Influence of ice degradation on planetary landscapes

Meven Philippe

COLLEGE DOCTORAL PAYS DE LA LOIRE
ED MATIERE, MOLECULES MATERIAUX ET GEOSCIENCES

Nantes Université

THESE DE DOCTORAT

NANTES UNIVERSITE

ECOLE DOCTORALE N° 596
Matière, Molécules, Matériaux et Géosciences
Spécialité : *Sciences de la Terre et des Planètes*

Par
Meven PHILIPPE

Influence of ice degradation on planetary landscapes

Thèse présentée et soutenue à Nantes, le 12/07/2023
Unité de recherche : Laboratoire de Planétologie et Géosciences

Rapporteurs avant soutenance :

Pascal Allemand — Professeur des Universités – Université Claude Bernard, Lyon
Reynald Delaloye — Professeur – Université de Fribourg (Suisse)

Composition du Jury :

Président : Nicolas Mangold — DR CNRS – Nantes Université
Examinateurs : Antoine Séjourné — Maître de Conférences – Université Paris-Saclay, Orsay

Dir. de thèse : Susan Conway — Chercheuse CNRS HDR – Nantes Université
Co-dir. de thèse : Marianne Font-Ertlen — Maître de Conférences HDR – UNICAEN, Caen

COLLEGE DOCTORAL PAYS DE LA LOIRE
ED MATIERE, MOLECULES MATERIAUX ET GEOSCIENCES

Nantes Université

Titre : Influence de la dégradation de la glace sur les paysages planétaires

Mots clés : permafrost, modélisation analogique, Mars, cartographie

Résumé : Cette thèse présente de nouvelles connaissances sur le lien entre glace du sol et géomorphologie, dans des contextes terrestres et martiens. J'étudie deux morphologies : les molards et les polygones de contraction thermique. Sur Terre, les molards sont des cônes de débris que l'on trouve dans les dépôts de glissements de terrain. Ils ont été récemment identifiés comme étant formés à partir de blocs de sédiments cimentés par la glace, transportés par un glissement de terrain, et s'étant dégradés dans ses dépôts. Ce sont potentiellement des marqueurs précis, à la fois temporels et spatiaux, de la dégradation du permafrost de montagne. Dans ma thèse, je propose donc d'étudier les molards de façon systématique grâce à une approche de modélisation analogique, dont les modèles sont reconstruits régulièrement grâce à un système de photogrammétrie automatisé que j'ai développé. Je présente également une étude qui suggère la présence de molards sur Mars dans les éjectas du cratère Hale, et qui les utilise pour obtenir des informations sur l'histoire géologique de ces éjectas. Dans cette thèse j'étudie également les polygones de contraction thermique, qui sont des réseaux de fractures résultant de la contraction thermique de la glace du sol. Sur Terre, la mise en place de glace d'eau ou de sédiments dans ces fractures peut former des polygones avec des morphologies différentes. Sur Mars, l'on observe des polygones ayant des dimensions et des morphologies similaires. Dans ma thèse, je présente donc une étude dans laquelle nous étudions les polygones de contraction thermique d'Utopia Planitia, et concluons à la présence d'eau liquide dans le proche passé de la planète. Je développe également une étude des polygones de contraction thermique en parallèle des unités géomorphologiques qui les portent, ce qui me permet d'obtenir des informations à la fois sur le timing de formation des polygones, et sur l'histoire géologique de ces unités.

Title : Influence of ice degradation on planetary landscapes

Keywords : permafrost, analogue modelling, Mars, mapping

Abstract : The present thesis aims at getting new understandings on how ground water ice and periglacial processes influence surface geomorphology on Earth and on Mars. I am hence investigating two periglacial landforms: molards and thermal-contraction polygons. On Earth, molards are cones of loose debris found in landslide deposits. It was recently attested that they are former ice-cemented blocks of sediment, that were transported by a landslide and progressively degraded within its deposits into conical shapes. They could represent accurate spatial and temporal markers of the degradation of mountain permafrost. Therefore, I provide here a systematic way to study molards, based on analogue modelling experiments monitored by an automated time-lapse photogrammetry system I developed. I also present a study on the firstly-identified potential martian molards, that provide insights into the geological setting of the ejecta from the Hale crater. Terrestrial thermal-contraction polygons are known to result from the thermal contraction of ground ice, which forms surficial networks of polygonal fractures. Water or lithic material can infill those fractures, and with repeated freeze-thaw cycles of water generate polygons with various morphologies. On Mars, polygons of similar dimensions and showing similar morphologies are observed. Therefore, I present here a study that investigates martian thermal-contraction polygons in Utopia Planitia, concluding on the geologically recent activity of liquid water in the area. I also present a study that investigates thermal-contraction polygons located on geomorphological units in Utopia Planitia, providing insights into both the timing of formation of thermal-contraction polygons and the geological history of the area.

Remerciements

C’est toujours compliqué de remercier les personnes qui nous ont entouré pendant une thèse. D’abord, car elles sont nombreuses. Dans mon cas précis, c’est également car j’avais oublié d’écrire ces lignes en avance – je le fais donc le jour même de la soumission du présent manuscrit. Quiconque me connaissant un peu ne sera pas surpris.

Je voudrais tout d’abord remercier Susan : ma patronne pendant 5 ans, modèle scientifique, maître à penser – mais cependant pas la dernière à participer aux activités extra-professionnelles (coucou le Little William). À ces multiples casquettes se rajoute celle de conseillère Pôle Emploi : tu as d’abord encadré mon stage de M1, puis tu m’as proposé un stage de M2, puis une thèse, et maintenant un postdoc. Tu as en quelque sorte façonné le scientifique que je suis aujourd’hui ; j’estime donc que toute erreur dans mes travaux passés, présents et futurs peut t’être directement imputée. J’espère que cela te convient. Plus sérieusement, on ne peut pas rêver meilleure directrice de thèse : toujours compréhensive, à l’écoute, scientifiquement quasi-omnisciente, et ayant une capacité à laisser de la liberté d’action à tes étudiants tout en les maintenant dans un cadre raisonnable. C’est tout cela (et bien plus encore) qui fait que travailler avec toi est un véritable plaisir. J’espère que la réciproque a été au moins un petit peu vraie – en omettant si tu le veux bien le lamentable épisode d’oubli de matériel de terrain…
Je me dois également de remercier Marianne, ma co-encadrante caennaise. Le covid a fait que nous ne nous sommes pas vus beaucoup, et je le déplore. Car pour le peu de temps que j’ai passé à Caen, j’ai pu me rendre compte qu’il est très agréable de travailler avec toi : bien que très occupée, tu trouves toujours le temps de venir voir comment se passent les expériences, de donner des pistes de réflexion, de relire les productions scientifiques… Et tu cuisines du Mont d’Or pour tes étudiants, ce qui en soit aurait été une raison suffisante pour vouloir travailler avec toi.
Bien entendu, je remercie également Olivier, mon encadrant officiel quasiment jusqu’à la fin du doctorat. Même en étant en-dehors du projet Permolards, tu as pris le temps de me prodiguer tes conseils avisés, et de m’accompagner scientifiquement et administrativement – surtout au début de la thèse.

Évidemment, mon ‘moi’ scientifique est également le produit de tous les collègues que j’ai pu rencontrer, de près ou de loin. Merci à Anthony, Axel, Anna, Calvin, Chimira, Jérémy, Lonneke, et aux nombreuses autres personnes qui sont provisoirement passées par les rituelles réunions d’équipe du jeudi, ces moments de rencontres scientifiques saupoudrés de fun. Merci à Calvin et Giulia pour le mirifique terrain en Islande – car les beaux paysages seuls ne suffisent pas à faire passer de bons moments. Merci à tous les collègues du projet Permolards, trop nombreux pour les citer tous, qui m’ont permis de replacer mon travail de thèse dans un cadre scientifique plus large. Cette vision d’ensemble a été particulièrement importante lors des moments où l’on a tellement la tête dans le guidon que l’on comprend à peine les tenants et aboutissants de notre travail. Merci à Richard et Lauren, collègues transatlantiques qui m’ont permis de me lancer sur un nouveau et passionnant sujet de recherche. Merci Costanza et François pour avoir accepté d’être membres de mon CSI. Ces rencontres annuelles ont été à chaque fois importantes pour mettre mes idées et études du moment à plat, en y apportant un regard extérieur et de nouvelles connaissances. Et pour finir, merci à Antoine, Nicolas, Pascal et Reynald d’avoir accepté de faire partie de mon jury de thèse. Les discussions que nous avons eues lors de la soutenance m’ont apporté de nouvelles pistes de réflexion, et vos remarques sur mon manuscrit l’ont sans aucun doute substantiellement amélioré.

De façon moins professionnelle, une thèse ne saurait bien se dérouler sans que l'on ne soit bien entouré. Et je pense pouvoir dire sans trop m'avancer que, bien entouré, je l'ai été pendant ces trois ans.
Tout d'abord, un remerciement mêlé d'excuses. Merci à mes collègues de bureau de m'avoir supporté pendant toutes ces années : Axel, Kelly, Pauline, et Benjamin (le petit dernier). Merci pour ces discussions, d'un intérêt parfois tout relatif, mais tellement importantes pour décrocher un peu du boulot. Et pas merci pour ces mêmes discussions, toujours d'un intérêt parfois tout relatif, qui m'ont empêché de travailler parfois pendant des heures. Plus sérieusement, avoir de tels collègues de bureau a été très appréciable, notamment dans les moments parfois difficiles que tout doctorant ne connait que trop bien. Je ne saurais remercier mes collègues de bureau sans mentionner Bill du Bigdil, qui a soutenu et surveillé ce bureau des années durant, tel un bienveillant chaperon.
Plus généralement, merci à tous mes collègues et amis, et anciens collègues (mais pas anciens amis) doctorants. Le mot 'collègue' est néanmoins un peu trop pompeux pour parler de l'ambiance incroyable qui règne au LPG. Peu nombreux sont les labos où tous les doctorants descendent en bande organisée pour des pauses café à rallonge, disent 'bonjour' aux marches d'escalier le matin, passent autant de soirées endiablées au bar, et partent en week-end au Parc Astérix – parfois au détriment de leurs horaires de travail. Heureusement qu'aucun de vos encadrants ne lira ça. Vous ne m'en voudrez pas de ne pas citer tous vos noms : vous vous reconnaîtrez, et si par un malheureux coup du sort l'un de vos encadrants lit ces lignes, vous pourrez toujours nier avoir participé aux activités listées plus haut – ne me remerciez pas. Et non, ce n'est pas une excuse de fainéant.
Je voudrais néanmoins faire une 'spéciale dédicace' à certaines personnes. Axel, ta propension à faire la fête et ta masse musculaire imposante ont fait de toi un des piliers de ma vie nantaise, après avoir été un des piliers de comptoir de ma vie brestoise. Tu le sais déjà, mais ton départ a été plus que regretté, surtout lorsque l'on a eu Benjamin à ta place. Arthur, merci pour beaucoup de choses, mais notamment les nombreuses soirées passées à geeker plus que de raison, et parfois dans des états plus que seconds. Dommage que tes nombreux faits d'arme soient entachés par ton agressivité après deux pintes, qui est d'ailleurs assez incompréhensible compte tenu de ta masse musculaire fort peu imposante. Anna et Victorine, merci pour m'avoir accompagné lors des derniers mois de rédaction en allant travailler dans divers cafés, tous ayant un niveau de bobo stratosphérique. Toute affirmation comme quoi j'en serais un moi-même ne serait que pure fantaisie. Victorine, merci également d'avoir été une coloc potable quand je n'avais plus de toit. Heureusement que le loyer était gratuit.
Je remercie également, bien entendu, le LPG et tous ses occupants. Vous contribuez grandement à maintenir la bonne ambiance au labo, notamment lors des désormais célèbres barbecue et raclette du labo (qui finissent régulièrement par des karaokés à des heures indues), mais également dans la vie de tous les jours. Je n'ai aucun exemple comparable de lieu de travail où les nouveaux arrivants se sentent aussi rapidement à la maison.

Merci à tous mes amis nantais, qui ont su égayer ma vie de façons diverses et variées (mais surtout en allant boire des coups, ne nous voilons pas la face). Merci aux plus beaux nantais pour toutes ces bamboches qui frisaient parfois la décadence. Merci Joubzy pour avoir été mon acolyte d'à peu près tout et n'importe quoi, depuis l'époque de nos jeunes années folles. Tu as fait passer le concept de 'bromance' de mythe à réalité. Merci Kémi pour avoir été un infatigable partenaire ces quatre dernières années. Je te pardonne les multiples tentatives d'homicide à mon encontre à base de restaurant avec buffet à volonté. Bien entendu, merci à Ludo et à toute l'équipe du Little William. Plus qu'un bar, plus qu'un QG, quasiment une deuxième maison… Néanmoins, ce manuscrit étant public, aucun chiffre ne sera dévoilé sur notre fréquentation de votre établissement. Disons simplement qu'Axel et moi en étions les principaux actionnaires. J'espère que votre chiffre d'affaires n'a pas trop chuté depuis notre départ.
Merci également à tous mes amis bretons : toute l'équipe du canton de Guingamp, les Oncles (et le Cousin Flo), la Mamènerie, et bien sûr toute la bande du collège (à jamais les neuf doigts de la main). Vous avez fait de mes rares vacances des vrais moments de décrochage du boulot. Les diverses soirées, festivals, Power Zénith ou autres virées pour le Nouvel An étaient toujours attendus avec impatience, et resteront parmi les souvenirs les plus mémorables de mes années de doctorat. Merci particulièrement à

ceux qui ont assisté à ma soutenance malgré leur QI limité. Mais ne changez rien et restez stupides : c'est comme ça qu'on vous aime.

Pour finir, merci évidemment à ma famille, qui m'a toujours soutenu en faisant des efforts, à des degrés variables, pour comprendre ce que je faisais. En a résulté une compréhension à des degrés variables également. C'était important pour moi de partager le moment de ma soutenance avec vous, et c'est principalement pour vous que je l'ai pensée. Heureusement que vous êtes venus, ça vous a permis de vous rendre compte qu'au final, j'avais un vrai travail.

En résumé, merci à tous ceux qui m'ont soutenu de près ou de loin dans le parcours parfois compliqué du doctorat. C'est en partie grâce à vous que j'ai pu, et que je peux encore, faire ce que j'aime : essayer de comprendre des trucs. Des fois ça ne marche pas et on ne comprend rien, des fois ça marche et on découvre encore plus de trucs auxquels on ne comprend rien. Mais après tout, est-ce que ce ne serait pas ça la beauté de la science ?

« Bizarre. Il est vrai que je ne suis jamais tombé sur un processus mathématique irréversible impliquant un canapé. Ça pourrait être un domaine nouveau. En avez-vous parlé à des spécialistes de la géométrie dans l'espace ? »

- Reg, dans 'Un cheval dans la salle de bain' de Douglas Adams

Résumé

Ce manuscrit de thèse a pour but général d'apporter de nouveaux éléments de compréhension sur la façon dont la glace du sol et les processus périglaciaires influent sur la géomorphologie de surface. Ce thème global y est exploré dans deux environnements planétaires différents, la Terre et Mars, et par le prisme de deux morphologies spécifiques : les molards (Section 2) et les polygones de contraction thermique (Section 3). La présente section va brièvement résumer ce manuscrit ; des simplifications seront donc faites, et la bibliographie y sera réduite.
La Section 1 introduit les concepts nécessaires à la compréhension des études suivantes, sur les molards (Section 2) et les polygones de contraction thermique (Section 3). La Section 4 résumera les conclusions de ce manuscrit.

1. Introduction

1.1. Milieu périglaciaire et pergélisol

Le concept d'« environnement périglaciaire » désigne des zones géographiques au climat froid, mais non glaciaire (Troll, 1944). Ces zones se trouvent en périphérie des environnements dits « glaciaires » : les calottes polaires (dans les latitudes élevées), et les glaciers (en haute altitude). Les environnements périglaciaires sont définis par leur climat, avec des variations de température qui permettent i. des cycles saisonniers de gel-dégel de l'eau en surface et en proche subsurface, et ii. la présence, en subsurface plus profonde, de sol gelé de façon pérenne (= dont la température reste ≤ 0°C toute l'année ; e.g. French, 2018 ; Permafrost Subcommittee, 1988 ; Tricart, 1968). Ce sol gelé de façon pérenne est appelé le « pergélisol ».
Le pergélisol est catégorisé en fonction de sa localisation géographique. Lorsqu'il est présent aux hautes latitudes, on parle de « pergélisol latitudinal » ; lorsqu'il est présent en haute altitude, on parle de « pergélisol de montagne ». On décrit également le pergélisol en termes de continuité : il est dit « continu » lorsqu'il constitue plus de 90% du sol d'une surface donnée ; « discontinu » lorsqu'il en constitue 50% à 90% ; « sporadique » lorsqu'il en constitue 10% à 50% ; et « isolé » lorsqu'il en constitue moins de 10% (Obu et al., 2019). De plus, le pergélisol peut être composé de différents types de glace du sol. Les deux principales catégories (simplifiées) de glace du sol sont les suivantes : i. la « glace interstitielle », qui se forme lorsque de l'eau gèle ou se condense *in situ* dans les pores d'un sédiment, augmentant par la même sa cohésion ; ii. la « glace en excès », dont le volume excède celui des pores du sédiment, et qui peut se former via différents processus impliquant la circulation d'eau liquide dans le sol (French, 2018). Stratigraphiquement, le pergélisol est compris entre la « couche active », qui gèle et dégèle saisonnièrement (Black, 1954), et le sol plus profond, non gelé, dont la température ne descend jamais sous 0°C (Figure 1). Lorsque la température augmente de façon pérenne au-dessus de 0°C, par exemple en conséquence du réchauffement climatique actuel (Christiansen et al., 2010), le pergélisol commence à fondre. Il s'amincit alors jusqu'à parfois disparaître complètement ; la couche active sus-jacente devient plus épaisse, et le sol non gelé sous-jacent commence moins profondément (Figure 1). On utilise le terme « thermokarst » pour désigner les morphologies et processus résultant d'une perte de volume due à la fonte de la glace en excès (Permafrost Subcommittee, 1988).
La formation et dégradation du pergélisol, ainsi que l'alternance de cycles gel-dégel, forment de nombreuses morphologies différentes dans les milieux périglaciaires. Le présent résumé ne détaillera pas toutes ces morphologies, mais se concentrera sur les deux qui font l'objet des études dans les sections suivantes : les molards (Section 1.2.) et les polygones de contraction thermique (Section 1.3.).

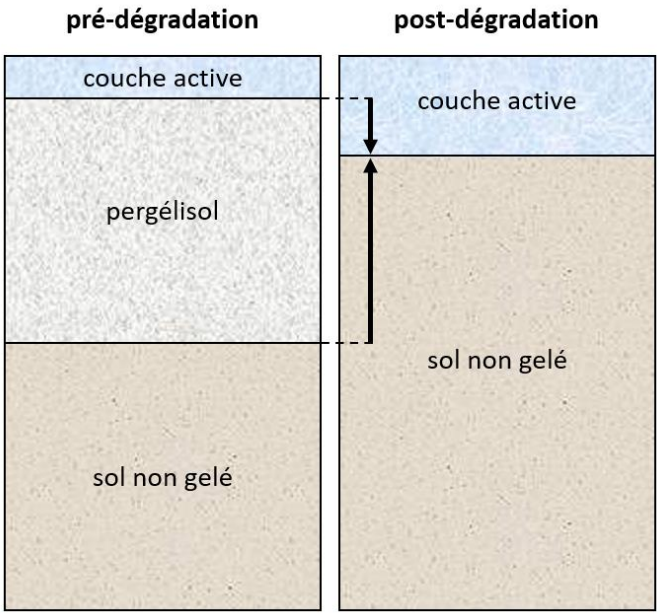

Figure 1 : schéma de l'organisation stratigraphique d'un sol en milieu périglaciaire, avant et après la fonte du permafrost qu'il contient.

1.2. Molards

La fonte du pergélisol de montagne, et donc la présence de pergélisol discontinu, peut notamment faire partie des facteurs déclenchants de glissements de terrain dans les milieux périglaciaires. Cela représente une menace pour les populations locales et infrastructures (Geertsema et al., 2009). Pour localiser les zones de pergélisol discontinu à l'échelle régionale, on utilise donc des modélisations numériques de température du sol, basées sur des mesures de température de l'air (Obu et al., 2019). Néanmoins, des facteurs locaux influant sur la présence de pergélisol rendent cette approche insuffisante à plus petite échelle. Pour pallier ce problème, une récente étude montre que les « molards » (des morphologies coniques constituées de débris que l'on observe dans les dépôts de glissements de terrain ; Figure 2b ; Brideau, 2009), représentent des marqueurs temporels et spatiaux de la dégradation du pergélisol de montagne (Morino et al., 2019b). Cette étude prouve que les molards se forment de la façon suivante : i. cimentation d'une pente de talus par la glace ; ii. fonte de ce pergélisol ; iii. déclenchement d'un glissement de terrain, mobilisant des blocs de débris encore gelés jusque dans ses dépôts (Figure 2a) ; iv. fonte progressive de la glace cimentant les blocs, rendant les débris non-cohésifs et formant petit à petit une forme conique (Figure 2b). La présence de molards dans des dépôts de glissement de terrain indique donc la présence d'un pergélisol en cours de dégradation, au niveau de la zone d'arrachement et au moment du glissement.

Cependant, étudier ces morphologies est compliqué. Elles ont été peu étudiées, donc peu sont identifiées. Elles ressemblent aux « hummocks », morphologies coniques observées dans les glissements de terrain mais n'étant pas liées à la dégradation du pergélisol. Une étude de terrain est donc nécessaire pour identifier les molards, or les glissements de terrain qui les forment surviennent parfois dans des endroits reculés et/ou difficiles d'accès. La Section 2.1. résume donc une étude permettant d'étudier les molards de façon plus systématique, par un dispositif expérimental utilisant des modèles analogues de molards. Cette étude fait partie du projet international ANR Permolards, dont le but est de produire la première base de données scientifique sur les molards. D'un point de vue plus large, les molards pourraient servir d'indicateurs de présence de glace du sol dans d'autres environnements planétaires que la Terre. La Section 2.2. résume donc une étude qui suggère la présence de molards sur Mars, dans les éjectas du cratère Hale.

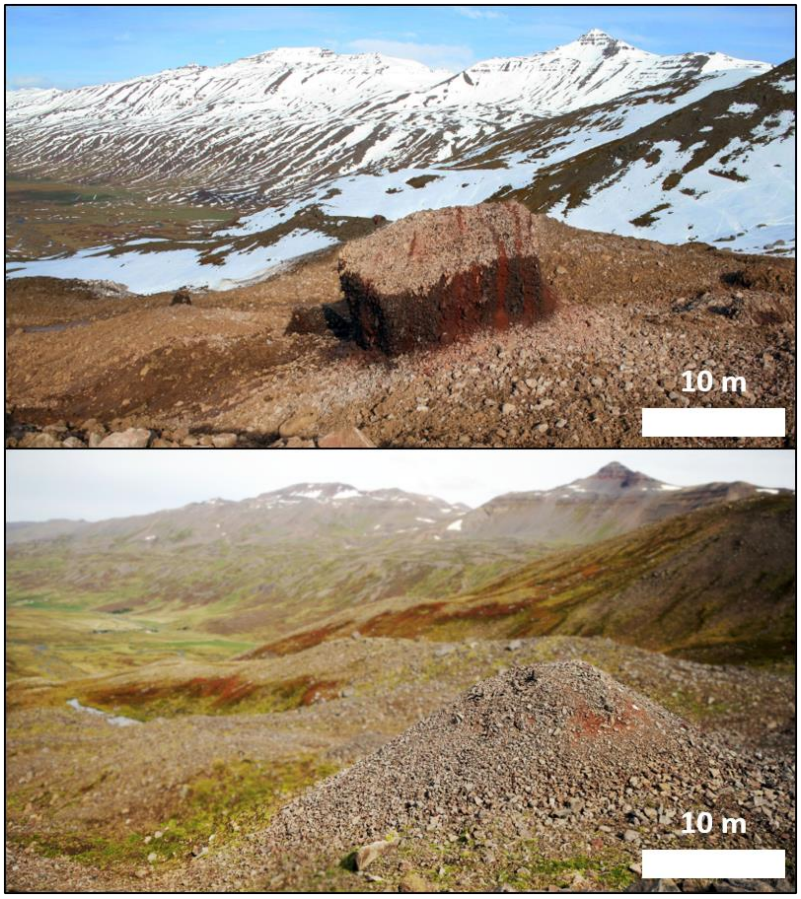

Figure 2 : dégradation d'un bloc de débris cimenté par la glace (Septembre 2012 ; Jón Kristinn Helgason), en un molard (Août 2022), en Islande.

1.3. Polygones de contraction thermique

Sur Terre, lorsqu'un sol cimenté par de la glace interstitielle subit une diminution importante de température sous 0°C, la glace du sol se contracte thermiquement (Butkovich, 1956). Cela peut causer la formation de fractures verticales dans le sol, qui peuvent se rejoindre et former un réseau de polygones en surface, appelés « polygones de contraction thermique » (5-25m de diamètres ; Figure 3a ; Mackay, 1974 ; Washburn, 1956). A ce stade, les polygones ne montrent pas de différences significatives d'élévation entre leur centre et leurs marges ; on les nommera par la suite « polygones à centre plat » (en anglais 'flat-centred polygons', FCPs ; Figure 3b ; Mackay, 2000). Dans un second temps, de l'eau liquide ou du sédiment peut se mettre en place dans les fractures et geler en hiver, formant des « coins de glace » (Black, 1976a) ou des « coins de sable » (Pewe, 1959). L'accumulation saisonnière de glace ou de sédiment cause ensuite la croissance de ces coins, donc l'élargissement progressif des fractures (Mackay, 1989). Cela a pour effet de surélever les marges des polygones par rapport à leur centre, formant des « polygones à centre bas » (en anglais 'low-centred polygons', LCPs ; Figure 3b ; Black, 1954). Il est ici important de noter que la croissance des coins de glace implique la présence saisonnière d'eau liquide, ce qui n'est pas le cas pour les coins de sable. Lorsque les coins se dégradent, par fonte (coins de glace) ou érosion mécanique (coins de sable), l'élévation des marges des polygones diminue sous celle de leur centre, formant des « polygones à centre haut » (en anglais 'high-centred polygons', HCPs ; Black, 1954 ; Ballantyne, 2018).

Ces processus de formation et d'évolution des polygones de contraction thermique sont également suggérés possibles sur Mars (Mellon, 1997). En effet, des polygones de dimensions et morphologies similaires y sont communs (Levy et al., 2009a), et de nombreuses études démontrent la présence de glace du sol, particulièrement dans les moyennes latitudes (Morgan et al., 2021). Cependant, il est encore incertain si ces polygones martiens possèdent des coins de glace ou de sable. Cette question est importante pour évaluer la possibilité que de l'eau liquide ait participé à la formation de ces polygones, malgré un climat récent suggéré hostile à la présence d'eau liquide en surface (Jakosky, 1985). La Section 3.1. résume donc une étude qui utilise la distribution latitudinale des différents types de polygones afin de conclure à la possible présence de coins de glace dans Utopia Planitia. De plus, bien que de nombreuses études suggèrent que ces polygones soient récents à l'échelle géologique (Mangold, 2005), la chronologie de leur formation et de leur évolution est encore mal contrainte. La Section 3.2. résume donc une étude qui apporte de nouveaux éléments de compréhension à cette question, en identifiant une unité géomorphologique sub-régionale qui comporte de nombreux polygones de contraction thermique. Cette étude montre également que les polygones peuvent être utilisés pour déterminer certaines propriétés géologiques de leur substrat.

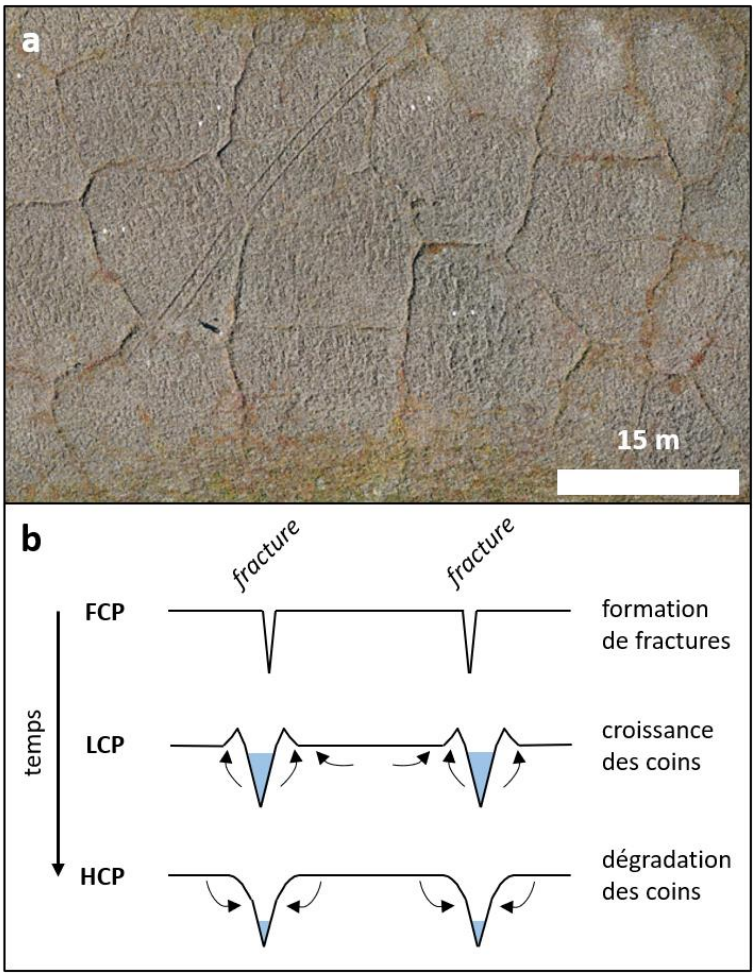

Figure 3 : ***a.*** *photo de polygones de contraction thermique en Islande ;*
b. *schéma d'évolution des polygones, de FCPs à LCPs à HCPs.*

2. Molards et dégradation du pergélisol

2.1. Modélisation analogique des molards

Les molards naturels étant difficiles à étudier de façon systématique (difficultés d'identification, zones difficiles d'accès), nous avons choisi de pallier ce problème par une approche de modélisation analogique. Nous reproduisons des molards en laboratoire de façon contrôlée, dans le dispositif expérimental du laboratoire M2C (Caen, France). Pour pouvoir prendre sur ces modèles des mesures nécessaires à une étude géomorphologique, nous avons mis en place un système photogrammétrique automatisé. La « photogrammétrie » est la méthode de vision par ordinateur permettant de reconstituer une scène en 3D à partir de photos (Bolles et al., 1987 ; Westoby et al., 2012). Dans notre cas, nous utilisons la photogrammétrie dite « Structure from Motion » (SfM), qui reconstruit une scène à partir d'une série de photos avec un fort recouvrement. A partir de ces modèles 3D, des Modèles Numériques de Terrain (MNT) peuvent être générés. Cette méthode, peu coûteuse et simple d'utilisation grâce aux récents développements de logiciels grand public, est très utilisée dans le cadre d'expériences de modélisation analogique à visée géomorphologique (e.g. Vérité et al., 2021).

Le but de notre dispositif expérimental est de reproduire la dégradation de blocs de sédiment gelés en molards. Le protocole est le suivant : i. remplissage d'un moule cubique de 30 cm d'arête par du sédiment de taille de grains connue ; ii. saturation des pores du sédiment par de l'eau ; iii. mise en gel du modèle dans une chambre froide à -20°C pendant 48h ; iv. démoulage du modèle sur une plateforme perforée ; v. suivi de la dégradation du modèle à température ambiante jusqu'à ce qu'aucun mouvement ne soit détectable (Figure 4).

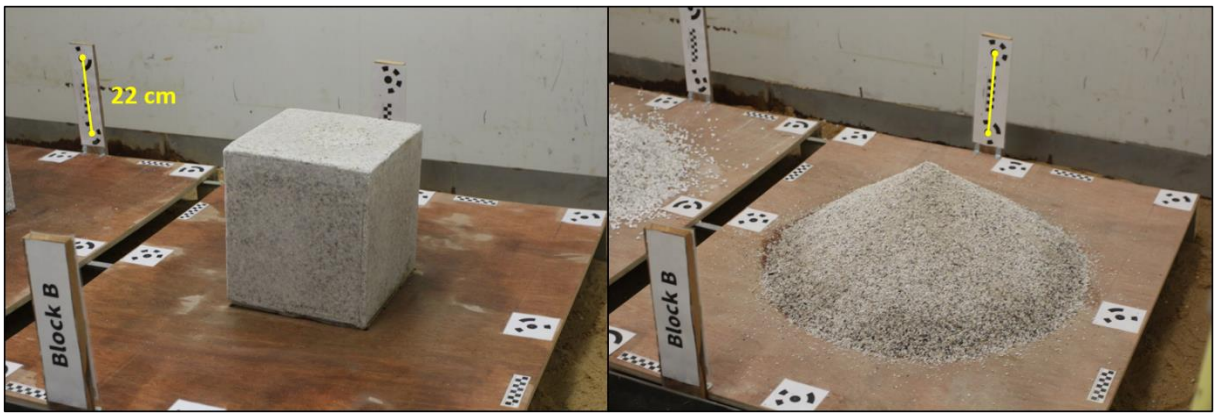

Figure 4 : photos d'un même modèle, avant et après une expérience.

Les modèles prenant plusieurs jours pour se dégrader, nous avons mis en place un système de photogrammétrie automatisé qui permet un suivi des modèles tout au long du processus. Ce dispositif est constitué de 18 micro-ordinateurs (Raspberry Pi 4, nommés par la suite « Pi ») connectés à des appareils photo haute résolution (12 megapixels). Les Pis sont disposés de façon radiale autour de deux modèles suivis simultanément (Figure 5). Chaque Pi est programmé pour prendre une photo à intervalle régulier (30 min). Un Pi principal (« Master Pi ») auquel sont connectés tous les Pis permet i. la synchronisation en temps des Pis ; ii. la collecte et le stockage des photos à chaque pas de temps ; iii. le lancement manuel d'une ligne de commande permettant l'arrêt du suivi à la fin de chaque expérience.
Les plateformes perforées sur lesquelles se dégradent les modèles possèdent des cibles (Figure 4). Ces cibles ont des coordonnées connues (X, Y et Z en mètres) dans un système de coordonnées propre à notre dispositif expérimental, ce qui permet de mettre à l'échelle les reconstructions 3D de nos modèles. Chaque set de 18 photos est ensuite traité de manière semi-automatique avec le logiciel Agisoft Metashape, permettant la création d'un MNT toutes les 30 min pour chaque expérience.

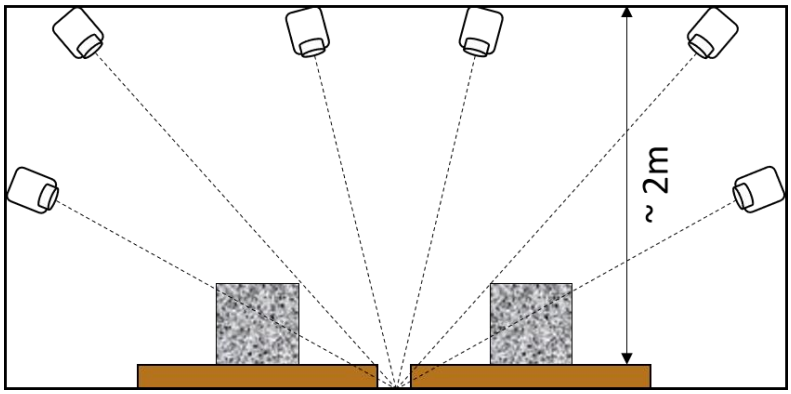

Figure 5 : schéma en coupe de la position des Pis par rapport aux modèles analogiques. Sur ce schéma, chaque représentation de Pi représente une ligne de 3 Pis.

Ces MNT réguliers nous permettent de suivre l'évolution de nos modèles de différentes façons :

- Profil topographique : nous utilisons un logiciel de SIG pour générer des profiles topographiques aux différents pas de temps. Cela permet une appréciation visuelle rapide de l'évolution morphologique des modèles.
- Profil radial : nous avons développé un script Python permettant, à partir du point sommital de notre modèle, d'en calculer un profil radial moyen (Figure 6). Ces profils permettent de calculer précisément la pente des flancs des modèles ($R^2 > 0.99$ pour la pente des flancs de la forme conique finale).
- Volume : avec un logiciel de SIG, nous calculons, à chaque pas de temps, le volume de nos modèles au-dessus de l'élévation Z = 0m (correspondant à l'élévation de la plateforme perforée). Nous avons calculé que l'erreur sur les volumes est < 1% du volume final.
- Détection de mouvements : avec un logiciel de SIG, nous avons généré des « MNT de Différence » (en anglais « DEM of Difference », DoD). Cette méthode consiste à soustraire un MNT à un pas de temps *t* d'un MNT à un pas de temps *t+1*. Cela permet de visualiser les zones où l'élévation a diminué et les zones où l'élévation a augmenté (Figure 7a). Appliqué à nos modèles, cela nous permet de visualiser quelles parties du modèle se sont dégradées, et où se sont déposés les sédiments ; des mouvements à l'échelle millimétrique peuvent ici être détectés (Figure 7b).

En conclusion, cette étude montre que le dispositif expérimental que nous avons développé est i. adapté à des études géomorphologiques à l'échelle de modèles analogiques ; ii. simple à mettre en place et à utiliser ; iii. novateur en cela qu'il permet un suivi régulier à un pas de temps adaptable, sur de longues durées, et dans des situations où une acquisition manuelle de photos est impossible (e.g. la nuit). Ce dispositif étant versatile (pas de temps modifiable, nombre de Pis adaptable, lentilles interchangeables), nous suggérons également qu'il pourrait être appliqué dans des contextes plus larges que le laboratoire (e.g. suivi de reliefs en extérieur, de structures d'ingénierie civile…).

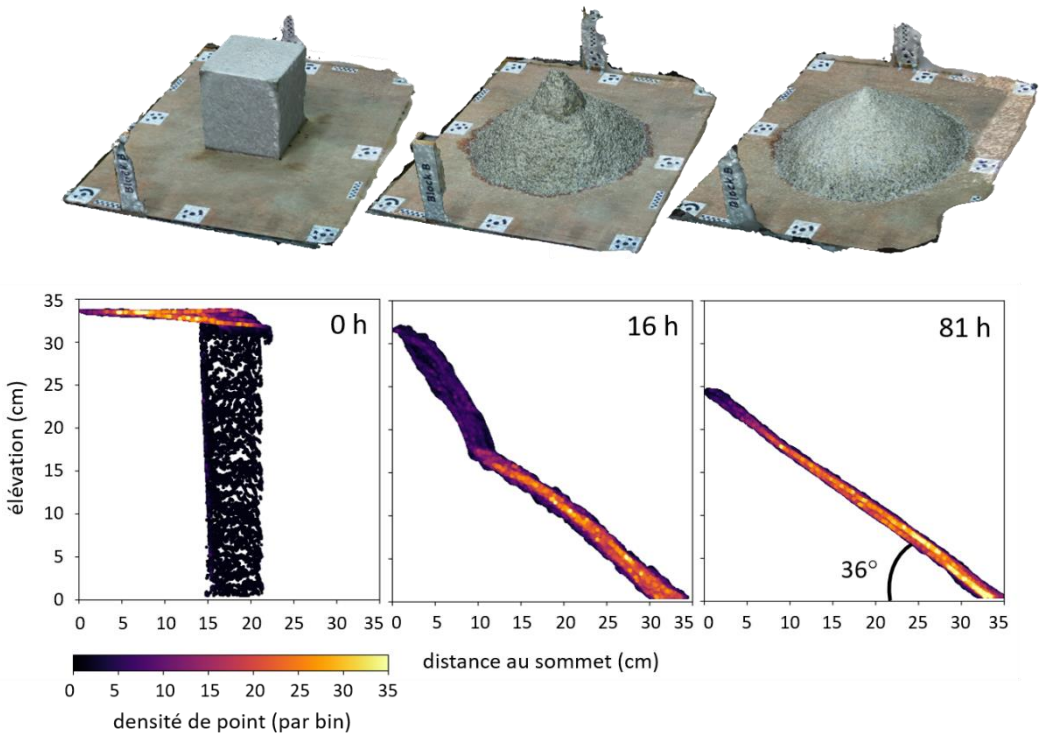

Figure 6 : modèles 3D et profils radiaux d'un modèle à trois pas de temps, avec sa forme initiale (0h), une forme intermédiaire (16h), et sa forme finale (81h). Les heures indiquent le temps écoulé depuis le début de l'expérience. Chaque pixel du MNT est placé sur le graphique en fonction de sa distance au sommet du modèle et de son élévation. Chaque graphique est quadrillé en 2000x2000 cases, chacune indiquée par un point dont la couleur représente la densité de point dans cette case.

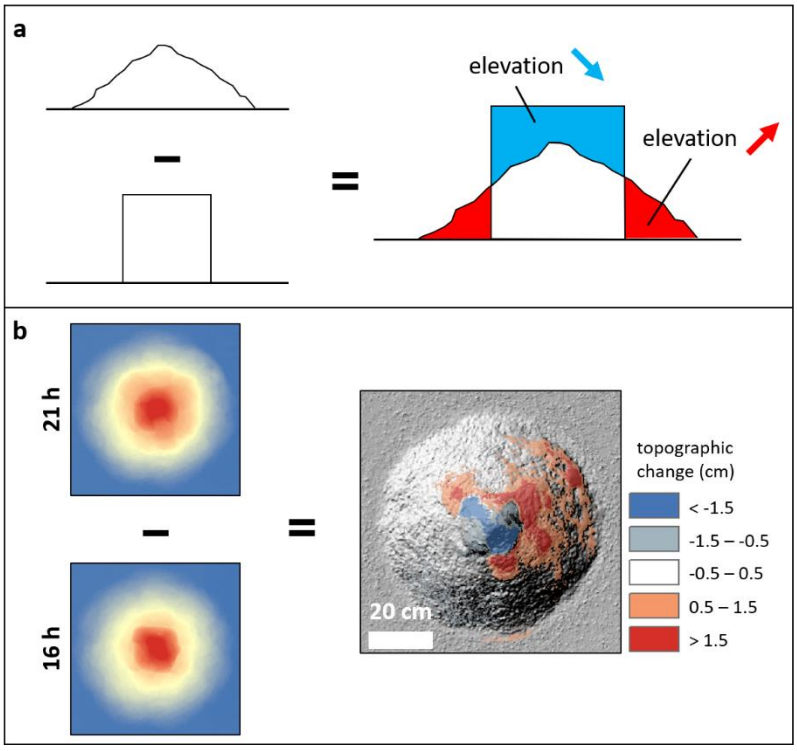

*Figure 7 : **a.** schéma explicatif de la création d'un MNT de Différence et **b.** exemple à partir d'un modèle expérimental.*

2.2. Molards martiens

Le sous-sol martien est connu pour contenir de grandes quantités de glace du sol (e.g. Morgan et al., 2021). De précédentes études ont souligné la présence de glace interstitielle et de glace en excès (Mellon et al., 2009 ; Smith et al., 2009). Faire la distinction entre ces deux catégories est une question importante dans un cadre martien : en effet, la glace interstitielle peut se mettre en place par condensation *in situ* de la vapeur d'eau de l'atmosphère dans les pores d'un sédiment superficiel (Dickson et al., 2015). En revanche, la formation de glace en excès implique la circulation d'eau liquide en subsurface (c.f. Section 1). Dans ce contexte, il a été suggéré que l'impacteur ayant formé le cratère Hale il y a ~ 1 milliard d'années (Jones et al., 2011) aurait mobilisé de la glace en subsurface, provoquant une fluidisation paetielle de ses éjectas et donc leur écoulement (Collins-May et al., 2020). Or, le type de glace (interstitielle/en excès) ainsi que son organisation dans le sol restent sujet à débat. Des morphologies coniques ont été observées dans ces éjectas ; le but de cette étude est donc d'évaluer si ces morphologies pourraient être des analogues martiens aux molards, et si oui quelles informations elles peuvent prodiguer sur l'état de la glace du sol au moment et au lieu de l'impact ayant formé le cratère Hale.

Pour répondre à ces questions, nous avons comparé :

- La distribution des morphologies coniques dans les éjectas avec la distribution de molards terrestres dans un glissement de terrain partiellement fluidisé (Mount Meager, Canada) ;
- La forme (hauteur, aire au sol, pente des flancs) des morphologies coniques (n = 2181) avec la forme de molards terrestres (n = 571) observés dans une avalanche de rochers (Niiortuut et Paatuut, Groënland).

Dans le glissement de terrain de Mount Meager, les molards sont retrouvés dans une phase du glissement suggérée visqueuse, donc ayant été fluidisée (Figure 8). Dans le cas de Hale, les morphologies coniques sont également retrouvées dans une phase des éjectas qui aurait été fluidisée (Figure 8 ; Collins-May et al., 2020).
Les morphologies coniques de Hale montrent des formes circulaires à sub-circulaires (vue planaire) et coniques (vue en coupe), comme les molards de Niiortuut et Paatuut (Figure 9). Les pentes de leurs flancs sont également du même ordre de grandeur (10° à 25°). En revanche, les morphologies coniques martiennes sont 1-2 ordres de grandeur plus hauts et plus larges que les molards groenlandais ; cela peut s'expliquer par une épaisseur plus importante de matériel gelé initialement mobilisé (Morino et al., 2019b).

Cette étude permet de tirer les conclusions suivantes :

- Les morphologies coniques martiennes étant similaires aux molards terrestres en termes de distribution et de forme, nous suggérons qu'elles sont les premiers molards martiens observés ;
- La présence de molards indique que la glace mobilisée lors de l'impact de Hale était présente, au moins en partie, sous forme de glace interstitielle ;
- Ces molards martiens faisant jusqu'à 55m de haut, il est probable que la couche de sol cimenté par la glace qui a été mobilisée faisait au moins ~ 60m d'épaisseur ;
- Les molards indiquent également que cette glace n'a pas fondu en totalité lors de l'impact – ce qui n'était jusqu'à présent pas pris en compte lors des calculs de quantité d'eau liquide formée lors des impacts mobilisant la cryosphère martienne.

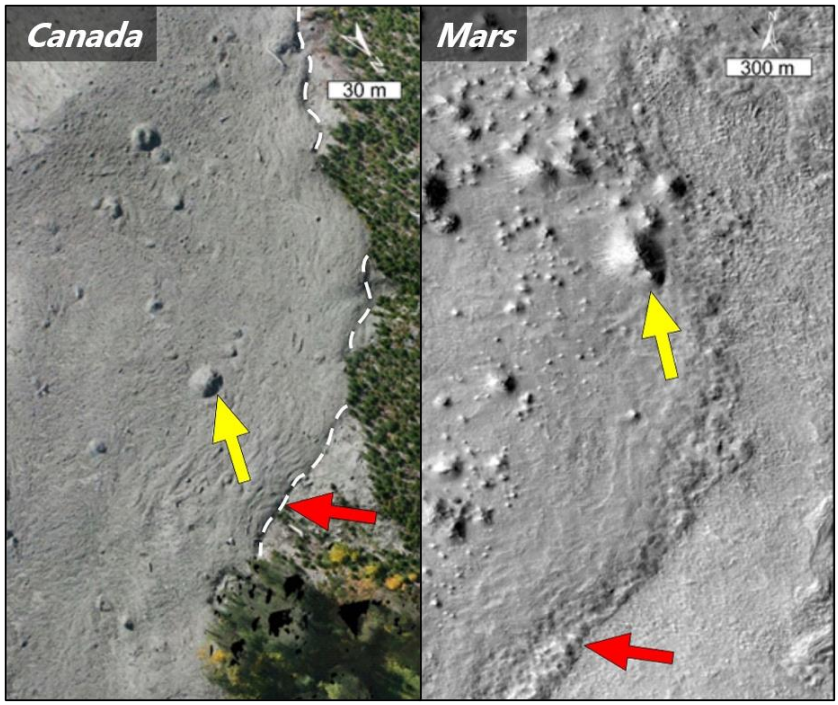

Figure 8 : des molards et morphologies coniques (flèches jaunes), proches de la bordure des phases visqueuses du glissement de terrain de Mount Meager et des éjectas du cratère Hale.

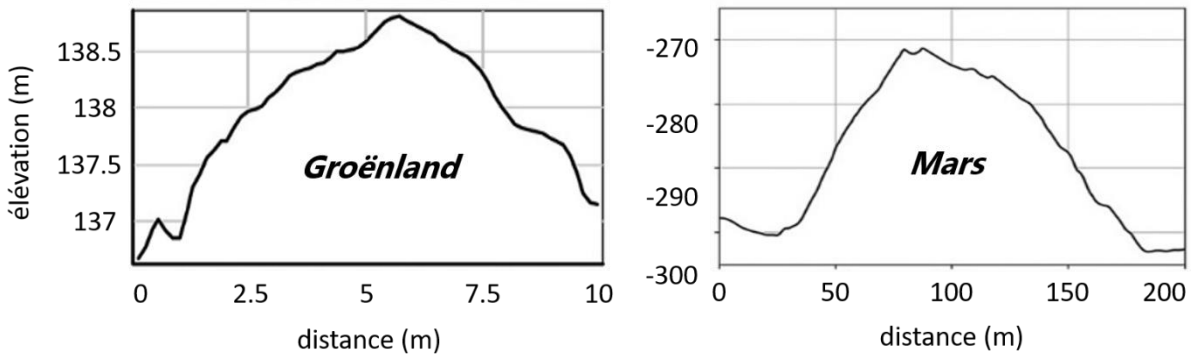

Figure 9 : profils topographiques d'un molard groenlandais et d'une morphologie conique martienne.

3. Polygones de contraction thermique et propriétés du sol

3.1. Polygones à coins de glace dans Utopia Planitia

Mars, comme la Terre, possède des polygones de contraction thermique. Ces polygones ont des dimensions et des morphologies (FCPs, LCPs, HCPs) similaires aux polygones de contraction thermique terrestres (Levy et al., 2009), mais le matériel constituant leurs coins (glace ou sédiment) est encore inconnu. Pour répondre à cette question, nous nous basons sur deux hypothèses de travail : i. la stabilité de la glace, et donc d'éventuels coins de glace, augmente avec la latitude ; et ii. la dégradation des coins de sable requiert une érosion mécanique, contrairement aux coins de glace (French, 2018). Cela signifie que, pour une population de polygones à coins de glace, une proportion plus importante de polygones ayant des coins (LCPs) est attendue aux latitudes plus élevées ; en revanche, cette tendance n'est pas attendue dans le cas de polygones à coins de sable.

Notre zone d'étude est située dans Utopia Planitia (40-50°N, 110°-125°E), une zone réputée pour être riche en polygones. Les polygones étant trop petits (5-25m de diamètre) et trop nombreux pour être cartographiés sur une telle étendue, nous utilisons une méthode dite « grid-based » (Ramsdale et al., 2017). Cette méthode consiste à quadriller une zone d'étude en cases de dimensions fixes, puis à cartographier la présence ou l'absence des différents types de polygones dans chaque case (Figure 10). Nous avons réalisé cette cartographie sur 108 images haute-résolution (HiRISE). Cela nous a permis de calculer, pour chaque intervalle d'un degré de latitude, le rapport *LCP/HCP* = [nombre de cases contenant des LCPs] / [nombre de cases contenant des HCPs]. Ce rapport indique donc, pour un intervalle de latitude donné et de façon semi-quantitative, la proportion de polygones dont les coins ont été préservés. Notons que les polygones de notre zone d'étude montrent une distribution particulière par rapport aux cratères, dans lesquels ils sont significativement plus nombreux – et en particulier les LCPs. Nous avons donc calculé le rapport *LCP/HCP* en excluant les cases comprises dans les cratères.

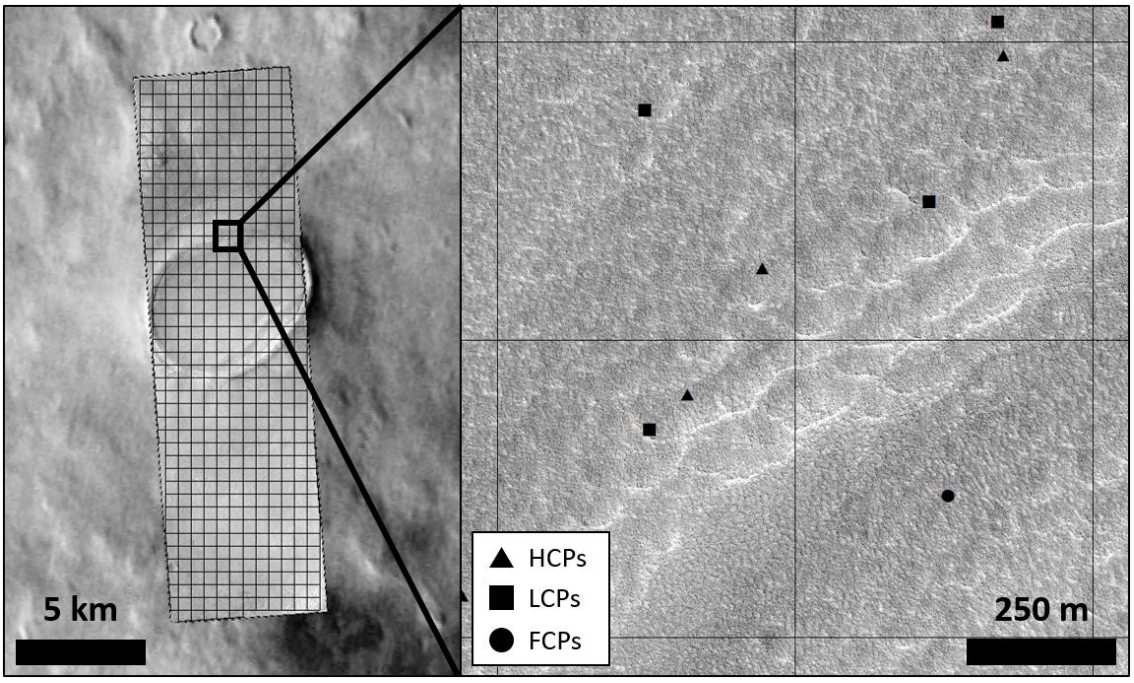

Figure 10 : illustration de la cartographie « grid-based », appliquée à nos polygones de différentes morphologies (FCPs, LCPs, HCPs).

En utilisant uniquement les polygones situés en-dehors des cratères, nous pouvons observer une tendance latitudinale à l'augmentation pour le rapport *LCP/HCP*, qui est statistiquement significative ($R^2 \approx 0.88$; *p-value* $\approx 6.65 \times 10^{-5}$; Figure 11). A l'inverse, lorsque les polygones intra-cratères sont inclus, aucune tendance ne peut être observée.

D'après nos hypothèses de travail, une telle distribution différentielle latitudinale est attendue uniquement dans le cas où les polygones étudiés sont des polygones à coins de glace, et non à coins de sable. Nous en concluons donc que les polygones de contraction thermique observés dans Utopia Planitia sont effectivement des polygones à coins de glace. Ces polygones sont récents à l'échelle géologique (quelques millions d'années ; Mangold, 2005 ; Séjourné et al., 2019), et leurs homologues terrestres se forment par la répétition de cycles gel-dégel de l'eau. Nous suggérons donc que, malgré un climat récent plutôt hostile à la présence d'eau liquide en surface (Jakosky, 1985), des cycles gel-dégel de l'eau auraient pu avoir lieu à la surface de Mars dans des temps géologiques récents – au moins dans Utopia Planitia.

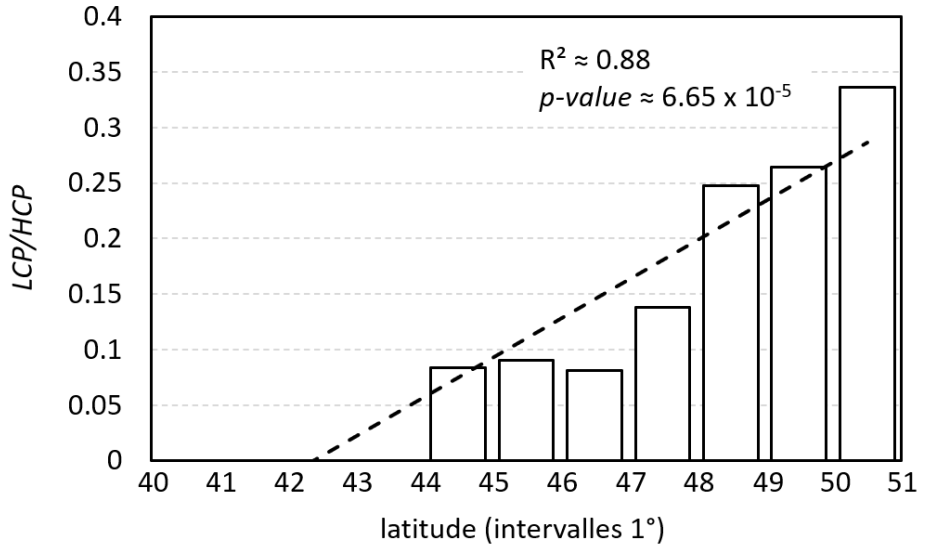

Figure 11 : rapport LCP/HCP pour chaque intervalle d'un degré de latitude sur l'ensemble de notre zone d'étude. La droite de régression linéaire y est tracée, ainsi que les R^2 et p-value correspondants.

3.2. Polygones de contraction thermique et propriétés du sol

Dans cette étude, nous investiguons i. la possibilité d'obtenir des informations sur les propriétés géologiques d'un substrat à partir des caractéristiques des polygones à coins de glace qu'il porte ; et ii. les informations que peuvent nous donner ce substrat sur la chronologie de formation et d'évolution de ces polygones. Pour cela, nous nous intéressons à deux zones d'étude : l'est d'Utopia Planitia (zone d'étude recoupant celle de la Section 3.1.), et la zone d'Erebus Montes dans Arcadia Planitia. Cependant, pour des raisons de simplicité et de synthèse, ne sera résumée ici que les travaux réalisés dans Utopia Planitia – qui représentent les réflexions et résultats principaux de l'étude.
Notre zone d'étude se situe au nord-ouest d'Elysium Mons, structure volcanique de laquelle proviennent de nombreux chenaux et systèmes de vallées. De précédentes études ont suggéré une géologie complexe pour notre zone d'étude : mise en place d'unité volcaniques (Russell et Head, 2007), dépôts de sédiments issus d'écoulements aqueux régionaux (Costard et Kargel, 1995), et plus récemment le dépôt d'unités régionales riches en glace, par condensation de vapeur d'eau de l'atmosphère (Mellon et Jakosky, 1995). De nombreux polygones sont observés dans cette zone, mais sont distribués de façon différentielle selon les unités ; ce contexte est donc idéal pour tester notre hypothèse selon laquelle les caractéristiques des polygones pourraient donner des informations sur les propriétés géologiques de leur substrat.

Nous avons donc cartographié, notamment, deux unités géomorphologiques dans la zone d'étude : une « unité sinueuse », qui est riche en polygones, et une « unité à rochers » (Figure 12), qui ne possède quasiment aucun polygone, mais est recouverte de rochers décamétriques. Nous avons investigué l'élévation relative de ces deux unités à partir de cette cartographie et de profils topographiques (Figure 13). Nous avons également cartographié les polygones de notre zone d'étude sur 104 images haute-résolution (dont 55 provenant de l'étude précédente), avec la même méthodologie que celle utilisée dans la Section 3.1. : une cartographie « grid-based » des différents types de polygones (FCPs, LCPs, HCPs). Pour chaque unité, la cartographie de ces polygones nous a permis de calculer trois paramètres, que nous suggérons étant des indicateurs de différentes propriétés du substrat :

- ρ_{pol} : le taux de polygonisation de l'unité, qui reflète sa cimentation par la glace ;
- ρ_{wf} : le taux de formation de coins, qui reflète la formation de glace en excès dans ce substrat ;
- ρ_{wp} : le taux de préservation des coins, qui reflète la capacité du substrat à préserver la glace.

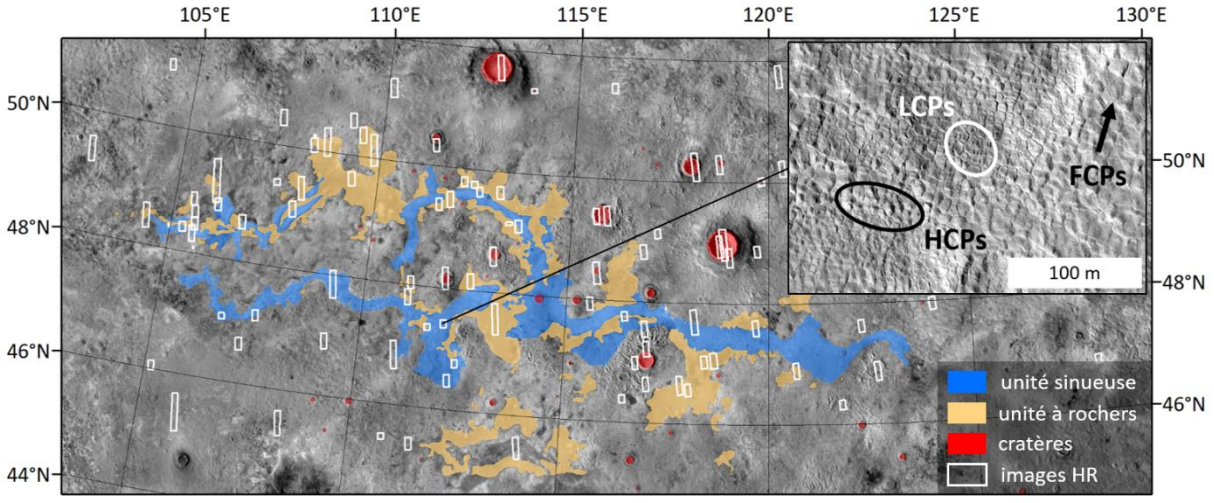

Figure 12 : la zone d'étude dans Utopia Planitia, montrant notamment l'étendue de l'unité sinueuse et de l'unité à rochers. Le zoom montre des polygones (FCPs, LCPs, HCPs) situés sur l'unité sinueuse.

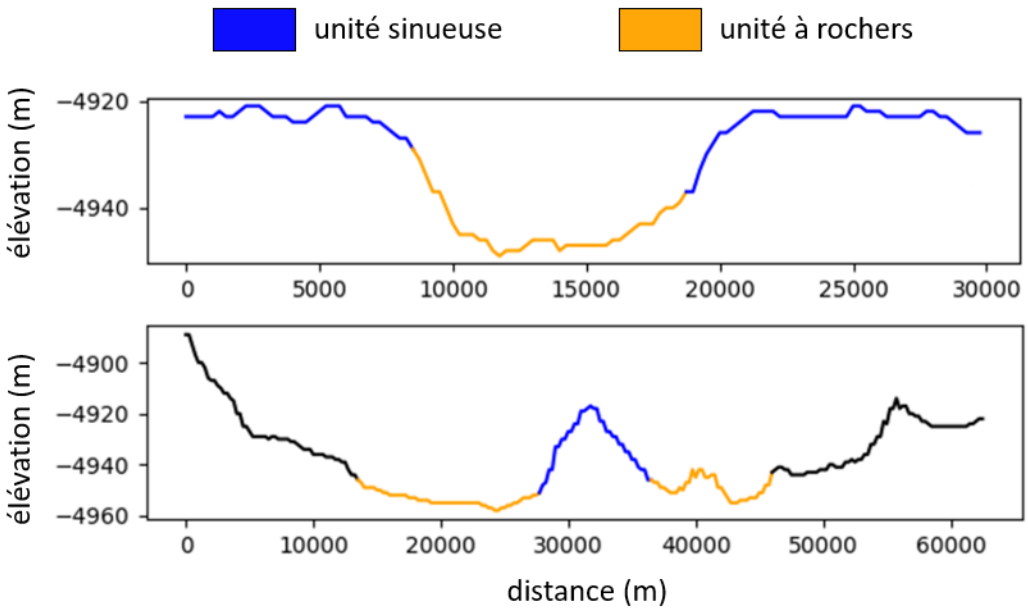

Figure 13 : profiles topographiques recoupant des contacts entre l'unité sinueuse (bleu) et l'unité à rochers (orange).

La combinaison de ces méthodes nous permet de faire des hypothèses quant à l'origine et la chronologie de mise en place de ces deux unités :

- L'unité à rochers ne montre quasiment aucun polygone, ce qui indique un matériel initial massif, qui a empêché la contraction thermique et donc la formation de polygones. Elle s'est mise en place avant l'unité sinueuse, probablement lors d'une importante activité volcanique autour de l'Amazonien précoce (Russell et Head, 2003).
- L'unité sinueuse est riche en glace, ce qui indique un matériel initialement poreux et susceptible à la contraction thermique. Elle aurait pu se mettre en place soit i. par condensation de vapeur d'eau dans un sédiment poreux, initialement en place ; soit ii. par solidification d'un large dépôt sédimentaire riche en eau. Elle s'est probablement mise en place autour de l'Amazonien moyen (hypothèse du dépôt aqueux ; Costard et Kargel, 1995), voire plus tardivement (hypothèse de la condensation de vapeur d'eau ; Morgenstern et al., 2007).

De plus, il était jusqu'à présent suggéré que les polygones s'étaient formés récemment (quelques derniers millions d'années ; Mangold, 2005 ; Séjourné et al., 2019). Or, la présence de polygones sur l'unité sinueuse montre que leur activité a pu avoir eu lieu depuis l'Amazonien moyen jusqu'au présent, sur une période de temps bien plus longue donc.

Cette étude nous permet de donner les conclusions suivantes :

- En calculant certains paramètres à partir des caractéristiques des polygones, il est possible d'obtenir des informations sur les propriétés géologiques de leur substrat ;
- Appliqués à Utopia Planitia, ces paramètres combinés à d'autres données ont permis de donner des hypothèses de formation de deux unités géomorphologiques, ainsi que leur chronologie de mise en place ;
- En retour, l'âge probable de mise en place de l'unité sinueuse nous a permis d'obtenir des informations sur la chronologie de formation et d'évolution des polygones, qui pourrait être plus ancienne (de l'Amazonien moyen jusqu'au présent) que ce qui était suggéré dans la littérature ;
- De façon générale, cette étude démontre l'importance de l'étude des polygones pour des questions d'habitabilité de la planète.

4. Conclusions

Les études présentées dans ce manuscrit et résumée ici ont permis, en s'intéressant aux morphologies spécifiques que sont les molards et les polygones de contraction thermique, d'améliorer notre compréhension de l'influence qu'a la glace du sol sur les paysages planétaires.

Les molards, marqueurs de la dégradation du pergélisol difficiles à étudier naturellement, ont pu être étudiés en laboratoire de manière contrôlée grâce à un protocole novateur, combinant modèles analogiques et photogrammétrie semi-automatisée. Cette étude en particulier ouvre la porte vers d'autre études qui permettront une meilleure compréhension de ces morphologies, et donc ultimement à une meilleure compréhension de la dégradation du pergélisol à l'échelle locale. De plus, de potentiels molards martiens ont permis de révéler d'importantes caractéristiques sur l'état de la glace du sol au moment et à l'endroit de l'impact ayant créé le cratère Hale. Cette étude a également permis une meilleure compréhension de la mécanique des éjectas impactant des surfaces en partie gelées.

Jusqu'à présent, il était incertain si les polygones de contractions thermique martiens se formaient par l'action de l'eau liquide ou non. Les études résumées ici ont permis de conclure à une potentielle activité d'eau liquide en surface de la planète, à une période où l'on pense le climat plutôt hostile à la présence d'eau liquide. De plus, cette activité aurait potentiellement pu s'étaler sur des périodes de temps à l'échelle du dernier milliard d'années, quand l'échelle précédemment suggérée était des quelques dernières dizaines de millions d'années au plus. Ces conclusions impactent de façon importante le potentiel d'habitabilité de la planète. De plus, ces études montrent que les polygones peuvent être utilisés pour révéler des informations sur l'histoire géologique des terrains qu'ils recouvrent ; et en retour, lier l'histoire ces terrains aux polygones qui les recouvrent permet d'obtenir des contraintes sur la chronologie de l'activité des polygones.

Table of contents

I. Introduction: permafrost and ground ice

1. Ground ice on Earth

In this section, I first explain the concept of periglacial environment (Section 1.1.). I then detail further the concepts of permafrost and ground ice (Section 1.2.), and the landforms typically associated with terrestrial permafrost (Section 1.3.). These first sections gather the general knowledge necessary to understand the further considerations of the present thesis. I finish this section by explaining what molards are, how they form, and what are the remaining scientific interrogations about them – highlighting the ones that will be addressed in the present thesis (Section 1.4.).

1.1. The periglacial environment

The term 'periglacial' and the concept of 'periglacial environment' were first introduced by von Lozinski (1909, 1912). He used them to describe the zone found on the periphery of ice sheets and glaciers, where cold but non-glacial processes occur – in opposition to glacial areas, where cold and glacial processes dominate. At the time, he already identified two main types of periglacial environments (von Lozinski, 1912): latitude-related ones, where periglacial environments occur at lower latitudes than glacial environments; and altitude-related ones, where periglacial environments occur on mountains, at lower altitudes than glacial environments. In both cases, periglacial environments were located between the tree line as a lower boundary (the limit at which tree growth is not possible anymore) and the snow line as a higher boundary (the limit between snow-covered and snow-free areas; Figure 1.1). This delimitation is however judged too simplistic. Nowadays, the current extent of periglacial environments is directly related to the occurrence of cold, but non-glacial climates (Troll, 1944), where temperature variations allow i. the occurrence of freeze-thaw cycles of water at the surface and subsurface of the ground, and ii. the presence of permafrost (i.e. frozen ground) in the subsurface (Abrahams and Dixon, 1992; French, 1979, 1987, 2000, 2018; French and Thorn, 2006; Permafrost Subcommittee, 1988; Slaymaker, 2009; Tricart, 1968). The freeze-thaw cycles of water typically occur on a seasonal and/or diurnal basis, depending on the season and on the depth considered (e.g. Cook, 1960; Fraser, 1959; French, 1987, 2018; Williams, 1964).

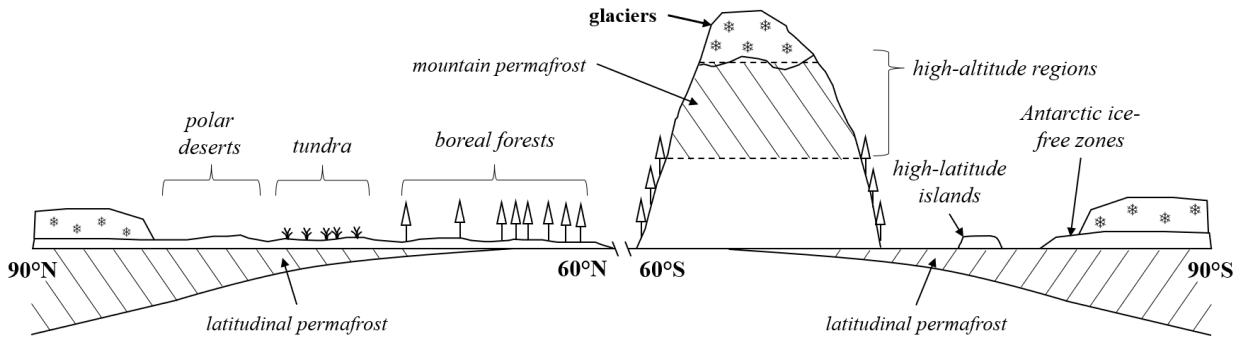

Figure 1.1: simplified diagram of the distribution of periglacial environments with respect to latitude and altitude on Earth. The various possible periglacial environments and the two types of permafrost (hatched areas) are named in italic.

The permafrost is a ground whose temperature remains below 0 °C for at least two consecutive years (Black, 1954; Dobinski, 2011; French, 2018; Muller, 1945; Permafrost Subcommittee, 1988; Section 1.2.). Geographically, periglacial environments are found in polar deserts and tundra of the northern high latitudes; in snow- and ice-free zones of Antarctic; in the low- and mid-latitude but high-altitude regions, below the snow line (e.g. Alps, Andes, Tibet plateau); on high-latitude oceanic islands; and in the northern parts of North America and Eurasia boreal forests (e.g. French, 2018; Figure 1.1).
The repetition of freeze-thaw cycles and the presence of permafrost are the causes of many geomorphological processes: freeze-thaw-related weathering (e.g. Hall et al., 2002; Matsuoka and Murton, 2008; Murton et al., 2006; von Lozinski, 1909; Walder and Hallet, 1985, 1986; White, 1976), aeolian abrasion or deflation (e.g. Koster, 1988; Matsuoka et al., 1996; McKenna Neuman, 1993; Powers, 1936; Seppälä, 2004; Whitney and Dietrich, 1973; Wright, 1946), processes related to bodies of liquid water (e.g. formation of sea ice; Koch, 1926; Meier et al., 2011; Tarr, 1897; Thomas, 2017; Walker, 1859), slow (e.g. Benedict, 1976; Harris, 1996; Harris et al., 2003; Matsuoka, 2001) or rapid mass-wasting processes (e.g. Dorren, 2003; Gruber and Haeberli, 2007; Haeberli et al., 2017; Krautblatter et al., 2013; Morino et al., 2019a, 2021; Rabatel et al., 2008; Sæmundsson et al., 2018), or processes linked with ground ice aggradation or degradation (Section 1.3.). However, extensively detailing all of these periglacial processes is out of the scope of the present thesis: I will focus exclusively on periglacial processes and subsequent landforms that are directly related to ground ice formation and degradation.

1.2. Permafrost and ground ice

As mentioned in Section 1.1., the term ‘permafrost’ refers to a ground whose temperature remains below 0 °C for at least two consecutive years, hence also during summer (Black, 1954; Dobinski, 2011; French, 2018; Permafrost Subcommittee, 1988; Washburn, 1980). Therefore, the recognition criterion for permafrost is solely based on thermal considerations (Figure 1.2; Dobinski, 2011; French, 2018; Permafrost Subcommittee, 1988). The term ‘cryotic’ is recommended by the Permafrost Subcommittee (1988) to define such thermal state. It is important to highlight that the cryotic state is different from the frozen state: permafrost can be cryotic (i.e. below 0 °C) but unfrozen. However, in the literature the term ‘cryotic’ was sometimes used to define specific and rare conditions, where ground temperature is below 0°C, liquid water is present, but the ground remains unfrozen because of high salt or clay content, or under high pressures (e.g. Dobinski, 2011; Dobinski et al., 2022). Therefore, to avoid any ambiguity and as only icy permafrost will be considered thereafter, the term ‘permafrost’ will be equivalent to ‘frozen ground’ in the present thesis.

On top of the permafrost, the surficial layer that undergoes seasonal freeze-thaw cycles of water is called the ‘active layer’ (Black, 1954, 1976a; Dobiński, 2011, 2020; French, 2018; Hinzman et al., 1991; Kane et al., 1991; Mackay, 1981; Figure 1.2). Its thickness depends on the air temperature and on the thermal conductivity of the ground, but also on slope orientation, vegetation, and/or snow cover – among others (e.g. Dobiński, 2020; French, 2018). During winter, the active layer can be totally frozen – and hence has properties similar to the underlying permafrost. With the presence of water in winter, freezing and ice segregation can occur within the active layer. During summer, temperatures rising above 0°C cause the active layer to thaw. However, because the energy received by the ground is partially or entirely used by the phase change to liquid water, the temperature of the thawed active layer can remain at ~ 0°C for a long period of time (‘zero-curtain effect’; Brewer, 1958; Muller, 1945; Nakano and Brown, 1972; Nelson et al., 1985; Outcalt et al., 1990). The seasonal repetition of freeze-thaw cycles of water causes various geomorphological processes within the active layer (e.g. frost heaving, formation of patterned ground, needle ice growth; Dobiński, 2020; Lawler, 1988; Rempel, 2010).

Then, some studies showed the existence of a layer that alternates between the perennially frozen and seasonally frozen states, on decadal to centennial cycles of temperature variations – the 'transient layer', or 'transition zone' (Figure 1.2; e.g. Dobiński, 2020; French, 2018; Shur et al., 2005). On shorter time scales (e.g. seasonal), this transient layer can hence be seen as part of the active layer or of the permafrost. The decadal or centennial freeze-thaw cycles of water can form perennial ice bodies within that transient layer (Dobiński, 2020; French, 2018; Shur et al., 2005).

Finally, frozen ground (permafrost, transient layer or frozen active layer) can be constituted of various types of ground ice (Figure 1.3; e.g. French, 2018):

1. 'pore ice', or 'interstitial ice', is ice that is emplaced within the pore of the sediment by *in-situ* freezing, and usually holds the sediment together (Figure 1.3a);
2. 'segregated ice' forms when pore water moves toward the freezing front by cryosuction, to form excess ice – and sometimes bodies of massive ice (Figure 1.3b). With respect to *in-situ* freezing, ice segregation happens preferentially in fine-grained, poorly-drained ground, that are then said to be 'frost-susceptible' (Hoekstra, 1969; Konrad, 1999; Sheng et al., 2013; Taber, 1929, 1930);
3. 'intrusive ice' forms when pressurised water intrudes a material and freezes in place (Figure 1.3c). Ice intrusion forms massive bodies of ice within the ground;
4. 'vein ice' forms when water fills pre-existing fractures and freezes in place (Figure 1.3d).

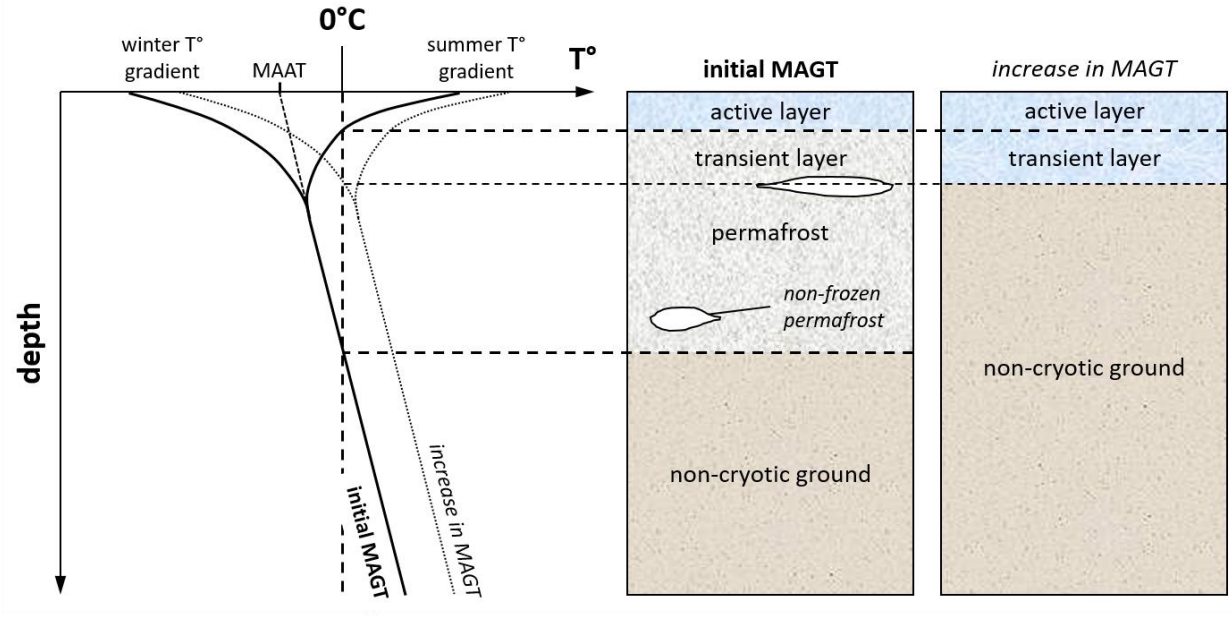

Figure 1.2: typical winter and summer Mean Annual Ground Temperature (MAGT) gradients in permafrost, with respect to depth. The theoretical Mean Annual Air Temperature (MAAT) is also indicated. The thick lines represent the thermal gradient of an initial MAGT, which remains perennially below 0°C at a certain depth range. The dotted lines represent the thermal gradient of an increased MAGT, which does not perennially remain below 0°C. The boxes represent the thermal states of the ground, in the case where the thermal gradient allows the presence of permafrost (initial MAGT; left box), and in the case where the thermal gradient does not allow the presence of permafrost (increased MAGT; right box). The surficial layer, whose temperature goes below and above 0°C seasonally, is the active layer. The layer whose temperature goes below and above 0°C on decadal to centennial time scales is the transition zone. The layer whose temperature perennially remains below 0°C is the permafrost. The deepest layer, whose temperature never goes below 0°C, is non-frozen. Modified from a figure in French (2018).

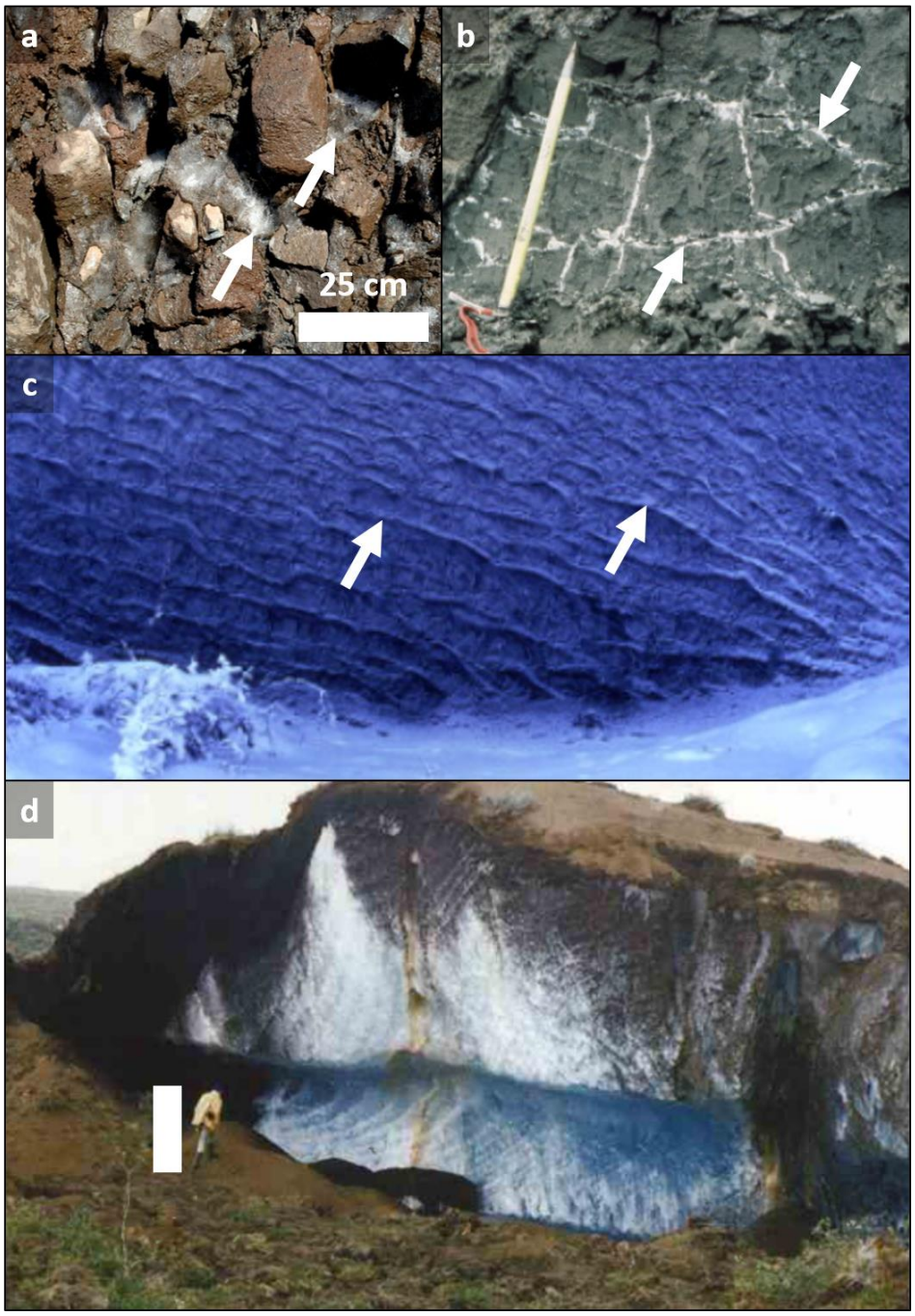

Figure 1.3: different types of ice; ***a.*** *pore ice within an ice-cemented block of coarse sediment in Iceland, pointed out by the white arrows (from Sæmundsson et al., 2018);* ***b.*** *vein ice in silty clay matrix in Canada, pointed out by the white arrows (from French and Shur, 2010);* ***c.*** *ice lenses (30-80 cm long, 5-10 cm thick) formed by ice segregation in silty clay in Canada, pointed out by white arrows (from French and Shur, 2010);* ***d.*** *intrusive ice within a pingo, with a person for the scale (from French, 2018 with photos from Mackay, 1990a).*

Frozen and unfrozen ground have different geological properties (e.g. Dobinski, 2011; French, 2018). First, water freezing can result in ice segregation (e.g. Arakawa, 1966; Coutard and Mücher, 1985; Guodong, 1983; Taber, 1929, 1930), which can form various surficial morphologies (Section 1.3.). Then, if permafrost degrades, its ice content will determine the intensity of ground subsidence (Gruber, 2020; Hjort et al., 2022; Nelson et al., 2001; Wagner et al., 2018; Walvoord and Kurylyk, 2016). In addition, frozen ground has hydrogeological properties that are different than unfrozen ground, because frozen ground prevents water infiltration and concentrates water drainage in the active layer or in unfrozen parts of the ground (Hinzman et al., 1991, Hinzman et al., 2005; Woo, 2012; Woo et al., 2000). Finally, as thermal conductivity of ice is approximately four times greater than that of liquid water, frozen ground has a higher thermal conductivity than unfrozen ground (e.g. Chuvilin et al., 2018; Penner, 1970; Slusarchuk and Watson, 1975). Therefore, the ice content of permafrost is the factor that has the most important impact on the geological properties of the permafrost.

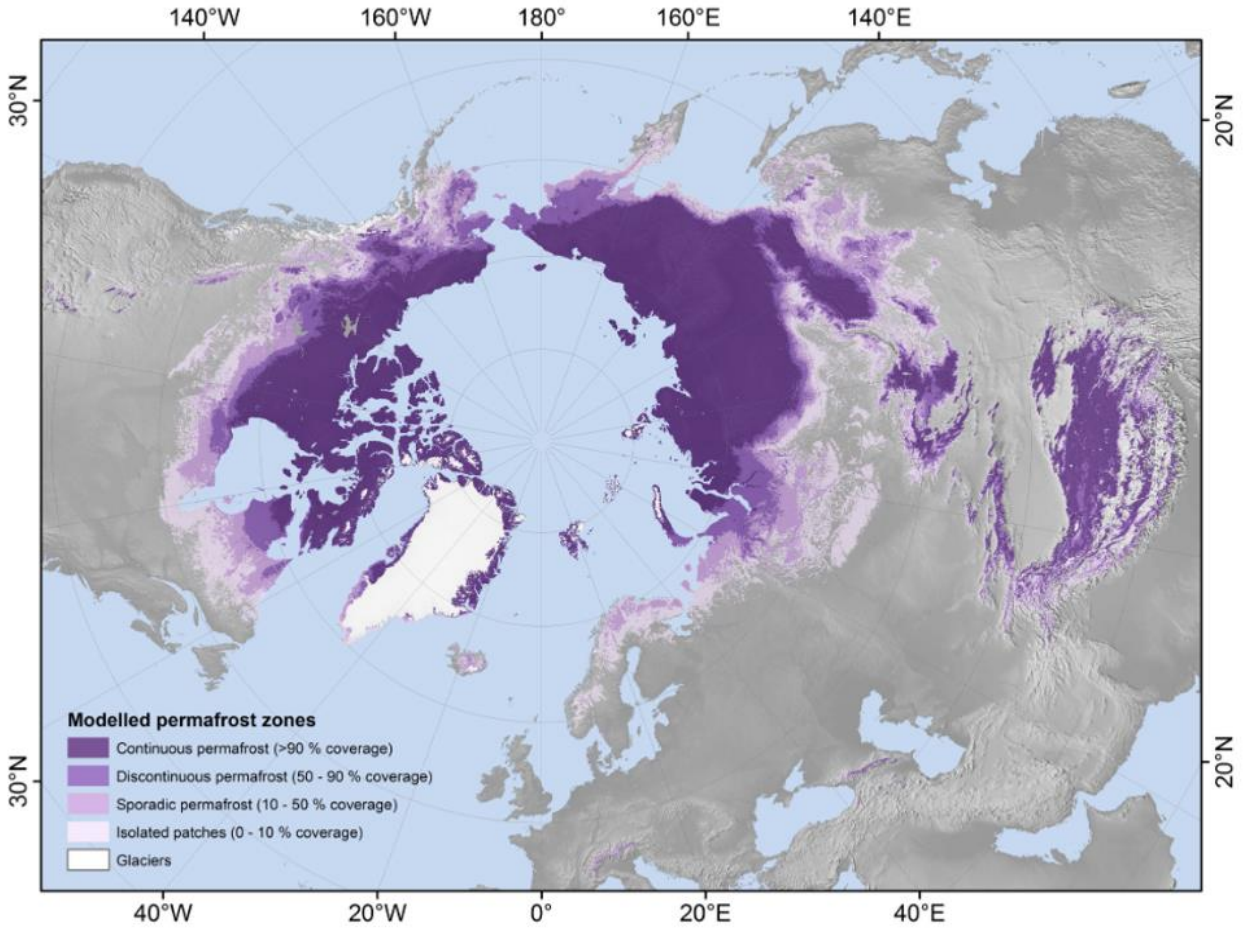

Figure 1.4: northern hemisphere distribution of the different types of permafrost on Earth, from Obu et al. (2019). The probability of presence of permafrost is computed from numerically modelled Mean Annual ground Temperature (MAGT), based on the Temperature at the Top Of Permafrost (TTOP) model (Smith and Riseborough, 1996).

Permafrost is usually described in terms of continuity: permafrost is said to be 'continuous' when it constitutes over 90% of the ground on a given area; 'discontinuous' when it constitutes 50-90% of the ground; 'sporadic' when it constitutes 10-50% of the ground; and 'isolated' when it constitutes less than 10% of the ground (e.g. Brown et al., 1997; Heginbottom, 2002; Obu et al., 2019; Zhang et al., 1999, 2000). Permafrost underlies approximately 15% of exposed land area on Earth (Obu et al., 2019), but the surface underlain by permafrost of any type (i.e. continuous to isolated) represents ~ 22% of the exposed land area of the northern hemisphere (Obu et al., 2019; ~ 24% in Zhang et al., 1999, 2000; Figure 1.4). Moreover, permafrost is also usually divided into two, geographical-dependent categories (Figure 1.1): latitudinal permafrost (in high-latitude regions; e.g. Dobiński, 2020; French et al., 2003; French, 2018; Nikiforoff, 1928; Permafrost Subcommittee, 1988) and mountain permafrost (or 'alpine permafrost', in high-altitude regions; e.g. Etzelmüller, 2013; Etzelmüller et al., 2001; Gruber and Haeberli, 2007, 2009; Guodong and Dramis, 1992; Haeberli et al., 1993, 2006, 2010; Harris et al., 2009; Permafrost Subcommittee, 1988).
The presence of ground ice and related liquid water activity form various types of landforms that are specific to periglacial areas. I review these landforms in the following section.

1.3. Ground-ice-related landforms

Periglacial landforms can be divided into two, process-related categories: aggradational and degradational landforms – i.e. formed by ground ice aggradation or degradation processes, respectively (e.g. French, 2018). Ground ice aggrades in different ways, forming different types of ice (Section 1.2.): pore ice, segregated ice, intrusive ice and vein ice.

1.3.1. Aggradational landforms

1.3.1.1. Pore ice and thermal-contraction polygons

Because pore ice simply fills the pore space of sediment, its emplacement does not directly cause the development of specific landforms. However, when ground is ice-cemented, subsequent high-magnitude decreases in temperature below 0°C cause ground ice to contract, as ice has a coefficient of linear expansion that decreases with temperature (e.g. Butkovich, 1959; Fukusako, 1990; La Placa and Post, 1960). If the thermal contraction of ice exceeds the yield strength, planar fractures will form perpendicularly to the axis of weakest yield strength, i.e. vertically. Those fractures can join, eventually after several iterations of the contraction process, to form a network of polygons at the surface (e.g. Plug and Werner, 2001, 2002, 2008). Such polygons are called 'thermal-contraction polygons' (Lachenbruch, 1962; Sletten et al., 2003; Washburn, 1956). They are typically around 5-25 m in diameter, and are one of the most common periglacial landforms (e.g. Beerten et al., 2021; Bernard-Grand'Maison and Pollard, 2018; Black, 1954; Dafflon et al., 2016; Kokelj and Burn, 2004; Mackay, 1974; Marchant et al., 2002). At this stage, there is no significant elevation difference between polygon centres and margins; they are further referred as 'flat-centred polygons' (FCPs; Figure 1.5; identified notably in Washburn, 1956; theoretical model showed in Ballantyne, 2018; French, 2018; Mackay, 2000; see also Bockheim, 2002; Engstrom et al., 2008; Pirk et al., 2017). Note that FCPs are never perfectly flat; however, the elevation difference between their centre and margins is not significant compared to the elevation differences exhibited by further stages of polygon morphologies. Once the polygonal fracture network is formed, in humid environments, water can flow within the fractures in summer and can form vein ice when freezing in winter. As the fractures are V-shaped, vein ice emplaces as wedge-shaped bodies of ice, called 'ice wedges' (Black, 1976a, 1976b, 1982; Christiansen et al., 2016; Harry and Gozdzik, 1988; Lachenbruch, 1962; Mackay, 1989, 1990b). Due to the volumetric expansion from liquid water to water ice and the cracking of the wedge itself during winter, these wedges grow larger seasonally with the repetition of freeze-thaw cycles of water (Mackay, 1989,

1990b, 1995; Murton, 2013). The direction of winter ground contraction is inward and null at the polygon centres, and the summer ground expansion is outward and unconstrained at the polygon margins. Hence, over a seasonal cycle, there is a small net material movement within the active layer, toward the polygon margins. However, as the presence of wedges prevents the ground to expand back into the fractures, displaced material raises at the polygon margins (Kokelj and Burn, 2004; Mackay, 2000). Therefore, over time, material accumulation at the polygon margins forms polygons that have a centre significantly lower in elevation than the margins, called 'low-centred polygons' (LCPs; Figure 1.5; e.g. Black, 1954; French, 2018; Harry and Gozdzik, 1988; Permafrost Subcommittee, 1988; Seppälä, 2011).

In arid periglacial environments, where little liquid water is available (e.g. Antarctica, Bockheim et al., 2009; the Gobi Desert, Li et al. 2014; the Canadian arctic, Murton, 1996a; the Atacama Desert, Sager et al., 2021), LCPs and HCPs morphologies can form through the deposition of sediment. In that case, once the polygonal fracture network is formed, sediment (e.g. carried by the wind) can deposit within the fractures, forming sediment veins. During the summer, the presence of sediment veins prevents the ground to expand back into the fractures; and during winter, the veins act as weakness zones, causing the ground to crack again at the same locations, creating space for the deposition of additional sediment within the widen fractures. Similarly to the growth of ice wedges, the repetition of this cycle causes the seasonal growth of what are then called 'sand wedges' (e.g. Leffingwell, 1915; Berg and Black, 1966; Christiansen et al., 2016; Hallet et al., 2011; Murton, 1996a; Murton et al., 2000; Pewe, 1959).

Ice wedges and sand wedges represent two endmembers of a compositional continuum. Therefore, 'composite wedges' can form in intermediate environments, where both liquid water and wind-blown sediment are available (e.g. Berg and Black, 1966; Christiansen et al., 2016; Murton, 1996a; Murton et al., 2000). Such wedges are closer to one or the other endmember, depending on the relative availability in liquid water and wind-blown sediment.

1.3.1.2. Segregated-ice mounds

Segregated ice typically forms ice lenses parallel to the freezing front in frost-susceptible ground, with thicknesses varying from a few millimetres to tens of metres (Konrad and Morgenstern, 1980; Mackay, 1972; Penner, 1986; Rempel, 2007; Takagi, 1970, 1979). Ice lenses can accumulate to form perennial icy mounds, up to several metres high, called 'palsas' and 'peat plateaus' (in organic-rich terrain; Figure 1.6; Martin et al., 2019; Pissart, 2002; Sæmundsson et al., 2012; Seppälä, 1982, 1986, 2011), or 'lithalsas' (in mineral-rich terrain; Calmels et al., 2008; Delisle et al., 2003; Pissart, 2000, 2002; Pissart et al., 2010). Smaller mounds (~ tens of centimetres), called 'thufurs' or 'hummocks', are common in periglacial areas and are also thought to form from ice segregation (e.g. Grab, 2005; Mackay, 1980; Utting et al., 2009; Van Vliet-Lanoë et al., 1998).

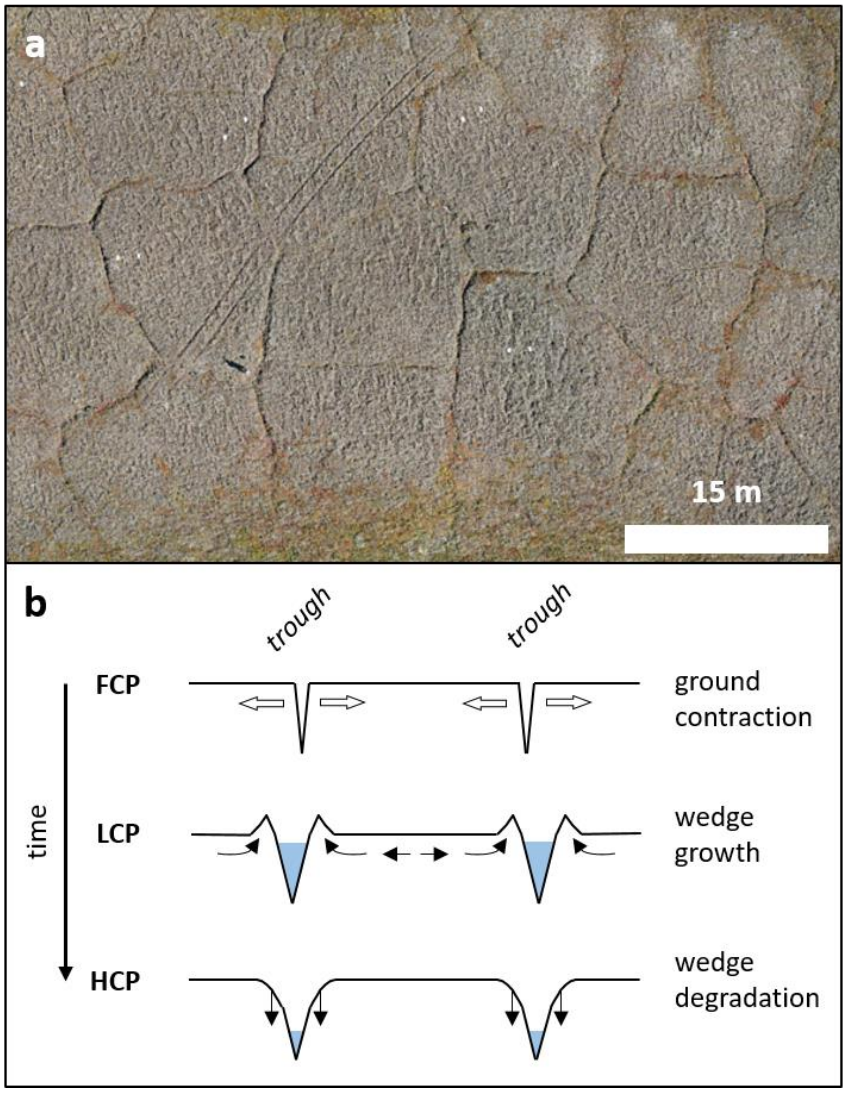

*Figure 1.5: **a.** photo of thermal-contraction polygons (65°17'32" N 15°30'30" W, Iceland); **b.** cross-section scheme of a thermal-contraction polygon, evolving from flat-centred, to low-centred, to high-centred polygon (FCP, LCP, HCP). At the flat-centred phase, fractures have formed because of thermal contraction of icy ground. At the low-centred phase, thermally-induced movements cause the progressive uplifting of the polygon margins. At the high-centred phase, the degradation of the ice wedges causes the collapse of the margins within the ice-wedge cast. Black arrows indicate directions of ground movements.*

1.3.1.3. Intrusive-ice mounds

Intrusive ice forms two types of structures: when pressurised liquid water is intruded into a confined material, it can fracture that material and freeze vertically ('ice dyke'; e.g. French, 2018; Permafrost Subcommittee, 1988) or emplace between two sedimentary layers ('ice sill'; e.g. French, 2018; Permafrost Subcommittee, 1988). When pressurised liquid water is expulsed toward the surface of the ground, it can freeze below the surface and form a 'pingo' (Figure 1.7; Gurney, 1998; Mackay, 1973, 1977, 1979, 1998; Mackay and Burn, 2011; Yoshikawa and Harada, 1995). Like palsas, pingos are perennial ice-cored mounds, but they are different in terms of ice formation process (segregation ice for palsas, intrusive ice for pingos). They can also be much larger than palsas – up to several tens of metres.

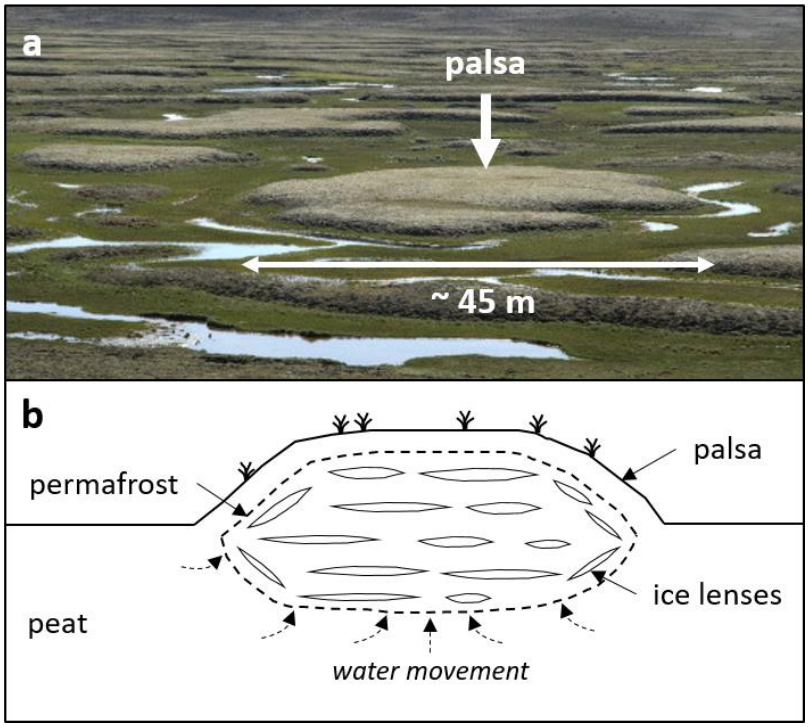

Figure 1.6: ***a.*** *photo of a palsa (credit: Þ. Sæmundsson, in Sæmundsson et al., 2012; 65°06'12" N, 18°32'36" W, Iceland);* ***b.*** *cross-section scheme of a palsa (modified from French, 2018).*

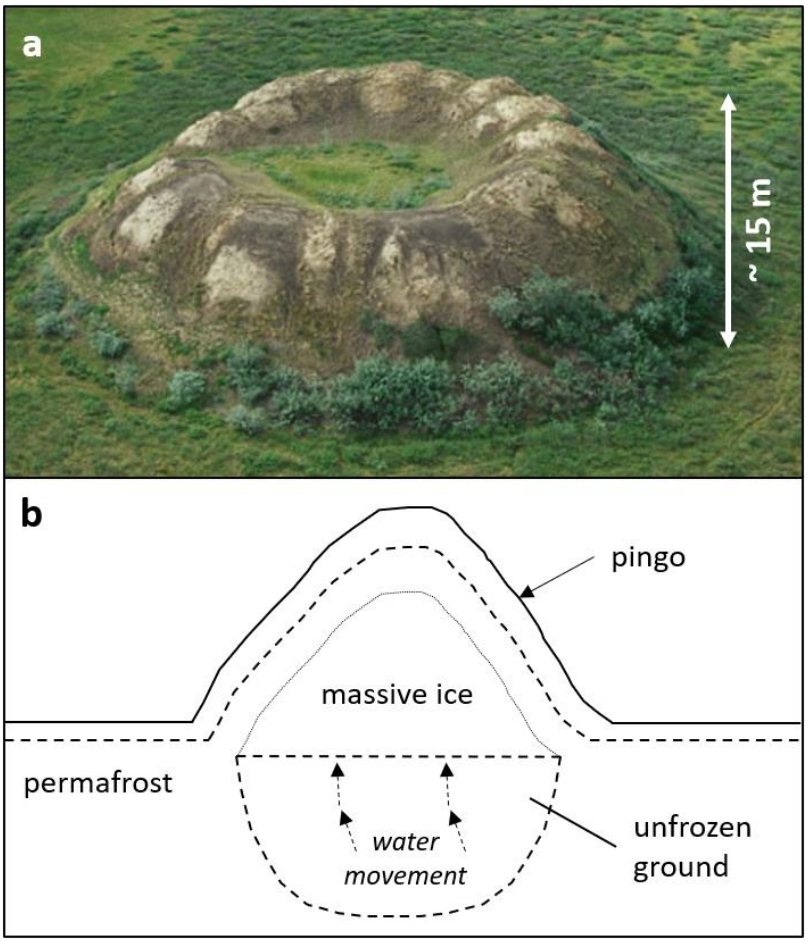

Figure 1.7: ***a.*** *photo of a pingo, with a collapsed summit (credit: C. R. Burn, in Mackay and Burn, 2011; 69°26' N, 124°53' W, Northwest Territories, Canada);* ***b.*** *cross-section scheme of a pingo (based on Mackay, 1998).*

1.3.2. Degradational landforms

When MAGT increases, for instance as a result of ongoing climate change (e.g. Christiansen et al., 2010; Romanovsky et al., 2010a, 2010b; Smith et al., 2010; Vieira et al., 2010; Zhao et al., 2010), the thermal gradient of the ground is perennially shifted towards higher temperatures. If the temperature increase is significant enough, permafrost – which represents a thermal state of the ground – gets thinner, and can even disappear completely (Figure 1.2; e.g. French, 2018). The active layer then extends downward, and becomes more frequently thawed than frozen (Figure 1.2). If permafrost totally disappears, the active layer is directly in contact with the underlying non-frozen ground. Therefore, all of the permafrost ice ultimately thaws, which modifies the hydrogeology of the area. Water can now infiltrate and drain, favouring mechanical and thermal erosion (i.e. melting of ice caused by the circulation of water above 0°C; e.g. Fortier et al., 2007; Murton, 2009; Randriamazaoro et al., 2007). Moreover, water is also directly provided by ground ice thaw, in quantities varying with respect to the ice content of the initial permafrost. The thawing of ground ice also decreases the cohesion of the ground, as pore ice can hold the sediment together, and causes the sediment to compact which leads to ground settlement (e.g. Anisimov and Reneva, 2006; Guo and Wang, 2017; Hjort et al., 2022; Hong et al., 2014; Ni et al., 2021). The term 'thermokarst' is used to describe features, landforms and processes associated with volume loss on degradation of excess ground ice (e.g. French, 2018; Kokelj and Jorgenson, 2013; Permafrost Subcommittee, 1988).

The most obvious thermokarst landforms directly result from ground settlement, subsequent to thawing of ground ice: thermokarst depressions (e.g. Czudek and Demek, 1970; Murton, 2009). When thermokarst depressions are filled with liquid water, they are referred to as 'thermokarst lakes' (Figure 1.8a; e.g. Burn and Smith, 2006; Grosse et al., 2013; Niu et al., 2011). Pingos can also melt and collapse, leaving a circled depression with raised rims (Figure 1.7a; Mackay, 1979, 1988; Mackay and Burn, 2011; Yoshikawa et al., 1996).

When ice wedges thaw, the elevated margins of LCPs collapse into the wedge casts, which lead to polygons that have margins lower in elevation than the centres, called 'high-centred polygons' (Figure 1.5b; Section 2.5.; Black, 1954; French, 2018; Permafrost Subcommittee, 1988). In the case of sand wedges, their degradation by mechanical erosion agents (e.g. precipitations, wind, flowing meltwater) also creates wedge casts in which polygon margins can collapse, thus also forming HCPs (Ballantyne, 2018; French, 2018).

'Pseudomorphs' are structures that are indirectly linked to permafrost degradation. They result from the degradation of ground ice features, and the replacement of missing ice by lithic or organic material that gets deposited within the empty space (e.g. aeolian deposition of sediment, or deposition of dead vegetation; French, 2018; Permafrost Subcommittee, 1988). Typically, ice-wedge pseudomorphs can be found in place of degraded ice wedges (Figure 1.8b; e.g. Harry and Gozdzik, 1988; Murton and French, 1993; Ewertowski, 2009).

Lastly, the low ground cohesion and the high water content of thawed ground lead to sediments that are easily mobilised (e.g. Patton et al., 2019), resulting in the occurrence of mass-wasting processes on slopes. In the case of latitudinal permafrost, thawed ground is frequently eroded by retrogressive-thaw-slumps (Figure 1.8c; Czudek and Demek, 1970; French, 1974; Kokelj and Jorgenson, 2013). They are slope failure with a headwall that retreats from year to year, and exhibit final retreat distances of metres to tens of metres (e.g. Burn and Lewkowicz, 1990; Lantz and Kokelj, 2008; Lewkowicz, 1987; Séjourné et al., 2015). In the case of mountain permafrost, degradation of ground ice can trigger various types of landslides (e.g. Dramis et al., 1995; Haeberli et al., 2017; Morino et al., 2021; Patton et al., 2019). It has also been suggested that 'molards', i.e. cones of loose debris found in landslide deposits, could constitute markers of permafrost degradation (Morino et al., 2019b, 2023). I detail further these morphologies in Section 1.4.

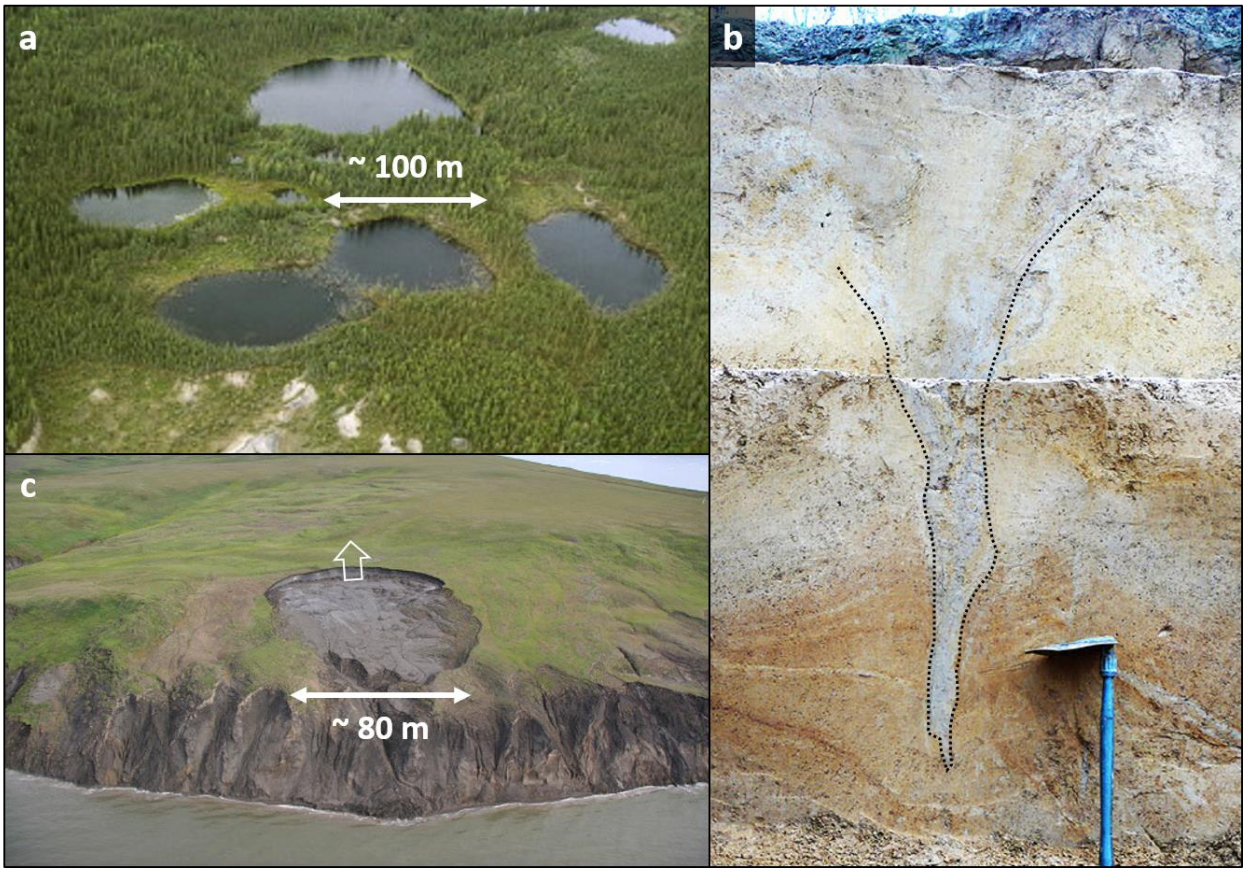

*Figure 1.8: photos of **a.** thermokarst lakes (credit: C. R. Burn, in Burn and Smith, 2006; 63°33'56" N, 135°53'59" W, Yukon, Canada); **b.** an ice-wedge sediment pseudomorph, outlined by the black dotted line (credit: P. Antoine in Andrieux et al., 2016; 50°7'12" N, 03°53'06" E, France); **c.** a retrogressive-thaw-slump. The hollow arrow indicates the direction of headwall retreat (credit: Pollard, 2018; 69°34'52" N, 139°04'34" W; Herschel Island, Yukon, Canada).*

1.4. Introduction to molards and permafrost degradation

1.4.1. Climate change and permafrost degradation

It is now consensual that ongoing climate change causes (among others) the global MAAT, and hence MAGT, to increase (e.g. Beltrami et al., 1992; Farbrot et al., 2007; Jorgenson et al., 2010; Smith and Riseborough, 1996; or the paper compilation published in 2010 for the International Polar Year: Christiansen et al., 2010; Romanovsky et al., 2010a, 2010b; Smith et al., 2010; Vieira et al., 2010; Zhao et al., 2010). When the increase in MAGT is significant, permafrost begins to thaw (Figure 1.2; Section 1.3.2.). Permafrost degradation in mountain areas causes mass-wasting hazards (e.g. Allen et al., 2009; Bell and Glade, 2004; Dramis et al., 1995; Fischer et al., 2006; Gruber and Haeberli, 2007; Haeberli et al., 2017; Harris et al., 2001; Kellerer-Pirklbauer et al., 2012; Patton et al., 2019; Wei et al., 2006), which represent a threat for local populations and infrastructures (e.g. Geertsema et al., 2009; Haque et al., 2016; Kjekstad and Highland, 2009; Petley, 2012). Unfortunately, estimating the extent of mountain permafrost is challenging: it involves numerical modelling of ground temperature (e.g. 'TTOP-models', for Temperature at the Top Of Permafrost; Obu et al., 2019; Way and Lewkowicz, 2016; Zhang et al., 2021), and is usually

of too-coarse scale to account for local factors, especially in areas of discontinuous permafrost. Moreover, few landforms exist that are indicative of active mountain permafrost degradation. Hence, assessing the hazard of landslides triggered by permafrost degradation is difficult at the local scale, as it is hard to know whether permafrost or its degradation were involved. However, studies suggested that molards – i.e. cones of loose debris found in landslide deposits (Figure 1.9) – could be linked to permafrost degradation (Brideau et al., 2009; Lyle et al., 2004; Milana, 2016). Morino et al. (2019b) confirmed that molards could represent accurate spatial and temporal markers of mountain permafrost presence and degradation.

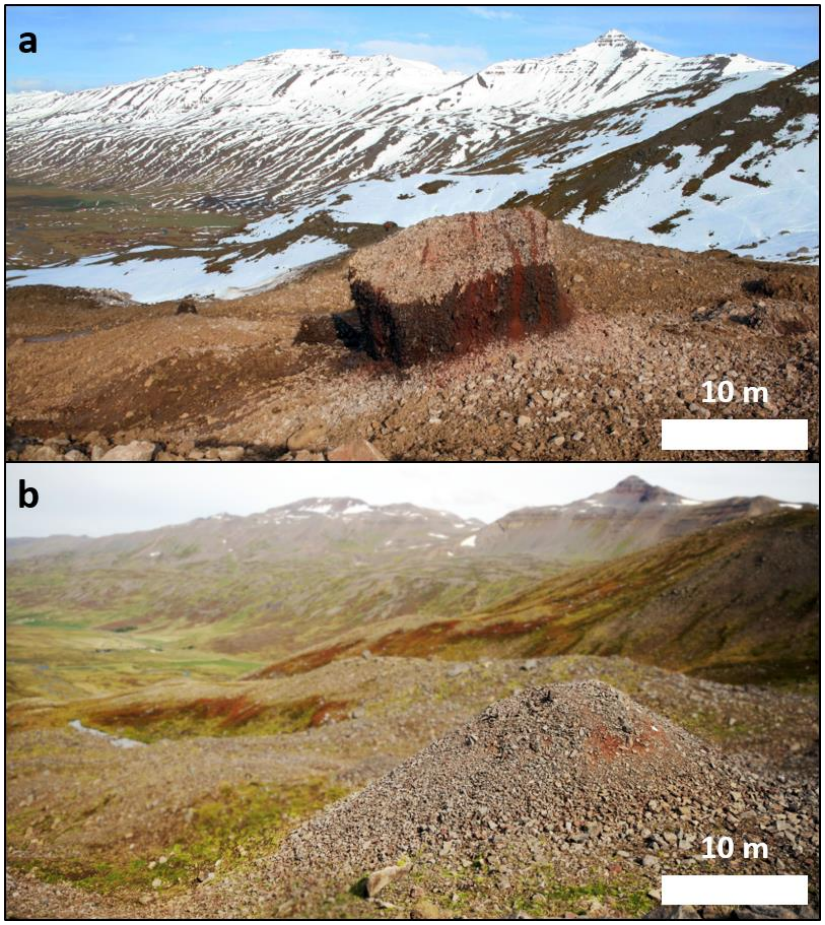

*Figure 1.9: degradation of **a.** an ice-cemented block of sediment (September 2012, a few days after the landslide; courtesy of Jón Kristinn Helgason) into **b.** an actual molard (August 2022), within the Móafellshyrna landslide deposits (20th September 2012, Iceland).*

1.4.2. Formation of molards

The formation of molards occur as follows (Morino et al., 2019b; Figure 1.10):

1. presence of mountain permafrost cementing debris located on a slope (Figure 1.10a);
2. an increase in MAGT – for instance due to a perennial increase in MAAT resulting from the ongoing climate change – causes the permafrost to degrade, forming patches of non-frozen ground (Figure 1.10b);
3. degradation of permafrost causes a loss of cohesion in the slope, and a landslide is triggered. This landslide transports blocks of ice-cemented sediment which come to rest in its deposits (Figure 1.10c);

4. with time, the ice within the blocks degrades, due to exposure to higher air temperatures at lower altitude and/or precipitation. Hence, the sediment within the blocks becomes loose and forms a cone of debris within the landslide deposits (Figure 1.10d and e). Eventually, patches of non-frozen ground form in the newly-exposed slope.

Therefore, finding molards in landslide deposits indicates that actively-degrading permafrost was present at the level of the detachment zone, when the landslide occurred (Morino et al., 2019b). Moreover, the existence of ice-cemented blocks of sediment indicates that the permafrost initially mobilised is constituted, at least partially, of pore ice. Previous studies estimated that the ice content of the initial blocks must be at least 50% to 80% for the block to withstand the landslide failure and subsequent transport (Brideau et al., 2009; Milana, 2016). Thus, presence of molards in landslide deposits also indicates that the mobilised permafrost layer has a relatively high ice content. Moreover, Morino et al. (2019b) suggested that higher initial ice content of the blocks are correlated with smaller molards, with gentler flank slopes and more rounded summits.

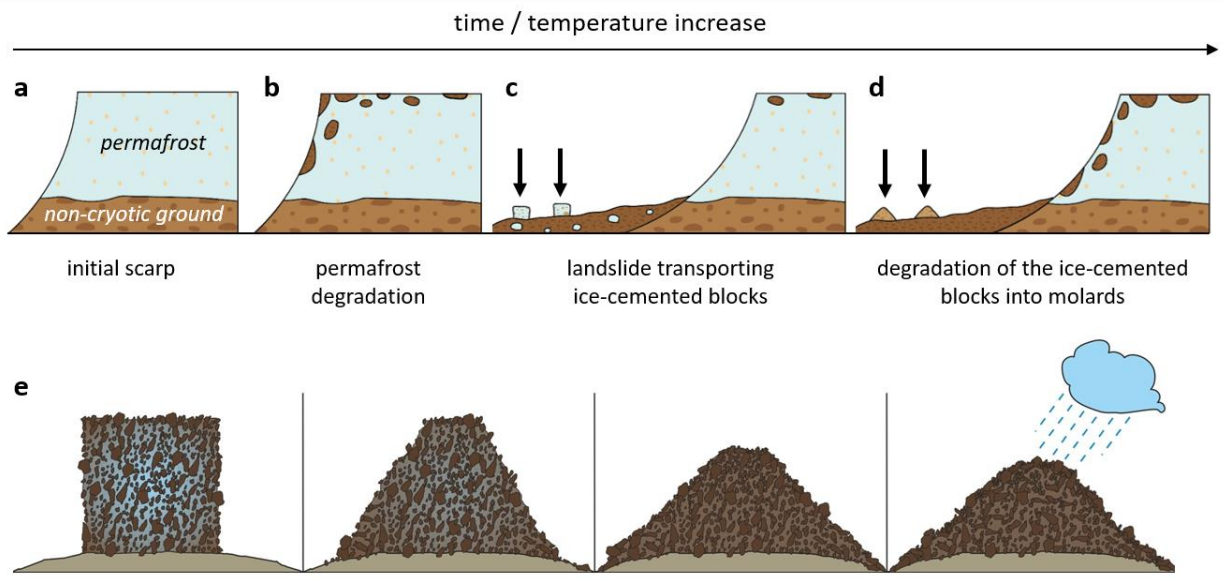

Figure 1.10: chronology of molard formation from degradation of mountain permafrost subsequent to an increase in MAGT. ***a.*** *presence of a slope cemented by mountain permafrost;* ***b.*** *permafrost degradation;* ***c.*** *destabilisation of the slope, generating a landslide that transports blocks of ice-cemented sediment (pointed out by black arrows);* ***d.*** *degradation of the ice-cemented blocks into molards (pointed out by black arrows), and eventual new permafrost degradation;* ***e.*** *progressive degradation of an ice-cemented block into a molard. Panel e. was modified from Morino et al. (2019b).*

1.4.3. Molards as an indicator of landslide processes

Morino et al. (2019b) also showed that the morphometrics of molards and their spatial distribution within landslide deposits can provide insights into the mass-wasting processes at play during the landslide. They investigated two case studies in Iceland: the Móafellshyrna and Árnesfjall landslides, in Iceland.
In the Móafellshyrna landslide (Figure 1.11a and b), molards show variable dimensions (< 10 m^3 to nearly 10,000 m^3), and overall circular planforms – with no preferential orientation of their long axis. They also

show flank slope angles that are radially consistent for a given molard. They are found as a cluster at the base of the slope, on or below a topographic bench with a relatively gentle slope (~ 17°). Such a setting indicates that the ice-cemented blocks had widely variable dimensions, and deposited on a slope break (Figure 1.11a). It points to a rockfall-like failure process for the Móafellshyrna landslide.
In the Árnesfjall landslide (Figure 1.11c and d), molards exhibit a different setting. They show shapes that are consistently elliptical, with the long axis orientated perpendicular to the flow direction of the landslide and parallel to the detachment scarp. They also show a steep scarp-facing flank and a gentler downslope-facing flank. They are clustered close to the base of the detachment scarp (< 30 m below), on a relatively steep slope (~ 26°). Such a setting indicates that the ice-cemented material was deposited as *en-echelon* elongated ridges, close to the detachment scarp (Figure 1.11c). It points to a rotational-sliding failure process for the Árnesfjall landslide.

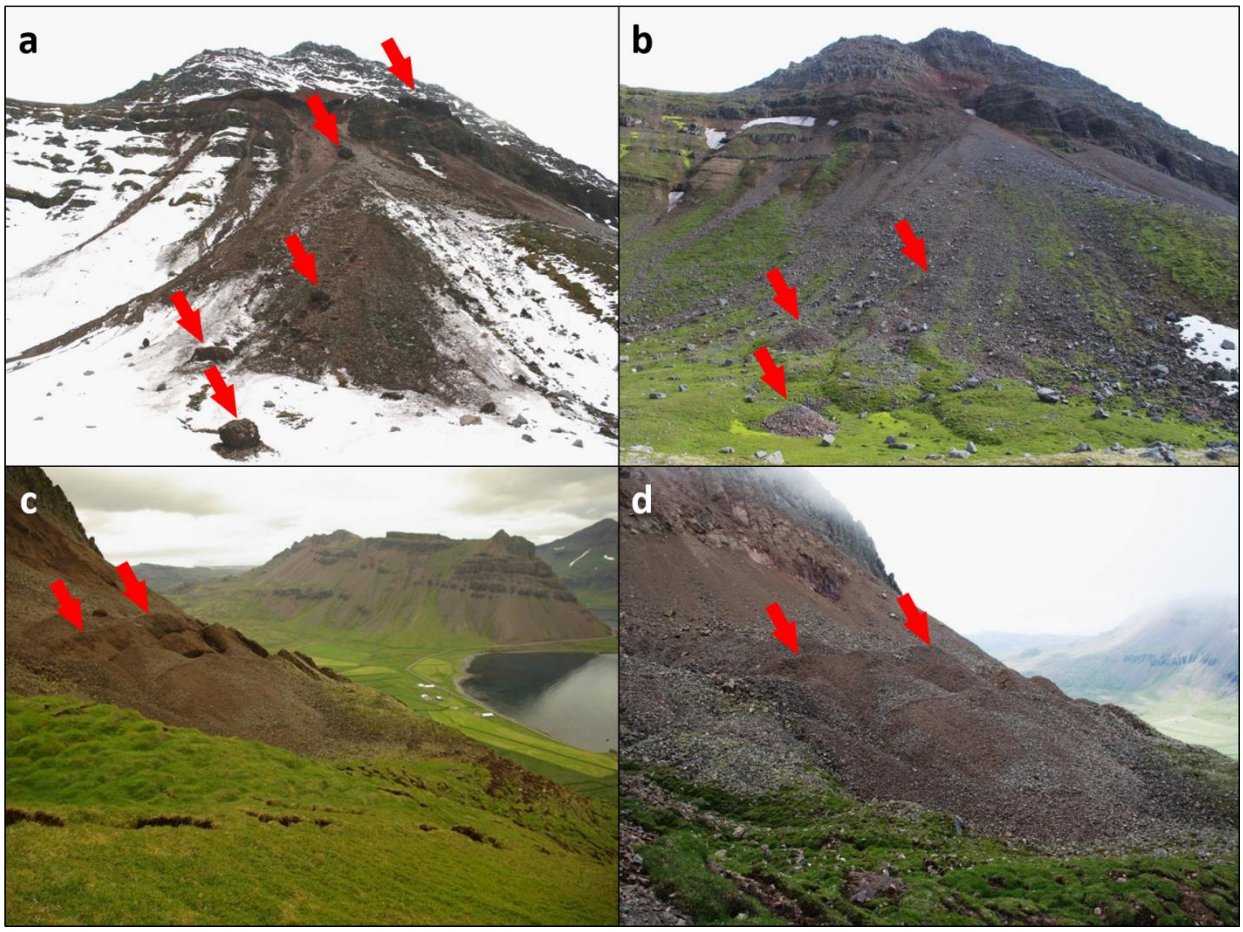

Figure 1.11: ***a.*** *ice-cemented blocks (one day after the failure; courtesy of G. Hansson) and* ***b.*** *resulting molards (three years after the failure), in the Móafellshyrna landslide (2012). The foreground block and resulting molard are ~ 7 m and ~ 9 m wide, respectively;* ***c.*** *ice-cemented ridges (two days after the failure; courtesy of V. Benediktsson) and* ***d.*** *resulting elongated molards (two years after the failure) in the Árnesfjall landslide (2014). Ridges and elongated molards are up to 4 m and 3.7 m high, respectively. Ice-cemented block/ridges and molard examples are pointed out by red arrows. Modified from Morino et al. (2019b).*

1.4.4. Remaining scientific questions

Several issues remain when studying molards. First, other conical features can be found in periglacial environment (e.g. ice-cored moraines), so the location of the conical mounds associated with a landslide is essential to identify them as molards. However, somewhat conical mounds can also form within landslide deposits by brittle failure of rocks transported within the landslide, without the involvement of ice – called hummocks (e.g. Paguican et al., 2014; Shea et al., 2008; Shea and Van Wyk De Vries, 2008; Yoshida et al., 2012). Moreover, molard-bearing landslides can occur in remote areas, and hence are difficult to access in the field – and sometimes not even identified. As fieldwork is currently necessary to distinguish between molards and landslide hummocks, a simple remote sensing study cannot definitively prove conical mounds are molards. Hence, we have only few observations of the degradation from ice-cemented blocks to molards, and studying that process is challenging due to the reasons I evoked above. I address this issue in Section II.1 by providing a protocol and setup to study the process of degradation from ice-cemented block of sediment into a molard. This experimental development is made in the framework of the Permolards project, which aims at creating the first scientific database on molards. The project combines various types of studies: fieldwork, remote sensing studies, experimental modelling, and numerical modelling. Its overarching goal is to allow the recognition of molards from remote sensing imagery, in order to map them at regional scales. Such maps will give accurate constraints on the current distribution of mountain permafrost over a given region, and hence on the location of zones with a high risk of landslide hazard.

In addition, as ground ice degradation occurs on other planetary bodies than the Earth (e.g. on Mars), the presence of molards could be used there as indicator of ground ice degradation. For instance, molards were suggested to have occurred on Mercury, by volatile loss within blocks mobilised by the Caloris crater ejecta (Wright et al., 2020). I address this question for Mars in Section II.2, in a study of suggesting the existence of martian molards.

2. Ground ice on Mars

Just like the Earth, Mars is a terrestrial planet over 4.5 Gyrs old, with a complex geological evolution. Figure 2.2 shows a global map of Mars, with the location of the principal geographic features and space probes mentioned in the following sections. I first give a brief overview of the space exploration of Mars and of the resulting datasets that are available (Section 2.1.), as well as an overview of the history of its climate and environment – and notably the evidence we have for occurrence of periglacial conditions (Section 2.2.). These two first sections will help to understand the scientific questions that remain concerning Mars, and the types of studies that are conducted to answer those questions. I then detail the direct and indirect evidence for the presence of martian ground ice (Section 2.3.), and the related potential periglacial landforms (Section 2.4.). I finish by detailing the knowledge we have on martian thermal-contraction polygons: the different polygon types, how they form, how they are distributed on Mars, as well as their link with the martian climate. I also identify the current knowledge gaps, highlighting those that will be addressed in the present thesis (Section 2.5.).

2.1. Overview of martian space probes and datasets

The exploration of Mars started with the Space Race, during the Cold War. Three space probes, Mariner 4, 6 and 7, launched by the National Aeronautics and Space Administration (NASA, from the USA), performed three flybys of Mars between 1965 and 1969 (Anderson, 1965; Leighton et al., 1965, 1969a, 1969b). These probes sent photographs to Earth that revealed a heavily-cratered surface, suggesting an inert desert similar to the lunar surface (Figure 2.1a; Chapman et al., 1969). However, the Mariner 9 orbiter reached Mars in 1971 (Masursky, 1973; McCauley et al., 1972; Sagan et al., 1972). It allowed the first detailed observations of major martian features, including: i. the northern and a southern polar caps (Masursky, 1973; Paige et al., 1990; Soderblom et al., 1973); ii. Valles Marineris, the largest set of canyons in the Solar System (around 3700 km long, and at most 10 km deep and 600 km wide; Figure 2.2; Sagan and Fox, 1975); iii. Olympus Mons, the largest volcano structure in the Solar System (22.5 km high; Figure 2.2; Carr, 1974; Davies, 1974; King and Riehle, 1974; Whitehead, 1974); iv. sinuous, branched valleys that are reminiscent of former drainage systems and rivers (Mars Channel Working Group, 1983; Pieri, 1980; Sagan et al., 1973). All of these observations suggested that Mars was actually a planet with a complex geological history. Notably, the presence of water-related features enhanced the interest of scientists for Mars, in the context of the research for extraterrestrial life (e.g. Klein, 1978, 1979).

From that point, the NASA, followed by other national and international space agencies, sent more and more space probes to Mars. I provide an overview of these martian probes and their major discoveries in Table 2.1. The scientific instruments onboard those probes have sent to Earth data that are of increasing variety and resolution. I summarise in Table 2.2. some of the existing datasets that can be used to study the martian surface and near subsurface and are mentioned in this thesis. Note that data from the Mars Orbiter Laser Altimeter (MOLA; Table 2.2.) are not the only topographic data available for Mars: photos can be used to generate small-scale and high-resolution Digital Elevation Models (DEMs) from stereophotogrammetry.

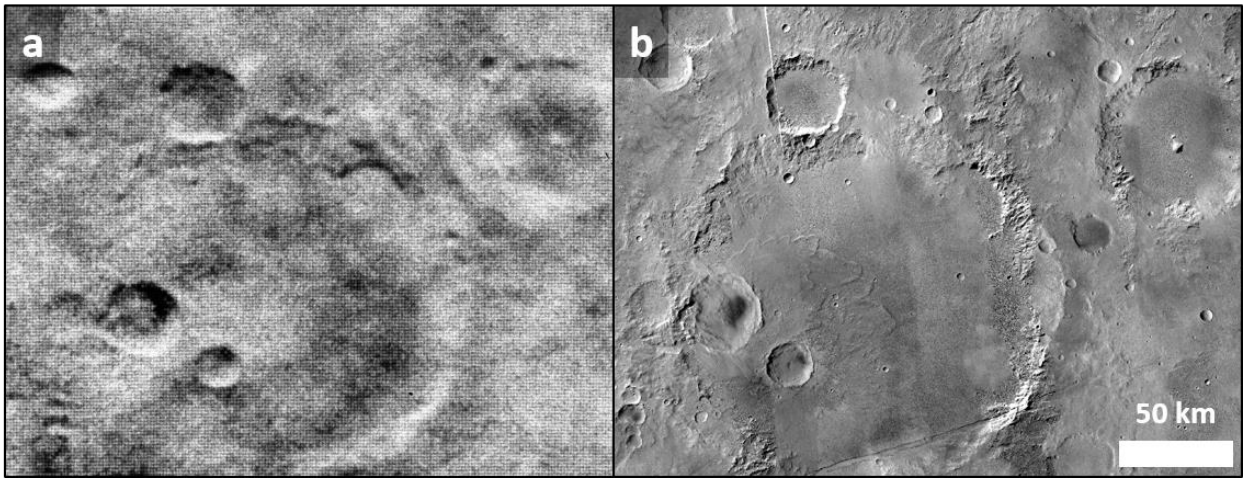

Figure 2.1: images of the same region of Mars taken by space probes launched approximately 40 years apart, showing the improvements made in imaging technologies; ***a.*** *the Mariner crater, imaged by the first probe successfully sent to Mars, Mariner 4 (credit: NASA/JPL);* ***b.*** *the same view as panel a using the global mosaic of the Context Camera images (CTX, 6 m/pixel), onboard the Mars Reconnaissance Orbiter probe (credit: NASA/JPL/MSSSS/The Murray Lab). North is up on both panels.*

Mission[1]	**Arrival**	**Type of probe**[2]	**Space agency**[3]	**Highlight**	**References**
Mariner 4	1965	orbiter (flyby)	NASA	observation of a heavily-cratered surface	Anderson, 1965; Leighton et al., 1965, 1969a, 1969b
Mariner 6	1969	orbiter (flyby)	NASA		
Mariner 7	1969	orbiter (flyby)	NASA		
Mariner 9	1971	orbiter	NASA	observation of former valley systems	Masursky, 1973; McCauley et al., 1972; Sagan et al., 1972
Viking 1 and 2	1976	2 orbiters and 2 landers	NASA	no detection of biological activity; past presence of liquid water confirmed; geologically recent periglacial conditions	Soffen, 1978; Soffen and Snyder, 1976; Soffen and Thomas Young, 1972
Mars Pathfinder - *Sojourner*	1997	lander + rover	NASA	first rover to operate on Mars	Golombek, 1997; Golombek et al., 1997
Mars Global Surveyor (MGS)	1997	orbiter	NASA	first global coverage of topography and visible/thermal imagery	Albee et al., 1998, 2001
Mars Odyssey	2001	orbiter	NASA	evidence for near-subsurface water ice	Saunders et al., 2004
Mars Express	2003	orbiter	ESA	detection of hydrated minerals	Chicarro et al., 2004
Mars Exploration Rover - *Spirit and Opportunity*	2004	2 rovers	NASA	evidence for surficial aqueous alteration	Crisp et al., 2003

Mars Reconnaissance Orbiter (MRO)	2006	orbiter	NASA	detection of active mass-wasting processes	Graf et al., 2005; Zurek and Smrekar, 2007
Phoenix	2008	lander	NASA	direct observation of ground ice	Shotwell, 2005; Smith, 2004
Mars Science Laboratory (MSL) - *Curiosity*	2012	rover	NASA	evidence for past persistent liquid water and environment suitable for life	Grotzinger et al., 2012; Rice et al., 2017; Vasavada et al., 2014
Mars Atmosphere and Volatile Evolution (MAVEN)	2014	orbiter	NASA	evidence that the martian atmosphere was blown away by solar winds	Jakosky et al., 2015a, 2015b; Lillis et al., 2015
Mars Orbiter Mission	2014	orbiter	ISRO	first national space agency other than NASA to send an orbiter to Mars	Arunan and Satish, 2015
ExoMars Trace Gas Orbiter (TGO)	2016	orbiter	ESA	absence of methane gas	Vago et al., 2015
InSight	2018	lander	NASA	location of the crust/mantle and mantle/core boundaries	Banerdt et al., 2020; Smrekar et al., 2019
Mars Hope	2021	orbiter	UAESA	first probe dedicated to the martian weather	Amiri et al., 2022; Sharaf et al., 2020
Tianwen-1 - *Zhurong*	2021	orbiter + lander + rover	CSA	first successful rover not sent by NASA	Zou et al., 2021
Mars 2020 - *Perseverance*	2021	rover + flight drone	NASA	collection of samples to be returned to Earth	Balaram et al., 2021; Farley et al., 2020; Williford et al., 2018

Table 2.1: information on the successful missions to Mars. [1]Rover names are indicated in italic, when applicable. [2]An orbiter is a space probe that orbits around a planetary body; when they perform a 'flyby', they do not remain in orbit but acquire data during a single pass only. A lander is a space probe that lands and stays static on a planetary body. A rover is a space probe that is mobile on the surface of a planetary body. [3]NASA: National Air and Space Agency (USA); ESA: European Space Agency; ISRO: Indian Space Research Organisation; UAESA: United Arab Emirates Space Agency; CSA: China Space Agency (China).

Instrument	Mission	Data type	Resolution	Coverage	References
High-Resolution Imaging Experiment (HiRISE)	MRO	multispectral (panchromatic, blue-green, red near-IR)	25-50 cm/pixel	local	McEwen et al., 2007
Context Camera (CTX)	MRO	visible imagery	6 m/pixel	global	Malin et al., 2007
Colour and Stereo Surface Imaging System (CaSSIS)	ExoMars	multispectral (panchromatic, blue-green, red, IR)	5 m/pixel	local	Thomas et al., 2017
High-Resolution Stereo Camera (HRSC)	Mars Express	multispectral (panchromatic, blue, green, red, infrared)	10-20 m/pixel (colour) 2.3 m/pixel (black and white)	global	Neukum and Jaumann, 2004
Mars Orbiter Camera (MOC)	MGS	Narrow-Angle Camera (NAC) black and white	1.5-12 m/pixel	global	Malin et al., 1992
		Wide-Angle Cameras (WAC) one in the blue, one in the red	230-7500 m/pixel	local	
Mars Orbiter Laser Altimeter (MOLA)	MGS	topography	463 m/pixel 30 m (vertical)	global	Abshire et al., 2000; Smith et al., 2001
Compact Reconnaissance Imaging Spectrometer (CRISM)	MRO	multispectral (72 channels) 362-3920 nm	100-200 m/pixel	near-complete between 65°N and 65°S	Murchie et al., 2007
		hyperspectral 362-3920 nm	18 m/pixel	local	
Observatoire pour la Minéralogie, l'Eau, les Glaces et l'Activité (OMEGA)	Mars Express	hyperspectral 0.38-5.1 µm	2-5 km/pixel	near-global	Bellucci et al., 2004
			< 350 m/pixel	local	
Shallow Radar (SHARAD)	MRO	radar profiles (1 km deep)	10 m (vertical)	global	Seu et al., 2007
Mars Advanced Radar for Subsurface and Ionosphere Sounding (MARSIS)	Mars Express	radar profiles (5 km deep)	~ 150 m (vertical)	global	Jordan et al., 2009; Picardi et al., 2004
Gamma Ray Spectrometer (GRS)	Mars Odyssey	gamma ray/neutron spectrometry of the shallow subsurface (< 1 m)	300 km/pixel	global	Boynton et al., 2004
Fine Resolution Epithermal	ExoMars TGO	gamma ray/neutron	60-200 km/pixel	global	Mitrofanov et al., 2018

Neutron Spectrometer (FREND)		spectrometry of the shallow subsurface (< 1 m)			
in-situ datasets from rovers and landers	Curiosity, InSight, Opportunity/Spirit, Perseverance, Phoenix, Sojourner, Viking 1and2, Zhurong	photographs; climate measurements (e.g. temperature, pressure, wind); sample and ground composition; radargrams; seismograms	variable	one-off	Banerdt et al., 2020; Crisp et al., 2003; Farley et al., 2020; Golombek, 1997; Grotzinger et al., 2012; Shotwell, 2005; Smith, 2004; Smrekar et al., 2019; Williford et al., 2018; Zou et al., 2021

Table 2.2: existing instruments and datasets that can be used to study the martian surface and near subsurface. Note that photos taken by space probes can be used to generate Digital Elevation Models (DEMs).

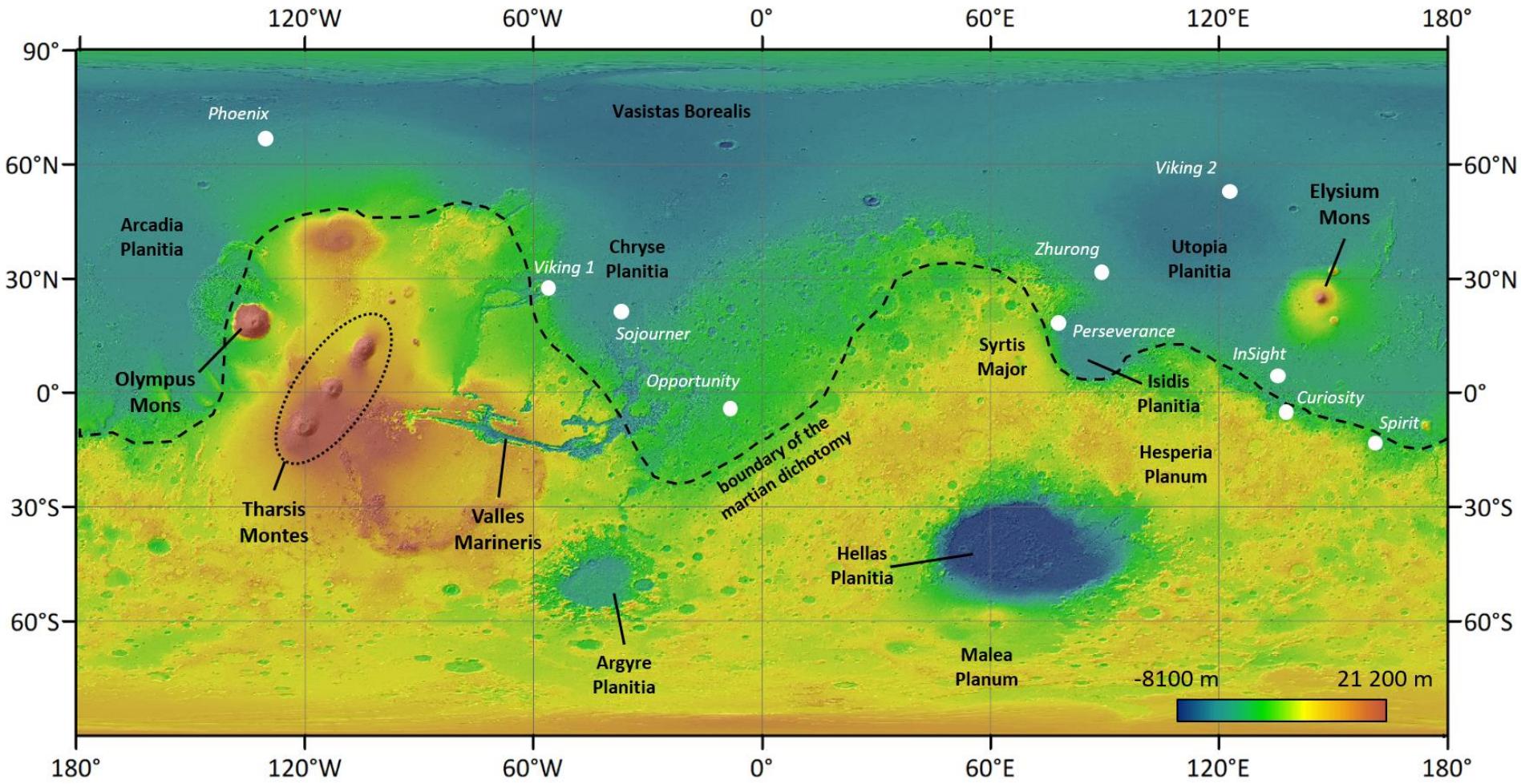

Figure 2.2: global topographic map of Mars. Selected major geological features are labelled, as well as the position of the various landers and rovers. Background is the colourised and hillshaded topographic data from the Mars Orbiter Laser Altimeter global gridded data (credit: MOLA Science Team).

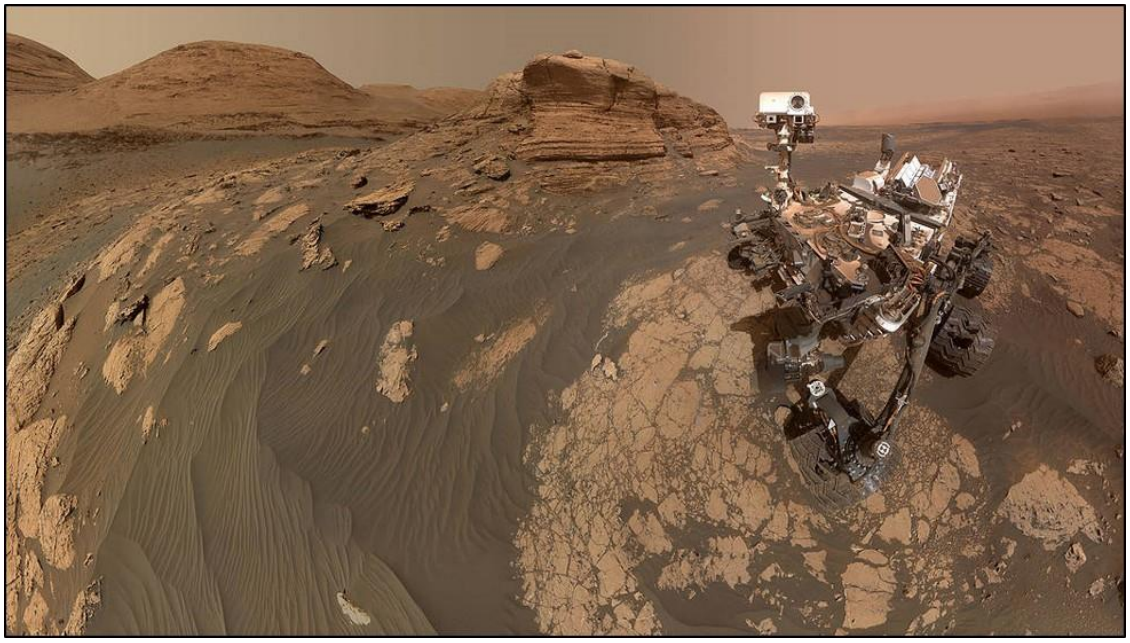

Figure 2.3: self-photograph of the Mars Science Laboratory Curiosity rover, in front of an outcrop ~ 6 m high. The panorama is made up from 60 images form the Mars Hand Lens Imager (MAHLI) camera and 11 images from the Mast Camera (Mastcam). Credit: NASA/JPL-Caltech/MSSS.

2.2. Martian climate and environment

The diversity of datasets returned from Mars has allowed scientists to gain a better understanding of its geological history. The geological history of Mars has been divided into different geological periods – just like the Earth. Bibring et al. (2006) proposed a classification based on the differential formation of minerals over Mars' history: the phyllosilicates found in the oldest terrains giving the 'phyllocian' period, the more recent sulfates giving the 'theiikian' period, and the even more recent ferric oxides giving the 'siderikian' period. However, the classification proposed by Scott and Carr, (1978) and Tanaka (1986), based on the intersection relationships between units and their dating by crater size-frequency distributions (Hartmann, 1977, 2005; Hartmann and Neukum, 2001; Ivanov, 2001; Neukum, 1983; Neukum et al., 2001; Platz et al., 2013), is more commonly used. Hence, this system is presented in Figure 2.4 and will be used throughout this manuscript. It divides martian geological history in three eras: the Noachian (4.1-3.7 Ga), Hesperian (3.7-3 Ga), and Amazonian (3.0 Ga to present).
One key point in the study of Mars is to understand the geological history of its liquid water, as it is essential for the life as we know it. Hence, in the scope of the search for extraterrestrial life or (organic components), all of the missions sent to Mars incorporate scientific instruments that are dedicated to investigations related to the current or past existence of liquid water. Therefore, understanding the global geological evolution of Mars is essential in order to understand the dynamic of water throughout its geological history. Hence, I briefly describe below the martian geological periods and the associated major events and environmental conditions.

The Pre-Noachian era (formation-4.1 Ga) is overall poorly understood, as geologic evidence from this period has almost completely been eroded or resurfaced (Carr and Head, 2010). During this period, Mars underwent differentiation into core/mantle/crust (e.g. Blichert-Toft et al., 1999; Foley et al., 2005; Kleine

et al., 2002; Nimmo and Kleine, 2007), volcanism may have been very active and quickly decreased in intensity (Carr and Head, 2010). The 'global dichotomy' formed from the Pre-Noachian to Early Hesperian (Carr, 2006; Frey, 2006; Irwin and Watters, 2010; McGill and Squyres, 1991; Nimmo and Tanaka, 2005; Watters et al., 2007). The 'global dichotomy' is the name given to the striking contract between the northern lowlands dominated by low-altitude plains, and the southern highlands dominated by higher-altitude plateaus, with an altitude difference of up to several kilometres (Figure 2.2; Frey et al., 1998). The martian crust is also thinner in the northern lowlands (~ 25 km thick in the lowlands, yet up to ~ 70 km thick in the highlands; Knapmeyer-Endrun et al., 2021; Neumann et al., 2004; Wieczorek and Zuber, 2004; Zuber, 2001). There is no consensus on the way the martian dichotomy formed. Some studies suggested the role of a mega-impact, leading to the formation of a large impact basin, now being the northern lowlands (Andrews-Hanna et al., 2008; Golabek et al., 2011; Leone et al., 2014; Marinova et al., 2008; Nimmo et al., 2008; Wilhelms and Squyres, 1984). Others suggested an internal origin for the dichotomy, linked with differential convecting modes between the highlands and the lowlands (Keller and Tackley, 2009; Neumann et al., 2004; Šrámek and Zhong, 2012; Zhong and Zuber, 2001), with a differential composition of the crust (Thiriet et al., 2018), or with a positive feedback between crustal growth and mantle melting (Bonnet Gibet et al., 2022).

Overall, little is known about the climate of the Pre-Noachian era. Several large impacts (e.g. creating the Chryse and Utopia basins; Figure 2.2) occurred during that period, which heated the surface of Mars and likely caused the release of volatiles in the atmosphere (Abramov and Mojzsis, 2016; Segura et al., 2002; Sleep and Zahnle, 1998). However, the environmental conditions between those catastrophic impacts is unknown (Carr and Head, 2010). The Pre-Noachian era ends with the formation of the Hellas impact basin, 4.1 to 3.8 Ga (Frey, 2008; Robbins et al., 2013; Tanaka and Leonard, 1995).

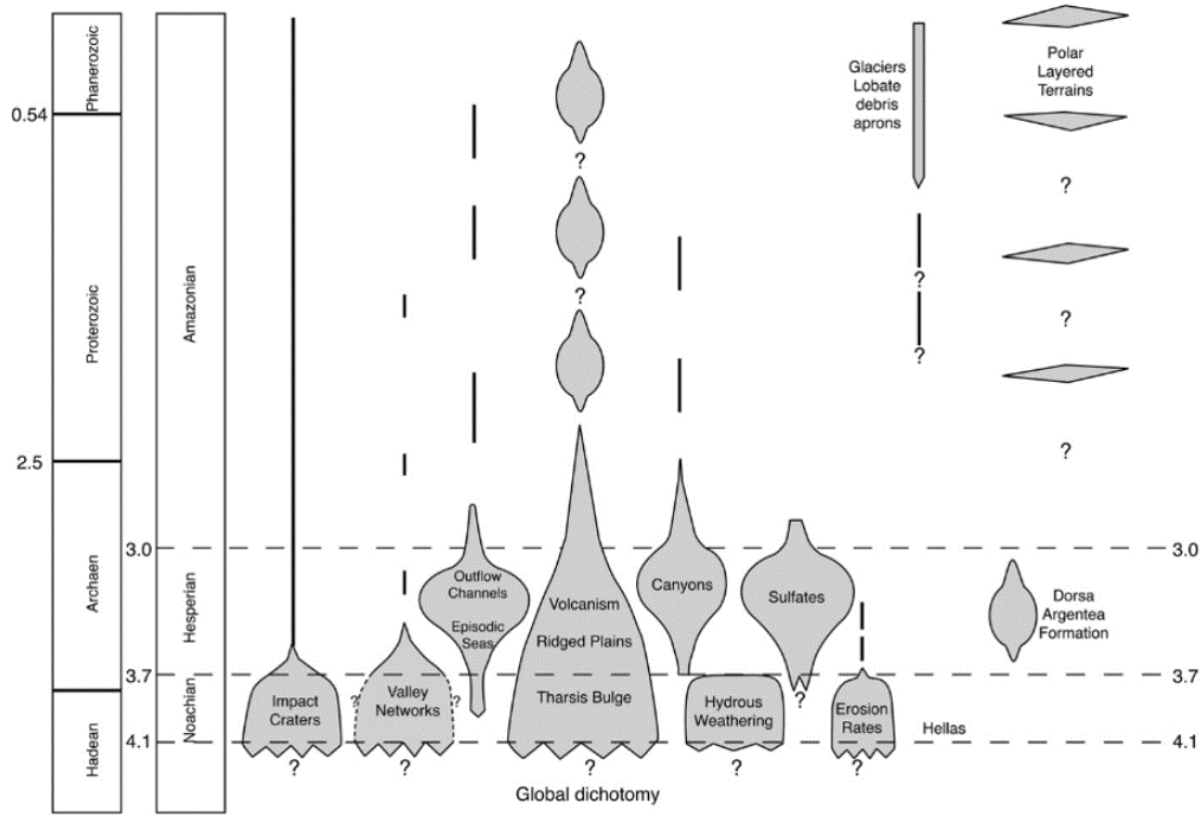

Figure 2.4: geological periods of Mars and associated geological activity, from (Carr and Head, 2010).

The Noachian era (4.1-3.7 Ga) is characterised by a high impact cratering rate compared to the following geological periods (Carr and Head, 2010; Hartmann, 2005; Hartmann and Neukum, 2001; Strom et al., 1992). Some of the largest impact basins formed during the Noachian, such as Argyre, Hellas or Isidis Planitiæ (Figure 2.2; Frey, 2008). Volcanism was also very active: the bulge of Tharsis, a large volcanic structure comprising the Tharsis Montes and Olympus Mons, may have started to build up at this time (Figure 2.2; Carr and Head, 2010; Johnson and Phillips, 2005; Williams et al., 2008).

The ubiquitous presence in Noachian terrains of minerals resulting from aqueous weathering (Bibring et al., 2006, 2005; Carter et al., 2023; Ehlmann et al., 2011; Loizeau et al., 2018; Poulet et al., 2005), paleolake evidence (Boatwright and Head, 2021, 2022; Goudge et al., 2016, 2021; Irwin, 2004; Irwin et al., 2005; Schon et al., 2012a; Stucky De Quay et al., 2020, 2021), valley networks (Figure 2.5a; Fassett and Head, 2008a, 2008b; Harrison and Grimm, 2005; Howard et al., 2005; Irwin and Howard, 2002; Seybold et al., 2018; Skinner et al., 2021; Wordsworth, 2016) or paleodeltas (Figure 2.5b; De Toffoli et al., 2021; Goudge et al., 2018; Wilson et al., 2021) suggest environmental conditions compatible with water precipitation and runoff (Hynek et al., 2010; Salese et al., 2020). It is still unknown for how long these conditions lasted, but martian valley profiles are not well-developed (e.g. Bahia et al., 2022; Grau Galofre et al., 2020a; Howard et al., 2005). This suggests that liquid water did not flow on Mars' surface during the whole Noachian era, but rather episodically (e.g. Ansan et al., 2008; Carr, 2006; Howard et al., 2005; Irwin and Howard, 2002). Some studies also hypothesised the existence of oceans within large basins during the Noachian (e.g. in Hellas Planitia or the northern lowlands; Baker et al., 1991; Carr and Head, 2010; Citron et al., 2018; Costard et al., 2017; Parker et al., 1993). However, the processes leading to a sustained wet and warm environment are still unknown (Carr and Head, 2010; Wordsworth, 2016), but atmospheric conditions (temperature, pressure and partial pressure of water vapour) are thought to have been conducive to stable liquid water during the Noachian (e.g. Boatwright and Head, 2021; Kite, 2019). In this regard, recent studies argue that valley networks could have formed under ice sheets, in a colder Noachian environment (e.g. Buffo et al., 2022; Cassanelli and Head, 2019; Fairén, 2010; Grau Galofre et al., 2020a, 2020b).

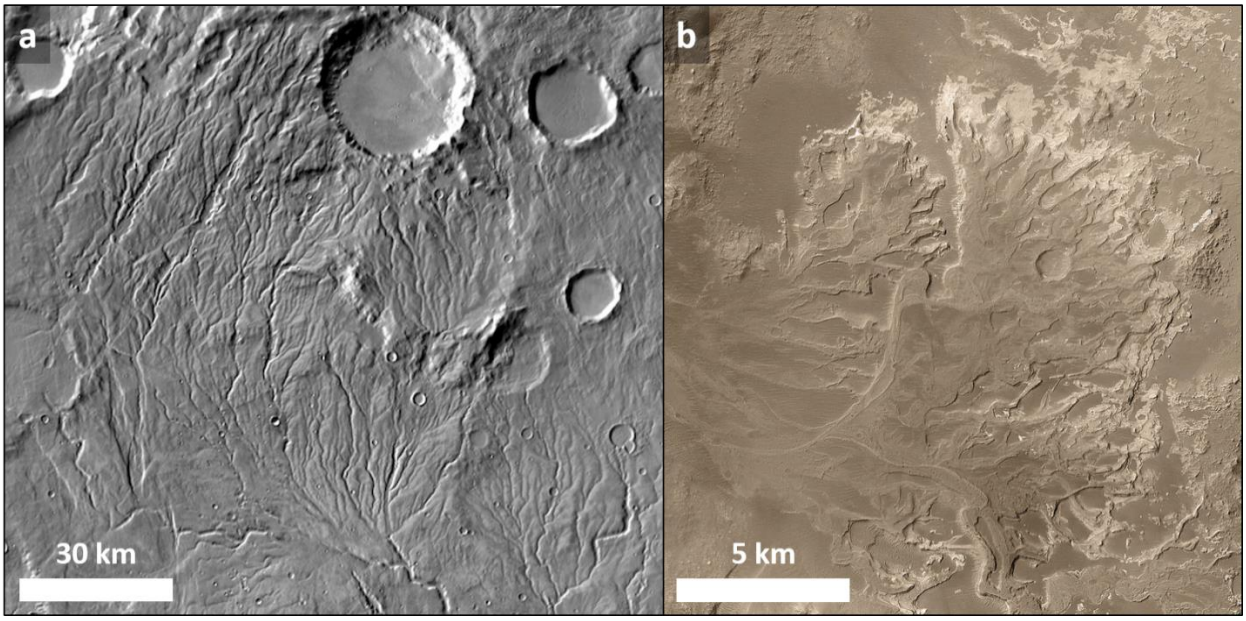

Figure 2.5: a. martian valley networks in Warrego Valles, imaged by Mariner 9 (41°35'S, 92°50' W; credit: NASA/JPL-Caltech/Arizona State University); b. the martian paleodelta Eberswalde, on a mosaic made from images of the Mars Orbiter Camera – Wide Angle mode (MOC-WA; 23°50' S, 33°35' W; credit: NASA/JPL/MSSS). North is up on both panels.

The Hesperian era (3.7-3 Ga) is seen as a transition period, between the wet environment of the Noachian and the cold and dry environment of the Amazonian (Carr and Head, 2010). It is notably characterised by the formation of Valles Marineris, by tectonic faulting radially from the Tharsis bulge (Figure 2.2; Blasius et al., 1977; Schultz, 1991; Sharp, 1973). Other geological processes may have participated in the deepening and lengthening of Valles Marineris (e.g. glacial erosion, Mège and Bourgeois, 2011; crustal stretching, Mège and Masson, 1996; erosion, Peulvast et al., 2001; localised subsidence, Schultz, 1998). Hesperian volcanism was sustained but episodic (Carr and Head, 2010): the Tharsis bulge continued to build up (Carr and Head, 2010; Johnson and Phillips, 2005; Williams et al., 2008), or started to build up in case of a late-formation hypothesis (Bouley et al., 2016). At the global scale, volcanism formed mainly shield volcano structures (e.g. Elysium Mons, Figure 2.2; Greeley and Spudis, 1981), and associated ridged plains, that are found notably around Tharsis (Scott and Tanaka, 1986; Watters and Maxwell, 1986), in Hellas Planitia or in the regions of Syrtis Major, Hesperia Planum or Malea Planum (Figure 2.2; Greeley and Guest, 1987). It was also suggested that Hesperian volcanic units could underlie, notably, parts of the northern plains (Fuller and Head, 2002).

The rate of valley formation diminished during the Hesperian (Fassett and Head, 2008b; Harrison and Grimm, 2005; Hynek et al., 2010), but sporadic evidence for Hesperian-age valley incision suggests episodic and local episodes of surface runoff (Fassett and Head, 2008b; Howard and Moore, 2011; Mangold et al., 2004b; Wilson et al., 2016). However, it is suggested that the runoff was caused by melting of snow, and not to liquid water precipitation (Fassett and Head, 2006, 2007, 2008b; Kamada et al., 2021; Wilson et al., 2016). Subsequently to the decrease in liquid water activity, aqueous alteration, common during the Noachian, occurred more rarely during the Hesperian and sulfates are the main mineral type found in Hesperian units (Bibring et al., 2006; Gendrin et al., 2005; Mangold et al., 2008; Murchie et al., 2009). The main liquid water activity during the Hesperian is represented by the formation of large outflow channels, resulting from the quick release of large volumes of water. The source for that water is proposed to be subsurface aquifers (Carr, 1979; Rodríguez et al., 2015a; Wilson et al., 2004) or lakes (Harrison and Chapman, 2008; Lucchitta et al., 1992; McCauley, 1978). These outflow channels are suggested to have formed large liquid water bodies (lakes/oceans), mostly in the northern plains and in the Hellas basin (Clifford and Parker, 2001; Mangold and Howard, 2013; Moore and Wilhelms, 2001; Parker et al., 1993; Warner et al., 2013). However, evidence is lacking to support this hypothesis (e.g. no detection of evaporites in the northern plains, Bibring et al., 2006; lack of explanation for the potential sink for that water, Carr and Head, 2010). Despite the scientific consensus being in favour of liquid water, a few studies suggest that the outflow channels could have been carved by low viscosity lava flows (Hopper and Leverington, 2014; Leverington, 2004, 2011). Other studies suggest that ice streams, i.e. rapidly-moving bodies of ice (hundreds of metres per year), could have carved the martian outflow channels (e.g. Lucchitta, 2001; Lucchitta et al., 1981). Moreover, alluvial fans have also been suggested to have formed during the Hesperian (e.g. Holo et al., 2021; Kite et al., 2017; Mangold et al., 2012; Wilson et al., 2021). They are conical-shaped bodies of accumulated sediment transported by liquid water, found on relatively flat surfaces at termini of confined channels. Hence, they also indicate flowing liquid water. Finally, it is thought that the polar water ice caps of the Hesperian were much bigger than the current ones, based on evidence that the Dorsa Argentea Formation is a remnant of that former polar ice cap (Butcher et al., 2016; Dickson and Head, 2006; Fastook et al., 2012; Head and Pratt, 2001). Overall, it suggests that the Hesperian saw a drastic climate change, between the wet Noachian environment, to a mostly dry and cold environment in the Amazonian, not suitable to liquid water stability (e.g. Carr and Head, 2010; Haberle et al., 2001; Skok et al., 2010).

The Amazonian era (3 Ga-present) is the current geological period of Mars. It is characterised by a general decrease in geological activity. Volcanism continued sporadically in the two main volcanic regions, the

Tharsis bulge and Elysium Mons, which kept building while depositing surrounding lava plains (e.g. Cassanelli and Head, 2018; Dohm et al., 2008; Pedersen et al., 2010; Pieterek et al., 2022; Plescia, 1990; Viviano et al., 2019). Some studies suggest that Mars could still be volcanically active today (Berman and Hartmann, 2002; Broquet and Andrews-Hanna, 2022; Edgett et al., 2010; Hauber et al., 2011a; Mangold et al., 2010).

Overall, ice is the major agent shaping the martian landscape during the Amazonian (Carr and Head, 2010). First, the obliquity of Mars (i.e. the angle between its rotation axis and the perpendicular to the ecliptic plane) is highly variable, from less than 10° to over 60° (Touma and Wisdom, 1993; Ward, 1973). During high-obliquity events, the Mean Annual Air Temperature (MAAT) is tens of degrees lower compared to the MAAT at the current obliquity. For instance, Schorghofer (2008) used climate modelling to show that MAAT would be below -90 °C at an obliquity of 60° - compared to the current -60 °C in the mid-latitudes (Martínez et al., 2017). Other orbital parameters than just the obliquity of the planet influence the MAAT, and the climatic response of a planet to these Milankovitch cycles is complex (e.g. Schorghofer, 2008). Generally, the combination of Milankovitch cycles – and notably the high-obliquity periods in the recent geological times – has caused numerous episodes of lower MAAT on Mars. During these 'high-obliquity events', the MAAT was low enough to cause the condensation of water ice in non-polar regions of Mars (e.g. Jakosky and Carr, 1985; Mellon and Jakosky, 1995; Mischna et al., 2003).

Consistently with climate model predictions, many studies conclude that subsurface water ice is common on Mars, notably in the mid-latitudes – and the state of martian ground ice is detailed further in Section 2.2. Concerning liquid water activity, few outflow channels and valley networks are reported to have formed during the Amazonian (Dickson et al., 2009; Fassett et al., 2010; Rodríguez et al., 2014, 2015b; Wilson et al., 2016). Some mass-wasting features are currently active on Mars, such as gullies (Dundas et al., 2010; Malin and Edgett, 2000; Pasquon et al., 2016, 2019; Raack et al., 2015, 2020), Recurring Slope Lineae (McEwen et al., 2011, 2021; Ojha et al., 2014, 2015; Stillman and Grimm, 2018), or slope streaks (Schorghofer et al., 2002, 2007; Schorghofer and King, 2011). Liquid water has been invoked to explain this activity (e.g. Malin and Edgett, 2000; McEwen et al., 2011; Ojha et al., 2014, 2015), especially when considering the morphological similarities with water-carved terrestrial features like gullies. However, evidence then accumulated in favour of other processes, like dry mass-wasting (for RSL: Dundas, 2020a; McEwen et al., 2021; Schmidt et al., 2017; Vincendon et al., 2019; and slope streaks: Chuang et al., 2007; Dundas, 2020b) or condensation/sublimation of CO_2 ice (for gullies; Raack et al., 2015, 2020; Vincendon, 2015). Despite the absence of liquid water at the surface, recent studies observed highly-reflective layers at the base of the southern polar cap that they attribute to subglacial water bodies (Khuller and Plaut, 2021; Lauro et al., 2020; Orosei et al., 2018; Sulcanese et al., 2023). However, other studies show that different material could form these highly-reflective layers: saline ice (Bierson et al., 2021), high-conductivity minerals like clays (Bierson et al., 2021; Smith et al., 2021), or even classical martian volcanic terrains (Grima et al., 2022).

At the present day the martian climate is cold and dry. The average temperature is around -60°C, but varies from around -150°C to +20°C (e.g. Hess et al., 1977; Martínez et al., 2017; Munguira et al., 2023; Spanovich et al., 2006). Its atmosphere is thin, at around 6 millibars (e.g. Bridger and Murphy, 1998; Hess et al., 1980, 1977; Martínez et al., 2017; Sánchez-Lavega et al., 2023; Spiga et al., 2007), and water vapour abundance in the atmosphere is also low (< 100 precipitable microns; e.g. Jakosky, 1985; Jakosky and Farmer, 1982; Smith, 2002; Sprague et al., 1996). Such temperature/pressure conditions mean that liquid water is not stable at the surface of Mars (Jakosky, 1985; Jakosky and Farmer, 1982; Jakosky and Phillips, 2001; Richardson, 2002). Hence, surficial activity of liquid water is considered to be unlikely and, if occurring at all, must be a marginal phenomenon (e.g. Carr and Head, 2010).

Overall, geological activity is subdued during the Amazonian, compared to the other epochs. One notable activity is due to CO_2, which constitutes most of the martian atmosphere (~ 96%; e.g. Encrenaz et al., 1991; Trainer et al., 2019) and a seasonal cycle of CO_2 condensation/sublimation is currently active on Mars (James et al., 1992; James and North, 1982; Kahre and Haberle, 2010; Piqueux et al., 2015). Hence, seasonal CO_2 ice deposits during winter, alternatively in each hemisphere (e.g. Piqueux et al., 2015). These seasonal ices extend down to ~ 50° of latitude, as a continuous surficial layer of CO_2 frost. Wind also plays an important geomorphological role during the Amazonian, as it mobilises dune fields (e.g. Hayward et al., 2007; Silvestro et al., 2010) and generates wind-blown morphologies (e.g. yardangs, Ward, 1979; Ward et al., 1985; Transverse Aeolian Ridges, Berman et al., 2011; Geissler, 2014; Zimbelman, 2010).
In addition, since water ice is present in the ground of the mid-latitudes, many studies suggest that processes similar to terrestrial periglacial ones could occur (e.g. Costard and Kargel, 1995; Lucchitta, 1981; Mangold et al., 2004a; Mangold, 2005; Mellon, 1997; Orgel et al., 2019; Séjourné et al., 2011, 2019; Soare et al., 2018). Notably, some suggest the involvement of near-surface liquid water during the Amazonian (e.g. Costard et al., 2016; Seibert and Kargel, 2001; Soare et al., 2014a). Therefore, as surficial liquid water is unlikely to be found at the surface, those potential periglacial processes could represent our best opportunities to seek for current liquid water on Mars. I hence detail in the following sections the evidence we have for the presence of ground ice (Section 2.3.), as well as the associated landforms (Section 2.4.).

2.3. Martian ground ice

As mentioned above, ground water ice is present on Mars, and nearly ubiquitous at the mid-to high-latitudes. Its presence can be attested by numerous direct observations or indirect evidence.

2.3.1. Direct observations

The first direct observations of ground ice were made by the Phoenix lander (Mellon et al., 2009a; Smith et al., 2009), which operated on a terrain covered in thermal-contraction polygons (Smith et al., 2009). Phoenix dug trenches which exposed ground ice in the form of pore ice (~ 90% of observed ice) and excess ice (~ 10% of observed ice; Figure 2.6a; Mellon et al., 2009a). Excess ice was found as an ice table as shallow as 5 to 18 centimetres deep (Smith et al., 2009).

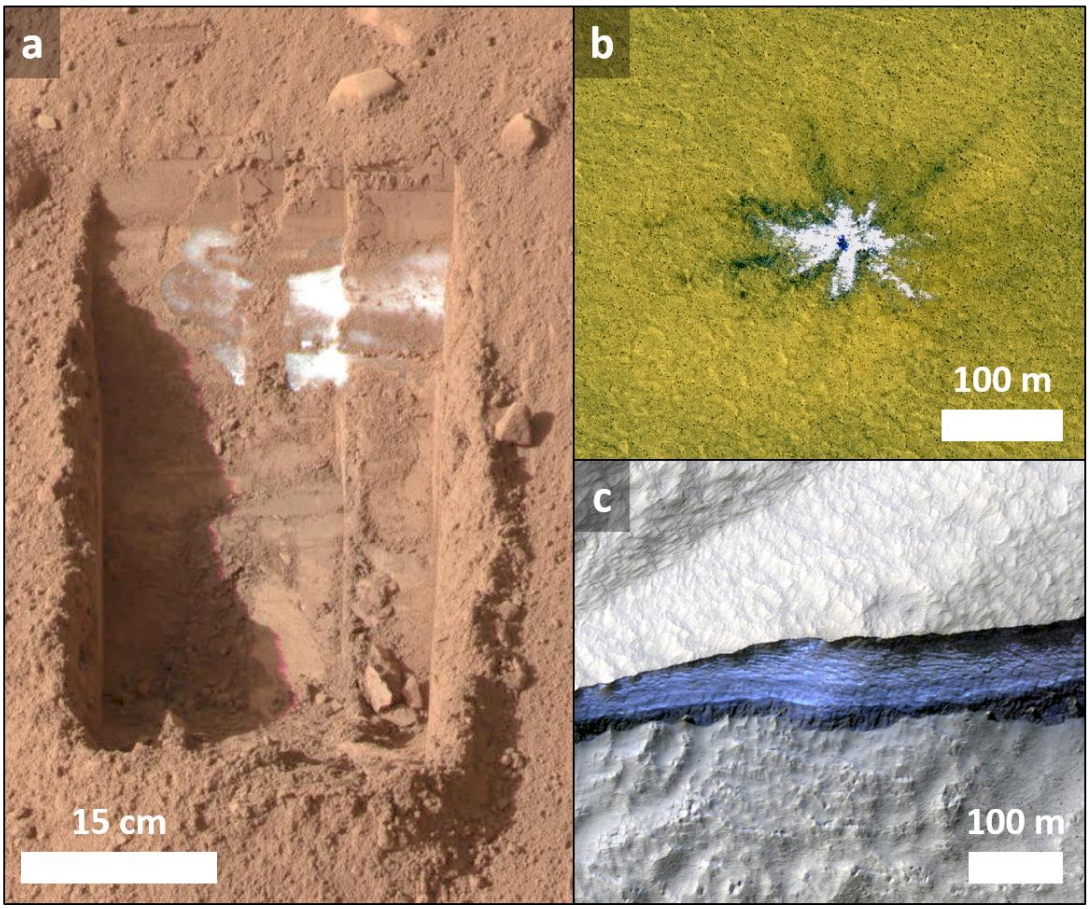

Figure 2.6: direct evidence of martian ground ice ***a.*** *in a trench dug by the Phoenix lander. white and translucent patches within the trench are water ice (credit: NASA/JPL-Caltech/University of Arizona/Texas A&M University);* ***b.*** *ice excavated by an impact crater. The white colour highlights water ice (HiRISE image ESP_017868_2440 in false colours; credit: NASA/JPL/University of Arizona);* ***c.*** *a pole-facing ice scarp. The blue colour highlights water ice (HiRISE image ESP_040772_1215 in false colours; credit: NASA/JPL/University of Arizona). North is up on panels b. and c.*

The Viking Lander 2 imaged diurnal frost formation at its landing site (Svitek and Murray, 1990). The Phoenix team also observed that H_2O was condensing and sublimating on the surface on a daily basis in late summer (Smith et al., 2009; Whiteway et al., 2009), as well as the sublimation of the ice exposed in the trenches within a few tens of sols (Smith et al., 2009). It shows that H_2O is highly interactive with the first tens of centimetres of the ground (Mellon et al., 2009b; Smith et al., 2009). Hence, they explain the pore ice formation by water vapour diffusion and condensation in place within the sediment (Cull et al., 2010a; Smith et al., 2009; Whiteway et al., 2009). However, they explain the formation of excess ice by terrestrial-like ice segregation processes, and subsequent formation of ice lenses and/or needle ice (e.g. Mellon et al., 2009a; Sizemore et al., 2015).

Byrne et al., (2009) analysed newly-formed impact craters with HiRISE imagery. They identified ice that was excavated by the impacts at the mid-latitudes (Figure 2.6b), with visible and near-infrared spectra indicative of water ice. Subsequent studies identified more of these ice-exposing craters (Dundas et al., 2014, 2021, 2023), at latitudes as low as 35° (Dundas et al., 2023). These studies also report the

disappearance of that ice within months (Byrne et al., 2009; Dundas et al., 2014) to years (Dundas et al., 2014), which is consistent with the expected sublimation rate of water ice (Dundas and Byrne, 2010). The spectral information and brightness of these ice blocks and the fact that they remain visible for months indicates nearly-pure ice rather than ice-cemented ground (Byrne et al., 2009; Dundas et al., 2014; Dundas and Byrne, 2010). Moreover, differences in terms of content of excavated ice between clustered craters suggests significant local differences in ice content (Dundas et al., 2014). This observation is more consistent with localised formation of ice lenses rather than a regional unit of massive ice, suggesting the occurrence of ice segregation in those locations (Dundas et al., 2014). Moreover, a more recent study on a single large crater (150 m in diameter) suggests the presence of a regional layer of ice at least several meters thick at low latitudes. It is interpreted as the remnant of a thicker layer deposited as snow and frost during high-obliquity periods (Dundas et al., 2023). In addition, this study suggests the presence of ice-cemented ground overlaying that ice layer.

Recently, high-resolution images allowed the observation of ice scarps in the high mid-latitudes, i.e. scarps constituted mostly of water ice (Figure 2.6c; Dundas et al., 2018, 2021). The scarps show layers of ice from a few meters below the surface, and extending downward to form layers up to ~ 100 m thick in some places (Dundas et al., 2018). Those ice layers are thought to have deposited from the atmosphere during high-obliquity excursions, and to be currently retreating due to ice sublimation (Dundas et al., 2018). Dundas et al. (2021) show that the ice scarps are found between 50° and 61° of latitude, near Milankovič crater in the northern hemisphere and southeast of Hellas Planitia in the southern hemisphere, suggesting that those regions may concentrate particularly thick and/or clean massive bodies of ice.

2.3.2. Indirect evidence

The presence of subsurface water ice can also be inferred from indirect sources: radar data, neutron spectrometry, and also from global climate models and from surface geomorphology. Orbital radars (MARSIS and SHARAD) have allowed the identification of highly-reflective subsurface layers in the mid-latitudes, that are interpreted as ice-rich deposits. Global MARSIS data (penetration depth of 5 km) also allowed the identification of nearly-global presence of subsurface water ice based on the inferred dielectric properties of the ground (first tens of metres below the surface; Mouginot et al., 2010). Data from SHARAD (penetration depth of 1 km) also suggested the presence of subsurface water ice layers in Arcadia and Utopia Planitiæ, with thicknesses of tens of meters (e.g. Bramson et al., 2015; Stuurman et al., 2016). These deposits are thought to have an ice content between 50% and 100%. These interpretations support the geomorphological evidence brought by the direct observations of ground ice mentioned above (ice at the Phoenix landing site, ice excavated by impacts and ice scarps). Moreover, the spectrometers GRS and FREND produced global maps of hydrogen content in the near subsurface of Mars (< 1 m deep). These instruments analyse the gamma rays and neutrons emitted by the martian surface interacting with cosmic rays, which allows to infer the presence of elements in the near subsurface (Mitrofanov et al., 2018; Saunders et al., 2004). As the hydrogen element is mostly present in H_2O molecules, measurements of hydrogen content by GRS and FREND allow us to infer the water or water ice content in the close subsurface of the planet (Mitrofanov et al., 2018; Saunders et al., 2004).

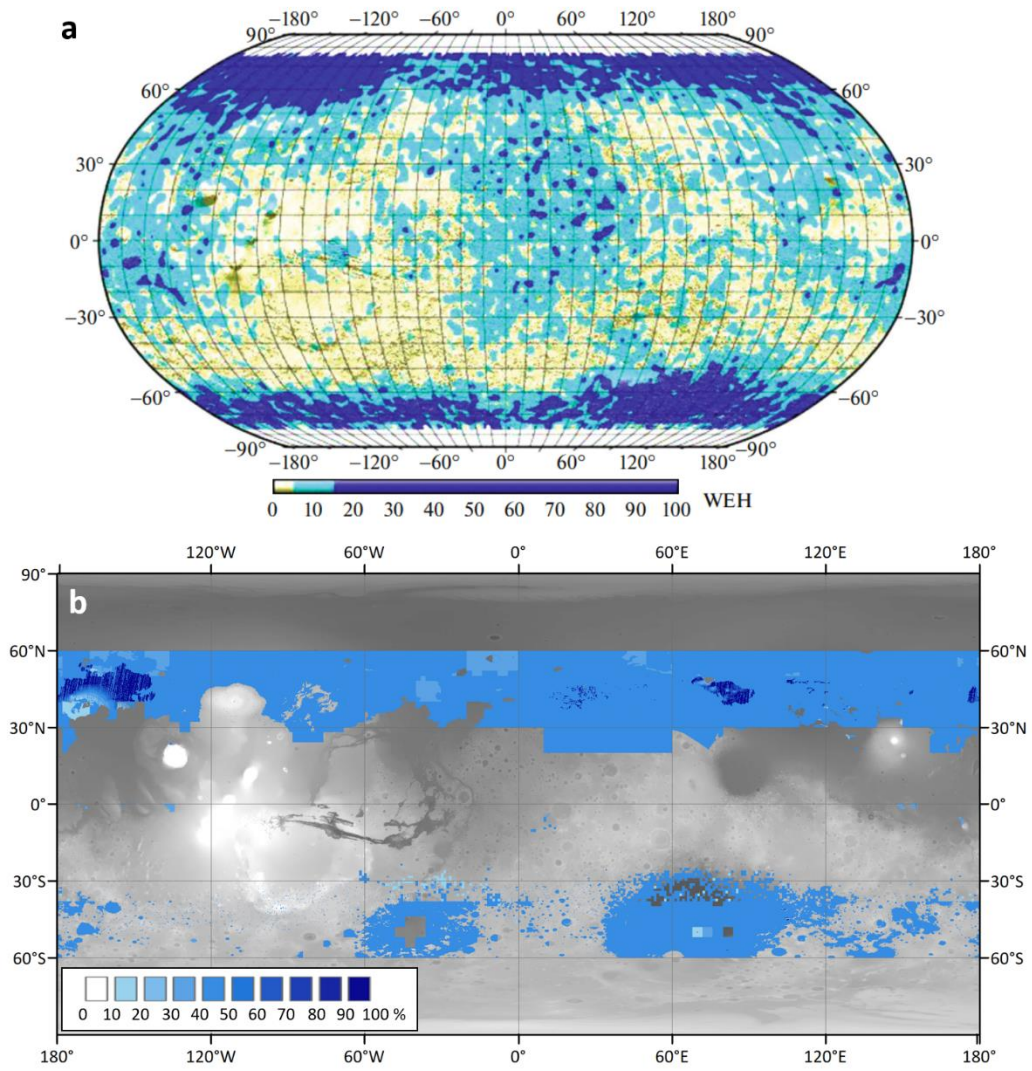

*Figure 2.7: global maps of **a.** the water-equivalent hydrogen content (WEH) by the Fine Resolution Epithermal Neutron Spectrometer (onboard the ESA ExoMars Trace Gas Orbiter; from Malakhov et al., 2020); **b.** the subsurface water ice consistency over 5 m deep between 60°S and 60°N, by the Subsurface Water Ice Mapper project (credit: SWIM Team/NASA/JPL/PSI) Background is the global DEM from Mars Orbiter Laser Altimeter data (credit: MOLA Science Team).*

The GRS and FREND maps show that the hydrogen content is consistent with a significant ground ice content, above ~ 50° latitude in both hemispheres (Figure 2.7a; Boynton et al., 2002; Feldman, 2004; Feldman et al., 2011; Jakosky et al., 2005; Kuzmin et al., 2004; Malakhov et al., 2020; Mitrofanov et al., 2004, 2002; Pathare et al., 2018). In addition, the Subsurface Water Ice Mapper project (SWIM; Morgan et al., 2021) aims at combining various datasets (geomorphology, radar dielectric estimates and surface power, presence of hydrogen from neutron spectrometry, thermal data) to produce global maps of ice consistency. Their maps show where those input data consistently indicate the presence of subsurface water ice at various depths. Their results suggest that water ice is present at shallow depths (first few metres) in the northern mid-latitudes and in some places in the southern mid-latitudes (Figure 2.7b; Morgan et al., 2021). Overall, the deposition of water ice in the mid-latitudes during – or subsequent to – high-obliquity events is also

supported by global climate models (e.g. Jakosky and Carr, 1985; Levrard et al., 2004, 2007; Mellon and Jakosky, 1995; Mischna et al., 2003), and ground ice stability is supported by ground temperature models (e.g. Bramson et al., 2015, 2017; Mellon and Jakosky, 1993, 1995; Piqueux et al., 2019). Some models also predict the formation of layers of excess ground ice, either at depth or close to the subsurface in the mid-latitudes (Fisher et al., 2022). Finally, geomorphological evidence indicates the presence of subsurface ground ice. I review these landforms in the following section.

2.4. Ground-ice-related landforms on Mars

Mars hosts numerous landforms that share geomorphological characteristics similar to terrestrial landforms associated with aggradational ground ice. First, morphologies called 'Viscous-Flow Features' (VFFs) were observed in the mid-latitudes (Milliken, 2003; Orgel et al., 2019; Ramsdale et al., 2019; Séjourné et al., 2019; Squyres, 1978, 1979). VFFs is an umbrella term comprising 'lineated valley fill', 'lobate debris apron' and 'concentric crater fill'. All of those landforms exhibit surficial lineated features that suggest a flowing viscous material, and as their surface is constituted of lithic material they were compared early with terrestrial cold-based, debris-covered glaciers (Colaprete and Jakosky, 1998; Hargitai, 2014; Head et al., 2005, 2010; Head and Marchant, 2003; Levy et al., 2014; Pierce and Crown, 2003). Lineated valley fills are found infilling valleys, and are typically hundreds of kilometres long and tens of kilometres wide. They exhibit surficial lineations parallel to their elongation, which resemble terrestrial medial moraine, and thus suggest a downslope flow (Figure 2.8a; Baker et al., 2010; Head et al., 2006; Kress and Head, 2008; Morgan et al., 2009). Lobate debris aprons are found on slopes, originating from a steep headwall, and spreading laterally at the slope foot with a lobate terminal shape (Figure 2.8b; Baker et al., 2010; Fastook et al., 2014; Li et al., 2005; Mangold, 2003). Smaller than the lineated valley fills (~ tens of kilometres), they have been compared to terrestrial piedmont glaciers (Head et al., 2010; Milkovich et al., 2006). Concentric crater fills are found infilling mid-latitude craters (e.g. Pearce et al., 2011). They exhibit concentric ridges that suggest a radial flow toward the centre of craters (Figure 2.9; Dickson et al., 2010; Fastook et al., 2014; Levy et al., 2010a, 2009b). Moreover, radar measurements show that LDAs are pure water ice covered in lithic debris (Degenhardt, 2003; Parsons and Holt, 2016; Petersen et al., 2018; Plaut et al., 2009). Overall, VFFs are glacial and not periglacial features. However, they are bodies of ice covered in lithic debris; hence I classified them as ground-ice features. Moreover, their surface exhibits patterned ground that are indicative of close-subsurface water ice: the 'brain terrains' (Figure 2.10c; first reported on MOC images, e.g. Malin and Edgett, 2001; Mangold, 2003). They are fields of small regularly patterned somewhat sinuous mounds (10-20 m wide, 10-100 m long; 'closed-cell' morphology) or depressions ('open-cell' morphology). The closed-cell morphology is thought to have an ice core, and the open-cell morphology is thought to be depressions resulting from the degradation of those ice cores (e.g. Levy et al., 2009b).

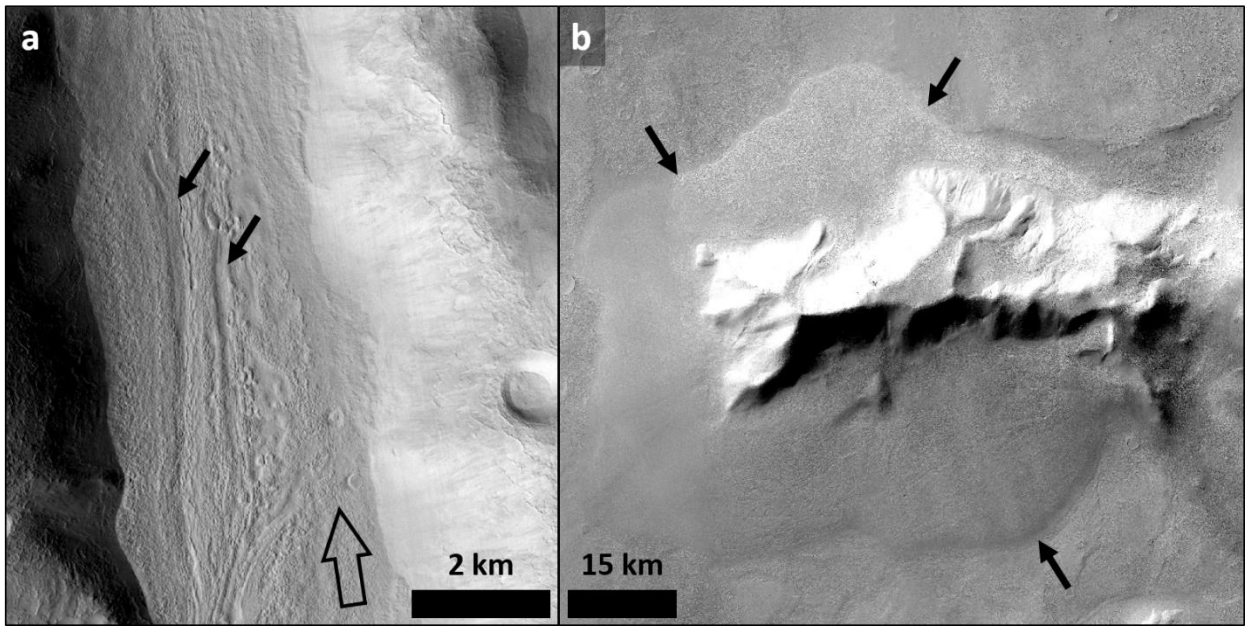

*Figure 2.8: Viscous Flow Features (VFFs): **a.** lineated valley fill on the global Context Camera mosaic (33°28' N, 68°38' E). Black arrows point to surface lineations, and the hollow arrow indicates the inferred flow direction; **b.** lobate debris aprons around a summit on the global Context Camera mosaic (44°50' S, 105°00' E; credit: NASA/JPL/MSSS/The Murray Lab). Black arrows point to the terminus of the lobate debris aprons. North is up on both panels.*

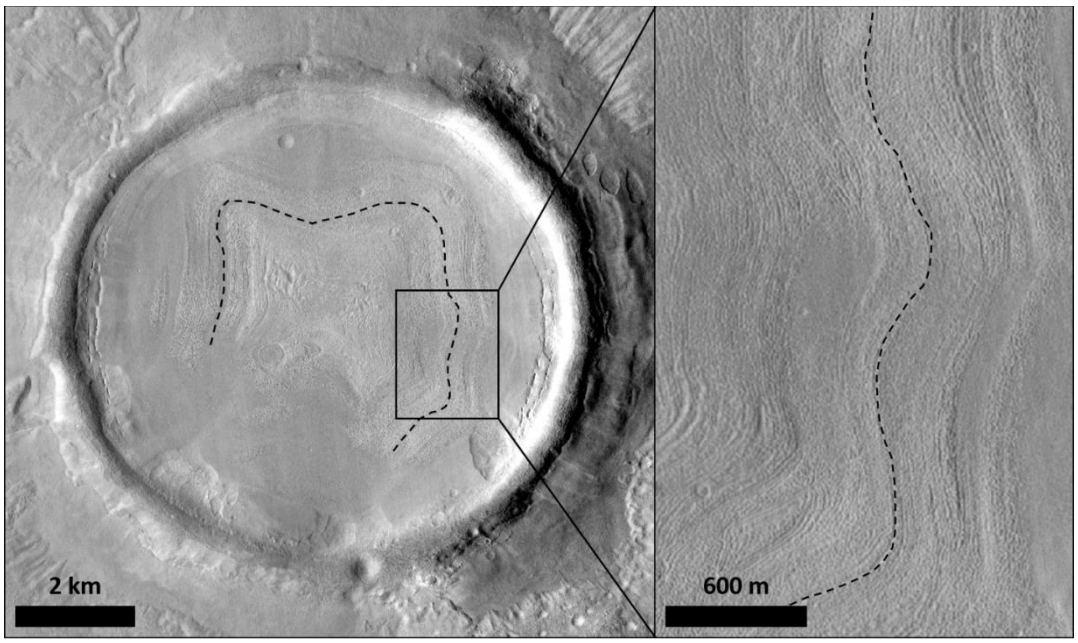

Figure 2.9: concentric crater fill on the global Context Camera mosaic (40°48' N, 99°30' E; credit: NASA/JPL/MSSS/The Murray Lab). The dashed line follows a concentric lineation. North is up.

Polygonal patterns, which are morphologies indicative of ground ice on Earth (Section 1.3.1.) are common in the martian mid-latitudes (Section 2.5.; Figure 2.10c; e.g. Levy et al., 2009a, 2009c, 2010b; Mangold, 2005; Mangold et al., 2004a; Orgel et al., 2019; Séjourné et al., 2011, 2019; Soare et al., 2018). They are generally accepted to be thermal-contraction polygons expressed in ice-cemented ground (Mangold et al., 2004a; Mellon, 1997). This hypothesis is supported by the spatial correspondence between their distribution and areas of high surficial ice content detected by the spectrometers GRS and now also FREND (Section 2.3.; Mangold et al., 2004a). I detail further these morphologies in Section 2.5.

Some studies have also identified mounds in the martian mid-latitudes that exhibit morphological characteristics similar to terrestrial pingos (Figure 2.10a) and collapsed pingos (Figure 2.10b; Section 1.3.; Burr et al., 2005, 2009; de Pablo and Komatsu, 2009; Dundas and McEwen, 2010; Soare et al., 2013a, 2013b, 2014b, 2020). If their interpretation is correct, it indicates that ice intrusion could have occurred in the mid-latitudes.

Another typical martian feature interpreted as ice-rich is the 'latitude-dependent mantle' (LDM). It is a series of Amazonian layers (as young as a few million years from Kostama et al., 2006; Levy et al., 2009c; Schon et al., 2012a), up to 100 m thick (Conway and Balme, 2014; Dundas et al., 2018, 2021), thought to be constituted of a mix of dust and ice (Head et al., 2003; Kreslavsky and Head, 2002), and that cover nearly-ubiquitously the martian mid-latitudes (approximately 23% of the surface of the planet from Kreslavsky and Head, 2002). It is thought that ice was deposited with dust by condensation from the atmosphere in many successive layers, and over time during multiple high-obliquity events (Dickson et al., 2015; Kostama et al., 2006; Levy et al., 2009c). The high ice content of those layers is suggested by surficial morphologies typical of terrestrial periglacial areas (e.g. thermal-contraction polygons; Levy et al., 2010b), and can be directly observed on ice-excavating impact craters and ice scarps (Section 2.3.; Dundas et al., 2018, 2021).

Only a few potential degradational periglacial landforms exist on Mars. Except for the closed-cells brain terrains, the most common features are called 'scalloped depressions'. They are scalloped-shaped depressions, up to a few kilometres wide and to tens of metres deep (Figure 2.11a; Costard and Kargel, 1995; Morgenstern et al., 2007; Séjourné et al., 2011, 2012; Soare et al., 2008). They typically show a steep pole-facing side and a gentle equator-facing side, which suggests insolation-driven degradation (Dundas et al., 2015; Séjourné et al., 2011, 2012; Ulrich et al., 2010). Their floor is covered in thermal-contraction polygons (e.g. Séjourné et al., 2011, 2012). Therefore, they are interpreted as thermokarst formed by sublimation of excess ground ice (Costard and Kargel, 1995; Dundas et al., 2015; Seibert and Kargel, 2001; Séjourné et al., 2011; Soare et al., 2008). In addition, some mid-latitude craters show depressions that are expanding radially from the crater (Figure 2.11b). These depressions are similar to scalloped depressions in terms of dimensions, and also host thermal-contraction polygons (Figure 2.11b). Hence, these 'expanded craters' are also thought to be thermokarstic landforms (e.g. Viola et al., 2015; Viola and McEwen, 2018).

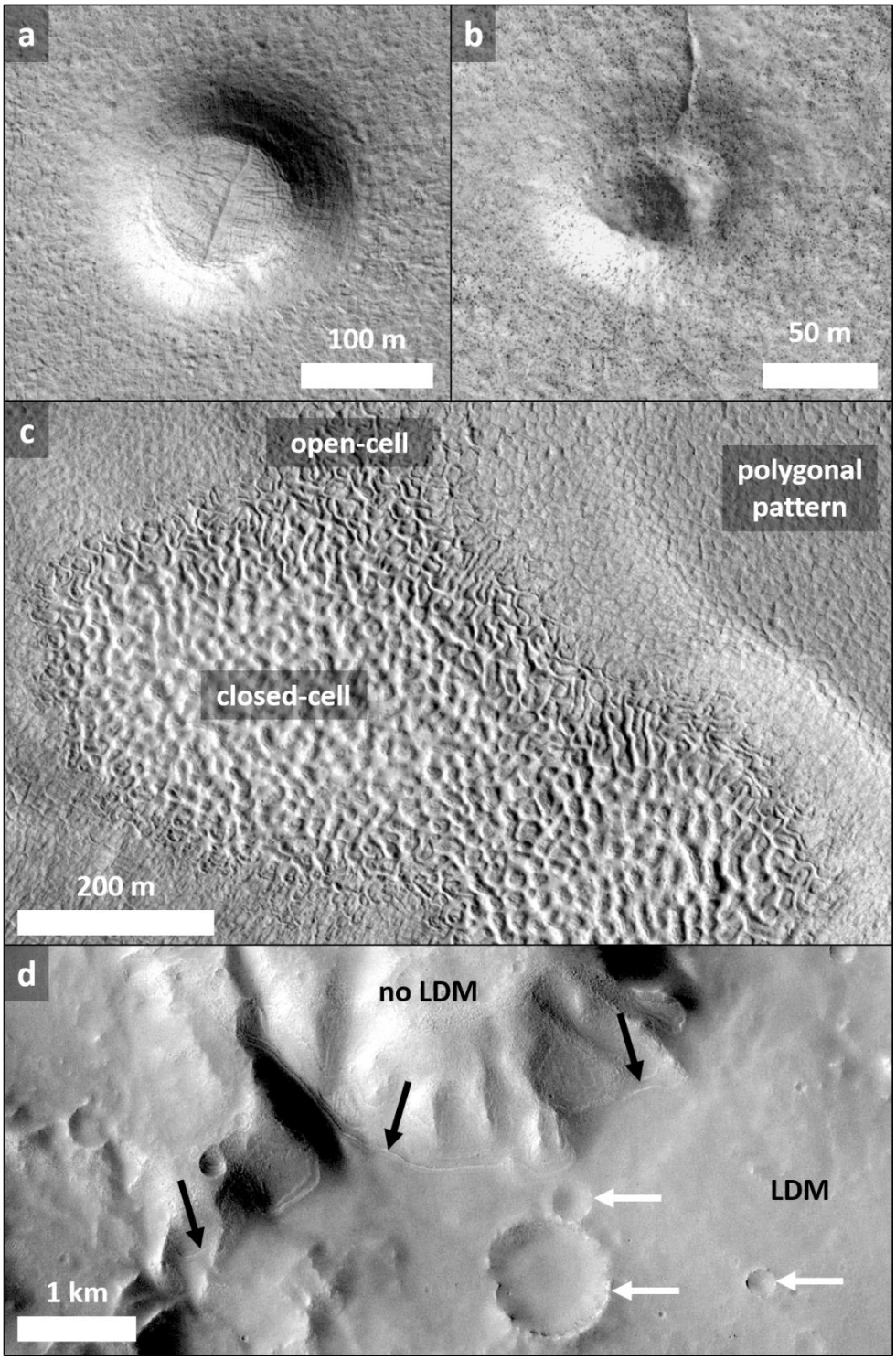

Figure 2.10: ***a.*** *potential pingo on HiRISE image PSP_005973_2200;* ***b.*** *potential collapsed pingo on HiRISE image PSP_006856_2215;* ***c.*** *closed-cell and open-cell morphologies of brain terrain on HiRISE image PSP_002175_2210 (credit: NASA/JPL/University of Arizona);* ***d.*** *Latitude-Dependent Mantle on the global Context Camera mosaic (35°06' S, 173°47' W; credit: NASA/JPL/MSSS/The Murray Lab). Black arrows point to the mantling boundary, and white arrows point to craters covered by the LDM. North is up on all panels.*

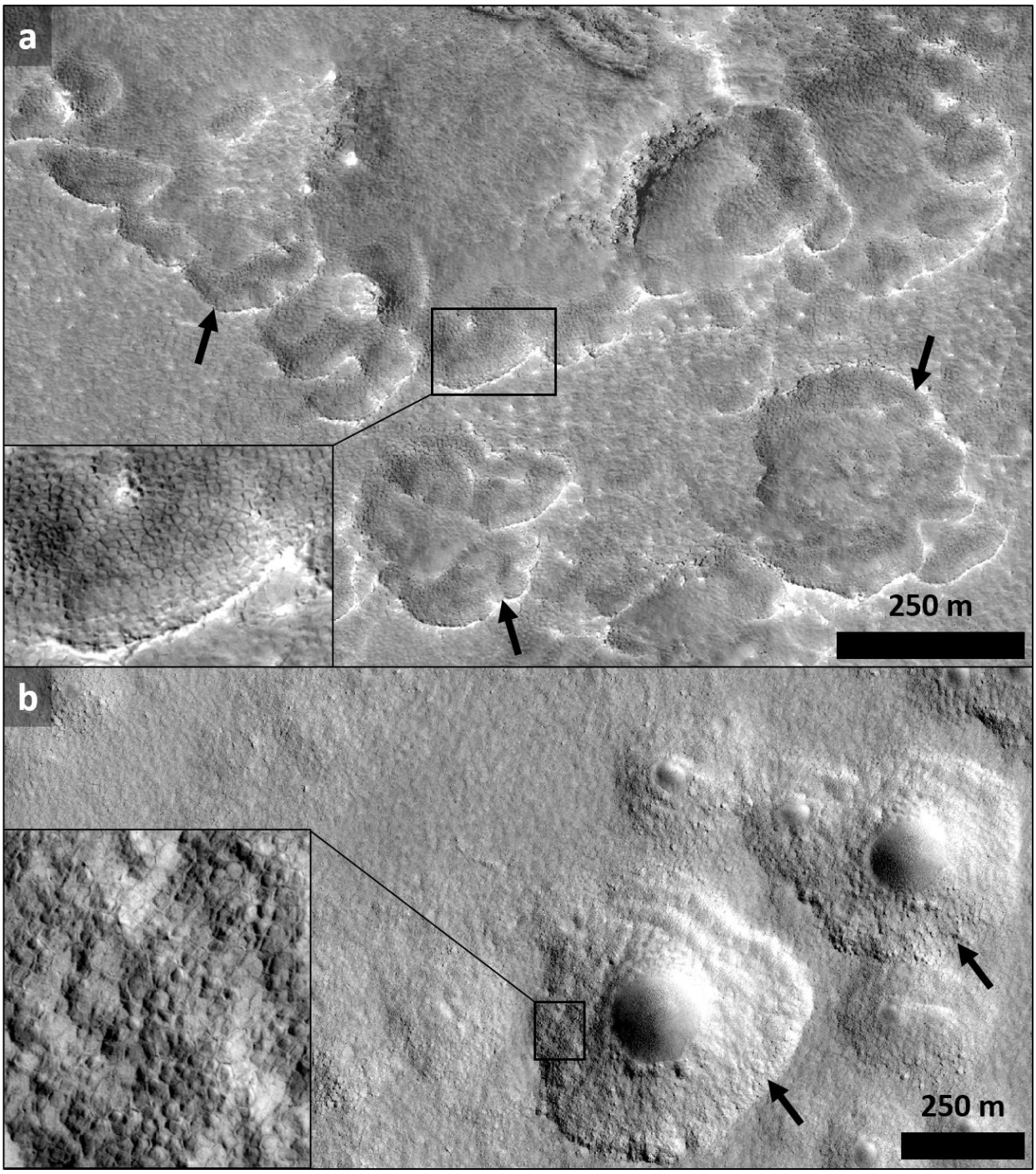

Figure 2.11: ***a.*** *cluster of scalloped depressions on HiRISE image ESP_044977_2270. Three scalloped depression examples are pointed out by black arrows. The zoomed panel shows polygons within a scalloped depression;* ***b.*** *cluster of expanded craters on HiRISE image ESP_028411_2330. Two expanded crater examples are pointed out by black arrows. The zoomed panel shows polygons within an expanded crater. North is up on both panels. HiRISE image credits: NASA/JPL/University of Arizona.*

2.5. Introduction to martian thermal-contraction polygons

2.5.1. Polygon types, formation and distribution on Mars

Mars hosts polygonal patterns of various dimensions: large-scale polygons with networks that extensively cover entire regions (up to several kilometres in diameter; e.g. Hiesinger and Head, 2000; McGill and Hills, 1992; Pechmann, 1980); medium-scale polygons (in the order of magnitude of a hundred metres in diameter; e.g. Mangold, 2005; Mangold et al., 2004a); and small-scale polygons (≤ 25 m in diameter; e.g. Levy et al., 2009a; Mangold, 2005; Mellon, 1997; Seibert and Kargel, 2001). Large-scale polygons are thought to have formed from tectonic stresses (e.g. Hiesinger and Head, 2000; Pechmann, 1980). Medium-scale polygons are thought to have formed similarly to terrestrial thermal-contraction polygons, and their larger dimensions were suggested to be due to a deep penetration of the thermal wave during past periods of sustained cold climate (Mangold, 2005; Mangold et al., 2004a).

Small-scale polygons are observed on HiRISE images (25-50 cm/pixel) to be common in the northern and southern mid-latitudes (Figure 2.12, from Levy et al., 2009a; see also Levy et al., 2010b; Mangold, 2005; Mangold et al., 2004a). Moreover, they are spatially correlated to the presence of surficial water ice detected by neutron spectrometers GRS and FREND (for spatial correlation with GRS, see Mangold et al., 2004a). Finally, i*n-situ* observation of ground ice by the Phoenix lander were done on a terrain hosting such small-scale polygons (Mellon et al., 2009b; Smith et al., 2009). Therefore, these small-scale polygons are thought to be thermal-contraction polygons (Section 2.4.) – which was already suggested since their first observations by the Viking orbiters and at the Viking 2 landing site, and validated by thermal stress modelling (Mellon, 1997). Several studies suggested that they are geologically recent (a few million years at most; Kostama et al., 2006; Levy et al., 2009a, 2010b; Mangold, 2005; Mangold et al., 2004a; Schon et al., 2012b; Séjourné et al., 2011, 2019). They are thought to form on the ice-rich units formed during the Amazonian by condensation of atmospheric water vapour (Section 2.2.).

A particularity of those small-scale thermal-contraction polygons, compared to the medium-scale ones, is that they exhibit varying morphologies: flat-centred (FCPs), low-centred (LCPs) and high-centred polygons (HCPs) (Figure 2.13). Such morphologies are reminiscent of the terrestrial processes forming ice-wedge polygons that are flat-centred, then low-centred and high-centred. They also have similar dimensions (≤ 25 m in diameter; Section 1.3.).

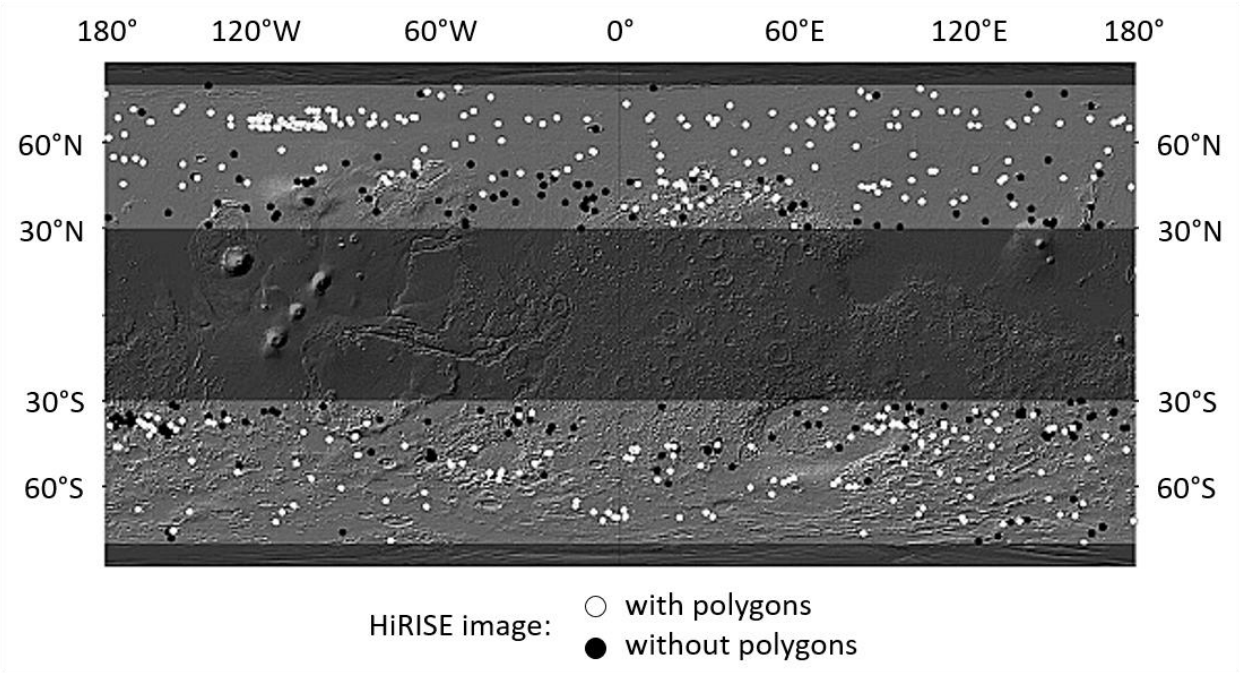

Figure 2.12: global distribution of small-scale polygons (≤ 25 m in diameter) on 823 HiRISE images (25-50 cm/pixel). HiRISE images with polygons are indicated by white circles, HiRISE images with no polygons are indicated by black circles. Modified from Levy et al. (2009a).

2.5.2. Thermal-contraction polygons and martian climate

As martian small-scale polygons are thought to form from thermal-contraction of ice-cemented ground, they have been associated with geologically recent (last few million years) occurrence of periglacial conditions in the mid-latitudes (e.g. Levy et al., 2009a, 2010b; Mangold, 2005; Mangold et al., 2004a; Mellon, 1997; Orgel et al., 2019; Séjourné et al., 2011, 2019; Soare et al., 2018). This is consistent with our knowledge of the Amazonian climate, i.e. cold conditions with strong seasonal and diurnal temperature gradients (Section 2.2.; e.g. Hess et al., 1977; Martínez et al., 2017; Munguira et al., 2023; Spanovich et al., 2006) that are conducive to thermal contraction of ground ice. Several studies suggested that they could indicate activity of liquid water in the surface or close subsurface (e.g. Baker, 2001; Costard et al., 2016; Mangold, 2005; Seibert and Kargel, 2001; Soare et al., 2008, 2014a). The first studies were based on polygon distribution and comparisons with terrestrial landforms (Baker, 2001; Mangold, 2005; Seibert and Kargel, 2001). More recent studies used the high-resolution HiRISE images (25-50 cm/pixel) to observe LCPs – i.e. polygons whose margins are underlain by ice or sand wedges – in spatial correlation with other landforms potentially linked with liquid water (Soare et al., 2008, 2014a). However, as liquid water is thought to be not stable at the surface of Mars during the Amazonian (Jakosky, 1985; Jakosky and Farmer, 1982; Jakosky and Phillips, 2001; Richardson, 2002), these studies suggesting involvement of liquid water are controversial. In that context, a study argues that liquid water is not required to form the ice wedges underlying martian LCPs (Fisher, 2005). The author suggests that diffusion of atmospheric water vapour could form ice wedges on Mars, if occurring episodically during a sufficiently long period of time, and interspersed with thermal cracking of the ice wedges.

2.5.3. Remaining scientific questions

Despite studies suggesting the recent activity of liquid water at the surface of Mars (Baker, 2001; Costard et al., 2016; Mangold, 2005; Seibert and Kargel, 2001; Soare et al., 2008, 2014a), our current knowledge of the Amazonian climate questions the presence of surficial liquid water (Jakosky, 1985; Jakosky and Farmer, 1982; Jakosky and Phillips, 2001; Richardson, 2002). Indeed, surficial liquid water is not compatible with the Amazonian environmental conditions: temperature, pressure and partial pressure of water vapour. In the specific case of thermal-contraction polygons, we know that sand-wedge formation can form, on Earth, FCPs, LCPs and HCPs without or with much less liquid water than for ice wedges. This process has also been suggested for martian thermal-contraction polygons (Levy et al., 2009a), so differentiating between the two hypotheses is an important matter in the investigation of potentially recent liquid water activity on Mars. I address this question in Section III. In addition, martian thermal-contraction polygons are suggested to be young (a few million years; Levy et al., 2009a, 2010b; Mangold, 2005; Mangold et al., 2004a; Séjourné et al., 2011). However, the timing of their activity is still not adequately constrained. By dating polygonally-patterned terrain I address this open question for an area in eastern Utopia Planitia in Section III. I also show that polygons themselves can be used to unveil geological properties of their substrate.

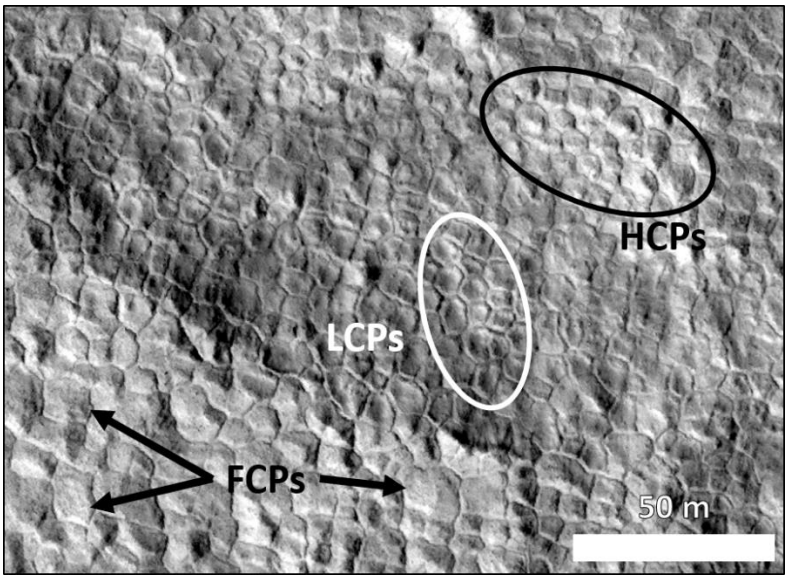

Figure 2.13: martian thermal-contraction polygons in UP. Three FCP examples are pointed out by black arrows, some LCPs are circled in white, and some HCPs are circled in black. North is up. HiRISE image ESP_063979_2280. HiRISE credits: NASA/JPL/University of Arizona.

3. Objectives and structure

3.1. Scientific objectives

The general objective of the present thesis is to gain new understanding on how ground ice and periglacial processes influence surface geomorphology in planetary environments – i.e., on Earth and on Mars. More specifically, I investigate molards (Section II) and martian thermal-contraction polygons (Section III).

Molards, i.e. cones of debris found in landslide deposits, were recently identified as potential spatial and temporal markers for permafrost degradation. This characteristic is interesting from a fundamental point of view: our knowledge of the extent of mountain permafrost is currently based on climate models, which are not accurate at the local scale. Molards could hence improve our understanding of permafrost extent and its evolution. From a more practical point of view, mass movements caused by permafrost degradation represent an increasing hazard in the context of climate change. The identification of molards, as markers of permafrost degradation, could hence improve our assessment of such hazards – which would be particularly useful for inhabitants of periglacial areas. However, molards resemble other conic landforms found in landslide deposits (i.e. hummocks). They also often occur in remote areas, hence are difficult to access in the field, and are sometimes not even formally identified. Therefore, the present thesis provides a way to study molards from analogue experimental models, in a controlled and systematic manner. More specifically, these experiments aim at improving our understanding of the degradation from ice-cemented blocks of sediment into molards – in terms, for instance, of shape or degradation processes. I also present a study that uses potential martian molards to investigate the state subsurface water ice during the impact that formed Hale crater (Mars), as well as the dynamics of the subsequent ejecta.

Thermal-contraction polygons are terrestrial periglacial landforms that necessitate the presence of ground ice, and some specific polygon morphologies (LCPs and HCPs) can require liquid water to form. They are also present on Mars, which poses the question as to potentially recent (Amazonian) liquid water activity in the mid-latitudes of the planet – despite the current cold and dry climate, hostile to liquid water stability. Improving our understanding of liquid water activity on Mars in turn leads to a better understanding of its past climate, its past and current habitability, and of its water resources for potential future human missions. Therefore, the present thesis aims at providing practical insights into the ways thermal-contraction polygons can be used to investigate martian periglacial processes and liquid water activity. I also suggest a methodology that uses thermal-contraction polygons in order to provide information on subsurface properties of their substrate.

3.2. Structure of the thesis

Section II focuses on terrestrial (and potential martian) molards. I first present a study I conducted, which is a proof-of-concept for a flexible, time-lapse automated setup, allowing the 3D monitoring of experimental analogue models of molards. I then present a study I participated in (Morino et al., 2023), where we identified potential martian molards and compared them to terrestrial ones, in terms of morphology and geological setting. I end Section II by summarising its content, and the scientific conclusions it allows me to draw.
Section III focuses on martian thermal-contraction polygons. I first detail the formation and evolution of thermal-contraction polygons, and explain the constraints they provide on the global climate and geological evolution of Mars. I then present a study I participated in (Soare et al., 2021), where we investigate the

latitudinal distribution of various thermal-contraction polygon types, which implies recent (Amazonian) surface activity of liquid water on Mars. I then present a study I conducted, where I use the distribution of thermal-contraction polygon types, as well as other geomorphologic evidence, in order to investigate subsurface properties of given substrates, and better constrain the timing of recent (Amazonian) surface water activity on Mars. I end Section III by summarising its content, and the scientific conclusions it allows me to draw.
Section IV provides a general synthesis of my thesis and summarises the scientific conclusions of the present work in the scope of the questions and objectives stated in Section I. I also provide an overview of the questions that remain, and of the next steps in the study of molards and martian thermal-contraction polygons.
In the Appendices are found various supplementary material linked to the different investigations presented in this thesis (mentioned individually in the text), as well as a published paper (Philippe et al., 2023; Appendix A.8) that is based on my master internship.

I wrote the entirety of the present thesis, and parts of this work are drawn from publications that were done in collaboration with other researchers as detailed below. Section II.2. is constituted of a paper (Philippe et al., submitted to *Geomorphology*) for which I: designed, built and programmed the experimental setup; designed the experimental protocol; performed data analysis and figure creation; designed and wrote the text. Co-authors on that paper performed the two experimental runs analysed in the study, and participated in the scientific interpretation and writing processes. Section II.3. is based on a paper I am co-author on (Morino et al., 2023), for which I performed parts of the mapping, data analysis and figure creation, as well as participated in the writing process. Section III.2. is constituted of a paper I am co-author on (Soare et al., 2021), for which I performed the mapping, data analysis and figure creation; I also wrote the Methods section, and participated in the scientific interpretation and writing processes. Section III.3. is constituted of a paper (Philippe et al., *in prep.*) for which I: designed the study; performed the mapping, data analysis and figure creation; designed and wrote the text. The co-author on that paper participated in the scientific interpretation and writing processes.

II. Molards and permafrost degradation

1. Introduction

In this section, I will focus on the research I performed on molards (Section I.1.4.). They are cones of loose debris found in landslide deposits, and were recently identified as spatial and temporal markers of permafrost degradation (Morino et al., 2019b). Therefore, they could help to better understand the current extent of mountain permafrost, but also to improve the assessment of landslide hazards in periglacial environments. However, little is known about their formation process, they often occur in remote areas which makes their identification and study difficult, and they are morphologically similar to other conical features found in landslide deposits – i.e. hummocks.

Therefore, Section 2. is constituted of an article (submitted to *Geomorphology*) that presents a controlled and systematic way to study molards. We perform analogue experiments of degradation from ice-cemented blocks of sediment to molards in cold-room facilities, in the Morphodynamique Continentale et Côtière laboratory (M2C; Caen, France). We provide details on an automated system we developed that allows time-lapse generation of DEMs, and hence the 3D-monitoring of our analogue models.

Then, Section 3. is an overview of an article (Morino et al., 2023) which suggests the presence of molards in the ejecta of Hale crater (Mars). In this study, we use the geological setting and the morphology of martian conical mounds to conclude on their origin. We then infer properties of subsurface water ice before the Hale impact, and get insights into the dynamics of Hale ejecta.

2. Analogue modelling of molards (Philippe et al., submitted to *Geomorphology*)

The following section is a direct copy of a submitted article. For that study, I: designed, built and programmed the experimental setup; designed the experimental protocol; performed data analysis and figure creation; designed and wrote the text. Co-authors on that paper performed the two experimental runs analysed in the study, and participated in the scientific interpretation and writing processes.

A cost-effective and flexible method for time-lapse Structure from Motion: application to analogue experiments in geomorphology

Meven Philippe[1], Calvin Beck[2], Susan J. Conway[1], Marianne Font[2], Liza Jabbour[2], Maxime Leguen[2], Jérémiah Clément[2], Costanza Morino[3], Christophe Marie[2]

[1]*Nantes Université/Université d'Angers/Le Mans Université, Laboratoire de Planétologie et Géosciences, CNRS UMR 6112, Nantes, France.*
[2]*Normandie Université/UNICAEN/UNIROUEN, CNRS UMR 6143 M2C, Laboratoire Morphodynamique Continentale et Côtière, Caen, France.*
[3]*Laboratoire EDYTEM, Université Savoie Mont Blanc, CNRS UMR 5204, Chambéry, France.*

2.1. Context of the experiments

In geosciences, topographic data are usually in the form of Digital Elevation Models (DEMs), 2D images which represent the ground surface as values of elevation attributed to each pixel. DEMs allow a wide range of quantitative measurements, e.g. heights, volumes or slopes of the studied objects. One popular way of obtaining the 3D shape of an object is by using photogrammetry techniques. Such techniques leverage the parallax obtained between images, taken from two (stereophotogrammetry; e.g. Chandler, 1999; Lane et al., 2000) or more points of view (SfM; Bolles et al., 1987; Snavely et al., 2008; Spetsakis and Aloimonos, 1991; Szeliski, 2011;Szeliski and Kang, 1994; Ullman, 1979; Westoby et al., 2012), in order to reconstruct a 3D scene.
The SfM technique allows the reconstruction of a static scene in 3D from a set of photos that is spatially dense - i.e., photos with high amount of overlap. It became more widely used in geosciences in the 2010's (e.g. Fonstad et al., 2013; Westoby et al., 2012), because of advances in computer vision and processing, and the widening availability of easy-to-use tools. Unlike traditional photogrammetry, SfM resolves automatically both the positions/orientations of the cameras and the geometry of the scene (Westoby et al., 2012). SfM algorithms identify and match the same features on several images, which produces self-consistent 3D models. Then, photos must contain spatial information in order to scale the 3D models, e.g. objects of known coordinates or dimension placed within the scene. The set of photos is processed semi-automatically with a dedicated software (e.g. Agisoft Metashape, IGN MicMac, Alice Vision Meshroom). The image processing and precise procedures from which the SfM technique originates are detailed in Bolles et al. (1987).
As it only requires photos of the studied scene, photogrammetry is a quick, easy to handle and cost-effective technique to produce 3D models (Anderson et al., 2019; Śledź et al., 2021; Smith et al., 2016; Westoby et al., 2012). Therefore, stereophotogrammetry and SfM are commonly used to study natural landforms (e.g. Casella et al., 2022 de Haas et al., 2021; Eltner et al., 2017; Filhol et al., 2019; Gabrieli et al., 2016; Kromer

et al., 2019; Lane et al., 2000; Marzolff and Poesen, 2009; Niethammer et al., 2012; Vassilopoulou et al., 2002; Westaway et al., 2000) or civil engineering structures (e.g. Haneberg, 2008; Hu et al., 2021; Reinoso et al., 2018). They represent alternatives to techniques that are more expensive and/or more complex in terms of logistic or data processing – like terrestrial (e.g. Haneberg, 2008; Heritage and Hetherington, 2007) and airborne (e.g. Fonstad et al., 2013; Jones et al., 2007; Lohani and Mason, 2001; Notebaert et al., 2009; Zhou et al., 2004) laser scanning (LiDAR), or field differential GPS campaigns (e.g. Brasington et al., 2000; Chassereau et al., 2011; Conway et al., 2010).

SfM is also widely employed at the laboratory scale to study experimental models – such as sediment sorting, rainfall erosion on sand beds, evolution of drainage basins, or formation of subglacial landforms (e.g. Balaguer-Puig et al., 2017; Brasington and Smart, 2003; Eltner et al., 2017; Fister et al., 2019; Hancock and Willgoose, 2001; Herny et al., 2019; Lane et al., 2001; Philippe et al., 2023; Rieke-Zapp and Nearing, 2005; Vérité et al., 2021; Wróżyński et al., 2017; Yang et al., 2021). Photogrammetry in this context can be cheaper, and/or more accurate and/or has simpler logistics or data processing than other techniques like manual cross-profile measurement (e.g. Conway et al., 2011; Lane et al., 2001), handheld (e.g. Dupeyrat et al., 2018; Lane et al., 2001) or fixed laser scanning (e.g. Jouannic et al., 2015; Morgan et al., 2017; Moussirou, 2017), and 3D scanning with structured light (e.g. Lanman et al., 2009; Rocchini et al., 2001; Zhuo et al., 2022). However, manual acquisition of photos for photogrammetry in experimental protocols is time-consuming. It is also not suitable to monitor experiments over long time periods, experiments involving fast processes (due to the time required to acquire a set of photos), or experiments where models are not physically accessible.

Here, we present a cost-effective setup installed at the Morphodynamique Continentale et Côtière laboratory (M2C; Caen, France), made of 18 microcomputers connected to cameras. They are programmed to take photos automatically and simultaneously at a given (and customisable) time step and sort them by acquisition time, allowing 3D reconstruction of experimental models at multiple time steps with the SfM technique.

We perform those experiments in the context of the study of molards. These are cones of loose debris found in landslide deposits in periglacial environments, typically tens of centimetres to ~ 15 metres high. They are the remnants of formerly ice-cemented blocks of sediment that were mobilised by a landslide, and then degraded progressively from blocks to cones due to melting of the ice that constitutes them (Figure 2.1; Brideau et al., 2009; Milana, 2016; Morino et al., 2019b; Sæmundsson et al., 2018). Their presence in landslide deposits implies the involvement of both ice-cemented and non-ice-cemented material within the mass movement, and thus the presence of degrading permafrost at the detachment zone. Therefore, they have been identified as key spatial and temporal markers of actively degrading mountain permafrost (Morino et al., 2019b). Molards could also be used to track ground ice in planetary environments, as potential molards were identified in the ejecta of Hale crater on Mars (Morino et al., 2023).

Degradation of mountain permafrost and subsequent mass movements represent a threat for population living in periglacial areas (e.g. Allen et al., 2009; Dramis et al., 1995; Fischer et al., 2006, 2011; Gruber and Haeberli, 2007; Haeberli et al., 2017; Kellerer-Pirklbauer et al., 2012; Morino et al., 2019b; Sæmundsson et al., 2018; Wei et al., 2006). Therefore, better understanding molards, and particularly being able to reliably identify them, would help to identify more accurately regions where there is a risk of mass movement caused by permafrost retreat.

In our experiments, we are investigating the degradation from ice-cemented blocks of sediment to molards, as such observations have not yet been made in the field. Hence, we developed analogue modelling experiments, that comprise two simultaneous cuboid models with an initial base of 30x30 cm and a height of 30 or 33 cm. The two models degrade within the same rectangular tray (310x140 cm), under ambient temperatures. In order to generate DEMs at regular time steps, both models have to be imaged

simultaneously by multiple cameras. We chose a time step of 30 min over the duration of the experiment and experiments can last up to four days. DEMs have to be accurate enough in order to monitor quantitatively the volume of sediment moving during the degradation of our models, as well as to identify the different transport processes. To quantify the degradation of the model we need to make morphological measurements on our models, such as topographic profiles, and slope gradient. Hence, our photogrammetry setup reflects these needs.

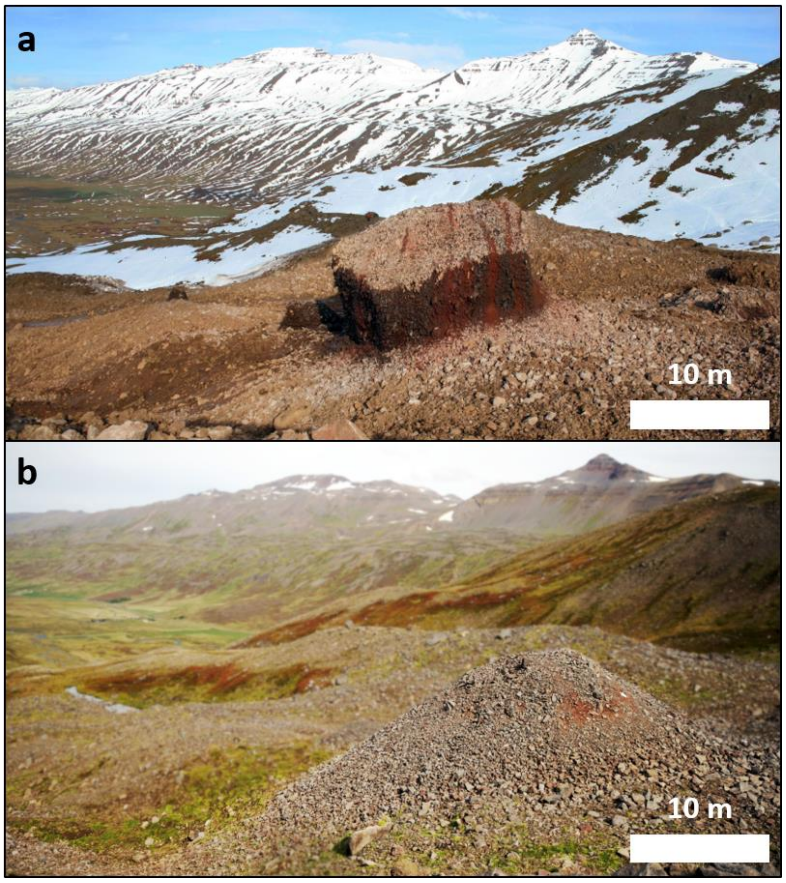

*Figure 2.1: degradation of **a.** an ice-cemented block of sediment (September 2012, a few days after the landslide; courtesy of Jón Kristinn Helgason) into **b.** an actual molard (August 2022), within the Móafellshyrna landslide deposits (20th September 2012, Iceland).*

2.2. Methods

In this section we first describe the equipment we use to acquire time-lapse photos (Section 2.2.1.), then we detail how we automated this process (Section 2.2.2.). We then explain how we generate the DEMs of our experimental models (Section 2.2.3.).

2.2.1. Equipment

The setup is constituted of 18 microcomputers (Raspberry Pi 4 Model B with 2 Gb RAM, referred to subsequently simply as 'Pi') including a 16 GB microSD card containing the operating system (Raspbian GNU/Linux v.10). Each Pi is connected to a high-resolution camera module (12 megapixels), with a lens of 30° of field of view (FOV). Lenses are independent of the cameras and can be changed. The camera focus and aperture are set manually. The ISO and shutter speed are adjusted automatically, taking into account the lighting conditions. Pis and cameras are attached to wooden supports that we designed and built

at M2C, allowing tilt and pan adjustments (Figure 2.2a). These supports are then mounted on metal rails on the ceiling and to the walls of the experimental chamber (Figure 2.2b). Each Pi is powered by a USB-C-power supply of 5.1V / 15.3W. We use another Pi (referred to as 'Master Pi') with an SD card with a higher storage capacity in order to gather and store photos from all devices. We use an ethernet cabled network to transfer data from the Pis to the Master Pi, via two ethernet hubs connected in series (Figure 2.2c). Two hubs were necessary as Pis were too numerous to be plugged into one hub all at once.

Two analogue models are monitored at a time. Those models degrade on 110x120x1.6 cm wooden platforms. The platforms are perforated in order to allow meltwater drainage, and they are placed in a 310x140 cm tray. The cameras are placed above the tray. We tested two different setups of camera positions: two arrays of 9 cameras pointed toward each model from a top-down point of view, from now on called the 'top-down setup' (Figure 2.3a); and all 18 cameras pointed toward the two models with a radial organisation - the 'radial setup' (Figure 2.3b). In the top-down setup, cameras are between 2 m and 2.2 m away from the models; in the radial setup, cameras are between 1.75 m and 2.5 m away from the models.

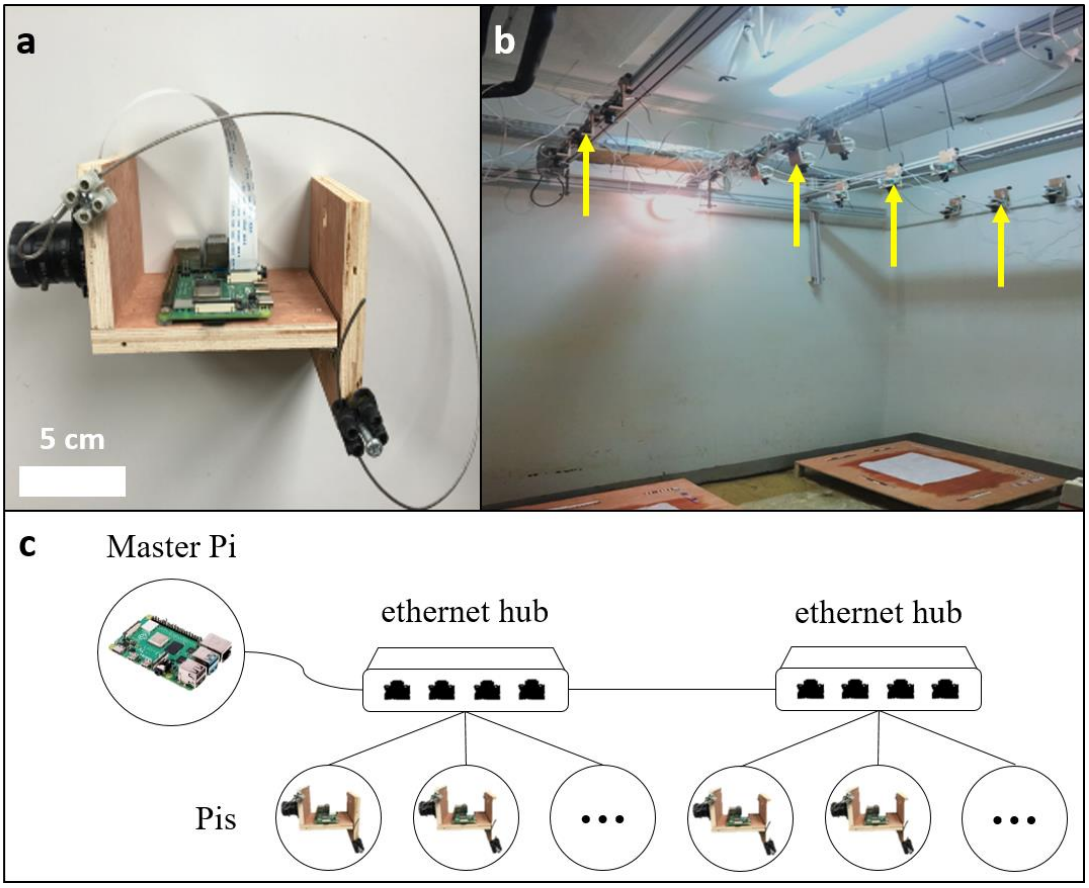

Figure 2.2: ***a.*** *a photo of one of the image acquisition devices, constituted of a Pi and a camera, fixed to its wooden support;* ***b.*** *devices installed on rails in the experimental chamber (yellow arrows highlight each row of devices on their supports);* ***c.*** *schematic representation of the LAN network of microcomputers.*

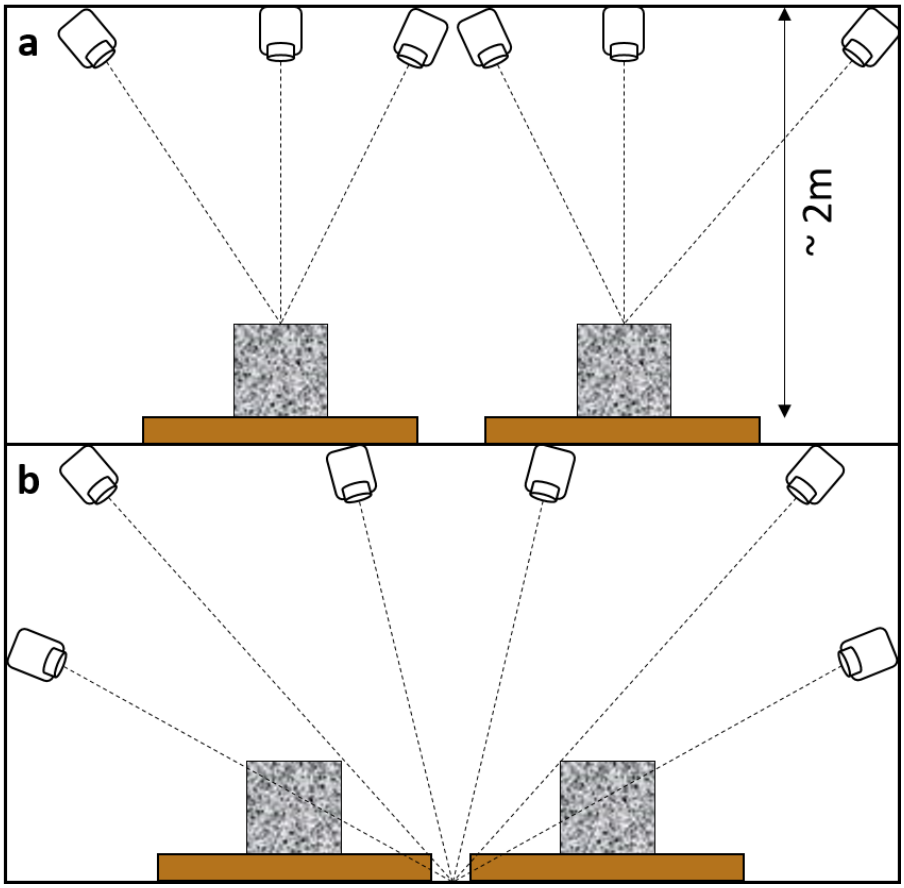

*Figure 2.3: schematic diagram of the camera positions with respect to the models in the chamber, for **a.** the top-down setup, and **b.** the radial setup.*

To allow the 3D reconstruction of our experiments, we place eight circular targets (radius = 3.5 cm) around each model (one at each corner and side of the wooden platforms; Figure 2.4), that are printed from the photogrammetry software (Agisoft Metashape). Their positions are measured in an X, Y coordinate system, the origin (0, 0) being a corner of each platform (top-down setup), or a corner of one of the two platforms (radial setup). In the top-down setup, a scale bar (40 cm) is added to the scene after the experiment (Figure 2.4a); in the radial setup, 2 pairs of vertical targets for two scales (22 cm) and three horizontal scales are placed on the platform for each model (Figure 2.4b). Those scales are used to generate errors on length within our models (Section 2.3.3.2.). The top-down setup treats the two platforms in two separate coordinate systems, and the radial setup treats the 16 markers on the two platforms in one and only coordinate system.

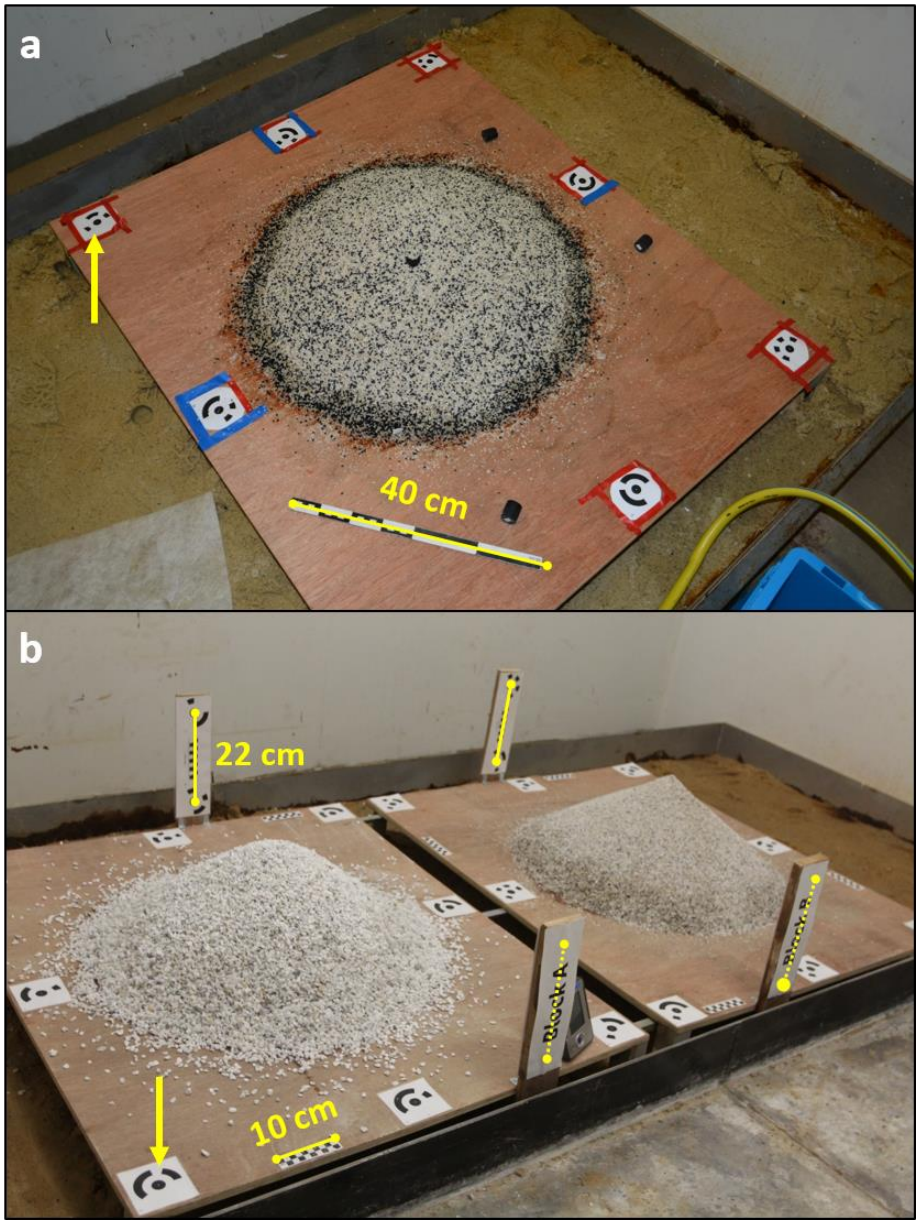

Figure 2.4: ***a.*** *targets (one example pointed out by the yellow arrow) and horizontal reference scale (40 cm, represented by the yellow line) used with the top-down setup;* ***b.*** *targets (one example pointed out by the yellow arrow) and vertical (22 cm, represented by the yellow lines) and horizontal reference scales (10 cm, one example represented by a yellow line) used with the radial setup. Two vertical reference scales are not visible since they are behind the vertical planks (represented by dotted lines).*

2.2.2. Setup for photo acquisition

A simplified sketch of our photo acquisition protocol is shown in Figure 2.5.
The Pi operating system (OS) includes a time-based scheduler application called CRON. It is a protocol in which you can specify a date/time, followed by a line of instruction which will be executed at the specified date/time.

In order to achieve simultaneous photo acquisitions, we first have to ensure that all devices have the same date and time settings. To achieve this, we wrote an instruction in CRON for each device that sets its date/time to the date/time of the Master Pi, twice a day. The date/time of the Master Pi itself is manually set at the beginning of each experiment. This means the devices should always have the correct date/time, except in case of power failure; and even in that case, all devices will have the same date/time as the Master Pi, and thus will continue taking photos simultaneously (see Section 2.3.3.1. for an evaluation of the synchronicity).

The cameras of the devices can be controlled by the Python programming language. Therefore, we implemented in each Pi a Python program which: i. switches the camera on, ii. waits for ten seconds (for the ISO and shutter speed to adapt to the light conditions), iii. takes a photo, iv. gives it a formatted name that includes the system date/time, and v. stores it in a specific folder with PNG format. This program is run regularly, from another line of instructions in CRON – in which the time step can be modified.

Between each photo acquisition, each Pi is programmed to connect, one after the other, to the Master Pi via a SSH (Secure Shell) protocol to send the last photo taken. Afterwards, each Pi stores the last photo taken into an archive folder. When all 18 photos are transferred, a line of instruction in the CRON of the Master Pi places them in a newly-created subfolder, which name is a number incremented by one at each iteration. Incrementation is done by counting the number of subfolders at each iteration, in order to avoid that the count reinitialises in the case of a power failure.

At the end of each experiment, as each Pi keeps its photos in its own storage (capacity of ~ 850-900 photos), the user can check if all the photos have been transferred to the Master Pi. The user can then manually run some code from the Master Pi, that will connect it to each Pi one by one, delete the photos and switch off the Pis. It is possible to run a similar code to delete the photos on each Pi during an experimental run, which would be useful in the case that free space in the memory of the Pis is needed during the experiment (e.g., experiment duration / timestep over 850).

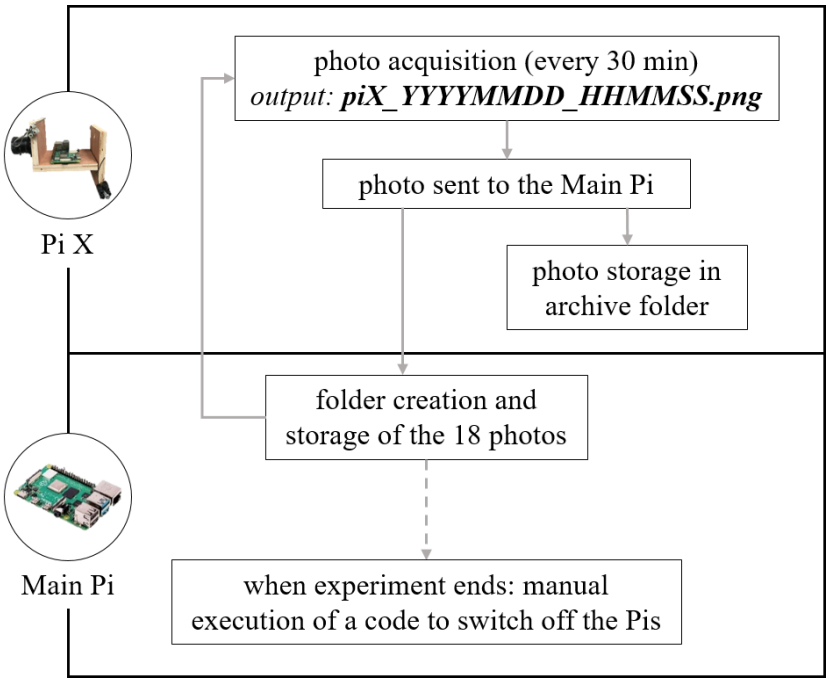

Figure 2.5: sketch of the flow of the automated photo acquisition setup. The photos are named with the number of the Pi (here X), the date (year = Y, month = M, day = D) and time (hour = H, minute = M, seconds = S).

2.2.3. DEM generation

We use the software Agisoft Metashape (version 1.7 to 1.8.4) to build 3D models of the experiments at regular time steps, from sets of 18 photos using the SfM technique. We also generate DEMs from sets of photos taken with a DSLR camera (models: Nikon D7100, FOV ≈ 62° for the top-down setup; Canon EOS 600D, FOV ≈ 32° for the radial setup): one at the beginning and one at the end of each experiment – i.e., before and after the degradation. We use them for redundancy and to provide a benchmark against which the models generated with the automated setup can be compared. We run Agisoft Metashape on two different computers, with the following specifications: i. OS Windows 10 v. 22H2, Intel® Core™ i9-9900 CPU (8 cores, 32GB RAM), graphic card NVIDIA GeForce RTX 2060; ii. OS Unbutu v. 22.04.2, AMD® Ryzen 7 4800hs CPU (8 cores, 40GB RAM), graphic card NVIDIA GeForce RTX 2060.
The workflow to process the images is organised as follows: i. co-alignment of all the sets of photos for one experiment (ensures that sets of photos of all time steps are aligned in the same coordinate reference system) via identification of sparse matching points, and importation of target coordinates; ii. automatic detection of the targets; iii. manual check of the target locations in each photo; iv. separation of the sets of photos by time step; v. generation of a dense cloud of matching points in the photos for each time step; vi. from the dense cloud, generation of a mesh (Triangulated Irregular Network of the surface of the model) for each time step; vii. from the mesh, generation of a DEM for each time step; viii. export of the DEM for each time step as a GIS-readable TIFF file. The duration of each time step within our workflow is detailed in Table 2.1. For both setups and for the first time step (i.e. the initial cuboid shape), generating the DEM from the mesh produces a curved shape along the edges of the model, which artificially makes the model larger and increases its volume. Therefore, DEMs of the first time step are generated directly from the dense cloud for both setups. To make further computations easier, within an experiment, DEMs are generated with the same spatial extent and with the same resolution (0.5 mm/pixel) – which results in DEMs with pixels that are perfectly overlapping. For complete details on the algorithmic processes taking place the reader is referred to the online documentation (Agisoft Metashape User Manual - Version 1.8).

	step	action	duration	remark
all time steps	**i.**	co-alignment of photos	6-8 min	/
	ii.	target detection	~ 1 min	/
	iii.	target location check	30-60 min	done by user
	iv.	separation of photos by time step	< 5 min	done by user
each time step	**v.**	dense cloud generation	1 min (Pis) > 10 min (DSLR)	done by batch processing
	vi.	mesh generation	< 2 min (Pis) > 5 min (DSLR)	
	vii.	DEM generation	seconds	
	viii.	DEM exportation	< 1 sec	
total common part			~ 1h	
total individual part			3 min (Pis) 15 min (DSLR)	

Table 2.1: detail of the duration of the DEM generation workflow.

2.3. Application: analogue modelling of molards

One of the aims of this paper is to provide a proof of concept for the automated time-lapse photo acquisition system we built. The following section provides an application of that system to analogue laboratory experiments of molards. The scientific results of the experiments will be discussed in upcoming work and are outside the scope of this paper.

2.3.1. Experimental protocol

In order to investigate the formation of molards we developed analogue experiments to model the degradation of ice-cemented blocks. These experiments implement the automated system described in Section 2.2. The simplified workflow is as follows: i. filling of a mould (30x30 cm base, varying filling height) with sediment of selected grain size; ii. saturation of sediment with liquid water; iii. freezing of the block in a cold room at -20°C for 48h; iv. removal of the block from the mould and placing on a perforated wooden platform; v. monitoring of the degradation of the model until no further movement can be detected. One experimental run comprises the monitoring of the degradation of two models simultaneously. This complete degradation can last several days. Note that the wooden moulds used for the two setups are different. The first mould, used in the top-down setup, bent during the freezing step under the force applied by the phase change from liquid water to water ice, which causes the sediment to uncompact slightly. The newly-built moulds used in the radial setup are more solid, bend less and allow the sediment to remain at the same level of compaction as before freezing. In order to test the performance of our photogrammetry setup, we focus on one grain size: fine gravel (2-4 mm; Figure 2.6). We also compare the performance of the top-down and radial setups in terms of 3D reconstruction and possible measurements.

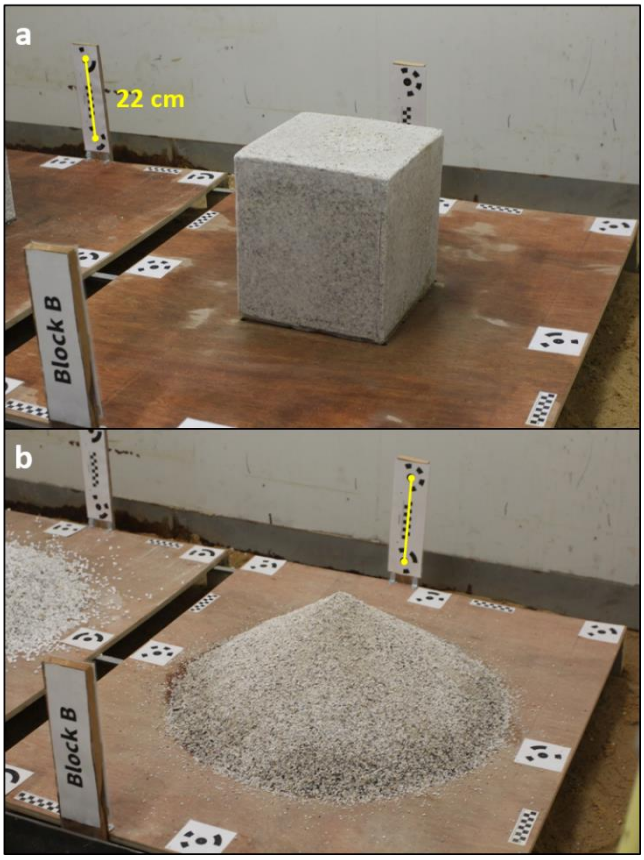

*Figure 2.6: photos **a.** before and **b.** after an experiment, with the radial setup and fine gravel (2-4 mm). Scales (yellow lines) measure 22 cm.*

2.3.2. Measurements

The following section is focused on two models: one of 30x30x30 cm monitored with the top-down setup, and one of 30x30x33 cm (i.e. 33 cm high) monitored with the radial setup.

2.3.2.1. Volume monitoring

For each experiment, we import the DEMs of the different time steps into ArcMap software (version 10.4.1). We then digitise a circle (elevation z = 0) around the final shape of each model, and for each DEM we compute the volume of the 3D model above this circle. This ensures that artefacts in the DEM caused by the textureless appearance of the platform (Section 2.3.2.2.) are not included in the volume calculation. We estimate the error on volume calculation for the top-down and the radial setup respectively at 0.20 dm^3 (0.8% of the final volume) and 0.06 dm^3 (0.2% of the final volume). They fall within the data points for both setups (Figure 2.7). For details on the calculation refer to Section 2.3.3.3.

For the DEMs made from the DSLR camera, we estimate the errors on volume calculation for the top-down setup at 0.9% of the volume (before: 0.26 dm^3; after: 0.23 dm^3), and for the radial setup at 0.6% of the volume (before: 0.20 dm^3; after: 0.19 dm^3). Those errors are derived from the errors on the length of the scales present in each setup (Figure 2.4; Section 2.3.3.2.) and fall within the data point in Figure 2.7.

The volume of the model with the top-down setup decreases with time (Figure 2.7). This is expected because ice is lost progressively by melting, decreasing the overall volume. The total volume loss calculated from the Pis DEMs is 2.5 ± 0.4 dm^3 (~ 9% of the initial volume). Note also that the Pis and DSLR DEMs show consistent volumes for the first and last time steps.

With the radial setup, the volume of the model first undergoes an abrupt decrease from 32.17 ± 0.06 dm^3 to 30.55 ± 0.06 dm^3 (t = 6h), then increases slowly up to 32.25 ± 0.06 dm^3 (t = 26h), then slowly decreases to a final volume of 31.01 ± 0.06 dm^3 at the end of the experiment (Figure 2.7). To further investigate this more complicated evolution in volume, we processed and analysed more time steps during the first ~ 10h of the experiment than for the top-down setup, and followed the experiment on a time-lapse video (Supplementary Material). This analysis allowed us to identify the gradual volume increase between t = 6h and t = 26h as arising from the decompaction of the sediment, which dominates over the volume decrease from ice loss. We do not observe the same phenomenon with the top-down setup because the sediment was initially uncompacted in the frozen state because of the mould-construction (Section 2.3.1.). Second, the abrupt decrease in volume at the beginning of the experiment is due to the melting of the excess ice present during the first time steps at the bottom of the model (as the mould does not expand in freezing the ice is forced to the surface of the mould, which is the bottom of the model). This ice degrades rapidly, causing the settling of the whole model. The settling of the model can be seen on the video in Supplementary Material. Note also that, similarly to the top-down setup, Pis and DSLR DEMs show consistent volumes for the first and last time steps.

Volumes computed for the top-down and the radial setups are presented in Appendices A.1 and A.2, respectively.

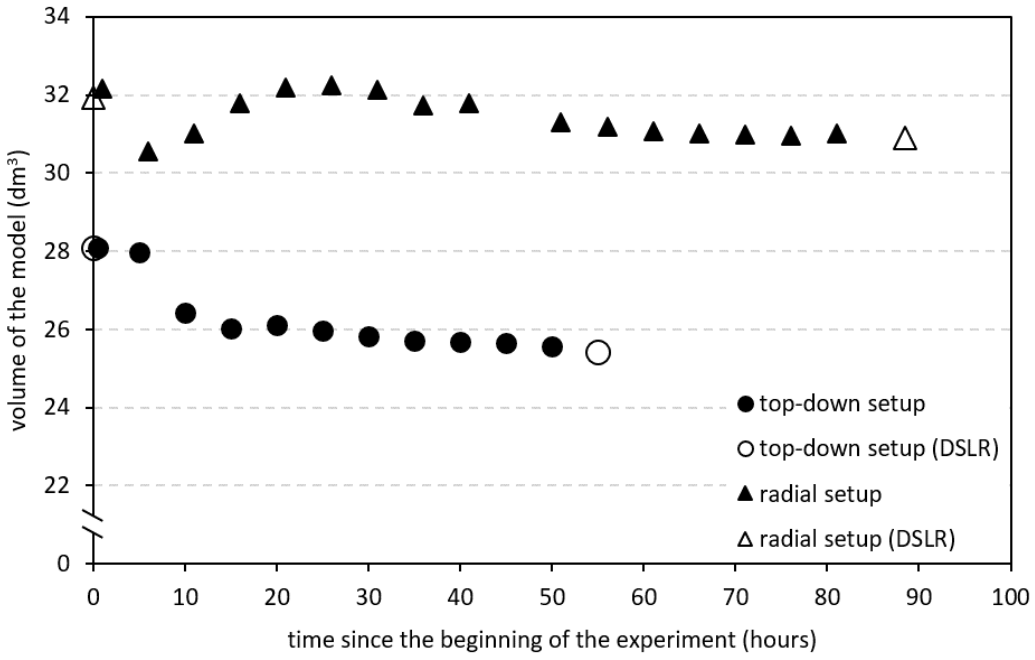

Figure 2.7: evolution with time of the volume of the models with the top-down and radial setups. The volumes calculated from the sets of photos taken with the DSLR camera before and after each experiment are also indicated. Error bars fall within the points. Missing data points are due to the recording of corrupted data (Section 2.4.3.2.).

2.3.2.2. DEMs of Difference (DoDs)

For a given experiment, we can subtract an earlier DEM from a later one to generate a DoD in ArcMap. This allows us to locate, between two time steps, the zones of the model where volume of material was eroded (negative values), deposited (positive values), or where the volume balance is neutral (null values). Note that we estimated the statistical variability in our DoDs in Section 2.3.3.3., and all the movements presented in the following section are significantly above that detection limit.

For the experiment with the top-down (Figure 2.8a to d) and the radial setup (Figure 2.8e to h), we generate two DoDs between the initial and final shapes of the models – one with the DSLR DEMs and one with the Pis DEMs (Figure 2.8a and e). In order to compare them, we generate a "DoD of comparison" by subtracting the final DEM made with the Pis from the final DEM made with the DSLR photos (Figure 2.8b and e). We also generate a DoD between two close time steps for each experiment (Figure 2.8d and h).
Overall, DoDs show a relatively high material erosion along the edges of the initial cubic shapes, and a lower erosion at its centre – as it is also the highest point of the final shape (Figure 2.8a and e). Apart from the initial cubic shape, material deposition decreases radially until the edge of the final shape, as it is expected with a conical shape.

For the radial setup, the DEM generated from the Pis is generally consistent with the one generated from the DSLR camera (Figure 2.8f). However, we see an elevation decrease at the summit of the model and some patches of elevation increase in the deposits (Figure 2.8f) between the last Pis DEM and the DSLR DEM. It can be explained by a settling of parts of the model under gravity, not linked to any volume loss

as final volumes are similar when calculated from the Pis or the DSLR DEMs (difference of 0.4%; Figure 2.7; Section 2.3.2.1.). Despite the fact that we wait several hours after the last visible movement to stop the experiments, it is still possible that small movements occur that we cannot spot visually. To ensure that these detections are not artefacts, we produced a DoD between the first and the last time step of the final, steady state of the model (Figure 2.8g): the location of patches of movements correspond to the DSLR of comparison Pis/DSLR (Figure 2.8f), which confirms our interpretation of those small movements. As an additional confirmation, the same phenomenon is observed with the top-down setup (Figure 2.8b and c). The enlargement of those patches on Figure 2.8f compared to Figure 2.8g can be explained as the occurrence of more small movements in the unstable parts of the model, for instance when we walk around the models to acquire the final DSLR set of photos.

For the top-down setup, final DEMs made from the DSLR and the Pis are significantly different: the summit of the model is lower in elevation and some parts of its flanks are higher on the DSLR DEM (Figure 2.8b). The majority of this difference can be attributed to the removal of a temperature sensor, measuring variations of inner temperature of the model, from the top of the model between the end of the Pi monitoring and the acquisition of the DSLR photos, which likely triggered some mass movements. Similarly to the radial setup, the DoD made between the first and last time steps of the final, steady state of the model (Figure 2.8c) shows small elevation differences – likely due to the settling of parts of the model. The location of the elevation differences is consistent between Figure 2.8b and c, but in Figure 2.8c they are less numerous and smaller – which shows that the removal of the temperature sensor is the cause of most of the elevation differences observed on Figure 2.8b.

These results demonstrate that our setup allows the monitoring of small-scale movements. During the very first stages of degradation of the model with the top-down setup (Figure 2.8d), the DoD shows the erosion of the edges of the model, which forms small piles of debris at the base, with individual grains scattered on the platform around it. This results from grain falls or small grain avalanches, which we visually observe at the beginning of the experiments. This material accumulates at the foot of the model, immediately below the erosion zones, and these patches of deposits intermittently grow. At a later stage of degradation of the model with the radial setup (Figure 2.8h), we see on the DoD that the remaining frozen part of the model fails in specific places; moreover, that material accumulation is seen consistently downslope of those erosion zones.
We can hence infer that frozen parts of the model failed *en-masse* and grain avalanches deposited right below, downslope. In the same panel (Figure 2.8h), we see material accumulation in the top-right quarter of the model. This accumulation does not have an associated upslope erosion zone, but is located further downslope the grain avalanches described above. Therefore, we can argue that this accumulation of material is a secondary debris avalanche that occurred because of the slope destabilisation induced by the upslope grain avalanches.

Artefacts (i.e. areas where the 3D shape of the scene is not well reconstructed) can form on DEMs when some Pis record corrupted data, or fail to record a photo due to memory overload. Those artefacts can lead to false detection of material erosion or deposition in the DoDs. We systematically exclude DEMs with artefacts on the experimental model itself, but keep those with artefacts elsewhere: this is the reason for the elevation change on the platform in Figure 2.8b and c. Note that the radial setup produces fewer artefacts than the top-down setup (Supplementary Material): this can be explained by the higher number of photos per model (Figure 2.2), which compensates for the eventual loss of one or several photos for a given time step.

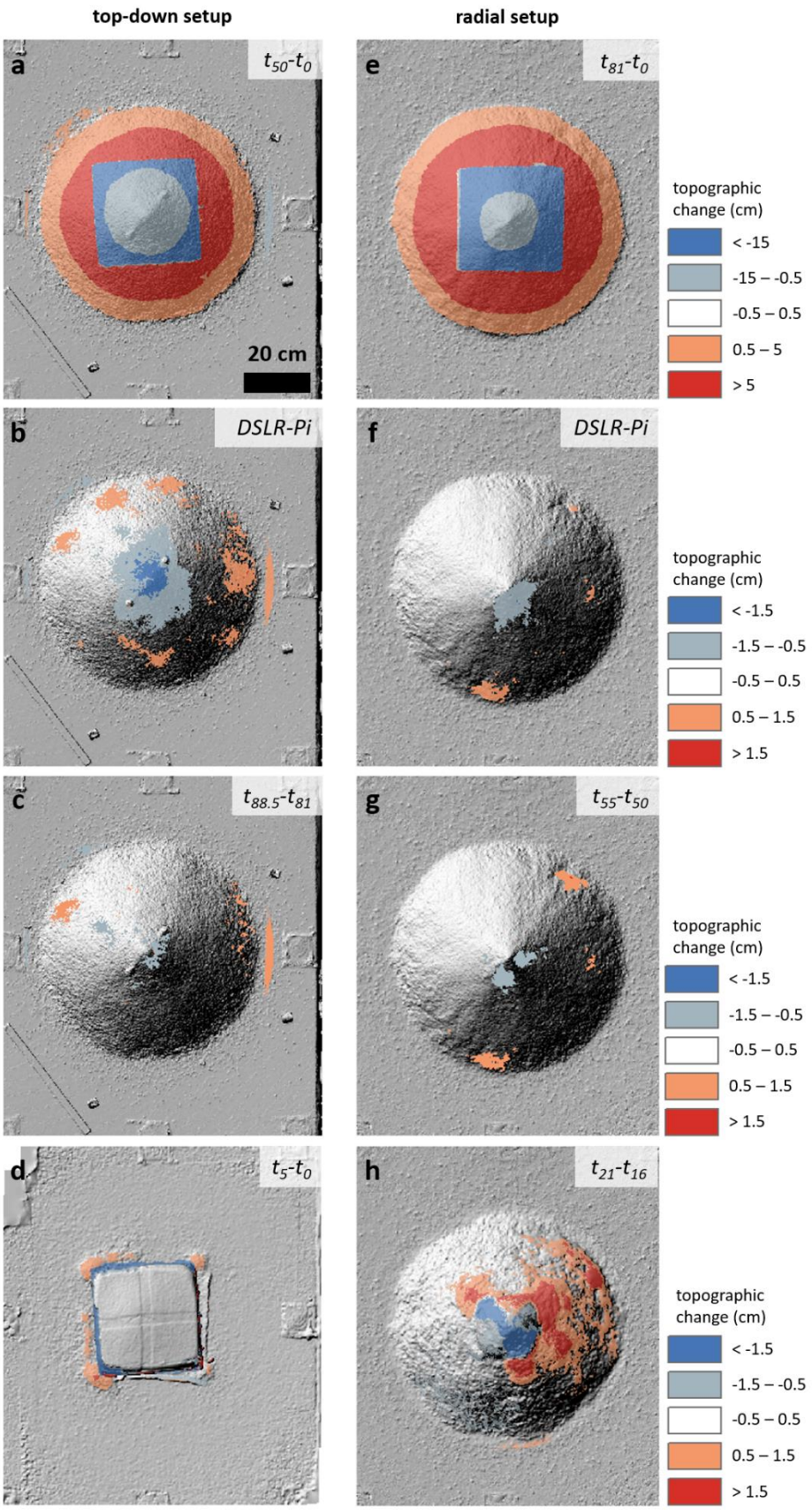

(caption on next page)

Figure 2.8: DoDs of the models with both setups, between various time steps. With the top-down setup: ***a.*** *$DoDt_{50}$-t_0 (final – initial),* ***b.*** *DoD of comparison (DSLR final – Pis final),* ***c.*** *$DoDt_{88.5}$-t_{81},* ***d.*** *$DoDt_5$-t_0; with the radial setup:* ***e.*** *$DoDt_{81}$-t_0 (final – initial),* ***f.*** *DoD of comparison (DSLR final – Pis final),* ***g.*** *$DoDt_{55}$-t_{50},* ***h.*** *$DoDt_{16}$-t_{11}. The cross shape appearing on the model on panel d. comes from the straps we placed inside the mould to lift the model up with the top-down setup. Values of t indicate the time in hours since the beginning of the experiment. The scale is the same for all panels, and the legend is expressed in elevation gain or loss in centimetres. The 'movement' that is detected on the platform (panels b. and c.) is due to artefacts that were formed on the edge of a DEM, without affecting the model itself. For each experiment the background is the hillshade of the latest DEM used to generate the DoD.*

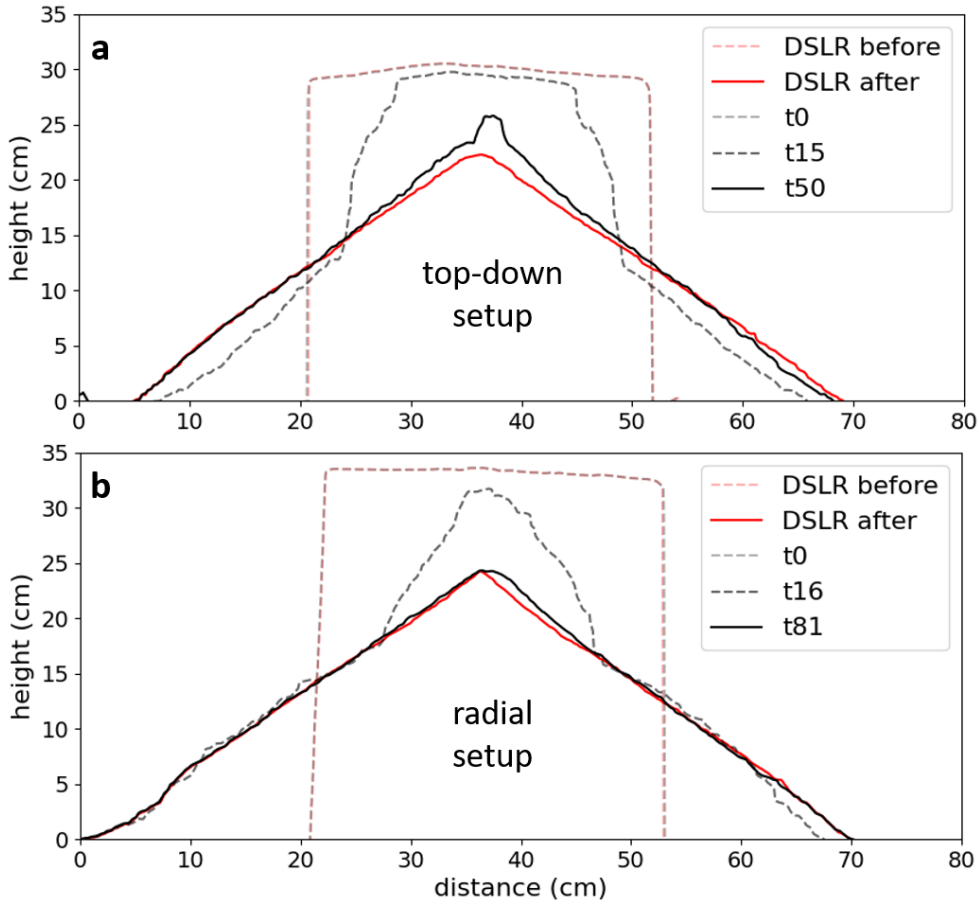

Figure 2.9: ***a.*** *topographic profiles of the top-down setup, from the Pis DEMs at t_0, t_{15}, t_{50}, and from the DSLR DEMs before and after the experiment;* ***b.*** *topographic profiles of the radial setup, from the Pis DEMs at t_0, t_{16}, t_{81}, and from the DSLR DEMs before and after the experiment. All profiles pass through the centre of the models. Scales of axes are 1:1 on both graphs. The subscript values of t indicate the time in hours since the beginning of the experiment.*

2.3.2.3. Morphometrics

The time-lapse DEMs allows the measurement of the morphometrics of the model during the experiments – e.g. the changing height or width of the model. We use a GIS software to compute topographic profiles of the models at various time steps (Figure 2.9). For both the top-down (Figure 2.9a) and the radial setup (Figure 2.9b), we compare the initial and final shape of the models on profiles computed from DEMs made from the Pis and from the DSLR camera. Note that on Figure 2.9a the difference between t_{50} and *DSLR after* profiles is due to a temperature sensor, which was protruding from the very top of the model being removed before the acquisition of DSLR photos. Otherwise, profiles made from the Pis and the DSLR DEMs are close, or even overlapping – especially for initial shape, for both setups. The slight differences observed for the radial setup can be explained by the slight settling of the model, described in Section 2.3.2.2. Our setup also allows to monitor the evolution of the profile of the models: for the top-down setup (Figure 2.9a), we see on the intermediate shape the erosion that started on the edges of the block, as well as a slight settling of the whole model when compared with the initial shape. On that intermediate time step, we also see that the slope of the debris is already close to the final slope. At a later stage of degradation, for the radial setup (Figure 2.9b), we see that the profile is getting closer to the final profile of the model.

A single topographic profile gives the shape of a model along one direction only. Therefore, we used ArcMap and a Python script to compute radial topographic profiles of our models, i.e. a visualisation of the average profile from the summit to the base of the models. It allows a visualisation of the variability in the data and the calculation of an average slope that is more representative than that extracted from a single profile. Our workflow is organized as follows: in ArcMap, i. digitisation of the summit point from the final shape of the model; ii. generation of a "distance raster", where each pixel value is the distance from the summit point. The extent and pixel size of the distance raster match those of the DEMs, so that they overlap perfectly. Then with a Python script, iii. import the DEM and the distance raster; iv. remove data points with an elevation below a certain value (here 5 mm), in order to keep only data points representing the model and not the platform; v. computation of a scatter plot showing the distance to the summit point (x-axis) against the elevation (y-axis) for each pixel of the rasters. For late stages of the experiments, i.e. when the slope is continuous, we also calculate the line of best fit and its slope. The result is a point cloud whose width represents the variability in elevation values, at a given distance from the summit. To better visualize the scatter in the data, we computed the density of data points in a grid of 2000x2000 bins, i.e. 2000 bins between the minimum and maximum input value for each axis (Figure 2.10; code available in Appendix A.6).

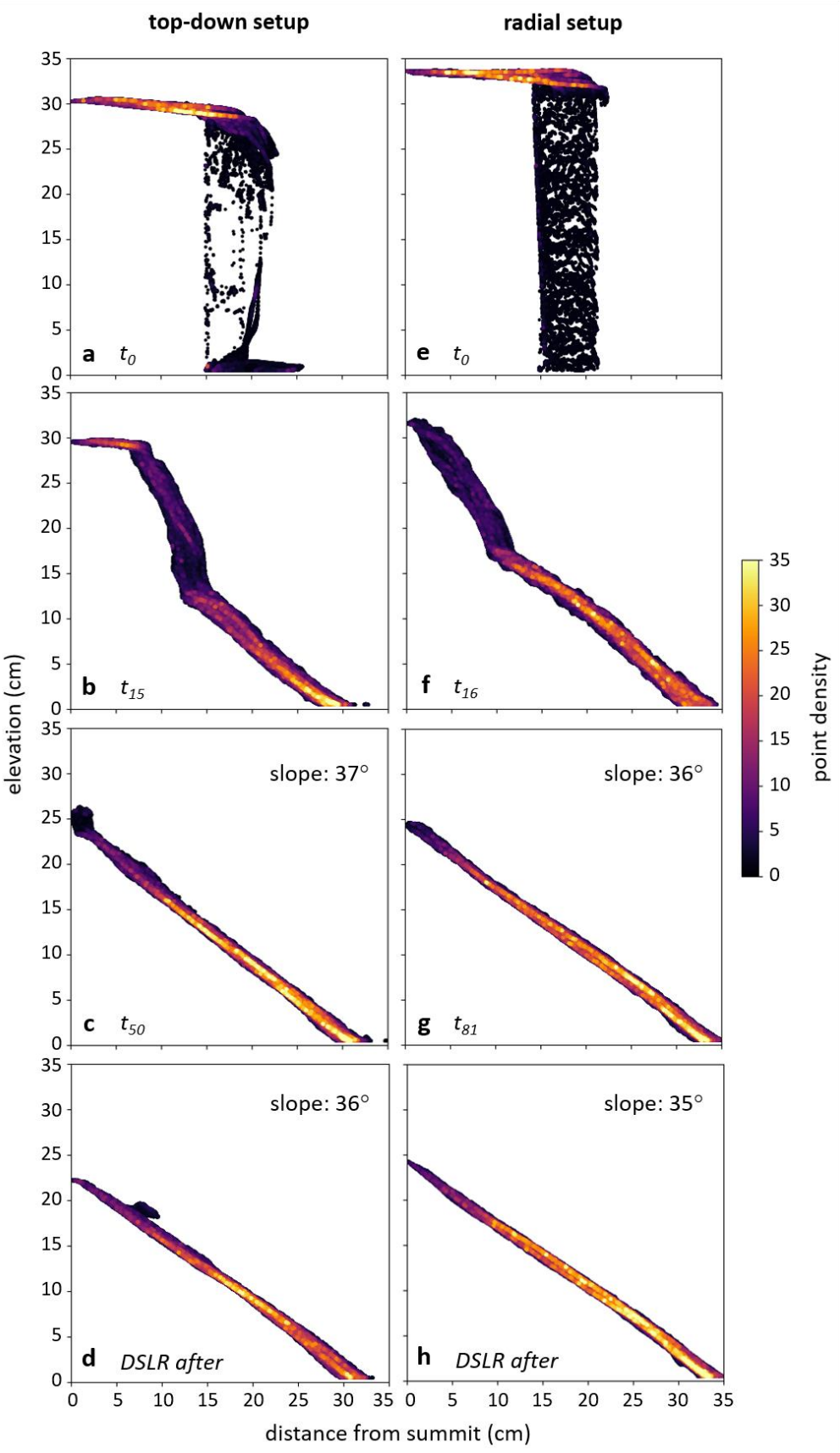

(caption on next page)

*Figure 2.10: average radial shapes of the model with the top-down setup for **a.** t_0, **b.** t_{15}, **c.** t_{50}, **d.** DSLR after; and with the radial setup for **e.** t_0, **f.** t_{16}, **g.** t_{81}, **h.** DSLR after. Subscript values of t indicate the time in hours since the beginning of the experiment. For each plot, axes scales are shown as 1:1. Each point is plotted from a value of distance from the summit (x-axis) and a value of elevation (y-axis). For each time step, we computed the data point density on a grid of 2000x2000 bins. The density scale is the same for all panels. The mean slope (i.e. slope of the best fitting line) is indicated for the final time steps, from the Pis and the DSLR DEMs for the both setups.*

We see that for the first time step (i.e. the initial cubic shape, t_0), the scatter plots are sparse at the level of the vertical face (Figure 2.10a and e). This is due to the fact that this initial shape has no radial symmetry, hence the vertical faces are located at a range of distances from the centre of the model.
Note that on the second time step (i.e. the intermediate shape, t_{15} and t_{16} respectively for the top-down and the radial setup; Figure 2.10b and f) horizontal surfaces show higher point densities than the more vertical ones. It can be explained by the radial irregularity of the sub-vertical faces, that are rapidly degrading.
The final shapes of the models are radially symmetrical, and are well-resolved (i.e. t_{50} and t_{81} respectively for the top-down and the radial setup, plus the final DSLR). This is reflected in high point density of the corresponding scatter plots (Figure 2.10c, d, g and h). Plots made from the Pis and the DSLR DEMs are similar for both setups (Figure 2.10c/d and g/h), with slight differences that are explained in Section 2.3.2.2. By using the least squares method we compute the best fit line to those plots, which allows to calculate the average radial slope of the whole models. With the DEMs made from the Pis, we obtain similar values for both setups, as well as low residuals: ~ 37° (top-down setup, Figure 2.10c; $R^2 > 0.98$; RMSE ≈ 0.69) and ~ 36° (radial setup, Figure 2.10f; $R^2 > 0.99$; RMSE ≈ 0.43), which is expected as the same sediment is used in both experiments. The slopes calculated from the DSLR DEMs are also slightly lower compared to those of the Pis DEMs (top-down setup: 36° *vs.* 37°; radial setup: 35° *vs.* 36°). It can also be explained by the slight settling of the models, described in Section 2.3.2.2.

2.3.3. Uncertainties

2.3.3.1. Time synchronisation of the Pis

The Pis are not equipped with Real-Time Clock (RTC) modules, which means that their internal clock is not set automatically. Therefore, to evaluate the variability on the time synchronisation between the Pis we perform a test in which we place a digital clock displaying a timer in the scene. For each Pi, we manually record the displayed time on the timer on the photos, for two early time steps (t = 0 and t = 0.5h) plus four consecutive time steps several hours after the beginning of the test (t = 18h, t = 18.5h, t = 19h, t = 19.5h). At each time step, we compute i. the average value of the time recorded by all the Pis; ii. from i., the shift between that average and the individual values of the Pis; iii. the standard deviation of recorded times at each time step (Figure 2.11).
Standard deviations range from 0.24s (t = 19h) to 0.39s (t = 18h) over the test. The maximum time shift observed is 0.62s (Pi 17 at t = 18h), and the maximum delay between earliest and latest Pis is 1.1s (Pis 3 and 17 at t = 18h). No statistically representative increase in time shift can be observed with time.
During our experiments, some movements (e.g. grain or debris avalanches) occur rapidly – a few seconds at most. Therefore, the maximum time delay we computed (1.1s) is not negligible compared to the speed of those movements. However, for our setup to fail capturing a steady scene, a movement (significant enough in terms of limit of detection) must occur during a time window of maximum 1.1s over a period of 30min. Moreover, such data loss at a given time step does not prevent us to analyse an experiment as other,

close time steps are still available. The table summarising the time synchronisation test is presented in Appendix A.3.

2.3.3.2. Absolute error on dimensions

The sets of photos for each time steps are all co-aligned (Section 2.2.3.), hence they all share the same coordinate reference system. Therefore, to estimate the absolute error of our DEMs, we can place scales of known dimensions in the scene and compute their estimated dimensions in the coordinate reference system of a given experiment. For the top-down setup, we used a scale of 40 cm (Figure 2.4a); for the radial setup, we used four pairs of vertical targets separated by 22 cm (Figure 2.4b) and three 10-cm horizontal scales. In the top-down setup, the absolute error on the scale is ~ 0.122 cm (0.3% of the total length of the scale bar). In the radial setup, the absolute error is ~ 0.024 cm (0.1%) on average of the four vertical scales, and ~ 0.025 cm (0.3%) on average of the three horizontal scales. The table summarising the absolute error on dimensions is presented in Appendix A.4.

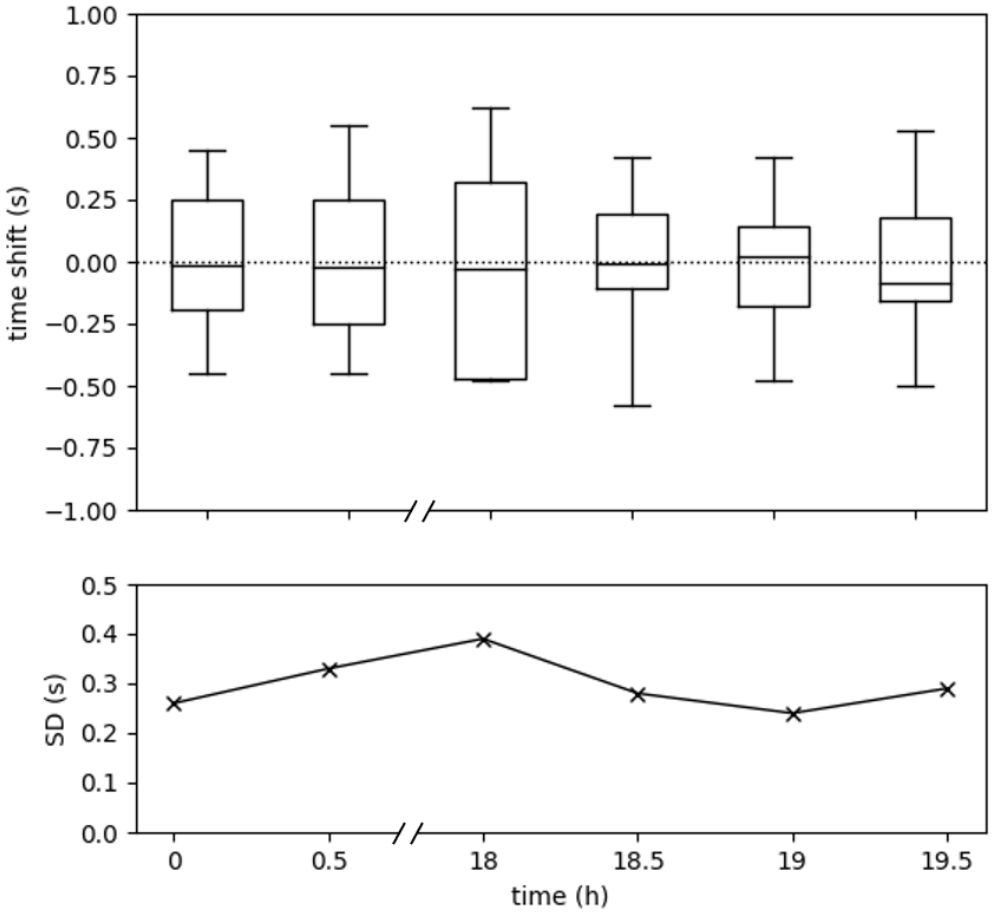

*Figure 2.11: **top**: boxplot of the time shifts, between each Pi and the average value of time displayed, at each time step of the synchronisation test. Time shifts are expressed in seconds. Each box extends from the first to third quartile values (Q1 to Q3), and the median value (Q2) is represented by the horizontal line within each box. Whiskers encompass all of the data points. The horizontal dotted line represents a zero time shift. **bottom:** standard deviation (SD) of the time shifts at each time step.*

2.3.3.3. Intra-experimental statistical variability

To estimate the statistical variability of the model volumes within an experiment, we computed the volumes of successive DEMs during a steady time series, when no more movement was observable (i.e. when degradation was finished). Volumes are here calculated above a reference plane (z = 0; Section 2.3.2.1.; Figure 2.7). We then calculated the standard deviation of the volume series.

The top-down setup (6 DEMs included) and the radial setup (8 DEMs included) respectively have standard deviations of 0.20 dm^3 (0.8% of the average computed volume) and 0.06 dm^3 (0.2% of the average computed volume) over the motionless time series. Note that the radial setup shows a smaller error compared to the top-down setup due to the higher number of photos available per model (Figure 2.2). The volumes of the DEMs used for error calculation are not shown in Figure 2.7, and are presented in Appendices A.1 and A.2 – for the top-down and radial setups, respectively.

To estimate the statistical variability of the DEMs, we also computed the pixel values of DoDs made from successive DEMs during the steady time series, within a zone on the platform which is totally immobile (Figure 2.12). For the top-down setup (Figure 2.12a), more than 97% of the pixels show absolute values of elevation shift below 2 mm, and less than 0.05% of the pixels show values above 5 mm. The radial setup (Figure 2.12b) shows significantly better performance, with more than 99.8% of the pixels showing absolute values of elevation shift below 2 mm. No systematic trend emerges from this analyse. Hence, we infer that patches of movements seen in DoDs are significant above 5 mm for the top-down setup, and above 2 mm for the radial setup (Section 2.3.2.2.). The table summarising the intra-experimental variability is presented in Appendix A.5.

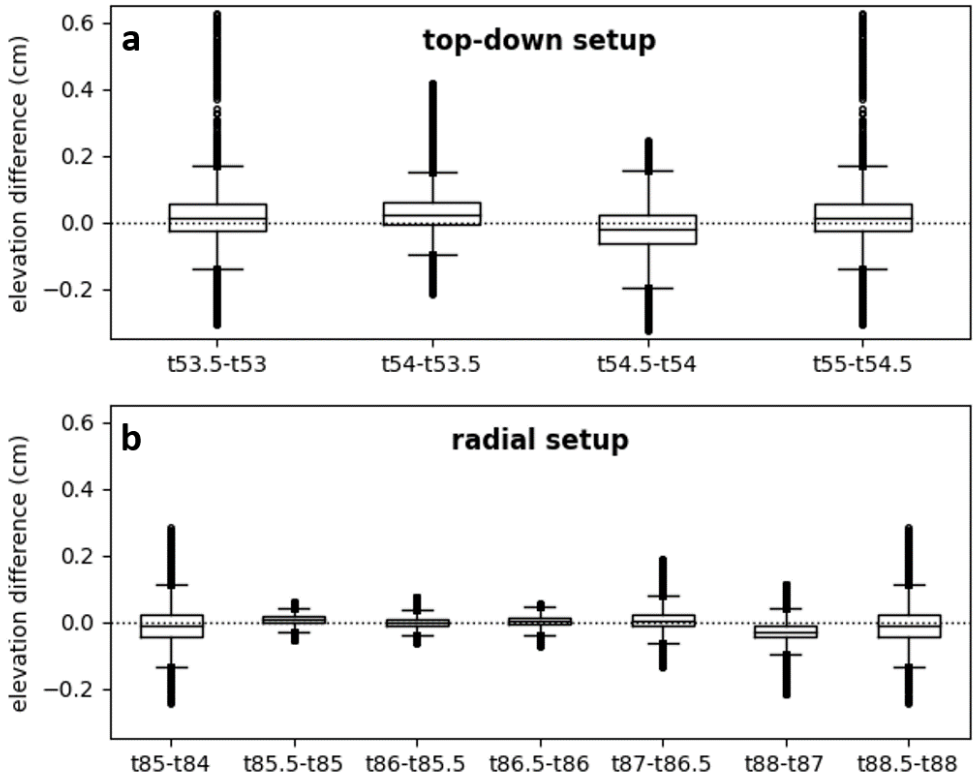

*Figure 2.12: boxplots of elevation shift measured from pixel values of DoDs made from successive DEMs, during a steady time series and within an immobile zone, for **a.** the top-down setup (n = 120120 pixels) and **b.** the radial setup (n = 120509 pixels). The elevation shift is expressed in centimetres. Values of t in the labels of the x-axis indicate which DEMs were used to compute the DoD, i.e. the time in hours since the beginning of the experiment.*

2.4. Discussion

2.4.1. Performance of the setup

With 18 microcomputers and cameras, our setup allows the production of DEMs of experimental models with a sub-millimetre horizontal resolution (here fixed at 0.5 mm; Section 2.2.3.) at a distance of 2 m. We also showed in Section 2.3.3. that, with the radial setup, the absolute error on distance measurements is sub-millimetre and the variability on volume computation is below 1% of the average volume for a motionless time series. In addition, the time synchronisation achieved by our setup allows the monitoring of morphometrics with a high temporal resolution: with a maximum of 1.1 s between the first and last photos (Section 2.3.3.1.), a time step of less than 1 min between two photo acquisitions would be feasible. However, we currently gather all photos acquired at a given time step before the next acquisition, and this process currently takes several minutes. Therefore, for short time steps, the photo transfer process would need to be modified – for example by sending all photos as a batch at the end of the experiment. Moreover, a time step below ~ 15 s (i.e. for a model evolving very quickly) is not recommended, unless improvements are made on the camera synchronisation and on the acquisition speed. To improve camera synchronisation, a solution could be to implement high-precision RTCs into each Pi, and set their date/time regularly on the RTC of the Master Pi. To improve photo acquisition speed, one could i. manually set camera parameters (in order to exposure time and shutter speed); ii. optimise the photo acquisition code, potentially by trying an OS-based program if quicker; iii. use Pis with high-precision RTCs and a photo-acquisition program running continuously. Point iii. would, however, favour instrumental drift between the different Pis, and would be sensitive to power failures as the aforementioned code would simply stop.
Overall, our setup achieves its initial goals. First, generating temporally regular DEMs over the duration of the experiments, with sufficient quality to allow the monitoring of sediment movements (here down to the millimetre-scale; Sections 2.3.2.2. and 2.3.3.3.) both qualitatively and quantitatively. The DEMs also allowed us to measure volumes, cross-profiles and radial profiles of our models over time. The DEMs generated from DSLR photos logically tend to be more accurate than the ones from the Pis because they incorporate larger sets of photos. Yet, our setup with 18 cameras is of acceptable accuracy for the measurements we want to make when compared to DEMs generated from DSLR photos. DEMs made from the Pis for the initial and final shape of the models are consistent with DEMs made from the DSLR camera (Section 2.3.3.), with a volume difference below 1% of the total volume (Section 2.3.2.1.). DoDs and profiles computed with both techniques are close or even overlapping, with millimetre-scale differences that are explained in Section 2.3.2.2.

Our radial setup shows better performance overall than the top-down setup: fewer artefacts appear in the DEMs (Supplementary Material), its absolute distance error is equal or smaller (0.3% of the total length for top-down setup; 0.1% and 0.3% for respectively the vertical and horizontal scales for the radial setup; Section 2.3.3.2.), and the intra-experimental variability is also smaller (0.2% of the average volume against 0.8% for the top-down setup; 99.8% of the absolute elevation shift values below 2 mm, against 97% for the top-down setup; Section 2.3.3.3.). For the final requirement of being able to detect the character and magnitude of individual or groups of mass-wasting events, the top-down setup allows the monitoring of vertical movements above 5 mm with a 99.5% certainty, and above 2 mm with a > 97% certainty. The radial setup allows to monitor vertical movements above 2 mm with a 99.8% certainty. However, these values are calculated from individual pixel values; hence, movements around the detection limit observed over larger areas have a lower uncertainty than similar small movements detected over smaller areas. Overall, the movements discussed in Section 2.3.2.2. are above our detection limit.

2.4.2. Comparison with similar setups

Our setup has a number of benefits compared to similar setups used in other published experiments, which we detail below. We compare the performance of our set up, discussed in the subsection above, to eleven recent articles (2010 or after) that used photogrammetry (stereophotogrammetry or SfM) at the laboratory scale.

Setups using manual photo acquisition, i.e. a single DSLR camera, whether for stereophotogrammetry (Bertin et al., 2014; Peter Heng et al., 2010) or SfM (Balaguer-Puig et al., 2017; Fister et al., 2019; Guo et al., 2016; Herny et al., 2019; Raack et al., 2017; Yang et al., 2021), are subject to the same limitation: it is difficult or impossible to acquire sets of photos during the experiment. Depending on what is experimentally possible, some studies choose to acquire only one set before and one after the experiment (Bertin et al., 2014; Peter Heng et al., 2010; Herny et al., 2019; Philippe et al., 2023; Raack et al., 2017; Yang et al., 2021); some stop the experiment and start it again after photo acquisition (Balaguer-Puig et al., 2017; Fister et al., 2019); and one acquires a single high-frame rate video (12-20 frames/s), shot by moving around the target at regular intervals during the experiment, and generates DEMs from the video frame stills (Guo et al., 2016). Overall, acquisition of photos during experiments adds extra steps either to the experimental protocol or to the data processing. For Herny et al. (2019), Philippe et al. (2023) and Raack et al. (2017) it is not physically possible because the experiments run in a sealed, low-pressure chamber. Also, using video frames as sets of photos requires a model that is not evolving too quickly – for instance, in Guo et al. (2016), a video of the whole scene requires 2 minutes to be taken. Our setup allows the monitoring of the experimental model at the desired time step, during the whole experiment, without the need to stop and restart the experiment. It also allows us to go further and perform the same experiments but over longer durations, and with a shorter time step between photo acquisitions compared to Guo et al. (2016).

Setups using automatic photo acquisition for SfM also have limitations. Eltner et al. (2017) use three digital SLR cameras that take photos at regular intervals. They have to trigger the initiation of the regular photo acquisition series manually, and individually for each camera. They estimate the initial offset to be below one second. This setup can only work for experiments running over a short time, because the instrumental drift of the camera clocks will lead to an increasing desynchronisation with time. Moreover, adding cameras to that setup would make it challenging to initially trigger the individual cameras, as more operators would be needed. Our setup applied to this case would allow us to monitor the experiment with greater spatial resolution because of the higher number of cameras. It would also allow the monitoring of similar experiments but over a longer duration, than used in this publication, ensuring a continuous camera synchronisation. Lelandais et al. (2016, 2018) and Vérité et al. (2021, 2022) use a grid network of 6 and 9 DSLR cameras, respectively, mounted on a metal structure that comprises an experimental box of 70x70 cm and 200x200 cm, respectively – for a depth of 5 cm. The cameras are triggered from a single computer, ensuring long-lasting synchronisation. The main advantage our setup has over this one is its capacity to be moved, reprogrammed and adapted to be reused in various situations and for various object sizes – whereas this setup has a fixed location and a spatially delimited experimental bed.

2.4.3. Evaluation of the setup

2.4.3.1. Advantages

This set up is relatively flexible compared to similar ones we discussed above. First, the number of cameras can be adjusted, with the quality of DEMs increasing with the number of cameras (e.g. Westoby et al., 2012). Multiplying the number of cameras also increases redundancy between images, which can

compensate for the loss of some images, or a camera malfunction. We suggest increasing the temporal redundancy as well, by using a shorter time step than is desired. This can compensate for a time step when data was lost or camera malfunctioned. The location of the cameras can also be selected freely, taking into account the shape of the object to study. It can also be entirely moved to different locations, e.g. different experimental rooms containing models that are difficult or impossible to move. The time step of photo acquisition is fully flexible: between < 1 min (Section 2.4.1.) for as long as the data storage allows (networking would allow this upper limit to be flexible); and, in practise, weeks or even months.

Another advantage of our setup is that it works automatically, which means that no operator is needed on site to activate the cameras during the period of monitoring – except at the start to switch on the Pis. As the photo sorting by time step is also automated, our setup is also particularly suitable in cases where further automation is wanted (e.g. automatic dense cloud or even DEM generation). This automation is particularly useful in case of monitoring periods that are overnight, that are in places difficult to access, or that have a time step too short to be achieved with a manual acquisition. Moreover, the use of the time-based scheduler application (CRON; Section 2.2.2.) means that no script is running continuously. Therefore, if power comes back after a failure the setup will work again normally without the need for an operator. Within the setup, cameras also are independent from each other, so if one becomes dysfunctional or even breaks, the rest of the setup will keep working normally.

The lenses used for the Pi cameras can be selected among a wide range of FOVs: from wide angle (FOV = 50°) to telephoto lenses (FOV = 14°), which could allow monitoring of objects at a wide range of distances from the cameras, although we did not test this possibility ourselves. Our is easily repurposed: by changing the time step of the photo acquisition and buying new lenses, the same Pis can be used to monitor distant and close objects, at a high or at low photo acquisition frequency.

All of this can be achieved with only basic skills in programming. The Raspbian OS of the Pis is a flavour of Linux and the code that controls the photo acquisition is written in Python. Python and Raspbian have an extensive documentation which makes it easy to adapt the programming process we describe in this study. Finally, our setup is relatively cheap considering the wide range of monitoring possibilities and its capacity to be reprogrammed and reused at will. One of the devices we used in this study can be purchased for less than 150 € - including the microcomputer, power supply, storage SD card, camera and lens.

2.4.3.2. Limitations

The major drawback is that the setup is time consuming to put in place. Cameras have to be individually attached to the Pis, supports have to be designed and built, and several programs have to be uploaded onto each Pi. The manual implementation of those programs also favours user mistakes. Power needs to be supplied to each Pi. If data needs to be streamed or backed up during the experiment, then a network (cabled or non-cabled) has to be set up. Just prior to the experiment, the devices need to have their orientation adjusted, pointing towards the object to study, and the cameras have to be focused and their aperture adjusted manually. This can be time-consuming, because the mechanism is fiddly and the Pis are not plugged into an individual monitor, so settings must be adjusted by opening a remote desktop on the monitor in which the Master Pi is plugged in.

Another issue we encountered was the corruption or loss of data during photo acquisitions (Section 2.3.2.2.). This was due to memory overloads caused by deleted photos being stored in the local garbage bin. To solve that issue, we strengthened our memory saving protocol by deleting images on each Pis more regularly and emptying the garbage bin.

In addition, if protection from environmental conditions is needed (e.g. physical shocks, cold, heat humidity…), special protective cases will have to be bought (or designed and built). We did not test our setup in such situation, and thus cannot provide any feedback for that specific case.

2.4.4. Potential other applications

In this study we show that our setup is well-suited for close-range (metres) monitoring of analogue models at the laboratory scale. The performance and versatility of our setup makes it applicable in the general context of studies in geosciences. Indeed, it can be adapted to be used outside (e.g., by using batteries and a specific protective case), has an acquisition time step which can be adapted to objects with rates of change slower than 15 s, and the number and type of cameras can be adapted to various distances and object shapes/sizes.

For instance, it could be used to study natural landscapes or landforms: study of snow depth (e.g. Filhol et al., 2019), landslide displacement (similarly to Gabrieli et al., 2016, but with generation of DEMs), or rockfall detection (e.g. Kromer et al., 2019). For monitoring landscape-scale changes outdoors, Pis cannot be connected to the same computer by ethernet cables. In that case, in order to keep the Pis synchronised over a long period of time, RTCs can be synchronised and implemented into each Pi. If the photos need to be downloaded at each time step, mobile broadband modules can be used for each Pi, both to synchronise their internal clocks and to allow data transfer.

Our setup could also be useful in civil engineering, for instance as a monitoring solution for hazardous rock slopes (e.g. Haneberg, 2008), deformation of large structures (e.g. Maas and Hampel, 2006; experiments from Hu et al., 2021), or crack monitoring (e.g. Nishiyama et al., 2015).

2.5. Conclusions

Our study leads to the following conclusions:

1. By using microcomputers with dedicated cameras and photogrammetry software, we set up an automated system to generate time-lapse DEMs. The installation of this setup does not require advanced skills, neither for its construction nor in programming;
2. The quality of output DEMs is suitable for geomorphologic studies: it allowed us to monitor the volumes and profiles of our models over time, and to detect millimetre-scale mass movements;
3. Our setup has several benefits compared to existing setups, including full automation, independence of the cameras, capacity to work again after power failure, possibility to monitor continuously, a variable time step, a potential for the same equipment to be reprogrammed and used in different situations;
4. The setup is particularly suited for situations where manual acquisition is difficult or impossible – e.g. photogrammetry with time steps under a few minutes, experiments running for several days or in sealed chambers, or monitoring of areas that are remote, dangerous or difficult to access (e.g. mountainous landforms or engineering structures);
5. The versatility of the setup means that a wide variety of objects could be monitored – from small analogue models in close-range photography to natural landscapes with telephoto lenses. The number of cameras can also be adjusted according to the geometry of the target and the desired quality of DEMs.

2.6. Supplementary Material

Supplementary Material is available on an online repository. It contains: DEMs, time-lapse video of the first time steps of the experiment with the radial setup, spreadsheets of volume and error calculations, and the Python code computing radial profiles (Figure 2.10). https://doi.org/10.6084/m9.figshare.22332076.v1

3. Molards on Mars (Morino et al., 2023, *Icarus*)

The following section is a summary of a published article (Morino et al., 2023). *For that study, I performed part of the mapping, data analysis and figure creation, as well as participated in the writing process. Some of the interpretations in the present section are my own and do not belong to Morino et al. (2023); it is explicitly stated when applicable.*

Permafrost molards as an analogue for ejecta-ice interactions at Hale Crater, Mars

Costanza Morino[1], Susan J. Conway[2], **Meven Philippe[2]**, Coralie Peignaux[2], Kristian Svennevig[3], Antoine Lucas[4], Axel Noblet[2], Gioachino Roberti[5], Frances Butcher[6], Jake Collins-May[7]

[1]*Université Savoie Mont Blanc, CNRS UMR 5204, Laboratoire Environnements, Dynamiques et Territoires de la Montagne, France*
[2]*Nantes Université, Université d'Angers, Le Mans Université, CNRS UMR 6112, Laboratoire de Planétologie et Géosciences, France*
[3]*Geological Survey of Denmark and Greenland, Denmark*
[4]*Université de Paris, Institut de physique du globe de Paris, CNRS, France*
[5]*Minerva Intelligence Inc., Canada*
[6]*The University of Sheffield, Department of Geography, UK*
[7]*The School of Geography, Politics and Sociology, Newcastle University, UK*

3.1. Context of the study

The subsurface of the martian mid-latitudes is known to be ice-rich (Section I.2.3.; e.g. Dundas et al., 2021; Holt et al., 2008; Mouginot et al., 2010; Mellon et al., 2009). Previous studies have reported evidence for the presence of both pore ice and excess ice (e.g. Mellon et al., 2009; Smith et al., 2009). Distinguishing between these two types of ice is an important matter, as their formation processes differ. Martian pore ice is thought to have formed during high-obliquity periods, when the mid-latitudes climate was colder (e.g. Dickson et al., 2015; Kostama et al., 2006; Levy et al., 2009c). However, the formation of excess ice implies either i. the occurrence of periglacial processes similar to terrestrial ones (e.g. French, 2018), i.e. movements of liquid water in the close subsurface of Mars (Section I.1.2.; e.g. Cull et al., 2010a; Mellon et al., 2009); or ii. the burial of massive ice (e.g. in the case of VFFs; Section I.2.4.; e.g. Milliken, 2003; Squyres, 1978, 1979).
The projectile that formed Hale Crater on Mars one billion years ago (35°42 S', 36°31' W; Hartmann, 2005; Jones et al., 2011) impacted a terrain which is thought to be an ice-rich subsurface (Barlow and Perez, 2003; El-Maarry et al., 2013; Jones et al., 2011; Tornabene et al., 2012). However, the type of subsurface water ice – pore or excess ice – is unknown, and so is its depth and quantity. The crater ejecta are thought to have been fluidised by the melting of subsurface ice, and hence are thought to have flowed downhill, radially from the impact crater (Collins-May et al., 2020; El-Maarry et al., 2013; Grant and Wilson, 2018; Jones et al., 2011). Moreover, conical mounds were found in the southeastern part of the ejecta (Collins-May et al., 2020). Therefore, our aim in the present study is to understand whether these conical mounds could be martian molards, i.e. former ice-cemented blocks of sediment that degraded in place to form cones of loose debris (e.g. Brideau et al., 2009; Milana, 2016; Morino et al., 2019b; Sæmundsson et al., 2018). Further, if these features could be molards, what insights do they give into the state of subsurface water ice at the time of the impact, as well as into the rheology of the ejecta.

3.2. Methods

We first compare the geological settings of the conical mounds in the Hale ejecta to those in the Mount Meager debris avalanche (2010, Canada; Roberti et al., 2017). For Mount Meager, we map the extent of the debris avalanche and the position of molards on an orthophoto (0.08 m/pixel) created from a 3D model constructed with photographs taken from helicopter. We map separately the deposits associated with the 'water-poor phase', the 'intermediate phase' and the 'water-rich phase' of the debris avalanche (based on Roberti et al., 2017). For Hale crater, we map separately the inner ejecta, the outer and continuous ejecta, and the outer and discontinuous ejecta (based on Jones et al., 2011; Figure 3.1). We use images from the Context Camera (CTX; 6 m/pixel) to map more precisely the southeastern ejecta and the surficial morphologies they exhibit, including the area where the conical mounds are located (Collins-May et al., 2020). We use images from the High-Resolution Stereo Camera (HRSC; 25 m/pixel) to map the extent of the whole ejecta blanket.

We then compute the morphometrics (height, area and slope) of 571 molards in the Niiortuut and Paatuut rock avalanches (occurring in 1952 and 2000 in Greenland, respectively; Dahl-Jensen et al., 2004; Schack Pedersen et al., 2002; Svennevig et al., 2023) and of 2181 conical mounds in the Hale crater ejecta. For the Niiortuut and Paatuut rock avalanches, morphometrics of molards are measured on two DEMs (15 cm/pixel), created from helicopter-based photographs. For the Hale conical mounds, we use two DEMs (Zone A and Zone B, Figure 3.1) made from images of the High-Resolution Imaging Science Experiment (HiRISE; 25-50 cm/pixel; resolution of DEMs up to 1 m/pixel).

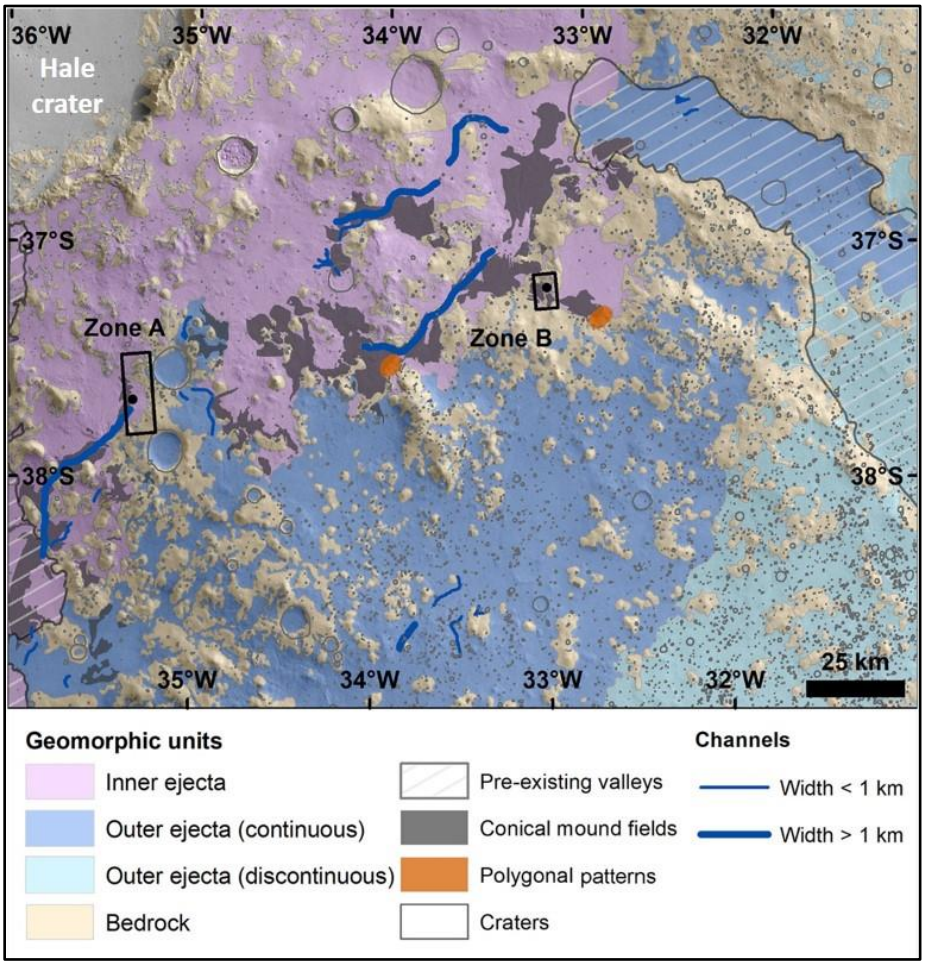

Figure 3.1: Geomorphological map of the southeast area of Hale Crater.

3.3. Geological setting and morphometrics of conical mounds

The molards of the Mount Meager debris avalanche (Figure 3.2a) are mostly found in the water-poor phase (84 % of the total number of molards), the intermediate and water-rich phase showing only a few patches of molards (8 % of the total number of molards for each phase). Indeed, the viscosity of the molard-bearing deposits had to be high enough in order to transport lithic debris and form terminal boundaries with a lobate shape. Hence, such deposits must have had a relatively low water content compared to the most fluidised phases. Similarly, the conical mounds around Hale crater are located in the distal part of the inner ejecta (Figure 3.2b), a unit which also shows lobate terminal boundaries (Figure 3.3). This unit is thought to contain meltwater and hence to be viscous (Collins-May et al., 2020).
Overall, the conical mounds in the Hale ejecta show circular to sub-circular planforms (Figure 3.2b) and conical shapes (Figure 3.4a) similar to terrestrial molards (Figure 3.2a; Figure 3.4b). They also have comparable flank slopes, between ~ 10° and 25° (Figure 3.5a). However, martian conical mounds are an order of magnitude taller (Figure 3.5b), and one to two orders of magnitude wider than the Greenland molards (Figure 3.5c). Such a difference between Earth and Mars could be explained by differences in thickness of frozen materials that were initially mobilised. As Morino et al. (2019b) suggested, the final height and area of molards should be positively correlated with the initial thickness of the frozen layer that is mobilised by a landslide.

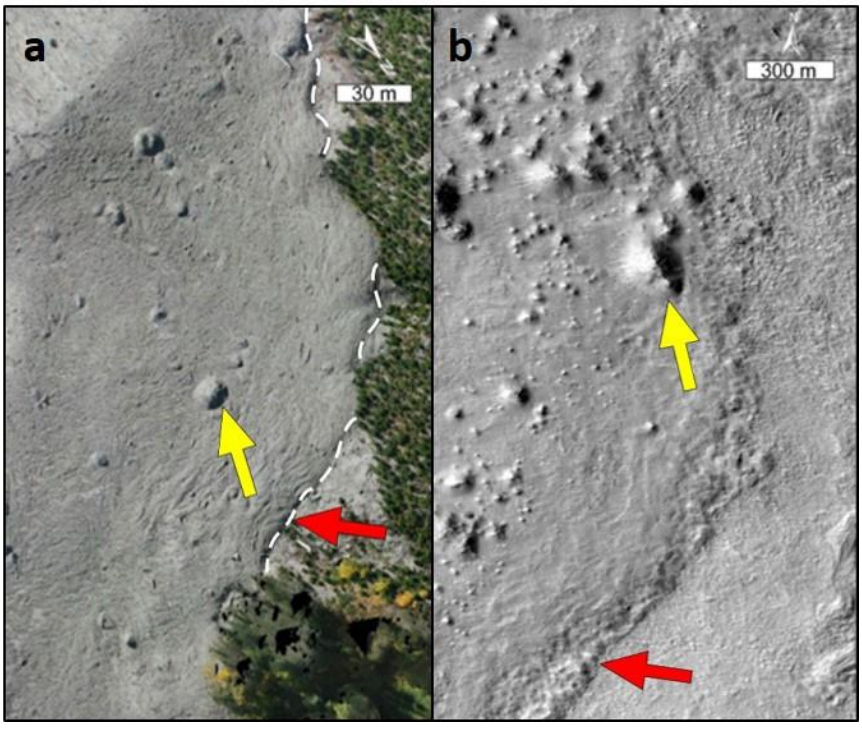

Figure 3.2: ***a.*** *boundary of the intermediate phase of the Mount Meager deposits, showing a patch of molards;* ***b.*** *boundary of the inner ejecta unit of Hale crater, showing a field of conical mounds. In both panels red arrows points to the unit boundaries, and the yellow arrows point to a molard (or conical mound), located near the boundary of the unit.*

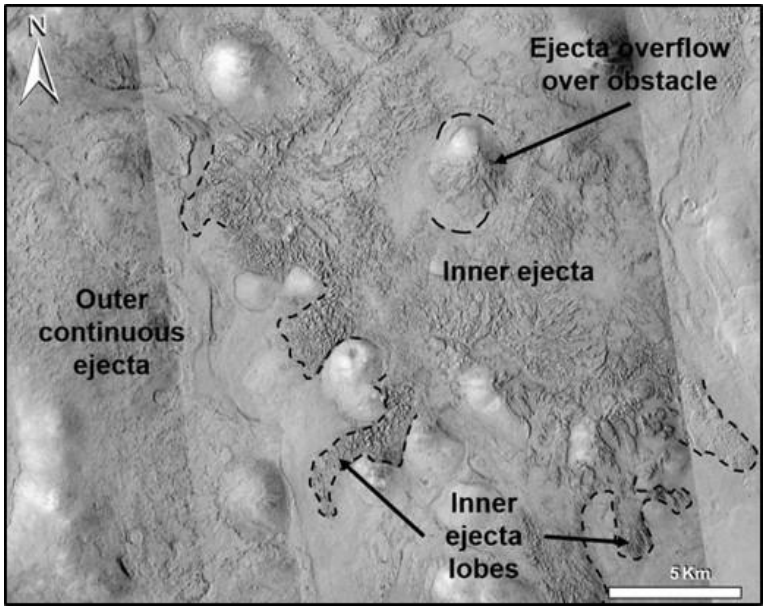

Figure 3.3: the boundary between inner and outer ejecta units, southeast of Hale crater. Note the lobate terminal shapes formed by the inner ejecta unit (CTX images: B03_010896_1425_XI_37S034W, B10_013665_1423_XN_37S035W and B11_013731_1426_XN_37S035W; credits: NASA/JPL/MSSS).

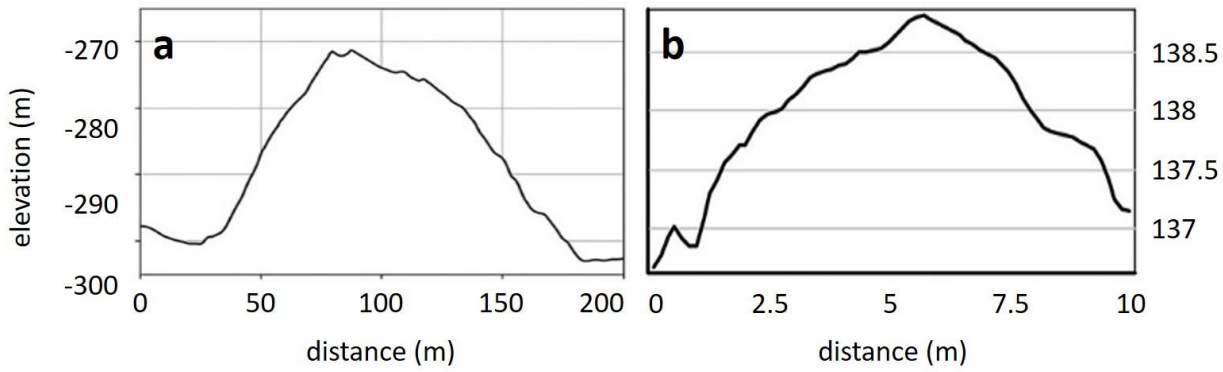

*Figure 3.4: cross-profiles of **a.** a martian conical mound, and **b.** a terrestrial molard. As martian conical mounds are globally taller and larger than the terrestrial molards, the vertical and horizontal scales are not identical on the two panels.*

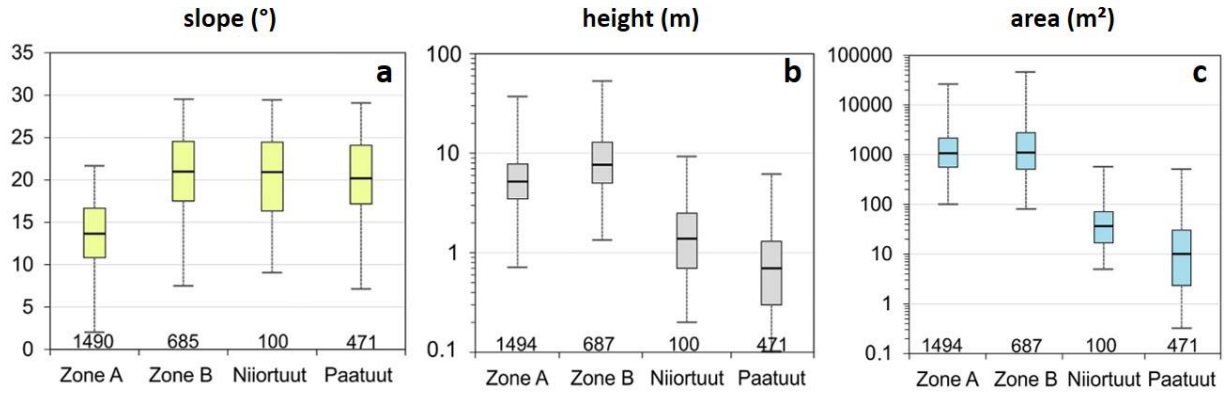

*Figure 3.5: boxplots of **a.** the flank slopes, **b.** the height, and **c.** the area of the mounds in Zone A and Zone B of Hale crater, and of molards in the Niiortuut and Paatuut rock avalanches. Note that the vertical axes for height and area use a logarithmic scale. The whiskers show the maximum and minimum values, the boxes mark the interquartile range, and the thick horizontal black lines are the medians of each population. The numbers on the x-axis show the number of mounds in each population.*

3.4. Interpretations and conclusions

1. The conical mounds found in the inner ejecta of Hale crater share similar geological settings with the molards from the Mount Meager debris avalanche; they also share similar shapes with molards from the Niiortuut and Paatuut rock avalanches. Therefore, we infer that those conical mounds are the first identified martian molards.
2. The presence of formerly ice-cemented sediment in the Hale ejecta indicates that subsurface ice existed in the form of pore ice at the time of the impact. Our observations rule out the presence of excess ice only, but it could have existed simultaneously with pore ice.
3. The larger size of the potential martian molards compared to the Greenland ones can be explained by a greater thickness of the ice-rich layer mobilised by the Hale impact, compared to the thickness of the ice-rich layer mobilised by the greenlandic rock avalanches.
4. Considering that potential martian molards are up to ~ 55 m high (Figure 3.5b), the lower limit for the thickness of the initial ice-rich layer is above 60 m. This conclusion is my own and does not belong to Morino et al. (2023).
5. We suggest the following chronological history for the Hale impact crater: one billion years ago, the Hale projectile impacted a terrain with an ice-rich subsurface. It volatilised part of the ground ice, but blocks of ice-cemented sediment withstood the impact and were incorporated into the ejecta. The dry ballistic ejecta formed the outer ejecta; the inner ejecta contained enough water to flow downslope, and were viscous enough in order to lobate terminal boundaries, and to transport the ice-cemented blocks of sediment to their distal part. These blocks then progressively degraded, probably because of ice sublimation, to form the molards we observe today.

III. Thermal-contraction polygons and subsurface properties

1. Introduction

In this section, I will focus on the research I performed on martian thermal-contraction polygons (Section I.2.5.). On Earth, thermal-contraction polygons form by thermal contraction of an ice-cemented ground. Subsequent liquid water activity can lead to polygons with various morphologies. Similar polygons are present on Mars, which raises question on potentially recent (Amazonian) activity of liquid water at the surface of the planet, despite the recent climate being thought to be too cold and dry to allow the sustained presence of surficial liquid water.
Therefore, Section 2. is constituted of an article (Soare et al., 2021) that presents a study of a population of thermal-contraction polygons, in Utopia Planitia (Mars). We investigate the relationship between the different polygon morphologies and the latitude, in order to conclude on the possible occurrence of geologically recent liquid water activity.
Then, Section 3. is constituted of an article (*in prep.*) which suggests that martian thermal-contraction polygons can be used to get insights into some geological properties of their substrate. We study the presence of the different polygon types for several geomorphological units in Utopia and Arcadia Planitiæ (Mars). In addition, we perform unit dating by crater size-frequency distribution and provide stratigraphic evidence that allow us to suggest geological origin for the studied units and the overall geological history of the studied areas.

The majority of the research effort presented in this section focuses on the northeastern part of Utopia Planitia, which leads to the necessity to introduce the geological story of the area.
Utopia Planitia is one of the martian northern plains, located in the Utopia impact basin (McGill, 1989), and northwest to the Elysium volcanic province. At a global scale, Utopia Planitia is covered in a regional geological unit – the Vastitas Borealis formation (Scott and Tanaka, 1986; Tanaka, 1986; Tanaka et al., 2005, 2014). This formation is interpreted as Late Hesperian regional sediment deposits, from an ocean/lake (e.g. Ivanov et al., 2014, 2015; Parker et al., 1993; Tanaka et al., 2014), and/or fluvial activity (e.g. Tanaka et al., 2014), and/or outflow channels (e.g. Costard and Kargel, 1995; Tanaka et al., 2005). This aqueous sedimentation could have been intercalated with volcanic material from the Elysium province (e.g. Russell and Head, 2003; Tanaka, 1986; Tanaka et al., 2014). It was suggested that Hesperian volcanic units from the main activity of the Elysium province underly the Vastitas Borealis formation (e.g. Fuller and Head, 2002, Russell and Head, 2003).
During the Amazonian, at the scale of our study area (northeastern part of Utopia Planitia), additional aqueous and volcanic material could have been deposited (e.g. Tanaka et al., 2005; Tanaka et al., 2014). It is also thought that the ice-rich material constituting the Vastitas Borealis formation was reworked by periglacial-like processes (e.g. Russell and Head, 2003; Tanaka et al., 2005; Tanaka et al., 2014), forming notably thermal-contraction polygons (REFs). In addition, numerous episodes of high obliquity during the Amazonian caused regular periods of lower temperatures (e.g. Jakosky and Carr, 1985; Mellon and Jakosky, 1995; Mischna et al., 2003), which led to the deposition of layers of mixed ice and dust in Utopia Planitia (Head et al., 2003; Kreslavsky and Head, 2002). The regularity of high-obliquity events caused the deposition of successive layers throughout the Amazonian (Dickson et al., 2015; Kostama et al., 2006; Levy et al., 2009c), with the most recent events being as young as a few million years (e.g. Kostama et al., 2006; Levy et al., 2009c; Schon et al., 2012a).

2. Potential ice-wedge polygons in Utopia Planitia (Soare et al., 2021, *Icarus*)

The following section is a direct copy of a published article (Soare et al., 2021). For that study, I: performed the mapping, data analysis and figure creation; wrote the Methods section; participated in the scientific interpretation and writing processes.

Possible ice-wedge polygonisation in Utopia Planitia, Mars and its latitudinal gradient of distribution

Richard J. Soare[1], Susan J. Conway[2], Jean-Pierre Williams[3], **Meven Philippe[2]**, Lauren E. McKeown[4], Etienne Godin[5], Jordan Hawkswell[6]

[1]*Geography Department, Dawson College, Montreal, QC, Canada*
[2]*Nantes Université/Université d'Angers/Le Mans Université, Laboratoire de Planétologie et Géosciences, CNRS UMR 6112, Nantes, France.*
[3]*Earth, Planetary and Space Sciences, University of California, Los Angeles, CA, USA.*
[4]*Earth Sciences Department, Natural History Museum. South Kensington, London. U.K.*
[5]*Centre for Northern Studies, Laval University, Quebec City, QC, Canada.*
[6]*Ocean Wise, PO Box 3232, Vancouver, BC, Canada.*

DOI: 10.1016/j.icarus.2020.114208

2.1. Introduction

On Earth, ice complexes (also referenced as ice-rich terrain) at or near the surface or to decametres of depth are ubiquitous within the permafrost of Arctic coastal-plains, i.e. the Tuktoyaktuk region of northern Canada (e.g. Murton et al., 2005; Rampton, 1988; Rampton and Bouchard, 1975) and the Laptev peninsula of northeastern Siberia (e.g. Grosse et al., 2007; Morgenstern et al., 2013; Schirrmeister et al., 2002, 2017; Strauss et al., 2017). Some examples of this terrain are:

a) Hummocky thermokarst (ballooned by aggraded excess-ice and deflated where the excess ice has been lost by evaporation, drainage or sublimation).

b) Thermokarst lakes, i.e. pooled meltwater resulting from the thaw of excess ice.

c) Alases (thermokarst-lake basins depleted of water).

d) Ice-wedge polygons, typically ≤ 25 m in diameter. Morphologically, they can be distinguished by three principal archetypes. 1. Low-centres relative to high margins/shoulders where the ice wedges have/are aggraded/aggrading (lcps); 2. high-centres relative to low margins/troughs where the ice wedges have/are degraded/degrading (hcps); or, 3. centres and margins that exhibit no discernable elevation difference, indicative of ice-wedge incipience or of a more mature and transitional stage between aggradation and degradation.

Pulses of ice-complex formation have been associated with inter-and intra-glacial mean-temperature rises and falls that reach back through the Holocene epoch (e.g. Grosse et al., 2007; Morgenstern et al., 2013; Murton et al., 2005; Rampton, 1988; Rampton and Bouchard, 1975; Schirrmeister et al., 2013), to the Wisconsinan glacial stage (e.g. Grosse et al., 2007; Morgenstern et al., 2013; Murton et al., 2005; Rampton, 1988; Rampton and Bouchard, 1975; Schirrmeister et al., 2013) and, even into the earlier periods of the Pleistocene Epoch (e.g. Kanevskiy et al., 2011; Rampton, 1988).

Ice-wedge polygon networks are current as well as paleo-markers of temperature variances. The nascent conditions required for the ice-wedges to form are continuous permafrost, thermal-contraction cracking, meltwater, hoarfrost (to a much lesser degree), and seasonal/annual (mean) temperature fluctuations above and below 0° C (e.g. Lachenbruch, 1962). Where low-centred (aggraded) and high-centred (degraded) polygons are closely set, this marks a system actively in thermal disequilibrium and transition (French, 2007; Grosse et al., 2007; Morgenstern et al., 2013; also, Rampton, 1988; Rampton and Bouchard, 1975; Schirrmeister et al., 2002; Washburn, 1976).

Mars-based lcps and hcps that are similar in shape and size to those observed on Earth have been reported antecedently in the literature (e.g. Lefort et al., 2009; Levy et al., 2009a, 2010b; Séjourné et al., 2011; Soare et al., 2014a, 2018). This having been said, questions concerning whether ice or sand underlies the margins of the Martian lcps and hcps remain open-ended, for two main principal reasons (e.g. Lefort et al., 2009; Levy et al., 2009a, 2010b; Séjourné et al., 2011; Soare et al., 2014a, 2018).
First, and based solely on the plan-based observation of lcps or hcps on Earth and on Mars, the identification or discrimination of sub-marginal materials is not possible. This is due to the similarity of form and scale between ice-and sand-wedge polygons when viewed planimetrically, from above (Hallet et al., 2011; Hauber et al., 2011b; Levy et al., 2009a, 2010b; Soare et al., 2014a, 2018).
Second, metres-wide ice wedges are not unusual amidst northern ice-complexes on Earth. Their development is incremental and episodically iterative, ranging through hundreds of seasonal/annual freeze-thaw cycles and meltwater fills (Lachenbruch, 1962). A similar or an even greater number of iterations would be required on Mars for similarly scaled ice-wedges to evolve. Current (mean) water-vapour pressures at or near the surface are as much as two orders of magnitude lower than on Earth (e.g. Rennó et al., 2009; Trokhimovskiy et al., 2015) and are inconsistent with the freeze-thaw cycling of water at a region-wide scale. There are areas, however, where the triple-point of water is exceeded (e.g. Haberle et al., 2001; Hecht, 2002). What is unclear is whether the temporal extent of this meta-stability, current, past or long past, could have supported the iterative requirements of ice-wedge formation.

In this article we plot, describe, discuss and statistically evaluate the distribution of lcps and hcps in Utopia Planitia [UP] (40-50° N; 100-125° E) (Fig. 2.1). The latter is one of the great northern plains of Mars. We assume that here in our study region, as elsewhere on Mars, the stability of ground ice increases with its poleward latitude. This is because (mean) annual surface and near-surface temperatures tend to remain below the atmospheric frost-point with poleward proximity, mitigating ice loss by sublimation (e.g. Clifford, 1993; Mellon and Jakosky, 1993, 1995). Consequently, ice-aggraded polygons should show a higher density of distribution with poleward proximity than ice-degraded polygons and vice versa.

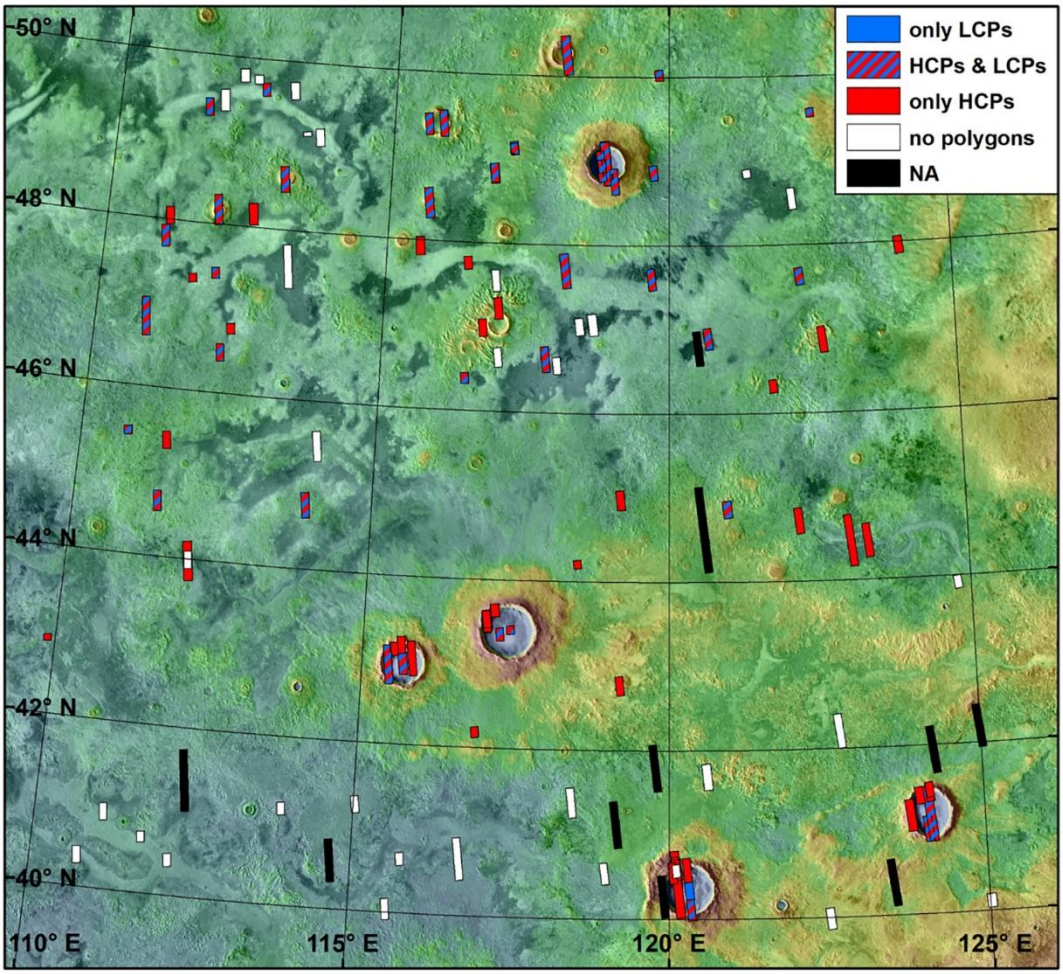

Fig. 2.1. View of the study region in Utopia Planitia (Lambert conformal conic-projection). The footprints of the 119 HiRISE images scanned for this study displayed with different colours according to the type(s) of polygons observed therein: blue, low-centred polygons (lcps); red, high-centred polygons (hcps); blue/red strips: lcps and hcps; white: no polygons; and, black: non-analysable image. Background: MOLA (Mars Orbiter Laser Altimeter) elevation data overlapping THEMIS (Thermal Emission Imaging System) daytime-IR mosaics. MOLA data credit: MOLA Science Team; Arizona State University; THEMIS image credit: Arizona State University. (For interpretation of the references to colour in this figure legend, the reader is referred to the web version of this article.)

2.2. Methods

All of the High Resolution Imaging Science Experiment (HiRISE) images (N = 135) in our study region (40-50° N; 110-125° E) were surveyed for the presence of low- or high-centered polygons (Fig. 2.1). To ensure the consistency of our observations and interpretations, multiple co-authors evaluated the images independently and our database (Table 2.1) integrates these evaluations.

***HiRISE* image ID**	**Center latitude**	**Center longitude**	**Resolution (centimetre/pixel)**	**HCPs**	**LCPs**	**Polygons (not possible to differentiate or showing no centre/margin elevation differences)**	**LCP/HCP ratio**
ESP_017127_2205	39.983	122.510	50	-	-	-	0.00
ESP_034243_2205	40.037	115.588	50	-	-	x	0.00
ESP_028652_2210	40.112	120.344	25	x	x	x	0.10
ESP_042801_2205	40.117	125.012	25	-	-	x	0.00
PSP_010679_2205	40.322	120.143	50	x	-	x	0.00
PSP_010257_2205	40.338	120.316	50	-	x	x	0.00
ESP_046441_2205	40.375	110.751	25	-	-	-	0.00
ESP_026028_2210	40.420	112.161	25	-	-	-	0.00
ESP_027597_2210	40.535	118.982	50	-	-	-	0.00
ESP_056937_2210	40.548	120.054	50	x	-	x	0.00
ESP_026542_2210	40.574	120.282	50	x	-	x	0.00
PSP_001528_2210	40.584	120.112	25	x	-	x	0.00
PSP_002214_2210	40.591	120.116	25	x	-	x	0.00
ESP_046454_2210	40.636	115.776	25	-	-	-	0.00
ESP_046797_2210	40.665	111.716	25	-	-	x	0.00
PSP_006249_2210	40.668	116.687	25	-	-	x	0.00
ESP_029338_2215	40.915	111.094	25	-	-	-	0.00
ESP_016705_2215	41.006	124.086	25	x	x	x	0.22
ESP_026595_2215	41.145	113.867	25	-	-	x	0.00
ESP_016283_2215	41.172	123.818	25	x	-	x	0.00
PSP_006908_2215	41.178	124.127	25	x	x	x	0.75
ESP_059245_2215	41.254	115.030	25	-	-	-	0.00
ESP_026041_2215	41.374	118.446	50	-	-	x	0.00
PSP_008846_2220	41.402	123.965	25	x	-	x	0.00
ESP_036603_2220	41.430	124.127	25	x	-	x	0.00
ESP_052796_2220	41.468	124.125	25	x	-	x	0.00
PSP_005972_2220	41.688	120.607	25	-	-	x	0.00
ESP_046032_2225	42.181	116.875	25	x	-	x	0.00
ESP_025632_2225	42.208	122.736	50	-	-	x	0.00
ESP_046322_2230	42.769	119.194	25	x	-	x	0.00
ESP_046652_2230	42.892	109.887	25	x	-	x	0.00
ESP_036366_2235	42.939	115.432	50	x	x	x	0.21
ESP_011523_2235	42.953	115.671	25	x	x	x	2.85
ESP_037223_2235	43.023	115.817	50	x	-	x	0.00
ESP_035456_2235	43.125	115.516	25	x	-	x	0.00
ESP_034744_2235	43.177	115.630	50	x	-	x	0.00
ESP_053205_2235	43.351	117.229	25	x	x	x	7.67
ESP_026608_2240	43.408	117.397	25	x	x	x	3.75

ESP_018960_2240	43.469	116.999	25	x	-	x	0.00
ESP_043566_2240	43.492	117.003	50	x	-	x	0.00
ESP_052704_2240	43.506	117.009	50	x	-	x	0.00
ESP_025896_2240	43.508	117.023	25	x	-	x	0.00
ESP_020516_2240	43.634	117.133	25	x	-	x	0.00
ESP_027821_2245	43.916	124.769	25	-	-	-	0.00
PSP_006882_2245	43.976	112.024	25	x	-	x	0.00
ESP_045610_2245	44.203	118.475	25	x	-	x	0.00
ESP_026410_2250	44.463	123.309	50	x	-	x	0.00
ESP_026621_2250	44.466	123.030	25	x	-	x	0.00
ESP_026094_2250	44.658	111.423	25	x	x	x	0.15
ESP_026265_2250	44.717	122.175	25	x	-	x	0.00
ESP_055038_2250	44.758	113.895	50	x	x	x	0.11
PSP_006618_2250	44.863	120.978	25	x	x	x	0.14
ESP_027808_2255	44.973	119.182	25	x	-	x	0.00
ESP_028072_2255	45.384	111.469	50	x	-	x	0.00
ESP_034164_2260	45.457	110.806	25	x	x	x	0.27
ESP_055671_2260	45.464	114.016	50	-	-	-	0.00
ESP_046401_2265	46.323	121.789	25	x	-	x	0.00
ESP_059390_2265	46.383	116.466	25	x	x	x	0.03
ESP_027650_2275	46.480	112.225	50	x	x	x	0.11
ESP_034823_2270	46.562	118.054	50	-	-	x	0.00
ESP_044977_2270	46.634	117.853	50	x	x	x	0.03
ESP_063992_2270	46.641	117.028	25	-	-	x	0.00
ESP_063768_2270	46.774	112.373	25	x	-	x	0.00
ESP_026450_2270	46.824	110.888	50	x	x	x	0.10
ESP_046757_2270	46.868	122.663	50	x	-	x	0.00
ESP_050304_2270	46.891	120.677	50	x	x	x	0.15
ESP_060168_2275	46.986	116.748	25	x	-	x	0.00
PSP_009334_2275	47.028	118.433	25	-	-	-	0.00
ESP_017549_2275	47.054	118.665	25	-	-	x	0.00
ESP_059746_2275	47.224	117.010	50	x	-	x	0.00
ESP_027861_2275	47.333	111.624	25	x	-	x	0.00
ESP_063979_2280	47.416	112.014	25	x	x	x	0.31
ESP_059957_2280	47.552	116.950	25	-	-	x	0.00
ESP_026384_2280	47.567	113.273	25	-	-	-	0.00
ESP_046467_2280	47.596	119.686	25	x	x	x	0.13
ESP_035614_2280	47.622	122.285	50	x	x	x	0.04
PSP_009901_2280	47.688	118.166	50	x	x	x	0.07
ESP_046388_2280	47.752	116.447	25	x	-	x	0.00
ESP_027505_2280	47.801	111.077	25	x	x	x	0.04
ESP_027096_2285	47.933	115.583	25	x	-	x	0.00
ESP_017206_2285	47.958	124.059	25	x	-	x	0.00

ESP_035021_2285	48.043	111.117	25	x	-	x	0.00
ESP_016046_2285	48.153	112.588	25	x	-	x	0.00
ESP_046164_2285	48.169	111.962	50	x	x	x	0.33
ESP_016336_2290	48.442	115.707	25	x	x	x	0.24
ESP_027043_2290	48.547	122.189	25	-	-	-	0.00
ESP_017035_2290	48.599	113.098	25	x	x	x	0.14
PSP_010125_2290	48.717	121.886	25	-	-	-	0.00
ESP_045399_2290	48.757	119.015	50	x	x	x	0.04
PSP_009756_2290	48.827	116.861	25	x	x	x	0.17
ESP_052506_2290	48.851	121.393	25	-	-	-	0.00
ESP_045544_2290	48.863	119.717	50	x	x	x	0.32
ESP_035535_2295	48.942	118.775	50	x	x	x	0.43
ESP_017760_2295	48.972	118.866	50	x	x	x	0.18
ESP_022850_2295	49.124	113.668	50	-	-	x	0.00
ESP_057768_2295	49.132	117.198	25	x	x	x	0.14
PSP_010244_2295	49.158	113.426	50	-	-	-	0.00
ESP_036432_2295	49.375	111.618	25	x	x	x	0.17
ESP_035667_2295	49.378	115.630	25	x	x	x	0.43
ESP_026885_2295	49.394	115.899	25	x	x	x	0.18
PSP_010521_2300	49.470	111.886	50	-	-	-	0.00
ESP_046546_2300	49.563	122.565	25	x	x	x	0.06
ESP_036577_2300	49.638	112.620	25	x	x	x	0.54
PSP_010455_2300	49.653	113.146	50	-	-	x	0.00
PSP_010099_2300	49.750	112.465	25	-	-	x	0.00
PSP_009888_2300	49.786	112.206	25	-	-	-	0.00
ESP_045333_2305	50.020	119.813	25	x	x	x	0.05
ESP_016837_2305	50.248	118.108	50	x	x	x	0.62

Table 2.1: Polygons in study region.

The survey itself was based on a grid-mapping approach (Ramsdale et al., 2017). Eleven images were too blurry to be evaluated; sixteen images were not surveyed because they were fully overlapped by images with higher resolution, or with equal resolution but greater spatial extent. These images have been excluded from the study and are not reported in Table 2.1. The remaining sample comprised 108 images, divided into two groups: 1) images whose resolution and/or quality support the unambiguous identification of lcps and/or hcps, if and when they are present (67 images, of which 41 have polygons); and, 2) images whose resolution and/or quality are of a lesser order, making the identification of lcps and hcps more difficult (41 images, of which 35 have polygons, Table 2.1).

The HiRISE image-footprints were gridded into reference squares of 250,000 m2 (37,639 squares) (Fig. 2.2a–b). Some squares were not fully within the HiRISE footprints. We excluded 4237 of those squares from our data base since they comprised less than half the area of a reference square, i.e. 125,000 m2. A further 111 squares were discounted because they overlapped with data gaps in the HiRISE image. As such, 33,291 squares were evaluated. If five or more candidate lcps or hcps were observed within each square

they were recorded. For grid squares where polygonised terrain was observed even in the absence of lcps or hcps, these grid squares were also recorded. Where fewer than five polygons were observed of any given type, they were not recorded for that grid square; highly localized if not stochastic boundary-conditions could have been responsible for the development of these small samples and would bias our evaluation of the larger population were they to be incorporated in our statistics. We are aware of and acknowledge that our five-unit (count/no count) threshold is arbitrary, but no more so than any other small unit-threshold that could have been used to differentiate meaningful samples from meaningless ones.

For each HiRISE image (Table 2.1) the number grid-squares containing lcp data-points was divided by the number of grid-squares containing hcp data-points to calculate the lcp/hcp ratio of each image (Fig. 1). Also, each scanned grid-square was related to: a) its centre latitude; b) the presence/absence of lcps or hcps; and, c) one of two terrain types (Type 1 and Type 2) by the location of their centre point. Type 1 comprises the whole study region exclusive of Type 2. The latter comprises the walls, rims and interiors of craters ≥ 2 km (in diameter). These outputs were used to evaluate the possible correlation between polygon type (i.e. the lcp/hcp ratio) and latitude/terrain type using regression analysis.

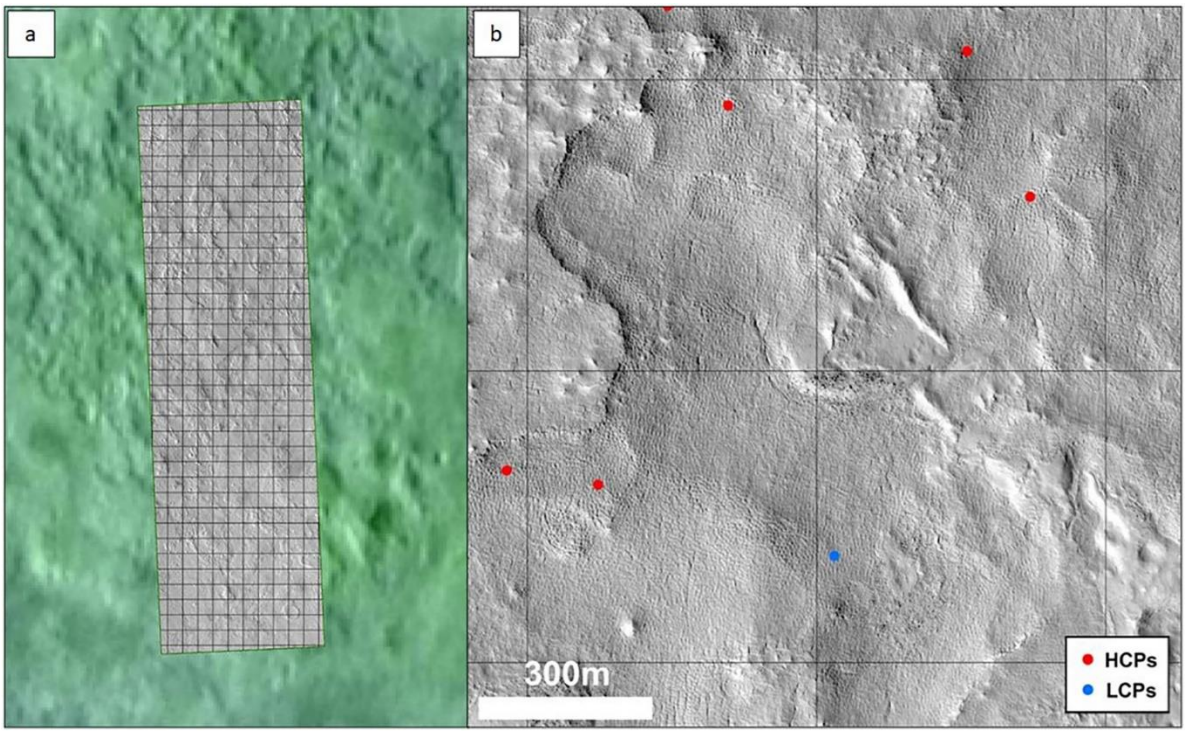

Fig. 2.2. a) HiRISE image ESP_055038_2250 gridded by 500 × 500 metres squares (background: MOLA elevation data overlapping a THEMIS daytime-IR mosaic). b) Zoom on four 500 × 500 metres-squares that illustrate the mapping method. Red and blue dots respectively locate lcps and hcps. North is up on all tiles. HiRISE image credit: NASA/JPL/University of Arizona; MOLA data credit: MOLA Science Team; Arizona State University; THEMIS image credit: Arizona State University. (For interpretation of the references to colour in this figure legend, the reader is referred to the web version of this article.)

Crater counts were conducted to derive information about the age of the polygonized terrain. HiRISE image ESP_026450_2270 (center longitude 110.880° E, center latitude 46.823° N) was selected within the study region as it contained polygons throughout the image; counts were conducted on the entire image covering 150 km2 at 0.5 m pix−1 resolution using the Cratertools plug-in for the ERSI ArcGIS to measure crater diameters (Kneissl et al., 2011). The crater-size frequency distribution (CSFD) was compared with modeled crater-retention age isochrons from Hartmann (2005) using Craterstats (Michael et al., 2016; Michael and Neukum, 2010).

2.3. Observations

Small-sized (~ ≤ 25 m in diameter) and clastically non-sorted polygons are ubiquitous in our study region. Typically, the polygons are hexagonal and enclosed by metre-scale margins. The margins exhibit: a) slightly-elevated (metre-high) shoulders (low-centred polygons, lcps), relative to the polygon centres (Fig. 2.3a, c); b) depressed troughs (high-centred polygons, hcps), relative to the polygon centres (Fig. 2.3b–c); or, c) variances of elevation between margins and centres that are small or non-existent (Fig. 2.3c), at the highest resolution available (~25 cm/pixel, HiRISE image).

Here, as elsewhere in Utopia Planitia (e.g. Costard and Kargel, 1995; Lefort et al., 2009; Levy et al., 2009a; Morgenstern et al., 2007; Seibert and Kargel, 2001; Séjourné et al., 2011, 2012; Soare et al., 2007, 2008; Ulrich et al., 2010), the small-sized polygons show distribution at or near the surface that is wide-ranging, often covering many square kilometres (Fig. 2.2a–b), and varied: 1) within rimless and sometimes scalloped depressions (Fig. 2.3a–c); 2) amidst inter-crater plains (Figs. 2b, 3d–e); and, 3) within impact craters (Fig. 2.3f–g). Frequently, the lcps are adjacent to the depression margins (e.g. Lefort et al., 2009; Séjourné et al., 2011). The hcps, by contrast, display no similar bias.

The depressions exhibit a variety of planforms: circular (Fig. 2.4a); sub-circular or elongated (Fig. 2.4b); and, scalloped on the margins (Fig. 2.4c). Their distribution is no less varied, being observed individually (Fig. 2.4a), clustered or coalesced (Fig. 2.4c), or in wave-like forms (Fig. 2.4d). Orientation, defined by the loss of elevation relative to the surface datum, is longitudinal and equatorward (e.g. Lefort et al., 2009; Morgenstern et al., 2007; Séjourné et al., 2011, 2012). Depths range from metres to decametres (Lefort et al., 2009; Morgenstern et al., 2007; Séjourné et al., 2011, 2012). Inward-oriented and roughly equatorial tiers or terraces often demarcate the changes of elevation and are commonplace amidst the scalloped depressions (Fig. 2.4c).

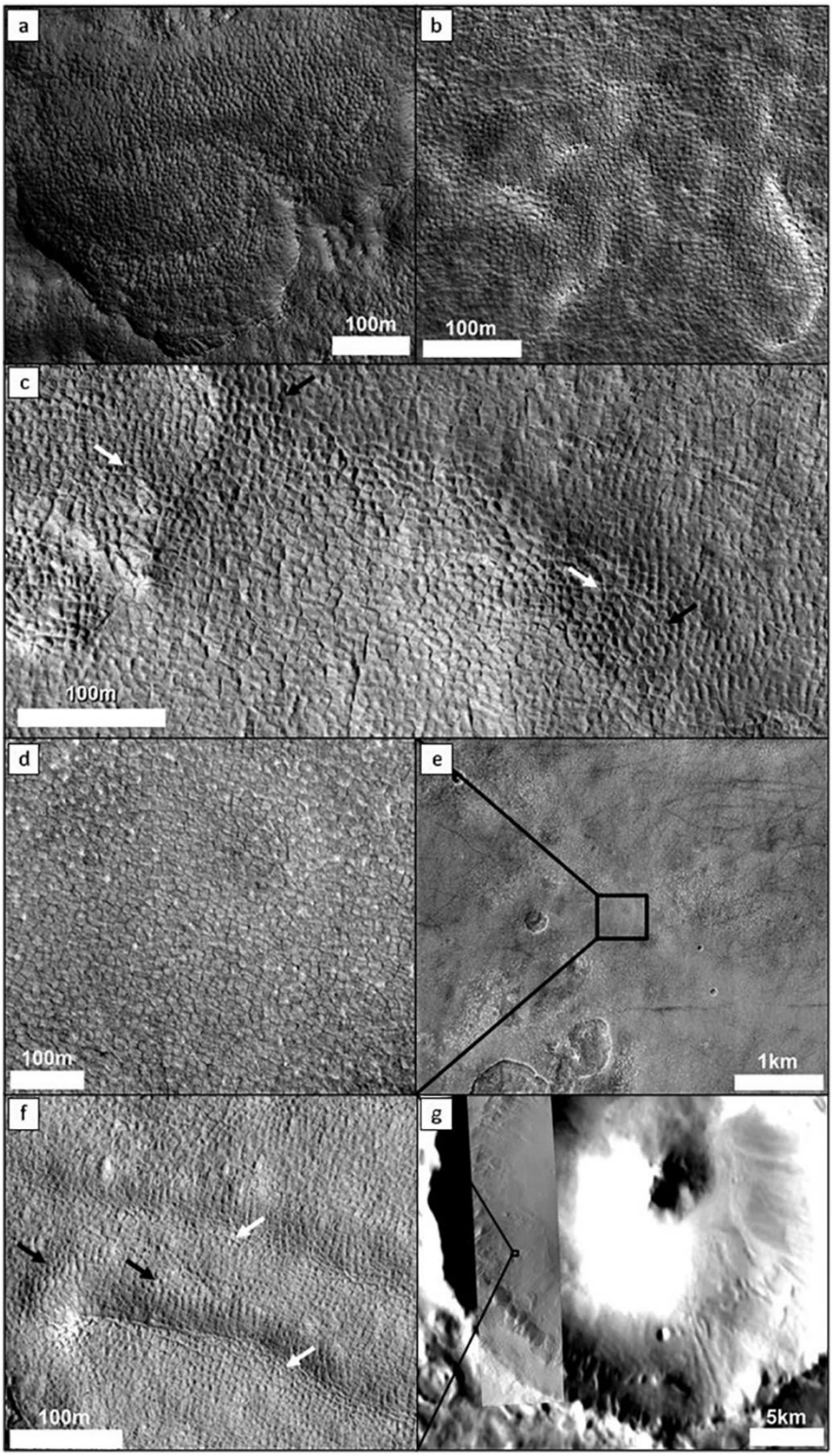

(caption on next page)

Fig. 2.3. Examples of the three polygon-types, categorised by the relative elevation-differences between polygon centres and margins, and disparate locations, in our study region. a) Scalloped depressions overprinted by lcps (HiRISE image PSP_006908_2215, 41.178° N, 124.130° E, 25 cm/pixel). b) Widespread hcp distribution in scalloped terrain (HiRISE image ESP_046467_2280, 47.594° N, 119.679° E, 25 cm/pixel). c) Proximal lcps (black arrows) and hcps (white arrows) (HiRISE image ESP_055038_2250, 44.757° N, 113.888° E, 50 cm/pixel). d) Polygons with no observable elevation-difference between centres and margins (HiRISE image ESP_026450_2270, 46.823o N, 110.880o E, 50 cm/pixel). e) Larger-scale view of panel d) within the inter-crater plains. f) Lcps (black arrows) and hcps (white arrows) in close proximity (HiRISE image ESP_036366_2235, 42.939o N, 115.428o E, 50 cm/pixel). g) Panel f) at a larger scale. Note: these polygons are in Type 2 terrain (background: THEMIS day-IR controlled mosaic). North is up in all images. HiRISE image credits: NASA/JPL/University of Arizona.

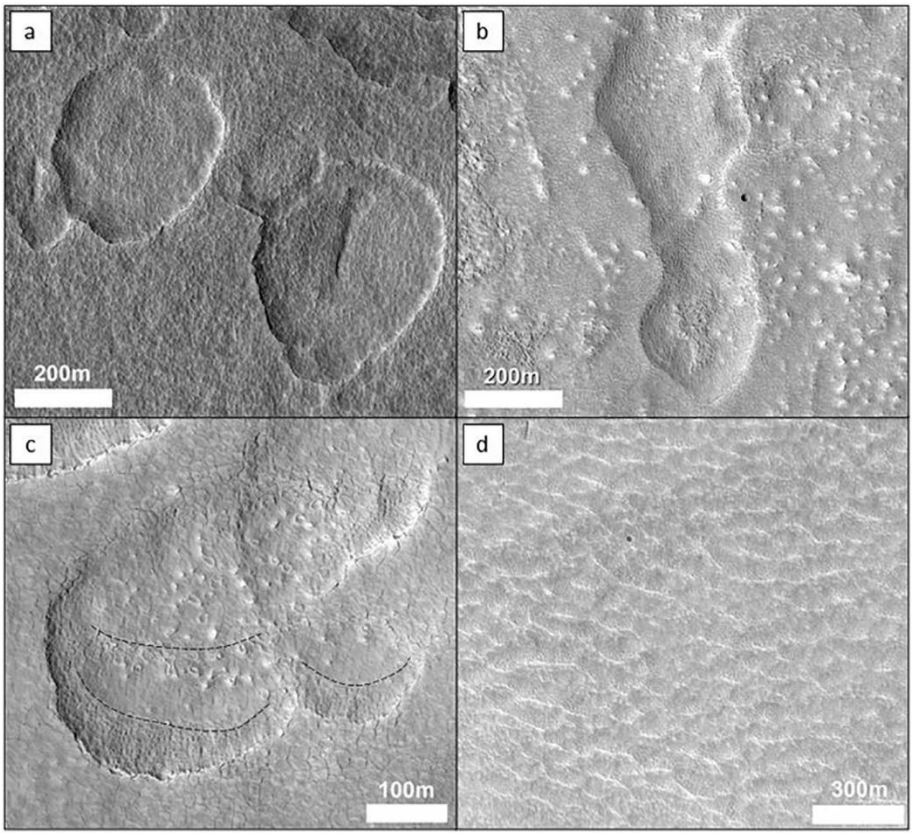

Fig. 2.4. a) Circular and individual rimless depressions (HiRISE image ESP_053205_2235, 43.350° N, 117.223° E, 25 cm/pixel). b) Elongated rimless-depression (HiRISE image ESP_026094_2250, 44.657° N, 111.415° E, 25 cm/pixel). c) Coalesced rimless depressions; note the scalloping of margins (HiRISE image ESP_026094_2250, 44.657° N, 111.415° E, 25 cm/pixel). Note the inward-facing tiers (black dashed lines). d) Wave-like depressions (HiRISE image ESP_035667_2295, 49.377° N, 115.622° E, 25 cm/pixel). North is up on all tiles. HiRISE image credits: NASA/JPL/University of Arizona.

2.4. Ice-complex constituents on Earth

2.4.1. Thermal-contraction cracking and ice wedge polygons

In low-lying and coastal regions of ice-rich permafrost such as the Tuktoyaktuk Coastlands small-sized (generally ≤ 25 m in diameter), clastically non-sorted, ice-wedge polygons are observed widely (French, 2007; Mackay, 1974; Rampton, 1988; Rampton and Bouchard, 1975). Here, mean monthly-temperatures (1971–2000) range from −26.3° to +10.9° C, and the mean annual-precipitation, inclusive of rain and snowfall, is 139.3 cm (water equivalent) (Environment Canada, 2010).

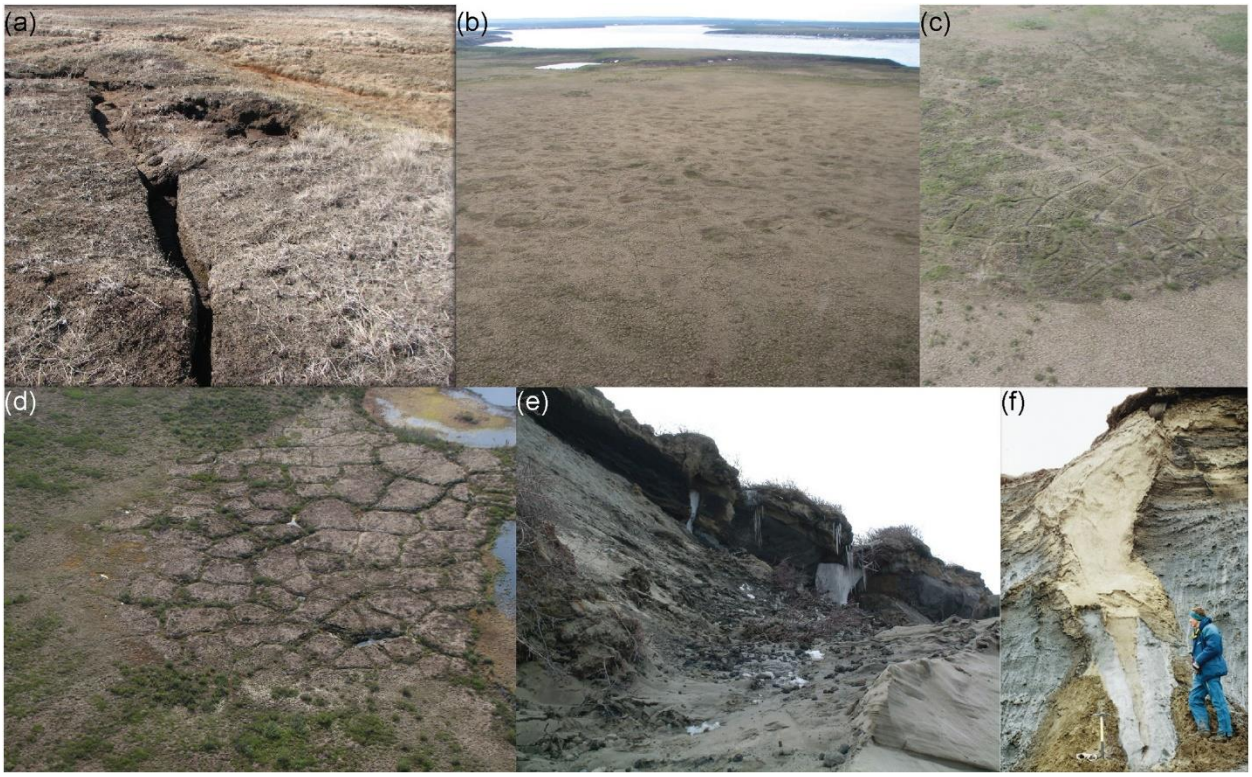

Fig. 2.5. a) Early-stage polygonization of continuous permafrost, by way of thermal contraction cracking (Tuktoyaktuk, Northwest Territories, Canada). b) Ubiquitous coverage of continuous permafrost by small-sized, possibly ice-wedge, polygons (Husky Lakes, [HL] midway between Tuktoyaktuk and Inuvik, Northwest Territories). c) Low-centred (ice-wedge) polygons, with marginal but elevated troughs hosting wedge-derived meltwater (HL). d) High-centred (ice-wedge) polygons, with marginal troughs filled with melt-water (HL). e) Ice-wedge exposure in scarp eroded by Beaufort Sea wave-action (Peninsula Point, ~6 km southwest of Tuktoyaktuk, Northwest Territories, Canada). Note the surface depressions above the large ice-wedge on the right and the dangling ice-wedge remnants to its left. The depressions, were they observed planimetrically, would comprise the marginal troughs of high-centred (degradational) polygons. The brownish sediments in whose midst the ice-wedges lie are silty clays. f) Exposed sand wedge (Tuktoyaktuk Coastlands) (Murton et al., 2000). Image credits for all panels other than f): R. Soare.

The polygons are the product of tensile stresses in frozen soil that arise from the sharp drop of sub-zero 0C temperatures (Lachenbruch, 1962). This fracturing, or thermal-contraction cracking, initially forms shallow, narrow and vertical veins (Fig. 2.5a). The type of fill depends on the ambient boundary-conditions and the availability of: 1) meltwater derived of thawed snow or ice; 2) winter hoarfrost; or, 3) windblown sand, mineral-soil, or a mixture of the two (e.g. Hallet et al., 2011; Lachenbruch, 1962; Leffingwell, 1915; Pewe, 1959; Sletten et al., 2003; Washburn, 1976).

The diurnal and seasonal iteration of cracking and filling may grow the sub-centimetre to centimetre- scale veins into wedges with metre-scale depth and width (Lachenbruch, 1962). As the cracks intercept one another they form individual polygons and, eventually, consolidated polygon networks (Mackay, 1974; Mackay and Matthews, 1983; Washburn, 1976). The latter may comprise hundreds of square kilometres of continuous or discontinuous coverage and represent hundreds of fill and crack-formation cycles (Black, 1954; Lachenbruch, 1962; Mackay, 1974; Washburn, 1976) (Fig. 2.5b).

Thermal-contraction (ice-wedge) polygons exhibit low (Fig. 2.5c) or high centres (Fig. 2.5d–e) relative to their margins or centres, or margins that are relatively-equal in elevation (Fig. 2.5b), depending upon their developmental stage. Ice-wedge aggradation is informed by the (seasonally) iterative infilling and freezing of meltwater at polygon margins, as well as by the active-layer expansion that moves sediment radially to the polygon margins from the centres. The former uplifts the sedimentary overburdens, generates raised shoulders (French, 2007; French and Guglielmin, 2000; Mackay, 1981) and gives the polygons a distinctly low-centred appearance (Czudek and Demek, 1970; Hallet et al., 2011; Rampton, 1988). Ice-wedge degradation follows from a sustained rise of thaw-tolerant mean temperatures. This deflates polygon-margin shoulders, perhaps sinking them below the elevation of polygon-centres, and morphs low-centred into high-centred polygons (Czudek and Demek, 1970; Hallet et al., 2011; Rampton, 1988). Regions or sub-regions where lcps and hcps are observed concurrently are in thermal flux (Czudek and Demek, 1970; Hallet et al., 2011; Rampton, 1988).

Of note; some polygon centres and their icy margins may exhibit little or no difference in their relative elevations. This either means that the ice has aggraded insufficiently to form marginal shoulders or degraded insufficiently to form marginal troughs.

2.4.2. Sand-wedge, composite and sublimation-enhanced polygons

Sand-wedge polygons with low and high centres are observed in relatively-temperate and ice-rich landscapes where ice-wedge polygons also are present (Mackay and Matthews, 1983; Murton et al., 2000) (Fig. 2.5f), as well as in the McMurdo Dry Valleys (MDVs), Antarctica, where ice-rich terrain and ice-wedge polygons are sparse (Berg and Black, 1966; Bockheim and Hall, 2002; French and Guglielmin, 2000; Hallet et al., 2011; Marchant et al., 2002; Pewe, 1959; Sletten et al., 2003). In either case the sand-wedge polygons are paleo-markers of climatic and hydrological regimes that are drier and/or colder than those associated with the origin and development of ice-wedge polygons (Mackay and Matthews, 1983; Murton et al., 2000; Washburn, 1976; Wolfe et al., 2018). For example, contrast the annual mean-temperatures and -precipitation at the Tuktoyaktuk coastlands (discussed above) with the mean annual air-temperatures and precipitation at Beacon Valley, one of the MDVs. Annual mean-temperatures Beacon Valley are ~ − 34° C and soil temperatures possibly do not exceed ~0° C (Marchant et al., 2002). Precipitation is meagre (<50 mm of water equivalent precipitation per annum) and is comprised solely of snowfall (Bockheim and Hall, 2002; Levy, 2015). Boundary conditions consistent with the iterative formation of ice-wedge polygons are rare, perhaps not exceeding a few days per annum.

Sand-wedge polygons originate and develop by the same thermal stresses that engender the formation of ice-wedge polygons (e.g. Berg and Black, 1966; French and Guglielmin, 2000; Hallet et al., 2011; Marchant et al., 2002; Pewe, 1959; Sletten et al., 2003). However, the rise and fall of polygon margins follows a

slightly different path. Sand-wedge polygon margins deform upwardly, forming (raised shoulders) lcps, as sand and other surface minerals accumulate by the work of wind; downward deformation, i.e. the transformation of raised shoulders into marginal troughs by aeolian erosion, creates hcps (e.g. French and Guglielmin, 2000; Hallet et al., 2011; Marchant et al., 2002; Pewe, 1959; Sletten et al., 2003). Sometimes, the evolution of hcps is enhanced or accelerated by the sublimation of underlying glacial ice (Marchant et al., 2002).

2.4.3. Thermokarst and ice-rich landscapes

Thermokarst refers to landforms developed by way of freeze-thaw cycling in permafrost composed of excess ice (e.g. Hussey and Michelson, 1966; Osterkamp et al., 2009; Permafrost Subcommittee, 1988; Rampton, 1988; Taber, 1930). Excess ice = "…the volume of ice in the ground that exceeds the total pore volume that the ground would have under unfrozen conditions" (Permafrost Subcommittee, 1988; also, see French, 2007; Murton, 1996b; Rampton, 1988; Rampton and Mackay, 1971; Taber, 1930; Washburn, 1976).

Excess ice comprises ice lenses, veins, wedges or larger masses of consolidated ice that are formed by ice segregation. Fine to medium-grained soils such as silts or silty clays are particularly adept at hosting segregation ice because they have relatively-small interstices (Abramov et al., 2008; Black, 1954; French, 2007; Rampton, 1988; Rampton and Mackay, 1971; Sone et al., 2006; Taber, 1930). Small interstices facilitate the migration of pore water to and the formation of discrete layers or lenses of segregation ice at the freezing front (French, 2007; Rampton, 1988; Rampton and Mackay, 1971; Taber, 1930). Were the grain-size too fine, pore-water migration would be overly constricted and ice lenses would not form; were the grain-size too coarse, pore-water migration would be overly expeditious and flush out of the system before segregation ice could form.

Where excess ice aggrades, frost heave follows (Rampton, 1988; Taber, 1930). Where excess ice thaws and degrades, the terrain subsides and settles under its own weight, until it reaches a consolidated state (Permafrost Subcommittee, 1988) (Fig. 2.6a–b). If thaw-generated meltwater pools then a thermokarst pond or lake forms; were the pooled meltwater to be lost by evaporation or drainage, an emptied basin or alas would form (French, 2007; Rampton, 1988; Washburn, 1976). Were the loss of pooled water partial and episodic, inwardly-oriented benches or terraces may develop on the alas margins; this imparts to the margins a distinctly-scalloped appearance (Brown, 1981; Soare et al., 2008, 2011).

Spatially, the dense or sparse distribution of heaved and subsided terrain, as well as of thermokarst lakes and alases, delineates two things: 1) the breadth and scale of thermal flux and disequilibrium in that region (French, 2007; Grosse et al., 2007; Pewe, 1959; Schirrmeister et al., 2013; Wetterich et al., 2014); and, 2) the volumetric loss of excess ice in that region (Czudek and Demek, 1970; French, 2007; Rampton, 1988; Rampton and Mackay, 1971; Washburn, 1976). This is no less true where ice-wedge associated lcps and hcps are observed concurrently.

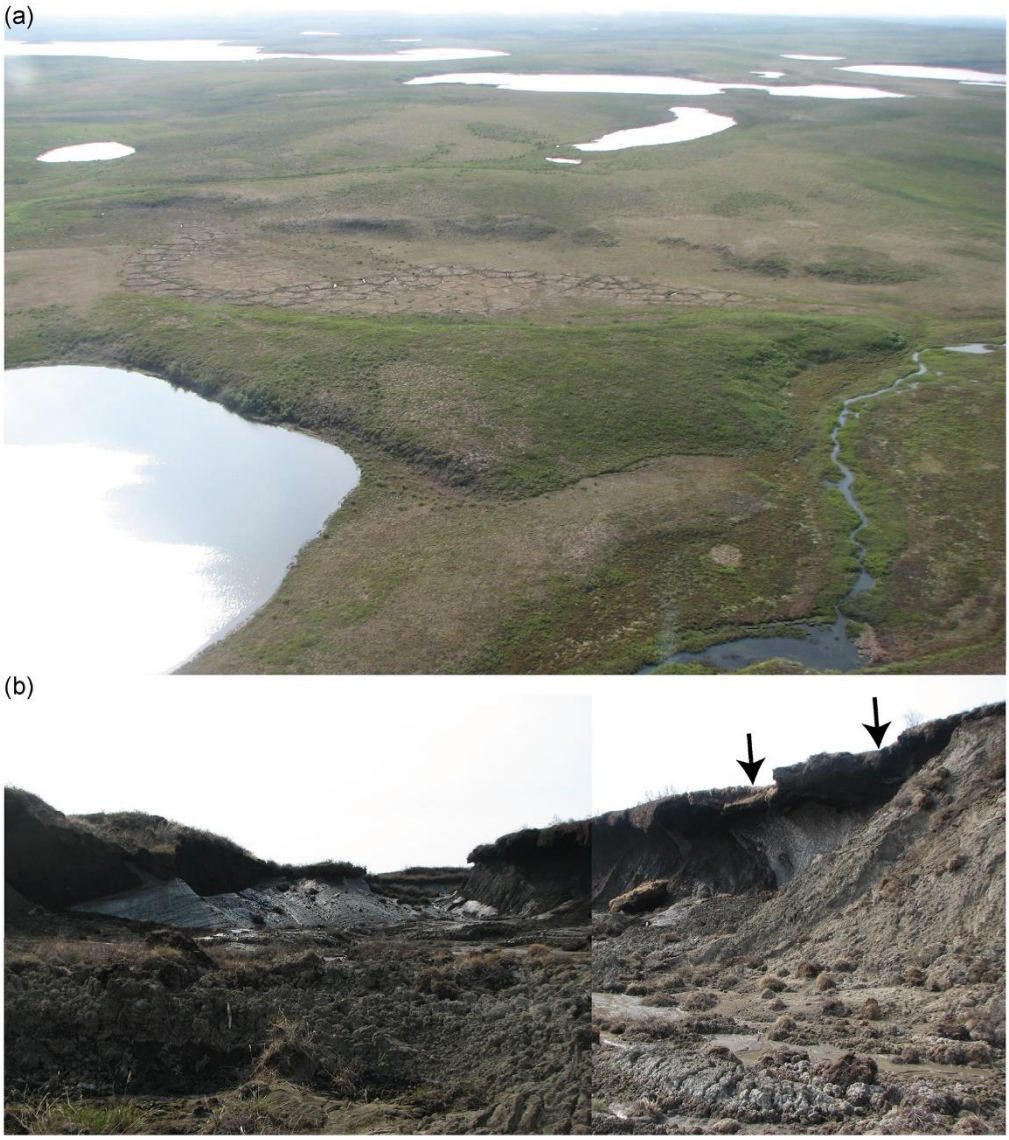

Fig. 2.6. a) Hummocky thermokarst, featuring thermokarst lakes, polygonised alases and beaded streams linking thaw pools of degraded ice-wedge polygons (Husky Lakes, Northwest Territories). b) Panoramic and cross-sectional view of an ice complex comprised of ice wedges (on the right-hand side) and massive ice. The small, surface depressions flanking the largest ice wedge (on the right-hand side, black arrows) mark the location of bilateral polygonal troughs associated with a field of high-centered polygons. In a wet permafrost-environment high-centered, ice-wedge polygons form when and if local or regional (mean) temperatures rise to the point of inducing thaw and melt at or near the surface where the ice wedges occur. Grayish-beige material on the right and throughout the floor of the terrace comprises silts and clays that have slumped to the floor from the near surface as retrogressive thaw has eroded this Beaufort Sea headland. The oblong block on the right-hand side of the terrace floor points to the recentness of thaw-based detachment as there is a gap in the overhang of the terrain immediately above the block location (Peninsula Point, Northwest Territories). Image credits: R. Soare.

2.5. Results

2.5.1. LCPs/HCPs and poleward latitude (Table 2.1)

All of the possible lcps or hcps, regardless of the group of the image they are located in (i.e. 1. images whose resolution/quality allows unambiguous identification of polygons; and, 2. images whose lower resolution/quality make the identification of polygons more uncertain), show similar changes of morphology with their poleward latitude. As such, both datasets are combined in the following results. We identified 313 squares with lcps and no hcps, 3325 squares with hcps and no lcps, 663 squares with both lcps and hcps, and 10,349 squares with polygons, generating a total of 14,650 polygonised grid-squares (Appendix A.7). The study area (40–50°N, 100–125°E) comprised 23,380 grid squares classified as terrain Type 1 and 9911 classified as terrain Type 2 (Appendix A.7).

Overall, the ratio of low to high-centered polygons does not show any correlation with increasing latitude ($R2 \sim 0.0143$) (Fig. 2.7), despite the frequency of polygonised squares increasing with latitude. However, when we exclude polygons in Type 2 terrain from the sample data, a statistically-significant linear correlation appears between the lcp-to-hcp ratio and latitude ($R2 > 0.87$, p-value < 0.05 (Fig. 2.8). Note that Fig. 2.8 and Appendix A.7 data include three latitudinal ranges without lcps (40°- < 41°, 42°- < 43°, 43°- < 44°; lcp/hcp = 0), and one range without polygons (41°- < 42°; lcp/hcp = no data).

Crater interiors (Type 2 terrain) host lower temperatures and slightly-higher atmospheric-pressures than the exterior terrain populated by them; these cold traps enhance the stability and preservation of volatiles (Conway et al., 2012; also, Dickson et al., 2010; Ingersoll et al., 1992). Low-centred ice-wedge polygons, formed under antecedent boundary conditions consistent with the freeze-thaw cycling of water but cold-trapped by recent or current conditions, would be able to avoid degradation at lower latitudes than similar polygons exposed to greater variances of temperature and pressure in the surrounding terrain (Type 1). Excluding the polygons in Type 2 terrain from our regression analysis prevents our results from being biased by these data.

Sixty-eight percent of the squares with lcps also have hcps. This increases to 83% if Type 2 grid squares are excluded from the count and decreases to 37% when Type 2 grid-squares alone are counted.

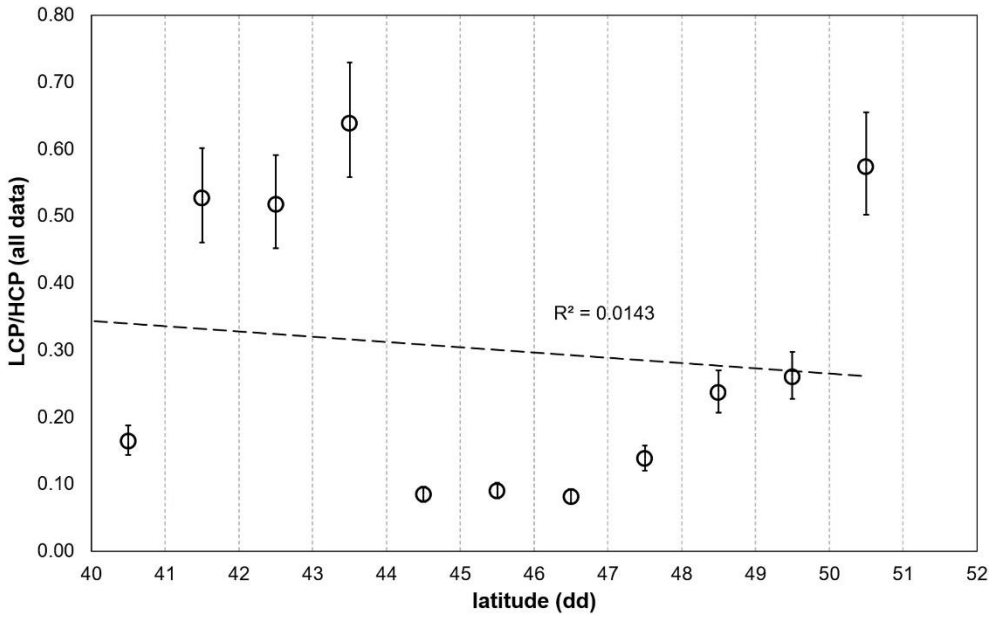

Fig. 2.7. Low-centred vs high-centred polygon latitudinal ratios for all terrain types. Data for all images have been binned for each degree of latitude excluding the upper bound. The black dashed line represents the linear correlation between lcp/hcp and latitude, its R2 value specified above it. No correlation is observable. Error bars are calculated by assuming one in 15 squares could be erroneously classified and are not visible if they fall within the points.

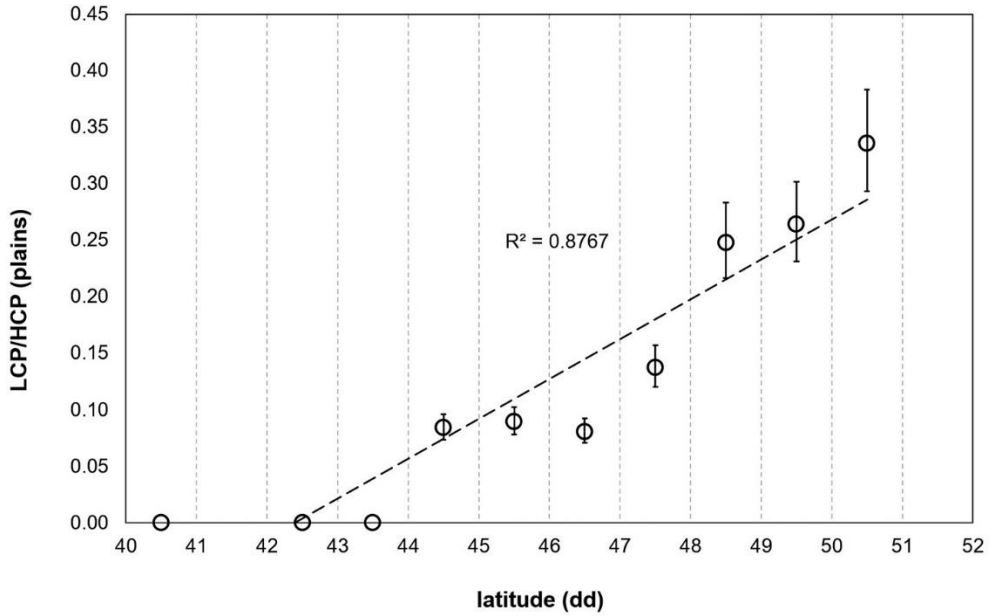

Fig. 2.8. Low-centred vs high-centred polygon latitudinal ratios for Type 1 terrain (plains, excluding large craters). Data for all images have been binned for each degree of latitude excluding the upper bound. The black dashed line represents the linear correlation between lcps/hcps and latitude. The R2 value is specified above it. A significant correlation is observed (p-value: 6.65 × 10−5). Error bars are calculated by assuming one in 15 squares could be erroneously classified and are not visible if they fall within the points.

2.5.2. Surface-age estimates

A general lack of craters in the region has been attributed to a very young age for the materials possibly linking them to recent past obliquity variations within the last ~100 kyr to several Myrs (Head et al., 2003; Lefort et al., 2009; Levy et al., 2009b, 2010b; Madeleine et al., 2009). However, recent analysis of the crater-size frequency distributions (CFSDs) on polygonized terrain to the west of our study region in UP found a crater population more consistent with an older surface (at least ~100 Myrs) (Soare et al., 2020). Here, the surface experienced a size-dependent loss of craters that removed many of the smaller craters (Soare et al., 2020).

Crater counts were conducted on the polygonised terrain in our study region using HiRISE image ESP_026450_2270 (Fig. 2.9). A total of 168 craters were identified in a 150 km2 area of the polygonised terrain. The results are consistent with those of Soare et al. (2020). The CSFD of the crater population has a much shallower power-law slope than predicted by production functions (e.g. Hartmann, 2005). This does not represent a formation age. Instead, it points to a "crater retention age" regulated by a destruction rate that tends to remove smaller craters preferentially (Hartmann, 1971; Kite and Mayer, 2017; Opik, 1965; Palucis et al., 2020; Smith et al., 2008; Williams et al., 2018). However, the number of craters D > 50 m in our count area suggests the material was emplaced and exposed to impact cratering for at least 10 Myrs, possibly longer, and precludes a surface as young as the most recent obliquity variations (Laskar et al., 2004). The size-dependent obliteration of craters apparent from the shallow power law slope is supported by the morphologies of the craters in various states of degradation; many of them exhibit shallow hollows. Moreover, this demonstrates that the polygonised surface has undergone erosion, the likely agent responsible for the removal of many of the craters in a size-dependent manner (e.g. Hartmann, 1971; Smith et al., 2008; Williams et al., 2018).

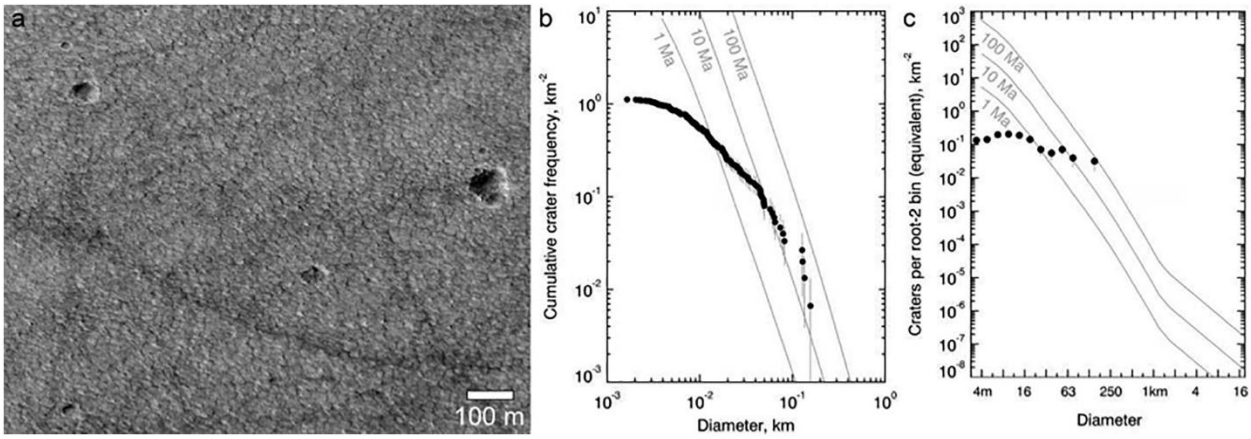

Fig. 2.9. a) Portion of HiRISE image ESP_026450_2270 within the study region (centered on 46.823o N, 110.880o E) showing impact craters on the polygonized terrain. b) Cumulative unbinned and c) log-incremental root-2 binned crater size-frequency distribution for the entire HiRISE image (Area: 150 km2) with absolute model age isochrons for 1 Ma, 10 Ma, and 100 Ma surfaces shown from Hartmann (2005). HiRISE image credit: NASA/JPL/University of Arizona.

2.6. A geochronology of periglaciation at the mid-latitudes of Utopia Planitia

Here, we present an integrated geochronology that comprises a baseline of generally-accepted ideas and reasoning within the community complemented by our own observations, deductions and statistical findings.

2.6.1. The origin and development of ice-rich terrain

2.6.1.1. Stage 1a

Atmospheric water-vapour (the Martian equivalent of winter hoar-frost on Earth) diffuses and charges the pore space of near-surface regolith (top few metres) with ice at all latitudes during one or more periods of high obliquity during the Late Amazonian Epoch (e.g. Clifford, 1993; Douglas and Mellon, 2019; Mellon and Jakosky, 1993, 1995). In concert (or not) with this diffusion-driven ice-charging of near-surface regolith, high obliquities engender enhanced periods of H2O-ice precipitation. The latter accumulates at the surface and forms an icy mantle (e.g. Forget et al., 2006; Head et al., 2003; Madeleine et al., 2009, 2014; Wetterich et al., 2014).

2.6.1.2. Stage 1b

Sub-aerial temperatures sufficient to host the freeze-thaw cycling of the icy mantle and near-surface regolith occur, potentially for a few hours per sol at the appropriate solar longitude (Rivera-Valentín et al., 2020) but through sufficient annual iterations for excess ice and ice-wedge polygons to form (Soare et al., 2014a, 2017, 2018). The presence of brine-bearing sediments could have facilitated the onset and iteration of this process because salt depresses the freezing point of water (e.g. Brass, 1980; Fairén et al., 2009; Martínez and Renno, 2013; Möhlmann and Thomsen, 2011; Rennó et al., 2009; Rivera-Valentín et al., 2020; Toner and Catling, 2018; Travis et al., 2013). The recent work of Rivera-Valentín et al. (2020) points to brines possibly being present today in our study region.

Further facilitation could have been provided, as is the case in ice-rich permafrost regions on Earth, by the presence of relatively fine-to medium-grained regolith (Soare et al., 2015; based on: Abramov et al., 2008; Black, 1954; French, 2007; Rampton, 1988; Rampton and Mackay, 1971; Sone et al., 2006; Taber, 1930. The latter would have been delivered to our study region by aeolian (Bristow and Moller, 2018) or volcanic surface processes (Hopper and Leverington, 2014; Wetterich et al., 2014).

2.6.1.3. Stage 2

As high obliquity/ies wanes/wane, near-surface ground ice at the lower mid-latitudes of our study region loses stability and sublimates (Mellon and Jakosky, 1995, 1993). Thermokarst or alas-like basins form where the volatile loss occurs (Dundas, 2017; Dundas et al., 2015; Lefort et al., 2009; Mangold, 2011; Morgenstern et al., 2007; Séjourné et al., 2011, 2012; Soare et al., 2014a; Ulrich et al., 2010). The episodic or intermittent return to higher obliquities, much like glacial inter-stades on Earth (Rampton, 1988; Rampton and Bouchard, 1975), could have replenished and recharged the volatile-depleted terrain with ice. Against this backdrop, the rimless and sometimes scalloped depressions in our study region and at the mid-latitudes of UP might be indicative of the net loss of ice-richness through the Late Amazonian Epoch to the present day. Their shape, size, depth, and location possibly reflect random differences in the distribution and depth of ground ice as well as in the reach of thermal disequilibrium (Soare et al., 2018). In this regard, the inwardly-oriented steps or tiers often observed within the depressions could be markers of an episodic loss of ice, much in the same way as tiered thermokarst basins in the Tuktoyaktuk region point to the episodic loss of water (Soare et al., 2007, 2008, 2017; also, Séjourné et al., 2011, 2012).

2.6.2. The origin and development of ice-wedge polygons

2.6.2.1. Stage 3

As we suggested in Section 2.5.2, thermal-contraction cracking polygonises the terrain within the depressions, perhaps 100 Mya. Additionally, we propose that thaw-derived meltwater is produced, whenever local/regional boundary conditions are fitting, with the possible assistance of near-surface brines, and maybe in conjunction with higher obliquities. The meltwater fills the polygonised cracks episodically. As the ice aggrades the regolith margins rise above the elevation datum of the polygon centres. This forms low-centred polygons (Séjourné et al., 2011, 2012; Soare et al., 2014a, 2018). As earlier, recharge by the atmospheric diffusion of water vapour could be of assistance in maintaining the volume and structural integrity of the ice wedges (Clifford, 1993; Mellon and Jakosky, 1993, 1995).

During later and lower obliquities, the stability of ground ice falls and may sublimate/degrade the ice-wedges preferentially at lower latitudes. This transforms high-shouldered margins into low-shouldered troughs, revises lcps into hcps, and decreases the ratio of lcps to hcps at these latitudes. Sand-wedge polygons would not be expected to fit the pattern of latitudinal distribution associated with the lcps and presented in Section 2.5.1, nor would the linear correlation between the lcp/hcp ratio and poleward latitudes.

2.6.2.2. Stage 4a

In conjunction with more recent high-obliquities a metres-deep icy and lightly-toned dusty mantle(s) accumulates in our study region (Forget et al., 2006; Head et al., 2003; Madeleine et al., 2009; Mustard et al., 2001). The mantle buries or mutes the thermokarstic (polygonised) depressions and the polygonised terrain incised by the depressions (Soare et al., 2017).

2.6.2.3. Stage 4b

As Mars moved cyclically back to lower obliquity(ies) the surface mantle began to sublimate and erode, uncovering and exhuming the terrain populated by the thermokarst-like depressions and possible ice-wedge polygons (Soare et al., 2017). Mirroring the antecedent and pre-mantling losses of ice, polygons at the lower latitudes show a higher observed-distribution of low shoulders or troughs (hcps) than polygons at higher latitudes.

2.7. Discussion and Conclusion

2.7.1. What if…

Questions concerning the possible existence of ice-rich terrain on Mars date back to the grainy Mariner-mission photographs of the 1960s and 1970s (e.g. Belcher et al., 1971; Sharp et al., 1971). In the aftermath, data-based validation of this hypothesis has been fleeting. “Looks-like” therefore “must-be” inferences of thermokarst-like landforms or of possible ice-wedge polygons are suggestive, even beguiling, but inadequate. Validation, however, requires ground-truth, i.e. direct evidence of near-surface ground ice by human or robotic sample analysis at the latitudes of our study or, possibly, a GPR operating at frequencies sufficient to identify discrete and heterogeneous emplacements of ground ice from the near-surface to depth. Current inferences of widespread water-equivalent hydrogen (possible near-surface ground-ice) derived from orbital spectrometry have been less than satisfying. The data have a relatively short/shallow skin-depth ($\leq$ 1 m) and a kilometre-scale footprint (e.g. Boynton et al., 2002; Feldman, 2004; Feldman et al., 2002; Mitrofanov et al., 2002).

More recent observations of Utopia Planitia (~70-90° E), slightly to the west of our study region and derived of the Shallow Radar (SHARAD, Mars Reconnaissance Orbiter), point to the possible presence of a large and near-surface but decametres-deep body of admixtured ice, air and dust (Stuurman et al., 2016). Whether this buried body comprises massive ice, excess ice or something else remains open-ended, as does the time-frame of its origin, i.e. late Noachian Epoch, early or mid-Amazonian Epochs, etc., and the process by which it came to be, i.e. glacial, fluvial, marine, periglacial, a combination thereof, or something else. North of our study region and substantially to the east (68.22° N, 234.30° E), shallow trenches dug by the Phoenix Lander revealed patches of light-toned ice that could be the work of ice/soil segregation (Mellon et al., 2009a). The light-toned near-surface ice is thought to be geologically young, perhaps no older than 100 kyr (Mellon et al., 2009a), much younger than the periglacial terrain discussed by us above. The depth and distribution of this segregated ice, at this location and possibly elsewhere, is unknown.

2.7.2. Poleward latitude, ice-wedging and the freeze-thaw cycling of water

1) Our study region in Utopia Planitia (40-50° N; 100-125° E) displays a statistically-significant and positive (linear) correlation between the ratio of low-centred to high-centred polygons (lcps vs hcps) and a poleward gradient of lcp/hcp distribution. As near-surface ground ice is more stable at higher latitudes than at lower ones, the increased (observed) occurrence of lcps at poleward latitudes would be expected were their margins underlain by ice-wedges. Also expected would be the lower prevalence of lcps at the equatorward latitudes where ice is less stable than at poleward ones.

2) This latitudinal gradient of lcp/hcp distribution would not be expected or predicted were the polygon margins underlain by sand wedges. The gains and losses of elevation in the margins of sand-wedge polygons are driven by aeolian accumulation or erosion or, in relatively unique periglacial contexts, by the sublimation of underlying glacial-ice. Variances in the stability of ground-ice, expressed on a local, regional or latitudinal scale, exercise no positive or negative effect on the relative elevations of sand-wedge polygon centres or margins.

3) The morphometric/statistical validation of ice-wedge polygonization along a latitudinal gradient of distribution at the mid-latitudes of UP accomplishes two things. First, it enhances the empirical/observational depth of excess-ice hypotheses and, second, it underpins the possibility that excess-ice could be present, even today, at lower than poleward (Phoenix-like) latitudes and closer to the surface in the northern plains than might otherwise be thought.

4) Equally important is a return to questions concerning the time-scale required to form metre-high ice-wedges on Ice-wedges on Earth may originate and evolve into mature landforms on relatively short scales of time. For example, within a few years of a thermokarst lake in the Tuktoyaktuk region having been drained of its water artificially, the newly-exposed basin underwent permafrost aggradation; thermal-contraction cracking also was observed, as were nascent ice-wedges (Mackay and Burn, 2002). Although hundreds of seasonal/annual freeze-thaw cycles are required to evolve mature and metre-scale ice wedges from sub-centimetre ice veins, even this somewhat extended period is relatively short, geologically speaking.

5) The crater counts (see Section 2.5.2) of the polygonised terrain in our region indicate that the latter is substantially older than previous studies of similar terrain in Utopia Planitia have suggested, perhaps by an order of magnitude. This attenuates the possible inconsistency between the more temperate boundary-

conditions required by the formation of ice-wedge polygons, under higher obliquities perhaps, and the current constraints of extreme aridity, low temperatures and low atmospheric-pressure. Additionally, slightly-higher temperatures in a volatile-rich environment could have induced an accompanying rise of atmospheric vapour-pressure. This would have shortened the period of time and the number of iterative (freeze-thaw) cycles required to originate and grow ice wedges.

6) Attention also ought to be cast on the possibility that disparate transformational-processes might be responsible for ice-wedge aggradation and ice-wedge degradation on Mars. The freeze-thaw cycling of water may be the most plausible means by which wedge ice, or even segregation ice, aggrade, on Mars as on Earth. On the other hand, the degradation of Martian wedge or segregation ice could and most probably is the work of sublimation. Reconciling the two end-processes may be no more difficult than ascribing a less than recent origin or aggradation period and a possibly very-late Amazonian Epoch and much more recent degradation period to the ice wedges.

3. Thermal-contraction polygons and subsurface properties (Philippe et al., *in prep.*)

The following section is a direct copy of an article that is in preparation. For that study, I: designed the study; performed the mapping, data analysis and figure creation; designed and wrote the text. The co-author on that paper participated in the scientific interpretation and writing processes.

Martian thermal-contraction polygons as sounders of subsurface properties: application to Utopia and Arcadia Planitiæ

Meven Philippe[1], Susan J. Conway[1]
[1]*Nantes Université/Université d'Angers/Le Mans Université, Laboratoire de Planétologie et Géosciences, CNRS UMR 6112, Nantes France.*

3.1. Introduction and context

3.1.1. General introduction

In terrestrial periglacial environments, ground is said to be 'ice-cemented' when pore water ice is present in sufficient proportions to bind the sediment together. When ice-cemented ground undergoes high-magnitude decreases in temperature below 0°C, ice-cemented ground contracts, making the overall volume of the ground decrease. With a significant volume decrease, the surface of the ground cracks, forming surficial fractures. Those fractures can join –with the cyclic repetition of that contraction process – to form polygonal patterns (Figure 3.1a; Washburn, 1956; Lachenbruch, 1962). These so-called 'thermal-contraction polygons' that constitute polygonal patterns are typically ~ 5-25 metres in diameter on Earth, and are a common feature in periglacial environments (e.g., Beerten et al., 2021; Bernard-Grand'Maison and Pollard, 2018; Black, 1954; Dafflon et al., 2016; Kokelj and Burn, 2004; Mackay, 1974; Marchant et al., 2002).
At this stage, thermal-contraction polygons are flat and thus are called 'flat-centred polygons' (FCPs; Figure 3.1b). In a second stage, material (aeolian sediment, liquid water, or a mix of both) can infill the fractures. This material freezes in winter, forming wedge-shaped bodies within the fractures called 'ice wedges' (when constituted mostly of ice; Lachenbruch, 1962), 'sand wedges' (when constituted mostly of sediment; Pewe, 1959), or 'soil wedges' (when constituted of a mix of both; White, 1971; Black, 1976a, 1976b). The volume of the wedges increases due to freezing, which opens the fractures even more. The wedges degrade partially and reform on a seasonal basis, with the repetition of freeze-thaw cycles of water (e.g. French, 2018; Mackay, 1990b). Their volume increases at each iteration, which exerts an outward force on the two faces of the fractures. The margins of the thermal-contraction polygons, in contact with the wedges, are thus pushed upward, which results in polygons where the margins are higher in elevation than the centre: they are called 'low-centred polygons' (LCPs, Figure 3.1b; Black, 1954; Harry and Gozdzik, 1988; Seppala et al., 1991; French, 2018). In a final stage, polygon wedges can degrade: ice wedges will progressively melt when Mean Annual Air Temperatures (MAAT) increase above 0°C, and sand wedges are eroded by mechanical erosion (e.g. from summer meltwater). When wedge material is lost, the outward force they apply on the nearby ground stops, and the polygon margins collapse into the wedge casts. This results in polygons with margins that are lower in elevation compared to their centre: they are called 'high-centred polygons' (HCPs, Figure 3.1b; Black, 1954; Harry and Gozdzik, 1988; French, 2018).

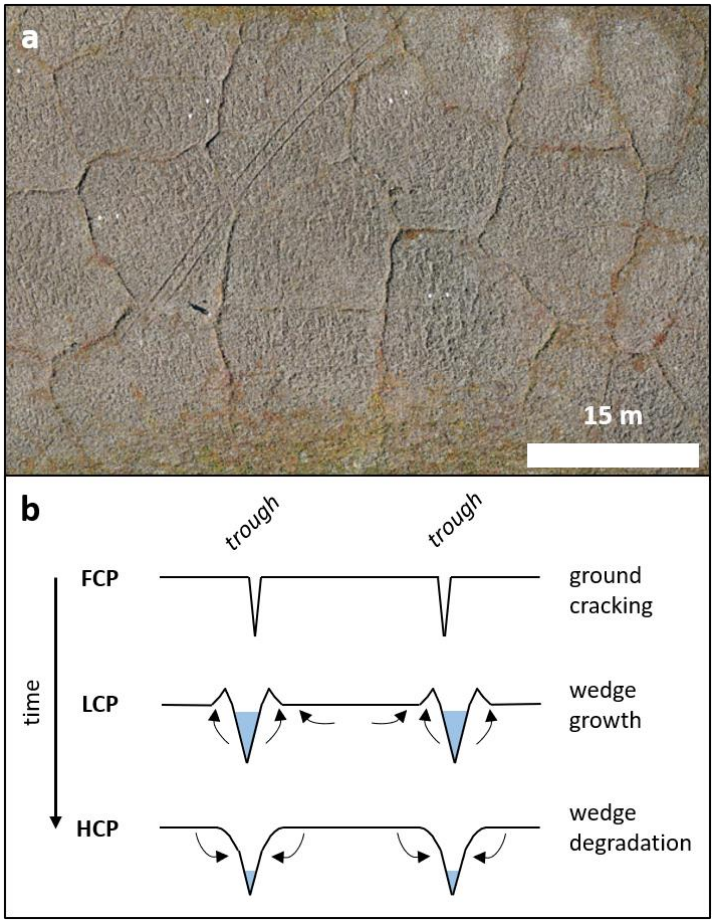

Figure 3.1: ***a.*** *Icelandic thermal-contraction polygons (65°17'32'' N 15°30'30'' W); b. schematic cross-sections of a given polygon, undergoing the evolution from flat-centred polygons (FCP) to low-centred polygons (LCP) and high-centred polygons (HCP). Black arrows indicate directions of ground movements.*

On Mars, polygons of similar dimensions (5 to 25 m) were first observed on the high-resolution images of the High-Resolution Imaging Science Experiment (HiRISE; 25-50 m/pixel), on board the Mars Reconnaissance Orbiter (MRO), notably by Mellon (1997). He concludes that they probably form similarly to terrestrial thermal-contraction polygons. Since then, numerous observations have revealed that polygons are a relatively common feature in the martian mid-latitudes, considered as Amazonian evidence for the occurrence of periglacial conditions (e.g. Mellon, 1997; Mangold, 2005; Mangold et al., 2004a; Levy et al., 2009a, 2009b, 2010; Orgel et al., 2019; Séjourné et al., 2011, 2019; Soare et al., 2018, 2021), or even liquid water activity (Seibert and Kargel, 2001; Costard et al., 2016; Soare et al., 2014a, 2021).

Martian thermal-contraction polygons also exhibit surficial morphologies similar to the terrestrial ones, i.e. FCPs, LCPs and HCPs (Figure 3.2; e.g. Séjourné et al., 2011; Soare et al., 2021). Note that FCPs never form with a perfectly flat shape; however, they exhibit no significant elevation difference between their centre and margins for that difference to be visible on HiRISE imagery. Recent work on thermal-contraction polygons in Utopia Planitia concluded that this population is constituted of ice-wedge polygons (Soare et al., 2021), supporting the hypothesis of previous studies (e.g. Soare et al., 2005). Those potential ice-wedge polygons are of central importance in the study of Mars, as they suggest the possibility of Amazonian activity of liquid water, and could constitute a potential source of near-surface water ice for future human missions (e.g. Morgan et al., 2021). The interest of Utopia Planitia as a primary target to investigate these questions is well demonstrated by its recent investigation by the Zhurong martian rover, from the chinese mission Tianwen-1 (Zou et al., 2021). Zhurong includes a ground-penetrating radar, and has an objective of water resource characterisation (Ye et al., 2021).

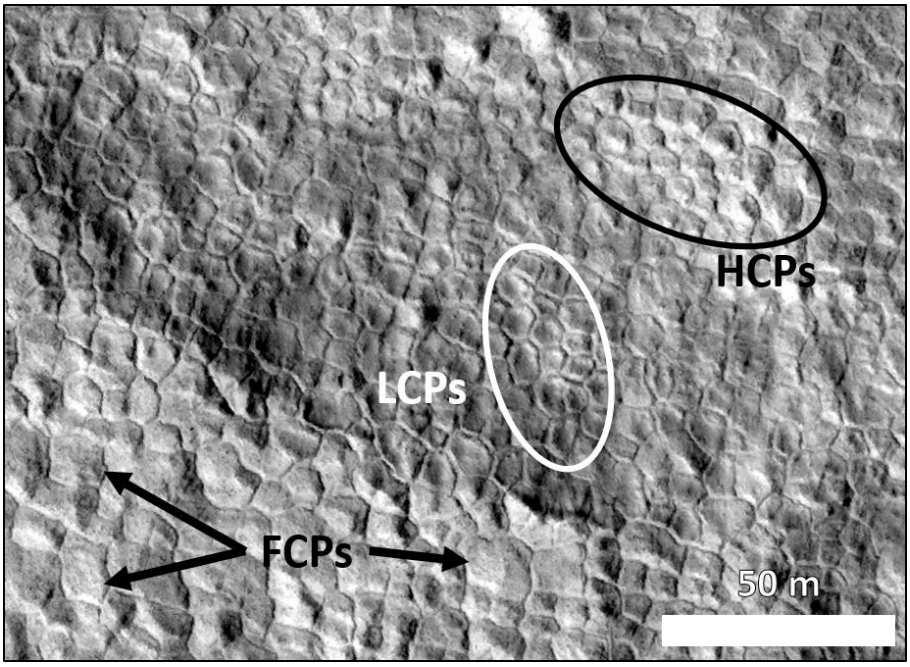

Figure 3.2: martian thermal-contraction polygons in UP. Three FCP examples are pointed out by black arrows, some LCPs are circled in white, and some HCPs are circled in black. North is up. HiRISE image ESP_063979_2280. HiRISE credits: NASA/JPL/University of Arizona.

In the present work, we are investigating two study zones (Figure 3.3a): one in Utopia Planitia (UP; Figure 3.3b) and one in Arcadia Planitia (AP; Figure 3.3c). UP is known to host extensive polygonal patterns (e.g. Haltigin et al., 2014; Morgenstern et al., 2007; Lefort et al., 2009; Levy et al., 2009a, 2009b, 2010; Ulrich et al., 2011; Séjourné et al., 2011, 2019; Soare et al., 2005, 2015, 2018, 2021). Observations of polygonal patterns in AP are much fewer, but they were described on specific units by Hibbard et al. (2021). Both of those northern plain areas have a complex geological history, involving Amazonian surface activity suspected to be caused by water ice, or even liquid water, to a certain extent.

3.1.2. Utopia Planitia: geological context and presence of ground ice

The study zone in UP is located to the northwest of Elysium Mons, from which multiple channels, valley systems and sinuous deposits originate (Figure 3.3b). Regional or local geological interpretations for the formation of channels and valley systems, such as Hrad Vallis, are diverse: carving by subsurface (de Hon, 1992) or surface liquid water (Costard and Kargel, 1995), phreatomagmatism (Wilson, 2003), low-viscosity lava flows (Hopper and Leverington, 2014), and/or aqueous flooding associated with effusive volcanism (Hamilton et al., 2018). Geological interpretations for the units in UP are equally diverse: outwash, lahar-type water-rich deposits, now frozen (Costard and Kargel, 1995; Russell and Head, 2003), which is supported by recent investigations of the Zhurong rover (Li et al., 2022); frozen paleolake deposits (Chapman, 1994); lava flows (Russell and Head, 2003); volcanoclastic flows generated by magma/volatile interactions (Tanaka et al., 2005); large lacustrine (Ivanov et al., 2014; Tanaka et al., 2014) or oceanic deposits (Ivanov et al., 2015; Tanaka et al., 2014); ice-rich mantling units deposited from the atmosphere during the Amazonian (Morgenstern et al., 2007; Stuurman et al., 2016; Soare et al., 2018), potentially formed in association with aeolian sediment (Séjourné et al., 2012) or water vapour diffusion and

condensation within the sediment pores (Jakosky and Carr, 1985; Mellon and Jakosky, 1993, 1995; Mischna et al., 2003; Schorghofer, 2008). Moreover, recent studies using data from the Zhurong rover confirmed the presence of hydrated minerals in UP, suggesting a potentially recent aqueous activity in the area (Liu et al., 2022; Wang et al., 2023; Zhao et al., 2023).
Our study zone in UP is partly included into geological units that were identified in previous mapping efforts, but at larger scales than our study zone – i.e. at the global scale (Tanaka et al., 2005, 2014) and the regional scale (Russell and Head, 2003):
1. Tanaka et al. (2005): 'Vastitas Borealis interior' unit (Late Hesperian ice-rich sediment, reworked by periglacial-like processes during the Amazonian); 'Tinjar Valles a' unit (Early Amazonian massive volcanoclastic flows);
2. Tanaka et al. (2014): 'Late Hesperian lowland' unit (corresponding to the Vastitas Borealis formation; ice-rich sediment, possibly intercalated with volcanic material, and modified by later periglacial processes); 'Early Amazonian basin' unit (late lacustrine and/or flood deposits, modified by later periglacial processes); patches of 'Middle Amazonian lowland' unit (ice-rich loess, modified by later periglacial processes);
3. Russell and Head (2003): 'Smooth Lobate' unit (Early Amazonian lava flows); 'Distal' unit (Middle Amazonian ice-rich sediment deposited by airfall, subsequently degraded; emplaced over the 'Smooth Lobate' unit).

The Mars Odyssey Gamma Ray Spectrometer (GRS) Neutron Spectrometer (NS) analyses the neutrons emitted by the interaction of cosmic rays and the martian close surface (< 1 m), which allows to infer the presence of the elements at those depths. As hydrogen is mostly present in H_2O molecules, measurements of hydrogen content by GRS allow to infer the water or water ice content of the upper ~ metre of the ground, and to produce 'water-equivalent hydrogen' maps. In Figure 3.4 we show the location of the study zone in UP on the water-equivalent hydrogen global map obtained from GRS-NS data. It is located on the boundary of excess ice defined by Butcher (2022), hence spanning a range of weight percentage of water-equivalent hydrogen around < 10% to > 30% (Figure 3.4).

We also locate the study zone on the global ice consistency maps (v. 2.0) produced by the Subsurface Water Ice Mapping project (SWIM; Morgan et al., 2021; Figure 3.5). The SWIM team combines multiple datasets and observations obtained from orbital instruments, that can give insights into the presence or absence of subsurface ice (e.g., mapping of glacial/periglacial landforms, thermal data, radar profiles, radar dielectric constant). Each one of the datasets is incorporated within the 'SWIM Equation' (Morgan et al., 2021), which combines the consistency of presence of subsurface ice for each input dataset, in order to evaluate the 'combined ice consistency' for a given area. The input terms for the SWIM Equation are modified to produce ice consistency maps at variable depths; here we show the ice consistency maps between 1 and 5 m depth and over 5 m depth. Between 1 and 5 m, the ice consistency is around 50 ± 15% (average ± standard deviation) over our study zone; no specific pattern can be observed (Figure 3.5a). Over 5 m deep, the ice consistency is around 51 ± 9% (Figure 3.5b). Despite overall similar values for the whole study zone on both maps, the spatial pattern of high-values on the > 5 m ice consistency map matches in some places the extent of the sinuous unit defined in Section 3.2.1.2. (Figure 3.5b), which shows values around 64 ± 20%. This high ice consistency value is the result of high values of the 'Radar Dielectric Estimates' term of the SWIM Equation, which is of 75 ± 26% over the sinuous unit.

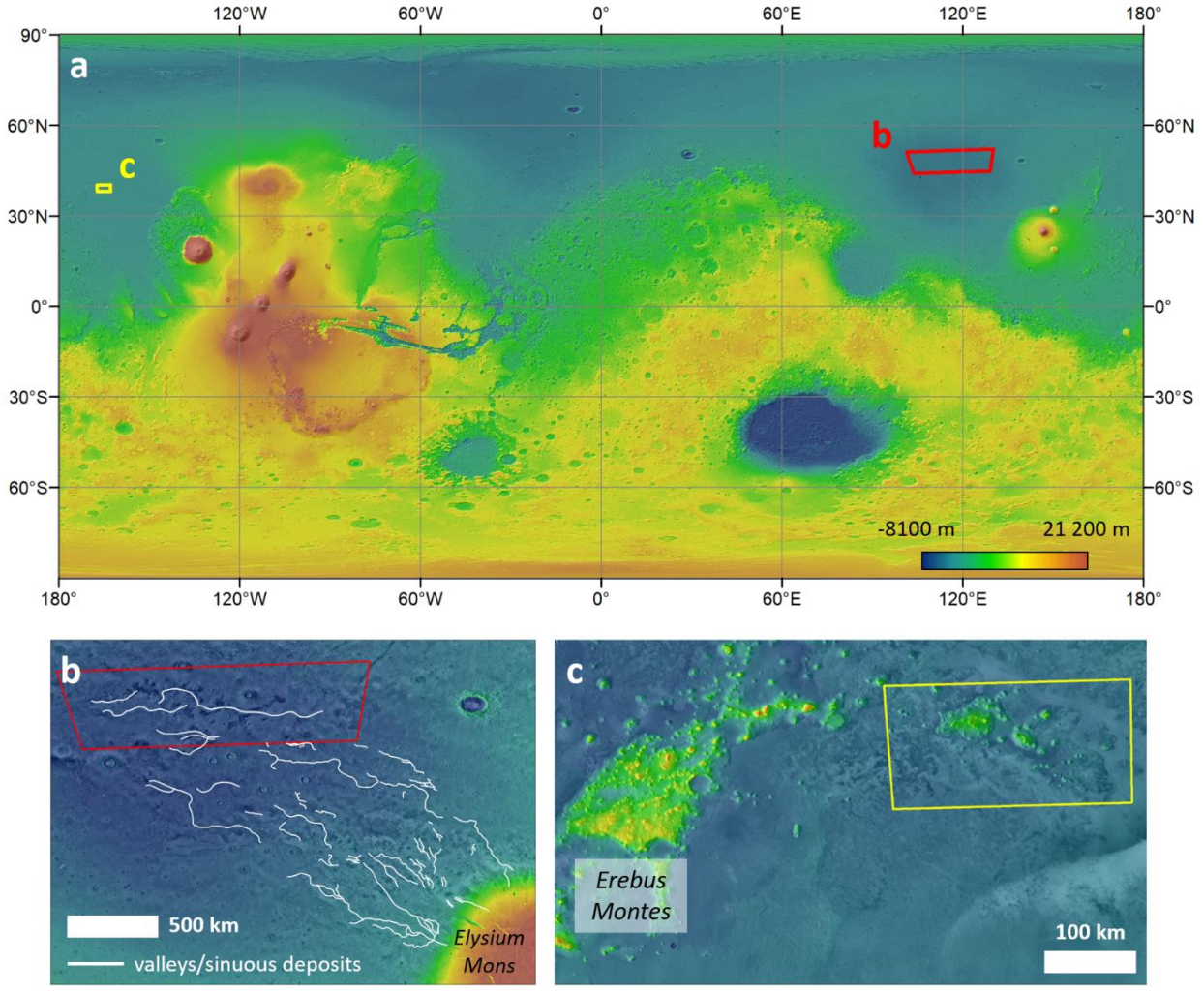

Figure 3.3: ***a.*** *the global context of the two study zones (background: MOLA global dataset of the Mars Orbiter Maser Altimeter over its hillshade);* ***b.*** *regional context of the study zone in Utopia Planitia, northwest of Elysium Mons. The study zone itself is outlined in red. The largest valley systems and potentially associated sinuous deposits are highlighted by white lines;* ***c.*** *regional context of the study zone in Arcadia Planitia, in the eastern Erebus Montes. The study zone itself is outlined in yellow (background: MOLA global mosaic over THEMIS day-IR mosaic). The extents of the two study zones do not appear rectangular as we perform mapping studies in locally-projected coordinate systems. MOLA credits: MOLA Science Team; THEMIS credits: Robin Fergason/USGS.*

3.1.3. Arcadia Planitia: geological context and presence of ground ice

The study zone in AP (Figure 3.3c) was extensively studied and mapped by Hibbard et al. (2021). They interpreted the geological origin of features observed in the area from surficial geomorphology, as well as radar, thermal and spectral data. They reported evidence of ice-cored moraines, ice-rich mantling, and Viscous Flow Features (VFFs; an umbrella term designating features that are interpreted as debris-covered glaciers, and exhibiting surficial morphologies indicating downslope movement deformation). More

specifically, they interpret the large-scale VFFs as ice streams; however, other studies suggested non-glacial origins (e.g. frozen former fluvial channels, Ramsdale et al., 2019; tunnel channels and eskers, Kargel et al., 1995). Hibbard et al. (2021) interpret the small-scale VFFs as Lobate Debris Aprons (LDAs), accordingly to previous studies (Head et al., 2010; Plaut et al., 2009; Ramsdale et al., 2019). They also reported thermal-contraction polygons on some of the units they mapped.
The study zone in AP is located below the excess ice boundary, on the water-equivalent hydrogen global map made from data of the Mars Odyssey GRS NS (Figure 3.4), with values ranging from around 10% to 20%. From the SWIM global maps, the ice consistency between 1 and 5 m is around 48 ± 19% (Figure 3.5a). At depth > 5 m, the ice consistency is around 34 ± 18%.

3.1.4. Objectives

We present here an analysis of the density and type of thermal-contraction polygons, for several units in UP and AP. We seek to understand whether the morphological characteristics of thermal-contraction polygons can be used as proxies to understand the subsurface properties of their substrates; and if yes, to what extent. We also date the units with a study of the crater size-frequency distribution in UP.
First, we detail our mapping workflow, the calculation of polygon morphological parameters, and the crater size-frequency distribution technique (Section 3.2.). We then provide the output results on both of our study zones, in Utopia (Section 3.3.) and Arcadia Planitiæ (Section 3.4.). Lastly, we discuss the implications of our results for the properties and geological origin of the studied units, and on the timing of formation of martian thermal-contraction polygons (Section 3.5.). Our findings are summarised in the conclusions.

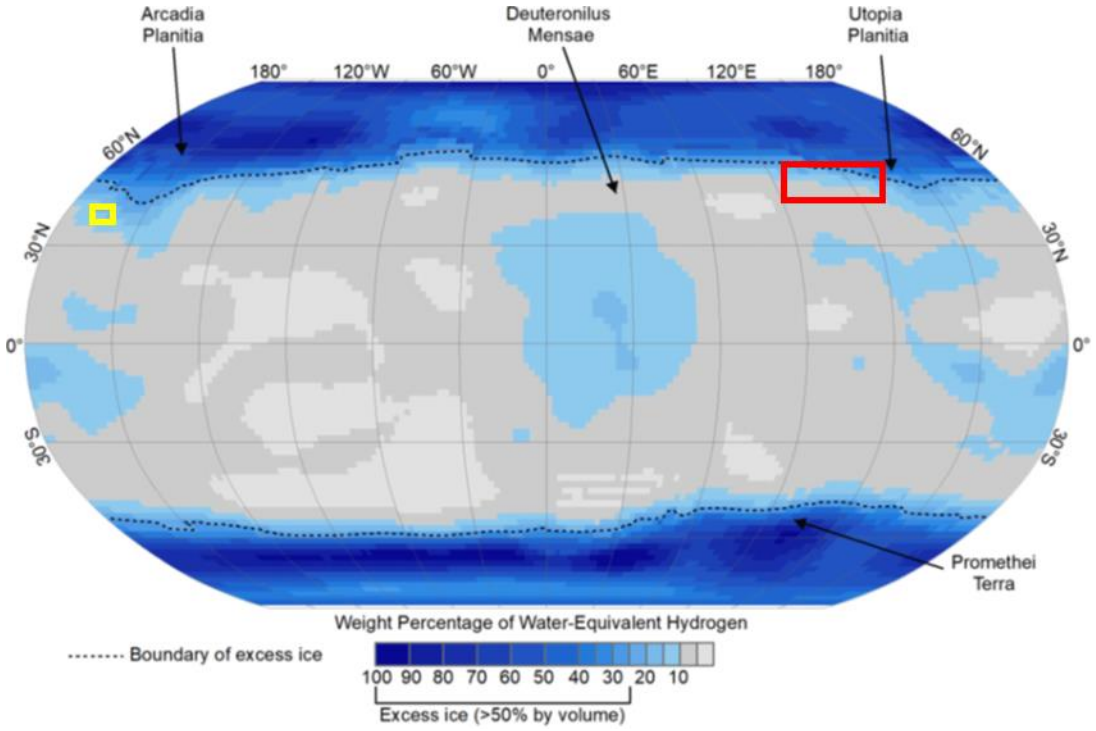

Figure 3.4: location of our two study zones (UP outlined in red, AP outlined in yellow) on the water-equivalent hydrogen global map from data of the Mars Odyssey GRS Neutron Spectrometer; modified from Butcher (2022). Resolution is 300 km/pixel. Credits: NASA/JPL/UA/LANL.

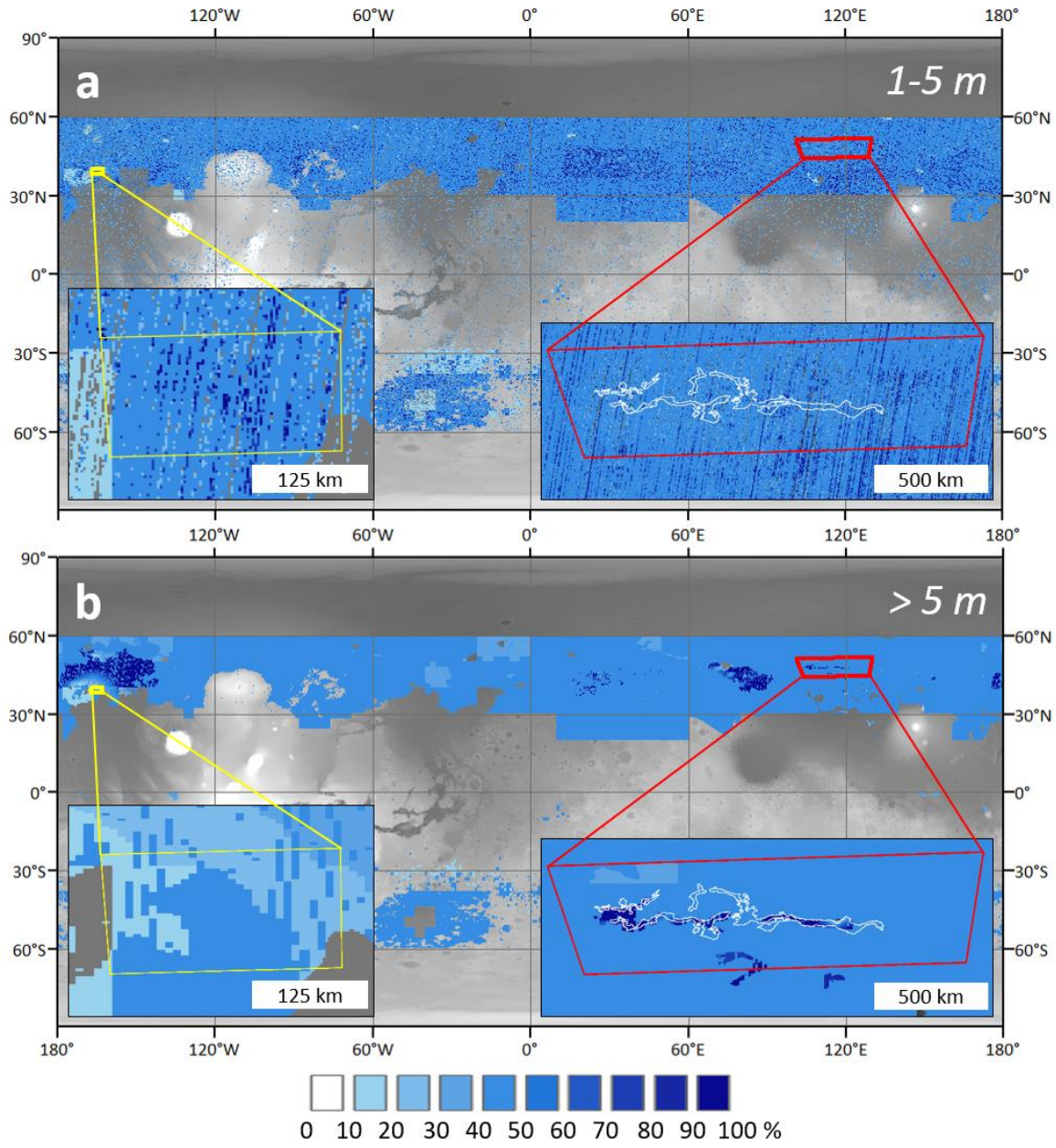

Figure 3.5: location of our two study zones (UP outlined in red, AP outlined in yellow) on the SWIM 2.0 global ice consistency maps. The ice consistency is calculated with the SWIM equations (Morgan et al., 2021), which combine several datasets and evaluates where they are consistently indicating the presence of subsurface ice; ***a.*** *shows the ice consistency at depths between 1 and 5m, based on the Shallow Geomorphology, Radar Surface Power and Radar Dielectric Estimates terms of the SWIM equation;* ***b.*** *indicates the ice consistency at depths over 5m, based on the Deep Geomorphology and Radar Dielectric Estimates terms of the SWIM equation. The sinuous unit in UP is outlined in white. In each panel, two sub-panels are providing zooms on the study zones in UP and AP. Background is the MOLA global DEM. MOLA credits: MOLA Science Team; SWIM credits: SWIM Team/NASA/JPL/PSI.*

3.2. Methods

3.2.1. Mapping

3.2.1.1. Polygon mapping

To perform the mapping of thermal-contraction polygons over our two study zones (Figure 3.3; Table 3.1), we use a grid-based technique (Orgel et al., 2019; Ramsdale et al., 2017, 2019; Séjourné et al., 2019). This technique is designed to efficiently map small features over large areas, and was shown to produce results that are consistent with the mapping of individual features (Ramsdale et al., 2017). It consists in the sub-division of the study zone into a regular grid. The grid squares are then surveyed individually and the presence of the studied features is reported for each square, when the number of features exceeds a predetermined threshold.

In our case, thermal-contraction polygons are 5-25 m in diameter, hence HiRISE images (25-50 cm/pixel) are necessary to map them. In UP (447,000 km^2), 104 images were surveyed – 55 from Soare et al. (2021) and 49 new ones. In AP, where we focus on a smaller study zone (27,500 km^2; studied in Hibbard et al., 2021), 25 images were surveyed. Table 3.1 presents a summary of information on the two study zones, as well as counts of HCPs, LCPs and FCPs data points within each surveyed HiRISE image. Images that are too blurry or grainy, preventing polygon detection, were systematically excluded and hence do not appear in the statistic given in that section nor in Table 3.1.

The valid HiRISE images are gridded in squares of 500x500 m (250,000 m^2; Figure 3.6a). As squares do not align with the extent of the images, we systematically exclude squares with less than 50% of their area overlapping an image, i.e. with an effective area below 125,000 m^2. We then survey each square manually and individually (UP: 35,269 squares; AP: 10,531 squares). In each of the squares, we record the presence of LCPs, HCPs and/or FCPs by digitising a data point within the concerned square, when five or more individuals are present (Figure 3.6b). Note that i. as several polygon types can be found in a single square, several data points can be digitised within the same square (Figure 3.6b); and ii. due to a systematic spatial correlation, squares containing HCPs and/or LCPs are considered by default to also contain FCPs – in addition to the squares containing FCPs only.

3.2.1.2. Unit mapping

In both study zones, we use a GIS software (ArcGIS 10.4 and 10.8) to map the different units at the sub-regional scale, using a mosaic of the infrared data acquired during the day by the Thermal Emission Imaging Sensor (THEMIS day-IR; 100 m/pixel; Arizona State University), a mosaic of visible images from the Context Camera (CTX; 5 m/pixel; NASA/JPL-Caltech), or, when applicable, visible images from the High-Resolution Imaging Experiment (HiRISE; 25-50 cm/pixel; NASA/JPL/University of Arizona).

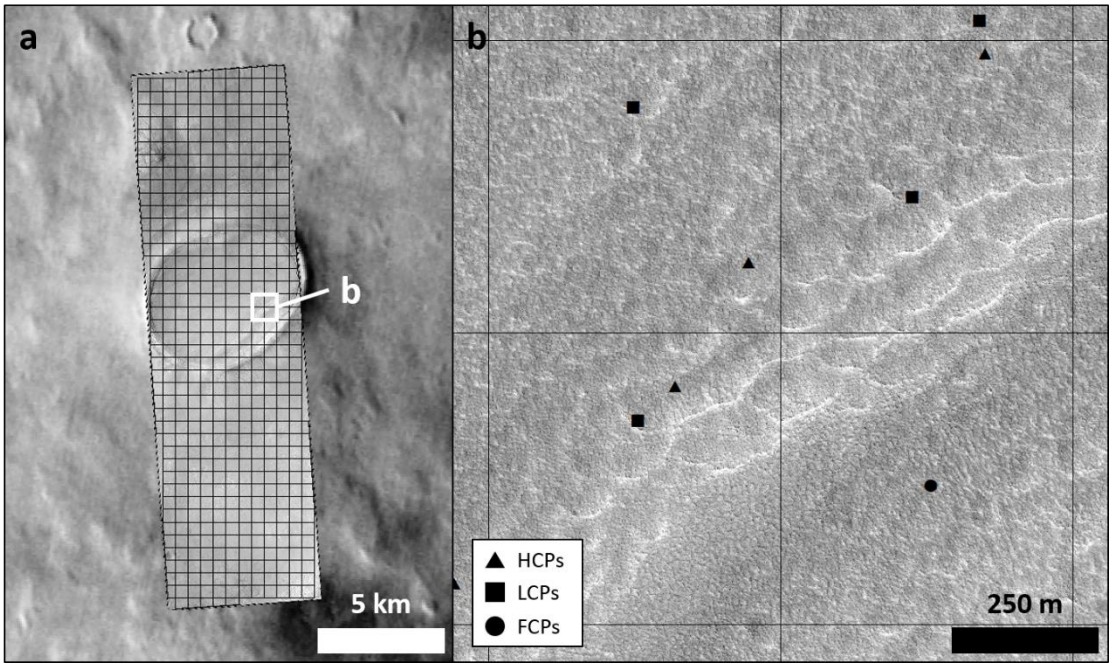

Figure 3.6: example of the grid-based mapping technique. ***a.*** *HiRISE image ESP_016336_2290, gridded into 500x500 m squares (background: THEMIS daytime-IR);* ***b.*** *detail of four grid squares containing data points. Triangles, squares and circles locate HCPs, LCPs and FCPs respectively. North is up on all panels. HiRISE credits: NASA/JPL/University of Arizona; THEMIS credits: Arizona State University.*

In UP, we mapped three different morphological units: the 'sinuous unit', the 'boulder unit' and the 'craters' (Figure 3.7a). The sinuous unit (Figure 3.7b and c) is defined as elongated, sinuous features appearing relatively bright on THEMIS day-IR imagery. The boulder unit (Figure 3.7d and e) is defined as patches appearing relatively dark in THEMIS day-IR imagery, often in contact with the sinuous unit. The craters (Figure 3.7f and g) comprise walls, rims and interior of craters ≥ 2 km in diameter (n = 88). Those units do not correspond to units described in previous studies (Russell and Head, 2003; Tanaka et al., 2005, 2014), as they are of smaller scale (Section 3.1.2.).

In AP, we mapped three different morphological units, based on the classification suggested by Hibbard et al. (2021): the 'sinuous features', the 'mantling unit', and the 'hills' (Figure 3.8a). The sinuous features (Figure 3.8b) are defined as elongated, sinuous features appearing relatively bright on THEMIS day-IR imagery. The mantling unit (Figure 3.8c) is defined as thermally dark (in THEMIS day-IR imagery) unit, surrounding the hills. The hills (Figure 3.8d) are defined as circular to elliptic hills, a few hundreds of metres high. For the hills, we mapped separately their summits and flanks as they exhibit different surficial morphologies (Section 3.4.1.). Those units do not correspond to units described in some previous studies (Russell and Head, 2003; Tanaka et al., 2005, 2014), as they are of smaller scale (Section 3.1.3.).

Study zone	Location	Images surveyed	Area (km^2)	Grid squares
Utopia Planitia	44°-52°N 100°-130°E	55 (Soare et al., 2021) 49 (this study)	447,167	35,269
Arcadia Planitia	38-40°N 193°-197°E	25	27,500	10,531

		Grid squares containing:		
HiRISE image ID	**Centre location**	**HCPs**	**LCPs**	**FCPs**
Utopia Planitia	ESP_016046_2285	48.15°N 112.59°E	1	-	13
	ESP_016336_2290	48.44°N 115.71°E	235	55	246
	ESP_016837_2305	50.25°N 118.11°E	390	247	123
	ESP_017035_2290	48.6°N 113.1°E	163	23	260
	ESP_017206_2285	47.96°N 124.06°E	1	-	290
	ESP_017549_2275	47.05°N 118.67°E	-	-	4
	ESP_017760_2295	48.97°N 118.87°E	185	31	328
	PSP_009334_2275	47.03°N 118.43°E	-	-	-
	PSP_009756_2290	48.83°N 116.86°E	4	1	95
	PSP_009888_2300	49.79°N 112.21°E	-	-	-
	PSP_009901_2280	47.69°N 118.17°E	88	6	274
	ESP_022850_2295	49.12°N 113.67°E	-	-	135
	PSP_010099_2300	49.75°N 112.47°E	-	-	2
	PSP_010125_2290	48.72°N 121.89°E	-	-	-
	PSP_010244_2295	49.16°N 113.43°E	-	-	-
	PSP_010455_2300	49.65°N 113.15°E	-	-	2
	PSP_010521_2300	49.47°N 111.89°E	-	-	-
	ESP_026384_2280	47.57°N 113.27°E	-	-	-
	ESP_026450_2270	46.82°N 110.89°E	208	22	370
	ESP_026885_2295	49.39°N 115.9°E	283	52	99
	ESP_027043_2290	48.55°N 122.19°E	-	-	-
	ESP_027096_2285	47.93°N 115.58°E	4	-	242
	ESP_027505_2280	47.8°N 111.08°E	48	2	93
	ESP_027650_2275	46.48°N 112.23°E	172	19	91
	ESP_027861_2275	47.33°N 111.62°E	4	-	39
	ESP_028072_2255	45.38°N 111.47°E	17	-	111
	ESP_034164_2260	45.46°N 110.81°E	22	6	72
	ESP_034823_2270	46.56°N 118.05°E	-	-	15
	ESP_035021_2285	48.04°N 111.12°E	18	-	128
	ESP_035535_2295	48.94°N 118.78°E	101	45	223
	ESP_035614_2280	47.62°N 122.29°E	54	2	197
	ESP_035667_2295	49.38°N 115.63°E	163	72	132
	ESP_036432_2295	49.38°N 111.62°E	29	4	62
	ESP_036577_2300	49.64°N 112.62°E	84	46	24
	ESP_044977_2270	46.63°N 117.85°E	31	1	67
	ESP_045333_2305	50.02°N 119.81°E	72	4	86
	ESP_045399_2290	48.76°N 119.02°E	112	5	244
	ESP_045544_2290	48.86°N 119.72°E	33	10	51
	ESP_046164_2285	48.17°N 111.96°E	166	53	227
	ESP_046401_2265	46.32°N 121.79°E	4	-	172
	ESP_046546_2300	49.56°N 122.57°E	45	3	49
	ESP_046467_2280	47.6°N 119.69°E	36	4	89
	ESP_046388_2280	47.75°N 116.45°E	8	-	130

ESP_046757_2270	46.87°N 122.66°E	22	-	334
ESP_050304_2270	46.89°N 120.68°E	17	3	56
ESP_052506_2290	48.85°N 121.39°E	-	-	-
ESP_055671_2260	45.46°N 114.02°E	-	-	-
ESP_057768_2295	49.13°N 117.2°E	34	5	163
ESP_059390_2265	46.38°N 116.47°E	97	3	58
ESP_059746_2275	47.22°N 117.01°E	2	-	296
ESP_059957_2280	47.55°N 116.95°E	-	-	163
ESP_060168_2275	46.99°N 116.75°E	6	-	260
ESP_063768_2270	46.77°N 112.37°E	38	-	63
ESP_063979_2280	47.42°N 112.01°E	130	41	44
ESP_063992_2270	46.64°N 117.03°E	-	-	178
ESP_011431_2290	48.87°N 106.08°E	10	-	89
ESP_011655_2315	51.19°N 110.13°E	-	-	-
ESP_016534_2305	50.35°N 109.48°E	-	-	-
ESP_016652_2315	50.97°N 128.58°E	16	5	21
ESP_016877_2295	49.25°N 105.95°E	-	-	1
ESP_017022_2310	50.46°N 107.38°E	-	-	7
ESP_017167_2310	50.57°N 109.19°E	-	-	2
PSP_006842_2310	50.73°N 123.87°E	326	205	308
ESP_018709_2290	48.73°N 127.55°E	38	30	35
PSP_006948_2305	50.14°N 109.81°E	-	-	-
ESP_019923_2290	48.4°N 105.29°E	-	-	83
PSP_009163_2270	46.65°N 107.14°E	109	24	163
PSP_009308_2295	48.99°N 107.95°E	-	-	108
PSP_009651_2290	48.48°N 104.36°E	-	-	29
PSP_009664_2305	50.09°N 108.27°E	-	-	-
PSP_009730_2290	48.65°N 106.75°E	-	-	39
PSP_009809_2300	49.62°N 109.33°E	-	-	-
PSP_009941_2290	48.49°N 105.59°E	-	-	7
PSP_008622_2305	50.29°N 118.73°E	10	1	124
PSP_010007_2285	48.38°N 104.97°E	-	-	3
PSP_010086_2295	49.39°N 107.46°E	-	-	21
PSP_010152_2290	48.09°N 105.66°E	-	-	-
PSP_010363_2290	48.68°N 105.55°E	-	-	149
PSP_010442_2305	50.23°N 108.24°E	-	-	-
ESP_026081_2290	48.89°N 105.47°E	-	-	4
ESP_026423_2270	46.84°N 128.02°E	-	-	35
ESP_026476_2315	51.08°N 121.47°E	-	-	7
ESP_034810_2305	50.34°N 111.39°E	-	-	178
ESP_036564_2260	45.45°N 108.34°E	115	64	282
ESP_036867_2315	51.37°N 113.82°E	-	-	9
ESP_037685_2295	49.38°N 102.69°E	-	-	85
ESP_042261_2315	51°N 104.3°E	-	-	-
ESP_043118_2275	47.06°N 106.62°E	18	4	101

	ESP_045254_2320	51.5°N 115.95°E	-	-	-
	ESP_045491_2300	49.51°N 127.45°E	-	-	13
	ESP_045847_2290	48.58°N 127.36°E	1	-	28
	ESP_046045_2320	51.75°N 120.26°E	-	-	1
	ESP_050344_2295	49.35°N 108.1°E	-	-	-
	ESP_050462_2310	50.65°N 126.01°E	1	1	35
	ESP_050357_2320	51.7°N 112.9°E	-	-	297
	ESP_050555_2275	47.16°N 107.43°E	20	6	167
	ESP_054392_2280	47.85°N 109.21°E	4	27	559
	ESP_055170_2270	46.9°N 109.17°E	1	2	110
	ESP_055302_2255	45.36°N 105.91°E	15	1	113
	ESP_058797_2290	48.32°N 105.56°E	-	-	35
	ESP_064651_2295	49.08°N 124.8°E	76	48	130
	ESP_065759_2305	50.23°N 120.35°E	-	-	-
	ESP_066960_2265	46.05°N 105.16°E	16	-	111
	PSP_001911_2305	50.17°N 108.59°E	-	-	-
Arcadia Planitia	ESP_015964_2195	39.18°N 193.85°E	-	-	23
	ESP_015964_2195	38.48°N 195.89°E	-	-	208
	ESP_015964_2195	38.99°N 195.41°E	-	-	155
	ESP_015964_2195	39.71°N 194.75°E	-	-	196
	ESP_015964_2195	39.59°N 193.88°E	-	-	108
	ESP_015964_2195	39.56°N 194.23°E	-	-	90
	ESP_015964_2195	40.06°N 194.77°E	-	-	156
	ESP_015964_2195	39.91°N 194.24°E	-	-	73
	ESP_015964_2195	39.42°N 194.03°E	-	-	154
	ESP_015964_2195	39.09°N 192.9°E	-	-	3
	ESP_015964_2195	39.51°N 193.38°E	-	-	22
	ESP_015964_2195	38.42°N 196.47°E	-	-	49
	ESP_015964_2195	40.02°N 195.51°E	40	-	227
	ESP_015964_2195	38.35°N 195.15°E	38	-	129
	ESP_015964_2195	40.01°N 195.32°E	69	-	224
	ESP_015964_2195	39.29°N 195.07°E	-	-	93
	ESP_015964_2195	38.92°N 193.57°E	5	-	124
	ESP_015964_2195	39.84°N 194.47°E	-	-	187
	ESP_015964_2195	39.11°N 196.57°E	28	-	212
	ESP_015964_2195	39.09°N 194.71°E	3	-	9
	ESP_015964_2195	39.1°N 196.71°E	-	-	97
	ESP_015964_2195	39.81°N 195.62°E	2	-	95
	ESP_015964_2195	39.18°N 195.61°E	-	-	108
	ESP_015964_2195	38.92°N 193.31°E	-	-	17
	ESP_015964_2195	39.18°N 193.85°E	-	-	97

Table 3.1: details of the two study zones in Utopia and Arcadia Planitiæ, and on the surveyed HiRISE images. The coordinates given for each image are the ones of their centre. A '-' sign indicates the absence of a given polygon morphology.

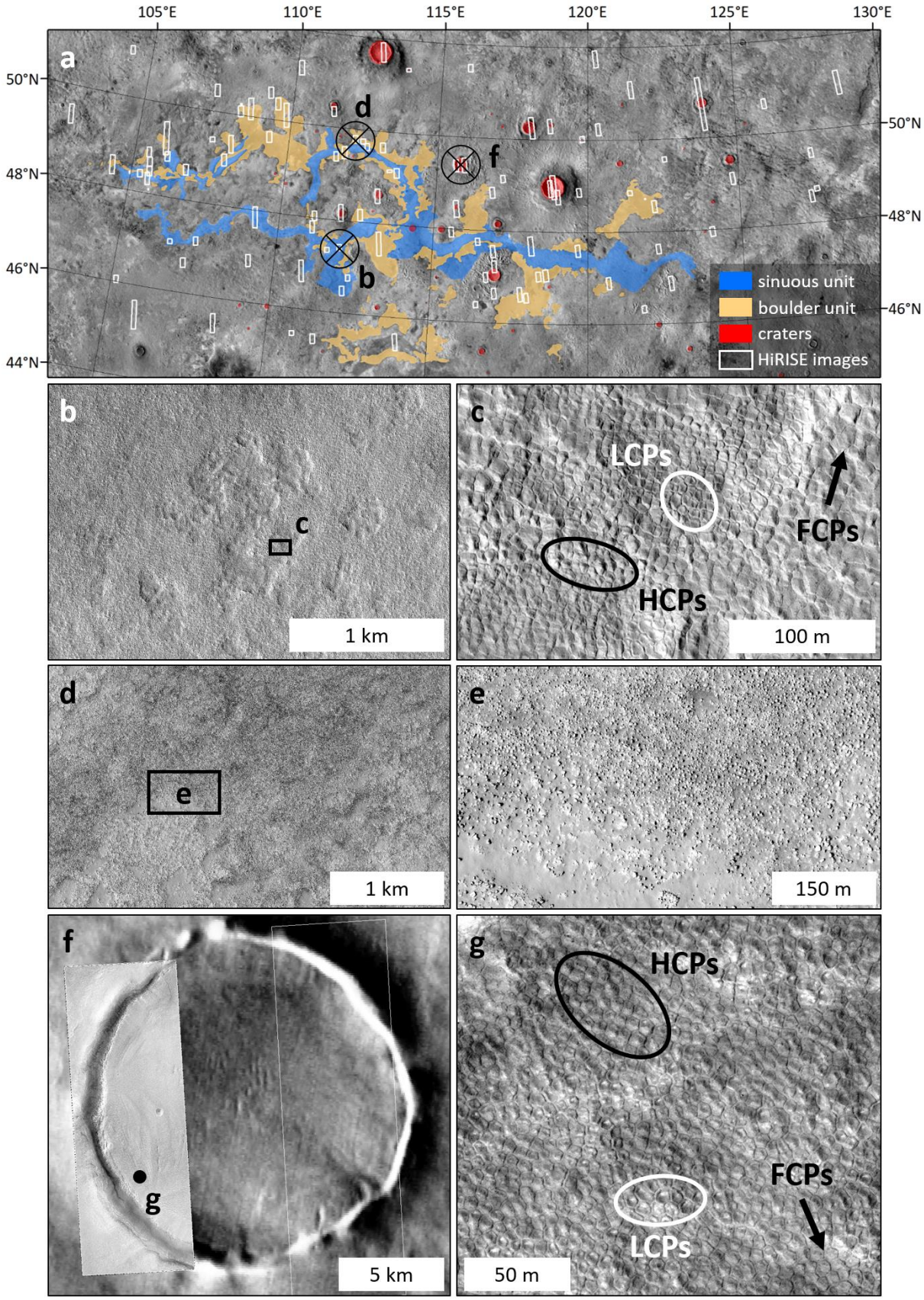

Figure 3.7: morphological units defined in UP. Full caption two pages ahead.

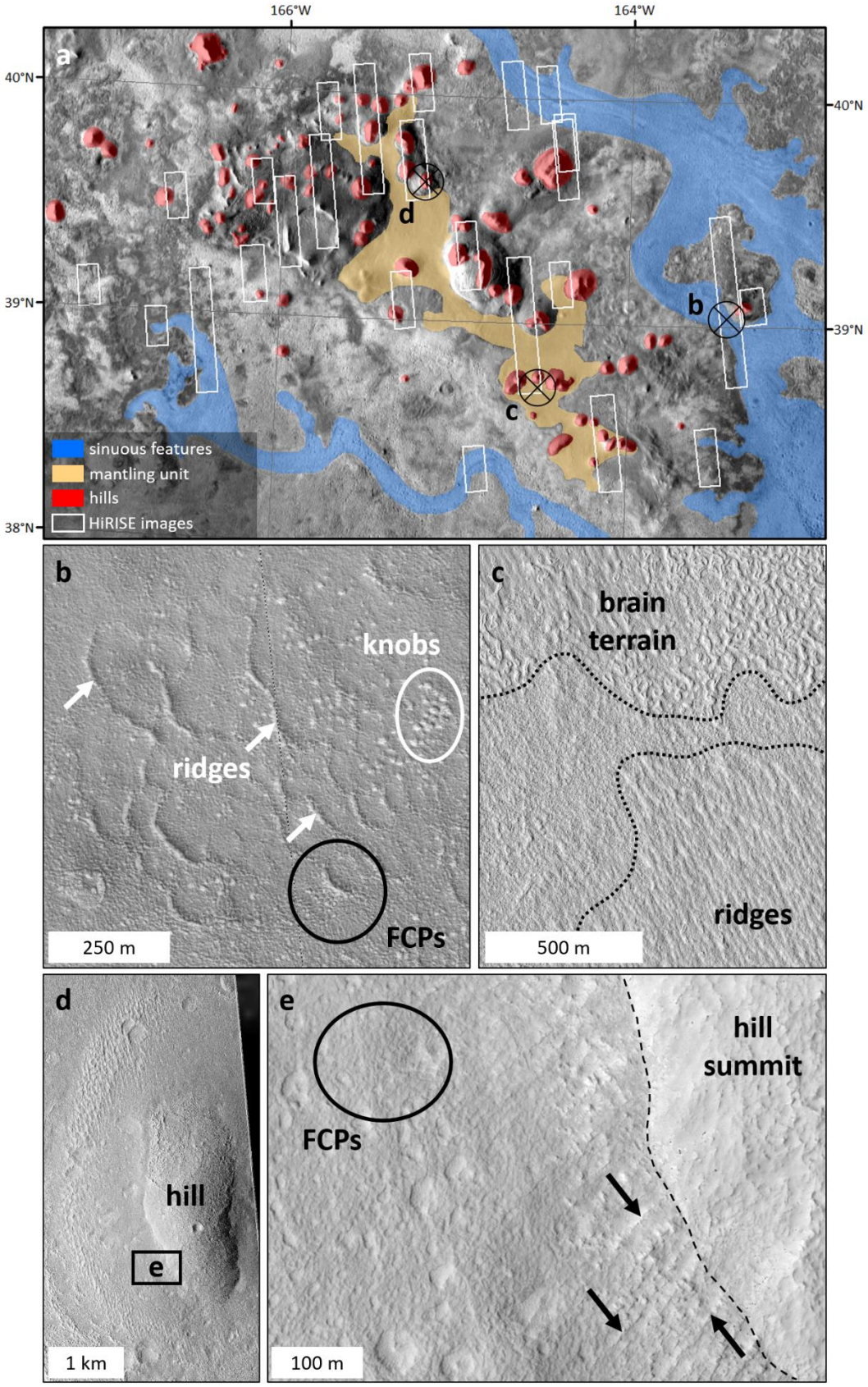

Figure 3.8: morphological units defined in AP. Full caption on next page.

*Figure 3.7: morphological units defined in UP. **a.** the whole study zone. Circled crosses point the location of panels b., d. and f. (background: THEMIS daytime-IR); **b.** detail of the sinuous unit showing scalloped depressions (HiRISE image ESP_063979_2280). **c.** detail of the scalloped depressions of panel b. LCPs and HCPs are found within the scalloped depression, and FCPs are mostly found outside. **d.** detail of the boulder unit showing a ubiquitous field of boulders (HiRISE image PSP_009888_2300). **e.** detail of panel d., boulders are tens of metres in diameter. **f.** a crater ~ 15 km in diameter. **g.** detail of the interior of the crater in panel f. Numerous LCPs, HCPs and FCPs are found (HiRISE image ESP_035667_2295). HiRISE credits: NASA/JPL/University of Arizona; THEMIS credits: Arizona State University.*

*Figure 3.8: morphological units defined in AP. **a.** the whole study zone in AP. Circled crosses point the location of panels b., c. and d. (background: THEMIS daytime-IR); **b.** detail of a sinuous feature. Arcuate ridges are pointed out by white arrows, FCP examples are circled in black and knob examples are circled in white (HiRISE image ESP_056710_2195); **c.** detail of the mantling unit. Note the spatial association between brain terrain and linear ridges (HiRISE image ESP_017243_2195); **d.** a hill in AP (HiRISE image PSP_009740_2200); e. detail of the hill shown in panel d. Note the presence of FCPs (circled in black) and linear ridges (black arrows) on the flank of the hill, and their absence on the summit. North is up on all panels. HiRISE credits: NASA/JPL/University of Arizona; THEMIS credits: Arizona State University.*

3.2.2. Parameter calculation

We defined three parameters based on polygon characteristics (Table 3.2): i. the polygonisation rate (ρ_{pol}), i.e. the proportion of a given substrate that has undergone thermal-contraction; ii. the wedge formation rate (ρ_{wf}), i.e. the proportion of the substrate that has undergone wedge formation; and iii. the wedge preservation rate (ρ_{wp}), i.e. the proportion of wedges that were preserved. These three parameters are calculated for each of the units defined in Section 3.2.1.2. The wedge preservation rate (ρ_{wp}) can be used in order to discriminate between the presence of ice wedges and sand wedges – as we did in Soare et al. (2021). Hence, the presence of LCPs on a study zone is required to perform such an investigation (Table 3.2).

We assume as working hypotheses that the studied units underwent temperature decreases that were of sufficiently high magnitude, and occurred a sufficient number of times, for thermal cracking of ground ice to occur. It implies that thermal-contraction polygons must have formed everywhere the substrate properties were conducive to thermal contraction. This hypothesis is likely to be true, as i. diurnal and seasonal temperature gradients are higher on Mars than on Earth (e.g. Leovy, 2001), and ii. similar temperature gradients probably occurred regularly throughout the Amazonian, i.e. for the last ~ 3 billion years (e.g. Mellon, 1997; Schorghofer, 2008). Therefore, we consider that the formation of thermal-contraction polygons on a given unit is solely dependent on internal properties of the substrate – or on environmental conditions that are specific to this unit. In addition, low-centred and high-centred polygon morphologies can be formed either by freezing of deposited sand or liquid water (Section 3.1.1.). However, we argued in Soare et al. (2021) that the polygons we study are ice-wedge polygons, and the study zones overlap with the present study. Therefore, we also use as a work hypothesis that the low-centred and high-centred polygon morphologies we investigate were formed by liquid water.

Hence, we suggest that each of the parameters we defined reflects a property of the substrate, at the scale of a study zone. As a substrate has to be ice-cemented – hence initially porous – in order to undergo thermal contraction, we suggest that the polygonisation rate of a given substrate (ρ_{pol}) is correlated with its cementation by ice. As liquid water has to accumulate within the polygonal fractures in order to form ice wedges, we suggest that the wedge formation rate of a substrate (ρ_{wf}) is correlated with the intensity of liquid water activity within that substrate, and hence its capacity to form ice wedges. Finally, the degradation of ice wedges depends on how deep the thermal wave penetrates the ground, and thus depends on the insulating properties of the substrate. Hence, we suggest that the wedge preservation rate of a substrate (ρ_{wp}) is correlated with the capacity of the substrate to preserve ground ice.
The parameters take values between 0 and 1 – with 0 indicating a property that the substrate does not express at all, and 1 indicating a property that the substrate expresses on the totality of its surface. Information on the calculation, the geologic significance, and the suggested property of the substrate the parameters reflect is summarised in Table 3.2.

	ρ_{pol}	ρ_{wf}	ρ_{wp}
calculation	squares in a unit containing polygons of any type as a proportion of the total number of squares	squares in a unit containing LCPs and/or HCPs, as a proportion of the squares including polygons	squares including LCPs, as a proportion of the squares including LCPs and/or HCPs
geologic significance	proportion of the substrate that has undergone thermal-contraction	proportion of the substrate that has undergone wedge formation	proportion of previously formed wedges that are preserved
reflects the	cementation of the substrate by ice	capacity of the substrate to form wedge ice	capacity of the substrate to preserve ground ice

Table 3.2: information on the calculation, the geologic significance, and the suggested property of the substrate reflected by each parameter – ρ_{pol}, ρ_{wf} and ρ_{wp}.

3.2.3. Crater size-frequency distribution

We also study the crater size-frequency distribution, which allows an estimate of the absolute ages of geological units (Hartmann, 1977, 2005; Hartmann and Neukum, 2001; Ivanov, 2001; Neukum, 1983; Neukum et al., 2001; Platz et al., 2013). We focus the study of crater size-frequency distribution on the sinuous and boulder units in our study zone in UP. We use the ArcGIS add-in 'CraterTools' (Kneissl et al., 2011, 2015) to map 625 craters on ~ 22,000 km² of the sinuous unit, and 1623 craters on ~ 29,000 km² of the boulder unit. Craters were systematically identified as circular depressions delimited by a rim. Craters that were stratigraphically overlapped by the studied unit were not included. The sinuous and boulder units cover sufficient area to produce statistically significant age estimates (Warner et al., 2015). Only craters with a diameter ≥ 100 m were included in order to avoid mapping secondary craters. We then use the output data within the CraterStats 2.0 analyst tool (developed at Freie Universität Berlin) in order to visualise the differential and cumulative crater density (Crater analysis techniques working group, 1979).

3.2.4. Topographic study

We use the global gridded data of the Mars Orbiter Laser Altimeter (MOLA; 463 m/pixel) in order to i. study the elevation of the sinuous and boulder units (using the Zonal Stats tool in ArcGIS); and ii. generate four topographic profiles, spanning contacts between the sinuous and boulder units.

3.3. Utopia Planitia: observations and measurements

3.3.1. Morphological observations

Large craters (≥ 2 km in diameter) in UP show extensive thermal-contraction polygons, of all types (Figure 3.7f and g). The surface of the sinuous unit (Figure 3.7b and c) is uneven, pitted with scallop-shaped depressions ('scalloped depressions'). Those scalloped depressions show a steep pole-facing flank and a gentle equator-facing flank, suggesting an insolation-driven degradation process similar to terrestrial thermokarst suggested in previous studies (Costard and Kargel, 1995; Dundas et al., 2015, 2017; Haltigin et al., 2014; Lefort et al., 2009; Morgenstern et al., 2007; Séjourné et al., 2011, 2012; Soare et al., 2018; Ulrich et al., 2010). The sinuous unit also hosts extensive polygonal patterns, within and outside of scalloped depressions (Figure 3.7b and c). From visual inspection, the vast majority of HCPs and LCPs are found within scalloped depressions (e.g. Séjourné et al., 2011); polygons outside of scalloped depressions are mostly FCPs. The surface of the boulder unit (Figure 3.7d and e) is covered in extensive boulder fields, with a diameter in the order of magnitude of tens of metres. We infer that the sediment found in-between the boulders is unconsolidated as it sometimes exhibits transverse aeolian ridges. Large blocks (~ 50-100 m in diameter) that seemingly shattered in place can also be observed (Figure 3.9).
Overall, the elevation of the sinuous unit is -4928 ± 10 m (average ± standard deviation); the elevation of the boulder unit is on average slightly lower: -4947 ± 15m, but there is significant overlap. The four topographic profiles we generate span two or three contacts between the sinuous and boulder units (Figure 3.10). From those profiles, the sinuous unit is a positive topographic relief that is higher in elevation than the boulder unit at the scale of a given profile. Furthermore, the boulder unit is found in areas that are local minima in elevation (Figure 3.10).

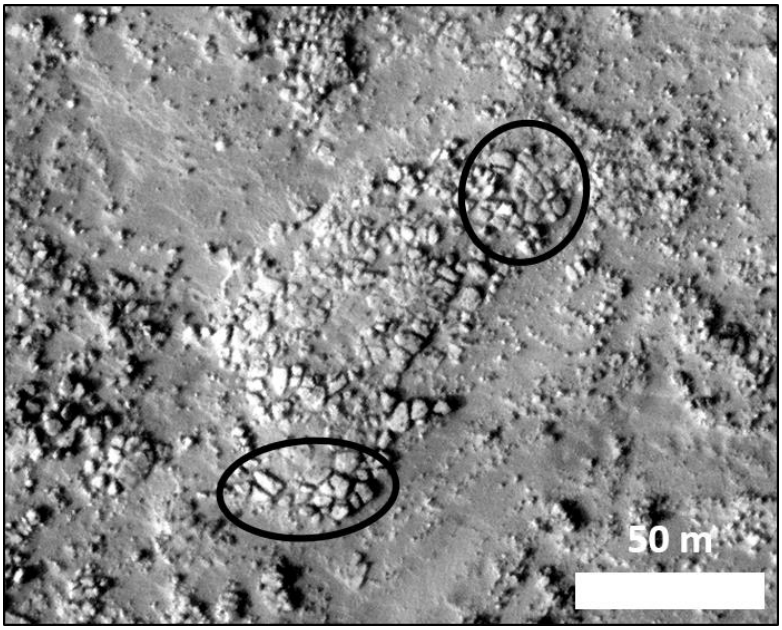

Figure 3.9: blocks that seem to have shattered in place within the boulder unit, circled in black (HiRISE image ESP_011431_2290). HiRISE credits: NASA/JPL/University of Arizona.

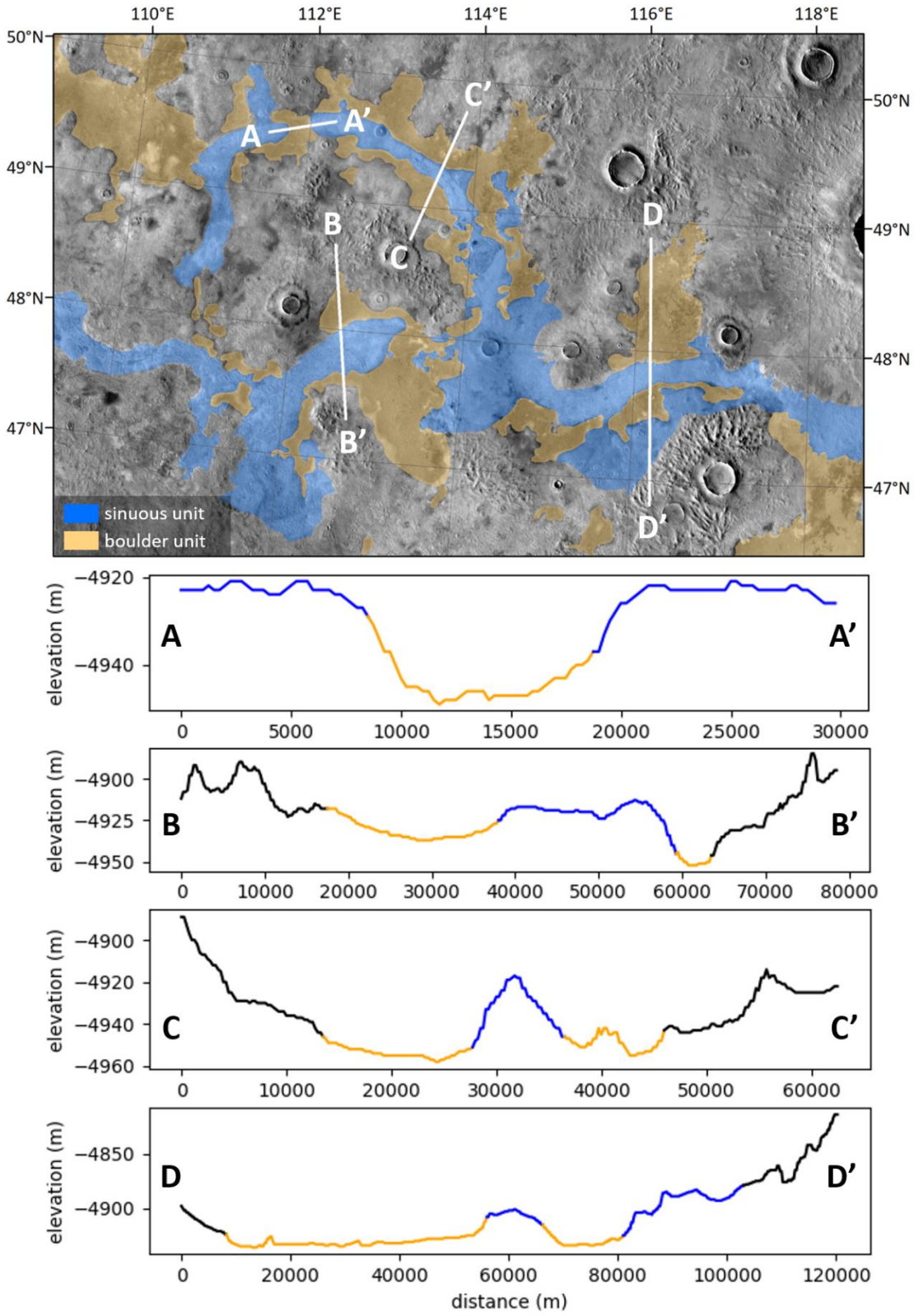

Figure 3.10: four topographic profiles cutting the sinuous and boulder units, made from the MOLA gridded elevation data. Vertical exaggeration is x200 for all profiles. Background is THEMIS day-IR mosaic. MOLA credits: MOLA Science Team; THEMIS credits: Arizona State University.

The expression of the contact between the sinuous and the boulder units varies. Where the sinuous unit is equator-facing (Figure 3.11a), the contact consists in a smooth strip of regularly-patterned material that follows the contact. From visual inspection, it seems to be in continuity with the sinuous unit in some places, and also exhibits features similar in shape to scalloped depressions, but without inner polygons (Figure 3.11a). The boulder unit can be observed at the bottom of these depressions. Where the sinuous unit is pole-facing (Figure 3.11b), the contact consists in an abrupt scarp, constituted of the same regularly-patterned material, and seemingly continuous with the sinuous unit. In that case, the boulder unit is found at the foot of the scarp. As the sinuous unit is elongated in an east-west direction, few east or west-facing contact exist with the boulder unit, and even fewer are imaged by HiRISE. One contact where the sinuous unit is facing the east (Figure 3.11c) shows a smooth strip of regular material that is similar to the equator-facing contacts (Figure 3.11a). These contact types are consistent everywhere HiRISE images allow to observe the contact between the sinuous and boulder units. Together with the topographic profiles we presented, the contacts between the sinuous and the boulder units support a stratigraphic order with the sinuous unit at the top.

3.3.2. Polygon parameters

We calculated the three parameters ρ_{pol}, ρ_{wf} *and* ρ_{wp} for the units of the study zone in UP: the sinuous unit, the boulder unit and the craters (Section 3.2.1.2.). The results are summarised in Table 3.3. The sinuous unit shows a relatively high ρ_{pol} (0.80), and intermediate values of ρ_{wf} *and* ρ_{wp} (0.28 and 0.22, respectively). The craters show similar ρ_{pol} (0.80) to the sinuous unit, but higher values of ρ_{wf} *and* ρ_{wp} (0.49 and 0.38, respectively). The boulder unit shows very low values of ρ_{pol} and ρ_{wf} relative to the other units (0.01 and 0.02, respectively). Calculating ρ_{wp} was not possible, as the boulder unit has no LCPs (see Table 3.2 for details).

	unit	ρ_{pol}	ρ_{wf}	ρ_{wp}
UP	sinuous unit	0.80	0.28	0.22
	boulder unit	0.01	0.02	-
	craters	0.80	0.49	0.38
AP	sinuous features	0.67	0.13	-
	mantling unit	0.24	-	-
	hill flanks	0.55	-	-

Table 3.3: results of the parameter calculation (ρ_{pol}, ρ_{wf} and ρ_{wp}), for the units of study zones in UP and AP. A '-' sign indicates that the parameter could not be calculated (i.e. one or several polygon types were absent on the unit).

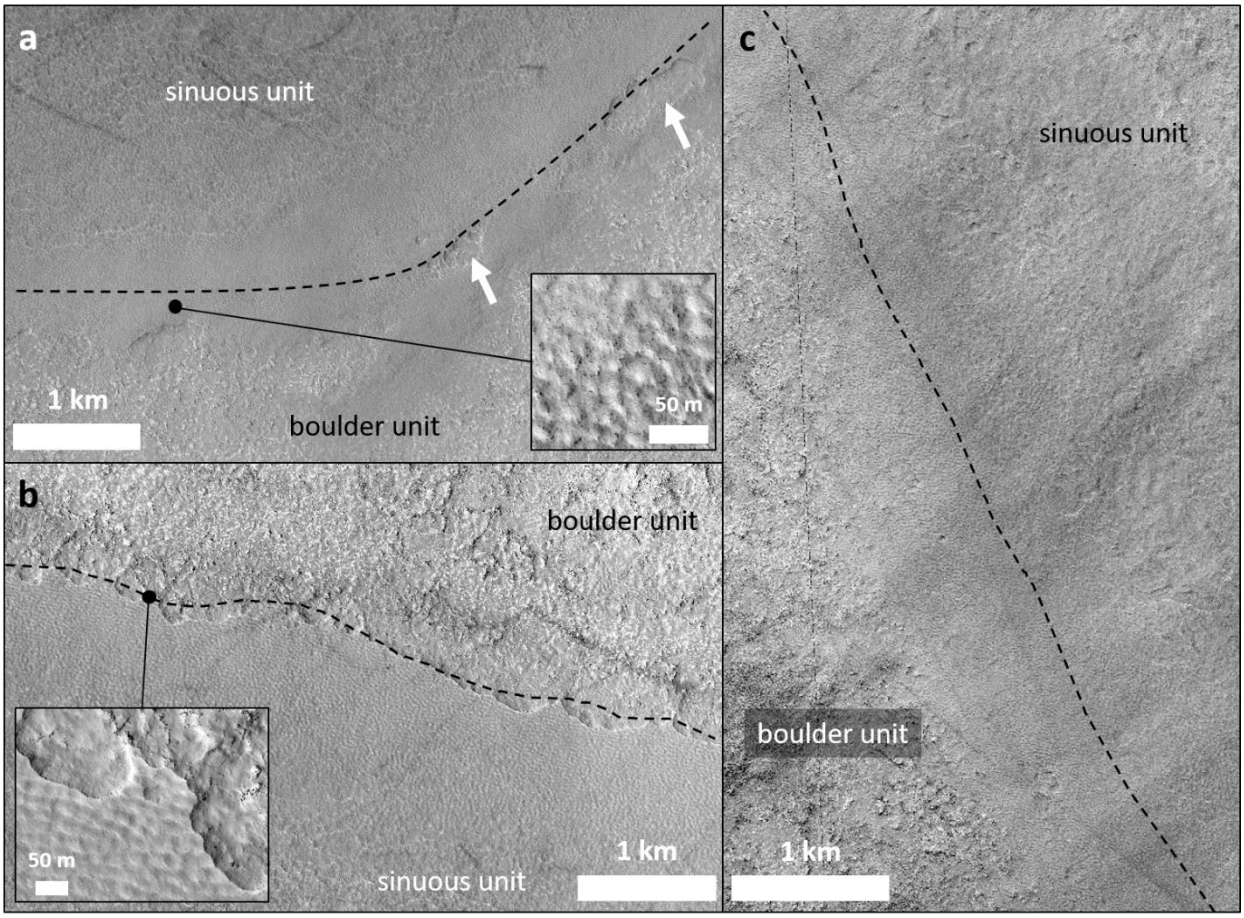

*Figure 3.11: contacts between the sinuous unit and the boulder unit, where **a.** the sinuous unit is facing toward the equator (HiRISE image ESP_036432_2295); **b.** the sinuous unit is facing toward the pole (HiRISE image ESP_036577_2300); **c.** the sinuous unit is facing toward the west (HiRISE image ESP_022850_2295). On panel a., scalloped shapes on the contact material are pointed out by white arrows. For panels a. and b., a sub-panel provides a zoom on the contact between the sinuous and the boulder units. HiRISE credits: NASA/JPL/University of Arizona.*

3.3.3. Results from crater size-frequency distribution

The differential and cumulative crater size-frequency distribution plots for the sinuous and boulder units show complex patterns (Figure 3.12), that do not overlap with the isochrones computed from the chronology and production functions defined in Hartmann, (2005). The sinuous unit seems to be depleted in craters with a relatively small diameter (< 400 m), which results in a gentler slope compared to the isochrones for that diameter range (Figure 3.12a). This gentle slope indicates that the smaller the craters, the more substantial the depletion is. The crater size-frequency distribution of the sinuous unit has two parts, that match isochrones of different ages (Figure 3.12a): craters ~ 400-700 m in diameter match an isochron around 340 ± 60 Ma, while craters ~ 1100-3000 m match an isochron around 1.4 ± 0.8 Ga. Craters between 700-1100 m overall form a slope gentler than the isochrones, joining the two crater sub-groups. However, data points do not align well with computed isochrones, indicating a complex cratering history. An outlier point constituted of two craters with a large diameter (7-8 km; Figure 3.12b) matches an older isochron

(around 3.8 Ga). As no other data point supports the age given by that isochron, and as no intermediate craters were found between those large craters and the rest of the crater population (maximum diameter < 3 km), we consider that data point as a statistical outlier.

The crater size-frequency distribution of the boulder unit is more complex than the distribution of the sinuous unit (Figure 3.12b). Craters 250-800 m match an isochron around 230 ± 20 Ma, and craters 1000-4000 m match an isochron around 1.3 ± 0.7 Ga. Craters between 800-1000 m are overall found in-between the two isochrones, joining the two crater sub-groups. However, similarly to the sinuous unit, data points do not align well with the computed isochrones, which indicates a complex cratering history.

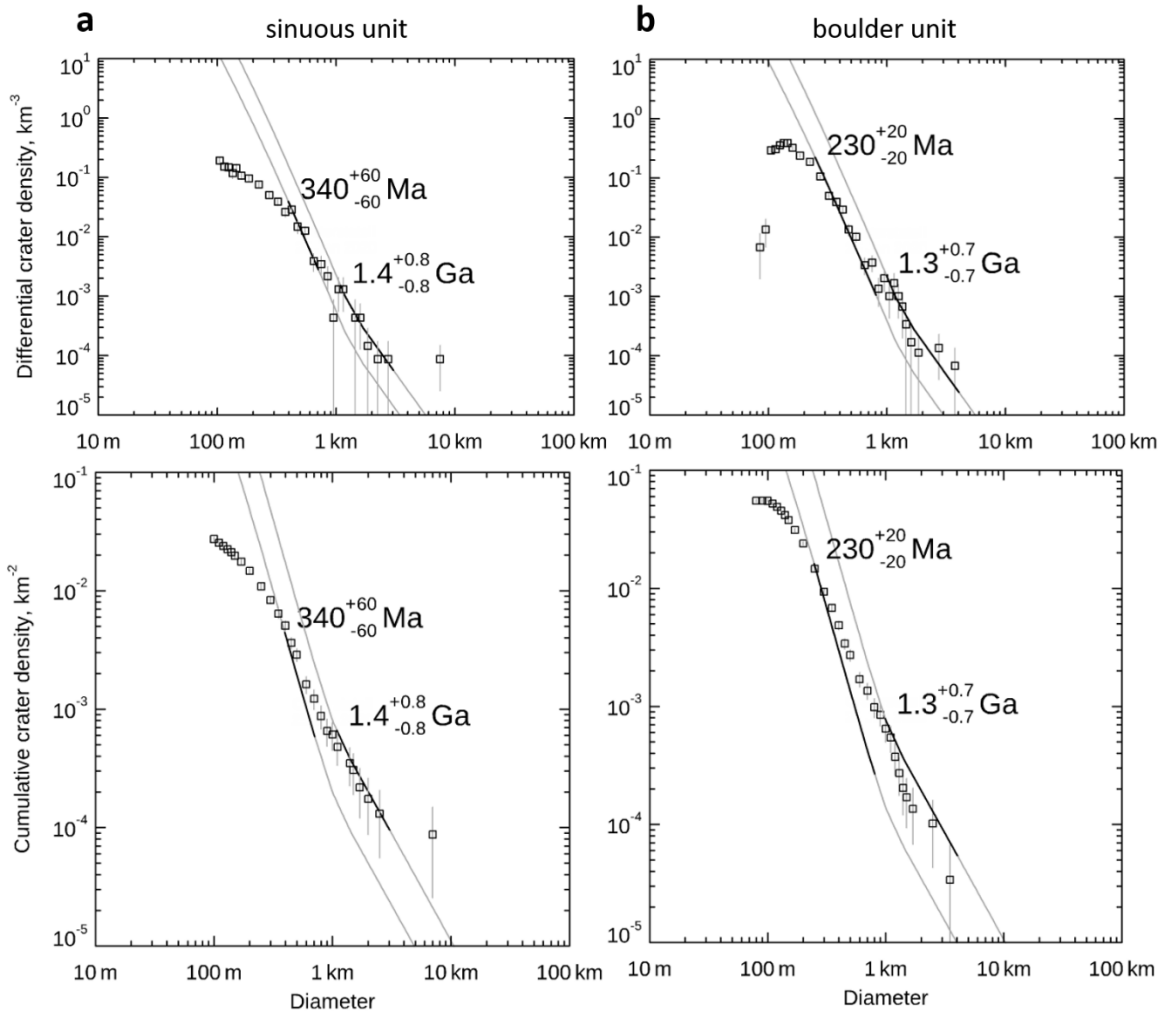

*Figure 3.12: differential and cumulative crater size-frequency distributions for **a.** the sinuous unit (~ 22,000 km²), and **b.** the boulder unit (~ 27,000 km²). Isochrones at 230 Ma and 1.2 Ga are plotted for the sinuous unit and isochrones at 260 Ma and 1.3 Ga are plotted for the boulder unit, computed from the chronology and production functions described in Hartmann (2005). We surveyed craters above 100 m in diameter only.*

3.4. Arcadia Planitia: observations and measurements

3.4.1. Morphological observations

The surface of the sinuous features in AP is knobbed and polygonised (Figure 3.8b). They also exhibit arcuate ridges, orientated NNW-SSE, and with the convex side facing the east. These sinuous features were interpreted as ice streams by Hibbard et al. (2021), and their arcuate ridges as evidence of the compressional deformation occurring at the surface of the flowing ice stream. The surface of the mantling unit (Figure 3.8c) exhibits knobs, brain terrain texture spatially associated with FCPs, and linear ridges. The brain terrain pattern is interpreted to be ice-cored mounds, equivalent to the terrestrial ice-cored hummocks (Levy et al., 2009b, 2010a). The ridges have an average spacing of ~ 25 m. The mantling unit was interpreted to be ice-rich by Hibbard et al. (2021). The hills (Figure 3.8d and e) are constituted i. at their summit, of heavily-cratered outcrops (interpreted as bedrock by Hibbard et al., 2021); ii. on their flanks, of downslope linear erosional features separated by < 10 m, in some places spatially associated with polygonal patterns. The flanks of the hills are interpreted as LDAs by Hibbard et al., 2021. Hence, we mapped separately the hill summits and flanks (Section 3.2.1.2.).

3.4.2. Polygon parameters

We calculate the three parameters ρ_{pol}, ρ_{wf} *and* ρ_{wp} for the units of the study zone in AP: the sinuous features, the mantling unit and the hills (Section 3.2.1.2.). Details on the significance of the parameters are provided in Table 3.2, and the results are summarised in Table 3.3. First, none of the studied units show LCPs, hence calculating ρ_{wp} is not possible for any unit. The sinuous features have a relatively high value of ρ_{pol} (0.67) compared to the other units in AP. They are the only unit showing HCPs, hence the only unit with a value of ρ_{wf} (0.13). The mantling unit has a relatively low value of ρ_{pol} (0.24), and shows no HCP – hence calculating ρ_{wf} is not possible. Concerning the hills, their summits show no polygon; hence we calculate the value of ρ_{pol} for their flanks only, which is intermediate compared to the values for the sinuous features and mantling unit (0.55).

3.5. Geological interpretations

3.5.1. Origin of the units in Utopia Planitia

3.5.1.1. Craters

Large craters in UP (> 2 km in diameter; Figure 3.7a, f and g) show a high polygonisation rate, equal to this of the sinuous unit, as well as a high wedge preservation rate compared to the other units in UP (Table 3.3; Section 3.3.3.). It shows that craters in our study zone are constituted of a material that is nearly ubiquitously cemented by ice, as well as prone to form massive ice – and hence must be initially porous. As crater floors are local elevation minima, they are depositional basins for aeolian and gravitational transport. Therefore, we infer that wind-blown sediment were enriched in ice within the craters after their deposition, and then underwent ground cracking and polygon formation. Craters in UP also show a high wedge preservation rate compared to the other units, which could either point toward an insulating material (such as the porous sediment aforementioned), or toward a climatic "cold-trap" effect (e.g. Conway et al., 2012) that would affect all large craters similarly. Such a climatic effect could also be the cause of ice deposition within an aeolian sediment, that we evoked above.

3.5.1.2. Sinuous unit

Overall, the whole study zone in UP seems to be ice-rich at the global scale (Figures 3.4. and 3.5.; Section 3.3.1.), especially the sinuous unit (Figure 3.7b and c) for which the radar dielectric estimates computed by the SWIM Team are highly consistent with the presence of subsurface ice (Figure 3.5b; Section 3.3.1.). Our parameters (Table 3.3; Section 3.3.3.) also point towards ice-rich material: the sinuous unit has a high polygonisation rate, equal to this of the craters, as well as intermediate values of wedge formation and wedge preservation rates – lower than those of the craters. Therefore, the sinuous unit is consistent with a porous material cemented by ice, which has preserved some of its ground ice. The high ice content of the sinuous unit is also confirmed by the presence of periglacial surficial features, such as thermokarst depressions (e.g. Costard and Kargel, 1995; Séjourné et al., 2012; Soare et al., 2018; Figure 3.7b; Section 3.3.2.). Moreover, the sinuous unit exhibits a sinuous, branched shape (Figure 3.7a), forms a positive relief feature (Figure 3.10; Section 3.3.2.), and overall seems to originate from the Elysium high-elevated area to the low-elevated Utopia Planitia. It suggests that the sinuous unit is a material that flowed over our study zone. A magmatic origin (i.e. a lava flow; Hamilton et al., 2018; Hopper and Leverington, 2014) can be ruled out for the sinuous unit as it is not compatible with a porous and ice-rich material. A glacial origin (e.g. debris-covered glacier) is also unlikely, considering the lack of high-elevation potential sources areas in the surroundings. Therefore, among all of the proposed origins for the units in our study zone (reviewed in Section 3.3.1.), several can be considered more likely: i. emplacement as sinuous, water-rich deposits from a large aqueous flow, potentially coming from the flanks of Elysium Mons (e.g. Costard and Kargel, 1995; Hamilton et al., 2018; Li et al., 2022; Russell and Head, 2003), which then froze in place; ii. emplacement as water-rich lacustrine (Chapman, 1994; Ivanov et al., 2014; Tanaka et al., 2014) or oceanic deposits (Ivanov et al., 2015) during an early 'wet' period of Mars, which then degraded in the observed sinuous shape; iii. emplacement from the condensation of atmospheric water vapour in ice within loose, porous sediment (Morgenstern et al., 2007; Séjourné et al., 2012; Soare et al., 2018, 2021; Stuurman et al., 2016), which then degraded in the observed sinuous shape.

The crater size-frequency distribution of the sinuous unit shows a lack of small craters (Figure 3.12a; Section 3.3.3.). It indicates that the sinuous unit is being resurfaced (e.g. Berman et al., 2015; Michael and Neukum, 2010; Michael, 2013): the most probable process is the formation of thermokarst, which can 'erase' the imprint of smallest craters with time (Hartmann, 1971). This process must be continuous, as the crater retention curve for craters < 400 m in diameter gets gentler with decreasing crater diameter. Hence, the age given by the most recent isochron most likely indicates the crater resurfacing rate, which is approximately equal to the crater production rate over a period of 340 ± 60 Ma (Figure 3.12a). Therefore, the age given by the largest craters, that cannot be erased by thermokarst formation, represents the minimum age of emplacement of the sinuous unit, which is Middle Amazonian (1.4 ± 0.8 Ga; Figure 3.12a).

Such a recent age rules out the geological origin of the sinuous unit as lacustrine or oceanic deposits (Chapman, 1994; Ivanov et al., 2014, 2015; Tanaka et al., 2014), as surface liquid water is thought to be not stable during the Amazonian (Jakosky, 1985; Jakosky and Farmer, 1982; Jakosky and Phillips, 2001; Richardson, 2002). Large liquid water bodies were suggested to exist on Mars but are thought to be older than the age given by our analysis of the crater size-frequency distribution (i.e. Noachian; Baker et al., 1991; Carr and Head, 2010; Citron et al., 2018; Costard et al., 2017; Parker et al., 1993). Despite that surface liquid water is thought to be unstable during the Amazonian (Jakosky, 1985; Jakosky and Farmer, 1982; Jakosky and Phillips, 2001; Richardson, 2002), the formation of the sinuous unit as a large water-rich flow (e.g. Costard and Kargel, 1995; Hamilton et al., 2018; Russell and Head, 2003) potentially coming from Elysium Mons can be considered, as outflow discharges were suggested to have occurred during the Middle Amazonian (Rodríguez et al., 2015b, 2014). Another possible formation process for the sinuous unit is the

condensation of atmospheric water vapour within porous sediment (e.g. Soare et al., 2018, 2021; Stuurman et al., 2016). This hypothesis is commonly invoked to explain mid-latitude ice-rich units (i.e. subsurface icy layers and the different layers of the Latitude-Dependent Mantle, LDM), as climate models and geomorphological observations agree that multiple high-obliquity excursions allowed the condensation of volatiles in the mid-latitudes during the Amazonian (e.g. Butcher, 2022; Conway et al., 2012; Conway and Balme, 2014; Dundas et al., 2018, 2021; Forget et al., 2006; Madeleine et al., 2009; Morgenstern et al., 2007; Séjourné et al., 2012, 2019; Soare et al., 2018; Stuurman et al., 2016).

Concerning the crater size-frequency distribution of the sinuous unit, an outlier data point matches an older isochron around 3.8 Ga (Late Noachian/Early Hesperian). We consider that data point as a statistical outlier (Section 3.3.3.) that does not accurately date the sinuous unit. Indeed, as stated above, the sinuous unit is undoubtedly ice-rich and emplaced either as a water-rich flow that subsequently froze, or as condensation of atmospheric water vapour within a sediment. Both of those geological origins are incompatible with a 3.8-Ga age: the Elysium volcanic structure started to build up during the Hesperian (hence after 3.7 Ga; Greeley and Spudis, 1981), which makes impossible the formation of outflow deposits coming from Elysium Mons at 3.8 Ga. In addition, the condensation of atmospheric water vapour at 3.8 Ga would require a rather cold environment, non-conducive to the stability of surface liquid water; however, the martian climate at the transition Noachian/Hesperian is thought to allow the sustained presence of surface liquid water (Fassett and Head, 2008a; Howard and Moore, 2011; Hynek et al., 2010; Mangold et al., 2004b; Salese et al., 2020; Wilson et al., 2016).

3.5.1.3. Boulder unit

The boulder unit (Figure 3.7d and e) shows extensive fields of boulders (~ 10 m in diameter), as well as blocks that shattered in place (Figure 3.7d and e; Section 3.3.2.). It suggests that the surface of the unit was extensively cracked, and underwent intense mechanical erosion that preferentially affected the cracks. Over time, it left individual boulders separated by fine-grained sediment derived from mechanical erosion. Moreover, the boulder unit has a polygonisation rate and a wedge formation rate that are nearly null, and the absence of LCPs prevented to calculate the wedge preservation rate (Table 3.3; Section 3.3.3.). Therefore, it must be a massive material, non-conducive to thermal contraction. These results point toward a volcanic origin for the boulder unit, coinciding with studies which suggested that channels on the flanks of Elysium Mons were carved by lava flows (e.g. Hamilton et al., 2018; Hopper and Leverington, 2014), or studies which concluded to the presence of volcanic units in UP (e.g. Russell and Head, 2003; Tanaka et al., 2005). It is also in agreement with the olivine signatures detected on and around the boulder unit by Soare et al. (2018).

We suggest that the overall complexity of the organisation of data points probably indicates that all of the patches of boulder unit were not subject to the same impact exposure times. However, we can infer that the age given by the most ancient isochron (for craters 1000-4000 m in diameter; Figure 3.12b) represents the earliest possible age of formation for the boulder unit, i.e. Middle Amazonian (1.3 ± 0.7 Ga; Figure 3.7b). Likewise, the age given by the most recent isochron – i.e. Late Amazonian (230 ± 20 Ma; Figure 3.7b) – corresponds to the latest crater retention age shown by a patch of boulder unit (see Section 3.5.1.4.).

3.5.1.4. Co-evolution of the sinuous and boulder units

Topographic profiles show that the sinuous unit is a positive relief, systematically found stratigraphically above the boulder unit (Figure 3.10); the boulder unit itself is found in local elevation minima (Figure 3.10). Moreover, both the sinuous and the boulder unit show a Middle-Amazonian age from the crater size-frequency distribution (Figure 3.12a and b; Sections 3.5.1.2. and 3.5.1.3.). Therefore, was the sinuous unit

emplaced on top of the boulder unit, or was the boulder unit emplaced around the sinuous unit as a low-viscosity lava flow?
Figure 3.11 shows two contact zones between the sinuous and boulder unit. Where the sinuous unit is facing the equator, the contact with the boulder unit is smooth and constituted of a patterned material; and where the sinuous unit is facing the pole, the same patterned material is observed, but ends up as an abrupt, scallop-shaped scarp above the boulder unit. This morphology is reminiscent of the dichotomy gentle equator-facing flank/steep pole-facing flank that the scalloped depressions exhibit in the area (Section 3.3.2.; Haltigin et al., 2014; Lefort et al., 2009; Morgenstern et al., 2007; Séjourné et al., 2011, 2012; Soare et al., 2018), and especially on the sinuous unit. This observation points toward a sinuous unit being degraded under insolation-driven processes, exposing the underlying boulder unit. This large-scale degradation is consistent with the origin of the sinuous unit as being ice-rich, and undergoing thermokarst degradation (Section 3.5.1.2.). It is also consistent with the complexity of the organisation of data points on the crater size-frequency distribution of the boulder unit (Figure 3.12b; Section 3.5.1.3.). If the boulder unit is indeed exposed part by part over time, the oldest age recorded (Middle Amazonian, 1.3 ± 0.7 Ga; Figure 3.12b) corresponds to its initial crater record, added to the crater record of the first period when the sinuous unit degraded sufficiently to expose the boulder unit. Then, the earliest age recorded on the boulder unit (Late Amazonian, 230 ± 20 Ma; Figure 3.12b) corresponds to the latest exposure of the boulder unit.

Therefore, we suggest the following chronology: first, the boulder unit emplaced during the Early to Middle Amazonian, as volcanic material potentially originating from Elysium Mons and taking (or carving) channels on its flanks, such as Hrad Vallis (Wilson, 2003; Hopper and Leverington, 2014). The newly-formed boulder unit started recording a crater retention age. This geological origin is consistent with that of the 'Smooth Lobate' unit from Russell and Head (2003) (Section 3.1.2.). Its timing of emplacement is also consistent with the 1.1-Ga minimum age of the rock basement suggested in Séjourné et al. (2019) in the western part of UP.
Later, the boulder unit was covered by the sinuous unit around the Middle Amazonian. The sinuous unit was emplaced either as deposits of a large, episodic outflow – potentially originating from Elysium Mons (e.g. Costard and Kargel, 1995; Hamilton et al., 2018; Russell and Head, 2003) – or by condensation of atmospheric water vapour within loose, porous sediment during a high-obliquity excursion (Morgenstern et al., 2007; Séjourné et al., 2012; Soare et al., 2018, 2021; Stuurman et al., 2016). Considering that our dating study gives minimum ages, the outflow origin could be consistent with the 'Early Amazonian basin' unit from Tanaka et al. (2014).
Then, due to the dry conditions of the Late Amazonian, the ice-rich sediment of the sinuous unit started to degrade via sublimation-driven thermokarst processes, exposing the underlying boulder unit. As the boulder unit is exposed slowly, part by part over time, it records various crater exposure ages – the most recent exposure event happening a few hundreds of million years ago (230 ± 20 Ma; Figure 3.12b). Hence, the lack of large craters on the boulder unit (Figure 3.12b; Section 3.3.4.) can be explained by the fact that the relatively small patches that are progressively exposed can easily be covered by ejecta of large craters, preventing their inclusion in the crater count for the boulder unit.

3.5.2. Origin of the units in Arcadia Planitia

Calculating the parameters we defined in Section 3.2.2. was challenging in AP. First, the absence of LCPs in the whole study area prevented us from evaluating the ice-wedge *vs.* sand-wedge hypothesis (Section 3.2.2.; Table 3.2). Second, HCPs are totally absent from both the mantling unit and the hills. Overall, we were able to calculate the polygonisation rate for all units, and the wedge formation rate only for the sinuous

features – but as the type of wedge is unknown, the wedge formation rate may not have the geological implications we are seeking (Table 3.2; Section 3.2.2.).
The hills (Figure 3.8d and e; Section 3.4.2.) show a summit of exposed bedrock according to Hibbard et al. (2021). We did not observe any polygon on these summits, which is consistent with this interpretation. However, polygons are nearly ubiquitous on the units on the flanks of the hills, which have a relatively high polygonisation rate (0.55). Therefore, we infer that hill flanks are superposed by an ice-rich material, which supports the interpretation made by Hibbard et al. (2021) that the flanks of the hills host LDAs, i.e. debris covered glaciers.
The mantling unit (Figure 3.8c; Section 3.4.2.) exhibits FCPs, and has a polygonisation rate of 0.24 – below that of the hills and sinuous features for the study zone in UP, but still indicative of ice-cemented ground. The main morphology that is expressed on the mantling unit is brain terrain, i.e. features indicative of degrading near-surface ice (Levy et al., 2009b, 2010a). Polygons are observed in spatial association with these brain terrains, but become more difficult to distinguish with increasing presence of brain terrain. Therefore, we infer that the mantling unit is indeed ice-rich. However, our parameters cannot help to decipher a specific geological origin for the mantling unit.
The sinuous features (Figure 3.8b; Section 3.4.2.) show the highest polygonisation rate among the units in AP (0.67), which indicates that the material that constitutes them is ice-cemented. Hibbard et al. (2021) interpreted them as ice streams, i.e. rapidly flowing bodies of nearly-pure ice (potentially covered by the layers of the LDM and dust), which is an interpretation that is supported by our results. Sinuous features exhibit not only FCPs, but also a few HCPs (wedge formation rate of 0.13), which could suggest that their surface underwent wedge formation. However, HCPs are found only on the arcuate ridges, interpreted to be features resulting from surficial compression due to the flowing of the ice stream. Therefore, we suggest that the HCPs observed are 'compressional HCPs', i.e. FCPs formed prior to the compression (and thus prior to the ice stream flow) that were pushed upward, favouring the degradation of their margins at the location of the fractures and resulting in a morphology resembling ice-wedge (or sand-wedge) HCPs. If our interpretation is correct, it further supports the ice-stream interpretation of Hibbard et al. (2021). Indeed, the formation of LCPs (which then degrade into HCPs) requires a substrate that can deform to produce high-elevation (LCPs) and low-elevation margins (HCPs) when wedges grow and degrade. Hence, LCPs and HCPs cannot form on pure bodies of ice such as ice streams.

3.5.3. Timing of polygon activity

In UP, previous studies investigated the timing of polygon activity in UP – although mostly in its western part, unlike the present study that focuses on its eastern part. Most of studies suggest that the observed thermal-contraction polygons formed in the ice/dust layered deposits of the LDM (e.g. Lefort et al., 2009; Levy et al., 2010b; Mangold et al., 2004a; Morgenstern et al., 2007; Séjourné et al., 2011, 2019; Ulrich et al., 2011). These layers are geologically recent, as young as a few million years (e.g. Kostama et al., 2006; Levy et al., 2009c; Schon et al., 2012a; Séjourné et al., 2019). Hence, polygon formation and degradation were also suggested to be geologically recent – logically more recent than the deposition of the layered deposits, i.e. within the last few million years (e.g. Levy et al., 2009a, 2010b; Mangold, 2005; Mangold et al., 2004a; Séjourné et al., 2011). Some studies also dated polygonised surfaces in UP by crater-size frequency distribution (Séjourné et al., 2019; Soare et al., 2020, 2021). Séjourné et al. (2019) dated in the western part of UP their "high-latitude assemblage", a geomorphological assemblage notably composed of polygons with dimensions that are of the same order of magnitude than the ones studied in the present work (20-50 m *vs.* 5-25 m in diameter, respectively). Their dating effort allowed to date the last deposition of ice-rich LDM material to the last million year. Therefore, the activity of polygons located on these LDM deposits must have occurred in the last million year. Soare et al. (2020) also dated an area in the western

part of UP, which extensively bears thermal-contraction polygons that are of similar dimensions than in the present work (5-25 m in diameter). The crater size-frequency distribution they obtained suggests an age probably over 100 Ma for the polygonised surface, as well as a likely resurfacing of that surface. Therefore, the timing of polygon activity can be extrapolated as being younger than 100 Ma. Soare et al. (2021) presents the only dating attempt in the western part of UP. Moreover, that dating was performed on an area that is comprised within the study zone of the present work. It suggests that the polygonised surface was at least 10 Ma, implying that polygon activity is younger than 10 Ma. Note that in Soare et al. (2020 and 2021), as no local polygon-covered unit (like the sinuous unit presented here) was observed yet, dating was performed on continuous polygon fields at the scale of a HiRISE image. In the present study, dating is performed over an area (22,000 km² on the sinuous unit) that is large enough to produce statistically significant age estimates (Warner et al., 2015), hence reducing the age uncertainties compared to Soare et al. (2021) within the same study area.

In our study zone, we observe polygons in association with thermokarst depressions on the sinuous unit (Figure 3.7b; Section 3.3.2.). We suggest that the sinuous unit was progressively degraded, exposing the underlying boulder unit, by the development of these thermokarst depressions (Section 3.5.1.2. and 3.5.1.4.). We dated the initial emplacement of the sinuous unit to at least at the Middle Amazonian (1.4 ± 0.8 Ga; Figure 3.12a), and the latest datable episode of degradation – i.e. the youngest age measured on the boulder unit – to the Late Amazonian (230 ± 20 Ma; Figure 3.12b). Hence, we infer that polygon activity, i.e. wedge formation and degradation, could have occurred from the Middle to Late Amazonian. Overall, compared to previous dating studies (e.g. Séjourné et al., 2019; Soare et al., 2020, 2021), our work shows that polygon activity was not constrained to the geologically recent LDM layers; hence, their period of activity could have been longer than the last few million years that were previously suggested. This interpretation is consistent with previous studies suggesting the occurrence of periglacial thermokarst processes (i.e. formation of scalloped depressions), on frozen outflow channel deposits in UP (Costard and Kargel, 1995).

Moreover, as polygons on our study zone in UP are suggested to be ice-wedge polygons (Soare et al., 2021), our interpretations suggest that liquid water could have been present at the surface or in the near-surface of Utopia Planitia during the Late Amazonian. It further raises the question of the possibility of having relatively recent liquid water activity in the near-surface of Mars in general. Such processes could be supported by the activity of brines rather than pure water, a hypothesis arising from the common presence of salts at the surface of Mars (Clark and Kounaves, 2016; Gasda et al., 2017; Gendrin et al., 2005; Hecht et al., 2009; Rivera-Valentín et al., 2020; Thomas et al., 2019) and more specifically in UP (Zhao et al., 2023). Salts are known to decrease the freezing point of water, hence brine should be more stable than pure water under martian conditions (Brass, 1980; Davila et al., 2010; Fischer et al., 2016; Rivera-Valentín et al., 2020). The possibility of forming ice-wedge polygons through the sporadic presence of surficial brines provides a potential solution to the paradox of the geomorphological evidence of surficial liquid water activity provided by ice-wedge polygons, and the thermodynamic instability of liquid water under the current martian climate. However, we cannot rule out the occurrence of other, more exotic formation mechanisms – for instance, condensation of atmospheric water vapour and its subsequent cracking, suggested by Fisher (2005). As liquid water is necessary for the life as we know it, attesting the presence of surficial liquid water on Mars during the Amazonian would have implications concerning its recent habitability.

In AP, the only polygon type present is FCP (Section 3.5.2.) – which provides no information on the potential liquid water activity in the area. Hence, a question arises concerning ice wedges: if climatic conditions allowed their formation in UP, why didn't they form in AP which is nearly at the same latitude (above 44° N for UP, below 40° N for AP) – for instance, on the hill flanks? Getting an answer to that

question will necessitate further investigations. In any case, a process leading to the formation of ice wedges (involving liquid water or not) in UP did not occur in AP. But depending on the formation mechanism of those ice wedges, answers to that question could be varied: for instance, if ice wedges in UP are formed by the transient existence of liquid brines, the availability of salts in AP could have prevented the existence of transient brines, and hence the formation of ice wedges.

Overall, the fact that the parameters could not be properly calculated in AP shows that the method we present in this paper cannot be applied everywhere. In order to calculate the three parameters, at least LCPs have to be present among the thermal-contraction polygons. Therefore, we suggest that a preliminary evaluation of the presence of such polygons has to be conducted within a potential study zone, before starting the grid-based mapping.

3.6. Conclusions

1. We defined three quantitative parameters based on characteristics of thermal-contraction polygons: i. the polygonisation rate (ρ_{pol}), ii. the wedge formation rate (ρ_{wf}), and iii. the wedge preservation rate (ρ_{wp}). We suggest that those reflect subsurface properties of the substrate: i. its cementation by ice, ii. its capacity to grow massive ice, and iii. its capacity to preserve ground ice, respectively;
2. Applied to Utopia Planitia, these parameters, along with geomorphological observations and a study of the crater size-frequency distribution, allowed us to infer the geological nature and the estimated age of the studied units. The sinuous unit is a Middle Amazonian ice-rich unit, resulting from water-rich deposits or from condensation of atmospheric water vapour within a porous sediment. The boulder unit is an Early to Middle Amazonian volcanic unit, potentially originating from Elysium Mons. We were also able to understand that the sinuous emplaced on the boulder unit, and were progressively degraded which exposed the underlying boulder unit;
3. Our parameters also allowed us to support the ‘cold-trap effect’ hypothesis raised by Conway et al. (2012) to explain the high concentration of water ice within mid-latitude craters;
4. Applied in Arcadia Planitia, our parameters allowed us to support the formation hypotheses of three units described by Hibbard et al. (2021). However, the absence of some polygon types (LCPs and HCPs) in the study zone prevented us investigating further the subsurface properties of those units, showing the limits of that method;
5. The combination of parameter calculation and crater size-frequency distribution revealed that formation and degradation of ice wedges (hence liquid water activity) could have occurred during the Middle to Late Amazonian in Utopia Planitia, when polygon activity was previously thought to be mainly constricted to the last few million years. It makes thermal-contraction polygons interesting study objects to assess recent habitability of Mars.

IV. Synthesis, outlook and conclusions

1. Synthesis

The objectives of the present thesis were to investigate specific morphologies in order to obtain a new understanding on how planetary landscapes – i.e. the Earth and Mars – are shaped by ground ice and periglacial processes. Within this framework, I investigated molards on Earth and Mars, with a combination of analogue experiments that I developed (Earth), and of terrestrial analogue and remote sensing studies that I participated in (Mars). I also investigated thermal-contraction polygons in Utopia Planitia (Mars), coupling existing mapping methods with stratigraphic, geomorphologic and dating studies, and with an analytical method that I developed. In the following sections, for both molards and martian thermal-contraction polygons, I summarise the objectives of my thesis and how I addressed the related scientific questions. I then summarise the main conclusions that my thesis allows me to draw, and discuss the implications of those conclusions for the concerned research fields, in the light of the current scientific knowledge and recent studies.

1.1. Molards

1.1.1. Summary of objectives and investigations

Molards are cones of loose debris found in landslide deposits. They are remnants of formerly ice-cemented blocks of sediment that were mobilised by a landslide and progressively degraded within its deposits, and thus are indicative of permafrost degradation in time and space. Hence, they represent an interesting tool to study the distribution and evolution of mountain permafrost, as well as to better evaluate potential future landslide-related hazards.

However, molards are morphologically similar to landslide hummocks – i.e. conical features found in landslide deposits that are not related to permafrost degradation. In addition, they often occur in remote areas, so the degradation process from ice-cemented block to molard has never been observed. Therefore, in this thesis I provide a way to study the degradation from ice-cemented blocks to molard, based on analogue modelling experiments performed in cold room facilities. I developed and programmed a photogrammetry system, constituted of 18 microcomputers and cameras, that automatically take photos of the analogue models at regular intervals. This setup allows to generate 3D models of the analogue molards at regular intervals, and hence to perform subsequent geomorphological analyses.

Moreover, molards can theoretically occur wherever ice-cemented ground is mobilised, including in icy planetary landscapes – on Mars, for instance. However, they have previously only been reported on Earth in the setting of degrading permafrost mobilised by mass-wasting processes. Therefore, in this thesis I presented a study which investigates conical mounds found in the ejecta of Hale crater (Mars), resembling terrestrial molards. The Hale impact is known to have mobilised ground ice, but the type and thickness of ice were not previously constrained. In this study, we mapped the conical mounds within the Hale ejecta, and we compared their distribution and morphometrics to those of confirmed terrestrial molards – in order to evaluate whether those conical mounds could be molards.

1.1.2. Conclusions and synthesis

1.1.2.1. Experimental setup

The main conclusions that draw from the experimental setup I developed are:

1. With 18 cameras, this setup produces DEMs that have a sufficient quality to perform geomorphological measurements on our models: volume monitoring, profiles, slope angle, and detection of millimetre-scale movements. Such measurements could be done at a 30-minutes time step.
2. The setup has various advantages compared to already existing setups, notably: ease of installation (in terms of programming or construction skills); full automation (i.e. the presence of an operator is not required for the duration of the experiment); possibility of continuous monitoring; independent functioning of the cameras;
3. The setup can easily be adapted to various studied objects and situations: the number of cameras can be modified, as well as their positions (adaptation to more or less complex shapes); the type of lenses can also be modified (adaptation to various required field of views or acquisition distances); the acquisition time step is fully flexible (adaptation to studied processes evolving more or less quickly);
4. The setup is particularly useful in cases where manual photo acquisition is difficult or impossible, or where the presence of an operator is complicated (e.g. experiments running overnight, in sealed chamber, in remote areas, or with short acquisition time steps).

This experimental development was made in the framework of the ANR funded Permolards project – whose aims are to produce the first global database and scientific knowledge on molards in order to improve our understanding of distribution of mountain permafrost and landslide-related hazards. Our analogue models allowed to observe, for the first time, the degradation process from an ice-cemented block of sediment into a molard. Not only the degradation could be observed, but thanks to the setup I developed, this degradation could be quantified. We were able to monitor millimetre-scale movements, which led to the identification of different degradation modes (e.g. grain falls or grain avalanches). We were also able to perform geomorphological measurements of height, topographic profile or slope angle on the models. Those types of measurements are typically the ones that are performed in studies of natural molards (e.g. Milana, 2016; Morino et al., 2019b, 2023; Wright et al., 2020), which makes our analogue models and experimental setup relevant tools in order to study molards. Moreover, our setup allows the monitoring of model morphometrics with a high temporal resolution (every 30 min for experiments that last several days), unveiling the stages of formation of a molard. Therefore, the setup I developed proves to fall perfectly within the scope of the study of molards for the Permolards project. It marks the first step toward a better understanding of those landforms, and toward a possibility to recognise them from remote sensing data only. From a broader point of view than molard-related studies, I showed from a review of existing photogrammetry that the one I developed could benefit to numerous studies of experimental or natural objects, and even potentially to geotechnical investigations.

1.1.2.2. Martian molards

The main conclusions that draw from the study of martian conical mounds I presented are:

1. We reported, for the first time, the occurrence of molards – i.e. cones of loose debris coming from the degradation of ice-cemented blocks of sediment – on Mars, in the ejecta of Hale crater;
2. Presence of molards in the Hale ejecta implies that, at the time and location of the impact, ground ice was present as pore ice in the subsurface, at least as one 60-metres thick layer. However, this is a lower boundary, and more numerous and/or thicker layers could have existed;
3. The inner ejecta of Hale were water-rich, and viscous enough in order to transport theoretically cubic blocks at least 60 metres high;
4. Chronologically, the ice-rich layer was obliterated by the impact, forming ice-cemented blocks which were transported within a relatively water-rich and viscous phase of the ejecta, and then degraded with the progressive sublimation of their pore ice.

The origin of terrestrial molards as former ice-cemented blocks of sediment mobilised by a landslide was already suggested (Brideau et al., 2009; Milana, 2016), but was only recently attested by observations before and after the degradation from block to molard (Morino et al., 2019b). Since then, molards gained attention and were reported as former ice-bearing landforms in other studies (e.g. Svennevig et al., 2023, 2022). Moreover, in this thesis I presented a study showing that molards are present on Mars, and they were also reported to have formed on Mercury (Wright et al., 2020). These observations indicate that molards, although they were first observed in terrestrial permafrost-related landslide, are actually features that could be common to various planetary bodies. Therefore, the studies conducted on terrestrial molards actually have planetary implications. Molards can indeed give constraints on the ice content and type within the material that is mobilised by a process – i.e. landslides on Earth (Morino et al., 2019b; Svennevig et al., 2023, 2022), or impact cratering on Mercury (Wright et al., 2020) and Mars (Morino et al., 2023 in this thesis).

One of the primary motivations for studying Mars is the activity of water throughout its geological history. Generally speaking, liquid water probably was commonly flowing at the surface of the planet during the Noachian (4.1-3.7 Ga; e.g. Hynek et al., 2010; Salese et al., 2020), and episodically and locally flowing during the Hesperian (3.7-3 Ga; e.g. Fassett and Head, 2008; Howard and Moore, 2011; Hynek et al., 2010; Mangold et al., 2004). However, during the Amazonian (3 Ga-present) liquid water was not stable at the surface of Mars (Jakosky, 1985; Jakosky and Farmer, 1982; Jakosky and Phillips, 2001; Richardson, 2002). A climate transition occurred, which marks the beginning of the Amazonian, and caused the trapping of liquid water as water ice, notably as ground ice within the mid-latitudes (e.g. Bramson et al., 2015; Stuurman et al., 2016). However, the climate mechanisms that led to the trapping of ground ice are still poorly understood. Pore ice can be formed by atmospheric condensation of water vapour within sediment pores (e.g. Jakosky and Carr, 1985; Schorghofer, 2008), but excess ice (i.e. ice exceeding the volumetric content of sediment pores) has to be formed by other mechanisms (e.g. burial of massive ice, Holt et al., 2008; or ice segregation, Sizemore et al., 2015). Moreover, such ice-rich deposits are thought to be condensing and sublimating following the obliquity incursions of Mars (e.g. Head et al., 2003; Schorghofer, 2005). Therefore, information on the current state of ground ice can give constraints on the past martian climate.

In the study of molards in the ejecta of Hale crater that I presented in this thesis, we showed that the material mobilised by the Hale impact (1 Ga, 35°42 S', 36°31' W; Jones et al., 2011) was cemented by pore ice, at least as a layer tens of metres thick. Several implications emerge from this point. First, pore ice on Mars is known to form by condensation of atmospheric water vapour within sediment pores (e.g. Jakosky and Carr,

1985; Schorghofer, 2008). However, this mechanism is thought to occur in the first few metres below the surface only (e.g. Mellon and Jakosky, 1995). Hence, an explanation still lacks for the formation of a thick (≥ 60 m) layer of pore ice. A cyclic deposition of layers of sediment and subsequent condensation of pore ice can be considered.
Second, thick regional layers of ground ice were detected in the mid-latitudes (Bramson et al., 2015; Stuurman et al., 2016), which is consistent with climate models that predict condensation of atmospheric water vapour in these relatively cold regions during high-obliquity events (e.g. Jakosky and Carr, 1985; Schorghofer, 2008). However, our results indicate that condensation of water vapour into thick layers of ground ice also occurred at the location of the Hale impact, i.e. around 35° S. It makes our study one of the few that shows evidence of relatively low-latitude and southern-hemisphere deposition of thick ice-rich layers (e.g. Dundas et al., 2023). Ice deposition as such low latitudes is predicted during periods of very high obliquity (e.g. Jakosky and Carr, 1985), but the mechanism that led to its preservation are not yet known, and represent a challenge for martian climate models. A possibility to break free from that constraint of ice preservation, in the case of Hale crater, would be that the impact itself occurred during a period of high obliquity – hence at a time when ice-rich deposits were stable at a latitude around 35° S.

In addition, our results indicate that ice-cemented blocks of sediment survived the initial impact, were transported by viscous ejecta and degraded later on. Several implications emerge. First, the fact that i. not all of the ice melts during an impact, and ii. blocks tens of metres in diameter can survive this impact, could be used as additional constraints in numerical models of impact physics. Second, as the Hale inner ejecta transported ice-cemented blocks tens of metres high, constraints on the rheology of those ejecta could be placed.
Finally, Jones et al. (2011) estimated the volume of liquid water necessary to fluidise the inner ejecta of Hale crater. They then compared it to a supposed initial volume of ground ice, calculated from a pre-impact topographic reconstruction and an estimated ground ice content of 10 %. They concluded that the volume of water ice that was supposed to melt was amply sufficient to fluidise the ejecta: around 1.9×10^{12} m^3, where 1.2×10^{10} m^3 would have been necessary. However, they assume in their calculation that all of the initial water ice melts, which we showed is not the case. We can get a quick estimate of the volume of ice within the initial ice-cemented blocks by assuming: i. an ice content of 10 %, like Jones et al. (2011); ii. a null loss of volume during the degradation from block to molard, as the ice was within the sediment pores; iii. a geometrically perfect conical shape for the molards. The measured median height of Hale molards is around 6 m and their median area around 1000 m^2, which results in molards with a volume around 2000 m^3. Assuming a 10 % ice content, each initial block could have contained 200 m^3 of ice. We measured 2181 molards on two HiRISE DEMs, which hence could have represented a total of around 4.4×10^4 m^3 of ice. It is far from negligible with respect to the volumes calculated by Jones et al. (2011), as it is two orders of magnitude above the difference they calculated between the volume of meltwater produced by the impact and the volume of water necessary to fluidise the ejecta. Note that Jones et al. (2011) mention additional sources for meltwater, like surficial ice or ice that was contained in the ground below the ejecta. Therefore, despite my quick calculation being nothing more than a rough estimate, this volume of ice is calculated for a small proportion of the total number of molards only (i.e. within the extent of two HiRISE DEMs). The volume of ice that survived the impact surely is several orders of magnitude above. In summary, ground ice can survive an impact, in volumes that are not negligible. Hence, it has to be considered when studying impacts that supposedly reached the martian cryosphere.

Overall, molards are landforms that can provide valuable information on the ice content and type within the material that was impacted, which can have broader implications. Typically, molards can give insights into the impact dynamics, or into the current and past distribution of ground ice – hence improving our

understanding of the martian climate. In addition, molards could be found within the ejecta of other Amazonian impact craters that would have reached the subsurface cryosphere, and hence that similar constraints could be put on other craters on Mars with conical mounds in their ejecta.

1.2. Thermal-contraction polygons

1.2.1. Summary of objectives and investigations

On Earth, when ice-cemented ground undergoes temperature drops below 0°C, ground ice contracts, which can form fractures. These fractures can join to form thermal-contraction polygons. Subsequently, sediment or water ice can infill the fractures and aggrade seasonally, forming sand or ice wedges, and rising the polygon margins to form low-centred polygons. When temperatures perennially rise, the wedges degrade, decreasing the elevation of the polygon margins to form high-centred polygons. The aggradation and degradation of wedges gives different polygon morphologies, and in the case of ice wedges, implies the activity of liquid water.
On Mars, polygons with the same morphologies are observed; however, it was unknown whether they are underlain by sand or ice wedges. This distinction directly impacts on the potential for surface activity of liquid water in geologically recent times in a climate under which liquid water is not stable. Therefore, in this thesis I presented a study in which we studied the latitudinal distribution of polygon morphologies in Utopia Planitia (Mars). We mapped polygons on high-resolution images, using a grid-based technique. Based on a correlation between latitude and presence of certain polygon types, we concluded to the presence of ice-wedge polygons in our study zone.
While completing this study, I found out that the density and types of thermal-contraction polygons varied depending on the geomorphological unit they are located on. This observation inspired the idea that, if geomorphological units that are spatially close express polygons differently, this discrepancy must be due to properties that are internal to the units. Hence, it should be possible to trace back the geological properties of these substrates by studying their polygon population. Therefore, in this thesis I presented an investigation of polygon density and types among three specific geomorphological units in Utopia Planitia and three units in Arcadia Planitia – the first time such an approach has been used. I created three quantitative parameters based on characteristics of thermal-contraction polygons, each one reflecting a property of the substrate. In Utopia Planitia, I also performed geomorphological measurements and a study of the crater size-frequency distribution on the studied units.

1.2.2. Conclusions and synthesis

The main conclusions that draw from the studies I presented and conducted are:

1. We provided evidence for the presence of ice-wedge polygons in Utopia Planitia (Mars), based on a correlation between latitude and presence of low-centred polygons. Indeed, such a correlation is expected if wedges are made of water ice and not of sediment, as ground ice stability increases with latitude;
2. The formation of these polygons and ice wedges occurred in geologically recent times (Late Amazonian), based on the dating by crater size-frequency distribution method of polygon-bearing units;

3. I developed an analytical method, based on parameters calculated from polygon characteristics (density and type). I show that these parameters can be used to infer geological properties of the polygon substrates;
4. This method allowed me to infer the presence of an ice-rich unit in Utopia Planitia. It emplaced during the Middle Amazonian, either as water-rich outflow deposits coming from Elysium Mons, or by condensation of atmospheric water vapour within a sediment;
5. This method also allowed me to infer the presence of a volcanic unit in Utopia Planitia. It emplaced during the Early to Middle Amazonian, potentially as lava deposits originating from Elysium Mons;
6. However, the analytical method I developed has some limitations, as it requires the presence of low-centred morphologies among the studied polygons. Due to a lack of such polygons in Arcadia Planitia I could not calculate all of the parameters I defined, which led to limited interpretations.

1.2.2.1. Ice wedges

On Earth, ice wedges form by seasonal thermal contraction and episodic presence of surficial liquid water. On Mars, surficial liquid water was present during the Noachian and Hesperian; however, our results indicate that ice-wedge polygons formed geologically recently (Late Amazonian), i.e. at a time when liquid water was not stable at the surface of the planet (e.g. Haberle et al., 2001). Therefore, a question arises concerning the mode of formation of those ice wedges. Previous studies identified several potential processes that could generate subsurface liquid water and/or massive ground ice during the Amazonian: sporadic existence of liquid brines (e.g. Kreslavsky, 2022); diffusion and condensation of water vapour within the ground, associated with thermal cracking (Fisher, 2005); and subsurface melting under specific conditions (e.g. Costard et al., 2016).

Spectral signatures of salts have been commonly detected on Mars, from remote sensing (e.g. Clark and Kounaves, 2016; Gendrin et al., 2005) and *in-situ* measurements (e.g. Clark and Kounaves, 2016; Gasda et al., 2017; Hecht et al., 2009; Thomas et al., 2019). The incorporation of salts in liquid water forms brines, i.e. aqueous solutions with high salt content. Brines are known to be more stable than pure water under martian conditions, due to the widening of their stability domain caused by the presence of dissolved salts. Therefore, the episodic and local existence of liquid brines was suggested to occur at the surface of Mars, potentially by the interaction of surficial salt minerals and atmospheric water vapour (e.g. Brass, 1980; Chevrier et al., 2009, 2020, 2022; Davila et al., 2010; Fischer et al., 2014, 2016; Rivera-Valentín et al., 2020; Vaniman et al., 2004; Zorzano et al., 2009). *In-situ* measurements support this hypothesis: liquid brines were detected at the Phoenix landing site (Cull et al., 2010b; Stillman and Grimm, 2011); recent surficial presence of brines was suggested by the observation of a potential duricrust by Zhurong (Liu et al., 2022); measurements of relative humidity, air and ground temperatures made by Curiosity are consistent with the existence of transient liquid brines in the close subsurface of Gale crater (Martín-Torres et al., 2015; Rivera-Valentín et al., 2018). These observations suggest that such liquid brines could occur on present-day Mars, on a seasonal basis, and rather as thin films than actual flows. Thermal contraction of the ground is also likely to have occurred on Mars throughout the Amazonian, as temperature gradient as higher than on Earth (e.g. Leovy, 2001; Martínez et al., 2017). Therefore, in this setting the requirements are met in order to form ice wedges on Mars during the Amazonian – or brine wedges, in that specific case. Even if small quantities of brines are formed at each iteration of the process, its long-term repetition throughout the Amazonian would allow to form brine wedges. This was recently suggested by Kreslavsky (2022; *conference abstract*).

On Mars, it is known that the climate variations – and especially the obliquity cycles – cause the cyclic condensation and sublimation of atmospheric water vapour within the sediment pores (e.g. Mellon and Jakosky, 1993; Schorghofer, 2005), which is also supported by experimental investigations (e.g. Hudson et

al., 2009). The depth at which water vapour can condense is typically estimated at a few metres (Mellon and Jakosky, 1993). Fisher (2005) suggested a process that could form excess ground ice on Mars by a water vapour condensation coupled to thermal contraction of ice. It was a novel approach as i. the condensation of atmospheric water vapour was supposed to form pore ice only (e.g. Mellon and Jakosky, 1993), and ii. on Earth, the formation of excess ice involves liquid water (e.g. French, 2018). The process suggested by Fisher (2005) works as follows: i. pore ice condenses within the martian ground during a period of relatively cold temperatures; ii. seasonal temperature decreases cause the thermal contraction of pore ice, and development of cracks within the ice; iii. secondary ice crystals condense within the cracks; iv. when temperature rises again, the newly-formed secondary ice crystals cause the overall volume of ice to increase above the initial volume of pore ice. Fisher (2005) suggests that an increase in ice content from 28% to 70% is possible in 10 Ma. Therefore, with sufficient cyclic repetitions, this process could form massive ground ice, including ice wedges.
Recently, Costard et al. (2016) observed unconnected, sinuous and elongated pits following the troughs of polygonal networks in Utopia Planitia – "polygon junction pits". They found terrestrial analogues for the polygon junction pits in Canada, where they are formed by subsurface melting and drainage of water ice along ice-wedge troughs. Therefore, they present a thermal model in which the deposition of a thick (at least 150 m) insulating layer of dust causes i. melting in an underlying ice-saturated layer, and ii. subsequent meltwater drainage following the troughs of the ice wedges present within the ice-saturated layer, forming junction pits. The insulating layer is then eroded, exposing the underlying layer that shows polygons and junction pits. Although potential subsurface liquid water in contact with ice wedges represents something worthy of further investigation (for habitability matters for instance), it is unlikely that this process can explain the formation of the ice wedges themselves. First, ice wedges require cyclic freeze-thaw cycles to form. However, the model presented in Costard et al. (2016) does not account for the cyclic deposition of the thick insulating layer that is required to cause subsurface melting. Second, this model accounts for ice-wedge melting and water drainage, but not for a mechanism for liquid water recharge and subsequent freezing.

As we dated the formation of ice wedges to the Late Amazonian, these mechanisms for the formation of ice wedges have different implications, depending on whether they imply the activity of liquid water or not. First, in the case that transient brines are involved in the formation of ice wedges (Kreslavsky, 2022; *conference abstract*), brines must have been cyclically present on Mars in geologically recent times, and in sufficient quantities to achieve metre-scale ice wedges (which is their typical dimensions, e.g. French, 2018). These brines would have been present in the close subsurface (upper few metres). It implies that the Late Amazonian climate, thought to prevent the existence of surficial liquid water (e.g. Haberle et al., 2001), would have actually been regularly conducive to the presence of significant volumes of liquid water (in the form of brines). In addition, as liquid water is essential for the life as we know it, the regular existence of liquid brines in the close subsurface of Mars implies that its potential for habitability may have to be revised – at least in regions bearing ice-wedge polygons.
Second, in case ice wedges are formed by condensation of atmospheric water vapour condensation and thermal cracking (Fisher, 2005), the existence of liquid water is not required. Hence, this formation mode is more consistent with our current knowledge on the Late Amazonian climate, which is thought to be conducive to such condensation of atmospheric water vapour (e.g. Mellon and Jakosky, 1993; Schorghofer, 2005). In the absence of liquid water in that process, the potential of habitability for such ice wedges is minor or non-existent.

Moreover, we mapped in Utopia Planitia spatially close high-centred and low-centred ice-wedge polygons. This close spatial correlation between degraded and non-degraded ice wedges indicates a landscape that is in disequilibrium with the climate – i.e. a transition climate between periods of ice-wedge stability and instability. Moreover, we dated the formation of ice wedges at the Late Amazonian. This implies that, during the last hundreds of million years, there first was a period of net accumulation of massive ground ice, followed by a period of net degradation of that ground ice. However, the degradation of ice wedges was not intense and/or not long enough to erode all the ice wedges that were previously formed. Taking into account the two formation mechanisms described above for ice wedges (i.e. transient brines or vapour condensation), it means that the activity of at least one of them is currently inactive, or at least significantly subdued, compared to its activity a few hundred of million years ago. A better understanding of that formation process of ice wedges would hence have important implications for the martian climate during the last few hundreds of million years. In addition, either i. the ice wedges currently are in disequilibrium with the mid-latitude climate and are actively degrading; ii. the ice wedges were in disequilibrium with the past climate and started degrading, but are now in equilibrium and their degradation stopped. However, it seems difficult to distinguish between the two possibilities without ground-truth evidence, as these landscapes are certainly evolving slowly. Terrestrial ice wedges typically degrade in tens of years (e.g. Kanevskiy et al., 2017), and martian ones could be evolving even slower, depending on the degradation process. For instance, if ice melts, thermal erosion would cause a positive feedback loop on the melting – which would not occur in the case of degradation by ice sublimation only. In addition, degradation events could occur less frequently on Mars than on Earth, following for instance obliquity cycles and not seasonal cycles, which would make the degradation process even slower.

Finally, ice wedges represent ideal targets for matters of *in-situ* resource utilisation (ISRU) of water – independently of their formation mode. Indeed, they are massive bodies of ice (metre scale) located in the near-surface (top few metres). Hence, they i. can provide water ice in rather large quantities, ii. are accessible, and iii. are easy to process – which matches three of the most important criteria for ISRU (e.g. Abbud-Madrid et al., 2016). Hence, ice-wedge polygons constitute primary landforms to study for ISRU-related scientific projects, such as the Subsurface Water Ice Mapper (SWIM; Morgan et al., 2021).

Overall, martian ice wedges are key features in order to investigate the primary scientific objectives of the current missions sent to Mars by all space agencies, i.e. the past and present habitability of the planet and its potential for ISRU of water. They can also provide important constraints on the Amazonian climate.

1.2.2.2. Sinuous unit in Utopia Planitia

In the present thesis, I reported the emplacement of an ice-rich unit in Utopia Planitia during the Middle Amazonian (around 1.4 Ga). I presented two hypotheses for its formation: i. deposits from a late, water-rich outflow, potentially coming from the Elysium volcanic structure, that subsequently froze in place; and ii. condensation of atmospheric water vapour within sediment pores. I discuss thereafter the implications of these two hypotheses; further investigations will have to be conducted to attest of the geological origin of the sinuous unit.

Martian outflow channels and associated deposits are thought to have formed mainly during the Hesperian (e.g. Carr, 1979; Carr and Head, 2010; Lucchitta et al., 1992; Wilson et al., 2004), but some studies suggested the occurrence of Middle Amazonian outflow discharges (Rodríguez et al., 2014, 2015b). Outflow deposits were reported in Utopia Planitia (e.g. Costard and Kargel, 1995), potentially during the Early Amazonian (Russell and Head, 2003). Moreover, a recharge mechanism via snowmelt was suggested as capable to provide liquid water in sufficient quantities in order to generate outflow discharges from Elysium during the Amazonian (Russell and Head, 2007). However, the occurrence of such outflow

discharges during the Amazonian is controversial (e.g. Carr and Head, 2010), as liquid water is thought to be unstable under the Amazonian climate (Jakosky, 1985; Jakosky and Farmer, 1982; Jakosky and Phillips, 2001; Richardson, 2002). Hence, attesting an outflow origin for the sinuous unit would provide constraints on the martian climate throughout the Amazonian, more specifically concerning the supposed stability of liquid water.

As we saw earlier, the process of water vapour condensation within sediment pores and subsequent formation of ice-rich layers during high-obliquity periods is a phenomenon that is supported by various types of studies and observations (Bramson et al., 2017; Jakosky and Carr, 1985; Mellon et al., 2009a; Mellon and Jakosky, 1995; Smith et al., 2009). These high-obliquity events occurred throughout the Amazonian (Schorghofer, 2008). If the sinuous unit indeed formed by condensation of atmospheric vapour in the Middle Amazonian, it would provide constraints on the quantity of atmospheric water that can be condensed in such events.

1.2.2.3. Polygon parameters

I presented in this thesis a novel analytical method that uses parameters based on characteristics of thermal-contraction polygons (density and type) to get insights into properties of the substrate. To calculate all of the three parameters that I defined, low-centred polygons have to be present in the study zone. I applied this method with success in Utopia Planitia, but the absence of low-centred polygons in the study zone in Arcadia Planitia prevented the calculation of all the parameters, leading to limited interpretations and showing the limits of that method. Potential target study zones are hence limited, but not uncommon: Levy et al. (2009a) surveyed 823 HiRISE images in the latitude range 30°-80° in both hemispheres, and 133 of them showed both low and high-centred polygons (what they called ‘mixed center polygons’). These positive-detection images are all located between 30° and 60° in both hemispheres, and at all longitudes. Moreover, this survey was done on a fraction of the whole HiRISE dataset; at present day, the total number of images showing low-centred polygons certainly is much higher. It shows that my method, backed up by an assessment of the existence of ice wedges in a given study zone, has the potential to be applied in a variety of study regions in the martian mid-latitudes.

In addition, I suggest that similar methods could be developed for other landforms than thermal-contraction polygons. For instance, on Mars, brain terrains are thought to be a type of ice-cored mound (e.g. Levy et al., 2009b), found on viscous-flow features (i.e. martian analogues to terrestrial debris-covered glaciers). Brain terrains exhibit two main morphological types: mounds forming the closed-cell morphology, and depressions forming the open-cell morphology. The mounds are thought to have an ice core, while the depressions are thought to result from the degradation of the ice core (Levy et al., 2009b). Therefore, my method could be applied to brain terrains by discriminating closed-cell and open-cell morphologies – similarly to the discrimination between low and high-centred polygons I presented in this thesis. For instance, the output results could be a quantification of the state of degradation of near-surface ice on martian debris-covered glaciers. Potential implications could emerge concerning the timing of ice degradation with respect to the Amazonian climate, or concerning the evolution of those martian glaciers.

2. Outlook

2.1. Molards

2.1.1. Experimental setup

Now that an experimental protocol has been established that allows the study of molard formation in a controlled and systematic way, experiments are currently being carried out in the cold room facilities at M2C laboratory (Caen, France). These experiments are conducted in the framework of the Permolards project. The goal of these experiments is i. to observe and quantify the degradation processes from ice-cemented block to molard, and ii. to investigate the effect of various parameters (e.g. grain size of the sediment, dimension of the initial ice-cemented block, initial ice-quantity) on the degradation processes and on the final shape of the molards. In addition to the systematic experiments with controlled grain sizes, we conducted fieldwork in Iceland in summer 2022 and brought back samples of an actual molard. This sample will be used as experimental sediment to build an analogue model as close as possible to a natural molard. Moreover, the degradation processes from ice-cemented block to molard is being studied under various settings. In the regular experiments, blocks are degrading in the open air, at ambient temperature. In some other experiments, models are degrading under hotter or colder temperature, or even underwater – as molard-bearing landslides reaching the sea were reported in Greenland (Svennevig et al., 2022, 2023). Moreover, the different datasets acquired during the analogue experiments (e.g. evolution of the shape, type of degradation processes, duration of the degradation) will be used to constrain a numerical model exploring the degradation from ice-cemented block to molard. This numerical model will be useful to investigate settings that are difficult or impossible to reproduce experimentally, for instance initial blocks with larger dimensions (tens of metres) or with coarse grain sizes.

Once again in the framework of the Permolards project, work is currently under progress in order to model numerically molard-bearing landslides. This part of the project will have as output to better understand the conditions for preservation of ice-cemented blocks during a landslide, as well as how they are distributed within landslide deposits.

Ultimately, understanding how molards are distributed within a landslide and the various shapes and dimensions they can have will lead to the possibility to recognise them on remote sensing data only, without the need to do fieldwork. It will be especially useful as molards often occur in remote areas. Recognising molards on remote sensing data will also enable the possibility to identify and map them at a larger scale than a single landslide. With a large-scale map of distribution of molard-bearing landslides, the current extent of mountain permafrost could be extrapolated at the regional scale. Eventually, this extent could be compared to the extent computed from current numerical models (e.g. Obu et al., 2019; Way and Lewkowicz, 2016; Zhang et al., 2021) – which could give new constraints on permafrost distribution in order to improve those numerical models. Knowing the extent of mountain permafrost will also allow us to locate accurately the zones with a high risk of landslide related to permafrost degradation (e.g. Geertsema et al., 2009; Haque et al., 2016; Kjekstad and Highland, 2009; Petley, 2012).

2.1.2. Martian molards

Concerning Mars, I presented a study in which we report the first molard population in the ejecta of Hale crater. Hence, a molard origin should be considered when investigating martian conical mounds in the future. This matter deserves attention, as their presence indicates that the material mobilised was at least partially constituted of sediment cemented by pore ice, which gives important insights into the geology of

a substrate – for instance in terms of ice content or porosity. However, it is still unknown how common martian molards are. This question could be addressed by surveying conical mounds in the ejecta of large craters, for instance based on existing crater catalogues (e.g. Robbins and Hynek, 2012a, 2012b; Salamunićcar et al., 2012). Such a survey would, first, indicate whether martian molards are common or not. Second, as molards indicate that the impacted material was ice-cemented, the presence of molards could be coupled with the age of the concerned impact craters. The results of that study could provide new constraints on the formation time of the current subsurface cryosphere on Mars, hence on the timing of the transition to a colder climate – and overall, on our understanding of the Amazonian climate. In addition, several studies reported the excavation of ground ice by recent craters (Byrne et al., 2009; Dundas et al., 2014, 2021, 2023). Despite that this ice was suggested to be nearly-pure (Byrne et al., 2009; Dundas et al., 2014; Dundas and Byrne, 2010), it is possible that some craters formed ice-cemented blocks of sediment that will ultimately form molards. As the presence of excess ice and pore ice have different implications in terms of substrate geology (porosity, ice content) and ice-formation processes (ice deposition within the pores *vs.* ice segregation or intrusion), it is important to differentiate between impacts excavating pure ice or ice-cemented blocks of sediment. Such a survey could be conducted using the recent catalogue of new impact craters provided by Daubar et al. (2022).
Up to that point, I only mentioned the formation of ice-cemented blocks by impact craters. However, it is possible that we can find molards in different geological settings on Mars – for instance, like on Earth, in mass-wasting deposits. Such a survey of martian landslide in search of molards could be performed using the inventory of martian landslides provided by Crosta et al. (2018). Combined with a dating of the landslides, that survey could unveil the evolution of the extent of martian ground ice at a regional scale.

In a broader view, molards are landforms that can potentially be found on every planetary environment where an ice-cemented sediment is mobilised by a destructive process, and with a surface environment conducive to ice degradation. As a mobilisation process, I already mentioned impact craters on Mars (Morino et al., 2023) and on Mercury (Wright et al., 2020), but this is also relevant for other planetary bodies – for instance the Moon (Moon et al., 2021), icy asteroids of dwarf planets like Vesta or Ceres (Hughson et al., 2018; Palmer et al., 2017; Schenk et al., 2021; B. E. Schmidt et al., 2017), or potentially the martian moons Phobos and Deimos (e.g. Avanesov et al., 1991; Basilevsky et al., 2014).

2.2. Thermal-contraction polygons

In this thesis I presented a study in which we show that investigating the latitudinal distribution of the different polygon types can provide insights into the type of wedge underlying a polygon population. At the time of writing, such a study has only been conducted in our study zone (eastern Utopia Planitia, 40°-50° N, 110°-125° E), where we provided evidence for the presence of ice wedges. First, conducting more investigations in other areas known to bear ground ice, similar to our study in Utopia Planitia, would help us to understand whether ice-wedge formation throughout the Amazonian was a local phenomenon or if it occurred globally. Depending on their formation mode, i.e. involvement of liquid water or not, important implications could be drawn concerning the stability of liquid water throughout the Amazonian.
Then, we discussed above the possibility to form ice wedges by the surficial activity of liquid brines rather than pure water (e.g. Kreslavsky, 2022; *conference abstract*). However, distinguishing ice-wedge polygons formed through the action of brines rather than pure water seems challenging. First, extensive polygon fields with a high density of the low-centred morphology (i.e. polygons that currently are underlain by wedges) will have to be identified. Their origin as ice-wedge polygons will have to be evaluated, by a study of the latitudinal distribution of their morphology types – as the one I presented in Utopia Planitia. Then,

different datasets will have to be combined in order to evaluate whether salts are present within the polygon field, and in what quantity – e.g. hyperspectral data (e.g. Ojha et al., 2015) or dielectric properties inferred from radar data (e.g. Mattei et al., 2022). Considering the (current) coarse resolution of such data, the selected polygon fields will have to be of sufficient size. As suggested numerous times throughout the manuscript, solving this question would have important implications concerning the stability of liquid water throughout the Amazonian.

Overall, not all of the knowledge we have on terrestrial thermal-contraction polygons has been applied to martian polygons. For instance, on Earth, some studies have investigated polygon fields in terms of fracture orientation, polygon subdivision, or network regularity in order to infer their development stage (e.g. Frappier and Lacelle, 2021; Goehring, 2013; Haltigin et al., 2012; Sletten et al., 2003); on Mars, this aspect has been poorly explored (e.g. Haltigin et al., 2014; Ulrich et al., 2011). However, understanding the stage of development of martian polygons based on terrestrial ones would give new insights on those landforms. For instance, we should be able to estimate how many cycles of temperature drops and/or freeze-thaw cycles were required to form martian polygon fields, or whether they are currently active landscapes. Therefore, getting a better understanding of the evolution of ice-wedge polygon fields would give new constraints on the recent martian climate. Such studies could be coupled to quantitative assessments of ground ice content, in order to get additional constraints on the potential volume of liquid water at play during these geologically recent times, but also on the amount of ground ice that currently exists. On Earth, estimations of the ice content of polygon fields can be obtained by various field techniques (e.g. ground-penetrating radar or electrical resistivity tomography; Forte et al., 2022; Munroe et al., 2007; Watanabe et al., 2013). Ongoing research projects are already planning on estimating the ground ice content of martian polygon fields based on comparison with terrestrial ones (e.g. Andres et al., 2020; *conference abstract*).

In this thesis, I also developed parameters that can be calculated for a given polygon-bearing unit, based on polygon characteristics (i.e. distribution and type). I suggested that these parameters can be used to trace geological properties of the substrate (its cementation by ice, its capacity to form massive ground ice, its capacity to preserve ground ice). Hence, by giving additional constraints on the geological origin of geomorphological units, the study of thermal-contraction polygon represents a complementary tool to more classic stratigraphic and geologic investigations. Therefore, these parameters could be used in other polygon-bearing regions within the martian mid-latitudes – with the condition, as stated above, that at least low-centred polygons are present. For instance, my parameters constitute valuable tools to be added to the investigation methods of current research projects on water ISRU (e.g. SWIM).
The method I developed could also benefit from a comparison with terrestrial ice-wedge polygons as, currently, the output values of parameters cannot be quantitatively related to the properties they reflect. However, calculating those parameters for terrestrial polygon fields with known properties could fill in this gap. I also acknowledge that, for the moment, the parameters I developed may reflect substrate properties in a way that is simplistic, and that their values could actually be affected by several different substrate properties. Conducting on Earth a study similar to the one I conducted in Utopia Planitia could unveil these potentially more complex relationships.

3. Conclusions

In this thesis, I addressed some of the scientific questions concerning the ways ground ice and periglacial processes shape the surfaces of the Earth and Mars. I particularly focused on molards and thermal-contraction polygons.
First, I provided an experimental system that allows to study analogue models of molards. These spatial and temporal markers of permafrost degradation are poorly understood. Such an experimental system will allow us to understand how these features form and evolve, which is currently unknown. Therefore, it will open the door to future studies which will, ultimately, improve the general understanding on the distribution of mountain permafrost, and on the landslide hazard assessment in these regions. These matters are particularly important in the current context of global climate change, as we can expect landslides to be more common in mountain permafrost areas in a near future. In addition, I expect that the experimental setup I developed could be adapted to study a variety of experimental or natural objects.
I also presented a study in which we investigate the first potential martian molards. It provides evidence that the studies we are conducting on terrestrial molards also have planetary applications, which widens the scope of potential future investigations. It suggests that molards could be a feature common to various planetary environments, where the environmental setting allows the presence of ice-cemented sediment. Applied to the case of Hale crater, it allowed to draw important conclusions on the post-impact evolution of its ejecta and on the initial ice content of the ground mobilised by the impact. I also suggested potential implications that the presence of a thick ice-rich layer at relatively low latitudes has for the Amazonian climate. Overall, I showed that molards represent a tool that can be used to investigate the type of ground ice – and its eventual degradation – in planetary environments.

Then, I presented a study in which we provided evidence for the presence of ice-wedge polygons in a study zone in Utopia Planitia. On Earth, they require liquid water to form; however, the recent martian climate is thought to be non-conducive to liquid water stability. I hence suggested two formation hypotheses for those ice wedges: one involving liquid water (or brines), and one involving condensation of atmospheric water vapour – and hence that does not require liquid water. Potential geologically recent liquid water could redefine our understanding of the martian climate at a global scale, but also our understanding of its habitability. In addition, the presence of ice wedges on Mars is interesting in terms of water ISRU for eventual human missions. Studying both the habitability and ISRU on Mars are prime objectives of the current missions sent to Mars by all space agencies, which makes investigations on martian thermal-contraction polygons currently very relevant. In addition, as the distribution and morphologies of thermal-contraction polygons is dependent on various properties of the ground, I showed in this thesis that polygons can be used to trace geological properties of their substrate. I applied this method I developed to specific geomorphological units, which was a novel approach. In return, I showed that identifying polygon-bearing geomorphological units and dating their emplacement gives constraints on the timing of polygon formation. Such constraints, as stated above, are important in order to adequately understand the Amazonian climate, and to evaluate the possibility of occurrence of liquid water in geologically recent times – with implications for the habitability of the planet. The method I developed allowed me to infer the geological origin of two units in Utopia Planitia, including a Middle Amazonian ice-rich unit. I suggested two different formation hypotheses for that unit: one involving large quantities of liquid water, the other involving condensation of atmospheric water vapour only. Similarly to the formation of ice wedges, the implications of those two formation hypotheses for the martian climate are different, as presence of surface liquid water during the Middle Amazonian could redefine our understanding of the liquid water stability – and hence of the habitability of Mars.

From a broader point of view, both molards and thermal-contraction polygons are indicators of specific settings of ground ice and periglacial processes. Molards are indicative of current degradation of ice-cemented ground; thermal-contraction polygons are indicative of the presence of ice-cemented ground, eventually liquid water, and their degraded morphology (high-centred polygons) are also indicative of ground ice degradation. Therefore, in this thesis, I investigated both of those morphologies and I provide additional knowledge on planetary periglacial processes – some of those processes being linked to ground ice degradation. But more importantly, I also provide novel investigation methods and open new doors for future studies that will investigate ground ice in a general way – both on Earth and/or on Mars.

References

Abbud-Madrid, A., Beaty, D., Boucher, D., Bussey, B., Davis, R., Gertsch, L., Hays, L., Kleinhenz, J., Meyer, M., Moats, M., Mueller, R., Paz, A., Suzuki, N., van Susante, P., Whetsel, C., Zbinden, E., 2016. Report of the Mars Water In-Situ Resource Utilization (ISRU) Planning (M-WIP) Study.

Abrahams, A.D., Dixon, J.C. (Eds.), 1992. Periglacial Geomorphology: Binghamton Geomorphology Symposium 22, 1st ed. Routledge. https://doi.org/10.4324/9781003028901

Abramov, A., Gruber, S., Gilichinsky, D., 2008. Mountain permafrost on active volcanoes: field data and statistical mapping, Klyuchevskaya volcano group, Kamchatka, Russia. Permafr. Periglac. Process. 19, 261–277. https://doi.org/10.1002/ppp.622

Abramov, O., Mojzsis, S.J., 2016. Thermal effects of impact bombardments on Noachian Mars. Earth Planet. Sci. Lett. 442, 108–120. https://doi.org/10.1016/j.epsl.2016.02.035

Abshire, J.B., Sun, X., Afzal, R.S., 2000. Mars Orbiter Laser Altimeter: receiver model and performance analysis. Appl. Opt. 39, 2449. https://doi.org/10.1364/AO.39.002449

Agisoft Metashape User Manual - Professional Edition, Version 1.8, n.d.

Albee, A.L., Palluconi, F.D., Arvidson, R.E., 1998. Mars Global Surveyor Mission: Overview and Status. Science 279, 1671–1672. https://doi.org/10.1126/science.279.5357.1671

Albee, A.L., Arvidson, R.E., Palluconi, F., Thorpe, T., 2001. Overview of the Mars Global Surveyor mission. J. Geophys. Res. Planets 106, 23291–23316. https://doi.org/10.1029/2000JE001306

Allen, S.K., Gruber, S., Owens, I.F., 2009. Exploring steep bedrock permafrost and its relationship with recent slope failures in the Southern Alps of New Zealand: Permafrost and Recent Slope Failures, New Zealand. Permafr. Periglac. Process. 20, 345–356. https://doi.org/10.1002/ppp.658

Amiri, H.E.S., Brain, D., Sharaf, O., Withnell, P., McGrath, M., Alloghani, M., Al Awadhi, M., Al Dhafri, S., Al Hamadi, O., Al Matroushi, H., Al Shamsi, Z., Al Shehhi, O., Chaffin, M., Deighan, J., Edwards, C., Ferrington, N., Harter, B., Holsclaw, G., Kelly, M., Kubitschek, D., Landin, B., Lillis, R., Packard, M., Parker, J., Pilinski, E., Pramman, B., Reed, H., Ryan, S., Sanders, C., Smith, M., Tomso, C., Wrigley, R., Al Mazmi, H., Al Mheiri, N., Al Shamsi, M., Al Tunaiji, E., Badri, K., Christensen, P., England, S., Fillingim, M., Forget, F., Jain, S., Jakosky, B.M., Jones, A., Lootah, F., Luhmann, J.G., Osterloo, M., Wolff, M., Yousuf, M., 2022. The Emirates Mars Mission. Space Sci. Rev. 218, 4. https://doi.org/10.1007/s11214-021-00868-x

Anderson, H.R., 1965. Mariner IV Measurements near Mars: Initial Results. Science 149, 1226–1228. https://doi.org/10.1126/science.149.3689.1226

Anderson, K., Westoby, M.J., James, M.R., 2019. Low-budget topographic surveying comes of age: Structure from motion photogrammetry in geography and the geosciences. Prog. Phys. Geogr. Earth Environ. 43, 163–173. https://doi.org/10.1177/0309133319837454

Andres, C.N., Osinski, G.R., Godin, E., Kukko, A., 2020. The Utility of 3D Ground Penetrating Radar Imaging to Quantify Subsurface Ice Volume: Considerations for Polygonal Terrain Network Development 1484.

Andrews-Hanna, J.C., Zuber, M.T., Banerdt, W.B., 2008. The Borealis basin and the origin of the martian crustal dichotomy. Nature 453, 1212–1215. https://doi.org/10.1038/nature07011

Andrieux, E., Bertran, P., Antoine, P., Deschodt, L., Lenoble, A., Coutard, S., Ajas, A., Borderie, Q., Coutard, J.-P., Didierjean, F., Dousteyssier, B., Ferrier, C., Gardère, P., Gé, T., Liard, M., Locht, J., Naton, H., Rué, M., Sitzia, L., Vliet-Lanoe, B.V., Vernet, G., 2016. Database of pleistocene periglacial featuresin France: description of the online version. Quaternaire 329–339. https://doi.org/10.4000/quaternaire.7717

Anisimov, O., Reneva, S., 2006. Permafrost and Changing Climate: The Russian Perspective. AMBIO J. Hum. Environ. 35, 169–175. https://doi.org/10.1579/0044-7447(2006)35[169:PACCTR]2.0.CO;2

Ansan, V., Mangold, N., Masson, P., Gailhardis, E., Neukum, G., 2008. Topography of valley networks on Mars from Mars Express High Resolution Stereo Camera digital elevation models. J. Geophys. Res. 113, E07006. https://doi.org/10.1029/2007JE002986

Arakawa, K., 1966. Theoretical Studies of Ice Segregation in Soil. J. Glaciol. 6, 255–260. https://doi.org/10.3189/S0022143000019274

Arunan, S., Satish, R., 2015. Mars Orbiter Mission spacecraft and its challenges. Curr. Sci. 109, 1061–1069.

Avanesov, G., Zhukov, B., Ziman, Ya., Kostenko, V., Kuzmin, A., Murav'ev, V., Fedotov, V., Bonev, B., Mishev, D., Petkov, D., Krumov, A., Simeonov, S., Boycheva, V., Uzunov, Yu., Weide, G.-G., Halmann, D., Pössel, W., Head, J., Murchie, S., Schkuratov, Yu.G., Berghänel, R., Danz, M., Mangoldt, T., Pihan, U., Weidlich, U., Lumme, K., Muinonen, K., Peltoniemi, J., Duxbury, T., Murray, B., Herkenhoff, K., Fanale, F., Irvine, W., Smith, B., 1991. Results of TV imaging of phobos (experiment VSK-FREGAT). Planet. Space Sci. 39, 281–295. https://doi.org/10.1016/0032-0633(91)90150-9

Bahia, R.S., Covey-Crump, S., Jones, M.A., Mitchell, N., 2022. Discordance analysis on a high-resolution valley network map of Mars: Assessing the effects of scale on the conformity of valley orientation and surface slope direction. Icarus 383, 115041. https://doi.org/10.1016/j.icarus.2022.115041

Baker, D.M.H., Head, J.W., Marchant, D.R., 2010. Flow patterns of lobate debris aprons and lineated valley fill north of Ismeniae Fossae, Mars: Evidence for extensive mid-latitude glaciation in the Late Amazonian. Icarus 207, 186–209. https://doi.org/10.1016/j.icarus.2009.11.017

Baker, V.R., 2001. Water and the martian landscape. Nature 412, 228–236. https://doi.org/10.1038/35084172

Baker, V.R., Strom, R.G., Gulick, V.C., Kargel, J.S., Komatsu, G., Kale, V.S., 1991. Ancient oceans, ice sheets and the hydrological cycle on Mars. Nature 352, 589–594. https://doi.org/10.1038/352589a0

Balaguer-Puig, M., Marqués-Mateu, Á., Lerma, J.L., Ibáñez-Asensio, S., 2017. Estimation of small-scale soil erosion in laboratory experiments with Structure from Motion photogrammetry. Geomorphology 295, 285–296. https://doi.org/10.1016/j.geomorph.2017.04.035

Balaram, J., Aung, M., Golombek, M.P., 2021. The Ingenuity Helicopter on the Perseverance Rover. Space Sci. Rev. 217, 56. https://doi.org/10.1007/s11214-021-00815-w

Ballantyne, C.K., 2018. Periglacial Geomorphology. Wiley-Blackwell

Banerdt, W.B., Smrekar, S.E., Banfield, D., Giardini, D., Golombek, M., Johnson, C.L., Lognonné, P., Spiga, A., Spohn, T., Perrin, C., Stähler, S.C., Antonangeli, D., Asmar, S., Beghein, C., Bowles, N., Bozdag, E., Chi, P., Christensen, U., Clinton, J., Collins, G.S., Daubar, I., Dehant, V., Drilleau, M., Fillingim, M., Folkner, W., Garcia, R.F., Garvin, J., Grant, J., Grott, M., Grygorczuk, J., Hudson, T., Irving, J.C.E., Kargl, G., Kawamura, T., Kedar, S., King, S., Knapmeyer-Endrun, B., Knapmeyer, M., Lemmon, M., Lorenz, R., Maki, J.N., Margerin, L., McLennan, S.M., Michaut, C., Mimoun, D., Mittelholz, A., Mocquet, A., Morgan, P., Mueller, N.T., Murdoch, N., Nagihara, S., Newman, C., Nimmo, F., Panning, M., Pike, W.T., Plesa, A.-C., Rodriguez, S., Rodriguez-Manfredi, J.A., Russell, C.T., Schmerr, N., Siegler, M., Stanley, S., Stutzmann, E., Teanby, N., Tromp, J., Van Driel, M., Warner, N., Weber, R., Wieczorek, M., 2020. Initial results from the InSight mission on Mars. Nat. Geosci. 13, 183–189. https://doi.org/10.1038/s41561-020-0544-y

Barlow, N.G., Perez, C.B., 2003. Martian impact crater ejecta morphologies as indicators of the distribution of subsurface volatiles. J. Geophys. Res. 108, 5085. https://doi.org/10.1029/2002JE002036

Basilevsky, A.T., Lorenz, C.A., Shingareva, T.V., Head, J.W., Ramsley, K.R., Zubarev, A.E., 2014. The surface geology and geomorphology of Phobos. Planet. Space Sci. 102, 95–118. https://doi.org/10.1016/j.pss.2014.04.013

Beerten, K., Meylemans, E., Kasse, C., Mestdagh, T., Van Rooij, D., Bastiaens, J., 2021. Networks of unusually large fossil periglacial polygons, Campine area, northern Belgium. Geomorphology 377, 107582. https://doi.org/10.1016/j.geomorph.2020.107582

Belcher, D., Veverka, J., Sagan, C., 1971. Mariner photography of Mars and aerial photography of Earth: Some analogies. Icarus 15, 241–252. https://doi.org/10.1016/0019-1035(71)90078-9

Bell, R., Glade, T., 2004. Quantitative risk analysis for landslides – Examples from Bíldudalur, NW-Iceland. Nat. Hazards Earth Syst. Sci. 4, 117–131. https://doi.org/10.5194/nhess-4-117-2004

Bellucci, G., Altieri, F., Bibring, J.P., OMEGA Team, 2004. The OMEGA Instrument on board Mars Express: First Results. Mem. Della Soc. Astron. Ital. Suppl. 5, 27.

Beltrami, H., Jessop, A.M., Mareschal, J.-C., 1992. Ground temperature histories in eastern and central Canada from geothermal measurements: evidence of climatic change. Glob. Planet. Change 6, 167–183. https://doi.org/10.1016/0921-8181(92)90033-7

Benedict, J.B., 1976. Frost Creep and Gelifluction Features: A Review. Quat. Res. 6, 55–76. https://doi.org/10.1016/0033-5894(76)90040-5

Berg, T.E., Black, R.F., 1966. Preliminary Measurements of Growth of Nonsorted Polygons, Victoria Land, Antarctica [1], in: Tedrow, J.C.F. (Ed.), Antarctic Research Series. American Geophysical Union, Washington, D. C., pp. 61–108. https://doi.org/10.1029/AR008p0061

Berman, D.C., Hartmann, W.K., 2002. Recent Fluvial, Volcanic, and Tectonic Activity on the Cerberus Plains of Mars. Icarus 159, 1–17. https://doi.org/10.1006/icar.2002.6920

Berman, D.C., Balme, M.R., Rafkin, S.C.R., Zimbelman, J.R., 2011. Transverse Aeolian Ridges (TARs) on Mars II: Distributions, orientations, and ages. Icarus 213, 116–130. https://doi.org/10.1016/j.icarus.2011.02.014

Berman, D.C., Crown, D.A., Joseph, E.C.S., 2015. Formation and mantling ages of lobate debris aprons on Mars: Insights from categorized crater counts. Planet. Space Sci. 111, 83–99. https://doi.org/10.1016/j.pss.2015.03.013

Bernard-Grand'Maison, C., Pollard, W., 2018. An estimate of ice wedge volume for a High Arctic polar desert environment, Fosheim Peninsula, Ellesmere Island. The Cryosphere 12, 3589–3604. https://doi.org/10.5194/tc-12-3589-2018

Bertin, S., Friedrich, H., Delmas, P., Chan, E., Gimel'farb, G., 2014. Dem quality assessment with a 3d printed gravel bed applied to stereo photogrammetry. Photogramm. Rec. 29, 241–264. https://doi.org/10.1111/phor.12061

Bibring, J.-P., Langevin, Y., Gendrin, A., Gondet, B., Poulet, F., Berthé, M., Soufflot, A., Arvidson, R., Mangold, N., Mustard, J., Drossart, P., the OMEGA team, 2005. Mars Surface Diversity as Revealed by the OMEGA/Mars Express Observations. Science 307, 1576–1581. https://doi.org/10.1126/science.1108806

Bibring, J.-P., Langevin, Y., Mustard, J.F., Poulet, F., Arvidson, Raymond, Gendrin, A., Gondet, B., Mangold, N., Pinet, P., Forget, F., Berthé, M., Bibring, J.-P., Gendrin, A., Gomez, C., Gondet, B., Jouglet, D., Poulet, F., Soufflot, A., Vincendon, M., Combes, M., Drossart, P., Encrenaz, T., Fouchet, T., Merchiorri, R., Belluci, G., Altieri, F., Formisano, V., Capaccioni, F., Cerroni, P., Coradini, A., Fonti, S., Korablev, O., Kottsov, V., Ignatiev, N., Moroz, V., Titov, D., Zasova, L., Loiseau, D., Mangold, N., Pinet, Patrick, Douté, S., Schmitt, B., Sotin, C., Hauber, E., Hoffmann, H., Jaumann, R., Keller, U., Arvidson, Ray, Mustard, J.F., Duxbury, T., Forget, François, Neukum, G., 2006. Global Mineralogical and Aqueous Mars History Derived from OMEGA/Mars Express Data. Science 312, 400–404. https://doi.org/10.1126/science.1122659

Bierson, C.J., Tulaczyk, S., Courville, S.W., Putzig, N.E., 2021. Strong MARSIS Radar Reflections From the Base of Martian South Polar Cap May Be Due to Conductive Ice or Minerals. Geophys. Res. Lett. 48. https://doi.org/10.1029/2021GL093880

Black, R.F., 1954. PERMAFROST: A REVIEW. Geol. Soc. Am. Bull. 65, 839. https://doi.org/10.1130/0016-7606(1954)65[839:PR]2.0.CO;2

Black, R.F., 1976a. Features Indicative of Permafrost. Annu. Rev. Earth Planet. Sci. 4, 75–94. https://doi.org/10.1146/annurev.ea.04.050176.000451

Black, R.F., 1976b. Periglacial Features Indicative of Permafrost: Ice and Soil Wedges. Quat. Res. 6, 3–26. https://doi.org/10.1016/0033-5894(76)90037-5

Black, R.F., 1982. Ice-Wedge Polygons of Northern Alaska, in: Coates, D.R. (Ed.), Glacial Geomorphology. Springer Netherlands, Dordrecht, pp. 247–275. https://doi.org/10.1007/978-94-011-6491-7_9

Blasius, K.R., Cutts, J.A., Guest, J.E., Masursky, H., 1977. Geology of the Valles Marineris: First analysis of imaging from the Viking 1 Orbiter Primary Mission. J. Geophys. Res. 82, 4067–4091. https://doi.org/10.1029/JS082i028p04067

Blichert-Toft, J., Gleason, J.D., Télouk, P., Albarède, F., 1999. The Lu–Hf isotope geochemistry of shergottites and the evolution of the Martian mantle–crust system. Earth Planet. Sci. Lett. 173, 25–39. https://doi.org/10.1016/S0012-821X(99)00222-8

Boatwright, B.D., Head, J.W., 2021. A Noachian Proglacial Paleolake on Mars: Fluvial Activity and Lake Formation within a Closed-source Drainage Basin Crater and Implications for Early Mars Climate. Planet. Sci. J. 2, 52. https://doi.org/10.3847/PSJ/abe773

Boatwright, B.D., Head, J.W., 2022. Noachian Proglacial Paleolakes on Mars: Regionally Recurrent Fluvial Activity and Lake Formation within Closed-source Drainage Basin Craters. Planet. Sci. J. 3, 38. https://doi.org/10.3847/PSJ/ac4d36

Bockheim, J.G., 2002. Landform and Soil Development in the McMurdo Dry Valleys, Antarctica: A Regional Synthesis. Arctic, Antarctic, and Alpine Research, 34:3, 308-317. https://doi.org/10.1080/15230430.2002.12003499

Bockheim, J.G., Hall, K.J., 2002. Permafrost, active-layer dynamics and periglacial environments of continental Antarctica : Periglacial and Permafrost Research in the Southern Hemisphere. South Afr. J. Sci. 98. https://hdl.handle.net/10520/EJC97385

Bockheim, J.G., Kurz, M.D., Soule, A., Burke, A., 2009. Genesis of active sand-filled polygons in lower and central Beacon Valley, Antarctica. Permafr. Periglac. Process. 20 (3), 295-398. https://doi.org/10.1002/ppp.661

Bolles, R.C., Baker, H.H., Marimont, D.H., 1987. Epipolar-plane image analysis: An approach to determining structure from motion. Int. J. Comput. Vis. 1, 7–55. https://doi.org/10.1007/BF00128525

Bonnet Gibet, V., Michaut, C., Wieczorek, M., Lognonné, P., 2022. A Positive Feedback Between Crustal Thickness and Melt Extraction for the Origin of the Martian Dichotomy. J. Geophys. Res. Planets 127. https://doi.org/10.1029/2022JE007472

Bouley, S., Baratoux, D., Matsuyama, I., Forget, F., Séjourné, A., Turbet, M., Costard, F., 2016. Late Tharsis formation and implications for early Mars. Nature 531, 344–347. https://doi.org/10.1038/nature17171

Boynton, W.V., Feldman, W.C., Squyres, S.W., Prettyman, T.H., Brückner, J., Evans, L.G., Reedy, R.C., Starr, R., Arnold, J.R., Drake, D.M., Englert, P.A.J., Metzger, A.E., Mitrofanov, I., Trombka, J.I., d'Uston, C., Wänke, H., Gasnault, O., Hamara, D.K., Janes, D.M., Marcialis, R.L., Maurice, S., Mikheeva, I., Taylor, G.J., Tokar, R., Shinohara, C., 2002. Distribution of Hydrogen in the Near Surface of Mars: Evidence for Subsurface Ice Deposits. Science 297, 81–85. https://doi.org/10.1126/science.1073722

Boynton, W.V., Feldman, W.C., Mitrofanov, I.G., Evans, L.G., Reedy, R.C., Squyres, S.W., Starr, R., Trombka, J.I., d'Uston, C., Arnold, J.R., Englert, P.A.J., Metzger, A.E., Wänke, H., Brückner, J., Drake, D.M., Shinohara, C., Fellows, C., Hamara, D.K., Harshman, K., Kerry, K., Turner, C., Ward, M., Barthe, H., Fuller, K.R., Storms, S.A., Thornton, G.W., Longmire, J.L., Litvak, M.L., Ton'chev, A.K., 2004. The Mars Odyssey Gamma-Ray Spectrometer Instrument Suite. Space Sci. Rev. 110, 37–83. https://doi.org/10.1023/B:SPAC.0000021007.76126.15

Bramson, A.M., Byrne, S., Putzig, N.E., Sutton, S., Plaut, J.J., Brothers, T.C., Holt, J.W., 2015. Widespread excess ice in Arcadia Planitia, Mars. Geophys. Res. Lett. 42, 6566–6574. https://doi.org/10.1002/2015GL064844

Bramson, A.M., Byrne, S., Bapst, J., 2017. Preservation of Midlatitude Ice Sheets on Mars: Mars Midlatitude Ice Sheet Preservation. J. Geophys. Res. Planets 122, 2250–2266. https://doi.org/10.1002/2017JE005357

Brasington, J., Rumsby, B.T., McVey, R.A., 2000. Monitoring and modelling morphological change in a braided gravel-bed river using high resolution GPS-based survey. Earth Surf. Process. Landf. 25, 973–990. https://doi.org/10.1002/1096-9837(200008)25:9<973::AID-ESP111>3.0.CO;2-Y

Brasington, J., Smart, R.M.A., 2003. Close range digital photogrammetric analysis of experimental drainage basin evolution. Earth Surf. Process. Landf. 28, 231–247. https://doi.org/10.1002/esp.480

Brass, G.W., 1980. Stability of brines on Mars. Icarus 42, 20–28. https://doi.org/10.1016/0019-1035(80)90237-7

Brewer, M.C., 1958. Some results of geothermal investigations of permafrost in northern Alaska. Trans. Am. Geophys. Union 39, 19. https://doi.org/10.1029/TR039i001p00019

Brideau, M., Stead, D., Lipovsky, P., Jaboyedoff, M., Hopkinson, C., Demuth, M., Barlow, J., Evans, S., Delaney, K., 2009. Preliminary description and slope stability analyses of the 2008 Little Salmon Lake and 2007 Mt . Steele landslides , Yukon. Yukon Explor. Geol. 119–134.

Bridger, A.F.C., Murphy, J.R., 1998. Mars' surface pressure tides and their behavior during global dust storms. J. Geophys. Res. Planets 103, 8587–8601. https://doi.org/10.1029/98JE00242

Bristow, C.S., Moller, T.H., 2018. Dust Production by Abrasion of Eolian Basalt Sands: Analogue for Martian Dust. J. Geophys. Res. Planets 123, 2713–2731. https://doi.org/10.1029/2018JE005682

Broquet, A., Andrews-Hanna, J.C., 2022. Geophysical evidence for an active mantle plume underneath Elysium Planitia on Mars. Nat. Astron. https://doi.org/10.1038/s41550-022-01836-3

Brown, J., Ferrians Jr., O.J., Heginbottom, J.A., Melnikov, E.S., 1997. Circum-Arctic map of permafrost and ground-ice conditions. https://doi.org/10.3133/cp45

Brown, R.J.E., 1981. Chapter 2: Permafrost distribution and terrain characteristics, in: Permafrost: Engineering Design and Construction. Johnston, GH Toronto, Ontario.

Buffo, J.J., Ojha, L., Meyer, C.R., Ferrier, K.L., Palucis, M.C., 2022. Revisiting subglacial hydrology as an origin for Mars' valley networks. Earth Planet. Sci. Lett. 594, 117699. https://doi.org/10.1016/j.epsl.2022.117699

Burn, C.R., Lewkowicz, A.G., 1990. CANADIAN LANDFORM EXAMPLES - 17 RETROGRESSIVE THAW SLUMPS. Can. Geogr. Géographe Can. 34, 273–276. https://doi.org/10.1111/j.1541-0064.1990.tb01092.x

Burn, C.R., Smith, M.W., 2006. Development of thermokarst lakes during the holocene at sites near Mayo, Yukon territory. Permafr. Periglac. Process. 1, 161–175. https://doi.org/10.1002/ppp.3430010207

Burr, D.M., Soare, R.J., Wan Bun Tseung, J.-M., Emery, J.P., 2005. Young (late Amazonian), near-surface, ground ice features near the equator, Athabasca Valles, Mars. Icarus 178, 56–73. https://doi.org/10.1016/j.icarus.2005.04.012

Burr, D.M., Tanaka, K.L., Yoshikawa, K., 2009. Pingos on Earth and Mars. Planet. Space Sci. 57, 541–555. https://doi.org/10.1016/j.pss.2008.11.003

Butcher, F.E.G., 2022. Water Ice at Mid-Latitudes on Mars, in: Oxford Research Encyclopedia of Planetary Science. Oxford University Press. https://doi.org/10.1093/acrefore/9780190647926.013.239

Butcher, F.E.G., Conway, S.J., Arnold, N.S., 2016. Are the Dorsa Argentea on Mars eskers? Icarus 275, 65–84. https://doi.org/10.1016/j.icarus.2016.03.028

Butkovich, T.R., 1959. Thermal Expansion of Ice. J. Appl. Phys. 30, 350–353. https://doi.org/10.1063/1.1735166

Byrne, S., Dundas, C.M., Kennedy, M.R., Mellon, M.T., McEwen, A.S., Cull, S.C., Daubar, I.J., Shean, D.E., Seelos, K.D., Murchie, S.L., Cantor, B.A., Arvidson, R.E., Edgett, K.S., Reufer, A., Thomas, N., Harrison, T.N., Posiolova, L.V., Seelos, F.P., 2009. Distribution of Mid-Latitude Ground Ice on Mars from New Impact Craters. Science 325, 1674–1676. https://doi.org/10.1126/science.1175307

Calmels, F., Allard, M., Delisle, G., 2008. Development and decay of a lithalsa in Northern Québec: A geomorphological history. Geomorphology 97, 287–299. https://doi.org/10.1016/j.geomorph.2007.08.013

Carr, M.H., 1974. Tectonism and volcanism of the Tharsis Region of Mars. J. Geophys. Res. 79, 3943–3949. https://doi.org/10.1029/JB079i026p03943

Carr, M.H., 1979. Formation of Martian flood features by release of water from confined aquifers. J. Geophys. Res. 84, 2995. https://doi.org/10.1029/JB084iB06p02995

Carr, M.H., 2006. The surface of Mars, Cambridge planetary science series. Cambridge university press, Cambridge.

Carr, M.H., Head, J.W., 2010. Geologic history of Mars. Earth Planet. Sci. Lett. 294, 185–203. https://doi.org/10.1016/j.epsl.2009.06.042

Carter, J., Riu, L., Poulet, F., Bibring, J.-P., Langevin, Y., Gondet, B., 2023. A Mars orbital catalog of aqueous alteration signatures (MOCAAS). Icarus 389, 115164. https://doi.org/10.1016/j.icarus.2022.115164

Casella, E., Lewin, P., Ghilardi, M., Rovere, A., Bejarano, S., 2022. Assessing the relative accuracy of coral heights reconstructed from drones and structure from motion photogrammetry on coral reefs. Coral Reefs 41, 869–875. https://doi.org/10.1007/s00338-022-02244-9

Cassanelli, J.P., Head, J.W., 2018. Large-scale lava-ice interactions on Mars: Investigating its role during Late Amazonian Central Elysium Planitia volcanism and the formation of Athabasca Valles. Planet. Space Sci. 158, 96–109. https://doi.org/10.1016/j.pss.2018.04.024

Cassanelli, J.P., Head, J.W., 2019. Assessing the formation of valley networks on a cold early Mars: Predictions for erosion rates and channel morphology. Icarus 321, 216–231. https://doi.org/10.1016/j.icarus.2018.11.020

Chandler, J., 1999. Effective application of automated digital photogrammetry for geomorphological research. Earth Surf. Process. Landf. 24, 51–63. https://doi.org/10.1002/(SICI)1096-9837(199901)24:1<51::AID-ESP948>3.0.CO;2-H

Chapman, C.R., Pollack, J.B., Sagan, C., 1969. An Analysis of the Mariner-4 Cratering Statistics. Astron. J. 74, 1039. https://doi.org/10.1086/110901

Chapman, M.G., 1994. Evidence, Age, and Thickness of a Frozen Paleolake in Utopia Planitia, Mars. Icarus 109, 393–406. https://doi.org/10.1006/icar.1994.1102

Chassereau, J.E., Bell, J.M., Torres, R., 2011. A comparison of GPS and lidar salt marsh DEMs: A COMPARISON OF GPS AND LIDAR SALT MARSH DEMS. Earth Surf. Process. Landf. 36, 1770–1775. https://doi.org/10.1002/esp.2199

Chevrier, V.F., Hanley, J., Altheide, T.S., 2009. Stability of perchlorate hydrates and their liquid solutions at the Phoenix landing site, Mars. Geophys. Res. Lett. 36, L10202. https://doi.org/10.1029/2009GL037497

Chevrier, V.F., Rivera-Valentín, E.G., Soto, A., Altheide, T.S., 2020. Global Temporal and Geographic Stability of Brines on Present-day Mars. Planet. Sci. J. 1, 64. https://doi.org/10.3847/PSJ/abbc14

Chevrier, V.F., Fitting, A.B., Rivera-Valentín, E.G., 2022. Limited Stability of Multicomponent Brines on the Surface of Mars. Planet. Sci. J. 3, 125. https://doi.org/10.3847/PSJ/ac6603

Chicarro, A., Martin, P., Trautner, R., 2004. The Mars Express mission: an overview 1240, 3–13.

Christiansen, H.H., Etzelmüller, B., Isaksen, K., Juliussen, H., Farbrot, H., Humlum, O., Johansson, M., Ingeman-Nielsen, T., Kristensen, L., Hjort, J., Holmlund, P., Sannel, A.B.K., Sigsgaard, C., Åkerman, H.J., Foged, N., Blikra, L.H., Pernosky, M.A., Ødegård, R.S., 2010. The thermal state of permafrost in the nordic area during the international polar year 2007-2009: Thermal state of permafrost in the Nordic area. Permafr. Periglac. Process. 21, 156–181. https://doi.org/10.1002/ppp.687

Christiansen, H.H., Matsuoka, N., Watanabe, T., 2016. Progress in Understanding the Dynamics, Internal Structure and Palaeoenvironmental Potential of Ice Wedges and Sand Wedges. Permafr. Periglac. Process. 24 (4), 365-376. https://doi.org/10.1002/ppp.1920

Chuang, F.C., Beyer, R.A., McEwen, A.S., Thomson, B.J., 2007. HiRISE observations of slope streaks on Mars. Geophys. Res. Lett. 34, L20204. https://doi.org/10.1029/2007GL031111

Chuvilin, E., Bukhanov, B., Cheverev, V., Motenko, R., Grechishcheva, E., 2018. Effect of Ice and Hydrate Formation on Thermal Conductivity of Sediments, in: Shahzad, A. (Ed.), Impact of Thermal Conductivity on Energy Technologies. InTech. https://doi.org/10.5772/intechopen.75383

Citron, R.I., Manga, M., Hemingway, D.J., 2018. Timing of oceans on Mars from shoreline deformation. Nature 555, 643–646. https://doi.org/10.1038/nature26144

Clark, B.C., Kounaves, S.P., 2016. Evidence for the distribution of perchlorates on Mars. Int. J. Astrobiol. 15, 311–318. https://doi.org/10.1017/S1473550415000385

Clifford, S.M., 1993. A model for the hydrologic and climatic behavior of water on Mars. J. Geophys. Res. 98, 10973. https://doi.org/10.1029/93JE00225

Clifford, S., Parker, T.J., 2001. The Evolution of the Martian Hydrosphere: Implications for the Fate of a Primordial Ocean and the Current State of the Northern Plains. Icarus 154, 40–79. https://doi.org/10.1006/icar.2001.6671

Colaprete, A., Jakosky, B.M., 1998. Ice flow and rock glaciers on Mars. J. Geophys. Res. Planets 103, 5897–5909. https://doi.org/10.1029/97JE03371

Collins-May, J.L., Carr, J.R., Balme, M.R., Ross, N., Russell, A.J., Brough, S., Gallagher, C., 2020. Postimpact Evolution of the Southern Hale Crater Ejecta, Mars. J. Geophys. Res. Planets 125. https://doi.org/10.1029/2019JE006302

Conway, S.J., Decaulne, A., Balme, M.R., Murray, J.B., Towner, M.C., 2010. A new approach to estimating hazard posed by debris flows in the Westfjords of Iceland. Geomorphology 114, 556–572. https://doi.org/10.1016/j.geomorph.2009.08.015

Conway, S.J., Lamb, M.P., Balme, M.R., Towner, M.C., Murray, J.B., 2011. Enhanced runout and erosion by overland flow at low pressure and sub-freezing conditions: Experiments and application to Mars. Icarus 211, 443–457. https://doi.org/10.1016/j.icarus.2010.08.026

Conway, S.J., Hovius, N., Barnie, T., Besserer, J., Le Mouélic, S., Orosei, R., Read, N.A., 2012. Climate-driven deposition of water ice and the formation of mounds in craters in Mars' north polar region. Icarus 220, 174–193. https://doi.org/10.1016/j.icarus.2012.04.021

Conway, S.J., Balme, M.R., 2014. Decameter thick remnant glacial ice deposits on Mars. Geophys. Res. Lett. 41, 5402–5409. https://doi.org/10.1002/2014GL060314

Cook, F.A., 1960. Periglacial-Geomorphological Investigations at Resolute, 1959. Arctic 13, 132–135.

Costard, F., Kargel, J.S., 1995. Outwash Plains and Thermokarst on Mars. Icarus 114, 93–112. https://doi.org/10.1006/icar.1995.1046

Costard, F., Sejourne, A., Kargel, J., Godin, E., 2016. Modeling and observational occurrences of near-surface drainage in Utopia Planitia, Mars. Geomorphology 275, 80–89. https://doi.org/10.1016/j.geomorph.2016.09.034

Costard, F., Séjourné, A., Kelfoun, K., Clifford, S., Lavigne, F., Di Pietro, I., Bouley, S., 2017. Modeling tsunami propagation and the emplacement of thumbprint terrain in an early Mars ocean. J. Geophys. Res. Planets 122, 633–649. https://doi.org/10.1002/2016JE005230

Coutard, J.P., Mücher, H.J., 1985. Deformation of laminated silt loam due to repeated freezing and thawing cycles. Earth Surf. Process. Landf. 10, 309–319. https://doi.org/10.1002/esp.3290100403

Crater analysis techniques working group, 1979. Standard techniques for presentation and analysis of crater size-frequency data. Icarus 37, 467–474. https://doi.org/10.1016/0019-1035(79)90009-5

Crisp, J.A., Adler, M., Matijevic, J.R., Squyres, S.W., Arvidson, R.E., Kass, D.M., 2003. Mars Exploration Rover mission: MARS EXPLORATION ROVER MISSION. J. Geophys. Res. Planets 108. https://doi.org/10.1029/2002JE002038

Crosta, G.B., De Blasio, F.V., Frattini, P., 2018. Global Scale Analysis of Martian Landslide Mobility and Paleoenvironmental Clues. J. Geophys. Res. Planets 123, 872–891. https://doi.org/10.1002/2017JE005398

Cull, S.C., Arvidson, R.E., Mellon, M., Wiseman, S., Clark, R., Titus, T., Morris, R.V., McGuire, P., 2010a. Seasonal H_2O and CO_2 ice cycles at the Mars Phoenix landing site: 1. Prelanding CRISM and HiRISE observations. J. Geophys. Res. 115, E00D16. https://doi.org/10.1029/2009JE003340

Cull, S.C., Arvidson, R.E., Catalano, J.G., Ming, D.W., Morris, R.V., Mellon, M.T., Lemmon, M., 2010b. Concentrated perchlorate at the Mars Phoenix landing site: Evidence for thin film liquid water on Mars: PHOENIX-CONCENTRATED PERCHLORATE. Geophys. Res. Lett. 37, n/a-n/a. https://doi.org/10.1029/2010GL045269

Czudek, T., Demek, J., 1970. Thermokarst in Siberia and Its Influence on the Development of Lowland Relief. Quat. Res. 1, 103–120. https://doi.org/10.1016/0033-5894(70)90013-X

Dafflon, B., Hubbard, S., Ulrich, C., Peterson, J., Wu, Y., Wainwright, H., Kneafsey, T.J., 2016. Geophysical estimation of shallow permafrost distribution and properties in an ice-wedge polygon-dominated Arctic tundra region. GEOPHYSICS 81, WA247–WA263. https://doi.org/10.1190/geo2015-0175.1

Dahl-Jensen, T., Larsen, L.M., Pedersen, S.A.S., Pedersen, J., Jepsen, H.F., Pedersen, G., Nielsen, T., Pedersen, A.K., Von Platen-Hallermund, F., Weng, W., 2004. Landslide and Tsunami 21 November 2000 in Paatuut, West Greenland. Nat. Hazards 31, 277–287. https://doi.org/10.1023/B:NHAZ.0000020264.70048.95

Daubar, I.J., Dundas, C.M., McEwen, A.S., Gao, A., Wexler, D., Piqueux, S., Collins, G.S., Miljkovic, K., Neidhart, T., Eschenfelder, J., Bart, G.D., Wagstaff, K.L., Doran, G., Posiolova, L., Malin, M., Speth, G., Susko, D., Werynski, A., 2022. New Craters on Mars: An Updated Catalog. J. Geophys. Res. Planets 127. https://doi.org/10.1029/2021JE007145

Davies, M.E., 1974. Photogrammetric measurements of Olympus Mons on Mars. Icarus 21, 230–236. https://doi.org/10.1016/0019-1035(74)90037-2

Davila, A.F., Duport, L.G., Melchiorri, R., Jänchen, J., Valea, S., de los Rios, A., Fairén, A.G., Möhlmann, D., McKay, C.P., Ascaso, C., Wierzchos, J., 2010. Hygroscopic Salts and the Potential for Life on Mars. Astrobiology 10, 617–628. https://doi.org/10.1089/ast.2009.0421

de Haas, T., Nijland, W., McArdell, B.W., Kalthof, M.W.M.L., 2021. Case Report: Optimization of Topographic Change Detection With UAV Structure-From-Motion Photogrammetry Through Survey Co-Alignment. Front. Remote Sens. 2, 626810. https://doi.org/10.3389/frsen.2021.626810

de Hon, R.A., 1992. Polygenetic Origin of Hrad Vallis Region of Mars, in: Proceedings of Lunar and Planetary Science. pp. 45–51.

de Pablo, M., Komatsu, G., 2009. Possible pingo fields in the Utopia basin, Mars: Geological and climatical implications. Icarus 199, 49–74. https://doi.org/10.1016/j.icarus.2008.09.007

De Toffoli, B., Plesa, A. -C., Hauber, E., Breuer, D., 2021. Delta Deposits on Mars: A Global Perspective. Geophys. Res. Lett. 48. https://doi.org/10.1029/2021GL094271

Degenhardt, J.J., 2003. Subsurface investigation of a rock glacier using ground-penetrating radar: Implications for locating stored water on Mars. J. Geophys. Res. 108, 8036. https://doi.org/10.1029/2002JE001888

Delisle, G., Allard, M., Fortier, R., Calmels, F., Larrivée, É., 2003. Umiujaq, northern Québec: innovative techniques to monitor the decay of a lithalsa in response to climate change: Monitoring Permafrost Properties. Permafr. Periglac. Process. 14, 375–385. https://doi.org/10.1002/ppp.469

Dickson, J.L., Head, J.W., 2006. Evidence for an Hesperian-aged South Circum-Polar Lake Margin Environment on Mars. Planet. Space Sci. 54, 251–272. https://doi.org/10.1016/j.pss.2005.12.010

Dickson, J.L., Fassett, C.I., Head, J.W., 2009. Amazonian-aged fluvial valley systems in a climatic microenvironment on Mars: Melting of ice deposits on the interior of Lyot Crater. Geophys. Res. Lett. 36, L08201. https://doi.org/10.1029/2009GL037472

Dickson, J.L., Head, J.W., Marchant, D.R., 2010. Kilometer-thick ice accumulation and glaciation in the northern mid-latitudes of Mars: Evidence for crater-filling events in the Late Amazonian at the Phlegra Montes. Earth Planet. Sci. Lett. 294, 332–342. https://doi.org/10.1016/j.epsl.2009.08.031

Dickson, J.L., Head, J.W., Goudge, T.A., Barbieri, L., 2015. Recent climate cycles on Mars: Stratigraphic relationships between multiple generations of gullies and the latitude dependent mantle. Icarus 252, 83–94. https://doi.org/10.1016/j.icarus.2014.12.035

Dobiński, W., 2011. Permafrost. Earth-Sci. Rev. 108, 158–169. https://doi.org/10.1016/j.earscirev.2011.06.007

Dobiński, W., 2020. Permafrost active layer. Earth-Sci. Rev. 208, 103301. https://doi.org/10.1016/j.earscirev.2020.103301

Dobiński, W., Szafraniec, J.E., Szypuła, B., 2022. Area and borders of Antarctic and permafrost—A review and synthesis. Permafr. Periglac. Process. 34, 37-51. https://doi.org/10.1002/ppp.2170

Dohm, J.M., Anderson, R.C., Barlow, N.G., Miyamoto, H., Davies, A.G., Jeffrey Taylor, G., Baker, V.R., Boynton, W.V., Keller, J., Kerry, K., Janes, D., Fairén, A.G., Schulze-Makuch, D., Glamoclija, M., Marinangeli, L., Ori, G.G., Strom, R.G., Williams, J.-P., Ferris, J.C., Rodríguez, J.A.P., De Pablo, M.A., Karunatillake, S., 2008. Recent geological and hydrological activity on Mars: The Tharsis/Elysium corridor. Planet. Space Sci. 56, 985–1013. https://doi.org/10.1016/j.pss.2008.01.001

Dorren, L.K.A., 2003. A review of rockfall mechanics and modelling approaches. Prog. Phys. Geogr. Earth Environ. 27, 69–87. https://doi.org/10.1191/0309133303pp359ra

Douglas, T.A., Mellon, M.T., 2019. Sublimation of terrestrial permafrost and the implications for ice-loss processes on Mars. Nat. Commun. 10, 1716. https://doi.org/10.1038/s41467-019-09410-8

Dramis, F., Govi, M., Guglielmin, M., Mortara, G., 1995. Mountain permafrost and slope instability in the Italian Alps: The Val Pola Landslide. Permafr. Periglac. Process. 6, 73–81. https://doi.org/10.1002/ppp.3430060108

Dundas, C.M., 2017. Effects of varying obliquity on Martian sublimation thermokarst landforms. Icarus 281, 115–120. https://doi.org/10.1016/j.icarus.2016.08.031

Dundas, C.M., 2020a. An aeolian grainflow model for Martian Recurring Slope Lineae. Icarus 343, 113681. https://doi.org/10.1016/j.icarus.2020.113681

Dundas, C.M., 2020b. Geomorphological evidence for a dry dust avalanche origin of slope streaks on Mars. Nat. Geosci. 13, 473–476. https://doi.org/10.1038/s41561-020-0598-x

Dundas, C.M., Byrne, S., 2010. Modeling sublimation of ice exposed by new impacts in the martian mid-latitudes. Icarus 206, 716–728. https://doi.org/10.1016/j.icarus.2009.09.007

Dundas, C.M., McEwen, A.S., 2010. An assessment of evidence for pingos on Mars using HiRISE. Icarus 205, 244–258. https://doi.org/10.1016/j.icarus.2009.02.020

Dundas, C.M., McEwen, A.S., Diniega, S., Byrne, S., Martinez-Alonso, S., 2010. New and recent gully activity on Mars as seen by HiRISE: RECENT GULLY ACTIVITY ON MARS. Geophys. Res. Lett. 37, n/a-n/a. https://doi.org/10.1029/2009GL041351

Dundas, C.M., Byrne, S., McEwen, A.S., Mellon, M.T., Kennedy, M.R., Daubar, I.J., Saper, L., 2014. HiRISE observations of new impact craters exposing Martian ground ice: ICY CRATERS ON MARS. J. Geophys. Res. Planets 119, 109–127. https://doi.org/10.1002/2013JE004482

Dundas, C.M., Byrne, S., McEwen, A.S., 2015. Modeling the development of martian sublimation thermokarst landforms. Icarus 262, 154–169. https://doi.org/10.1016/j.icarus.2015.07.033

Dundas, C.M., Bramson, A.M., Ojha, L., Wray, J.J., Mellon, M.T., Byrne, S., McEwen, A.S., Putzig, N.E., Viola, D., Sutton, S., Clark, E., Holt, J.W., 2018. Exposed subsurface ice sheets in the Martian mid-latitudes. Science 359, 199–201. https://doi.org/10.1126/science.aao1619

Dundas, C.M., Mellon, M.T., Conway, S.J., Daubar, I.J., Williams, K.E., Ojha, L., Wray, J.J., Bramson, A.M., Byrne, S., McEwen, A.S., Posiolova, L.V., Speth, G., Viola, D., Landis, M.E., Morgan, G.A., Pathare, A.V., 2021. Widespread Exposures of Extensive Clean Shallow Ice in the Midlatitudes of Mars. J. Geophys. Res. Planets 126. https://doi.org/10.1029/2020JE006617

Dundas, C.M., Mellon, M.T., Posiolova, L.V., Miljković, K., Collins, G.S., Tornabene, L.L., Rangarajan, V.G., Golombek, M.P., Warner, N.H., Daubar, I.J., Byrne, S., McEwen, A.S., Seelos, K.D., Viola, D., Bramson, A.M., Speth, G., 2023. A Large New Crater Exposes the Limits of Water Ice on Mars. Geophys. Res. Lett. 50, e2022GL100747. https://doi.org/10.1029/2022GL100747

Dupeyrat, L., Hurault, B., Costard, F., Marmo, C., Gautier, E., 2018. Satellite image analysis and frozen cylinder experiments on thermal erosion of periglacial fluvial islands. Permafr. Periglac. Process. 29, 100–111. https://doi.org/10.1002/ppp.1973

Edgett, K.S., Cantor, B.A., Harrison, T.N., Kennedy, M.R., Lipkaman, L.J., Malin, M.C., Posiolova, L.V., Shean, D.E., 2010. Active and Recent Volcanism and Hydrogeothermal Activity on Mars 42, 34.06.

Ehlmann, B.L., Mustard, J.F., Murchie, S.L., Bibring, J.-P., Meunier, A., Fraeman, A.A., Langevin, Y., 2011. Subsurface water and clay mineral formation during the early history of Mars. Nature 479, 53–60. https://doi.org/10.1038/nature10582

El-Maarry, M.R., Dohm, J.M., Michael, G., Thomas, N., Maruyama, S., 2013. Morphology and evolution of the ejecta of Hale crater in Argyre basin, Mars: Results from high resolution mapping. Icarus 226, 905–922. https://doi.org/10.1016/j.icarus.2013.07.014

Eltner, A., Kaiser, A., Abellan, A., Schindewolf, M., 2017. Time lapse structure-from-motion photogrammetry for continuous geomorphic monitoring: Time-lapse photogrammetry for continuous geomorphic monitoring. Earth Surf. Process. Landf. 42, 2240–2253. https://doi.org/10.1002/esp.4178

Encrenaz, T., Lellouch, E., Rosenqvist, J., Drossart, P., Combes, M., Billebaud, F., de Pater, I., Gulkis, S., Maillard, J.P., Paubert, G., 1991. The atmospheric composition of Mars: ISM and ground-based observational data. Ann. Geophys. 9, 797–803.

Engstrom, R., Hope, A., Kwon, H., Stow, D., 2008. The Relationship Between Soil Moisture and NDVI Near Barrow, Alaska. Physical Geography, 29:1, 38-53. https://doi.org/10.2747/0272-3646.29.1.38

Etzelmüller, B., 2013. Recent Advances in Mountain Permafrost Research: Recent Advances in Mountain Permafrost Research. Permafr. Periglac. Process. 24, 99–107. https://doi.org/10.1002/ppp.1772

Etzelmüller, B., Hoelzle, M., Flo Heggem, E.S., Isaksen, K., Mittaz, C., Mühll, D.V., ødegård, R.S., Haeberli, W., Sollid, J.L., 2001. Mapping and modelling the occurrence and distribution of mountain permafrost. Nor. Geogr. Tidsskr. - Nor. J. Geogr. 55, 186–194. https://doi.org/10.1080/00291950152746513

Ewertowski, M., 2009. Ice-wedge pseudomorphs and frost-cracking structures in Weichselian sediments, central-west Poland. Permafr. Periglac. Process. 20, 316–330. https://doi.org/10.1002/ppp.657

Fairén, A.G., 2010. A cold and wet Mars. Icarus 208, 165–175. https://doi.org/10.1016/j.icarus.2010.01.006

Fairén, A.G., Davila, A.F., Gago-Duport, L., Amils, R., McKay, C.P., 2009. Stability against freezing of aqueous solutions on early Mars. Nature 459, 401–404. https://doi.org/10.1038/nature07978

Farbrot, H., Etzelmüller, B., Schuler, T.V., Guðmundsson, Á., Eiken, T., Humlum, O., Björnsson, H., 2007. Thermal characteristics and impact of climate change on mountain permafrost in Iceland. J. Geophys. Res. 112, F03S90. https://doi.org/10.1029/2006JF000541

Farley, K.A., Williford, K.H., Stack, K.M., Bhartia, R., Chen, A., de la Torre, M., Hand, K., Goreva, Y., Herd, C.D.K., Hueso, R., Liu, Y., Maki, J.N., Martinez, G., Moeller, R.C., Nelessen, A., Newman, C.E., Nunes, D., Ponce, A., Spanovich, N., Willis, P.A., Beegle, L.W., Bell, J.F., Brown, A.J., Hamran, S.-E., Hurowitz, J.A., Maurice, S., Paige, D.A., Rodriguez-Manfredi, J.A., Schulte, M., Wiens, R.C., 2020. Mars 2020 Mission Overview. Space Sci. Rev. 216, 142. https://doi.org/10.1007/s11214-020-00762-y

Fassett, C.I., Dickson, J.L., Head, J.W., Levy, J.S., Marchant, D.R., 2010. Supraglacial and proglacial valleys on Amazonian Mars. Icarus 208, 86–100. https://doi.org/10.1016/j.icarus.2010.02.021

Fassett, C.I., Head, Iii, J.W., 2006. Valleys on Hecates Tholus, Mars: origin by basal melting of summit snowpack. Planet. Space Sci. 54, 370–378. https://doi.org/10.1016/j.pss.2005.12.011

Fassett, C.I., Head, J.W., 2007. Valley formation on martian volcanoes in the Hesperian: Evidence for melting of summit snowpack, caldera lake formation, drainage and erosion on Ceraunius Tholus. Icarus 189, 118–135. https://doi.org/10.1016/j.icarus.2006.12.021

Fassett, C.I., Head, J.W., 2008a. Valley network-fed, open-basin lakes on Mars: Distribution and implications for Noachian surface and subsurface hydrology. Icarus 198, 37–56. https://doi.org/10.1016/j.icarus.2008.06.016

Fassett, C.I., Head, J.W., 2008b. The timing of martian valley network activity: Constraints from buffered crater counting. Icarus 195, 61–89. https://doi.org/10.1016/j.icarus.2007.12.009

Fastook, J.L., Head, J.W., Marchant, D.R., Forget, F., Madeleine, J.-B., 2012. Early Mars climate near the Noachian–Hesperian boundary: Independent evidence for cold conditions from basal melting of the south polar ice sheet (Dorsa Argentea Formation) and implications for valley network formation. Icarus 219, 25–40. https://doi.org/10.1016/j.icarus.2012.02.013

Fastook, J.L., Head, J.W., Marchant, D.R., 2014. Formation of lobate debris aprons on Mars: Assessment of regional ice sheet collapse and debris-cover armoring. Icarus 228, 54–63. https://doi.org/10.1016/j.icarus.2013.09.025

Feldman, W.C., 2004. Global distribution of near-surface hydrogen on Mars. J. Geophys. Res. 109, E09006. https://doi.org/10.1029/2003JE002160

Feldman, W.C., Boynton, W.V., Tokar, R.L., Prettyman, T.H., Gasnault, O., Squyres, S.W., Elphic, R.C., Lawrence, D.J., Lawson, S.L., Maurice, S., McKinney, G.W., Moore, K.R., Reedy, R.C., 2002. Global Distribution of Neutrons from Mars: Results from Mars Odyssey. Science 297, 75–78. https://doi.org/10.1126/science.1073541

Feldman, W.C., Pathare, A., Maurice, S., Prettyman, T.H., Lawrence, D.J., Milliken, R.E., Travis, B.J., 2011. Mars Odyssey neutron data: 2. Search for buried excess water ice deposits at nonpolar latitudes on Mars. J. Geophys. Res. 116, E11009. https://doi.org/10.1029/2011JE003806

Filhol, S., Perret, A., Girod, L., Sutter, G., Schuler, T.V., Burkhart, J.F., 2019. Time-Lapse Photogrammetry of Distributed Snow Depth During Snowmelt. Water Resour. Res. 55, 7916–7926. https://doi.org/10.1029/2018WR024530

Fischer, E., Martínez, G.M., Elliott, H.M., Rennó, N.O., 2014. Experimental evidence for the formation of liquid saline water on Mars. Geophys. Res. Lett. 41, 4456–4462. https://doi.org/10.1002/2014GL060302

Fischer, E., Martínez, G.M., Rennó, N.O., 2016. Formation and Persistence of Brine on Mars: Experimental Simulations throughout the Diurnal Cycle at the Phoenix Landing Site. Astrobiology 16, 937–948. https://doi.org/10.1089/ast.2016.1525

Fischer, L., Kääb, A., Huggel, C., Noetzli, J., 2006. Geology, glacier retreat and permafrost degradation as controlling factors of slope instabilities in a high-mountain rock wall: the Monte Rosa east face. Nat. Hazards Earth Syst. Sci. 6, 761–772. https://doi.org/10.5194/nhess-6-761-2006

Fischer, L., Eisenbeiss, H., Kääb, A., Huggel, C., Haeberli, W., 2011. Monitoring topographic changes in a periglacial high-mountain face using high-resolution DTMs, Monte Rosa East Face, Italian Alps: Topographic Investigation of Steep Periglacial Rock Walls. Permafr. Periglac. Process. 22, 140–152. https://doi.org/10.1002/ppp.717

Fisher, D., 2005. A process to make massive ice in the martian regolith using long-term diffusion and thermal cracking. Icarus 179, 387–397. https://doi.org/10.1016/j.icarus.2005.07.024

Fisher, D., Lacelle, D., Pollard, W., 2022. A possible perchlorate-enabled mechanism for forming thick near surface excess ice layers; in the Amazonian regolith of Mars. Icarus 387, 115198. https://doi.org/10.1016/j.icarus.2022.115198

Fister, W., Goldman, N., Mayer, M., Suter, M., Kuhn, N.J., 2019. Testing of photogrammetry for differentiation of soil organic carbon and biochar in sandy substrates. Geogr. Helvetica 74, 81–91. https://doi.org/10.5194/gh-74-81-2019

Foley, C.N., Wadhwa, M., Borg, L.E., Janney, P.E., Hines, R., Grove, T.L., 2005. The early differentiation history of Mars from 182W-142Nd isotope systematics in the SNC meteorites. Geochim. Cosmochim. Acta 69, 4557–4571. https://doi.org/10.1016/j.gca.2005.05.009

Fonstad, M.A., Dietrich, J.T., Courville, B.C., Jensen, J.L., Carbonneau, P.E., 2013. Topographic structure from motion: a new development in photogrammetric measurement: TOPOGRAPHIC STRUCTURE FROM MOTION. Earth Surf. Process. Landf. 38, 421–430. https://doi.org/10.1002/esp.3366

Forget, F., Haberle, R.M., Montmessin, F., Levrard, B., Head, J.W., 2006. Formation of Glaciers on Mars by Atmospheric Precipitation at High Obliquity. Science 311, 368–371. https://doi.org/10.1126/science.1120335

Forte, E., French, H.M., Raffi, R., Santin, I., Guglielmin, M., 2022. Investigations of polygonal patterned ground in continuous Antarctic permafrost by means of ground penetrating radar and electrical resistivity tomography: Some unexpected correlations. Permafr. Periglac. Process. 33, 226–240. https://doi.org/10.1002/ppp.2156

Fortier, D., Allard, M., Shur, Y., 2007. Observation of rapid drainage system development by thermal erosion of ice wedges on Bylot Island, Canadian Arctic Archipelago. Permafr. Periglac. Process. 18, 229–243. https://doi.org/10.1002/ppp.595

Frappier, R., Lacelle, D., 2021. Distribution, morphometry, and ice content of ice-wedge polygons in Tombstone Territorial Park, central Yukon, Canada. Permafr. Periglac. Process. 32, 587–600. https://doi.org/10.1002/ppp.2123

Fraser, J.K., 1959. Freeze-Thaw Frequencies and Mechanical Weathering in Canada. Arctic 12, 40–53.

French, H.M., 2007. The Periglacial Environment. John Wiley & Sons. Ltd.

French, H.M., 2018. The Periglacial Environment. John Wiley & Sons. Ltd.

French, H.M., 1974. Active Thermokarst Processes, Eastern Banks Island, Western Canadian Arctic. Can. J. Earth Sci. 11, 785–794. https://doi.org/10.1139/e74-078

French, H.M., 1979. Periglacial geomorphology. Prog. Phys. Geogr. Earth Environ. 3, 264–273. https://doi.org/10.1177/030913337900300206

French, H.M., 1987. Periglacial geomorphology in North America: current research and future trends. Prog. Phys. Geogr. Earth Environ. 11, 533–551. https://doi.org/10.1177/030913338701100404

French, H.M., 2000. Does Lozinski's periglacial realm exist today? A discussion relevant to modern usage of the term ?periglacial? Permafr. Periglac. Process. 11, 35–42. https://doi.org/10.1002/(SICI)1099-1530(200001/03)11:1<35::AID-PPP334>3.0.CO;2-6

French, H.M., Guglielmin, M., 2000. Frozen ground phenomena in the vicinity of terra nova bay, northern victoria land, antarctica: a preliminary report. Geogr. Ann. Ser. Phys. Geogr. 82, 513–526. https://doi.org/10.1111/j.0435-3676.2000.00138.x

French, H., Shur, Y., 2010. The principles of cryostratigraphy. Earth-Sci. Rev. 101, 190–206. https://doi.org/10.1016/j.earscirev.2010.04.002

French, H., Thorn, C.E., 2006. The changing nature of periglacial geomorphology. Géomorphologie Relief Process. Environ. 12. https://doi.org/10.4000/geomorphologie.119

French, H.M., Demitroff, M., Forman, S.L., 2003. Evidence for late-Pleistocene permafrost in the New Jersey Pine Barrens(latitude 39°N), eastern USA. Permafr. Periglac. Process. 14, 259–274. https://doi.org/10.1002/ppp.456

Frey, H.V., 2006. Impact constraints on the age and origin of the lowlands of Mars. Geophys. Res. Lett. 33, L08S02. https://doi.org/10.1029/2005GL024484

Frey, H.V., 2008. Ages of very large impact basins on Mars: Implications for the late heavy bombardment in the inner solar system. Geophys. Res. Lett. 35, L13203. https://doi.org/10.1029/2008GL033515

Frey, H.V., Sakimoto, S.E., Roark, J., 1998. The MOLA Topographic signature at the crustal dichotomy boundary zone on Mars. Geophys. Res. Lett. 25, 4409–4412. https://doi.org/10.1029/1998GL900095

Fukusako, S., 1990. Thermophysical properties of ice, snow, and sea ice. Int. J. Thermophys. 11, 353–372. https://doi.org/10.1007/BF01133567

Fuller, E.R., Head, J.W., 2002. Amazonis Planitia: The role of geologically recent volcanism and sedimentation in the formation of the smoothest plains on Mars. J. Geophys. Res. 107, 5081. https://doi.org/10.1029/2002JE001842

Gabrieli, F., Corain, L., Vettore, L., 2016. A low-cost landslide displacement activity assessment from time-lapse photogrammetry and rainfall data: Application to the Tessina landslide site. Geomorphology 269, 56–74. https://doi.org/10.1016/j.geomorph.2016.06.030

Gasda, P.J., Haldeman, E.B., Wiens, R.C., Rapin, W., Bristow, T.F., Bridges, J.C., Schwenzer, S.P., Clark, B., Herkenhoff, K., Frydenvang, J., Lanza, N.L., Maurice, S., Clegg, S., Delapp, D.M., Sanford, V.L., Bodine, M.R., McInroy, R., 2017. In situ detection of boron by ChemCam on Mars: First Detection of Boron on Mars. Geophys. Res. Lett. 44, 8739–8748. https://doi.org/10.1002/2017GL074480

Geertsema, M., Highland, L., Vaugeouis, L., 2009. Environmental Impact of Landslides, in: Sassa, K., Canuti, P. (Eds.), Landslides – Disaster Risk Reduction. Springer Berlin Heidelberg, Berlin, Heidelberg, pp. 589–607. https://doi.org/10.1007/978-3-540-69970-5_31

Geissler, P.E., 2014. The birth and death of transverse aeolian ridges on Mars: Transverse Aeolian Ridges on Mars. J. Geophys. Res. Planets 119, 2583–2599. https://doi.org/10.1002/2014JE004633

Gendrin, A., Mangold, N., Bibring, J.-P., Langevin, Y., Gondet, B., Poulet, F., Bonello, G., Quantin, C., Mustard, J., Arvidson, R., LeMouélic, S., 2005. Sulfates in Martian Layered Terrains: The OMEGA/Mars Express View. Science 307, 1587–1591. https://doi.org/10.1126/science.1109087

Goehring, L., 2013. Evolving fracture patterns: columnar joints, mud cracks and polygonal terrain. Philos. Trans. R. Soc. Math. Phys. Eng. Sci. 371, 20120353. https://doi.org/10.1098/rsta.2012.0353

Golabek, G.J., Keller, T., Gerya, T.V., Zhu, G., Tackley, P.J., Connolly, J.A.D., 2011. Origin of the martian dichotomy and Tharsis from a giant impact causing massive magmatism. Icarus 215, 346–357. https://doi.org/10.1016/j.icarus.2011.06.012

Golombek, M.P., 1997. The Mars Pathfinder Mission. J. Geophys. Res. Planets 102, 3953–3965. https://doi.org/10.1029/96JE02805

Golombek, M.P., Cook, R.A., Economou, T., Folkner, W.M., Haldemann, A.F.C., Kallemeyn, P.H., Knudsen, J.M., Manning, R.M., Moore, H.J., Parker, T.J., Rieder, R., Schofield, J.T., Smith, P.H., Vaughan, R.M., 1997. Overview of the Mars Pathfinder Mission and Assessment of Landing Site Predictions. Science 278, 1743–1748. https://doi.org/10.1126/science.278.5344.1743

Goudge, T.A., Fassett, C.I., Head, J.W., Mustard, J.F., Aureli, K.L., 2016. Insights into surface runoff on early Mars from paleolake basin morphology and stratigraphy. Geology 44, 419–422. https://doi.org/10.1130/G37734.1

Goudge, T.A., Mohrig, D., Cardenas, B.T., Hughes, C.M., Fassett, C.I., 2018. Stratigraphy and paleohydrology of delta channel deposits, Jezero crater, Mars. Icarus 301, 58–75. https://doi.org/10.1016/j.icarus.2017.09.034

Goudge, T.A., Morgan, A.M., Stucky De Quay, G., Fassett, C.I., 2021. The importance of lake breach floods for valley incision on early Mars. Nature 597, 645–649. https://doi.org/10.1038/s41586-021-03860-1

Grab, S., 2005. Aspects of the geomorphology, genesis and environmental significance of earth hummocks (thúfur, pounus): miniature cryogenic mounds. Prog. Phys. Geogr. Earth Environ. 29, 139–155. https://doi.org/10.1191/0309133305pp440ra

Graf, J.E., Zurek, R.W., Eisen, H.J., Jai, B., Johnston, M.D., DePaula, R., 2005. The Mars Reconnaissance Orbiter Mission. Acta Astronaut. 57, 566–578. https://doi.org/10.1016/j.actaastro.2005.03.043

Grant, J.A., Wilson, S.A., 2018. The nature and emplacement of distal aqueous-rich ejecta deposits from Hale crater, Mars. Meteorit. Planet. Sci. 53, 839–856. https://doi.org/10.1111/maps.12843

Grau Galofre, A., Bahia, R.S., Jellinek, A.M., Whipple, K.X., Gallo, R., 2020a. Did Martian valley networks substantially modify the landscape? Earth Planet. Sci. Lett. 547, 116482. https://doi.org/10.1016/j.epsl.2020.116482

Grau Galofre, A., Jellinek, A.M., Osinski, G.R., 2020b. Valley formation on early Mars by subglacial and fluvial erosion. Nat. Geosci. 13, 663–668. https://doi.org/10.1038/s41561-020-0618-x

Greeley, R., Guest, J.E., 1987. Geologic map of the eastern equatorial region of Mars. https://doi.org/10.3133/i1802B

Greeley, R., Spudis, P.D., 1981. Volcanism on Mars. Rev. Geophys. 19, 13. https://doi.org/10.1029/RG019i001p00013

Grima, C., Mouginot, J., Kofman, W., Hérique, A., Beck, P., 2022. The Basal Detectability of an Ice-Covered Mars by MARSIS. Geophys. Res. Lett. 49. https://doi.org/10.1029/2021GL096518

Grosse, G., Jones, B., Arp, C., 2013. 8.21 Thermokarst Lakes, Drainage, and Drained Basins, in: Treatise on Geomorphology. Elsevier, pp. 325–353. https://doi.org/10.1016/B978-0-12-374739-6.00216-5

Grosse, G., Schirrmeister, L., Siegert, C., Kunitsky, V.V., Slagoda, E.A., Andreev, A.A., Dereviagyn, A.Y., 2007. Geological and geomorphological evolution of a sedimentary periglacial landscape in Northeast Siberia during the Late Quaternary. Geomorphology 86, 25–51. https://doi.org/10.1016/j.geomorph.2006.08.005

Grotzinger, J.P., Crisp, J., Vasavada, A.R., Anderson, R.C., Baker, C.J., Barry, R., Blake, D.F., Conrad, P., Edgett, K.S., Ferdowski, B., Gellert, R., Gilbert, J.B., Golombek, M., Gómez-Elvira, J., Hassler, D.M., Jandura, L., Litvak, M., Mahaffy, P., Maki, J., Meyer, M., Malin, M.C., Mitrofanov, I.,

Simmonds, J.J., Vaniman, D., Welch, R.V., Wiens, R.C., 2012. Mars Science Laboratory Mission and Science Investigation. Space Sci. Rev. 170, 5–56. https://doi.org/10.1007/s11214-012-9892-2

Gruber, S., 2020. Ground subsidence and heave over permafrost: hourly time series reveal interannual, seasonal and shorter-term movement caused by freezing, thawing and water movement. The Cryosphere 14, 1437–1447. https://doi.org/10.5194/tc-14-1437-2020

Gruber, S., Haeberli, W., 2007. Permafrost in steep bedrock slopes and its temperature-related destabilization following climate change. J. Geophys. Res. 112, F02S18. https://doi.org/10.1029/2006JF000547

Gruber, S., Haeberli, W., 2009. Mountain Permafrost, in: Margesin, R. (Ed.), Permafrost Soils, Soil Biology. Springer Berlin Heidelberg, Berlin, Heidelberg, pp. 33–44. https://doi.org/10.1007/978-3-540-69371-0_3

Guo, D., Wang, H., 2017. Permafrost degradation and associated ground settlement estimation under 2 °C global warming. Clim. Dyn. 49, 2569–2583. https://doi.org/10.1007/s00382-016-3469-9

Guo, M., Shi, H., Zhao, J., Liu, P., Welbourne, D., Lin, Q., 2016. Digital close range photogrammetry for the study of rill development at flume scale. CATENA 143, 265–274. https://doi.org/10.1016/j.catena.2016.03.036

Guodong, C., 1983. The mechanism of repeated-segregation for the formation of thick layered ground ice. Cold Reg. Sci. Technol. 8, 57–66. https://doi.org/10.1016/0165-232X(83)90017-4

Guodong, C., Dramis, F., 1992. Distribution of mountain permafrost and climate. Permafr. Periglac. Process. 3, 83–91. https://doi.org/10.1002/ppp.3430030205

Gurney, S.D., 1998. Aspects of the genesis and geomorphology of pingos: perennial permafrost mounds. Prog. Phys. Geogr. Earth Environ. 22, 307–324. https://doi.org/10.1177/030913339802200301

Haberle, R.M., McKay, C.P., Schaeffer, J., Cabrol, N.A., Grin, E.A., Zent, A.P., Quinn, R., 2001. On the possibility of liquid water on present-day Mars. J. Geophys. Res. Planets 106, 23317–23326. https://doi.org/10.1029/2000JE001360

Haeberli, W., Guodong, C., Gorbunov, A.P., Harris, S.A., 1993. Mountain permafrost and climatic change. Permafr. Periglac. Process. 4, 165–174. https://doi.org/10.1002/ppp.3430040208

Haeberli, W., Hallet, B., Arenson, L., Elconin, R., Humlum, O., Kääb, A., Kaufmann, V., Ladanyi, B., Matsuoka, N., Springman, S., Mühll, D.V., 2006. Permafrost creep and rock glacier dynamics. Permafr. Periglac. Process. 17, 189–214. https://doi.org/10.1002/ppp.561

Haeberli, W., Noetzli, J., Arenson, L., Delaloye, R., Gärtner-Roer, I., Gruber, S., Isaksen, K., Kneisel, C., Krautblatter, M., Phillips, M., 2010. Mountain permafrost: development and challenges of a young research field. J. Glaciol. 56, 1043–1058. https://doi.org/10.3189/002214311796406121

Haeberli, W., Schaub, Y., Huggel, C., 2017. Increasing risks related to landslides from degrading permafrost into new lakes in de-glaciating mountain ranges. Geomorphology 293, 405–417. https://doi.org/10.1016/j.geomorph.2016.02.009

Hall, K., Thorn, C.E., Matsuoka, N., Prick, A., 2002. Weathering in cold regions: some thoughts and perspectives. Prog. Phys. Geogr. Earth Environ. 26, 577–603. https://doi.org/10.1191/0309133302pp353ra

Hallet, B., Sletten, R., Whilden, K., 2011. Micro-relief development in polygonal patterned ground in the Dry Valleys of Antarctica. Quat. Res. 75, 347–355. https://doi.org/10.1016/j.yqres.2010.12.009

Haltigin, T.W., Pollard, W.H., Dutilleul, P., Osinski, G.R., 2012. Geometric Evolution of Polygonal Terrain Networks in the Canadian High Arctic: Evidence of Increasing Regularity over Time: Polygon Geometry Evolution. Permafr. Periglac. Process. 23, 178–186. https://doi.org/10.1002/ppp.1741

Haltigin, T.W., Pollard, W.H., Dutilleul, P., Osinski, G.R., Koponen, L., 2014. Co-evolution of polygonal and scalloped terrains, southwestern Utopia Planitia, Mars. Earth Planet. Sci. Lett. 387, 44–54. https://doi.org/10.1016/j.epsl.2013.11.005

Hamilton, C.W., Mouginis-Mark, P.J., Sori, M.M., Scheidt, S.P., Bramson, A.M., 2018. Episodes of Aqueous Flooding and Effusive Volcanism Associated With Hrad Vallis, Mars. J. Geophys. Res. Planets 123, 1484–1510. https://doi.org/10.1029/2018JE005543

Hancock, G., Willgoose, G., 2001. The production of digital elevation models for experimental model landscapes. Earth Surf. Process. Landf. 26, 475–490. https://doi.org/10.1002/esp.187

Haneberg, W.C., 2008. Using close range terrestrial digital photogrammetry for 3-D rock slope modeling and discontinuity mapping in the United States. Bull. Eng. Geol. Environ. 67, 457–469. https://doi.org/10.1007/s10064-008-0157-y

Haque, U., Blum, P., Da Silva, P.F., Andersen, P., Pilz, J., Chalov, S.R., Malet, J.-P., Auflič, M.J., Andres, N., Poyiadji, E., Lamas, P.C., Zhang, W., Peshevski, I., Pétursson, H.G., Kurt, T., Dobrev, N., García-Davalillo, J.C., Halkia, M., Ferri, S., Gaprindashvili, G., Engström, J., Keellings, D., 2016. Fatal landslides in Europe. Landslides 13, 1545–1554. https://doi.org/10.1007/s10346-016-0689-3

Hargitai, H., 2014. Viscous Flow Features (Mars), in: Encyclopedia of Planetary Landforms. Springer New York, New York, NY, pp. 1–4. https://doi.org/10.1007/978-1-4614-9213-9_596-1

Harris, C., 1996. Physical modelling of periglacial solifluction: Review and future strategy. Permafr. Periglac. Process. 7, 349–360. https://doi.org/10.1002/(SICI)1099-1530(199610)7:4<349::AID-PPP235>3.0.CO;2-O

Harris, C., Arenson, L.U., Christiansen, H.H., Etzelmüller, B., Frauenfelder, R., Gruber, S., Haeberli, W., Hauck, C., Hölzle, M., Humlum, O., Isaksen, K., Kääb, A., Kern-Lütschg, M.A., Lehning, M., Matsuoka, N., Murton, J.B., Nötzli, J., Phillips, M., Ross, N., Seppälä, M., Springman, S.M., Vonder Mühll, D., 2009. Permafrost and climate in Europe: Monitoring and modelling thermal, geomorphological and geotechnical responses. Earth-Sci. Rev. 92, 117–171. https://doi.org/10.1016/j.earscirev.2008.12.002

Harris, C., Davies, M.C.R., Etzelmüller, B., 2001. The assessment of potential geotechnical hazards associated with mountain permafrost in a warming global climate: Potential Geotechnical Hazards. Permafr. Periglac. Process. 12, 145–156. https://doi.org/10.1002/ppp.376

Harris, C., Davies, M.C.R., Rea, B.R., 2003. Gelifluction: viscous flow or plastic creep? Earth Surf. Process. Landf. 28, 1289–1301. https://doi.org/10.1002/esp.543

Harrison, K.P., Chapman, M.G., 2008. Evidence for ponding and catastrophic floods in central Valles Marineris, Mars. Icarus 198, 351–364. https://doi.org/10.1016/j.icarus.2008.08.003

Harrison, K.P., Grimm, R.E., 2005. Groundwater-controlled valley networks and the decline of surface runoff on early Mars. J. Geophys. Res. 110, E12S16. https://doi.org/10.1029/2005JE002455

Harry, D.G., Gozdzik, J.S., 1988. Ice wedges: Growth, thaw transformation, and palaeoenvironmental significance. J. Quat. Sci. 3, 39–55. https://doi.org/10.1002/jqs.3390030107

Hartmann, W.K., 1971. Martian cratering III: Theory of crater obliteration. Icarus 15, 410–428. https://doi.org/10.1016/0019-1035(71)90119-9

Hartmann, W.K., 1977. Relative crater production rates on planets. Icarus 31, 260–276. https://doi.org/10.1016/0019-1035(77)90037-9

Hartmann, W.K., 2005. Martian cratering 8: Isochron refinement and the chronology of Mars. Icarus 174, 294–320. https://doi.org/10.1016/j.icarus.2004.11.023

Hartmann, W.K., Neukum, G., 2001. Cratering Chronology and the Evolution of Mars, in: Kallenbach, R., Geiss, J., Hartmann, W.K. (Eds.), Chronology and Evolution of Mars, Space Sciences Series of ISSI. Springer Netherlands, Dordrecht, pp. 165–194. https://doi.org/10.1007/978-94-017-1035-0_6

Hauber, E., Brož, P., Jagert, F., Jodłowski, P., Platz, T., 2011a. Very recent and wide-spread basaltic volcanism on Mars: RECENT WIDE-SPREAD VOLCANISM ON MARS. Geophys. Res. Lett. 38, n/a-n/a. https://doi.org/10.1029/2011GL047310

Hauber, E., Reiss, D., Ulrich, M., Preusker, F., Trauthan, F., Zanetti, M., Hiesinger, H., Jaumann, R., Johansson, L., Johnsson, A., Olvmo, M., Carlsson, E., Johansson, H.A.B., McDaniel, S., 2011b. Periglacial landscapes on Svalbard: Terrestrial analogs for cold-climate landforms on Mars, in: Analogs for Planetary Exploration. Geological Society of America. https://doi.org/10.1130/2011.2483(12)

Hayward, R.K., Mullins, K.F., Fenton, L.K., Hare, T.M., Titus, T.N., Bourke, M.C., Colaprete, A., Christensen, P.R., 2007. Mars Global Digital Dune Database and initial science results. J. Geophys. Res. 112, E11007. https://doi.org/10.1029/2007JE002943

Head, J.W., Marchant, D.R., 2003. Cold-based mountain glaciers on Mars: Western Arsia Mons. Geology 31, 641. https://doi.org/10.1130/0091-7613(2003)031<0641:CMGOMW>2.0.CO;2

Head, J.W., Pratt, S., 2001. Extensive Hesperian-aged south polar ice sheet on Mars: Evidence for massive melting and retreat, and lateral flow and ponding of meltwater. J. Geophys. Res. Planets 106, 12275–12299. https://doi.org/10.1029/2000JE001359

Head, J.W., Marchant, D.R., Agnew, M.C., Fassett, C.I., Kreslavsky, M.A., 2006. Extensive valley glacier deposits in the northern mid-latitudes of Mars: Evidence for Late Amazonian obliquity-driven climate change. Earth Planet. Sci. Lett. 241, 663–671. https://doi.org/10.1016/j.epsl.2005.11.016

Head, J.W., Mustard, J.F., Kreslavsky, M.A., Milliken, R.E., Marchant, D.R., 2003. Recent ice ages on Mars. Nature 426, 797–802. https://doi.org/10.1038/nature02114

Head, J.W., Neukum, G., Jaumann, R., Hiesinger, H., Hauber, E., Carr, M., Masson, P., Foing, B., Hoffmann, H., Kreslavsky, M., Werner, S., Milkovich, S., Van Gasselt, S., The HRSC Co-Investigator Team, 2005. Tropical to mid-latitude snow and ice accumulation, flow and glaciation on Mars. Nature 434, 346–351. https://doi.org/10.1038/nature03359

Head, J.W., Marchant, D.R., Dickson, J.L., Kress, A.M., Baker, D.M., 2010. Northern mid-latitude glaciation in the Late Amazonian period of Mars: Criteria for the recognition of debris-covered glacier and valley glacier landsystem deposits. Earth Planet. Sci. Lett. 294, 306–320. https://doi.org/10.1016/j.epsl.2009.06.041

Hecht, M., 2002. Metastability of Liquid Water on Mars. Icarus 156, 373–386. https://doi.org/10.1006/icar.2001.6794

Hecht, M. H., Kounaves, S.P., Quinn, R.C., West, S.J., Young, S.M.M., Ming, D.W., Catling, D.C., Clark, B.C., Boynton, W.V., Hoffman, J., DeFlores, L.P., Gospodinova, K., Kapit, J., Smith, P.H., 2009. Detection of Perchlorate and the Soluble Chemistry of Martian Soil at the Phoenix Lander Site. Science 325, 64–67. https://doi.org/10.1126/science.1172466

Heginbottom, J.A., 2002. Permafrost mapping: a review. Prog. Phys. Geogr. Earth Environ. 26, 623–642. https://doi.org/10.1191/0309133302pp355ra

Heritage, G., Hetherington, D., 2007. Towards a protocol for laser scanning in fluvial geomorphology. Earth Surf. Process. Landf. 32, 66–74. https://doi.org/10.1002/esp.1375

Herny, C., Conway, S.J., Raack, J., Carpy, S., Colleu-Banse, T., Patel, M.R., 2019. Downslope sediment transport by boiling liquid water under Mars-like conditions: experiments and potential implications for Martian gullies. Geol. Soc. Lond. Spec. Publ. 467, 373–410. https://doi.org/10.1144/SP467.10

Hess, S.L., Henry, R.M., Leovy, C.B., Ryan, J.A., Tillman, J.E., 1977. Meteorological results from the surface of Mars: Viking 1 and 2. J. Geophys. Res. 82, 4559–4574. https://doi.org/10.1029/JS082i028p04559

Hess, S.L., Ryan, J.A., Tillman, J.E., Henry, R.M., Leovy, C.B., 1980. The annual cycle of pressure on Mars measured by Viking Landers 1 and 2. Geophys. Res. Lett. 7, 197–200. https://doi.org/10.1029/GL007i003p00197

Hibbard, S.M., Williams, N.R., Golombek, M.P., Osinski, G.R., Godin, E., 2021. Evidence for widespread glaciation in Arcadia Planitia, Mars. Icarus 359, 114298. https://doi.org/10.1016/j.icarus.2020.114298

Hiesinger, H., Head, J.W., 2000. Characteristics and origin of polygonal terrain in southern Utopia Planitia, Mars: Results from Mars Orbiter Laser Altimeter and Mars Orbiter Camera data. J. Geophys. Res. Planets 105, 11999–12022. https://doi.org/10.1029/1999JE001193

Hinzman, L.D., Kane, D.L., Gieck, R.E., Everett, K.R., 1991. Hydrologic and thermal properties of the active layer in the Alaskan Arctic. Cold Reg. Sci. Technol. 19, 95–110. https://doi.org/10.1016/0165-232X(91)90001-W

Hinzman, L.D., Kane, D.L., Woo, M., 2005. Permafrost Hydrology, in: Anderson, M.G., McDonnell, J.J. (Eds.), Encyclopedia of Hydrological Sciences. John Wiley & Sons, Ltd, Chichester, UK, p. hsa178. https://doi.org/10.1002/0470848944.hsa178

Hjort, J., Streletskiy, D., Doré, G., Wu, Q., Bjella, K., Luoto, M., 2022. Impacts of permafrost degradation on infrastructure. Nat. Rev. Earth Environ. 3, 24–38. https://doi.org/10.1038/s43017-021-00247-8

Hoekstra, P., 1969. Water Movement and Freezing Pressures. Soil Sci. Soc. Am. J. 33, 512–518. https://doi.org/10.2136/sssaj1969.03615995003300040011x

Holo, S.J., Kite, E.S., Wilson, S.A., Morgan, A.M., 2021. The Timing of Alluvial Fan Formation on Mars. Planet. Sci. J. 2, 210. https://doi.org/10.3847/PSJ/ac25ed

Holt, J.W., Safaeinili, A., Plaut, J.J., Head, J.W., Phillips, R.J., Seu, R., Kempf, S.D., Choudhary, P., Young, D.A., Putzig, N.E., Biccari, D., Gim, Y., 2008. Radar Sounding Evidence for Buried Glaciers in the Southern Mid-Latitudes of Mars. Science 322, 1235–1238. https://doi.org/10.1126/science.1164246

Hong, E., Perkins, R., Trainor, S., 2014. Thaw Settlement Hazard of Permafrost Related to Climate Warming in Alaska. ARCTIC 67, 93. https://doi.org/10.14430/arctic4368

Hopper, J.P., Leverington, D.W., 2014. Formation of Hrad Vallis (Mars) by low viscosity lava flows. Geomorphology 207, 96–113. https://doi.org/10.1016/j.geomorph.2013.10.029

Howard, A.D., Irwin, R.P., Craddock, R.A., Moore, J.M., 2005. An intense terminal epoch of widespread fluvial activity on early Mars: 2. Increased runoff and paleolake development. J. Geophys. Res. 110, E12S15. https://doi.org/10.1029/2005JE002460

Howard, A.D., Moore, J.M., 2011. Late Hesperian to early Amazonian midlatitude Martian valleys: Evidence from Newton and Gorgonum basins. J. Geophys. Res. 116, E05003. https://doi.org/10.1029/2010JE003782

Hu, J., Liu, E., Yu, J., 2021. Application of Structural Deformation Monitoring Based on Close-Range Photogrammetry Technology. Adv. Civ. Eng. 2021, 1–11. https://doi.org/10.1155/2021/6621440

Hudson, T.L., Aharonson, O., Schorghofer, N., 2009. Laboratory experiments and models of diffusive emplacement of ground ice on Mars. J. Geophys. Res. 114, E01002. https://doi.org/10.1029/2008JE003149

Hughson, K.H.G., Russell, C.T., Williams, D.A., Buczkowski, D.L., Mest, S.C., Pasckert, J.H., Scully, J.E.C., Combe, J.-P., Platz, T., Ruesch, O., Preusker, F., Jaumann, R., Nass, A., Roatsch, T., Nathues, A., Schaefer, M., Schmidt, B.E., Chilton, H.T., Ermakov, A., Singh, S., McFadden, L.A., Raymond, C.A., 2018. The Ac-5 (Fejokoo) quadrangle of Ceres: Geologic map and geomorphological evidence for ground ice mediated surface processes. Icarus 316, 63–83. https://doi.org/10.1016/j.icarus.2017.09.035

Hussey, K.M., Michelson, R.W., 1966. Tundra Relief Features near Point Barrow, Alaska. Arctic 19, 162–184.

Hynek, B.M., Beach, M., Hoke, M.R.T., 2010. Updated global map of Martian valley networks and implications for climate and hydrologic processes. J. Geophys. Res. 115, E09008. https://doi.org/10.1029/2009JE003548

Ingersoll, A.P., Svitek, T., Murray, B.C., 1992. Stability of polar frosts in spherical bowl-shaped craters on the Moon, Mercury, and Mars. Icarus 100, 40–47. https://doi.org/10.1016/0019-1035(92)90016-Z

Irwin, R.P., 2002. Drainage basin evolution in Noachian Terra Cimmeria, Mars. J. Geophys. Res. 107, 5056. https://doi.org/10.1029/2001JE001818

Irwin, R.P., 2004. Geomorphology of Ma'adim Vallis, Mars, and associated paleolake basins. J. Geophys. Res. 109, E12009. https://doi.org/10.1029/2004JE002287

Irwin, R.P., Watters, T.R., 2010. Geology of the Martian crustal dichotomy boundary: Age, modifications, and implications for modeling efforts. J. Geophys. Res. 115, E11006. https://doi.org/10.1029/2010JE003658

Irwin, R.P., Howard, A.D., Craddock, R.A., Moore, J.M., 2005. An intense terminal epoch of widespread fluvial activity on early Mars: 2. Increased runoff and paleolake development. J. Geophys. Res. 110, E12S15. https://doi.org/10.1029/2005JE002460

Ivanov, B.A., 2001. Mars/Moon Cratering Rate Ratio Estimates. Space Sci. Rev. 96, 87–104. https://doi.org/10.1023/A:1011941121102

Ivanov, M.A., Hiesinger, H., Erkeling, G., Reiss, D., 2014. Mud volcanism and morphology of impact craters in Utopia Planitia on Mars: Evidence for the ancient ocean. Icarus 228, 121–140. https://doi.org/10.1016/j.icarus.2013.09.018

Ivanov, M.A., Hiesinger, H., Erkeling, G., Reiss, D., 2015. Evidence for large reservoirs of water/mud in Utopia and Acidalia Planitiae on Mars. Icarus 248, 383–391. https://doi.org/10.1016/j.icarus.2014.11.013

Jakosky, B.M., 1985. The seasonal cycle of water on Mars. Space Sci. Rev. 41. https://doi.org/10.1007/BF00241348

Jakosky, B.M., Carr, M.H., 1985. Possible precipitation of ice at low latitudes of Mars during periods of high obliquity. Nature 315, 559–561. https://doi.org/10.1038/315559a0

Jakosky, B.M., Farmer, C.B., 1982. The seasonal and global behavior of water vapor in the Mars atmosphere: Complete global results of the Viking Atmospheric Water Detector Experiment. J. Geophys. Res. 87, 2999. https://doi.org/10.1029/JB087iB04p02999

Jakosky, B.M., Phillips, R.J., 2001. Mars' volatile and climate history. Nature 412, 237–244. https://doi.org/10.1038/35084184

Jakosky, B.M., Grebowsky, J.M., Luhmann, J.G., Brain, D.A., 2015a. Initial results from the MAVEN mission to Mars: Results From the MAVEN Mission. Geophys. Res. Lett. 42, 8791–8802. https://doi.org/10.1002/2015GL065271

Jakosky, B.M., Lin, R.P., Grebowsky, J.M., Luhmann, J.G., Mitchell, D.F., Beutelschies, G., Priser, T., Acuna, M., Andersson, L., Baird, D., Baker, D., Bartlett, R., Benna, M., Bougher, S., Brain, D., Carson, D., Cauffman, S., Chamberlin, P., Chaufray, J.-Y., Cheatom, O., Clarke, J., Connerney, J., Cravens, T., Curtis, D., Delory, G., Demcak, S., DeWolfe, A., Eparvier, F., Ergun, R., Eriksson, A., Espley, J., Fang, X., Folta, D., Fox, J., Gomez-Rosa, C., Habenicht, S., Halekas, J., Holsclaw, G., Houghton, M., Howard, R., Jarosz, M., Jedrich, N., Johnson, M., Kasprzak, W., Kelley, M., King, T., Lankton, M., Larson, D., Leblanc, F., Lefevre, F., Lillis, R., Mahaffy, P., Mazelle, C., McClintock, W., McFadden, J., Mitchell, D.L., Montmessin, F., Morrissey, J., Peterson, W., Possel, W., Sauvaud, J.-A., Schneider, N., Sidney, W., Sparacino, S., Stewart, A.I.F., Tolson, R., Toublanc, D., Waters, C., Woods, T., Yelle, R., Zurek, R., 2015b. The Mars Atmosphere and Volatile Evolution (MAVEN) Mission. Space Sci. Rev. 195, 3–48. https://doi.org/10.1007/s11214-015-0139-x

Jakosky, B.M., Mellon, M., Varnes, E., Feldman, W., Boynton, W., Haberle, R., 2005. Mars low-latitude neutron distribution: Possible remnant near-surface water ice and a mechanism for its recent emplacement. Icarus 175, 58–67. https://doi.org/10.1016/j.icarus.2004.11.014

James, P.B., North, G.R., 1982. The seasonal CO_2 cycle on Mars: An application of an energy balance climate model. J. Geophys. Res. 87, 10271. https://doi.org/10.1029/JB087iB12p10271

James, P.B., Kieffer, H.H., Paige, D.A., 1992. The seasonal cycle of carbon dioxide on Mars., Mars.

Johnson, C.L., Phillips, R.J., 2005. Evolution of the Tharsis region of Mars: insights from magnetic field observations. Earth Planet. Sci. Lett. 230, 241–254. https://doi.org/10.1016/j.epsl.2004.10.038

Jones, A.F., Brewer, P.A., Johnstone, E., Macklin, M.G., 2007. High-resolution interpretative geomorphological mapping of river valley environments using airborne LiDAR data. Earth Surf. Process. Landf. 32, 1574–1592. https://doi.org/10.1002/esp.1505

Jones, A.P., McEwen, A.S., Tornabene, L.L., Baker, V.R., Melosh, H.J., Berman, D.C., 2011. A geomorphic analysis of Hale crater, Mars: The effects of impact into ice-rich crust. Icarus 211, 259–272. https://doi.org/10.1016/j.icarus.2010.10.014

Jordan, R., Picardi, G., Plaut, J., Wheeler, K., Kirchner, D., Safaeinili, A., Johnson, W., Seu, R., Calabrese, D., Zampolini, E., Cicchetti, A., Huff, R., Gurnett, D., Ivanov, A., Kofman, W., Orosei, R., Thompson, T., Edenhofer, P., Bombaci, O., 2009. The Mars express MARSIS sounder instrument. Planet. Space Sci. 57, 1975–1986. https://doi.org/10.1016/j.pss.2009.09.016

Jorgenson, M.T., Romanovsky, V., Harden, J., Shur, Y., O'Donnell, J., Schuur, E.A.G., Kanevskiy, M., Marchenko, S., 2010. Resilience and vulnerability of permafrost to climate changeThis article is one of a selection of papers from The Dynamics of Change in Alaska's Boreal Forests: Resilience

and Vulnerability in Response to Climate Warming. Can. J. For. Res. 40, 1219–1236. https://doi.org/10.1139/X10-060

Jouannic, G., Gargani, J., Conway, S.J., Costard, F., Balme, M.R., Patel, M.R., Massé, M., Marmo, C., Jomelli, V., Ori, G.G., 2015. Laboratory simulation of debris flows over sand dunes: Insights into gully-formation (Mars). Geomorphology 231, 101–115. https://doi.org/10.1016/j.geomorph.2014.12.007

Kahre, M.A., Haberle, R.M., 2010. Mars CO2 cycle: Effects of airborne dust and polar cap ice emissivity. Icarus 207, 648–653. https://doi.org/10.1016/j.icarus.2009.12.016

Kamada, A., Kuroda, T., Kasaba, Y., Terada, N., Nakagawa, H., 2021. Global climate and river transport simulations of early Mars around the Noachian and Hesperian boundary. Icarus 368, 114618. https://doi.org/10.1016/j.icarus.2021.114618

Kane, D.L., Hinzman, L.D., Zarling, J.P., 1991. Thermal response of the active layer to climatic warming in a permafrost environment. Cold Reg. Sci. Technol. 19, 111–122. https://doi.org/10.1016/0165-232X(91)90002-X

Kanevskiy, M., Shur, Y., Fortier, D., Jorgenson, M.T., Stephani, E., 2011. Cryostratigraphy of late Pleistocene syngenetic permafrost (yedoma) in northern Alaska, Itkillik River exposure. Quat. Res. 75, 584–596. https://doi.org/10.1016/j.yqres.2010.12.003

Kanevskiy, M., Shur, Y., Jorgenson, T., Brown, D.R.N., Moskalenko, N., Brown, J., Walker, D.A., Raynolds, M.K., Buchhorn, M., 2017. Degradation and stabilization of ice wedges: Implications for assessing risk of thermokarst in northern Alaska. Geomorphology 297, 20–42. https://doi.org/10.1016/j.geomorph.2017.09.001

Kargel, J.S., Baker, V.R., Begét, J.E., Lockwood, J.F., Péwé, T.L., Shaw, J.S., Strom, R.G., 1995. Evidence of ancient continental glaciation in the Martian northern plains. J. Geophys. Res. 100, 5351. https://doi.org/10.1029/94JE02447

Keller, T., Tackley, P.J., 2009. Towards self-consistent modeling of the martian dichotomy: The influence of one-ridge convection on crustal thickness distribution. Icarus 202, 429–443. https://doi.org/10.1016/j.icarus.2009.03.029

Kellerer-Pirklbauer, A., Lieb, G.K., Avian, M., Carrivick, J., 2012. Climate change and rock fall events in high mountain areas: numerous and extensive rock falls in 2007 at mittlerer burgstall, central austria. Geogr. Ann. Ser. Phys. Geogr. 94, 59–78. https://doi.org/10.1111/j.1468-0459.2011.00449.x

Khuller, A.R., Plaut, J.J., 2021. Characteristics of the Basal Interface of the Martian South Polar Layered Deposits. Geophys. Res. Lett. 48. https://doi.org/10.1029/2021GL093631

King, J.S., Riehle, J.R., 1974. A proposed origin of the olympus Mons escarpment. Icarus 23, 300–317. https://doi.org/10.1016/0019-1035(74)90008-6

Kite, E.S., 2019. Geologic Constraints on Early Mars Climate. Space Sci. Rev. 215, 10. https://doi.org/10.1007/s11214-018-0575-5

Kite, E.S., Mayer, D.P., 2017. Mars sedimentary rock erosion rates constrained using crater counts, with applications to organic-matter preservation and to the global dust cycle. Icarus 286, 212–222. https://doi.org/10.1016/j.icarus.2016.10.010

Kite, E.S., Sneed, J., Mayer, D.P., Wilson, S.A., 2017. Persistent or repeated surface habitability on Mars during the late Hesperian - Amazonian. Geophys. Res. Lett. 44, 3991–3999. https://doi.org/10.1002/2017GL072660

Kjekstad, O., Highland, L., 2009. Economic and Social Impacts of Landslides, in: Sassa, K., Canuti, P. (Eds.), Landslides – Disaster Risk Reduction. Springer Berlin Heidelberg, Berlin, Heidelberg, pp. 573–587. https://doi.org/10.1007/978-3-540-69970-5_30

Klein, H.P., 1978. The Viking biological experiments on Mars. Icarus 34, 666–674. https://doi.org/10.1016/0019-1035(78)90053-2

Klein, H.P., 1979. The Viking mission and the search for life on Mars. Rev. Geophys. 17, 1655. https://doi.org/10.1029/RG017i007p01655

Kleine, T., Münker, C., Mezger, K., Palme, H., 2002. Rapid accretion and early core formation on asteroids and the terrestrial planets from Hf–W chronometry. Nature 418, 952–955. https://doi.org/10.1038/nature00982

Knapmeyer-Endrun, B., Panning, M.P., Bissig, F., Joshi, R., Khan, A., Kim, D., Lekić, V., Tauzin, B., Tharimena, S., Plasman, M., Compaire, N., Garcia, R.F., Margerin, L., Schimmel, M., Stutzmann, É., Schmerr, N., Bozdağ, E., Plesa, A.-C., Wieczorek, M.A., Broquet, A., Antonangeli, D., McLennan, S.M., Samuel, H., Michaut, C., Pan, L., Smrekar, S.E., Johnson, C.L., Brinkman, N., Mittelholz, A., Rivoldini, A., Davis, P.M., Lognonné, P., Pinot, B., Scholz, J.-R., Stähler, S., Knapmeyer, M., Van Driel, M., Giardini, D., Banerdt, W.B., 2021. Thickness and structure of the martian crust from InSight seismic data. Science 373, 438–443. https://doi.org/10.1126/science.abf8966

Kneissl, T., van Gasselt, S., Neukum, G., 2011. Map-projection-independent crater size-frequency determination in GIS environments—New software tool for ArcGIS. Planet. Space Sci. 59, 1243–1254. https://doi.org/10.1016/j.pss.2010.03.015

Kneissl, T., Michael, G.G., Platz, T., Walter, S.H.G., 2015. Age determination of linear surface features using the Buffered Crater Counting approach – Case studies of the Sirenum and Fortuna Fossae graben systems on Mars. Icarus 250, 384–394. https://doi.org/10.1016/j.icarus.2014.12.008

Koch, L., 1926. Ice Cap and Sea Ice in North Greenland. Geogr. Rev. 16, 98. https://doi.org/10.2307/208506

Kokelj, S.V., Burn, C.R., 2004. Tilt of Spruce Trees near Ice Wedges, Mackenzie Delta, Northwest Territories, Canada. Arct. Antarct. Alp. Res. 36, 615–623. https://doi.org/10.1657/1523-0430(2004)036[0615:TOSTNI]2.0.CO;2

Kokelj, S.V., Jorgenson, M.T., 2013. Advances in Thermokarst Research: Recent Advances in Research Investigating Thermokarst Processes. Permafr. Periglac. Process. 24, 108–119. https://doi.org/10.1002/ppp.1779

Konrad, J.-M., 1999. Frost susceptibility related to soil index properties. Can. Geotech. J. 36, 403–417. https://doi.org/10.1139/t99-008

Konrad, J.-M., Morgenstern, N.R., 1980. A mechanistic theory of ice lens formation in fine-grained soils. Can. Geotech. J. 17, 473–486. https://doi.org/10.1139/t80-056

Kostama, V. -P., Kreslavsky, M.A., Head, J.W., 2006. Recent high-latitude icy mantle in the northern plains of Mars: Characteristics and ages of emplacement. Geophys. Res. Lett. 33, 2006GL025946. https://doi.org/10.1029/2006GL025946

Koster, E.A., 1988. Ancient and modern cold-climate aeolian sand deposition: A review. J. Quat. Sci. 3, 69–83. https://doi.org/10.1002/jqs.3390030109

Krautblatter, M., Funk, D., Günzel, F.K., 2013. Why permafrost rocks become unstable: a rock-ice-mechanical model in time and space: A ROCK-ICE-MECHANICAL MODEL FOR PERMAFROST ROCKS. Earth Surf. Process. Landf. 38, 876–887. https://doi.org/10.1002/esp.3374

Kreslavsky, M.A., 2022. Seasonal Brine Formation in Shallow Subsurface on Mars. Presented at the Lunar and Planetary Science Conference, LPI Contribution, The Woodlands, Texas. https://doi.org/2022LPICo2678.2628K

Kreslavsky, M.A., Head, J.W., 2002. Mars: Nature and evolution of young latitude-dependent water-ice-rich mantle: MARS. Geophys. Res. Lett. 29, 14-1-14–4. https://doi.org/10.1029/2002GL015392

Kress, A.M., Head, J.W., 2008. Ring-mold craters in lineated valley fill and lobate debris aprons on Mars: Evidence for subsurface glacial ice. Geophys. Res. Lett. 35, L23206. https://doi.org/10.1029/2008GL035501

Kromer, R., Walton, G., Gray, B., Lato, M., Group, R., 2019. Development and Optimization of an Automated Fixed-Location Time Lapse Photogrammetric Rock Slope Monitoring System. Remote Sens. 11, 1890. https://doi.org/10.3390/rs11161890

Kuzmin, R.O., Zabalueva, E.V., Mitrofanov, I.G., Litvak, M.L., Boynton, W.V., Saunders, R.S., 2004. Regions of Potential Existence of Free Water (Ice) in the Near-Surface Martian Ground: Results

from the Mars Odyssey High-Energy Neutron Detector (HEND). Sol. Syst. Res. 38, 1–11. https://doi.org/10.1023/B:SOLS.0000015150.61420.5b

La Placa, S.J., Post, B., 1960. Thermal expansion of ice. Acta Crystallogr. 13, 503–505. https://doi.org/10.1107/S0365110X60001205

Lachenbruch, A. H., 1962. Mechanics of Thermal Contraction Cracks and Ice-Wedge Polygons in Permafrost, in: Geological Society of America Special Papers. Geological Society of America, pp. 1–66. https://doi.org/10.1130/SPE70-p1

Lane, S.N., James, T.D., Crowell, M.D., 2000. Application of Digital Photogrammetry to Complex Topography for Geomorphological Research. Photogramm. Rec. 16, 793–821. https://doi.org/10.1111/0031-868X.00152

Lane, S.N., Chandler, J.H., Porfiri, K., 2001. Monitoring River Channel and Flume Surfaces with Digital Photogrammetry. J. Hydraul. Eng. 127, 871–877. https://doi.org/10.1061/(ASCE)0733-9429(2001)127:10(871)

Lanman, D., Crispell, D., Taubin, G., 2009. Surround structured lighting: 3-D scanning with orthographic illumination. Comput. Vis. Image Underst. 113, 1107–1117. https://doi.org/10.1016/j.cviu.2009.03.016

Lantz, T.C., Kokelj, S.V., 2008. Increasing rates of retrogressive thaw slump activity in the Mackenzie Delta region, N.W.T., Canada. Geophys. Res. Lett. 35, L06502. https://doi.org/10.1029/2007GL032433

Laskar, J., Correia, A.C.M., Gastineau, M., Joutel, F., Levrard, B., Robutel, P., 2004. Long term evolution and chaotic diffusion of the insolation quantities of Mars. Icarus 170, 343–364. https://doi.org/10.1016/j.icarus.2004.04.005

Lauro, S.E., Pettinelli, E., Caprarelli, G., Guallini, L., Rossi, A.P., Mattei, E., Cosciotti, B., Cicchetti, A., Soldovieri, F., Cartacci, M., Di Paolo, F., Noschese, R., Orosei, R., 2020. Multiple subglacial water bodies below the south pole of Mars unveiled by new MARSIS data. Nat. Astron. 5, 63–70. https://doi.org/10.1038/s41550-020-1200-6

Lawler, D.M., 1988. A bibliography of needle ice. Cold Reg. Sci. Technol. 15, 295–310. https://doi.org/10.1016/0165-232X(88)90076-6

Leffingwell, E.D.K., 1915. Ground-Ice Wedges: The Dominant Form of Ground-Ice on the North Coast of Alaska. J. Geol. 23, 635–654. https://doi.org/10.1086/622281

Lefort, A., Russell, P.S., Thomas, N., McEwen, A.S., Dundas, C.M., Kirk, R.L., 2009. Observations of periglacial landforms in Utopia Planitia with the High Resolution Imaging Science Experiment (HiRISE). J. Geophys. Res. 114, E04005. https://doi.org/10.1029/2008JE003264

Leighton, R.B., Murray, B.C., Sharp, R.P., Allen, J.D., Sloan, R.K., 1965. Mariner IV Photography of Mars: Initial Results. Science 149, 627–630. https://doi.org/10.1126/science.149.3684.627

Leighton, R.B., Horowitz, N.H., Murray, B.C., Sharp, R.P., Herriman, A.G., Young, A.T., Smith, B.A., Davies, M.E., Leovy, C.B., 1969a. Mariner 6 Television Pictures: First Report. Science 165, 685–690. https://doi.org/10.1126/science.165.3894.685

Leighton, R.B., Horowitz, N.H., Murray, B.C., Sharp, R.P., Herriman, A.H., Young, A.T., Smith, B.A., Davies, M.E., Leovy, C.B., 1969b. Mariner 6 and 7 Television Pictures: Preliminary Analysis. Science 166, 49–67. https://doi.org/10.1126/science.166.3901.49

Lelandais, T., Mourgues, R., Ravier, É., Pochat, S., Strzerzynski, P., Bourgeois, O., 2016. Experimental modeling of pressurized subglacial water flow: Implications for tunnel valley formation: Experimental Modeling of Tunnel Valleys. J. Geophys. Res. Earth Surf. 121, 2022–2041. https://doi.org/10.1002/2016JF003957

Lelandais, T., Ravier, É., Pochat, S., Bourgeois, O., Clark, C., Mourgues, R., Strzerzynski, P., 2018. Modelled subglacial floods and tunnel valleys control the life cycle of transitory ice streams. The Cryosphere 12, 2759–2772. https://doi.org/10.5194/tc-12-2759-2018

Leone, G., Tackley, P.J., Gerya, T.V., May, D.A., Zhu, G., 2014. Three-dimensional simulations of the southern polar giant impact hypothesis for the origin of the Martian dichotomy: Southern Impact

for Martian Dichotomy. Geophys. Res. Lett. 41, 8736–8743. https://doi.org/10.1002/2014GL062261

Leovy, C., 2001. Weather and climate on Mars. Nature 412, 245–249. https://doi.org/10.1038/35084192

Leverington, D.W., 2011. A volcanic origin for the outflow channels of Mars: Key evidence and major implications. Geomorphology 132, 51–75. https://doi.org/10.1016/j.geomorph.2011.05.022

Leverington, D.W., 2004. Volcanic rilles, streamlined islands, and the origin of outflow channels on Mars. J. Geophys. Res. 109, E10011. https://doi.org/10.1029/2004JE002311

Levrard, B., Forget, F., Montmessin, F., Laskar, J., 2007. Recent formation and evolution of northern Martian polar layered deposits as inferred from a Global Climate Model. J. Geophys. Res. 112, E06012. https://doi.org/10.1029/2006JE002772

Levrard, B., Forget, F., Montmessin, F., Laskar, J., 2004. Recent ice-rich deposits formed at high latitudes on Mars by sublimation of unstable equatorial ice during low obliquity. Nature 431, 1072–1075. https://doi.org/10.1038/nature03055

Levy, J. S., 2015. A hydrological continuum in permafrost environments: The morphological signatures of melt-driven hydrology on Earth and Mars. Geomorphology 240, 70–82. https://doi.org/10.1016/j.geomorph.2014.02.033

Levy, J. S., Head, J., Marchant, D., 2009a. Thermal contraction crack polygons on Mars: Classification, distribution, and climate implications from HiRISE observations. J. Geophys. Res. 114, E01007. https://doi.org/10.1029/2008JE003273

Levy, J. S., Head, J.W., Marchant, D.R., 2009b. Concentric crater fill in Utopia Planitia: History and interaction between glacial "brain terrain" and periglacial mantle processes. Icarus 202, 462–476. https://doi.org/10.1016/j.icarus.2009.02.018

Levy, J. S., Head, J.W., Marchant, D.R., Dickson, J.L., Morgan, G.A., 2009c. Geologically recent gully–polygon relationships on Mars: Insights from the Antarctic Dry Valleys on the roles of permafrost, microclimates, and water sources for surface flow. Icarus 201, 113–126. https://doi.org/10.1016/j.icarus.2008.12.043

Levy, J. S., Head, J.W., Marchant, D.R., 2010a. Concentric crater fill in the northern mid-latitudes of Mars: Formation processes and relationships to similar landforms of glacial origin. Icarus 209, 390–404. https://doi.org/10.1016/j.icarus.2010.03.036

Levy, J. S., Marchant, D.R., Head, J.W., 2010b. Thermal contraction crack polygons on Mars: A synthesis from HiRISE, Phoenix, and terrestrial analog studies. Icarus 206, 229–252. https://doi.org/10.1016/j.icarus.2009.09.005

Levy, J.S., Fassett, C.I., Head, J.W., Schwartz, C., Watters, J.L., 2014. Sequestered glacial ice contribution to the global Martian water budget: Geometric constraints on the volume of remnant, midlatitude debris-covered glaciers: Buried martian glaciers. J. Geophys. Res. Planets 119, 2188–2196. https://doi.org/10.1002/2014JE004685

Lewkowicz, A.G., 1987. Headwall retreat of ground-ice slumps, Banks Island, Northwest Territories. Can. J. Earth Sci. 24, 1077–1085. https://doi.org/10.1139/e87-105

Li, C., Zheng, Y., Wang, X., Zhang, J., Wang, Y., Chen, L., Zhang, L., Zhao, P., Liu, Yike, Lv, W., Liu, Yang, Zhao, X., Hao, J., Sun, W., Liu, X., Jia, B., Li, J., Lan, H., Fa, W., Pan, Y., Wu, F., 2022. Layered subsurface in Utopia Basin of Mars revealed by Zhurong rover radar. Nature 610, 308–312. https://doi.org/10.1038/s41586-022-05147-5

Li, H., Robinson, M., Jurdy, D., 2005. Origin of martian northern hemisphere mid-latitude lobate debris aprons. Icarus 176, 382–394. https://doi.org/10.1016/j.icarus.2005.02.011

Li, H., Wang, W., Wu, F., Zhan, H., Zhang, G., Qiu, F., 2014. A new sand-wedge–forming mechanism in an extra-arid area. Geomorphology 211, 43-51. https://doi.org/10.1016/j.geomorph.2013.12.028

Lillis, R.J., Brain, D.A., Bougher, S.W., Leblanc, F., Luhmann, J.G., Jakosky, B.M., Modolo, R., Fox, J., Deighan, J., Fang, X., Wang, Y.C., Lee, Y., Dong, C., Ma, Y., Cravens, T., Andersson, L., Curry, S.M., Schneider, N., Combi, M., Stewart, I., Clarke, J., Grebowsky, J., Mitchell, D.L., Yelle, R., Nagy, A.F., Baker, D., Lin, R.P., 2015. Characterizing Atmospheric Escape from Mars Today and

Through Time, with MAVEN. Space Sci. Rev. 195, 357–422. https://doi.org/10.1007/s11214-015-0165-8

Liu, Y., Wu, X., Zhao, Y.-Y.S., Pan, L., Wang, C., Liu, J., Zhao, Z., Zhou, X., Zhang, C., Wu, Y., Wan, W., Zou, Y., 2022. Zhurong reveals recent aqueous activities in Utopia Planitia, Mars. Sci. Adv. 8, eabn8555. https://doi.org/10.1126/sciadv.abn8555

Lohani, B., Mason, D.C., 2001. Application of airborne scanning laser altimetry to the study of tidal channel geomorphology. ISPRS J. Photogramm. Remote Sens. 56, 100–120. https://doi.org/10.1016/S0924-2716(01)00041-7

Loizeau, D., Quantin-Nataf, C., Carter, J., Flahaut, J., Thollot, P., Lozac'h, L., Millot, C., 2018. Quantifying widespread aqueous surface weathering on Mars: The plateaus south of Coprates Chasma. Icarus 302, 451–469. https://doi.org/10.1016/j.icarus.2017.11.002

Lucchitta, B., 1981. Mars and Earth: Comparison of cold-climate features. Icarus 45, 264–303. https://doi.org/10.1016/0019-1035(81)90035-X

Lucchitta, B.K., Anderson, D.M., Shoji, H., 1981. Did ice streams carve martian outflow channels? Nature 290, 759–763. https://doi.org/10.1038/290759a0

Lucchitta, B.K., McEwen, A.S., Clow, G.D., Geissler, P.E., Singer, R.B., Schultz, R.A., Squyres, S.W., 1992. The canyon system on Mars., Mars.

Lucchitta, B.K., 2001. Antarctic ice streams and outflow channels on Mars. Geophys. Res. Lett. 28, 403–406. https://doi.org/10.1029/2000GL011924

Lyle, R.R., Hutchinson, D.J., Preston, Y., 2004. Landslide processes in discontinuous permafrost, Little Salmon Lake (NTS 105L/1 and 2), south-central Yukon. Yukon Explor. Geol. 193–204.

Maas, H.-G., Hampel, U., 2006. Photogrammetric Techniques in Civil Engineering Material Testing and Structure Monitoring. Photogramm. Eng. Remote Sens. 72, 39–45. https://doi.org/10.14358/PERS.72.1.39

Mackay, J.R., 1972. THE WORLD OF UNDERGROUND ICE. Ann. Assoc. Am. Geogr. 62, 1–22. https://doi.org/10.1111/j.1467-8306.1972.tb00839.x

Mackay, J.R., 1973. The Growth of Pingos, Western Arctic Coast, Canada. Can. J. Earth Sci. 10, 979–1004. https://doi.org/10.1139/e73-086

Mackay, J.R., 1974. Ice-Wedge Cracks, Garry Island, Northwest Territories. Can. J. Earth Sci. 11, 1366–1383. https://doi.org/10.1139/e74-133

Mackay, J.R., 1977. Pulsating pingos, Tuktoyaktuk Peninsula, N.W.T. Can. J. Earth Sci. 14, 209–222. https://doi.org/10.1139/e77-023

Mackay, J.R., 1979. Pingos of the Tuktoyaktuk Peninsula Area, Northwest Territories. Géographie Phys. Quat. 33, 3–61. https://doi.org/10.7202/1000322ar

Mackay, J.R., 1980. The origin of hummocks, western Arctic coast, Canada. Can. J. Earth Sci. 17, 996–1006. https://doi.org/10.1139/e80-100

Mackay, J.R., 1981. Active layer slope movement in a continuous permafrost environment, Garry Island, Northwest Territories, Canada. Can. J. Earth Sci. 18, 1666–1680. https://doi.org/10.1139/e81-154

Mackay, J.R., Matthews Jr., J.V., 1983. Pleistocene ice and sand wedges, Hooper Island, Northwest Territories. Can. J. Earth Sci. 20, 1087–1097. https://doi.org/10.1139/e83-097

Mackay, J.R., 1988. Pingo collapse and paleoclimatic reconstruction. Can. J. Earth Sci. 25, 495–511. https://doi.org/10.1139/e88-050

Mackay, J.R., 1989. ICE-WEDGE CRACKS, WESTERN ARCTIC COAST. Can. Geogr. Géographe Can. 33, 365–368. https://doi.org/10.1111/j.1541-0064.1989.tb00923.x

Mackay, J.R., 1990a. Seasonal growth bands in pingo ice. Can. J. Earth Sci. 27, 1115–1125. https://doi.org/10.1139/e90-116

Mackay, J.R., 1990b. Some observations on the growth and deformation of epigenetic, syngenetic and anti-syngenetic ice wedges. Permafr. Periglac. Process. 1, 15–29. https://doi.org/10.1002/ppp.3430010104

Mackay, J.R., 1995. Ice wedges on hillslopes and landform evolution in the late Quaternary, western Arctic coast, Canada. Can. J. Earth Sci. 32, 1093–1105. https://doi.org/10.1139/e95-091

Mackay, J.R., 1998. Pingo Growth and collapse, Tuktoyaktuk Peninsula Area, Western Arctic Coast, Canada: a long-term field study. Géographie Phys. Quat. 52, 271–323. https://doi.org/10.7202/004847ar

Mackay, J.R., 2000. Thermally induced movements in ice-wedge polygons, western arctic coast: a long-term study. Géographie Phys. Quat. 54, 41–68. https://doi.org/10.7202/004846ar

Mackay, J.R., Burn, C.R., 2002. The first 20 years (1978-1979 to 1998–1999) of ice-wedge growth at the Illisarvik experimental drained lake site, western Arctic coast, Canada. Can. J. Earth Sci. 39, 95–111. https://doi.org/10.1139/e01-048

Mackay, J.R., Burn, C.R., 2011. A Century (1910-2008) of Change in a Collapsing Pingo, Parry Peninsula, Western Arctic Coast, Canada: Pingo Collapse, Parry Peninsula. Permafr. Periglac. Process. n/a-n/a. https://doi.org/10.1002/ppp.723

Madeleine, J.-B., Forget, F., Head, J.W., Levrard, B., Montmessin, F., Millour, E., 2009. Amazonian northern mid-latitude glaciation on Mars: A proposed climate scenario. Icarus 203, 390–405. https://doi.org/10.1016/j.icarus.2009.04.037

Madeleine, J.-B., Head, J.W., Forget, F., Navarro, T., Millour, E., Spiga, A., Colaïtis, A., Määttänen, A., Montmessin, F., Dickson, J.L., 2014. Recent Ice Ages on Mars: The role of radiatively active clouds and cloud microphysics. Geophys. Res. Lett. 41, 4873–4879. https://doi.org/10.1002/2014GL059861

Malakhov, A.V., Mitrofanov, I.G., Litvak, M.L., Sanin, A.B., Golovin, D.V., Djachkova, M.V., Nikiforov, S.Yu., Anikin, A.A., Lisov, D.I., Lukyanov, N.V., Mokrousov, M.I., 2020. Ice Permafrost ‘“Oases”’ Close to Martian Equator: Planet Neutron Mapping Based on Data of FREND Instrument Onboard TGO Orbiter of Russian-European ExoMars Mission. Astron. Lett. 46, 407–421. https://doi.org/10.1134/S1063773720060079

Malin, M.C., Edgett, K.S., 2000. Evidence for Recent Groundwater Seepage and Surface Runoff on Mars. Science 288, 2330–2335. https://doi.org/10.1126/science.288.5475.2330

Malin, M.C., Edgett, K.S., 2001. Mars Global Surveyor Mars Orbiter Camera: Interplanetary cruise through primary mission. J. Geophys. Res. Planets 106, 23429–23570. https://doi.org/10.1029/2000JE001455

Malin, M.C., Danielson, G.E., Ingersoll, A.P., Masursky, H., Veverka, J., Ravine, M.A., Soulanille, T.A., 1992. Mars Observer camera. J. Geophys. Res. 97, 7699. https://doi.org/10.1029/92JE00340

Malin, M.C., Bell, J.F., Cantor, B.A., Caplinger, M.A., Calvin, W.M., Clancy, R.T., Edgett, K.S., Edwards, L., Haberle, R.M., James, P.B., Lee, S.W., Ravine, M.A., Thomas, P.C., Wolff, M.J., 2007. Context Camera Investigation on board the Mars Reconnaissance Orbiter. J. Geophys. Res. 112, E05S04. https://doi.org/10.1029/2006JE002808

Mangold, N., 2003. Geomorphic analysis of lobate debris aprons on Mars at Mars Orbiter Camera scale: Evidence for ice sublimation initiated by fractures. J. Geophys. Res. 108, 8021. https://doi.org/10.1029/2002JE001885

Mangold, N., Maurice, S., Feldman, W.C., Costard, F., Forget, F., 2004a. Spatial relationships between patterned ground and ground ice detected by the Neutron Spectrometer on Mars. J. Geophys. Res. 109, E08001. https://doi.org/10.1029/2004JE002235

Mangold, N., Quantin, C., Ansan, V., Delacourt, C., Allemand, P., 2004b. Evidence for Precipitation on Mars from Dendritic Valleys in the Valles Marineris Area. Science 305, 78–81. https://doi.org/10.1126/science.1097549

Mangold, N., 2005. High latitude patterned grounds on Mars: Classification, distribution and climatic control. Icarus 174, 336–359. https://doi.org/10.1016/j.icarus.2004.07.030

Mangold, N., Gendrin, A., Gondet, B., LeMouelic, S., Quantin, C., Ansan, V., Bibring, J.-P., Langevin, Y., Masson, P., Neukum, G., 2008. Spectral and geological study of the sulfate-rich region of West Candor Chasma, Mars. Icarus 194, 519–543. https://doi.org/10.1016/j.icarus.2007.10.021

Mangold, N., Roach, L., Milliken, R., Le Mouélic, S., Ansan, V., Bibring, J.P., Masson, Ph., Mustard, J.F., Murchie, S., Neukum, G., 2010. A Late Amazonian alteration layer related to local volcanism on Mars. Icarus 207, 265–276. https://doi.org/10.1016/j.icarus.2009.10.015

Mangold, N., 2011. Ice sublimation as a geomorphic process: A planetary perspective. Geomorphology 126, 1–17. https://doi.org/10.1016/j.geomorph.2010.11.009

Mangold, N., Carter, J., Poulet, F., Dehouck, E., Ansan, V., Loizeau, D., 2012. Late Hesperian aqueous alteration at Majuro crater, Mars. Planet. Space Sci. 72, 18–30. https://doi.org/10.1016/j.pss.2012.03.014

Mangold, N., Howard, A.D., 2013. Outflow channels with deltaic deposits in Ismenius Lacus, Mars. Icarus 226, 385–401. https://doi.org/10.1016/j.icarus.2013.05.040

Marchant, D.R., Lewis, A.R., Phillips, W.M., Moore, E.J., Souchez, R.A., Denton, G.H., Sugden, D.E., Potter Jr., N., Landis, G.P., 2002. Formation of patterned ground and sublimation till over Miocene glacier ice in Beacon Valley, southern Victoria Land, Antarctica. Geol. Soc. Am. Bull. 114, 718–730. https://doi.org/10.1130/0016-7606(2002)114<0718:FOPGAS>2.0.CO;2

Marinova, M.M., Aharonson, O., Asphaug, E., 2008. Mega-impact formation of the Mars hemispheric dichotomy. Nature 453, 1216–1219. https://doi.org/10.1038/nature07070

Mars Channel Working Group, 1983. Channels and valleys on Mars. Geol. Soc. Am. Bull. 94, 1035. https://doi.org/10.1130/0016-7606(1983)94<1035:CAVOM>2.0.CO;2

Martin, L.C.P., Nitzbon, J., Aas, K.S., Etzelmüller, B., Kristiansen, H., Westermann, S., 2019. Stability Conditions of Peat Plateaus and Palsas in Northern Norway. J. Geophys. Res. Earth Surf. 124, 705–719. https://doi.org/10.1029/2018JF004945

Martínez, G.M., Renno, N.O., 2013. Water and Brines on Mars: Current Evidence and Implications for MSL. Space Sci. Rev. 175, 29–51. https://doi.org/10.1007/s11214-012-9956-3

Martínez, G.M., Newman, C.N., De Vicente-Retortillo, A., Fischer, E., Renno, N.O., Richardson, M.I., Fairén, A.G., Genzer, M., Guzewich, S.D., Haberle, R.M., Harri, A.-M., Kemppinen, O., Lemmon, M.T., Smith, M.D., De La Torre-Juárez, M., Vasavada, A.R., 2017. The Modern Near-Surface Martian Climate: A Review of In-situ Meteorological Data from Viking to Curiosity. Space Sci. Rev. 212, 295–338. https://doi.org/10.1007/s11214-017-0360-x

Martín-Torres, F.J., Zorzano, M.-P., Valentín-Serrano, P., Harri, A.-M., Genzer, M., Kemppinen, O., Rivera-Valentin, E.G., Jun, I., Wray, J., Bo Madsen, M., Goetz, W., McEwen, A.S., Hardgrove, C., Renno, N., Chevrier, V.F., Mischna, M., Navarro-González, R., Martínez-Frías, J., Conrad, P., McConnochie, T., Cockell, C., Berger, G., R. Vasavada, A., Sumner, D., Vaniman, D., 2015. Transient liquid water and water activity at Gale crater on Mars. Nat. Geosci. 8, 357–361. https://doi.org/10.1038/ngeo2412

Marzolff, I., Poesen, J., 2009. The potential of 3D gully monitoring with GIS using high-resolution aerial photography and a digital photogrammetry system. Geomorphology 111, 48–60. https://doi.org/10.1016/j.geomorph.2008.05.047

Masursky, H., 1973. An overview of geological results from Mariner 9. J. Geophys. Res. 78, 4009–4030. https://doi.org/10.1029/JB078i020p04009

Matsuoka, N., 2001. Solifluction rates, processes and landforms: a global review. Earth-Sci. Rev. 55, 107–134. https://doi.org/10.1016/S0012-8252(01)00057-5

Matsuoka, N., Murton, J., 2008. Frost weathering: recent advances and future directions. Permafr. Periglac. Process. 19, 195–210. https://doi.org/10.1002/ppp.620

Matsuoka, N., Moriwaki, K., Hirakawa, K., 1996. FIELD EXPERIMENTS ON PHYSICAL WEATHERING AND WIND EROSION IN AN ANTARCTIC COLD DESERT. Earth Surf. Process. Landf. 21, 687–699. https://doi.org/10.1002/(SICI)1096-9837(199608)21:8<687::AID-ESP614>3.0.CO;2-J

Mattei, E., Pettinelli, E., Lauro, S.E., Stillman, D.E., Cosciotti, B., Marinangeli, L., Tangari, A.C., Soldovieri, F., Orosei, R., Caprarelli, G., 2022. Assessing the role of clay and salts on the origin of MARSIS basal bright reflections. Earth Planet. Sci. Lett. 579, 117370. https://doi.org/10.1016/j.epsl.2022.117370

McCauley, J.F., 1978. Geologic map of the Coprates Quadrangle of Mars. https://doi.org/10.3133/i897

McCauley, J.F., Carr, M.H., Cutts, J.A., Hartmann, W.K., Masursky, H., Milton, D.J., Sharp, R.P., Wilhelms, D.E., 1972. Preliminary mariner 9 report on the geology of Mars. Icarus 17, 289–327. https://doi.org/10.1016/0019-1035(72)90003-6

McEwen, A.S., Eliason, E.M., Bergstrom, J.W., Bridges, N.T., Hansen, C.J., Delamere, W.A., Grant, J.A., Gulick, V.C., Herkenhoff, K.E., Keszthelyi, L., Kirk, R.L., Mellon, M.T., Squyres, S.W., Thomas, N., Weitz, C.M., 2007. Mars Reconnaissance Orbiter's High Resolution Imaging Science Experiment (HiRISE). J. Geophys. Res. 112, E05S02. https://doi.org/10.1029/2005JE002605

McEwen, A.S., Ojha, L., Dundas, C.M., Mattson, S.S., Byrne, S., Wray, J.J., Cull, S.C., Murchie, S.L., Thomas, N., Gulick, V.C., 2011. Seasonal Flows on Warm Martian Slopes. Science 333, 740–743. https://doi.org/10.1126/science.1204816

McEwen, A.S., Schaefer, E.I., Dundas, C.M., Sutton, S.S., Tamppari, L.K., Chojnacki, M., 2021. Mars: Abundant Recurring Slope Lineae (RSL) Following the Planet-Encircling Dust Event (PEDE) of 2018. J. Geophys. Res. Planets 126. https://doi.org/10.1029/2020JE006575

McGill, G.E., 1989. Buried topography of Utopia, Mars: Persistence of a giant impact depression. Solid Earth 94 (B3), 2753-2759. https://doi.org/10.1029/JB094iB03p02753

McGill, G.E., Hills, L.S., 1992. Origin of giant Martian polygons. J. Geophys. Res. 97, 2633. https://doi.org/10.1029/91JE02863

McGill, G.E., Squyres, S.W., 1991. Origin of the Martian crustal dichotomy: Evaluating hypotheses. Icarus 93, 386–393. https://doi.org/10.1016/0019-1035(91)90221-E

McKenna Neuman, C., 1993. A review of aeolian transport processes in cold environments. Prog. Phys. Geogr. Earth Environ. 17, 137–155. https://doi.org/10.1177/030913339301700203

Mège, D., Bourgeois, O., 2011. Equatorial glaciations on Mars revealed by gravitational collapse of Valles Marineris wallslopes. Earth Planet. Sci. Lett. 310, 182–191. https://doi.org/10.1016/j.epsl.2011.08.030

Mège, D., Masson, P., 1996. Amounts of crustal stretching in Valles Marineris, Mars. Planet. Space Sci. 44, 749–781. https://doi.org/10.1016/0032-0633(96)00013-X

Meier, W., Gerland, S., Granskog, M.A., Key, J.R., Haas, C., Hovelsrud, G.K., Kovacs, K.M., Makshtas, A., Michel, C., Perovich, D., Reist, J., van Oort, B., 2011. Sea Ice, in: Snow, Water, Ice and Permafrost in the Arctic (SWIPA): Climate Change and the Cryosphere. Arctic Monitoring and Assessment Programme, Oslo, Norway, p. 538.

Mellon, M.T., 1997. Small-scale polygonal features on Mars: Seasonal thermal contraction cracks in permafrost. J. Geophys. Res. Planets 102, 25617–25628. https://doi.org/10.1029/97JE02582

Mellon, M.T., Jakosky, B.M., 1993. Geographic variations in the thermal and diffusive stability of ground ice on Mars. J. Geophys. Res. Planets 98, 3345–3364. https://doi.org/10.1029/92JE02355

Mellon, M.T., Jakosky, B.M., 1995. The distribution and behavior of Martian ground ice during past and present epochs. J. Geophys. Res. 100, 11781. https://doi.org/10.1029/95JE01027

Mellon, M.T., Arvidson, R.E., Sizemore, H.G., Searls, M.L., Blaney, D.L., Cull, S., Hecht, M.H., Heet, T.L., Keller, H.U., Lemmon, M.T., Markiewicz, W.J., Ming, D.W., Morris, R.V., Pike, W.T., Zent, A.P., 2009a. Ground ice at the Phoenix Landing Site: Stability state and origin. J. Geophys. Res. 114, E00E07. https://doi.org/10.1029/2009JE003417

Mellon, M.T., Malin, M.C., Arvidson, R.E., Searls, M.L., Sizemore, H.G., Heet, T.L., Lemmon, M.T., Keller, H.U., Marshall, J., 2009b. The periglacial landscape at the Phoenix landing site. J. Geophys. Res. 114, E00E06. https://doi.org/10.1029/2009JE003418

Michael, G.G., 2013. Planetary surface dating from crater size–frequency distribution measurements: Multiple resurfacing episodes and differential isochron fitting. Icarus 226, 885–890. https://doi.org/10.1016/j.icarus.2013.07.004

Michael, G.G., Neukum, G., 2010. Planetary surface dating from crater size–frequency distribution measurements: Partial resurfacing events and statistical age uncertainty. Earth Planet. Sci. Lett. 294, 223–229. https://doi.org/10.1016/j.epsl.2009.12.041

Michael, G.G., Kneissl, T., Neesemann, A., 2016. Planetary surface dating from crater size-frequency distribution measurements: Poisson timing analysis. Icarus 277, 279–285. https://doi.org/10.1016/j.icarus.2016.05.019

Milana, J.P., 2016. Molards and Their Relation to Landslides Involving Permafrost Failure: Molards and permafrost degradation. Permafr. Periglac. Process. 27, 271–284. https://doi.org/10.1002/ppp.1878

Milkovich, S.M., Head, J.W., Marchant, D.R., 2006. Debris-covered piedmont glaciers along the northwest flank of the Olympus Mons scarp: Evidence for low-latitude ice accumulation during the Late Amazonian of Mars. Icarus 181, 388–407. https://doi.org/10.1016/j.icarus.2005.12.006

Milliken, R.E., 2003. Viscous flow features on the surface of Mars: Observations from high-resolution Mars Orbiter Camera (MOC) images. J. Geophys. Res. 108, 5057. https://doi.org/10.1029/2002JE002005

Mischna, M.A., Richardson, M.I., John Wilson, R., McCleese, D.J., 2003. On the orbital forcing of Martian water and CO_2 cycles: A general circulation model study with simplified volatile schemes. J. Geophys. Res. 108, 5062. https://doi.org/10.1029/2003JE002051

Mitrofanov, I., Anfimov, D., Kozyrev, A., Litvak, M., Sanin, A., Tret'yakov, V., Krylov, A., Shvetsov, V., Boynton, W., Shinohara, C., Hamara, D., Saunders, R.S., 2002. Maps of Subsurface Hydrogen from the High Energy Neutron Detector, Mars Odyssey. Science 297, 78–81. https://doi.org/10.1126/science.1073616

Mitrofanov, I., Litvak, M.L., Kozyrev, A.S., Sanin, A.B., Tret'yakov, V.I., Grin'kov, V.Yu., Boynton, W.V., Shinohara, C., Hamara, D., Saunders, R.S., 2004. Soil Water Content on Mars as Estimated from Neutron Measurements by the HEND Instrument Onboard the 2001 Mars Odyssey Spacecraft. Sol. Syst. Res. 38, 253–257. https://doi.org/10.1023/B:SOLS.0000037461.70809.45

Mitrofanov, I., Malakhov, A., Bakhtin, B., Golovin, D., Kozyrev, A., Litvak, M., Mokrousov, M., Sanin, A., Tretyakov, V., Vostrukhin, A., Anikin, A., Zelenyi, L.M., Semkova, J., Malchev, S., Tomov, B., Matviichuk, Y., Dimitrov, P., Koleva, R., Dachev, T., Krastev, K., Shvetsov, V., Timoshenko, G., Bobrovnitsky, Y., Tomilina, T., Benghin, V., Shurshakov, V., 2018. Fine Resolution Epithermal Neutron Detector (FREND) Onboard the ExoMars Trace Gas Orbiter. Space Sci. Rev. 214, 86. https://doi.org/10.1007/s11214-018-0522-5

Möhlmann, D., Thomsen, K., 2011. Properties of cryobrines on Mars. Icarus 212, 123–130. https://doi.org/10.1016/j.icarus.2010.11.025

Moon, S., Paige, D.A., Siegler, M.A., Russell, P.S., 2021. Geomorphic Evidence for the Presence of Ice Deposits in the Permanently Shadowed Regions of Scott-E Crater on the Moon. Geophys. Res. Lett. 48. https://doi.org/10.1029/2020GL090780

Moore, J., Wilhelms, D.E., 2001. Hellas as a Possible Site of Ancient Ice-Covered Lakes on Mars. Icarus 154, 258–276. https://doi.org/10.1006/icar.2001.6736

Morgan, G.A., Head, J.W., Marchant, D.R., 2009. Lineated valley fill (LVF) and lobate debris aprons (LDA) in the Deuteronilus Mensae northern dichotomy boundary region, Mars: Constraints on the extent, age and episodicity of Amazonian glacial events. Icarus 202, 22–38. https://doi.org/10.1016/j.icarus.2009.02.017

Morgan, G.A., Putzig, N.E., Perry, M.R., Sizemore, H.G., Bramson, A.M., Petersen, E.I., Bain, Z.M., Baker, D.M.H., Mastrogiuseppe, M., Hoover, R.H., Smith, I.B., Pathare, A., Dundas, C.M., Campbell, B.A., 2021. Availability of subsurface water-ice resources in the northern mid-latitudes of Mars. Nat. Astron. 5, 230–236. https://doi.org/10.1038/s41550-020-01290-z

Morgan, J.A., Brogan, D.J., Nelson, P.A., 2017. Application of Structure-from-Motion photogrammetry in laboratory flumes. Geomorphology 276, 125–143. https://doi.org/10.1016/j.geomorph.2016.10.021

Morgenstern, A., Hauber, E., Reiss, D., van Gasselt, S., Grosse, G., Schirrmeister, L., 2007. Deposition and degradation of a volatile-rich layer in Utopia Planitia and implications for climate history on Mars. J. Geophys. Res. 112, E06010. https://doi.org/10.1029/2006JE002869

Morgenstern, A., Ulrich, M., Günther, F., Roessler, S., Fedorova, I.V., Rudaya, N.A., Wetterich, S., Boike, J., Schirrmeister, L., 2013. Evolution of thermokarst in East Siberian ice-rich permafrost: A case study. Geomorphology 201, 363–379. https://doi.org/10.1016/j.geomorph.2013.07.011

Morino, C., Conway, S.J., Balme, M.R., Hillier, J., Jordan, C., Saemundsson, Þ., Argles, T., 2019a. Debris-flow release processes investigated through the analysis of multi-temporal LiDAR datasets in north-western Iceland: Debris-flow processes investigated by multi-temporal LiDAR datasets. Earth Surf. Process. Landf. 44, 144–159. https://doi.org/10.1002/esp.4488

Morino, C., Conway, S.J., Sæmundsson, Þ., Helgason, J.K., Hillier, J., Butcher, F.E.G., Balme, M.R., Jordan, C., Argles, T., 2019b. Molards as an indicator of permafrost degradation and landslide processes. Earth Planet. Sci. Lett. 516, 136–147. https://doi.org/10.1016/j.epsl.2019.03.040

Morino, C., Conway, S.J., Balme, M.R., Helgason, J.K., Sæmundsson, Þ., Jordan, C., Hillier, J., Argles, T., 2021. The impact of ground-ice thaw on landslide geomorphology and dynamics: two case studies in northern Iceland. Landslides 18, 2785–2812. https://doi.org/10.1007/s10346-021-01661-1

Morino, C., Conway, S., Philippe, M., Peignaux, C., Svennevig, K., Lucas, A., Noblet, A., Roberti, G., Butcher, F., Collins-May, J., 2023. Permafrost molards as an analogue for ejecta-ice interactions at Hale Crater, Mars. Icarus 391, 115363. https://doi.org/10.1016/j.icarus.2022.115363

Mouginot, J., Pommerol, A., Kofman, W., Beck, P., Schmitt, B., Herique, A., Grima, C., Safaeinili, A., Plaut, J.J., 2010. The 3–5MHz global reflectivity map of Mars by MARSIS/Mars Express: Implications for the current inventory of subsurface H2O. Icarus 210, 612–625. https://doi.org/10.1016/j.icarus.2010.07.003

Moussirou, B., 2017. Modélisation expérimentale de la dynamique long-terme des reliefs en réponse aux forçages climatiques et tectoniques.

Muller, S., 1945. Permafrost or Permanently Frozen Ground and Related Engineering Problems, Strategic Engineering Studies.

Munguira, A., Hueso, R., Sánchez-Lavega, A., De La Torre-Juarez, M., Martínez, G.M., Newman, C.E., Sebastian, E., Lepinette, A., Vicente-Retortillo, A., Chide, B., Lemmon, M.T., Bertrand, T., Lorenz, R.D., Banfield, D., Gómez-Elvira, J., Martín-Soler, J., Navarro, S., Pla-García, J., Rodríguez-Manfredi, J.A., Romeral, J., Smith, M.D., Torres, J., 2023. Near Surface Atmospheric Temperatures at Jezero From Mars 2020 MEDA Measurements. J. Geophys. Res. Planets 128, e2022JE007559. https://doi.org/10.1029/2022JE007559

Munroe, J.S., Doolittle, J.A., Kanevskiy, M.Z., Hinkel, K.M., Nelson, F.E., Jones, B.M., Shur, Y., Kimble, J.M., 2007. Application of ground-penetrating radar imagery for three-dimensional visualisation of near-surface structures in ice-rich permafrost, Barrow, Alaska: 3D GPR Application Near Barrow, Alaska. Permafr. Periglac. Process. 18, 309–321. https://doi.org/10.1002/ppp.594

Murchie, S.L., Arvidson, R., Bedini, P., Beisser, K., Bibring, J.-P., Bishop, J., Boldt, J., Cavender, P., Choo, T., Clancy, R.T., Darlington, E.H., Des Marais, D., Espiritu, R., Fort, D., Green, R., Guinness, E., Hayes, J., Hash, C., Heffernan, K., Hemmler, J., Heyler, G., Humm, D., Hutcheson, J., Izenberg, N., Lee, R., Lees, J., Lohr, D., Malaret, E., Martin, T., McGovern, J.A., McGuire, P., Morris, R., Mustard, J., Pelkey, S., Rhodes, E., Robinson, M., Roush, T., Schaefer, E., Seagrave, G., Seelos, F., Silverglate, P., Slavney, S., Smith, M., Shyong, W.-J., Strohbehn, K., Taylor, H., Thompson, P., Tossman, B., Wirzburger, M., Wolff, M., 2007. Compact Reconnaissance Imaging Spectrometer for Mars (CRISM) on Mars Reconnaissance Orbiter (MRO). J. Geophys. Res. 112, E05S03. https://doi.org/10.1029/2006JE002682

Murchie, S.L., Mustard, J.F., Ehlmann, B.L., Milliken, R.E., Bishop, J.L., McKeown, N.K., Noe Dobrea, E.Z., Seelos, F.P., Buczkowski, D.L., Wiseman, S.M., Arvidson, R.E., Wray, J.J., Swayze, G., Clark, R.N., Des Marais, D.J., McEwen, A.S., Bibring, J.-P., 2009. A synthesis of Martian aqueous mineralogy after 1 Mars year of observations from the Mars Reconnaissance Orbiter. J. Geophys. Res. 114, E00D06. https://doi.org/10.1029/2009JE003342

Murton, J.B., 1996a. Morphology and paleoenvironmental significance of Quaternary sand veins, sand wedges, and composite wedges, Tuktoyaktuk coastlands, western Arctic Canada. Journal of

Sedimentary Research, 66 (1), 17-25. https://doi.org/10.1306/D4268298-2B26-11D7-8648000102C1865D

Murton, J.B., 1996b. Thermokarst-lake-basin sediments, Tuktoyaktuk Coastlands, western arctic Canada. Sedimentology 43, 737–760. https://doi.org/10.1111/j.1365-3091.1996.tb02023.x

Murton, J.B., French, H.M., 1993. Thaw modification of frost-fissure wedges, Richards Island, Pleistocene Mackenzie Delta, Western Arctic Canada. J. Quat. Sci. 8, 185–196. https://doi.org/10.1002/jqs.3390080302

Murton, J.B., Worsley, P., Gozdzik, J., 2000. Sand veins and wedges in cold aeolian environments. Quat. Sci. Rev. 19, 899–922. https://doi.org/10.1016/S0277-3791(99)00045-1

Murton, J.B., Whiteman, C.A., Waller, R.I., Pollard, W.H., Clark, I.D., Dallimore, S.R., 2005. Basal ice facies and supraglacial melt-out till of the Laurentide Ice Sheet, Tuktoyaktuk Coastlands, western Arctic Canada. Quat. Sci. Rev. 24, 681–708. https://doi.org/10.1016/j.quascirev.2004.06.008

Murton, J.B., Peterson, R., Ozouf, J.-C., 2006. Bedrock Fracture by Ice Segregation in Cold Regions. Science 314, 1127–1129. https://doi.org/10.1126/science.1132127

Murton, J.B., 2009. Global Warming and Thermokarst, in: Margesin, R. (Ed.), Permafrost Soils, Soil Biology. Springer Berlin Heidelberg, Berlin, Heidelberg, pp. 185–203. https://doi.org/10.1007/978-3-540-69371-0_13

Murton, J., 2013. PERMAFROST AND PERIGLACIAL FEATURES | Ice Wedges and Ice-Wedge Casts, in: Encyclopedia of Quaternary Science. Elsevier, pp. 436–451. https://doi.org/10.1016/B978-0-444-53643-3.00097-2

Mustard, J.F., Cooper, C.D., Rifkin, M.K., 2001. Evidence for recent climate change on Mars from the identification of youthful near-surface ground ice. Nature 412, 411–414. https://doi.org/10.1038/35086515

Nakano, Y., Brown, J., 1972. Mathematical modelling and validation of the thermal regimes in tundra soils, Barrow, Alaska. Arct Alp Res 4, 19–38.

Nelson, F.E., Outcalt, S.I., Goodwin, C.W., Hinkel, K.M., 1985. Diurnal thermal regime in a peat-covered palsa, Toolik Lake, Alaska. Arctic 38, 310–315.

Nelson, F.E., Anisimov, O.A., Shiklomanov, N.I., 2001. Subsidence risk from thawing permafrost. Nature 410, 889–890. https://doi.org/10.1038/35073746

Neukum, G., 1983. Meteoritenbombardement und Datierung Planetarer Oberflaechen.

Neukum, G., Ivanov, B.A., Hartmann, W.K., 2001. Cratering Records in the Inner Solar System in Relation to the Lunar Reference System, in: Kallenbach, R., Geiss, J., Hartmann, William K. (Eds.), Chronology and Evolution of Mars, Space Sciences Series of ISSI. Springer Netherlands, Dordrecht, pp. 55–86. https://doi.org/10.1007/978-94-017-1035-0_3

Neukum, G., Jaumann, R., 2004. HRSC: the High Resolution Stereo Camera of Mars Express 1240, 17–35.

Neumann, G.A., Zuber, M.T., Wieczorek, M.A., McGovern, P.J., Lemoine, F.G., Smith, D.E., 2004. Crustal structure of Mars from gravity and topography. J. Geophys. Res. 109, E08002. https://doi.org/10.1029/2004JE002262

Ni, J., Wu, T., Zhu, X., Wu, X., Pang, Q., Zou, D., Chen, J., Li, R., Hu, G., Du, Y., Hao, J., Li, X., Qiao, Y., 2021. Risk assessment of potential thaw settlement hazard in the permafrost regions of Qinghai-Tibet Plateau. Sci. Total Environ. 776, 145855. https://doi.org/10.1016/j.scitotenv.2021.145855

Niethammer, U., James, M.R., Rothmund, S., Travelletti, J., Joswig, M., 2012. UAV-based remote sensing of the Super-Sauze landslide: Evaluation and results. Eng. Geol. 128, 2–11. https://doi.org/10.1016/j.enggeo.2011.03.012

Nikiforoff, C., 1928. The perpetually frozen subsoil of Siberia. Soil Sci. 26, 61–82.

Nimmo, F., Hart, S.D., Korycansky, D.G., Agnor, C.B., 2008. Implications of an impact origin for the martian hemispheric dichotomy. Nature 453, 1220–1223. https://doi.org/10.1038/nature07025

Nimmo, F., Kleine, T., 2007. How rapidly did Mars accrete? Uncertainties in the Hf–W timing of core formation. Icarus 191, 497–504. https://doi.org/10.1016/j.icarus.2007.05.002

Nimmo, F., Tanaka, K., 2005. EARLY CRUSTAL EVOLUTION OF MARS. Annu. Rev. Earth Planet. Sci. 33, 133–161. https://doi.org/10.1146/annurev.earth.33.092203.122637

Nishiyama, S., Minakata, N., Kikuchi, T., Yano, T., 2015. Improved digital photogrammetry technique for crack monitoring. Adv. Eng. Inform. 29, 851–858. https://doi.org/10.1016/j.aei.2015.05.005

Niu, F., Lin, Z., Liu, H., Lu, J., 2011. Characteristics of thermokarst lakes and their influence on permafrost in Qinghai–Tibet Plateau. Geomorphology 132, 222–233. https://doi.org/10.1016/j.geomorph.2011.05.011

Notebaert, B., Verstraeten, G., Govers, G., Poesen, J., 2009. Qualitative and quantitative applications of LiDAR imagery in fluvial geomorphology. Earth Surf. Process. Landf. 34, 217–231. https://doi.org/10.1002/esp.1705

Obu, J., Westermann, S., Bartsch, A., Berdnikov, N., Christiansen, H.H., Dashtseren, A., Delaloye, R., Elberling, B., Etzelmüller, B., Kholodov, A., Khomutov, A., Kääb, A., Leibman, M.O., Lewkowicz, A.G., Panda, S.K., Romanovsky, V., Way, R.G., Westergaard-Nielsen, A., Wu, T., Yamkhin, J., Zou, D., 2019. Northern Hemisphere permafrost map based on TTOP modelling for 2000–2016 at 1 km2 scale. Earth-Sci. Rev. 193, 299–316. https://doi.org/10.1016/j.earscirev.2019.04.023

Ojha, L., McEwen, A., Dundas, C., Byrne, S., Mattson, S., Wray, J., Masse, M., Schaefer, E., 2014. HiRISE observations of Recurring Slope Lineae (RSL) during southern summer on Mars. Icarus 231, 365–376. https://doi.org/10.1016/j.icarus.2013.12.021

Ojha, L., Wilhelm, M.B., Murchie, S.L., McEwen, A.S., Wray, J.J., Hanley, J., Massé, M., Chojnacki, M., 2015. Spectral evidence for hydrated salts in recurring slope lineae on Mars. Nat. Geosci. 8, 829–832. https://doi.org/10.1038/ngeo2546

Opik, E.J., 1965. Mariner IV and Craters on Mars. Ir. Astron. J. 7, 92.

Orgel, C., Hauber, E., Gasselt, S., Reiss, D., Johnsson, A., Ramsdale, J.D., Smith, I., Swirad, Z.M., Séjourné, A., Wilson, J.T., Balme, M.R., Conway, S.J., Costard, F., Eke, V.R., Gallagher, C., Kereszturi, Á., Łosiak, A., Massey, R.J., Platz, T., Skinner, J.A., Teodoro, L.F.A., 2019. Grid Mapping the Northern Plains of Mars: A New Overview of Recent Water- and Ice-Related Landforms in Acidalia Planitia. J. Geophys. Res. Planets 124, 454–482. https://doi.org/10.1029/2018JE005664

Orosei, R., Lauro, S.E., Pettinelli, E., Cicchetti, A., Coradini, M., Cosciotti, B., Di Paolo, F., Flamini, E., Mattei, E., Pajola, M., Soldovieri, F., Cartacci, M., Cassenti, F., Frigeri, A., Giuppi, S., Martufi, R., Masdea, A., Mitri, G., Nenna, C., Noschese, R., Restano, M., Seu, R., 2018. Radar evidence of subglacial liquid water on Mars. Science 361, 490–493. https://doi.org/10.1126/science.aar7268

Osterkamp, T.E., Jorgenson, M.T., Schuur, E.A.G., Shur, Y.L., Kanevskiy, M.Z., Vogel, J.G., Tumskoy, V.E., 2009. Physical and ecological changes associated with warming permafrost and thermokarst in Interior Alaska: Physical and Ecological Changes Associated with Thermokarst. Permafr. Periglac. Process. 20, 235–256. https://doi.org/10.1002/ppp.656

Outcalt, S.I., Nelson, F.E., Hinkel, K.M., 1990. The zero-curtain effect: Heat and mass transfer across an isothermal region in freezing soil. Water Resour. Res. 26, 1509–1516. https://doi.org/10.1029/WR026i007p01509

Paguican, E.M.R., Van Wyk De Vries, B., Lagmay, A.M.F., 2014. Hummocks: how they form and how they evolve in rockslide-debris avalanches. Landslides 11, 67–80. https://doi.org/10.1007/s10346-012-0368-y

Paige, D.A., Herkenhoff, K.E., Murray, B.C., 1990. Mariner 9 observations of the south polar cap of Mars: Evidence for residual CO_2 frost. J. Geophys. Res. 95, 1319. https://doi.org/10.1029/JB095iB02p01319

Palmer, E.M., Heggy, E., Kofman, W., 2017. Orbital bistatic radar observations of asteroid Vesta by the Dawn mission. Nat. Commun. 8, 409. https://doi.org/10.1038/s41467-017-00434-6

Palucis, M.C., Jasper, J., Garczynski, B., Dietrich, W.E., 2020. Quantitative assessment of uncertainties in modeled crater retention ages on Mars. Icarus 341, 113623. https://doi.org/10.1016/j.icarus.2020.113623

Parker, T.J., Gorsline, D.S., Saunders, R.S., Pieri, D.C., Schneeberger, D.M., 1993. Coastal geomorphology of the Martian northern plains. J. Geophys. Res. 98, 11061. https://doi.org/10.1029/93JE00618

Parsons, R., Holt, J., 2016. Constraints on the formation and properties of a Martian lobate debris apron: Insights from high-resolution topography, SHARAD radar data, and a numerical ice flow model: EURIPUS MONS LDA ANALYSIS. J. Geophys. Res. Planets 121, 432–453. https://doi.org/10.1002/2015JE004927

Pasquon, K., Gargani, J., Massé, M., Conway, S.J., 2016. Present-day formation and seasonal evolution of linear dune gullies on Mars. Icarus 274, 195–210. https://doi.org/10.1016/j.icarus.2016.03.024

Pasquon, K., Gargani, J., Massé, M., Vincendon, M., Conway, S.J., Séjourné, A., Jomelli, V., Balme, M.R., Lopez, S., Guimpier, A., 2019. Present-day development of gully-channel sinuosity by carbon dioxide gas supported flows on Mars. Icarus 329, 296–313. https://doi.org/10.1016/j.icarus.2019.03.034

Pathare, A.V., Feldman, W.C., Prettyman, T.H., Maurice, S., 2018. Driven by excess? Climatic implications of new global mapping of near-surface water-equivalent hydrogen on Mars. Icarus 301, 97–116. https://doi.org/10.1016/j.icarus.2017.09.031

Patton, A.I., Rathburn, S.L., Capps, D.M., 2019. Landslide response to climate change in permafrost regions. Geomorphology 340, 116–128. https://doi.org/10.1016/j.geomorph.2019.04.029

Pearce, G., Osinski, G.R., Soare, R.J., 2011. Intra-crater glacial processes in central Utopia Planitia, Mars. Icarus 212, 86–95. https://doi.org/10.1016/j.icarus.2010.12.001

Pechmann, J.C., 1980. The origin of polygonal troughs on the Northern Plains of Mars. Icarus 42, 185–210. https://doi.org/10.1016/0019-1035(80)90071-8

Pedersen, G.B.M., Head, J.W., Wilson, L., 2010. Formation, erosion and exposure of Early Amazonian dikes, dike swarms and possible subglacial eruptions in the Elysium Rise/Utopia Basin Region, Mars. Earth Planet. Sci. Lett. 294, 424–439. https://doi.org/10.1016/j.epsl.2009.08.010

Penner, E., 1970. Thermal conductivity of frozen soils. Can. J. Earth Sci. 7, 982–987. https://doi.org/10.1139/e70-091

Penner, E., 1986. Aspects of ice lens growth in soils. Cold Reg. Sci. Technol. 13, 91–100. https://doi.org/10.1016/0165-232X(86)90011-X

Permafrost Subcommittee, 1988. Glossary of Permafrost and Related Ground-Ice Terms.

Peter Heng, B.C., Chandler, J.H., Armstrong, A., 2010. Applying close range digital photogrammetry in soil erosion studies: Applying close range digital photogrammetry in soil erosion studies. Photogramm. Rec. 25, 240–265. https://doi.org/10.1111/j.1477-9730.2010.00584.x

Petersen, E.I., Holt, J.W., Levy, J.S., 2018. High Ice Purity of Martian Lobate Debris Aprons at the Regional Scale: Evidence From an Orbital Radar Sounding Survey in Deuteronilus and Protonilus Mensae. Geophys. Res. Lett. 45, 11,595-11,604. https://doi.org/10.1029/2018GL079759

Petley, D., 2012. Global patterns of loss of life from landslides. Geology 40, 927–930. https://doi.org/10.1130/G33217.1

Peulvast, J.-P., Mège, D., Chiciak, J., Costard, F., Masson, P.L., 2001. Morphology, evolution and tectonics of Valles Marineris wallslopes (Mars). Geomorphology 37, 329–352. https://doi.org/10.1016/S0169-555X(00)00085-4

Pewe, T.L., 1959. Sand-wedge polygons (tesselations) in the McMurdo Sound region, Antarctica; a progress report. Am. J. Sci. 257, 545–552. https://doi.org/10.2475/ajs.257.8.545

Philippe, M., Conway, S.J., Raack, J., Carpy, S., Massé, M., Patel, M.R., Sylvest, M.E., Lewis, S.R., Morino, C., 2023. Experimental study of sediment transport processes by liquid water and brine under Martian pressure. Icarus 395, 115475. https://doi.org/10.1016/j.icarus.2023.115475

Picardi, G., Biccari, D., Seu, R., Marinangeli, L., Johnson, W.T.K., Jordan, R.L., Plaut, J., Safaenili, A., Gurnett, D.A., Ori, G.G., Orosei, R., Calabrese, D., Zampolini, E., 2004. Performance and surface scattering models for the Mars Advanced Radar for Subsurface and Ionosphere Sounding (MARSIS). Planet. Space Sci. 52, 149–156. https://doi.org/10.1016/j.pss.2003.08.020

Pierce, T.L., Crown, D.A., 2003. Morphologic and topographic analyses of debris aprons in the eastern Hellas region, Mars. Icarus 163, 46–65. https://doi.org/10.1016/S0019-1035(03)00046-0

Pieri, D.C., 1980. Martian Valleys: Morphology, Distribution, Age, and Origin. Science 210, 895–897. https://doi.org/10.1126/science.210.4472.895

Pieterek, B., Ciazela, J., Lagain, A., Ciazela, M., 2022. Late Amazonian dike-fed distributed volcanism in the Tharsis volcanic province on Mars. Icarus 386, 115151. https://doi.org/10.1016/j.icarus.2022.115151

Piqueux, S., Kleinböhl, A., Hayne, P.O., Kass, D.M., Schofield, J.T., McCleese, D.J., 2015. Variability of the martian seasonal CO2 cap extent over eight Mars Years. Icarus 251, 164–180. https://doi.org/10.1016/j.icarus.2014.10.045

Piqueux, S., Buz, J., Edwards, C.S., Bandfield, J.L., Kleinböhl, A., Kass, D.M., Hayne, P.O., The MCS, THEMIS Teams, 2019. Widespread Shallow Water Ice on Mars at High Latitudes and Mid Latitudes. Geophys. Res. Lett. 46, 14290–14298. https://doi.org/10.1029/2019GL083947

Pirk, N., Sievers, J., Mertes, J., Parmentier, F.-J., Mastepanov, M., Christensen, T.R., 2017. Spatial variability of CO2 uptake in polygonal tundra: assessing low-frequency disturbances in eddy covariance flux estimates. Biogeosciences, 14, 3157–3169. https://doi.org/10.5194/bg-14-3157-201

Pissart, A., 2000. Remnants of Lithalsas of the Hautes Fagnes, Belgium: A Summary of Present-day Knowledge. Permafr. Periglac. Process. 11, 327–355. https://doi.org/10.1002/1099-1530(200012)11:4<327::AID-PPP370>3.0.CO;2-Q

Pissart, A., 2002. Palsas, lithalsas and remnants of these periglacial mounds. A progress report. Prog. Phys. Geogr. Earth Environ. 26, 605–621. https://doi.org/10.1191/0309133302pp354ra

Pissart, A., Calmels, F., Wastiaux, C., 2010. The potential lateral growth of lithalsas. Quat. Res. 75, 371–377. https://doi.org/10.1016/j.yqres.2011.01.001

Platz, T., Michael, G., Tanaka, K.L., Skinner, J.A., Fortezzo, C.M., 2013. Crater-based dating of geological units on Mars: Methods and application for the new global geological map. Icarus 225, 806–827. https://doi.org/10.1016/j.icarus.2013.04.021

Plaut, J.J., Safaeinili, A., Holt, J.W., Phillips, R.J., Head, J.W., Seu, R., Putzig, N.E., Frigeri, A., 2009. Radar evidence for ice in lobate debris aprons in the mid-northern latitudes of Mars: RADAR EVIDENCE FOR MID-LATITUDE MARS ICE. Geophys. Res. Lett. 36, n/a-n/a. https://doi.org/10.1029/2008GL036379

Plescia, J.B., 1990. Recent flood lavas in the Elysium region of Mars. Icarus 88, 465–490. https://doi.org/10.1016/0019-1035(90)90095-Q

Plug, L. J., Werner B. T., 2001. Fracture networks in frozen ground. Solid Earth 106 (B5), 8599-8613. https://doi.org/10.1029/2000JB900320

Plug, L. J., Werner B. T., 2002. Nonlinear dynamics of ice-wedge networks and resulting sensitivity to severe cooling events. Nature 417, 929-933. https://doi.org/10.1038/nature00796

Plug, L. J., Werner B. T., 2008. Modelling of ice-wedge networks. Permafr. Periglac. Process. 19 (1), 63-69. https://doi.org/10.1002/ppp.604

Pollard, W., 2018. Periglacial Processes in Glacial Environments, in: Past Glacial Environments. Elsevier, pp. 537–564. https://doi.org/10.1016/B978-0-08-100524-8.00016-6

Poulet, F., Bibring, J.-P., Mustard, J.F., Gendrin, A., Mangold, N., Langevin, Y., Arvidson, R.E., Gondet, B., Gomez, C., The OMEGA Team, 2005. Phyllosilicates on Mars and implications for early martian climate. Nature 438, 623–627. https://doi.org/10.1038/nature04274

Powers, W.E., 1936. The Evidences of Wind Abrasion. J. Geol. 44, 214–219. https://doi.org/10.1086/624419

Raack, J., Reiss, D., Appéré, T., Vincendon, M., Ruesch, O., Hiesinger, H., 2015. Present-day seasonal gully activity in a south polar pit (Sisyphi Cavi) on Mars. Icarus 251, 226–243. https://doi.org/10.1016/j.icarus.2014.03.040

Raack, J., Conway, S.J., Herny, C., Balme, M.R., Carpy, S., Patel, M.R., 2017. Water induced sediment levitation enhances downslope transport on Mars. Nat. Commun. 8, 1151. https://doi.org/10.1038/s41467-017-01213-z

Raack, J., Conway, S.J., Heyer, T., Bickel, V.T., Philippe, M., Hiesinger, H., Johnsson, A., Massé, M., 2020. Present-day gully activity in Sisyphi Cavi, Mars – Flow-like features and block movements. Icarus 350, 113899. https://doi.org/10.1016/j.icarus.2020.113899

Rabatel, A., Deline, P., Jaillet, S., Ravanel, L., 2008. Rock falls in high-alpine rock walls quantified by terrestrial lidar measurements: A case study in the Mont Blanc area: ROCK FALLS QUANTIFIED BY LIDAR. Geophys. Res. Lett. 35. https://doi.org/10.1029/2008GL033424

Rampton, V.N., 1988. Quaternary geology of the Tuktoyaktuk coastlands, Northwest Territories (No. EMR-M46-423E; MICROLOG-88-02809). Department of Energy, Mines and Resources, Canada.

Rampton, V.N., Bouchard, M., 1975. Surficial geology of Tuktoyaktuk, District of Mackenzie.

Rampton, V.N., Mackay, J.R., 1971. Massive Ice and Icy Sediments Throughout the Tuktoyaktuk Peninsula, Richards Island: And Nearby Areas, District of Mackenzie.

Ramsdale, J.D., Balme, M.R., Conway, S.J., Gallagher, C., van Gasselt, S.A., Hauber, E., Orgel, C., Séjourné, A., Skinner, J.A., Costard, F., Johnsson, A., Losiak, A., Reiss, D., Swirad, Z.M., Kereszturi, A., Smith, I.B., Platz, T., 2017. Grid-based mapping: A method for rapidly determining the spatial distributions of small features over very large areas. Planet. Space Sci. 140, 49–61. https://doi.org/10.1016/j.pss.2017.04.002

Ramsdale, J.D., Balme, M.R., Gallagher, C., Conway, S.J., Smith, I.B., Hauber, E., Orgel, C., Séjourné, A., Costard, F., Eke, V.R., Gasselt, S.A., Johnsson, A., Kereszturi, A., Losiak, A., Massey, R.J., Platz, T., Reiss, D., Skinner, J.A., Swirad, Z.M., Teodoro, L.F.A., Wilson, J.T., 2019. Grid Mapping the Northern Plains of Mars: Geomorphological, Radar, and Water-Equivalent Hydrogen Results From Arcadia Plantia. J. Geophys. Res. Planets 124, 504–527. https://doi.org/10.1029/2018JE005663

Randriamazaoro, R., Dupeyrat, L., Costard, F., Gailhardis, E.C., 2007. Fluvial thermal erosion: heat balance integral method. Earth Surf. Process. Landf. 32, 1828–1840. https://doi.org/10.1002/esp.1489

Reinoso, J.F., Gonçalves, J.E., Pereira, C., Bleninger, T., 2018. Cartography for Civil Engineering Projects: Photogrammetry Supported by Unmanned Aerial Vehicles. Iran. J. Sci. Technol. Trans. Civ. Eng. 42, 91–96. https://doi.org/10.1007/s40996-017-0076-x

Rempel, A.W., 2007. Formation of ice lenses and frost heave. J. Geophys. Res. 112, F02S21. https://doi.org/10.1029/2006JF000525

Rempel, A.W., 2010. Frost heave. J. Glaciol. 56, 1122–1128. https://doi.org/10.3189/002214311796406149

Rennó, N.O., Bos, B.J., Catling, D., Clark, B.C., Drube, L., Fisher, D., Goetz, W., Hviid, S.F., Keller, H.U., Kok, J.F., Kounaves, S.P., Leer, K., Lemmon, M., Madsen, M.B., Markiewicz, W.J., Marshall, J., McKay, C., Mehta, M., Smith, M., Zorzano, M.P., Smith, P.H., Stoker, C., Young, S.M.M., 2009. Possible physical and thermodynamical evidence for liquid water at the Phoenix landing site. J. Geophys. Res. 114, E00E03. https://doi.org/10.1029/2009JE003362

Rice, M.S., Gupta, S., Treiman, A.H., Stack, K.M., Calef, F., Edgar, L.A., Grotzinger, J., Lanza, N., Le Deit, L., Lasue, J., Siebach, K.L., Vasavada, A., Wiens, R.C., Williams, J., 2017. Geologic overview of the Mars Science Laboratory rover mission at the Kimberley, Gale crater, Mars: Overview of MSL at the Kimberley. J. Geophys. Res. Planets 122, 2–20. https://doi.org/10.1002/2016JE005200

Richardson, M.I., 2002. Investigation of the nature and stability of the Martian seasonal water cycle with a general circulation model. J. Geophys. Res. 107, 5031. https://doi.org/10.1029/2001JE001536

Rieke-Zapp, D.H., Nearing, M.A., 2005. Digital close range photogrammetry for measurement of soil erosion. Photogramm. Rec. 20, 69–87. https://doi.org/10.1111/j.1477-9730.2005.00305.x

Rivera-Valentín, E.G., Gough, R.V., Chevrier, V.F., Primm, K.M., Martínez, G.M., Tolbert, M., 2018. Constraining the Potential Liquid Water Environment at Gale Crater, Mars. J. Geophys. Res. Planets 123, 1156–1167. https://doi.org/10.1002/2018JE005558

Rivera-Valentín, E.G., Chevrier, V.F., Soto, A., Martínez, G., 2020. Distribution and habitability of (meta)stable brines on present-day Mars. Nat. Astron. 4, 756–761. https://doi.org/10.1038/s41550-020-1080-9

Robbins, S.J., Hynek, B.M., 2012a. A new global database of Mars impact craters ≥1 km: 2. Global crater properties and regional variations of the simple-to-complex transition diameter: MARS CRATER DATABASE-RESULTS. J. Geophys. Res. Planets 117, n/a-n/a. https://doi.org/10.1029/2011JE003967

Robbins, S.J., Hynek, B.M., 2012b. A new global database of Mars impact craters ≥1 km: 1. Database creation, properties, and parameters: MARS CRATER DATABASE-CONSTRUCTION. J. Geophys. Res. Planets 117, n/a-n/a. https://doi.org/10.1029/2011JE003966

Robbins, S.J., Hynek, B.M., Lillis, R.J., Bottke, W.F., 2013. Large impact crater histories of Mars: The effect of different model crater age techniques. Icarus 225, 173–184. https://doi.org/10.1016/j.icarus.2013.03.019

Roberti, G., Friele, P., Van Wyk De Vries, B., Ward, B., Clague, J.J., Perotti, L., Giardino, M., 2017. Rheological evolution of the Mount Meager 2010 debris avalanche, southwestern British Columbia. Geosphere 13, 369–390. https://doi.org/10.1130/GES01389.1

Rocchini, C., Cignoni, P., Montani, C., Pingi, P., Scopigno, R., 2001. A low cost 3D scanner based on structured light. Comput. Graph. Forum 20, 299–308. https://doi.org/10.1111/1467-8659.00522

Rodríguez, J.A.P., Gulick, V.C., Baker, V.R., Platz, T., Fairén, A.G., Miyamoto, H., Kargel, J.S., Rice, J.W., Glines, N., 2014. Evidence for Middle Amazonian catastrophic flooding and glaciation on Mars. Icarus 242, 202–210. https://doi.org/10.1016/j.icarus.2014.06.008

Rodríguez, J.A.P., Kargel, J.S., Baker, V.R., Gulick, V.C., Berman, D.C., Fairén, A.G., Linares, R., Zarroca, M., Yan, J., Miyamoto, H., Glines, N., 2015a. Martian outflow channels: How did their source aquifers form and why did they drain so rapidly? Sci. Rep. 5, 13404. https://doi.org/10.1038/srep13404

Rodríguez, J.A.P., Platz, T., Gulick, V., Baker, V.R., Fairén, A.G., Kargel, J., Yan, J., Miyamoto, H., Glines, N., 2015b. Did the martian outflow channels mostly form during the Amazonian Period? Icarus 257, 387–395. https://doi.org/10.1016/j.icarus.2015.04.024

Romanovsky, V.E., Drozdov, D.S., Oberman, N.G., Malkova, G.V., Kholodov, A.L., Marchenko, S.S., Moskalenko, N.G., Sergeev, D.O., Ukraintseva, N.G., Abramov, A.A., Gilichinsky, D.A., Vasiliev, A.A., 2010a. Thermal state of permafrost in Russia. Permafr. Periglac. Process. 21, 136–155. https://doi.org/10.1002/ppp.683

Romanovsky, V. E., Smith, S.L., Christiansen, H.H., 2010b. Permafrost thermal state in the polar Northern Hemisphere during the international polar year 2007-2009: a synthesis. Permafr. Periglac. Process. 21, 106–116. https://doi.org/10.1002/ppp.689

Russell, P.S., Head, J.W., 2003. Elysium-Utopia flows as mega-lahars: A model of dike intrusion, cryosphere cracking, and water-sediment release. J. Geophys. Res. 108, 5064. https://doi.org/10.1029/2002JE001995

Russell, P.S., Head, J.W., 2007. The Martian hydrologic system: Multiple recharge centers at large volcanic provinces and the contribution of snowmelt to outflow channel activity. Planet. Space Sci. 55, 315–332. https://doi.org/10.1016/j.pss.2006.03.010

Sæmundsson, T., Arnalds, O., Kneisel, C., Jonsson, H.P., Decaulne, A., 2012. The Orravatnsrustir palsa site in Central Iceland—Palsas in an aeolian sedimentation environment. Geomorphology 167–168, 13–20. https://doi.org/10.1016/j.geomorph.2012.03.014

Sæmundsson, Þ., Morino, C., Helgason, J.K., Conway, S.J., Pétursson, H.G., 2018. The triggering factors of the Móafellshyrna debris slide in northern Iceland: Intense precipitation, earthquake activity and thawing of mountain permafrost. Sci. Total Environ. 621, 1163–1175. https://doi.org/10.1016/j.scitotenv.2017.10.111

Sagan, C., Fox, P., 1975. The canals of Mars: An assessment after Mariner 9. Icarus 25, 602–612. https://doi.org/10.1016/0019-1035(75)90042-1

Sagan, C., Veverka, J., Fox, P., Dubisch, R., Pollack, J.B., Smith, B.A., 1972. Variable Features on Mars: Preliminary Mariner 9 Television Results. Icarus 17, 346–372.

Sagan, C., Veverka, J., Fox, P., Dubisch, R., French, R., Gierasch, P., Quam, L., Lederberg, J., Levinthal, E., Tucker, R., Eross, B., Pollack, J.B., 1973. Variable features on Mars, 2, Mariner 9 global results. J. Geophys. Res. 78, 4163–4196. https://doi.org/10.1029/JB078i020p04163

Sager, C., Airo, A., Arens, F. L., Schulze-Makuch, D., 2021. New type of sand wedge polygons in the salt cemented soils of the hyper-arid Atacama Desert. Geomorphology 373, 107481. https://doi.org/10.1016/j.geomorph.2020.107481

Salamunićcar, G., Lončarić, S., Mazarico, E., 2012. LU60645GT and MA132843GT catalogues of Lunar and Martian impact craters developed using a Crater Shape-based interpolation crater detection algorithm for topography data. Planet. Space Sci. 60, 236–247. https://doi.org/10.1016/j.pss.2011.09.003

Salese, F., McMahon, W.J., Balme, M.R., Ansan, V., Davis, J.M., Kleinhans, M.G., 2020. Sustained fluvial deposition recorded in Mars' Noachian stratigraphic record. Nat. Commun. 11, 2067. https://doi.org/10.1038/s41467-020-15622-0

Sánchez-Lavega, A., Del Rio-Gaztelurrutia, T., Hueso, R., Juárez, M.D.L.T., Martínez, G.M., Harri, A. -M., Genzer, M., Hieta, M., Polkko, J., Rodríguez-Manfredi, J.A., Lemmon, M.T., Pla-García, J., Toledo, D., Vicente-Retortillo, A., Viúdez-Moreiras, D., Munguira, A., Tamppari, L.K., Newman, C., Gómez-Elvira, J., Guzewich, S., Bertrand, T., Apéstigue, V., Arruego, I., Wolff, M., Banfield, D., Jaakonaho, I., Mäkinen, T., 2023. Mars 2020 Perseverance Rover Studies of the Martian Atmosphere Over Jezero From Pressure Measurements. J. Geophys. Res. Planets 128. https://doi.org/10.1029/2022JE007480

Saunders, R.S., Arvidson, R.E., Badhwar, G.D., Boynton, W.V., Christensen, P.R., Cucinotta, F.A., Feldman, W.C., Gibbs, R.G., Kloss Jr., C., Landano, M.R., Mase, R.A., McSmith, G.W., Meyer, M.A., Mitrofanov, I.G., Pace, G.D., Plaut, J.J., Sidney, W.P., Spencer, D.A., Thompson, T.W., Zeitlin, C.J., 2004. 2001 Mars Odyssey Mission Summary. Space Sci. Rev. 110, 1–36. https://doi.org/10.1023/B:SPAC.0000021006.84299.18

Schack Pedersen, S.A., Melchior Larsen, L., Dahl-Jensen, T., Jepsen, H.F., Krarup Pedersen, G., Nielsen, T., Pedersen, A.K., Von Platen-Hallermund, F., Weng, W., 2002. Tsunami-generating rock fall and landslide on the south coast of Nuussuaq, central West Greenland. Geol. Greenl. Surv. Bull. 191, 73–93. https://doi.org/10.34194/ggub.v191.5131

Schenk, P., Castillo-Rogez, J., Otto, K.A., Marchi, S., O'Brien, D., Bland, M., Hughson, K., Schmidt, B., Scully, J., Buczkowski, D., Krohn, K., Hoogenboom, T., Kramer, G., Bray, V., Neesemann, A., Hiesinger, H., Platz, T., De Sanctis, M.C., Schroeder, S., Le Corre, L., McFadden, L., Sykes, M., Raymond, C., Russell, C.T., 2021. Compositional control on impact crater formation on mid-sized planetary bodies: Dawn at Ceres and Vesta, Cassini at Saturn. Icarus 359, 114343. https://doi.org/10.1016/j.icarus.2021.114343

Schirrmeister, L., Siegert, C., Kunitzky, V.V., Grootes, P.M., Erlenkeuser, H., 2002. Late Quaternary ice-rich permafrost sequences as a paleoenvironmental archive for the Laptev Sea Region in northern Siberia. Int. J. Earth Sci. 91, 154–167. https://doi.org/10.1007/s005310100205

Schirrmeister, L., Froese, D., Tumskoy, V., Grosse, G., Wetterich, S., 2013. PERMAFROST AND PERIGLACIAL FEATURES | Yedoma: Late Pleistocene Ice-Rich Syngenetic Permafrost of Beringia, in: Encyclopedia of Quaternary Science. Elsevier, pp. 542–552. https://doi.org/10.1016/B978-0-444-53643-3.00106-0

Schirrmeister, L., Schwamborn, G., Overduin, P.P., Strauss, J., Fuchs, M.C., Grigoriev, M., Yakshina, I., Rethemeyer, J., Dietze, E., Wetterich, S., 2017. Yedoma Ice Complex of the Buor Khaya Peninsula (southern Laptev Sea). Biogeosciences 14, 1261–1283. https://doi.org/10.5194/bg-14-1261-2017

Schmidt, B.E., Hughson, K.H.G., Chilton, H.T., Scully, J.E.C., Platz, T., Nathues, A., Sizemore, H., Bland, M.T., Byrne, S., Marchi, S., O'Brien, D.P., Schorghofer, N., Hiesinger, H., Jaumann, R., Pasckert, J.H., Lawrence, J.D., Buzckowski, D., Castillo-Rogez, J.C., Sykes, M.V., Schenk, P.M., DeSanctis, M.-C., Mitri, G., Formisano, M., Li, J.-Y., Reddy, V., LeCorre, L., Russell, C.T., Raymond, C.A., 2017. Geomorphological evidence for ground ice on dwarf planet Ceres. Nat. Geosci. 10, 338–343. https://doi.org/10.1038/ngeo2936

Schmidt, F., Andrieu, F., Costard, F., Kocifaj, M., Meresescu, A.G., 2017. Formation of recurring slope lineae on Mars by rarefied gas-triggered granular flows. Nat. Geosci. 10, 270–273. https://doi.org/10.1038/ngeo2917

Schon, S.C., Head, J.W., Fassett, C.I., 2012a. An overfilled lacustrine system and progradational delta in Jezero crater, Mars: Implications for Noachian climate. Planet. Space Sci. 67, 28–45. https://doi.org/10.1016/j.pss.2012.02.003

Schon, S.C., Head, J.W., Fassett, C.I., 2012b. Recent high-latitude resurfacing by a climate-related latitude-dependent mantle: Constraining age of emplacement from counts of small craters. Planet. Space Sci. 69, 49-61. https://doi.org/10.1016/j.pss.2012.03.015

Schorghofer, N., Aharonson, O., Khatiwala, S., 2002. Slope streaks on Mars: Correlations with surface properties and the potential role of water: SLOPE STREAKS ON MARS. Geophys. Res. Lett. 29, 41-1-41–4. https://doi.org/10.1029/2002GL015889

Schorghofer, N., 2005. Stability and exchange of subsurface ice on Mars. J. Geophys. Res. 110, E05003. https://doi.org/10.1029/2004JE002350

Schorghofer, N., Aharonson, O., Gerstell, M., Tatsumi, L., 2007. Three decades of slope streak activity on Mars. Icarus 191, 132–140. https://doi.org/10.1016/j.icarus.2007.04.026

Schorghofer, N., 2008. Temperature response of Mars to Milankovitch cycles. Geophys. Res. Lett. 35, L18201. https://doi.org/10.1029/2008GL034954

Schorghofer, N., King, C.M., 2011. Sporadic formation of slope streaks on Mars. Icarus 216, 159–168. https://doi.org/10.1016/j.icarus.2011.08.028

Schultz, R.A., 1991. Structural development of Coprates Chasma and Western Ophir Planum, Valles Marineris Rift, Mars. J. Geophys. Res. 96, 22777. https://doi.org/10.1029/91JE02556

Schultz, R.A., 1998. Multiple-process origin of Valles Marineris basins and troughs, Mars. Planet. Space Sci. 46, 827–834. https://doi.org/10.1016/S0032-0633(98)00030-0

Scott, D.H., Carr, M.H., 1978. Geologic map of Mars. https://doi.org/10.3133/i1083

Scott, D.H., Tanaka, K.L., 1986. Geologic map of the western equatorial region of Mars. https://doi.org/10.3133/i1802A

Segura, T.L., Toon, O.B., Colaprete, A., Zahnle, K., 2002. Environmental Effects of Large Impacts on Mars. Science 298, 1977–1980. https://doi.org/10.1126/science.1073586

Seibert, N.M., Kargel, J.S., 2001. Small-scale Martian polygonal terrain: Implications for liquid surface water. Geophys. Res. Lett. 28, 899–902. https://doi.org/10.1029/2000GL012093

Séjourné, A., Costard, F., Gargani, J., Soare, R.J., Fedorov, A., Marmo, C., 2011. Scalloped depressions and small-sized polygons in western Utopia Planitia, Mars: A new formation hypothesis. Planet. Space Sci. 59, 412–422. https://doi.org/10.1016/j.pss.2011.01.007

Séjourné, A., Costard, F., Gargani, J., Soare, R.J., Marmo, C., 2012. Evidence of an eolian ice-rich and stratified permafrost in Utopia Planitia, Mars. Planet. Space Sci. 60, 248–254. https://doi.org/10.1016/j.pss.2011.09.004

Séjourné, A., Costard, F., Fedorov, A., Gargani, J., Skorve, J., Massé, M., Mège, D., 2015. Evolution of the banks of thermokarst lakes in Central Yakutia (Central Siberia) due to retrogressive thaw slump activity controlled by insolation. Geomorphology 241, 31–40. https://doi.org/10.1016/j.geomorph.2015.03.033

Séjourné, A., Costard, F., Swirad, Z.M., Łosiak, A., Bouley, S., Smith, I., Balme, M.R., Orgel, C., Ramsdale, J.D., Hauber, E., Conway, S.J., Gasselt, S., Reiss, D., Johnsson, A., Gallagher, C., Skinner, J.A., Kereszturi, Á., Platz, T., 2019. Grid Mapping the Northern Plains of Mars: Using Morphotype and Distribution of Ice-Related Landforms to Understand Multiple Ice-Rich Deposits in Utopia Planitia. J. Geophys. Res. Planets 124, 483–503. https://doi.org/10.1029/2018JE005665

Seppälä, M., 1982. An experimental study of the formation of palsas. Proc. Fourth Can. Permafr. Conf. 36.

Seppälä, M., 1986. The Origin of Palsas. Geogr. Ann. Ser. Phys. Geogr. 68, 141–147. https://doi.org/10.1080/04353676.1986.11880167

Seppala, M., Gray, J., Ricard, J., 1991. Development of low-centred ice-wedge polygons in the northernmost Ungava Peninsual, Queébec, Canada. Boreas 20, 259–285. https://doi.org/10.1111/j.1502-3885.1991.tb00155.x

Seppälä, M., 2004. Wind as a Geomorphic Agent in Cold Climates, Studies in Polar Research. Cambridge University Press.

Seppälä, M., 2011. Synthesis of studies of palsa formation underlining the importance of local environmental and physical characteristics. Quat. Res. 75, 366–370. https://doi.org/10.1016/j.yqres.2010.09.007

Seu, R., Phillips, R.J., Biccari, D., Orosei, R., Masdea, A., Picardi, G., Safaeinili, A., Campbell, B.A., Plaut, J.J., Marinangeli, L., Smrekar, S.E., Nunes, D.C., 2007. SHARAD sounding radar on the Mars Reconnaissance Orbiter. J. Geophys. Res. 112, E05S05. https://doi.org/10.1029/2006JE002745

Seybold, H.J., Kite, E., Kirchner, J.W., 2018. Branching geometry of valley networks on Mars and Earth and its implications for early Martian climate. Sci. Adv. 4, eaar6692. https://doi.org/10.1126/sciadv.aar6692

Sharaf, O., Amiri, S., AlDhafri, S., Withnell, P., Brain, D., 2020. Sending hope to Mars. Nat. Astron. 4, 722–722. https://doi.org/10.1038/s41550-020-1151-y

Sharp, R.P., 1973. Mars: Troughed terrain. J. Geophys. Res. 78, 4063–4072. https://doi.org/10.1029/JB078i020p04063

Sharp, R.P., Soderblom, L.A., Murray, B.C., Cutts, J.A., 1971. The surface of Mars 2. Uncratered terrains. J. Geophys. Res. 76, 331–342. https://doi.org/10.1029/JB076i002p00331

Shea, T., Van Wyk De Vries, B., 2008. Structural analysis and analogue modeling of the kinematics and dynamics of rockslide avalanches. Geosphere 4, 657. https://doi.org/10.1130/GES00131.1

Shea, T., Van Wyk De Vries, B., Pilato, M., 2008. Emplacement mechanisms of contrasting debris avalanches at Volcán Mombacho (Nicaragua), provided by structural and facies analysis. Bull. Volcanol. 70, 899–921. https://doi.org/10.1007/s00445-007-0177-7

Sheng, D., Zhang, S., Yu, Z., Zhang, J., 2013. Assessing frost susceptibility of soils using PCHeave. Cold Reg. Sci. Technol. 95, 27–38. https://doi.org/10.1016/j.coldregions.2013.08.003

Shotwell, R., 2005. Phoenix—the first Mars Scout mission. Acta Astronaut. 57, 121–134. https://doi.org/10.1016/j.actaastro.2005.03.038

Shur, Y., Hinkel, K.M., Nelson, F.E., 2005. The transient layer: implications for geocryology and climate-change science. Permafr. Periglac. Process. 16, 5–17. https://doi.org/10.1002/ppp.518

Silvestro, S., Fenton, L.K., Vaz, D.A., Bridges, N.T., Ori, G.G., 2010. Ripple migration and dune activity on Mars: Evidence for dynamic wind processes: RIPPLE AND DUNE ACTIVITY ON MARS. Geophys. Res. Lett. 37, n/a-n/a. https://doi.org/10.1029/2010GL044743

Sizemore, H.G., Zent, A.P., Rempel, A.W., 2015. Initiation and growth of martian ice lenses. Icarus 251, 191–210. https://doi.org/10.1016/j.icarus.2014.04.013

Skinner, J.A., Fortezzo, C.M., Mouginis-Mark, P.J., 2021. Exposure of an Early to Middle Noachian valley network in three dimensions on Mars. Icarus 354, 114071. https://doi.org/10.1016/j.icarus.2020.114071

Skok, J.R., Mustard, J.F., Murchie, S.L., Wyatt, M.B., Ehlmann, B.L., 2010. Spectrally distinct ejecta in Syrtis Major, Mars: Evidence for environmental change at the Hesperian-Amazonian boundary. J. Geophys. Res. 115, E00D14. https://doi.org/10.1029/2009JE003338

Slaymaker, O., 2009. Proglacial, periglacial or paraglacial? Geol. Soc. Lond. Spec. Publ. 320, 71–84. https://doi.org/10.1144/SP320.6

Śledź, S., Ewertowski, M.W., Piekarczyk, J., 2021. Applications of unmanned aerial vehicle (UAV) surveys and Structure from Motion photogrammetry in glacial and periglacial geomorphology. Geomorphology 378, 107620. https://doi.org/10.1016/j.geomorph.2021.107620

Sleep, N.H., Zahnle, K., 1998. Refugia from asteroid impacts on early Mars and the early Earth. J. Geophys. Res. Planets 103, 28529–28544. https://doi.org/10.1029/98JE01809

Sletten, R.S., Hallet, B., Fletcher, R.C. 2003. Resurfacing time of terrestrial surfaces by the formation and maturation of polygonal patterned ground. J. Geophys. Res. 108, 8044. https://doi.org/10.1029/2002JE001914

Slusarchuk, W.A., Watson, G.H., 1975. Thermal Conductivity of Some Ice-rich Permafrost Soils. Can. Geotech. J. 12, 413–424. https://doi.org/10.1139/t75-045

Smith, D.E., Zuber, M.T., Frey, H.V., Garvin, J.B., Head, J.W., Muhleman, D.O., Pettengill, G.H., Phillips, R.J., Solomon, S.C., Zwally, H.J., Banerdt, W.B., Duxbury, T.C., Golombek, M.P., Lemoine, F.G., Neumann, G.A., Rowlands, D.D., Aharonson, O., Ford, P.G., Ivanov, A.B., Johnson, C.L., McGovern, P.J., Abshire, J.B., Afzal, R.S., Sun, X., 2001. Mars Orbiter Laser Altimeter: Experiment summary after the first year of global mapping of Mars. J. Geophys. Res. Planets 106, 23689–23722. https://doi.org/10.1029/2000JE001364

Smith, I.B., Lalich, D.E., Rezza, C., Horgan, B.H.N., Whitten, J.L., Nerozzi, S., Holt, J.W., 2021. A Solid Interpretation of Bright Radar Reflectors Under the Mars South Polar Ice. Geophys. Res. Lett. 48. https://doi.org/10.1029/2021GL093618

Smith, M.D., 2002. The annual cycle of water vapor on Mars as observed by the Thermal Emission Spectrometer: MARS WATER VAPOR. J. Geophys. Res. Planets 107, 25-1-25–19. https://doi.org/10.1029/2001JE001522

Smith, M.R., Gillespie, A.R., Montgomery, D.R., 2008. Effect of obliteration on crater-count chronologies for Martian surfaces: MARTIAN SURFACE CRATER-COUNT CHRONOLOGIES. Geophys. Res. Lett. 35. https://doi.org/10.1029/2008GL033538

Smith, M.W., Riseborough, D.W., 1996. Permafrost monitoring and detection of climate change. Permafr. Periglac. Process. 7, 301–309. https://doi.org/10.1002/(SICI)1099-1530(199610)7:4<301::AID-PPP231>3.0.CO;2-R

Smith, M.W., Carrivick, J.L., Quincey, D.J., 2016. Structure from motion photogrammetry in physical geography. Prog. Phys. Geogr. Earth Environ. 40, 247–275. https://doi.org/10.1177/0309133315615805

Smith, P.H., 2004. The Phoenix mission to Mars, in: 2004 IEEE Aerospace Conference Proceedings (IEEE Cat. No.04TH8720). Presented at the 2004 IEEE Aerospace, IEEE, Big Sky, MT, USA, pp. 337–342. https://doi.org/10.1109/AERO.2004.1367617

Smith, P.H., Tamppari, L.K., Arvidson, R.E., Bass, D., Blaney, D., Boynton, W.V., Carswell, A., Catling, D.C., Clark, B.C., Duck, T., DeJong, E., Fisher, D., Goetz, W., Gunnlaugsson, H.P., Hecht, M.H., Hipkin, V., Hoffman, J., Hviid, S.F., Keller, H.U., Kounaves, S.P., Lange, C.F., Lemmon, M.T., Madsen, M.B., Markiewicz, W.J., Marshall, J., McKay, C.P., Mellon, M.T., Ming, D.W., Morris, R.V., Pike, W.T., Renno, N., Staufer, U., Stoker, C., Taylor, P., Whiteway, J.A., Zent, A.P., 2009. H_2O at the Phoenix Landing Site. Science 325, 58–61. https://doi.org/10.1126/science.1172339

Smith, S.L., Romanovsky, V.E., Lewkowicz, A.G., Burn, C.R., Allard, M., Clow, G.D., Yoshikawa, K., Throop, J., 2010. Thermal state of permafrost in North America: a contribution to the international polar year. Permafr. Periglac. Process. 21, 117–135. https://doi.org/10.1002/ppp.690

Smrekar, S.E., Lognonné, P., Spohn, T., Banerdt, W.B., Breuer, D., Christensen, U., Dehant, V., Drilleau, M., Folkner, W., Fuji, N., Garcia, R.F., Giardini, D., Golombek, M., Grott, M., Gudkova, T., Johnson, C., Khan, A., Langlais, B., Mittelholz, A., Mocquet, A., Myhill, R., Panning, M., Perrin, C., Pike, T., Plesa, A.-C., Rivoldini, A., Samuel, H., Stähler, S.C., Van Driel, M., Van Hoolst, T., Verhoeven, O., Weber, R., Wieczorek, M., 2019. Pre-mission InSights on the Interior of Mars. Space Sci. Rev. 215, 3. https://doi.org/10.1007/s11214-018-0563-9

Snavely, N., Seitz, S.M., Szeliski, R., 2008. Modeling the World from Internet Photo Collections. Int. J. Comput. Vis. 80, 189–210. https://doi.org/10.1007/s11263-007-0107-3

Soare, R.J., Burr, D.M., Wan Bun Tseung, J.M., 2005. Possible pingos and a periglacial landscape in northwest Utopia Planitia. Icarus 174, 373–382. https://doi.org/10.1016/j.icarus.2004.11.013

Soare, R., Kargel, J., Osinski, G., Costard, F., 2007. Thermokarst processes and the origin of crater-rim gullies in Utopia and western Elysium Planitia. Icarus 191, 95–112. https://doi.org/10.1016/j.icarus.2007.04.018

Soare, R.J., Osinski, G.R., Roehm, C.L., 2008. Thermokarst lakes and ponds on Mars in the very recent (late Amazonian) past. Earth Planet. Sci. Lett. 272, 382–393. https://doi.org/10.1016/j.epsl.2008.05.010

Soare, R.J., Séjourné, A., Pearce, G., Costard, F., Osinski, G.R., 2011. The Tuktoyaktuk Coastlands of northern Canada: A possible "wet" periglacial analog of Utopia Planitia, Mars, in: Analogs for Planetary Exploration. Geological Society of America. https://doi.org/10.1130/2011.2483(13)

Soare, R.J., Conway, S.J., Pearce, G.D., Costard, F., Séjourné, A., 2013a. Sub-kilometre (intra-crater) mounds in Utopia Planitia, Mars: character, occurrence and possible formation hypotheses. Icarus 225, 982–991. https://doi.org/10.1016/j.icarus.2012.06.003

Soare, R.J., Conway, S.J., Pearce, G.D., Dohm, J.M., Grindrod, P.M., 2013b. Possible crater-based pingos, paleolakes and periglacial landscapes at the high latitudes of Utopia Planitia, Mars. Icarus 225, 971–981. https://doi.org/10.1016/j.icarus.2012.08.041

Soare, R.J., Conway, S.J., Dohm, J.M., 2014a. Possible ice-wedge polygons and recent landscape modification by "wet" periglacial processes in and around the Argyre impact basin, Mars. Icarus 233, 214–228. https://doi.org/10.1016/j.icarus.2014.01.034

Soare, R.J., Conway, S.J., Dohm, J.M., El-Maarry, M.R., 2014b. Possible open-system (hydraulic) pingos in and around the Argyre impact region of Mars. Earth Planet. Sci. Lett. 398, 25–36. https://doi.org/10.1016/j.epsl.2014.04.044Soare, R.J., Horgan, B., Conway, S.J., Souness, C., El-Maarry, M.R., 2015. Volcanic terrain and the possible periglacial formation of "excess ice" at the mid-latitudes of Utopia Planitia, Mars. Earth Planet. Sci. Lett. 423, 182–192. https://doi.org/10.1016/j.epsl.2015.04.033

Soare, R.J., Conway, S.J., Gallagher, C., Dohm, J.M., 2017. Ice-rich (periglacial) vs icy (glacial) depressions in the Argyre region, Mars: a proposed cold-climate dichotomy of landforms. Icarus 282, 70–83. https://doi.org/10.1016/j.icarus.2016.09.009

Soare, Richard J., Conway, S.J., Gallagher, C.J., Williams, J.-P., Osinski, G.R., 2018. Paleo-Periglacial and "Ice-Rich" Complexes in Utopia Planitia, in: Dynamic Mars. Elsevier, pp. 209–237. https://doi.org/10.1016/B978-0-12-813018-6.00007-8

Soare, R.J., Conway, S.J., Williams, J.-P., Gallagher, C., Keown, L.E.M., 2020. Possible (closed system) pingo and ice-wedge/thermokarst complexes at the mid latitudes of Utopia Planitia, Mars. Icarus 342, 113233. https://doi.org/10.1016/j.icarus.2019.03.010

Soare, R.J., Conway, S.J., Williams, J.-P., Philippe, M., Mc Keown, L.E., Godin, E., Hawkswell, J., 2021. Possible ice-wedge polygonisation in Utopia Planitia, Mars and its latitudinal gradient of distribution. Icarus 358, 114208. https://doi.org/10.1016/j.icarus.2020.114208

Soderblom, L.A., Malin, M.C., Cutts, J.A., Murray, B.C., 1973. Mariner 9 observations of the surface of Mars in the north polar region. J. Geophys. Res. 78, 4197–4210. https://doi.org/10.1029/JB078i020p04197

Soffen, G.A., Thomas Young, A., 1972. The Viking missions to Mars. Icarus 16, 1–16. https://doi.org/10.1016/0019-1035(72)90133-9

Soffen, G.A., Snyder, C.W., 1976. The First Viking Mission to Mars. Science 193, 759–766. https://doi.org/10.1126/science.193.4255.759

Soffen, G.A., 1978. Mars and the Remarkable Viking Results. J. Spacecr. Rockets 15, 193–200. https://doi.org/10.2514/3.57305

Sone, T., Yamagata, K., Otsuki, Y., Sawada, Y., Vyatkina, M., 2006. Distribution of permafrost on the west slope of Mt. Ichinsky, Kamchatka, Russia. Bull. Glaciol. Res. 23, 69.

Spanovich, N., Smith, M.D., Smith, P.H., Wolff, M.J., Christensen, P.R., Squyres, S.W., 2006. Surface and near-surface atmospheric temperatures for the Mars Exploration Rover landing sites. Icarus 180, 314–320. https://doi.org/10.1016/j.icarus.2005.09.014

Spetsakis, M., Aloimonos, J.Y., 1991. A multi-frame approach to visual motion perception. Int. J. Comput. Vis. 6, 245–255. https://doi.org/10.1007/BF00115698

Spiga, A., Forget, F., Dolla, B., Vinatier, S., Melchiorri, R., Drossart, P., Gendrin, A., Bibring, J.-P., Langevin, Y., Gondet, B., 2007. Remote sensing of surface pressure on Mars with the Mars

Express/OMEGA spectrometer: 2. Meteorological maps: REMOTE SENSING OF SURFACE PRESSURE ON MARS, 2. J. Geophys. Res. Planets 112. https://doi.org/10.1029/2006JE002870
Sprague, A.L., Hunten, D.M., Hill, R.E., Rizk, B., Wells, W.K., 1996. Martian water vapor, 1988-1995. J. Geophys. Res. Planets 101, 23229–23241. https://doi.org/10.1029/96JE02265
Squyres, S.W., 1978. Martian fretted terrain: Flow of erosional debris. Icarus 34, 600–613. https://doi.org/10.1016/0019-1035(78)90048-9
Squyres, S.W., 1979. The distribution of lobate debris aprons and similar flows on Mars. J. Geophys. Res. 84, 8087. https://doi.org/10.1029/JB084iB14p08087
Šrámek, O., Zhong, S., 2012. Martian crustal dichotomy and Tharsis formation by partial melting coupled to early plume migration: MARTIAN DICHOTOMY BY MELTING AND THARSIS. J. Geophys. Res. Planets 117. https://doi.org/10.1029/2011JE003867
Stillman, D.E., Grimm, R.E., 2011. Dielectric signatures of adsorbed and salty liquid water at the Phoenix landing site, Mars. J. Geophys. Res. Planets 116, 2011JE003838. https://doi.org/10.1029/2011JE003838
Stillman, D.E., Grimm, R.E., 2018. Two pulses of seasonal activity in martian southern mid-latitude recurring slope lineae (RSL). Icarus 302, 126–133. https://doi.org/10.1016/j.icarus.2017.10.026
Strauss, J., Schirrmeister, L., Grosse, G., Fortier, D., Hugelius, G., Knoblauch, C., Romanovsky, V., Schädel, C., Schneider Von Deimling, T., Schuur, E.A.G., Shmelev, D., Ulrich, M., Veremeeva, A., 2017. Deep Yedoma permafrost: A synthesis of depositional characteristics and carbon vulnerability. Earth-Sci. Rev. 172, 75–86. https://doi.org/10.1016/j.earscirev.2017.07.007
Strom, R.G., Croft, S.K., Barlow, N.G., 1992. The Martian impact cratering record., Mars.
Stucky De Quay, G., Goudge, T.A., Fassett, C.I., 2020. Precipitation and aridity constraints from paleolakes on early Mars. Geology 48, 1189–1193. https://doi.org/10.1130/G47886.1
Stucky De Quay, G., Goudge, T.A., Kite, E.S., Fassett, C.I., Guzewich, S.D., 2021. Limits on Runoff Episode Duration for Early Mars: Integrating Lake Hydrology and Climate Models. Geophys. Res. Lett. 48. https://doi.org/10.1029/2021GL093523
Stuurman, C.M., Osinski, G.R., Holt, J.W., Levy, J.S., Brothers, T.C., Kerrigan, M., Campbell, B.A., 2016. SHARAD detection and characterization of subsurface water ice deposits in Utopia Planitia, Mars: SHARAD DETECTION OF ICE UTOPIA PLANITIA. Geophys. Res. Lett. 43, 9484–9491. https://doi.org/10.1002/2016GL070138
Sulcanese, D., Mitri, G., Genova, A., Petricca, F., Andolfo, S., Chiarolanza, G., 2023. Topographical analysis of a candidate subglacial water region in Ultimi Scopuli, Mars. Icarus 392, 115394. https://doi.org/10.1016/j.icarus.2022.115394
Svennevig, K., Hermanns, R.L., Keiding, M., Binder, D., Citterio, M., Dahl-Jensen, T., Mertl, S., Sørensen, E.V., Voss, P.H., 2022. A large frozen debris avalanche entraining warming permafrost ground—the June 2021 Assapaat landslide, West Greenland. Landslides 19, 2549–2567. https://doi.org/10.1007/s10346-022-01922-7
Svennevig, K., Keiding, M., Korsgaard, N.J., Lucas, A., Owen, M., Poulsen, M.D., Priebe, J., Sørensen, E.V., Morino, C., 2023. Uncovering a 70-year-old permafrost degradation induced disaster in the Arctic, the 1952 Niiortuut landslide-tsunami in central West Greenland. Sci. Total Environ. 859, 160110. https://doi.org/10.1016/j.scitotenv.2022.160110
Svitek, T., Murray, B., 1990. Winter frost at Viking Lander 2 site. J. Geophys. Res. 95, 1495. https://doi.org/10.1029/JB095iB02p01495
Szeliski, R., Kang, S.B., 1994. Recovering 3D Shape and Motion from Image Streams Using Nonlinear Least Squares. J. Vis. Commun. Image Represent. 5, 10–28. https://doi.org/10.1006/jvci.1994.1002
Szeliski, R., 2011. Structure from motion, in: Computer Vision, Texts in Computer Science. Springer London, London, pp. 303–334. https://doi.org/10.1007/978-1-84882-935-0_7
Taber, S., 1929. Frost Heaving. J. Geol. 37, 428–461. https://doi.org/10.1086/623637
Taber, S., 1930. The Mechanics of Frost Heaving. J. Geol. 38, 303–317. https://doi.org/10.1086/623720
Takagi, S., 1970. An Analysis of Ice Lens Formation. Water Resour. Res. 6, 736–749. https://doi.org/10.1029/WR006i003p00736

Takagi, S., 1979. Segregation Freezing as the Cause of Suction Force for Ice Lens Formation, in: Developments in Geotechnical Engineering. Elsevier, pp. 93–100. https://doi.org/10.1016/B978-0-444-41782-4.50013-0

Tanaka, K.L., 1986. The stratigraphy of Mars. J. Geophys. Res. 91, E139. https://doi.org/10.1029/JB091iB13p0E139

Tanaka, K.L., Leonard, G.J., 1995. Geology and landscape evolution of the Hellas region of Mars. J. Geophys. Res. 100, 5407. https://doi.org/10.1029/94JE02804

Tanaka, K.L., Skinner, J.A., Hare, T.M., 2005. Geologic Map of the Northern Plains of Mars. U.S. Geological Survey Science Investigations Map.

Tanaka, K.L., Robbins, S.J., Fortezzo, C.M., Skinner, J.A., Hare, T.M., 2014. The digital global geologic map of Mars: Chronostratigraphic ages, topographic and crater morphologic characteristics, and updated resurfacing history. Planet. Space Sci. 95, 11–24. https://doi.org/10.1016/j.pss.2013.03.006

Tarr, R.S., 1897. The Arctic Sea Ice as a Geological Agent. Am. J. Sci. 3, 223.

Thiriet, M., Michaut, C., Breuer, D., Plesa, A.-C., 2018. Hemispheric Dichotomy in Lithosphere Thickness on Mars Caused by Differences in Crustal Structure and Composition: MARTIAN LITHOSPHERE DICHOTOMY. J. Geophys. Res. Planets 123, 823–848. https://doi.org/10.1002/2017JE005431

Thomas, D.N., 2017. Sea Ice, 3rd Edition, 3rd Edition. ed. Wiley Blackwell.

Thomas, N., Cremonese, G., Ziethe, R., Gerber, M., Brändli, M., Bruno, G., Erismann, M., Gambicorti, L., Gerber, T., Ghose, K., Gruber, M., Gubler, P., Mischler, H., Jost, J., Piazza, D., Pommerol, A., Rieder, M., Roloff, V., Servonet, A., Trottmann, W., Uthaicharoenpong, T., Zimmermann, C., Vernani, D., Johnson, M., Pelò, E., Weigel, T., Viertl, J., De Roux, N., Lochmatter, P., Sutter, G., Casciello, A., Hausner, T., Ficai Veltroni, I., Da Deppo, V., Orleanski, P., Nowosielski, W., Zawistowski, T., Szalai, S., Sodor, B., Tulyakov, S., Troznai, G., Banaskiewicz, M., Bridges, J.C., Byrne, S., Debei, S., El-Maarry, M.R., Hauber, E., Hansen, C.J., Ivanov, A., Keszthelyi, L., Kirk, R., Kuzmin, R., Mangold, N., Marinangeli, L., Markiewicz, W.J., Massironi, M., McEwen, A.S., Okubo, C., Tornabene, L.L., Wajer, P., Wray, J.J., 2017. The Colour and Stereo Surface Imaging System (CaSSIS) for the ExoMars Trace Gas Orbiter. Space Sci. Rev. 212, 1897–1944. https://doi.org/10.1007/s11214-017-0421-1

Thomas, N. H., Ehlmann, B.L., Meslin, P. -Y., Rapin, W., Anderson, D.E., Rivera-Hernández, F., Forni, O., Schröder, S., Cousin, A., Mangold, N., Gellert, R., Gasnault, O., Wiens, R.C., 2019. Mars Science Laboratory Observations of Chloride Salts in Gale Crater, Mars. Geophys. Res. Lett. 46, 10754–10763. https://doi.org/10.1029/2019GL082764

Toner, J.D., Catling, D.C., 2018. Chlorate brines on Mars: Implications for the occurrence of liquid water and deliquescence. Earth Planet. Sci. Lett. 497, 161–168. https://doi.org/10.1016/j.epsl.2018.06.011

Tornabene, L.L., Osinski, G.R., McEwen, A.S., Boyce, J.M., Bray, V.J., Caudill, C.M., Grant, J.A., Hamilton, C.W., Mattson, S., Mouginis-Mark, P.J., 2012. Widespread crater-related pitted materials on Mars: Further evidence for the role of target volatiles during the impact process. Icarus 220, 348–368. https://doi.org/10.1016/j.icarus.2012.05.022

Touma, J., Wisdom, J., 1993. The Chaotic Obliquity of Mars. Science 259, 1294–1297. https://doi.org/10.1126/science.259.5099.1294

Trainer, M.G., Wong, M.H., McConnochie, T.H., Franz, H.B., Atreya, S.K., Conrad, P.G., Lefèvre, F., Mahaffy, P.R., Malespin, C.A., Manning, H.L.K., Martín-Torres, J., Martínez, G.M., McKay, C.P., Navarro-González, R., Vicente-Retortillo, Á., Webster, C.R., Zorzano, M., 2019. Seasonal Variations in Atmospheric Composition as Measured in Gale Crater, Mars. J. Geophys. Res. Planets 124, 3000–3024. https://doi.org/10.1029/2019JE006175

Travis, B.J., Feldman, W.C., Maurice, S., 2013. A mechanism for bringing ice and brines to the near surface of Mars: BRINE CONVECTION ON MARS. J. Geophys. Res. Planets 118, 877–890. https://doi.org/10.1002/jgre.20074

Tricart, J., 1968. Periglacial landscapes, in: Geomorphology, Encyclopedia of Earth Science. Kluwer Academic Publishers, Dordrecht, pp. 829–833. https://doi.org/10.1007/3-540-31060-6_279

Trokhimovskiy, A., Fedorova, A., Korablev, O., Montmessin, F., Bertaux, J.-L., Rodin, A., Smith, M.D., 2015. Mars' water vapor mapping by the SPICAM IR spectrometer: Five martian years of observations. Icarus 251, 50–64. https://doi.org/10.1016/j.icarus.2014.10.007

Troll, C., 1944. Strukturböden, Solifluktion und Frostklimate der Erde. Geol. Rundsch. 34, 545–694. https://doi.org/10.1007/BF01803103

Ullman, S., 1979. The interpretation of structure from motion. Proc. R. Soc. Lond. B Biol. Sci. 203, 405–426. https://doi.org/10.1098/rspb.1979.0006

Ulrich, M., Morgenstern, A., Günther, F., Reiss, D., Bauch, K.E., Hauber, E., Rössler, S., Schirrmeister, L., 2010. Thermokarst in Siberian ice-rich permafrost: Comparison to asymmetric scalloped depressions on Mars. J. Geophys. Res. 115, E10009. https://doi.org/10.1029/2010JE003640

Ulrich, M., Hauber, E., Herzschuh, U., Härtel, S., Schirrmeister, L., 2011. Polygon pattern geomorphometry on Svalbard (Norway) and western Utopia Planitia (Mars) using high-resolution stereo remote-sensing data. Geomorphology 134, 197–216. https://doi.org/10.1016/j.geomorph.2011.07.002

Ulrich, M., Wagner, D., Hauber, E., de Vera, J.-P., Schirrmeister, L., 2012. Habitable periglacial landscapes in martian mid-latitudes. Icarus 219, 345-357. https://doi.org/10.1016/j.icarus.2012.03.019

Utting, D.J., Ward, B.C., Little, E.C., 2009. Genesis of hummocks in glaciofluvial corridors near the Keewatin Ice Divide, Canada. Boreas 38, 471–481. https://doi.org/10.1111/j.1502-3885.2008.00074.x

Vago, J., Witasse, O., Svedhem, H., Baglioni, P., Haldemann, A., Gianfiglio, G., Blancquaert, T., McCoy, D., De Groot, R., 2015. ESA ExoMars program: The next step in exploring Mars. Sol. Syst. Res. 49, 518–528. https://doi.org/10.1134/S0038094615070199

Van Vliet-Lanoë, B., Bourgeois, O., Dauteuil, O., 1998. Thufur formation in northern Iceland and its relation to holocene climate change. Permafr. Periglac. Process. 9, 347–365. https://doi.org/10.1002/(SICI)1099-1530(199810/12)9:4<347::AID-PPP299>3.0.CO;2-4

Vaniman, D.T., Bish, D.L., Chipera, S.J., Fialips, C.I., William Carey, J., Feldman, W.C., 2004. Magnesium sulphate salts and the history of water on Mars. Nature 431, 663–665. https://doi.org/10.1038/nature02973

Vasavada, A.R., Grotzinger, J.P., Arvidson, R.E., Calef, F.J., Crisp, J.A., Gupta, S., Hurowitz, J., Mangold, N., Maurice, S., Schmidt, M.E., Wiens, R.C., Williams, R.M.E., Yingst, R.A., 2014. Overview of the Mars Science Laboratory mission: Bradbury Landing to Yellowknife Bay and beyond. J. Geophys. Res. Planets 119, 1134–1161. https://doi.org/10.1002/2014JE004622

Vassilopoulou, S., Hurni, L., Dietrich, V., Baltsavias, E., Pateraki, M., Lagios, E., Parcharidis, I., 2002. Orthophoto generation using IKONOS imagery and high-resolution DEM: a case study on volcanic hazard monitoring of Nisyros Island (Greece). ISPRS J. Photogramm. Remote Sens. 57, 24–38. https://doi.org/10.1016/S0924-2716(02)00126-0

Vérité, J., Ravier, É., Bourgeois, O., Pochat, S., Lelandais, T., Mourgues, R., Clark, C.D., Bessin, P., Peigné, D., Atkinson, N., 2021. Formation of ribbed bedforms below shear margins and lobes of palaeo-ice streams. The Cryosphere 15, 2889–2916. https://doi.org/10.5194/tc-15-2889-2021

Vérité, J., Ravier, É., Bourgeois, O., Bessin, P., Livingstone, S.J., Clark, C.D., Pochat, S., Mourgues, R., 2022. Formation of murtoos by repeated flooding of ribbed bedforms along subglacial meltwater corridors. Geomorphology 408, 108248. https://doi.org/10.1016/j.geomorph.2022.108248

Vieira, G., Bockheim, J., Guglielmin, M., Balks, M., Abramov, A.A., Boelhouwers, J., Cannone, N., Ganzert, L., Gilichinsky, D.A., Goryachkin, S., López-Martínez, J., Meiklejohn, I., Raffi, R., Ramos, M., Schaefer, C., Serrano, E., Simas, F., Sletten, R., Wagner, D., 2010. Thermal state of permafrost and active-layer monitoring in the antarctic: Advances during the international polar year 2007-2009: Thermal State of Permafrost in the Antarctic. Permafr. Periglac. Process. 21, 182–197. https://doi.org/10.1002/ppp.685

Vincendon, M., 2015. Identification of Mars gully activity types associated with ice composition: ICE COMPOSITION AT ACTIVE MARS GULLIES. J. Geophys. Res. Planets 120, 1859–1879. https://doi.org/10.1002/2015JE004909

Vincendon, M., Pilorget, C., Carter, J., Stcherbinine, A., 2019. Observational evidence for a dry dust-wind origin of Mars seasonal dark flows. Icarus 325, 115–127. https://doi.org/10.1016/j.icarus.2019.02.024

Viola, D., McEwen, A.S., Dundas, C.M., Byrne, S., 2015. Expanded secondary craters in the Arcadia Planitia region, Mars: Evidence for tens of Myr-old shallow subsurface ice. Icarus 248, 190–204. https://doi.org/10.1016/j.icarus.2014.10.032

Viola, D., McEwen, A.S., 2018. Geomorphological Evidence for Shallow Ice in the Southern Hemisphere of Mars. J. Geophys. Res. Planets 123, 262–277. https://doi.org/10.1002/2017JE005366

Viviano, C.E., Murchie, S.L., Daubar, I.J., Morgan, M.F., Seelos, F.P., Plescia, J.B., 2019. Composition of Amazonian volcanic materials in Tharsis and Elysium, Mars, from MRO/CRISM reflectance spectra. Icarus 328, 274–286. https://doi.org/10.1016/j.icarus.2019.03.001

von Lozinski, W., 1909. Über die mechanische Verwitterung der Sandsteine im gemässigten klima. Bull. Int. Académie Sci. Crac. Cl. Sci. Mathématique Nat. 1, 1–25.

von Lozinski, W., 1912. Die periglaziale fazies der mechanischen Verwitterung, in: Comptes Rendus, XI Congrès Internationale Géologie, Stockholm. Presented at the XI Congrès Internationale Géologie, pp. 1039–1053.

Wagner, A.M., Lindsey, N.J., Dou, S., Gelvin, A., Saari, S., Williams, C., Ekblaw, I., Ulrich, C., Borglin, S., Morales, A., Ajo-Franklin, J., 2018. Permafrost Degradation and Subsidence Observations during a Controlled Warming Experiment. Sci. Rep. 8, 10908. https://doi.org/10.1038/s41598-018-29292-y

Walder, J., Hallet, B., 1985. A theoretical model of the fracture of rock during freezing. Geol. Soc. Am. Bull. 96, 336. https://doi.org/10.1130/0016-7606(1985)96<336:ATMOTF>2.0.CO;2

Walder, J.S., Hallet, B., 1986. The Physical Basis of Frost Weathering: Toward a More Fundamental and Unified Perspective. Arct. Alp. Res. 18, 27–32.

Walker, D., 1859. II. Ice observations. Proc. R. Soc. Lond. 9, 609–611. https://doi.org/10.1098/rspl.1857.0118

Walvoord, M.A., Kurylyk, B.L., 2016. Hydrologic Impacts of Thawing Permafrost-A Review. Vadose Zone J. 15, vzj2016.01.0010. https://doi.org/10.2136/vzj2016.01.0010

Wang, J., Zhao, Jiannan, Xiao, L., Peng, S., Zhang, L., Zhang, Z., Gao, A., Qiao, H., Wang, L., Zhang, S., Xiao, X., Shi, Y., Zhao, S., Zhao, Jiawei, Qian, Y., Zhang, J., Zhang, X., Huang, J., 2023. Recent Aqueous Activity on Mars Evidenced by Transverse Aeolian Ridges in the Zhurong Exploration Region of Utopia Planitia. Geophys. Res. Lett. 50, e2022GL101650. https://doi.org/10.1029/2022GL101650

Ward, A.W., 1979. Yardangs on Mars: Evidence of recent wind erosion. J. Geophys. Res. 84, 8147. https://doi.org/10.1029/JB084iB14p08147

Ward, A.W., Doyle, K.B., Helm, P.J., Weisman, M.K., Witbeck, N.E., 1985. Global map of eolian features on Mars. J. Geophys. Res. 90, 2038. https://doi.org/10.1029/JB090iB02p02038

Ward, W.R., 1973. Large-Scale Variations in the Obliquity of Mars. Science 181, 260–262. https://doi.org/10.1126/science.181.4096.260

Warner, N.H., Sowe, M., Gupta, S., Dumke, A., Goddard, K., 2013. Fill and spill of giant lakes in the eastern Valles Marineris region of Mars. Geology 41, 675–678. https://doi.org/10.1130/G34172.1

Warner, N.H., Gupta, S., Calef, F., Grindrod, P., Boll, N., Goddard, K., 2015. Minimum effective area for high resolution crater counting of martian terrains. Icarus 245, 198–240. https://doi.org/10.1016/j.icarus.2014.09.024

Washburn, A.L., 1956. CLASSIFICATION OF PATTERNED GROUND AND REVIEW OF SUGGESTED ORIGINS. Geol. Soc. Am. Bull. 67, 823. https://doi.org/10.1130/0016-7606(1956)67[823:COPGAR]2.0.CO;2

Washburn, A.L., 1976. Periglacial processes and environments. London, Edward Arnold, 1973. [viii], 320 p., illus. £8.50. J. Glaciol. 17, 359–360. https://doi.org/10.3189/S0022143000013654

Washburn, A.L., 1980. Permafrost features as evidence of climatic change. Earth-Sci. Rev. 15, 327–402. https://doi.org/10.1016/0012-8252(80)90114-2

Watanabe, T., Matsuoka, N., Christiansen, H.H., 2013. Ice- and Soil-Wedge Dynamics in the Kapp Linné Area, Svalbard, Investigated by Two- and Three-Dimensional GPR and Ground Thermal and Acceleration Regimes: Ice- and Soil-Wedge Dynamics in the Kapp Linné Area, Svalbard. Permafr. Periglac. Process. 24, 39–55. https://doi.org/10.1002/ppp.1767

Watters, T.R., Maxwell, T.A., 1986. Orientation, relative age, and extent of the Tharsis Plateau Ridge System. J. Geophys. Res. 91, 8113. https://doi.org/10.1029/JB091iB08p08113

Watters, T.R., McGovern, P.J., Irwin Iii, R.P., 2007. Hemispheres Apart: The Crustal Dichotomy on Mars. Annu. Rev. Earth Planet. Sci. 35, 621–652. https://doi.org/10.1146/annurev.earth.35.031306.140220

Way, R.G., Lewkowicz, A.G., 2016. Modelling the spatial distribution of permafrost in Labrador–Ungava using the temperature at the top of permafrost. Can. J. Earth Sci. 53, 1010–1028. https://doi.org/10.1139/cjes-2016-0034

Wei, M., Fujun, N., Satoshi, A., Dewu, J., 2006. Slope instability phenomena in permafrost regions of Qinghai-Tibet Plateau, China. Landslides 3, 260–264. https://doi.org/10.1007/s10346-006-0045-0

Westaway, R.M., Lane, S.N., Hicks, D.M., 2000. The development of an automated correction procedure for digital photogrammetry for the study of wide, shallow, gravel-bed rivers. Earth Surf. Process. Landf. 25, 209–226. https://doi.org/10.1002/(SICI)1096-9837(200002)25:2<209::AID-ESP84>3.0.CO;2-Z

Westoby, M.J., Brasington, J., Glasser, N.F., Hambrey, M.J., Reynolds, J.M., 2012. 'Structure-from-Motion' photogrammetry: A low-cost, effective tool for geoscience applications. Geomorphology 179, 300–314. https://doi.org/10.1016/j.geomorph.2012.08.021

Wetterich, S., Tumskoy, V., Rudaya, N., Andreev, A.A., Opel, T., Meyer, H., Schirrmeister, L., Hüls, M., 2014. Ice Complex formation in arctic East Siberia during the MIS3 Interstadial. Quat. Sci. Rev. 84, 39–55. https://doi.org/10.1016/j.quascirev.2013.11.009

White, E.M., 1971. Contemporary Soil Wedge Formation in Western South Dakota. Soil Sci. Soc. Am. J. 35, 306–309. https://doi.org/10.2136/sssaj1971.03615995003500020036x

White, S.E., 1976. Rock Glaciers and Block fields, Review and new data. Quat. Res. 6, 77–97. https://doi.org/10.1016/0033-5894(76)90041-7

Whitehead, A.B., 1974. The elevation of Olympus Mons from limb photography. Icarus 22, 189–196. https://doi.org/10.1016/0019-1035(74)90117-1

Whiteway, J.A., Komguem, L., Dickinson, C., Cook, C., Illnicki, M., Seabrook, J., Popovici, V., Duck, T.J., Davy, R., Taylor, P.A., Pathak, J., Fisher, D., Carswell, A.I., Daly, M., Hipkin, V., Zent, A.P., Hecht, M.H., Wood, S.E., Tamppari, L.K., Renno, N., Moores, J.E., Lemmon, M.T., Daerden, F., Smith, P.H., 2009. Mars Water-Ice Clouds and Precipitation. Science 325, 68–70. https://doi.org/10.1126/science.1172344

Whitney, M.I., Dietrich, R.V., 1973. Ventifact Sculpture by Windblown Dust. Geol. Soc. Am. Bull. 84, 2561. https://doi.org/10.1130/0016-7606(1973)84<2561:VSBWD>2.0.CO;2

Wieczorek, M.A., 2004. Thickness of the Martian crust: Improved constraints from geoid-to-topography ratios. J. Geophys. Res. 109, E01009. https://doi.org/10.1029/2003JE002153

Wilhelms, D.E., Squyres, S.W., 1984. The martian hemispheric dichotomy may be due to a giant impact. Nature 309, 138–140. https://doi.org/10.1038/309138a0

Williams, J., Van Der Bogert, C.H., Pathare, A.V., Michael, G.G., Kirchoff, M.R., Hiesinger, H., 2018. Dating very young planetary surfaces from crater statistics: A review of issues and challenges. Meteorit. Planet. Sci. 53, 554–582. https://doi.org/10.1111/maps.12924

Williams, J.-P., Nimmo, F., Moore, W.B., Paige, D.A., 2008. The formation of Tharsis on Mars: What the line-of-sight gravity is telling us. J. Geophys. Res. 113, E10011. https://doi.org/10.1029/2007JE003050

Williams, L., 1964. REGIONALIZATION OF FREEZE-THAW ACTIVITY. Ann. Assoc. Am. Geogr. 54, 597–611. https://doi.org/10.1111/j.1467-8306.1964.tb01787.x

Williford, K.H., Farley, K.A., Stack, K.M., Allwood, A.C., Beaty, D., Beegle, L.W., Bhartia, R., Brown, A.J., De La Torre Juarez, M., Hamran, S.-E., Hecht, M.H., Hurowitz, J.A., Rodriguez-Manfredi, J.A., Maurice, S., Milkovich, S., Wiens, R.C., 2018. The NASA Mars 2020 Rover Mission and the Search for Extraterrestrial Life, in: From Habitability to Life on Mars. Elsevier, pp. 275–308. https://doi.org/10.1016/B978-0-12-809935-3.00010-4

Wilson, L., 2003. Phreatomagmatic explosive origin of Hrad Vallis, Mars. J. Geophys. Res. 108, 5082. https://doi.org/10.1029/2002JE001927

Wilson, L., Ghatan, G.J., Head, J.W., Mitchell, K.L., 2004. Mars outflow channels: A reappraisal of the estimation of water flow velocities from water depths, regional slopes, and channel floor properties. J. Geophys. Res. 109, E09003. https://doi.org/10.1029/2004JE002281

Wilson, S.A., Howard, A.D., Moore, J.M., Grant, J.A., 2016. A cold-wet middle-latitude environment on Mars during the Hesperian-Amazonian transition: Evidence from northern Arabia valleys and paleolakes. J. Geophys. Res. Planets 121, 1667–1694. https://doi.org/10.1002/2016JE005052

Wilson, S.A., Morgan, A.M., Howard, A.D., Grant, J.A., 2021. The Global Distribution of Craters With Alluvial Fans and Deltas on Mars. Geophys. Res. Lett. 48. https://doi.org/10.1029/2020GL091653

Wolfe, S.A., Morse, P.D., Neudorf, C.M., Kokelj, S.V., Lian, O.B., O'Neill, H.B., 2018. Contemporary sand wedge development in seasonally frozen ground and paleoenvironmental implications. Geomorphology 308, 215–229. https://doi.org/10.1016/j.geomorph.2018.02.015

Woo, M., 2012. Permafrost Hydrology. Springer Berlin Heidelberg, Berlin, Heidelberg. https://doi.org/10.1007/978-3-642-23462-0

Woo, M., Marsh, P., Pomeroy, J.W., 2000. Snow, frozen soils and permafrost hydrology in Canada, 1995-1998. Hydrol. Process. 14, 1591–1611. https://doi.org/10.1002/1099-1085(20000630)14:9<1591::AID-HYP78>3.0.CO;2-W

Wordsworth, R.D., 2016. The Climate of Early Mars. Annu. Rev. Earth Planet. Sci. 44, 381–408. https://doi.org/10.1146/annurev-earth-060115-012355

Wright, H.E., 1946. Sand Grains and Periglacial Climate: A Discussion. J. Geol. 54, 200–205. https://doi.org/10.1086/625342

Wright, J., Conway, S.J., Morino, C., Rothery, D.A., Balme, M.R., Fassett, C.I., 2020. Modification of Caloris ejecta blocks by long-lived mass-wasting: A volatile-driven process? Earth Planet. Sci. Lett. 549, 116519. https://doi.org/10.1016/j.epsl.2020.116519

Wróżyński, R., Pyszny, K., Sojka, M., Przybyła, C., Murat-Błażejewska, S., 2017. Ground volume assessment using 'Structure from Motion' photogrammetry with a smartphone and a compact camera. Open Geosci. 9. https://doi.org/10.1515/geo-2017-0023

Yang, Y., Shi, Y., Liang, X., Huang, T., Fu, S., Liu, B., 2021. Evaluation of structure from motion (SfM) photogrammetry on the measurement of rill and interrill erosion in a typical loess. Geomorphology 385, 107734. https://doi.org/10.1016/j.geomorph.2021.107734

Ye, B., Qian, Y., Xiao, L., Michalski, J.R., Li, Y., Wu, B., Qiao, L., 2021. Geomorphologic exploration targets at the Zhurong landing site in the southern Utopia Planitia of Mars. Earth Planet. Sci. Lett. 576, 117199. https://doi.org/10.1016/j.epsl.2021.117199

Yoshida, H., Sugai, T., Ohmori, H., 2012. Size–distance relationships for hummocks on volcanic rockslide-debris avalanche deposits in Japan. Geomorphology 136, 76–87. https://doi.org/10.1016/j.geomorph.2011.04.044

Yoshikawa, K., Harada, K., 1995. Observations on nearshore pingo growth, Adventdalen, Spitsbergen. Permafr. Periglac. Process. 6, 361–372. https://doi.org/10.1002/ppp.3430060407

Yoshikawa, K., Nakamura, T., Igarashi, Y., 1996. Growth and collapse history of pingos, Kuganguaq, Disko island, Greenland. Polarforschung 64, 109–113.

Zhang, T., Barry, R.G., Knowles, K., Heginbottom, J.A., Brown, J., 1999. Statistics and characteristics of permafrost and ground-ice distribution in the Northern Hemisphere. Polar Geogr. 31, 47–68. https://doi.org/10.1080/10889370802175895

Zhang, T., Heginbottom, J.A., Barry, R.G., Brown, J., 2000. Further statistics on the distribution of permafrost and ground ice in the Northern Hemisphere [1]. Polar Geogr. 24, 126–131. https://doi.org/10.1080/10889370009377692

Zhang, Y., Zang, S., Li, M., Shen, X., Lin, Y., 2021. Spatial Distribution of Permafrost in the Xing'an Mountains of Northeast China from 2001 to 2018. Land 10, 1127. https://doi.org/10.3390/land10111127

Zhao, L., Wu, Q., Marchenko, S.S., Sharkhuu, N., 2010. Thermal state of permafrost and active layer in Central Asia during the international polar year. Permafr. Periglac. Process. 21, 198–207. https://doi.org/10.1002/ppp.688

Zhao, Y.-Y.S., Yu, J., Wei, G., Pan, L., Liu, X., Lin, Y., Liu, Y., Sun, C., Wang, X., Wang, J., Xu, Weijie, Rao, Y., Xu, Weiming, Sun, T., Chen, F., Zhang, B., Lin, H., Zhang, Z., Hu, S., Li, X.-Y., Yu, X.-W., Qu, S.-Y., Zhou, D.-S., Wu, X., Zeng, X., Li, X., Tang, H., Liu, J., 2023. In situ analysis of surface composition and meteorology at the Zhurong landing site on Mars. Natl. Sci. Rev. nwad056. https://doi.org/10.1093/nsr/nwad056

Zhong, S., Zuber, M.T., 2001. Degree-1 mantle convection and the crustal dichotomy on Mars. Earth Planet. Sci. Lett. 189, 75–84. https://doi.org/10.1016/S0012-821X(01)00345-4

Zhou, G., Song, C., Simmers, J., Cheng, P., 2004. Urban 3D GIS From LiDAR and digital aerial images. Comput. Geosci. 30, 345–353. https://doi.org/10.1016/j.cageo.2003.08.012

Zhuo, Z., Zhu, C., Tang, C.-S., Xu, H., Shi, X., Mark, V., 2022. 3D characterization of desiccation cracking in clayey soils using a structured light scanner. Eng. Geol. 299, 106566. https://doi.org/10.1016/j.enggeo.2022.106566

Zimbelman, J.R., 2010. Transverse Aeolian Ridges on Mars: First results from HiRISE images. Geomorphology 121, 22–29. https://doi.org/10.1016/j.geomorph.2009.05.012

Zorzano, M.-P., Mateo-Martí, E., Prieto-Ballesteros, O., Osuna, S., Renno, N., 2009. Stability of liquid saline water on present day Mars. Geophys. Res. Lett. 36, L20201. https://doi.org/10.1029/2009GL040315

Zou, Y., Zhu, Y., Bai, Y., Wang, L., Jia, Y., Shen, W., Fan, Y., Liu, Y., Wang, C., Zhang, A., Yu, G., Dong, J., Shu, R., He, Z., Zhang, T., Du, A., Fan, M., Yang, J., Zhou, B., Wang, Y., Peng, Y., 2021. Scientific objectives and payloads of Tianwen-1, China's first Mars exploration mission. Adv. Space Res. 67, 812–823. https://doi.org/10.1016/j.asr.2020.11.005

Zuber, M.T., 2001. The crust and mantle of Mars. Nature 412, 220–227. https://doi.org/10.1038/35084163

Zurek, R.W., Smrekar, S.E., 2007. An overview of the Mars Reconnaissance Orbiter (MRO) science mission. J. Geophys. Res. 112, E05S01. https://doi.org/10.1029/2006JE002701

Appendices

Appendix A.1 (Section II.2.): table of the volumes of the analogue models at each time step, for the experiment with the top-down setup. The last six rows were used to calculate the intra-experimental variability on computed volumes.

top-down setup				
DEM	Area (m2)	Volume (m3)	Volume (dm3)	Time (hours)
DSLR_before	0.106793	0.028084	28.08	0
DSLR_after	0.327759	0.025427	25.43	55
Pis_DTM1	0.105258	0.028086	28.09	0.5
Pis_DTM10	0.114535	0.027961	27.96	5
Pis_DTM20	0.245267	0.026428	26.43	10
Pis_DTM30	0.291349	0.026023	26.02	15
Pis_DTM40	0.310482	0.026116	26.12	20
Pis_DTM50	0.312802	0.025956	25.96	25
Pis_DTM60	0.313555	0.025837	25.84	30
Pis_DTM70	0.314300	0.025704	25.70	35
Pis_DTM80	0.315880	0.025678	25.68	40
Pis_DTM90	0.318814	0.025653	25.65	45
Pis_DTM100	0.330732	0.025572	25.57	50
Pis_DTM101	0.350394	0.026076	26.08	50.5
Pis_DTM106	0.323517	0.025544	25.54	53
Pis_DTM107	0.323874	0.025532	25.53	53.5
Pis_DTM108	0.322798	0.025528	25.53	54
Pis_DTM109	0.322867	0.025542	25.54	54.5
Pis_DTM110	0.322226	0.025549	25.55	55
Pis_DTM101	0.350394	0.026076	26.08	50.5
Pis_DTM106	0.323517	0.025544	25.54	53
Pis_DTM107	0.323874	0.025532	25.53	53.5
Pis_DTM108	0.322798	0.025528	25.53	54
Pis_DTM109	0.322867	0.025542	25.54	54.5
Pis_DTM110	0.322226	0.025549	25.55	55

Appendix A.2 (Section II.2.): table of the volumes of the analogue models at each time step, for the experiment with the radial setup. The last eight rows were used to calculate the intra-experimental variability on computed volumes.

radial setup				
DEM	Area (m2)	Volume (m3)	Volume (dm3)	Time (hours)
DSLR_before	0.099425	0.031927	31.93	0
DSLR_after	0.379729	0.030891	30.89	88.5
Pis_DTM2	0.101216	0.032168	32.17	1
Pis_DTM12	0.252190	0.030551	30.55	6
Pis_DTM22	0.339964	0.031020	31.02	11
Pis_DTM32	0.354762	0.031797	31.80	16
Pis_DTM42	0.353763	0.032186	32.19	21
Pis_DTM52	0.354713	0.032252	32.25	26
Pis_DTM62	0.357652	0.032126	32.13	31
Pis_DTM72	0.352287	0.031729	31.73	36
Pis_DTM82	0.350167	0.031782	31.78	41
Pis_DTM102	0.356577	0.031291	31.29	51
Pis_DTM112	0.358759	0.031185	31.18	56
Pis_DTM122	0.362532	0.031058	31.06	61
Pis_DTM132	0.370464	0.031002	31.00	66
Pis_DTM142	0.373465	0.030979	30.98	71
Pis_DTM152	0.373876	0.030944	30.94	76
Pis_DTM162	0.380140	0.031013	31.01	81
Pis_DTM168	0.378866	0.030884	30.88	84
Pis_DTM170	0.379500	0.030964	30.96	85
Pis_DTM171	0.379294	0.030998	31.00	85.5
Pis_DTM172	0.379766	0.030977	30.98	86
Pis_DTM173	0.379416	0.030996	31.00	86.5
Pis_DTM174	0.378005	0.030814	30.81	87
Pis_DTM176	0.378269	0.030995	30.99	88
Pis_DTM177	0.378025	0.030942	30.94	88.5

Appendix A.3 (Section II.2.): table of the time synchronization of the Pis. The value is the seconds displayed on a timer located within the scene. The first row is the time in hours since the beginning of the synchronisation test.

Pi	0	0.5	18	18.5	19	19.5
1	35.36	34.03	56.83	55.46	37.23	35.83
2	35.16	34.43	57.23	56.46	37.43	35.93
3	34.96	34.16	56.43	56.13	37.26	36.76
4	35.73	34.93	56.43	55.46	37.13	36.36
5	35.36	33.93	57.36	55.83	37.13	36.36
6	35.43	34.73	56.43	56.23	37.23	36.16
7	35.36	34.63	56.93	56.46	37.46	36.16
8	35.43	34.13	57.23	55.93	36.63	36.13
9	35.16	34.56	57.43	56.36	37.03	35.96
10	35.26	33.96	56.46	56.13	36.73	36.76
11	35.63	34.13	56.43	55.93	37.36	36.13
12	35.63	34.36	57.16	56.03	36.93	36.53
13	34.96	34.93	56.73	56.03	37.16	35.73
14	35.83	34.63	57.13	55.93	37.53	36.13
15	35.63	34.13	56.83	56.23	37.03	36.06
16	35.33	34.03	56.43	55.83	36.86	36.13
17	35.63	34.36	57.53	56.36	36.93	36.63
18	34.93	34.83	57.36	55.93	36.93	36.43
average	35.38	34.38	56.91	56.04	37.11	36.23
SD	0.26	0.33	0.39	0.28	0.24	0.29
max-min	0.90	1.00	1.10	1.00	0.90	1.03

Appendix A.4 (Section II.2.): table of the absolute error on the scales for the top-down and radial setups.

	scale	true distance	estimated distance	error	average total error
radial setup	vertical	220	219.721	-0.279	0.242
		220	220.052	0.052	
		220	219.611	-0.389	
		220	219.954	-0.046	
	horizontal	100	99.584	-0.416	0.253
		100	99.88	-0.12	
		100	99.929	-0.071	
top-down setup	horizontal	400	398.778	-1.222	1.222

Appendix A.5 (Section II.2.): table of the intra-experimental statistical variability on the elevation of DEMs.

Due to a large number of rows (> 120,000), to access this table please refer to the online repository: https://doi.org/10.6084/m9.figshare.22332076.v1

Appendix A.6 (Section II.2.): Python code generating the radial profiles shown in Figure 2.10.

```
"""Compute average radial profiles"""
from os import listdir
import matplotlib.pyplot as plt
import numpy as np
import pandas as pd
from PIL import Image
from scipy.optimize import curve_fit

def compute_profile(path,DEMfile): #compute average radial profile from a DEM
and a raster of distance from summit of model
 #import DEM & distance raster
 DEM = Image.open(path + '/DEMs/' + DEMfile)
 Dist = Image.open(path + 'DistanceRaster.tif')

 #transform images in list of arrays - one array per line of pixel
 DEMarray = np.array(DEM)
 Distarray = np.array(Dist)

 #concatenate list of arrays in single 1D arrays
 DEMconc = np.concatenate(DEMarray)
 Distconc = np.concatenate(Distarray)

 #transform 1D arrays into lists
 DEMlist = DEMconc.tolist()
 Distlist = Distconc.tolist()

 #find the indexes of the negative (NoData) values in Distlit and of the low
elevations in DEMlist
 NegativeItems = []

 for i in range(len(Distlist)):
     if (Distlist[i]) < 0 or (DEMlist[i]) < 0.005:
         NegativeItems.append(i)

 #delete those items in both lists
 DistlistDel = Distlist
 DEMlistDel = DEMlist

 for j in reversed(NegativeItems): #reversed to delete items from the end as
subsequent indexes are messed up
     del DistlistDel[j]
     del DEMlistDel[j]

 ###plot as density scatter plot###

     #transform lists in arrays to use array functions for density
 x = np.array(DistlistDel)*100
 y = np.array(DEMlistDel)*100

     #histogram definition
 bins = [2000, 2000] # number of bins in both dimensions
```

```
    #histogram the data
 hh, locx, locy = np.histogram2d(x, y, bins=bins)

    #sort the points by density, so that the densest points are plotted last
 z = np.array([hh[np.argmax(a<=locx[1:]),np.argmax(b<=locy[1:])] for a,b in
zip(x,y)])
 idx = z.argsort()
 x2, y2, z2 = x[idx], y[idx], z[idx]

    #find best fit
 a, b = np.polyfit(x, y, 1)

    #plot scatter, best fit, average slope
 fig, ax = plt.subplots(figsize=(6,5))
 ax.set(xlabel='distance from summit (cm)', ylabel='elevation (cm)',
        size=16, xlim=(0,35), ylim=(0,35),
        aspect='equal')
 ax.xaxis.labelpad = 10
 ax.yaxis.labelpad = 10
 plt.scatter(x2, y2, c=z2, cmap='inferno', marker='.', s=15)
 cb = plt.colorbar(fraction=0.05)
 plt.clim(0,35)
 cb.set_label('point density (point per bin)', labelpad=5, size=16)
 #plt.plot(x, a*x+b, linestyle='dashed', color='white')   #plot best fit line
 plt.text(25, 30, 'slope: '+ str(round(np.degrees(np.arctan(-a)), 1)) + '°',
size=16)
 plt.savefig(path + 'Profiles/' + DEMfile[:(len(DEMfile))-4] +
'_profile.png', bbox_inches='tight')
 #plt.show()
 plt.close()

################################

#specify here the path to the folder containing the distance raster and the
DEMs folder
Paths = ['F:/PhD/_papers/2_setup
photogrammetry/data/OldSetup/OldSetup_FineGravel/',
         'F:/PhD/_papers/2_setup
photogrammetry/data/NewSetup/NewSetup_FineGravel/']

#specify here the names of the DEMs to be processed
DEMs =
('Pis_DTM2.tif','Pis_DTM22.tif','Pis_DTM32.tif','Pis_DTM42.tif','Pis_DTM52.ti
f',
        'Pis_DTM62.tif','Pis_DTM72.tif','Pis_DTM82.tif','Pis_DTM92.tif')

#main code: call of the compute_profile function for each DEM in each path
for path in Paths:
    DEMs = listdir(path + 'DEMs')
    for DEMfile in DEMs:
        compute_profile(path,DEMfile)
```

Appendix A.7 (Section III.2.): table of the details on presence of polygons for each grid square.

Due to a large number of rows (> 30,000), to access this table please refer to the online version of the paper: https://www.sciencedirect.com/science/article/pii/S0019103520305418#s0120

Appendix A.8: paper based on my master internship (see next page).

Icarus 395 (2023) 115475

Contents lists available at ScienceDirect

Icarus

journal homepage: www.elsevier.com/locate/icarus

Experimental study of sediment transport processes by liquid water and brine under Martian pressure

M. Philippe [a,*], S.J. Conway [a], J. Raack [b,c], S. Carpy [a], M. Massé [a], M.R. Patel [d], M.E. Sylvest [d], S.R. Lewis [d], C. Morino [e]

[a] Nantes Université/Université d'Angers/Le Mans Université, Laboratoire de Planétologie et Géosciences, CNRS UMR 6112, 2 chemin de la Houssinière, Nantes, France
[b] Innomago GmbH, Ludgeristraße 110, 48143 Münster, Germany
[c] Institut für Planetologie, Westfälische Wilhelms-Universität Münster, Wilhelm-Klemm-Str. 10, 48149 Münster, Germany
[d] School of Physical Sciences, Open University, Milton Keynes, UK
[e] Laboratoire EDYTEM, Université Savoie Mont Blanc, CNRS UMR 5204, 5 Bd de la Mer Caspienne, 73370, Le Bourget-du-Lac, France

ARTICLE INFO

Original content: BrineExperiments_2022 (Original data)

Keywords:
Mars, surface
Mars, climate
Experimental techniques
Geological processes

ABSTRACT

We present here an experimental study to compare the behaviour of water and brine releases over loose sediments under present-day Martian pressure. Water has been invoked to explain current or past Martian surface features for decades. Recent studies have indicated that current surface conditions are, in certain times and places, compatible with the transient existence of liquid water or brine. However, the behaviour of water or brine releases over loose sediments under low Martian atmospheric pressure has been poorly studied.

We performed 33 experiments of water and brine ($MgSO_4$ at 19 wt%) releases over sandy slopes of various temperatures (0 °C to 20 °C), in a chamber allowing the reproduction of Martian pressure 6–7 millibars (mbar). We observe sediment transport mechanisms, that do not occur on Earth, caused by the boiling of water or brine at Martian pressures: grain ejection and "levitation" of sand pellets on cushions of vapour. The main parameter controlling the behaviour of the flow is the temperature of the substrate. Water and brine flows transport similar volumes of sediment under Martian pressure. We show that the grain ejection is the most efficient transport mechanism, dominating the volumes of sediment transported. Pellet "levitation" should lead to longer features formed with brine than with pure water on Mars. Boiling induced sediment transport requires much less water than sediment transport by overland flow to form morphologies similar in size or volume. Moreover, our one-dimensional climate model runs reveal that the temperatures at which we observe those types of transport are predicted to occur at the Martian surface today and in the past. When scaled to Mars, the morphologies we observe with water and brine experiments should be resolvable using the High-Resolution Science Experiment (HiRISE) camera at ~25 cm/pix. Overall, our results show that boiling must be taken into account when considering sediment-rich flows under recent or current Martian conditions.

1. Introduction

Whether water or brine has flowed recently over the Martian surface has been debated for decades as these fluids have been proposed to form gullies (Malin and Edgett, 2000; Fig. 1a-c), recurring slope lineae (RSL; McEwen et al., 2011; Fig. 1d-e) and slope streaks (Schorghofer et al., 2002; Fig. 1f). This debate has been fuelled by the fact that water is vital for all life as we know it. Searching for signs of past or extant extraterrestrial life is one of the main objectives of space exploration programmes (e.g., Farley et al., 2020; Graf et al., 2002; Grotzinger et al., 2012; Schmidt, 2003; Zelenyi et al., 2015). However, what we know about Mars' current surface conditions makes it highly unlikely that enough stable liquid water is available to enable terrestrial-like water-driven mass-wasting processes (Haberle et al., 2001).

Liquid water is not thermodynamically stable at the surface of Mars (Haberle et al., 2001), because the air temperature and atmospheric pressure generally are too low (−60 °C and 6 mbar on average), which means water is stable only in the form of ice or vapour. Hence, any liquid water on the surface would be in a metastable state. This condition means that small perturbations of temperature or vapour partial

* Corresponding author at: 2 chemin de la Houssinière, 44300, Nantes, France.
E-mail address: philippe.meven@gmail.com (M. Philippe).

https://doi.org/10.1016/j.icarus.2023.115475
Received 26 July 2022; Received in revised form 8 February 2023; Accepted 8 February 2023
Available online 22 February 2023

pressure of water (p[H_2O]) would lead to freezing or boiling. For products other than pure water their vapour partial pressure (p[H2O]) can be related to their boiling temperature. For example, with salt in water, the higher the vapour pressure (at a given temperature) of the product, the lower its boiling temperature will be compared with a product with a lower vapour pressure at the same temperature. Salts have been detected on the surface of Mars and are widely distributed (Clark and Kounaves, 2016; Gasda et al., 2017; Gendrin, 2005; Hecht et al., 2009; Rivera-Valentín et al., 2020; Thomas et al., 2019). Therefore, liquid water at the surface would likely incorporate salt(s), forming a brine. This incorporation widens the domain of liquid stability of the solution, therefore brines would be more stable than pure water on the surface of Mars (Brass, 1980; Davila et al., 2010; Fischer et al., 2016; Rivera-Valentín et al., 2020).

Despite the existence of landforms that resemble terrestrial landforms formed from aqueous flows (e.g. gullies Malin and Edgett, 2000 or RSL McEwen et al., 2011) on the Martian surface, there is a lack of information on how that metastable water interacts with the substrate to engender sediment transport and to produce these landforms. In this context, several experimental studies have reported on sediment transport by water under Martian conditions (Massé et al., 2016; Raack et al., 2017; Herny et al., 2019), but only one has studied sediment transport by flowing brine (Massé et al., 2016). Massé et al. (2016) highlighted a new sediment transport process: grain ejection by boiling water and brine, brought about by the low atmospheric pressure and contact with "hot" sediment (>15 °C). In these experiments, brines were observed to transport less sediment by grain ejection than pure water. Massé et al. (2016), Raack et al. (2017) and Herny et al. (2019) all noted that boiling water was more efficient at transporting sediment than overland flows of stable water. Therefore, they proposed boiling as a way to solve the problem of the relatively large amount of water needed to form Martian features. These experiments also showed that the intensity of boiling-driven transport is determined by the temperature of the sediment the liquid is flowing over. However, Massé et al. (2016) only studied grain ejection, caused by seeping water and brine flows. Raack et al. (2017) and Herny et al. (2019) studied higher flow rates, but only used water. Therefore, this study aims at combining these two approaches by studying all the transport processes that boiling liquid can lead to, comparing the efficiency of both water and brine flows.

This study, therefore, pursues an experimental approach that:

1. follows the experimental protocol of Raack et al. (2017) and Herny et al. (2019) to expand the experimental dataset over a wider range of temperatures, which will lead to a better understanding of the processes at play beyond the known limits of the boiling phenomenon;
2. performs a comparative study (both qualitative and quantitative) of water and brine flows under Martian pressure at different sand temperatures, to understand how the type of liquid and the sand temperatures combine to drive the sediment transport.

First, we will describe our experimental setup and protocol as well as our data processing method. We will then present the results we obtained, followed by a discussion of the impact of our results on the potential for contemporary Martian aqueous flows.

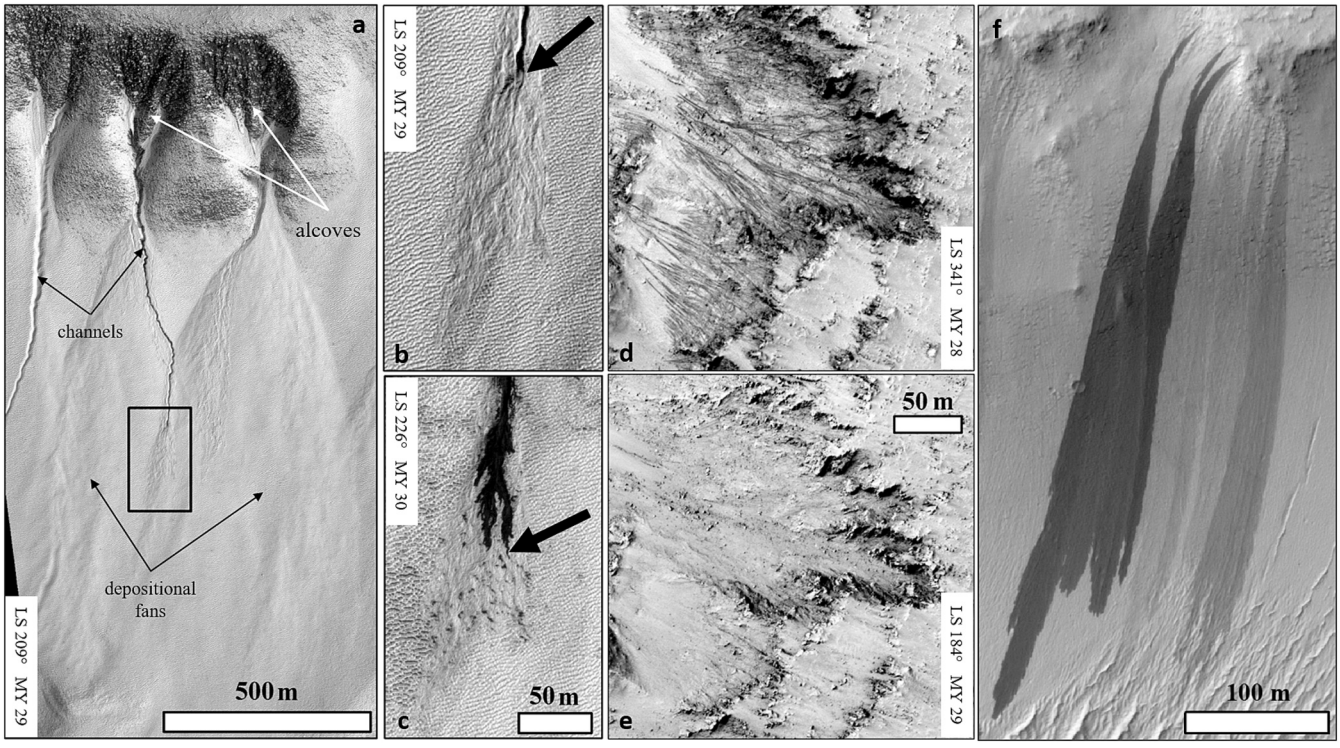

Fig. 1. Recently active gullies, RSL and slope streaks. Solar Longitude (Ls) is an angular value (0° - 360°) giving the position of the planet on its orbit and thus indicates the season (Ls 0° being the northern spring equinox). (a) Typical gully systems in Sisyphi Cavi (68.544°S, 1.444°E) with alcoves, channels and depositional fans. The downslope direction is from top to bottom of the image and north is down. Taken from HiRISE image ESP_011963_1115. The black box delimits the extent of the images b & c. (b) and (c) Active depositional fan during the spring for Mars Year (MY) 29 and 30. Black arrows point to the terminus of the freshest deposits. Images b & c have the same scale and are taken from HiRISE images ESP_011963_1115 and ESP_012319_1115, respectively. (d) RSL originating from bedrock outcrops in the rim of Palikir Crater (41.65°S, 157.705°W) in late summer in Mars Year 28. The downslope direction is from right to left of the image, and north is up. Taken from HiRISE image PSP_005943_1380. (e) RSL have faded by the early spring of the next Mars Year. Taken from HiRISE image ESP_011428_1380. Images d and e have the same scale. (f) Recent (darker) slope streaks, nearby more ancient (lighter) ones (0.148°N, 36.840°E). Taken from HiRISE image ESP_017605_1800. Image credits: NASA/JPL/UofA.

2. Method

2.1. Protocol and setup

The experiments were performed in the Mars Simulation Chamber (MSC) at The Open University (Milton Keynes, UK), which provides an experimental environment at Mars-like pressures (e.g., Conway et al., 2011; Herny et al., 2019; Massé et al., 2016; Raack et al., 2017; Sylvest et al., 2016, 2019).

For each experiment, we placed a levelled-out sand bed of 5 cm depth in a rectangular tray (90 × 40 cm) inclined at 25°. We chose this angle to be consistent with the experiments of Raack et al. (2017) and Herny et al. (2019). Moreover, Martian features such as gullies and RSL are commonly found on slopes with similar angles (Heldmann and Mellon, 2004; Dickson et al., 2007; McEwen et al., 2011; Ojha et al., 2014). Each experiment began with depressurisation of the MSC using a vacuum pump, with the pressure maintained at ~7 mbar. A water pump transferred 550 to 600 g of liquid (water or $MgSO_4$ brine at 19 wt%), in one minute, from a reservoir outside the MSC to an outlet 5 cm above the sand bed (Fig. 2). As liquid temperature only had a minor influence on experiments by Herny et al. (2019), water and brine were always at ambient temperature in the reservoir (19.7 ± 2.5 °C). We performed three replicates of five sand temperatures: 0, 5, 15, 17.5 and 20 °C. The sand was stored in a freezer before the experiment and was left to warm at room temperature in the MSC. The sand temperature was not maintained, and hence increased during the experiments but at a very slow rate (0.2 °C on average along the experiments). We started the depressurisation just before the target sand temperature was reached, and started the flow when the target sand temperature and the target pressure were both reached. When no further motion was observed inside the MSC, we repressurised the MSC and stopped the experiment.

The sand used was sieved and was composed of grains with diameters from 125 µm to 450 µm (~96 wt%), with a median diameter of 250–300 µm. This fractionation is within the range of grain sizes observed on Mars' surface (Rivera-Hernández et al., 2019; Squyres et al., 2004; Weitz et al., 2018). We chose a $MgSO_4$ brine (the freezing point at eutectic is about −3.5 °C; Brass, 1980) because this salt is common on Mars (Gendrin, 2005). Moreover it is easy to acquire, and no specific precautions have to be taken to work with it. Twelve photogrammetric targets were located at different heights along the edges of the tray (Fig. 3). Fifteen thermocouples recorded temperatures (time step = 1 s) at the following locations: eight at the base of the sand layer along the middle of the tray; four on 2.5-cm-high pillars within the sand bed; one at the surface of the sand; one in the liquid outlet; one in the liquid reservoir outside the MSC (Fig. 3). Inside the MSC, there was one Pirani pressure gauge to record inner pressure (time step = 1 s), an ibutton sensor recording air temperature and relative humidity (time step = 1 s), and two webcams. Outside the MSC there was one high-resolution video camera which was used to record each experiment. All devices were recording/monitoring from before the depressurisation until after the repressurisation. The protocol that we employed has been used by Raack et al. (2017) and Herny et al. (2019) (with water flows only).

To summarise, the parameters we varied from one experiment to the other were the sand temperature (0, 5, 15, 17.5 and 20 °C) and the type of liquid (water or $MgSO_4$ brine at 19 wt%). The slope angle and the pressure were kept constant. We monitored the relative humidity, liquid temperature, and air temperature, but did not attempt to control them.

2.2. Data processing

2.2.1. Analysis of morphologies and volumes

Similarly to Raack et al. (2017) and Herny et al. (2019), we used Agisoft Photoscan (version 1.3) software to create Digital Terrain Models (DTMs) at 1 mm/pixel and orthomosaics at 0.2 mm/pixel from

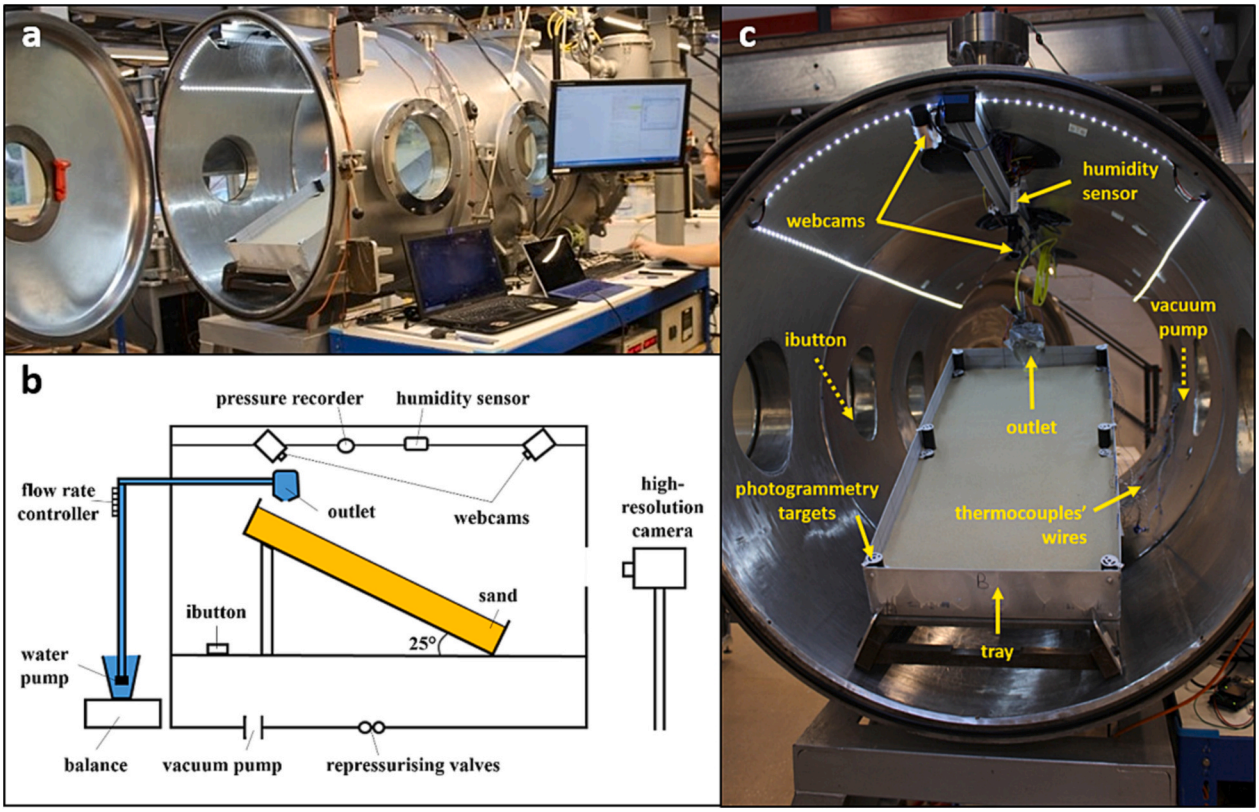

Fig. 2. a. photograph of the outside of the MSC with the tray visible through the open door; b. schematic of the MSC. The "ibutton" is a temperature and humidity sensor; c. annotated photograph of the MSC interior showing the positions of the main pieces of equipment. Dashed lines point to devices that are hidden in this photograph. The MSC is approximately 2 m long and 0.9 m in diameter.

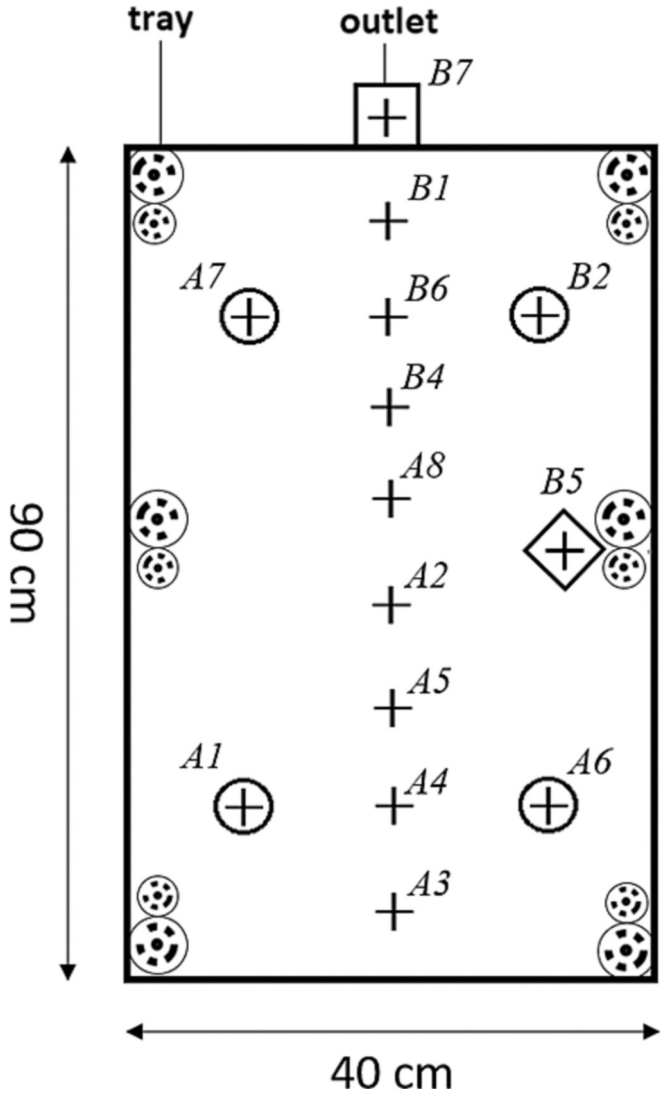

Fig. 3. Top-down schematic of the experimental tray with the position of the 15 thermocouples in the tray, labelled as they are in the software and in the Supplementary Table S1. Crosses represent the thermocouples at the base of the sand bed, circled crosses represent the thermocouples within the sand bed on pillars at 2.5 cm above the base of the tray and the diamond-cross represents the thermocouple at the surface of the sand bed. The twelve photogrammetric targets attached to the tray are also located on the sketch.

series of 100–150 photographs of the sand bed (Structure from Motion technique - Bolles et al., 1987; Westoby et al., 2012). The photographs were taken before and after each experiment with a handheld commercial camera (Casio EX-FH20–9 Mpixel, focal length = 5 mm). The software aligns the photographs by recognising the overlapping parts and calculates the scale using the user-input coordinates of the photogrammetric targets. For each experiment, we obtained two DTMs and two orthomosaics of the sand bed, before and after the flow (Fig. 4a & b). A hillshaded relief image for each DTM was produced using ArcGIS (version 10.4). The difference between the values of the DTMs after and before (DTM of difference - DoD, e.g., Herny et al., 2019; Morino et al., 2019, 2021; Williams, 2012; Raack et al., 2017) was computed in order to visualise the erosion zones (negative values) and the deposition zones (positive values), and to calculate the volume of sediment moved during each experiment (DoDs available in Supplementary Files).

We observed four different sediment transport processes: overland flow (the liquid flowing at the surface of the sand bed, carrying sediment); percolation (the liquid infiltrating within the sand bed around the point of liquid supply); boiling (the liquid changing to gas phase on the sand bed, leading to grain ejection; Massé et al., 2016); and "levitation" (liquid-saturated pellets of sand and changing to the gas phase, leading to these pellets to move downslope quickly, supported by cushions of water vapour; Raack et al., 2017).

Based on the observation of those four processes and on the surface morphology of the sand bed after the experiments, we identified six different landforms (six "morphological units"; Fig. 4b):

- unit 1: the channel and its associated deposits. The channel is a few centimetres wide and deep, it originates from a pit located right below the water supply and extends downslope. The sediment that was initially filling the channel is found at its terminus, deposited downslope as several tongues of sediment – similarly to an alluvial fan. Channel and associated deposits form by overland flow, progressively, from the liquid supply point;
- unit 2: the saturated zone. It is a volume of sand around the liquid supply point which is water-saturated and appears darker. The channel and often its associated deposits (unit 1) overprint the saturated zone and, when applicable, the saturated zone lays at the bottom of the depression (unit 3). The saturated zone forms by the progressive percolation of water through the sand bed during the experiments;
- unit 3: the depression and its associated avalanche deposits. The depression is a pit located below the liquid supply, around ten centimetres deep and extending radially for tens of centimetres; the saturated zone is at its base. The sediment initially filling the depression forms avalanche deposits, elongated positive relief features found downslope the depression, 10 to 20 cm wide and up to nearly one metre long. The depression and associated avalanche deposits are formed by boiling water. Boiling is first observed at the liquid supply point when liquid encounters the relatively hot sand bed. It then follows the edges of the growing saturated zone (unit 2). This continuous process ejects sand grains downslope, which progressively forms the depression within the sand bed around the saturated zone, and associated avalanche deposits downslope;
- unit 4: the pellets. They are pellets of water-saturated sediment, of maximum a few centimetres wide and long. They are located downslope, often far away from the liquid supply point – most of them being found in the lowest ~ quarter of the tray. They form at the very beginning of the experiments by "levitation": the water they contain undergoes a phase change from liquid to gas, which generates a cushion of vapour between the pellet and the sand bed, allowing it to move downslope quickly;
- unit 5: the fine deposits. They are a thin layer of the finest grain sizes of the sand we use, and are located around the depression and avalanche deposits (unit 3). They form by boiling, which ejects fine grains further than the avalanche deposits;
- unit 6: the covered pellets. They are regular pellets, but they were covered during the experiments by avalanche deposits (unit 3).

Units 1 to 4 are consistent with those defined by Raack et al. (2017) and Herny et al. (2019); we added units 5 and 6.

To estimate the volume of sediment moved within each unit, we mapped them individually for each experiment (outlines available in Supplementary Files), using the hillshaded reliefs, the orthomosaics and videos of the experiment. For unit 6 we only used the video recordings to map its extent, because this unit was buried during the experiment. First, for each pellet, we used recordings from different angles to estimate its height. Then we chose a frame of the video when the pellet had formed, but was not moving anymore and had not yet been covered by the avalanche deposits. We projected that frame onto the corresponding orthomosaic and proceeded with the mapping.

The volumes of sediment deposited within each unit were calculated for each experiment using the DoD. The total volume transported was the sum of the volumes of sediment deposited within each unit. The

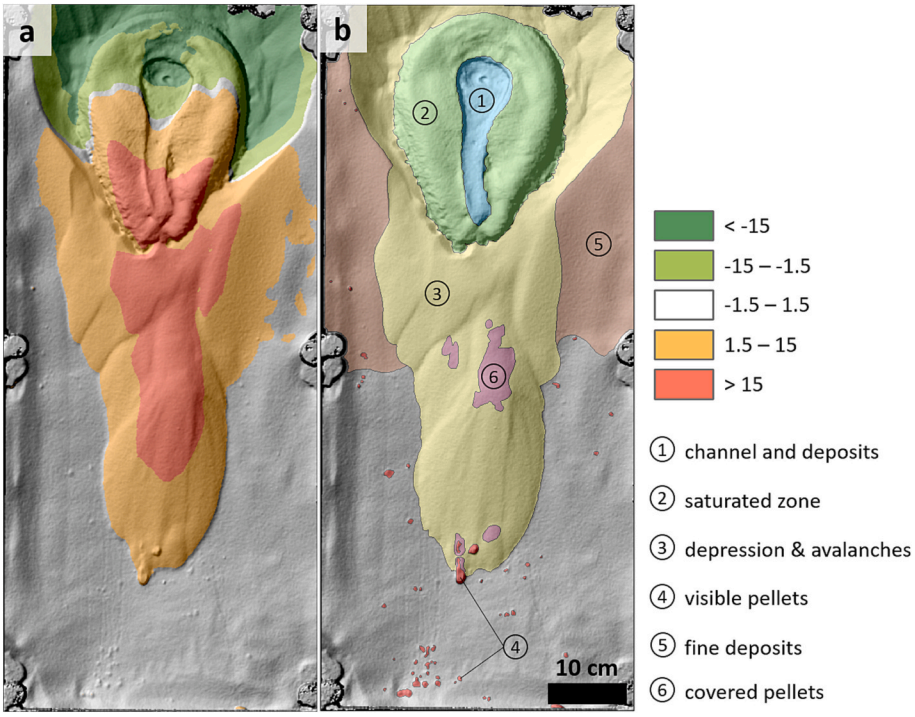

Fig. 4. Example of the experiment 01. a. The hillshaded DTM after the experiment, overlain by the zones of erosion (blue) and of deposition (red). The legend is expressed in millimetres. b. The hillshaded DTM after the experiment, overlain by the polygons representing the different units used to estimate the volumes moved by each process: the channel and deposits formed by overland flow (unit 1); the saturated zone formed by water percolation (unit 2); the depression and avalanche deposits resulting from grain ejection by boiling (unit 3); the visible pellets, formed by "levitation" of sand on cushions of vapour (unit 4); the fine deposits resulting from fine grain ejection by boiling (unit 5); the pellets covered by the avalanche deposits (unit 6). (For interpretation of the references to colour in this figure legend, the reader is referred to the web version of this article.)

volume of the saturated zone (unit 2), pellets (unit 4) and fine deposits (unit 5) were simply the deposited volumes within these units. The volumes of covered pellets (unit 6) were obtained by multiplying the area of each pellet by their height (previously estimated – see above). The overall volume of pellets was the sum of the volumes of the visible pellets (unit 4) and covered pellets (unit 6). The volumes of the avalanche deposits were the deposited volumes within unit 3 (which comprises the depression and avalanche deposits), from which were subtracted the volumes of covered pellets (unit 6).

To provide a realistic estimate of the volume mobilised by overland flow (unit 1), we needed to topographically isolate this unit to remove the influence of the depression caused by the ejection of saltation deposits (unit 3). To do this we created a "reference DTM" for unit 1 that roughly described the surface over which the liquid flowed. To construct this reference DTM we extracted the elevation values within a 0.5 cm buffer around the exterior of the polygon describing the unit 1. These values were used to interpolate the values within the area of unit 1 using a Natural Neighbour algorithm. By computing the difference between the "after" DTM and the new reference DTM we estimated the erosion and deposition volumes for unit 1 (overland flow), being respectively the volume of runoff channel and the volume of runoff deposits. Length and width of the channels and deposits also were measured manually in ArcGIS, the length being considered as the distance between the liquid supply point and the point of the deposits that are the furthest downslope (digitised as a broken line following the middle of the channel and deposits as much as possible), and width is considered as the distance between the two high points at the very top of the channel, itself located at the base of the depression (unit 3).

To calculate the uncertainty in the calculation of the volumes transported derived from the DTMs, we drew a "reference polygon" (a square of ~5 to 15 cm side depending on the available space) for each experiment in an area where we could not see any sand movement using the orthomosaics and the hillshaded relief images (Raack et al., 2017; Herny et al., 2019). Using the DoD we calculated the eroded and deposited volume within the reference polygon per unit area (which if the DTMs were perfect should equal zero). We estimated the potential error for the depositional and erosional volumes derived for each unit by scaling this error to their areas. For unit 6 (covered pellets), we estimated the error on the height at 0.2 cm and multiplied it by the area of the unit. The uncertainty on the total volume of pellets hence is the resulting value, summed with the error on visible pellets calculated with the reference polygon.

2.2.2. Physical parameters

To understand which parameters were controlling the transport processes we observed, we first identified the transport period for each run, i.e. the time interval between the start of liquid release and the end of visible movements on the video. Then, we calculated the mean and standard deviation (to account respectively for the values and variability associated with each run) of pressure, air temperature, relative humidity, liquid temperature and surface temperature over this time period (full records available in Supplementary Table S1). The error of the air temperature is the accuracy of the sensor, i.e. 0.5 °C. The sand temperature was calculated using all the data from the four thermocouples located within the sand bed. The mass of liquid used is the difference between the weight of the liquid container immediately before and immediately after the liquid flowed, with an accuracy of 5 g. The length and width of the channels have been estimated with 1 cm and 5 mm uncertainty, respectively.

2.3. Scaling

In the following subsections we summarise the calculations made by Massé et al. (2016) and Raack et al. (2017) to scale their experiments to the lower Martian gravity compared to their experiments. We use their results to perform our own scaling calculations presented in Section 4.3.

2.3.1. Grain ejection by boiling (Massé et al., 2016)

Massé et al. (2016) performed experiments of flowing water within sand beds under Martian pressure (6.5 to 9 mbar), and they also observed sand grain ejection due to water boiling. They calculated the gas speed expected during their experiments, from an adapted equation initially created to calculate phase change gas speed in capillary tubes (Massé et al., 2016 in Supplementary Discussion). They then created a numerical model to simulate the grain initial acceleration and ballistic trajectory under the reduced Martian gravity, with the gas speed

previously calculated. They conclude that the reduced gravity results in a higher initial grain ejection speed compared to Earth, inducing a travel distance 2.5 to 3 times greater on Mars than on Earth.

2.3.2. Pellet "levitation" (Raack et al., 2017)

Raack et al. (2017) performed experiments of water flows over sand beds, with the same setup as the present article. They observed, among other processes, formation of pellets by "levitation" that we also observe during our experiments (see Section 2.2.1.). To estimate how efficient the "levitation" force would be under the reduced Martian gravity, they calculated and compared two opposing forces over time: the friction force (inhibiting the pellet sliding downslope) and the levitation force (favouring the pellet sliding downslope). They stated that pellets can "levitate" only if the levitation force overcomes the friction force – i.e. if the ratio [levitation force]/[friction force] is >1. Therefore, they studied those forces in the scope of the reduced Martian gravity, and concluded that the friction force would be lower on Mars, resulting in pellets sliding for a time up to 48 times longer.

3. Results

We performed a total of 33 experiments involving ten combinations with the two types of liquids (water and magnesium sulphate brine at 19 wt%) and five sand temperatures (0, 5, 15, 17.5 and 20 °C; Table 1). Runs 19 and 33 are not taken into account in the results and do not appear in Table 1 because of operator error: pressure that went too low and sand temperature too high (run 19), and a too-rapid depressurisation that caused an avalanche before the liquid release (run 33). A triplicate of each combination was our aim but the difficulty in always obtaining the same average surface temperatures caused deficits or additions in some series (Table 1). We separate the experiments into two groups, based on the occurrence of boiling or not: "hot" (15 to 20 °C, where boiling occurs) and "cold" (0–5 °C, where boiling is minimal). In the following section we present first the transport processes that we observed during the experiments, and then the quantification of these processes on both "hot" and "cold" sediment. Supplementary Videos show four typical experiments combining hot or cold sand and water or brine. Supplementary Table S1 shows the physical parameters measured in each experiment, with the full records of sand temperature, air temperature & pressure and relative humidity for the duration of the experiments.

3.1. Observations on transport processes

Consistent with the results reported by Massé et al. (2016), Raack et al. (2017) and Herny et al. (2019), we observed intense boiling of both water and brine due to the low pressure, with sediments from 10 °C to 20 °C ("hot experiments", Fig. 5). With sediments from 0 °C to 5 °C ("cold experiments"), the boiling manifested itself in bubble formation visible at the surface of the flows and was not intense enough to induce sediment movement by ejection. We observed several processes that are known on Earth: formation of erosion channels and subsequent deposits by overland flow, and sediment saturation by percolation. However several processes were caused by the phase change of water from liquid to gas, and so are unknown in natural settings on Earth: i. grain ejection forming a depression at the source, avalanche deposits along the sand bed and fine deposits layers on the sides (Massé et al., 2016; Fig. 5); ii. downslope movement of wet sand pellets, levitating on cushions of vapour formed by boiling of the water they contain (Raack et al., 2017; Fig. 6); and iii. mm-sized pellet ejection around the saturated zone. All of these processes (overland flow, percolation, boiling, "levitation") occur on hot sediments (10 °C to 20 °C). On colder sediment (0 °C to 5 °C) only overland flow, percolation and mm-sized pellet ejection are observed (Fig. 7, Fig. 8; Supplementary Videos). These differences in terms of active processes lead to important differences in terms of morphology between cold and hot experiments.

Experiments with water and brine flow both showed the same transport processes and sequences of events, which are described in the following text. Experiments with hot sediment begin with pellet "levitation" immediately after the liquid comes into contact with the sand (Fig. 6), and mm-sized pellets are ejected at the same time (Fig. 5). Intense boiling starts immediately after the first pellets are ejected (Fig. 5), and in a few seconds a depression starts forming. Percolation starts immediately after the first few tenths of a second of boiling and forms a growing saturated zone; there is no further pellet "levitation" or ejection. Some small avalanche deposits start forming. Overland flow forms channels and deposits after a few tens of seconds, when the saturated zone is already several centimetres wide. After that, we observed a slow but continuous decrease in boiling intensity, and the boiling can last from 45 s to nearly 2 min (extending after the one-minute-long liquid release has stopped); the depression continues to get bigger and the avalanche deposits longer and wider; the percolation progresses and makes the saturated zone grow continuously during the one-min flow; channel and deposits become longer and wider. Avalanche deposits can cover some pellets during their progression (Fig. 5).

Cold sediment experiments immediately start with overland flow forming channels and deposits (Fig. 8). Some small pellets levitate over a few centimetres but will be covered by the flow deposits before the end of the experiment. The percolation starts forming a saturated zone around the channel, which progressively gets longer and wider. Channel deposits extend, and spread to form a depositional fan. Bubbles formed by boiling are visible at the surface of the flow. Millimetre-sized pellets are ejected throughout the experiment when bubbles explode. The overland flow stops when the liquid release stops, but the percolation continues (Fig. 8).

It should be noted that some morphologies can overlap other ones. As an example, avalanche deposits form constantly during the hot experiments and they cover pellets most of the time since those are preferentially formed at the very beginning of the hot experiments.

3.2. Quantification of transport

Our morphological analysis allowed us to quantify the volumes of sediment moved by the different processes described above. The relative volumes moved by these processes differ between hot and cold sediment (Fig. 9), we will therefore present the results of these two types of experiments separately.

3.2.1. Hot experiments

On sediment ≥10 °C grain ejection induced by boiling is the main sediment transport process because it represents about 55–60% of the total transported volume (Fig. 9). The fine deposits formed by boiling (unit 5) represent only small amounts of sediment that are very difficult to discern on orthoimages or hillshades, and are therefore negligible. We also observed that intense boiling lasts longer for water than for brines at these temperatures: from ~15 s longer at 20 °C to ~25 s longer at 15 °C (Fig. 10).

Experiments with water also show larger volumes transported through grain ejection caused by boiling (depression/avalanche deposits) than experiments with brine, and larger total volumes transported (Fig. 11). Water transports 1.6 times more sediments than brine at 20 °C and 1.5 times more at 17.5 °C. The mean transported volumes at 15 °C are however similar. The volumes of depression/avalanche deposits and the total volume transported increase with temperature (Fig. 11).

3.2.2. Cold experiments

At sand temperatures of 0–5 °C sediment transport is mainly driven by overland flow (Fig. 9). The volumes transported are negligible compared with the hot experiments (< 100 cm^3), and no difference can be seen between water and brine flows (Fig. 12). Volumes of sediment

Table 1
Summary of parameters and measurements for each run.

Run	Type of liquid	Water weight (g)	Sand temperature (°C)	Air temperature (°C)	Pressure (mbar)	Relative humidity (%)	Runoff length (cm)	Runoff width (cm)	Strong saltation duration (s)	Total volume transported	Transported volumes (cm3)			
											Volume of overland flow	Volume of percolation	Volume of avalanches	Volume of pellets
1	water	625 ± 5	20.38 ± 0.12	19.38 ± 0.5	8.48 ± 0.62	26.99 ± 10.59	21.54 ± 1	4.27 ± 0.5	103 ± 3	1355.1 ± 11.5	55.9 ± 0.1	300.5 ± 0.4	936.1 ± 1.4	62.6 ± 9.6
2	water	570 ± 5	20.43 ± 0.11	20.11 ± 0.5	8.3 ± 0.67	33.12 ± 6.62	21.84 ± 1	5.55 ± 0.5	107 ± 3	1300.9 ± 16.3	71.1 ± 0.1	174.4 ± 0.4	837 ± 2.2	218.3 ± 13.6
3	water	605 ± 5	20.85 ± 0.11	20.35 ± 0.5	8.6 ± 0.71	32.13 ± 10.05	23.32 ± 1	5.23 ± 0.5	107 ± 3	2064.2 ± 29.7	89.3 ± 0.1	176.6 ± 0.5	1578.8 ± 3.7	219.5 ± 25.4
4	brine	560 ± 5	19.08 ± 0.12	18.54 ± 0.5	7.99 ± 0.42	27.91 ± 9.36	22.52 ± 1	2 ± 0.5	76 ± 3	784.4 ± 10.1	31.9 ± 0	187.7 ± 0.6	489.6 ± 1.4	75.2 ± 8.1
5	brine	575 ± 5	20.89 ± 0.12	20.19 ± 0.5	8.24 ± 0.52	28.16 ± 8.2	28.38 ± 1	2.68 ± 0.5	99 ± 3	1101.6 ± 51.9	62.2 ± 0.2	93 ± 1.2	729.7 ± 7.6	216.8 ± 42.8
6	brine	595 ± 5	20.19 ± 0.09	18.54 ± 0.5	8.3 ± 0.53	26.22 ± 11.18	43.2 ± 1	4.07 ± 0.5	94 ± 3	883.4 ± 19.3	142.5 ± 1.1	113.5 ± 1.1	554.7 ± 5.1	72.7 ± 12
7	brine	565 ± 5	5.06 ± 1.27	20.38 ± 0.5	7.83 ± 0.61	27.24 ± 5.66	34.96 ± 1	1.64 ± 0.5	/	91.1 ± 3.9	76.7 ± 2.3	5.9 ± 1	/	8.5 ± 0.6
8	brine	600 ± 5	5.09 ± 1.13	18.54 ± 0.5	8.21 ± 0.22	16.81 ± 6.2	40.66 ± 1	1.47 ± 0.5	/	75.1 ± 1.9	70.2 ± 1.2	1.9 ± 0.3	/	3.1 ± 0.4
9	brine	590 ± 5	4.88 ± 0.74	18.54 ± 0.5	8.19 ± 0.28	16.47 ± 5.49	35.29 ± 1	2.16 ± 0.5	/	68.5 ± 1.7	62.3 ± 1.2	3.8 ± 0.3	/	2.4 ± 0.2
10	brine	580 ± 5	15.65 ± 0.13	14.35 ± 0.5	8 ± 0.41	14.21 ± 6.91	39.14 ± 1	2.66 ± 0.5	47 ± 3	668.1 ± 12.2	75.5 ± 0.3	190.8 ± 1.2	326.3 ± 1.7	75.5 ± 9
11	brine	595 ± 5	16.08 ± 0.1	14.54 ± 0.5	8.2 ± 0.48	23.83 ± 9.65	38.86 ± 1	2.71 ± 0.5	98 ± 3	959.1 ± 19.3	76.9 ± 0.5	286.8 ± 1.9	557 ± 4.6	38.4 ± 12.3
12	brine	595 ± 5	16.27 ± 0.17	14.54 ± 0.5	8.18 ± 0.3	24.3 ± 11.69	40.12 ± 1	2.93 ± 0.5	69 ± 3	782 ± 15.6	95.4 ± 0.9	198.2 ± 1.8	424.2 ± 5	64.1 ± 7.9
13	water	590 ± 5	14.85 ± 0.14	12.8 ± 0.5	8.12 ± 0.25	30 ± 13.73	22.79 ± 1	3.7 ± 0.5	97 ± 3	878.9 ± 13.4	72.1 ± 0.5	168 ± 1.3	603.3 ± 4.3	35.5 ± 7.3
14	water	585 ± 5	15.51 ± 0.14	13.54 ± 0.5	8.09 ± 0.29	31.61 ± 12.95	22.56 ± 1	4.23 ± 0.5	116 ± 3	494.5 ± 10.2	52.2 ± 0.5	134.9 ± 2	285.3 ± 4.1	22.1 ± 3.7
15	water	590 ± 5	15.54 ± 0.14	14.35 ± 0.5	7.99 ± 0.51	34.18 ± 11.04	21.19 ± 1	3.99 ± 0.5	113 ± 3	980.6 ± 8.9	58.2 ± 0.2	130.1 ± 0.8	774.8 ± 3	17.4 ± 4.8
16	water	595 ± 5	5.06 ± 0.41	16.36 ± 0.5	7.8 ± 0.17	23.34 ± 7.57	26.26 ± 1	4.08 ± 0.5	/	65.3 ± 0.7	49.7 ± 0.3	13.7 ± 0.3	/	1.9 ± 0.1
17	water	600 ± 5	10.12 ± 0.72	18.45 ± 0.5	8.12 ± 0.5	19.37 ± 8.87	24.91 ± 1	3.61 ± 0.5	92 ± 3	474.5 ± 8	65.4 ± 0.8	67.8 ± 1.2	334 ± 3.8	7.3 ± 2.2
18	water	595 ± 5	5.23 ± 1.14	18.04 ± 0.5	7.95 ± 0.31	24.12 ± 6.62	27 ± 1	3.54 ± 0.5	/	60.9 ± 1.3	51.6 ± 0.6	8.4 ± 0.6	/	0.9 ± 0.1
20	brine	565 ± 5	−0.37 ± 1.26	18.45 ± 0.5	7.09 ± 0.08	19.48 ± 4.91	40.77 ± 1	1.99 ± 0.5	/	54.4 ± 4.2	52.5 ± 2.9	0.6 ± 0.4	/	1.3 ± 0.8
21	brine	545 ± 5	0.24 ± 1.71	18.37 ± 0.5	7.23 ± 0.24	18.66 ± 4.02	42.82 ± 1	1.64 ± 0.5	/	55 ± 1.9	52.5 ± 1.4	0.8 ± 0.1	/	1.6 ± 0.4
22	water	590 ± 5	−0.11 ± 1.96	18.37 ± 0.5	7.34 ± 0.28	18.12 ± 4.73	27.14 ± 1	3.03 ± 0.5	/	75.8 ± 1.9	72 ± 1.2	3.1 ± 0.4	/	0.7 ± 0.3
23	water	590 ± 5	−0.35 ± 1.59	18.37 ± 0.5	/	20.73 ± 5.25	28.31 ± 1	2.7 ± 0.5	/	78 ± 0.7	73.2 ± 0.4	3.9 ± 0.2	/	0.9 ± 0.1
24	water	600 ± 5	0.09 ± 1.08	17.54 ± 0.5	7.25 ± 0.23	21.48 ± 4.77	27.57 ± 1	4.5 ± 0.5	/	84.2 ± 5.8	70.8 ± 2	12.7 ± 3.5	/	0.7 ± 0.3
25	water	585 ± 5	17.32 ± 0.13	15.54 ± 0.5	7.69 ± 0.54	30.94 ± 10.44	25.64 ± 1	2.67 ± 0.5	106 ± 3	1331.9 ± 16.7	73.2 ± 0.4	272.9 ± 1.9	952.7 ± 6	33.1 ± 8.4
26	water	590 ± 5	15.82 ± 1.42	15.86 ± 0.5	7.79 ± 0.47	29.16 ± 10.1	26.24 ± 1	3.43 ± 0.5	92 ± 3	1032.7 ± 12	85.2 ± 0.3	213.4 ± 0.8	688.1 ± 2.4	46 ± 8.5
27	water	595 ± 5	17.55 ± 0.1	15.68 ± 0.5	7.86 ± 0.55	29.07 ± 11.46	20.78 ± 1	4.41 ± 0.5	101 ± 3	1288.4 ± 12.6	74.2 ± 0.2	335 ± 1.2	830.4 ± 3.8	48.7 ± 7.4
28	water	595 ± 5	−0.4 ± 1.64	15.36 ± 0.5	6.89 ± 0.2	29.19 ± 5.01	27.98 ± 1	2.32 ± 0.5	/	80.2 ± 4.8	77.8 ± 3.9	2.3 ± 0.7	/	0.1 ± 0.2
29	brine	555 ± 5	17.15 ± 0.16	17.96 ± 0.5	7.71 ± 0.55	22.93 ± 9.78	35.34 ± 1	2.73 ± 0.5	93 ± 3	768.6 ± 11.8	61.3 ± 0.2	223.4 ± 1.1	410.3 ± 2.7	73.6 ± 7.9
30	brine	590 ± 5	17.52 ± 0.08	16.54 ± 0.5	7.55 ± 0.38	27.42 ± 9.42	37.49 ± 1	2.4 ± 0.5	89 ± 3	918 ± 13.4	105.2 ± 0.8	147.7 ± 1.3	558.6 ± 5.2	106.5 ± 6.1
31	brine	590 ± 5	17.17 ± 0.22	16.36 ± 0.5	7.74 ± 0.54	27.67 ± 9.81	22.89 ± 1	1.76 ± 0.5	92 ± 3	873.3 ± 9	25.5 ± 0.1	283.3 ± 1.6	486.3 ± 3.1	78.1 ± 4.2
32	brine	585 ± 5	0.67 ± 1.04	17.54 ± 0.5	7.29 ± 0.26	20.34 ± 4.8	45.07 ± 1	1.43 ± 0.5	/	68.3 ± 1.4	66.9 ± 1	0.7 ± 0.2	/	0.7 ± 0.2

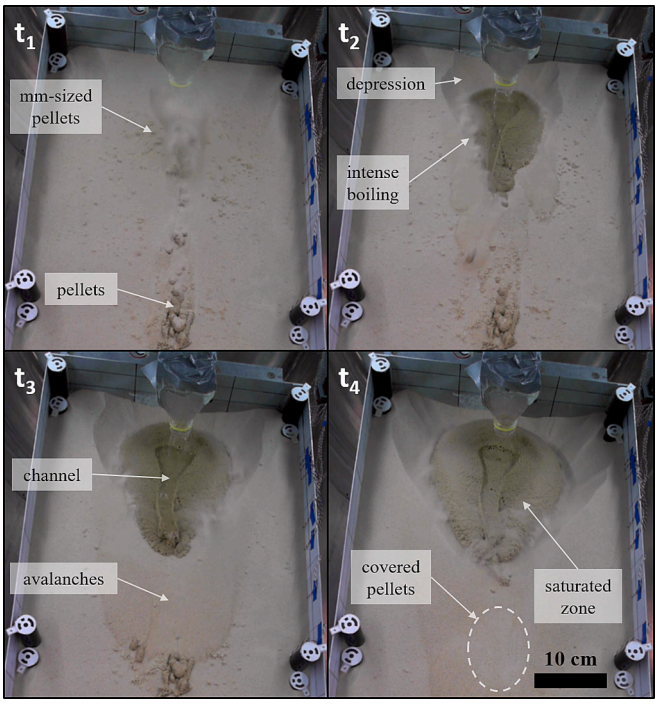

Fig. 5. images of the top of the sand bed from the webcam recording of experiment 01 (water, 20 °C) at $t_1 = 5$ s, $t_2 = 30$ s, $t_3 = 60$ s, $t_4 = 90$ s after the beginning of the experiment. We observe the progressive formation of the channel, the saturated zone and the depression/avalanche deposits. Note that the pellet "levitation" occurs within the very first seconds of the experiment.

transported during the cold experiments also seem to be steady against sand temperature, unlike the volumes transported during hot experiments (Fig. 12).

3.3. Morphological differences

Channels formed by brine overland flows are longer and narrower than those formed by water overland flows (Fig. 13). This difference is even more visible in cold experiments because the main feature forming at those temperatures is the channel (Fig. 7). Moreover, both water and brine channels tend to be shorter and wider with increasing temperature (Fig. 13). Brine flows tend to produce larger volumes of pellets than water flows (Fig. 14), which most of the time leads to more chaotic morphologies (Fig. 15). We observed a jump in the volume of pellets transported for our three hottest experiments (Fig. 14). Our values of volume of pellets transported by water flows are in agreement with the ones measured by Herny et al. (2019). They also observed a jump in the volume of pellets transported for some of their experiments (Fig. 14), despite not counting buried pellets.

4. Discussion

In the following section, we will first detail the similarities we observed between our experimental water and brine releases. We will then discuss qualitatively and quantitatively on how sediment is transported during our experiments, and how it links to the physical parameters we measure. We then attempt to scale up our experiments to Mars, based on calculations made in the literature of similar experiments (Section 2.3). Finally, we compare our physical parameter measurements to the Martian surface conditions, either measured from orbit or computed with a one-dimensional climate model.

4.1. Similarity water/brine

We observed slightly larger volumes of sediment transported by water flows in contrast to brine flows (Fig. 11). This result can be explained by the instability of water under our experimental conditions, which leads to a longer duration of boiling of water flows (Fig. 10). Moreover, our brine solution has a higher density than pure water (1.21 compared with 1 g/cm^3), so for the same weight of liquid used, brine releases were 1.21 times less voluminous. Hence, water releases form larger volumes of avalanche deposits formed by grain ejection (Fig. 11) - which is the main sediment transport process at those temperatures (Fig. 9), leading to greater total volumes of sediment moved. We found similar ratios of volume of sediment transported/volume of liquid release between water and brine flows (see Section 4.2).

To summarise, differences between water and brine flows in terms of transported volumes are small on hot sediment (10 °C – 20 °C). On cold sediment (0 °C – 5 °C) the difference is even smaller (Fig. 12).

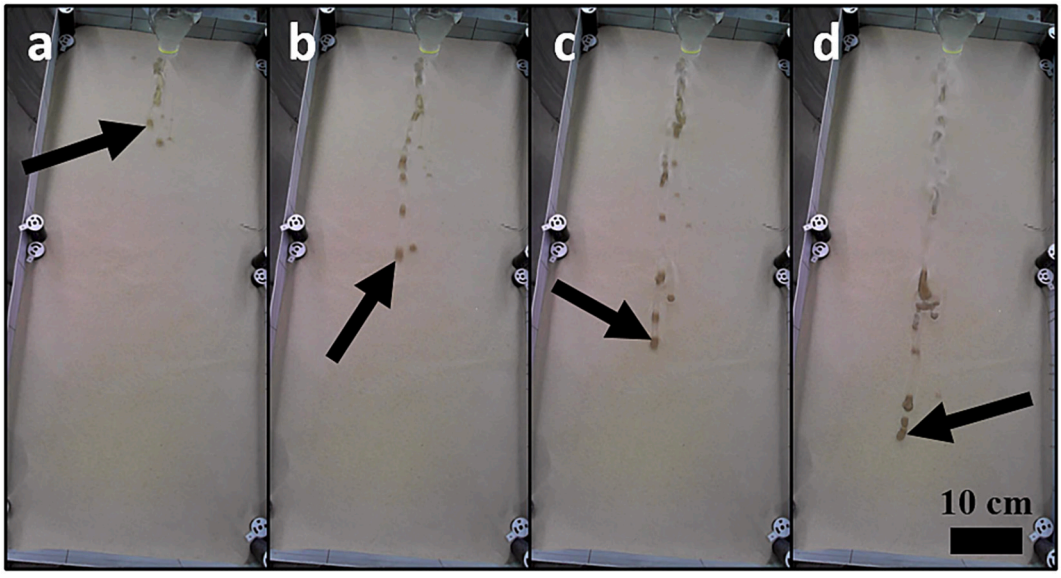

Fig. 6. tracking of a pellet undergoing "levitation" (black arrow). The pellet travels around 50 cm in approximately 1 s. Images are taken from the webcam recording of experiment 01.

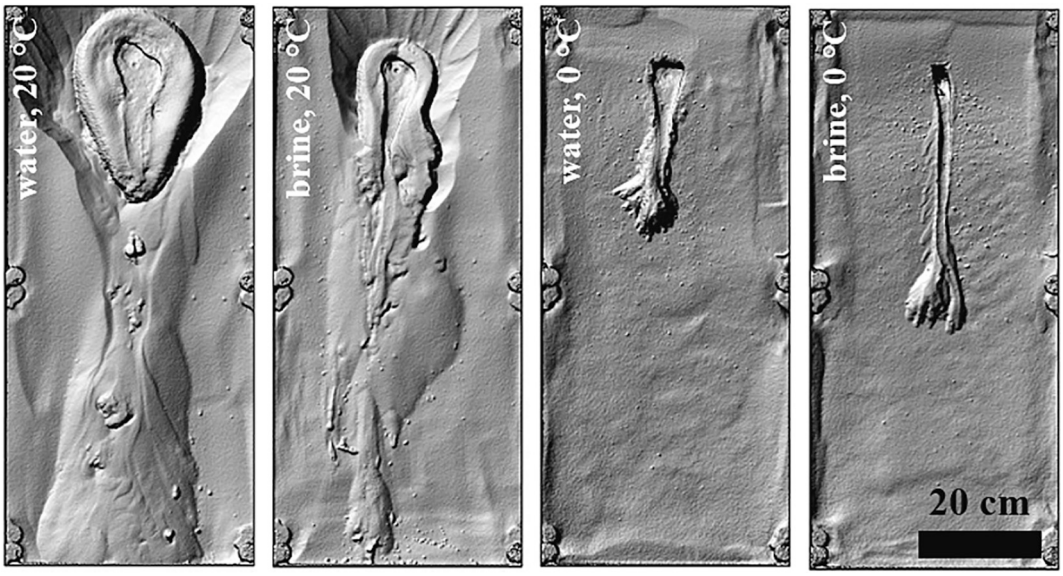

Fig. 7. comparison between water and brine flows, at 20 °C and 0 °C. The hillshades displayed here are from experiments 03 (water, 20 °C), 06 (brine, 20 °C), 23 (water, 0 °C) and 20 (brine, 0 °C).

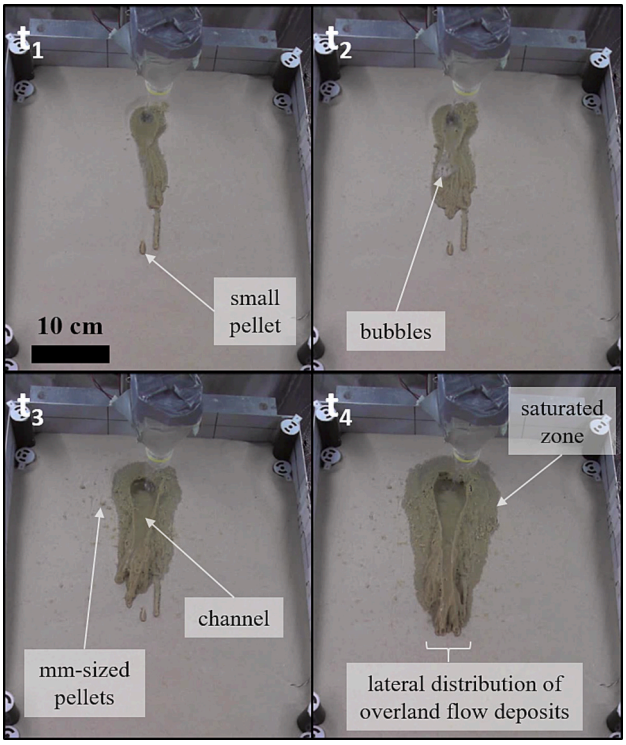

Fig. 8. images from experiment 16 (water, 5 °C) at $t_1 = 5$ s, $t_2 = 10$ s, $t_3 = 30$ s, $t_4 = 60$ s after the beginning of the experiment. We observe the growth of the channel and its deposits, enlargement of the saturated zone and ejection of mm-sized pellets.

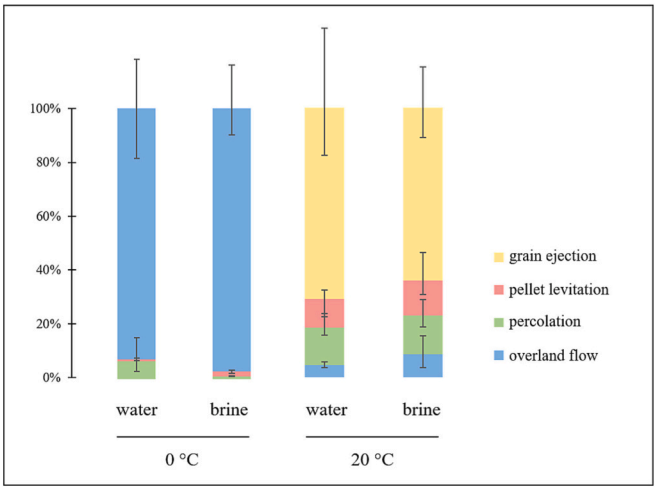

Fig. 9. relative contribution of the different processes in the total transported sediment for experiments at 20 °C (left) and 0 °C (right). The relative contributions are averages of all the experiments in each combination of liquid-sand temperature. The error bars show the minimum and maximum values observed in each given combination.

4.2. Sediment transport & comparison with previous studies

Water and brine flows have similar behaviours under Martian pressure, despite slightly larger volumes of sediment transported by water flows (see Section 4.1) – a behaviour already noted by Massé et al. (2016). Because they used the same protocol, we can combine our results with the ones obtained by Herny et al. (2019) (Fig. 12). The results from Raack et al. (2017) are not displayed here as they come from the same experiments as Herny et al. (2019). Also, compared with Raack et al. (2017) and Herny et al. (2019), we extended the temperature range at which the experiments were conducted.

Total volumes transported during the cold experiments (0 °C – 5 °C) seem to be steady against sand temperature, but experiments on hot sand (10 °C – 20 °C) appear to transport more sediment with increasing temperature (Fig. 12) – in accordance with Herny et al. (2019). On a cold substrate, fluid parameters such as viscosity or flow speed drive the capacity to erode and carry sediments, which is expressed by the different morphologies of channels (Fig. 13; Section 3.3). On hot sediment the volume transported by a liquid release (water or brine) mostly is due to boiling (Fig. 11; Section 3.1.2); it therefore strongly depends on the intensity and duration of boiling, which is driven by the physical parameters: temperature, atmospheric pressure and $p[H_2O]$. At 7 mbar and 0 °C, water is around the triple point, where the three states of water coexist. When its temperature increases, for example when in contact

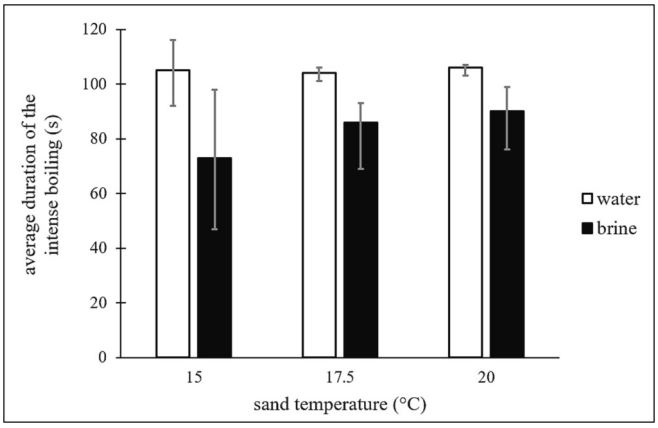

Fig. 10. average duration of the intense boiling for water and brine at 15, 17.5 and 20 °C. The error bars are defined as the shortest and the longest boiling durations observed at the different sand temperatures.

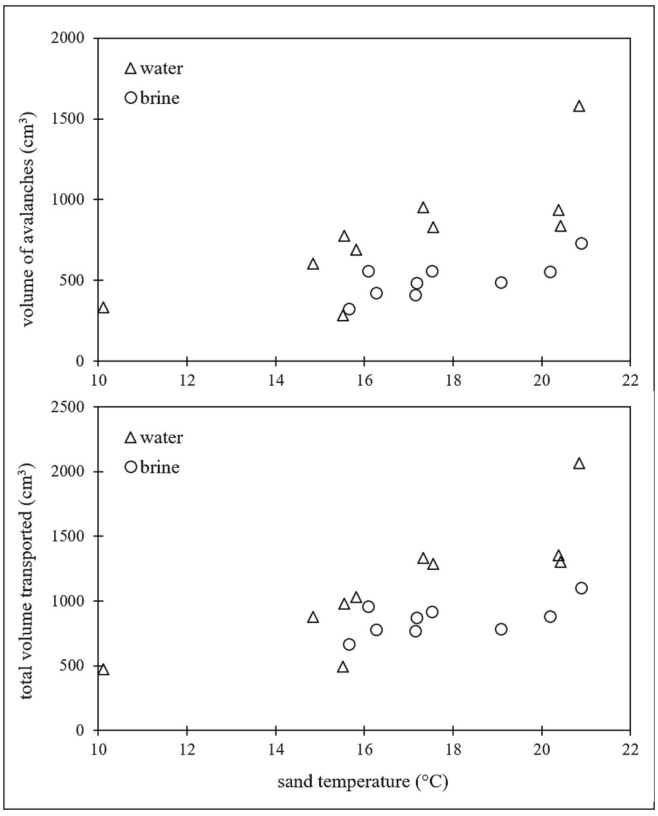

Fig. 11. volume transported through avalanche deposits (top) and total volume transported (bottom) in water (triangles) and brine experiments (circles) vs. sand temperature. The experiments displayed here are the "hot" ones (temperatures from 10 °C to 20 °C). The errors are presented in Table 1 and fall within the symbols.

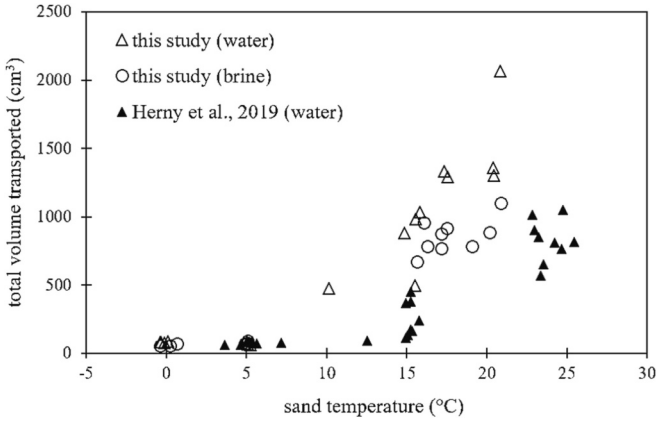

Fig. 12. total volume of sediment moved vs. sand temperature in our experiments (water = hollow triangles, brine = hollow circles), and in the experiments of Herny et al. (2019) (filled triangles), which were exclusively experiments with water. The errors are presented in Table 1 and fall within the symbols.

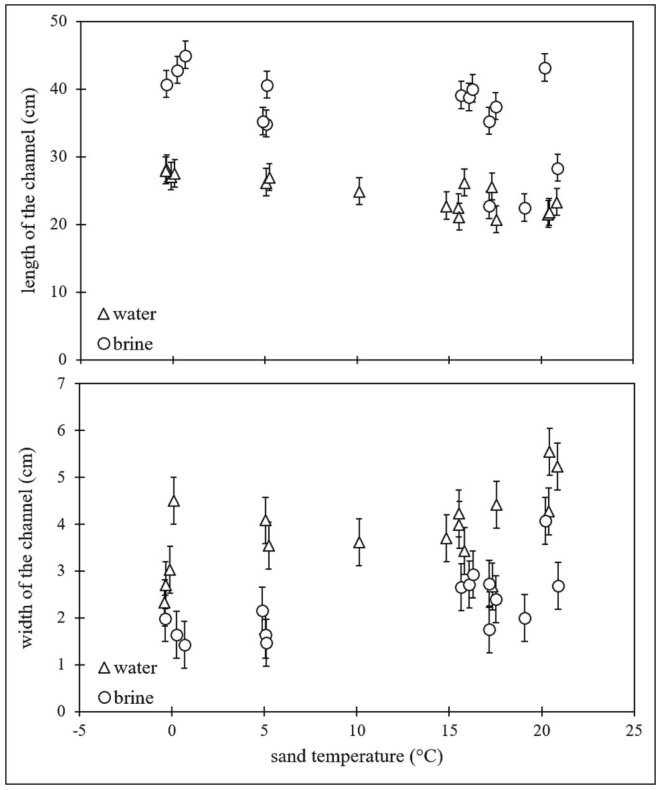

Fig. 13. length (top) and width (bottom) of the channel vs. sand temperature, for water (triangles) and brine experiments (circles). The errors in the sand temperature fall within the symbols. The errors in the length and width of the channels have been estimated at respectively 2 cm and 0.5 cm.

with the sand in our experiments, the temperature increases above the liquidus on the phase diagram of water. The further temperature is from its liquidus, the more intensely water will boil, and therefore larger volumes of sediment are transported during the hot experiments. Adding salt to pure water, as we did, induces changes in the phase diagram, which are "freezing-point depression" and "boiling-point elevation". A brine solution, therefore, boils at a higher temperature. It means that at the same temperature (15–20 °C in our case), the temperature is further from the liquidus of water than the liquidus of a brine, and thus pure water boils more intensely. Note that the intensity of boiling, and thus the volume of avalanche deposits and the total volume of sediment moved, depends more specifically on $p[H_2O]$ – and not exactly on the sand temperature. However the boiling occurs within the sand, and we cannot access the relative humidity of the sand bed from our setup – which is necessary to calculate $p[H_2O]$.

We observe that the trend that emerges from the data of Herny et al. (2019) is similar to the one that emerges from our data: very small amounts of sediment are transported on cold sand (which seem to be

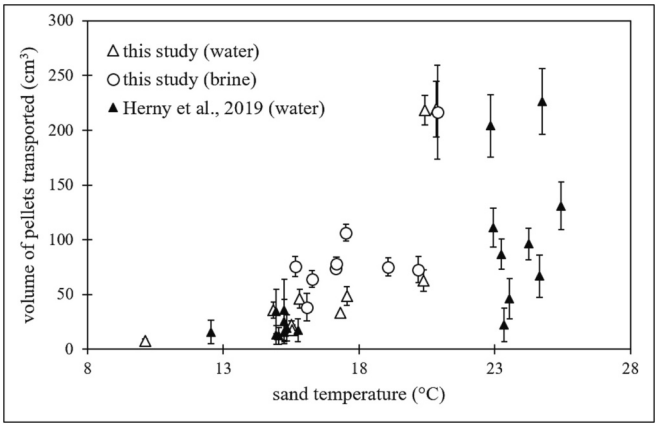

Fig. 14. volume of pellets moved vs. sand temperature. The experiments displayed here are the "hot" ones (sand temperature from 10 °C to 20 °C). The data from Herny et al. (2019) are added as small black triangles, and are water flows experiments only. The volume of covered pellets (our unit 6) was not measured by Herny et al. (2019). The error bars on the sand temperature are negligible.

independent of the sand temperature); then a jump in transported volumes occurs, after which transported volumes increase proportionally to the increase in sand temperature. The position of the jump is correlated to the onset of intense boiling. However, the data of Herny et al. (2019) show systematically lower volumes moved (Fig. 12). This difference can be explained by the fact that the vacuum pump we used during our experiments was able to maintain more stable pressures than the one used by Raack et al. (2017) and Herny et al. (2019). Relative humidity and pressure in the MSC tend to increase before decreasing at the beginning of each experiment which causes negative feedback in the boiling process. If this effect is limited, then the atmosphere of the MSC remains more favourable to intense boiling, and therefore to larger volumes of sediment transported by grain ejection. This outcome is consistent with the peaks of pressure observed: during our experiments at 15 °C it rose to 8.6 mbar on average, compared with 11.4 mbar during the experiments of Herny et al. (2019). It also seems that the jump observed by Herny et al. (2019) happens at a higher temperature than ours: their experiments at 15 °C show a range of volumes moved which is between the volumes moved by their 5 °C-experiments and their 25 °C-ones (Fig. 12). In our study, the volumes transported during the experiments at 15 °C are much larger than the volumes transported during the "cold" ones; moreover, we also observed intense boiling during our only experiment at 10 °C (Fig. 12). This result suggests that if the pressure and relative humidity increase is limited at the beginning of the experiment, the boiling is more intense and it can be active at colder surface temperatures. Because this increase would be nearly null on the surface of Mars, this would mean that boiling could be more efficient in transporting sediment and would be triggered at colder temperatures than those observed during our experiments.

We also find that boiling is a very efficient way to transport sediment under Martian conditions: our water releases can transport from 1.6 (at 15 °C) to 3.3 times (at 20 °C) their volumes in sediment. Brine experiments show ratios of the same order of magnitude: 2.0 (at 15 °C) to 2.6 times (at 20 °C) their volume in sediment. Hence, boiling is at least ten times more efficient than overland flows in transporting sediment (ratio volume of sediment transported/volume of liquid release ≈ 0.1–0.2).

4.3. Scaling up to Mars

In the following Section, our attempt to scale our experiments up to Mars is based on scaling calculations made for similar experiments, in Massé et al. (2016) and Raack et al. (2017). In their calculations, they take into consideration the effect of the reduced Martian gravity on the physical processes they observed or measured during their experiments. We summarise their methodology in Section 2.3.

Massé et al. (2016) scaled the grain transport by boiling to reduced Martian gravity and concluded that it would be around three times more efficient in terms of volumes of sediment transported, and would lead to morphologies ~2.5 times bigger. Using our previous calculations on the ratio volume of sediment moved/volume of water, it means that water or brine flows on a 20 °C sediment could transport from ~ four to eight times the volume of water in sediment. Our experiments on 20 °C sediment showed that water can transport sediment far from the release source (in 2/3 of the experiments avalanche deposits progress was blocked by the tray). Assuming a reasonable length of around one metre for our experiments, the same process on Mars would form morphologies of several metres in length which would be visible at least on

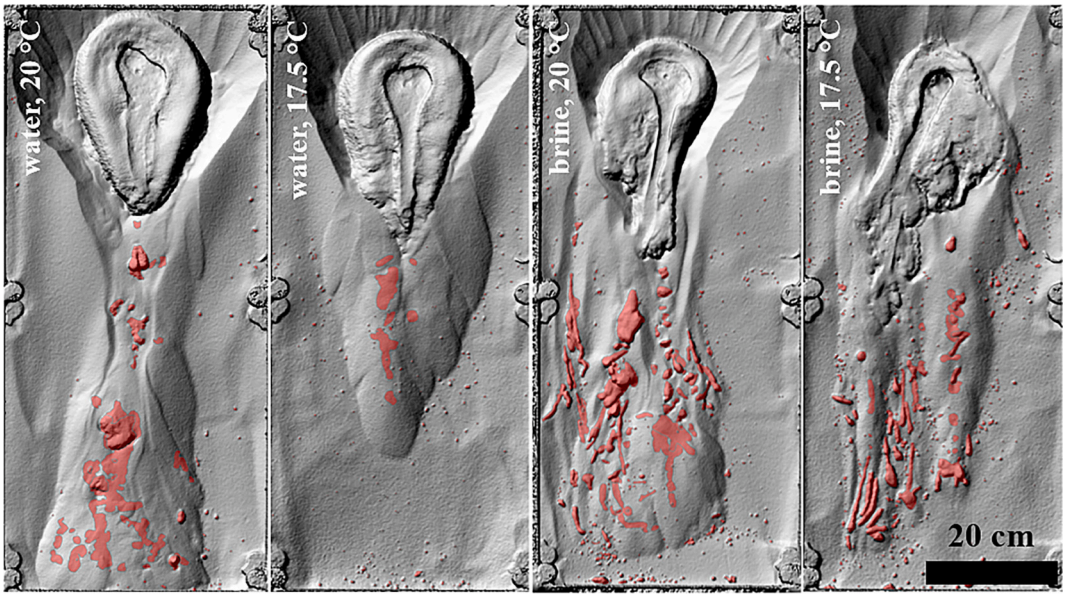

Fig. 15. comparison between water and brine flows, at 20 °C and 17.5 °C. Pellets are identified with the light red colour. A lot more pellets are formed with the brine flows and the resulting morphologies seem more chaotic. The hillshades displayed here are from experiments 03 (water, 20 °C), 05 (brine, 20 °C), 25 (water, 17.5 °C) and 30 (brine, 17.5 °C).

images from the High Resolution Imaging Science Experiment (HiRISE) at 25 cm/pixel. Based on our previous calculations, brine flows containing an equivalent amount of water should transport similar volumes of sediment. It is however worth noticing that brine releases produce more pellets than water releases (Fig. 14). Considering that pellet "levitation" is thought to last much longer under the reduced Martian gravity (~48 times longer; Raack et al., 2017), and that brine flows are more likely to occur than pure water flows, brine releases on Mars could result in morphologies much longer than those we calculated (potentially of an order of magnitude), with similar amounts of water. It allows us to confirm and extend the conclusion of Raack et al. (2017), that the boiling phenomenon could create morphologies with much less water or brine than has been estimated previously (Chojnacki et al., 2016; Grimm et al., 2014; Malin and Edgett, 2000; Stillman et al., 2016). However, scaling morphologies to Mars is challenging, and many more parameters should be taken into account to describe the potential boiling of a Martian aqueous flow (e.g. the flow rate, temperature variations, potential slow temperature increase, a potential cyclicity). The simple-scaling arguments made above demonstrate that the boiling phenomenon should be explored to resolve the issue of the high water budget thought to form some aqueous mass movement features on Mars.

4.4. Comparison with Mars surface conditions

Our experiments show that intense boiling is triggered at a sand temperature between 5 °C and 15 °C (Fig. 12). Because a non-intense boiling (i.e. bubbling) is observed during 0 °C-experiments and 5 °C-experiments and as the only experiment at 10 °C also shows intense boiling (Fig. 12), we think it could even be triggered between 5 °C and 10 °C. Also, both water and brine have been observed to remain liquid when flowing on 0 °C-sand and 5 °C-sand (water starts forming ice features at 0 °C but remains mostly liquid).

We applied a 1D version of the LMD Mars climate model physics (Forget et al., 1999; Spiga and Forget, 2008) to the Martian slopes, in a similar way to Conway et al. (2018). This model takes into account several parameters: latitude, slope angle and orientation, the thermal inertia of the substrate, orbital obliquity and solar longitude of perihelion (LsP; solar longitude at which the planet is the closest from the Sun) as variables; surface pressure and soil albedo were fixed, respectively 6.1 mbar and 0.2 (Conway et al., 2018). We compute from the model results the number of hours per year when the surface conditions allow to reach or exceed a certain temperature (Fig. 16). This model shows that positive surface temperatures are common on Mars at the present day (current obliquity = 25°; current LsP = 251°; standard Mars thermal inertia ≈ 250 $Jm^{-2}K^{-1}s^{-1/2}$, Putzig et al., 2005). Slopes at large ranges of latitudes and angles experience surface temperatures exceeding 0 °C for >1000 h/yr (> 40 sols), and temperatures above 5 °C are not uncommon either (nearly all equator-facing slopes with an angle ≥20°). Temperatures of 15 °C are more difficult to reach, but still possible (Fig. 16). Trends can be identified (Fig. 16): i. on equator-facing slopes, temperatures are more often positive and go higher than on pole-facing ones; ii. equator-facing slopes with greater angles also reach more recurrent and higher positive temperatures; the reverse is observable on pole-facing slopes; iii. Positive temperatures are more common at mid-latitudes. All these trends stem from the orbital parameters of Mars. Here the southern hemisphere undergoes more positive-temperature periods than the northern hemisphere due to the closeness of its summer solstice with the current LsP of Mars.

Moreover, McEwen et al. (2011, 2014) and Ojha et al. (2014) reported from orbital thermal data surface temperatures exceeding ~15 °C to over 25 °C during summer, in the southern mid-latitudes and in some places at equatorial latitudes (e.g. Valles Marineris).

Linking our experimental data with surface temperature measurements and modelling, we can determine that liquid water and brine flow should boil on Mars' surface at the present day given a water source. Surface temperatures required to maintain and boil a water flow would be reached quite easily; brine flows could occur at even lower temperatures than 0 °C because of their freezing point depression, and therefore are even more likely to occur (Brass, 1980). Moreover, Rivera-Valentín et al. (2020) concluded that, thanks to metastability, brines could be

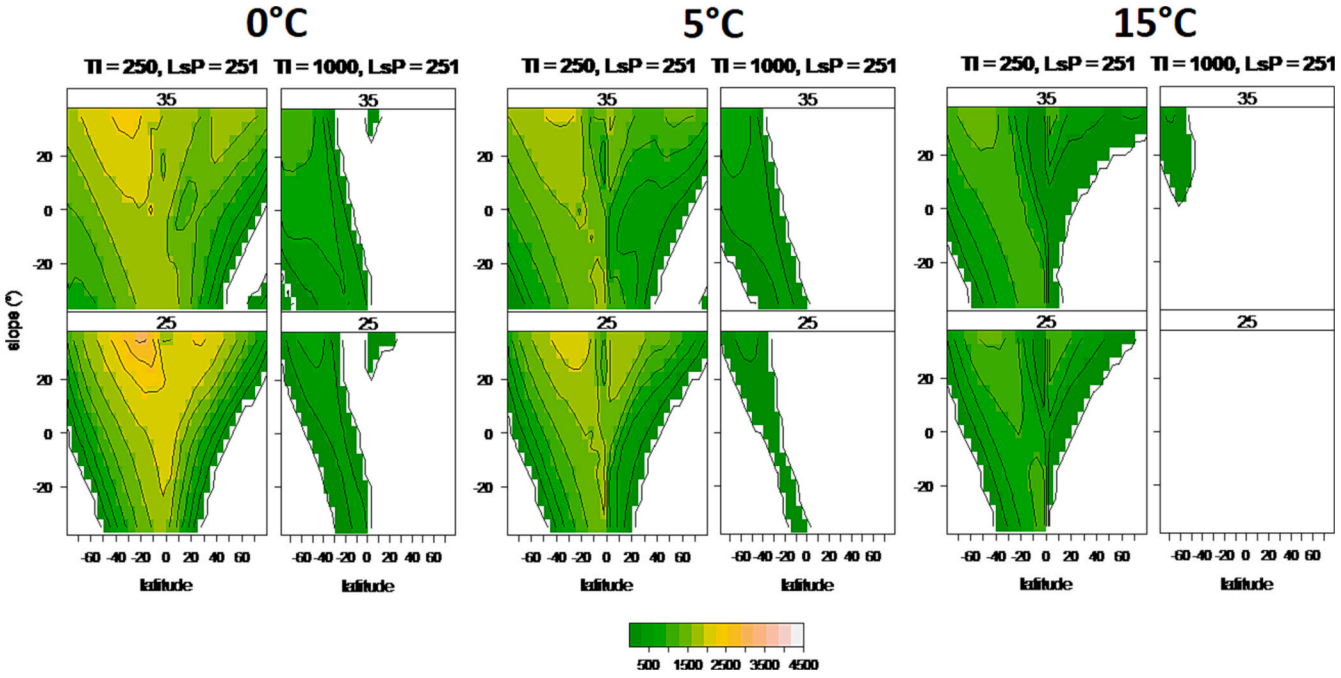

Fig. 16. slope angle vs. latitude, with the number of hours per year (h/yr) when the surface temperature exceeds 0 °C (left columns), 5 °C (middle columns) and 15 °C (right columns) given in the colour scale. Positive slope angles indicate equator-facing slopes, negative slope angles indicate pole-facing ones. For each surface temperature, columns have thermal inertia of 250 $Jm^{-2}K^{-1}s^{-1/2}$ (left column) and 1000 $Jm^{-2}K^{-1}s^{-1/2}$ (right column), values we chose to represent respectively mean Mars and bedrock (Fergason et al., 2006; Putzig et al., 2005). On the top line are the calculations with an orbital obliquity of 35°, representing Mars' recent past; on the bottom line are calculations with an obliquity of 25° (current value). The LsP here is fixed at its current value (251°).

found at even more locations than previously thought (Davila et al., 2010); for instance, the $Ca(ClO_4)_2$ brine is thought to be stable or metastable for ~2% of the Martian year, on ~40% of the Martian surface. Moreover, previous studies confirmed that brines tend to persist beyond their predicted stability region, as metastable aqueous (Fischer et al., 2016) or supercooled solutions (Toner et al., 2014). Therefore, liquid brines have the potential to be found nearly everywhere on the surface of Mars.

Also, in the past few million years positive surface temperatures were even more widespread, as well as overall higher than today because of higher orbital obliquity (Fig. 16; Kreslavsky et al., 2008). Such temperatures should have led to metastable and boiling water (or more likely brines) for a higher number of sols per year compared with the present day. Therefore, their boiling could have triggered the formation of mass-wasting features in the mid-latitudes to high-latitudes.

Overall, these observations show that it has been, and still is, possible to reach surface conditions on Mars where water and brine can flow and boil. The questions remain, however, whether (1) these phenomena occur (or occurred) and led to mass-wasting features, and (2) today we can observe those features – active or as remnants of past activity. The potential source of water is still unknown and has been debated in several studies (e.g., Abotalib and Heggy, 2019; Grimm et al., 2014; Stillman et al., 2014, 2016).

5. Conclusions

Several conclusions emerge from our study:

1. During our experiments, we observed similar flow behaviours compared with Raack et al. (2017) and Herny et al. (2019) – indicating good reproducibility of those experiments. In "cold" experiments (≤ 5 °C), sediment transport mainly is driven by overland flows. In "hot" experiments, above a certain threshold in temperature (between 5 °C and 10 °C), boiling is triggered and becomes the process transporting the largest volumes of sediment. It can transport over three times the weight of water in sediment, which is ~ ten times more efficient than overland flows.
2. Water and brine flows produce similar volumes of sediment moved, but they present morphological differences: brine flows tend to produce more levitating pellets, which produce longer morphologies than grain ejection by boiling.
3. Scaled to Mars, the morphologies formed by grain ejection would be several metres long. Moreover, pellet "levitation" should occur for longer under Martian conditions: morphologies resulting from brine releases could thus be an order of magnitude longer than those resulting from water releases, for a similar amount of water. In both cases, metre or tens-of-metre-long features would be visible on HiRISE imagery.
4. Comparing our experimental results to a 1D-climatic model and direct surface temperature measurements, we find that it is possible to reach atmospheric conditions favourable to water stability and boiling on present-day Mars. In particular, a wide range of slopes undergo over 40 sols per year of positive temperatures. Atmospheric conditions favourable to brine stability and boiling are even more widespread thanks to the depression of their freezing point. Moreover, within the last million years, periods of higher obliquity have led to higher temperatures overall, suggesting that water and brine stability and boiling could have been sporadically even more widespread during the recent past.

Declaration of Competing Interest

Authors declare no competing interest.

Data availability

Due to a large dataset, some data are available on an open-source repository. The rest is available on request.

BrineExperiments_2022 (Original data) (Figshare)

Acknowledgements

We thank the reviewer Paul Carling and the editors Alessandro Morbidelli and Elizabeth Rampe for constructive comments that greatly improved the quality of the manuscript. The laboratory work was supported by the Europlanet 2020 RI which has received funding from the European Union's Horizon 2020 research and innovation program under grant agreement No 654208, by Région Pays de la Loire project GeoPlaNet (convention N° 2016-10982) and by the French Space Agency (CNES). SRL thanks the UK Space Agency for support under grants ST/R001405/1, ST/W002949/1 and ST/S00145X/1. CM is funded by the Agence Nationale de la Recherche in the framework of the project ANR-19-CE01-0010 PERMOLARDS. MRP acknowledges funding from the UK Space Agency under grants ST/V005332/1 and ST/V002295/1.

Appendix A. Supplementary data

Supplementary data to this article can be found online at https://doi.org/10.1016/j.icarus.2023.115475.

References

Abotalib, A.Z., Heggy, E., 2019. A deep groundwater origin for recurring slope lineae on Mars. Nat. Geosci. 12, 235–241. https://doi.org/10.1038/s41561-019-0327-5.

Bolles, R.C., Baker, H.H., Marimont, D.H., 1987. Epipolar-plane image analysis: an approach to determining structure from motion. Int. J. Comput. Vis. 1, 7–55. https://doi.org/10.1007/BF00128525.

Brass, G.W., 1980. Stability of brines on Mars. Icarus 42, 20–28. https://doi.org/10.1016/0019-1035(80)90237-7.

Chojnacki, M., McEwen, A., Dundas, C., Ojha, L., Urso, A., Sutton, S., 2016. Geologic context of recurring slope lineae in Melas and Coprates Chasmata, Mars: GEOLOGY OF MELAS AND COPRATES RSL. J. Geophys. Res. Planets 121, 1204–1231. https://doi.org/10.1002/2015JE004991.

Clark, B.C., Kounaves, S.P., 2016. Evidence for the distribution of perchlorates on Mars. Int. J. Astrobiol. 15, 311–318. https://doi.org/10.1017/S1473550415000385.

Conway, S.J., Lamb, M.P., Balme, M.R., Towner, M.C., Murray, J.B., 2011. Enhanced runout and erosion by overland flow at low pressure and sub-freezing conditions: experiments and application to Mars. Icarus 211, 443–457. https://doi.org/10.1016/j.icarus.2010.08.026.

Conway, S.J., Harrison, T.N., Lewis, S.R., 2018. Martian gullies and their connection with the Martian climate. In: Dynamic Mars. Elsevier, pp. 87–119. https://doi.org/10.1016/B978-0-12-813018-6.00003-0.

Davila, A.F., Duport, L.G., Melchiorri, R., Jänchen, J., Valea, S., de los Rios, A., Fairén, A. G., Möhlmann, D., McKay, C.P., Ascaso, C., Wierzchos, J., 2010. Hygroscopic salts and the potential for life on Mars. Astrobiology 10, 617–628. https://doi.org/10.1089/ast.2009.0421.

Dickson, J.L., Head, J.W., Kreslavsky, M., 2007. Martian gullies in the southern mid-latitudes of Mars: evidence for climate-controlled formation of young fluvial features based upon local and global topography. Icarus 188, 315–323. https://doi.org/10.1016/j.icarus.2006.11.020.

Farley, K.A., Williford, K.H., Stack, K.M., Bhartia, R., Chen, A., de la Torre, M., Hand, K., Goreva, Y., Herd, C.D.K., Hueso, R., Liu, Y., Maki, J.N., Martinez, G., Moeller, R.C., Nelessen, A., Newman, C.E., Nunes, D., Ponce, A., Spanovich, N., Willis, P.A., Beegle, L.W., Bell, J.F., Brown, A.J., Hamran, S.-E., Hurowitz, J.A., Maurice, S., Paige, D.A., Rodriguez-Manfredi, J.A., Schulte, M., Wiens, R.C., 2020. Mars 2020 mission overview. Space Sci. Rev. 216, 142. https://doi.org/10.1007/s11214-020-00762-y.

Fergason, R.L., Christensen, P.R., Kieffer, H.H., 2006. High-resolution thermal inertia derived from the thermal emission imaging system (THEMIS): thermal model and applications: THEMIS THERMAL INERTIA. J. Geophys. Res. 111, n/a–n/a. https://doi.org/10.1029/2006JE002735.

Fischer, E., Martínez, G.M., Rennó, N.O., 2016. Formation and persistence of brine on Mars: experimental simulations throughout the diurnal cycle at the Phoenix landing site. Astrobiology 16, 937–948. https://doi.org/10.1089/ast.2016.1525.

Forget, F., Hourdin, F., Fournier, R., Hourdin, C., Talagrand, O., Collins, M., Lewis, S.R., Read, P.L., Huot, J.-P., 1999. Improved general circulation models of the Martian atmosphere from the surface to above 80 km. J. Geophys. Res. 104, 24155–24175. https://doi.org/10.1029/1999JE001025.

Gasda, P.J., Haldeman, E.B., Wiens, R.C., Rapin, W., Bristow, T.F., Bridges, J.C., Schwenzer, S.P., Clark, B., Herkenhoff, K., Frydenvang, J., Lanza, N.L., Maurice, S., Clegg, S., Delapp, D.M., Sanford, V.L., Bodine, M.R., McInroy, R., 2017. In situ detection of boron by ChemCam on Mars: first detection of boron on Mars. Geophys. Res. Lett. 44, 8739–8748. https://doi.org/10.1002/2017GL074480.

Gendrin, A., 2005. Sulfates in Martian layered terrains: the OMEGA/Mars express view. Science 307, 1587–1591. https://doi.org/10.1126/science.1109087.

Graf, J., Zurek, R., Jones, R., Eisen, H., Johnston, M.D., Jai, B., Mateer, B., 2002. An overview of the Mars reconnaissance orbiter mission. In: Proceedings, IEEE Aerospace Conference. Presented at the 2002 IEEE Aerospace Conference. IEEE, Big Sky, MT, USA, pp. 1–180. https://doi.org/10.1109/AERO.2002.1036837.

Grimm, R.E., Harrison, K.P., Stillman, D.E., 2014. Water budgets of martian recurring slope lineae. Icarus 233, 316–327. https://doi.org/10.1016/j.icarus.2013.11.013.

Grotzinger, J.P., Crisp, J., Vasavada, A.R., Anderson, R.C., Baker, C.J., Barry, R., Blake, D.F., Conrad, P., Edgett, K.S., Ferdowski, B., Gellert, R., Gilbert, J.B., Golombek, M., Gómez-Elvira, J., Hassler, D.M., Jandura, L., Litvak, M., Mahaffy, P., Maki, J., Meyer, M., Malin, M.C., Mitrofanov, I., Simmonds, J.J., Vaniman, D., Welch, R.V., Wiens, R.C., 2012. Mars science laboratory mission and science investigation. Space Sci. Rev. 170, 5–56. https://doi.org/10.1007/s11214-012-9892-2.

Haberle, R.M., McKay, C.P., Schaeffer, J., Cabrol, N.A., Grin, E.A., Zent, A.P., Quinn, R., 2001. On the possibility of liquid water on present-day Mars. J. Geophys. Res. 106, 23317–23326. https://doi.org/10.1029/2000JE001360.

Hecht, M.H., Kounaves, S.P., Quinn, R.C., West, S.J., Young, S.M.M., Ming, D.W., Catling, D.C., Clark, B.C., Boynton, W.V., Hoffman, J., DeFlores, L.P., Gospodinova, K., Kapit, J., Smith, P.H., 2009. Detection of perchlorate and the soluble chemistry of Martian soil at the Phoenix Lander site. Science 325, 64–67. https://doi.org/10.1126/science.1172466.

Heldmann, J.L., Mellon, M.T., 2004. Observations of martian gullies and constraints on potential formation mechanisms. Icarus 168, 285–304. https://doi.org/10.1016/j.icarus.2003.11.024.

Herny, C., Conway, S.J., Raack, J., Carpy, S., Colleu-Banse, T., Patel, M.R., 2019. Downslope sediment transport by boiling liquid water under Mars-like conditions: experiments and potential implications for Martian gullies. Geol. Soc. Lond., Spec. Publ. 467, 373–410. https://doi.org/10.1144/SP467.10.

Kreslavsky, M.A., Head, J.W., Marchant, D.R., 2008. Periods of active permafrost layer formation during the geological history of Mars: implications for circum-polar and mid-latitude surface processes. Planet. Space Sci. 56, 289–302. https://doi.org/10.1016/j.pss.2006.02.010.

Malin, M.C., Edgett, K.S., 2000. Evidence for recent groundwater seepage and surface runoff on Mars. Science 288, 2330–2335. https://doi.org/10.1126/science.288.5475.2330.

Massé, M., Conway, S.J., Gargani, J., Patel, M.R., Pasquon, K., McEwen, A., Carpy, S., Chevrier, V., Balme, M.R., Ojha, L., Vincendon, M., Poulet, F., Costard, F., Jouannic, G., 2016. Transport processes induced by metastable boiling water under Martian surface conditions. Nat. Geosci. 9, 425–428. https://doi.org/10.1038/ngeo2706.

McEwen, A.S., Ojha, L., Dundas, C.M., Mattson, S.S., Byrne, S., Wray, J.J., Cull, S.C., Murchie, S.L., Thomas, N., Gulick, V.C., 2011. Seasonal flows on warm Martian slopes. Science 333, 740–743. https://doi.org/10.1126/science.1204816.

McEwen, A.S., Dundas, C.M., Mattson, S.S., Toigo, A.D., Ojha, L., Wray, J.J., Chojnacki, M., Byrne, S., Murchie, S.L., Thomas, N., 2014. Recurring slope lineae in equatorial regions of Mars. Nat. Geosci. 7, 53–58. https://doi.org/10.1038/ngeo2014.

Morino, C., Conway, S.J., Balme, M.R., Hillier, J., Jordan, C., Saemundsson, Þ., Argles, T., 2019. Debris-flow release processes investigated through the analysis of multi-temporal LiDAR datasets in North-Western Iceland: debris-flow processes investigated by multi-temporal LiDAR datasets. Earth Surf. Process. Landf. 44, 144–159. https://doi.org/10.1002/esp.4488.

Morino, C., Conway, S.J., Balme, M.R., Helgason, J.K., Sæmundsson, Þ., Jordan, C., Hillier, J., Argles, T., 2021. The impact of ground-ice thaw on landslide geomorphology and dynamics: two case studies in northern Iceland. Landslides 18, 2785–2812. https://doi.org/10.1007/s10346-021-01661-1.

Ojha, L., McEwen, A., Dundas, C., Byrne, S., Mattson, S., Wray, J., Masse, M., Schaefer, E., 2014. HiRISE observations of recurring slope Lineae (RSL) during southern summer on Mars. Icarus 231, 365–376. https://doi.org/10.1016/j.icarus.2013.12.021.

Putzig, N.E., Mellon, M.T., Kretke, K.A., Arvidson, R.E., 2005. Global thermal inertia and surface properties of Mars from the MGS mapping mission. Icarus 173, 325–341. https://doi.org/10.1016/j.icarus.2004.08.017.

Raack, J., Conway, S.J., Herny, C., Balme, M.R., Carpy, S., Patel, M.R., 2017. Water induced sediment levitation enhances downslope transport on Mars. Nat. Commun. 8, 1151. https://doi.org/10.1038/s41467-017-01213-z.

Rivera-Hernández, F., Sumner, D.Y., Mangold, N., Stack, K.M., Forni, O., Newsom, H., Williams, A., Nachon, M., L'Haridon, J., Gasnault, O., Wiens, R., Maurice, S., 2019. Using ChemCam LIBS data to constrain grain size in rocks on Mars: proof of concept and application to rocks at Yellowknife Bay and Pahrump Hills, Gale crater. Icarus 321, 82–98. https://doi.org/10.1016/j.icarus.2018.10.023.

Rivera-Valentín, E.G., Chevrier, V.F., Soto, A., Martínez, G., 2020. Distribution and habitability of (meta)stable brines on present-day Mars. Nat. Astron. 4, 756–761. https://doi.org/10.1038/s41550-020-1080-9.

Schmidt, R., 2003. Mars express—ESA's first mission to planet Mars. Acta Astronaut. 52, 197–202. https://doi.org/10.1016/S0094-5765(02)00157-1.

Schorghofer, N., Aharonson, O., Khatiwala, S., 2002. Slope streaks on Mars: correlations with surface properties and the potential role of water: SLOPE STREAKS ON MARS. Geophys. Res. Lett. 29 https://doi.org/10.1029/2002GL015889, 41-1-41–4.

Spiga, A., Forget, F., 2008. Fast and accurate estimation of solar irradiance on Martian slopes. Geophys. Res. Lett. 35, L15201. https://doi.org/10.1029/2008GL034956.

Squyres, S.W., Grotzinger, J.P., Arvidson, R.E., Bell, J.F., Calvin, W., Christensen, P.R., Clark, B.C., Crisp, J.A., Farrand, W.H., Herkenhoff, K.E., Johnson, J.R., Klingelhöfer, G., Knoll, A.H., McLennan, S.M., McSween, H.Y., Morris, R.V., Rice, J. W., Rieder, R., Soderblom, L.A., 2004. In situ evidence for an ancient aqueous environment at Meridiani Planum, Mars. Science 306, 1709–1714. https://doi.org/10.1126/science.1104559.

Stillman, D.E., Michaels, T.I., Grimm, R.E., Harrison, K.P., 2014. New observations of martian southern mid-latitude recurring slope lineae (RSL) imply formation by freshwater subsurface flows. Icarus 233, 328–341. https://doi.org/10.1016/j.icarus.2014.01.017.

Stillman, D.E., Michaels, T.I., Grimm, R.E., Hanley, J., 2016. Observations and modeling of northern mid-latitude recurring slope lineae (RSL) suggest recharge by a present-day martian briny aquifer. Icarus 265, 125–138. https://doi.org/10.1016/j.icarus.2015.10.007.

Sylvest, M.E., Conway, S.J., Patel, M.R., Dixon, J.C., Barnes, A., 2016. Mass wasting triggered by seasonal CO2 sublimation under Martian atmospheric conditions: laboratory experiments. Geophys. Res. Lett. 43 https://doi.org/10.1002/2016GL071022.

Sylvest, M.E., Dixon, J.C., Conway, S.J., Patel, M.R., McElwaine, J.N., Hagermann, A., Barnes, A., 2019. CO2 sublimation in Martian gullies: laboratory experiments at varied slope angle and regolith grain sizes. Geol. Soc. Lond., Spec. Publ. 467, 343–371. https://doi.org/10.1144/SP467.11.

Thomas, N.H., Ehlmann, B.L., Meslin, P.-Y., Rapin, W., Anderson, D.E., Rivera-Hernández, F., Forni, O., Schröder, S., Cousin, A., Mangold, N., Gellert, R., Gasnault, O., Wiens, R.C., 2019. Mars science laboratory observations of chloride salts in Gale crater. Mars. Geophys. Res. Lett. 46, 10754–10763. https://doi.org/10.1029/2019GL082764.

Toner, J.D., Catling, D.C., Light, B., 2014. The formation of supercooled brines, viscous liquids, and low-temperature perchlorate glasses in aqueous solutions relevant to Mars. Icarus 233, 36–47. https://doi.org/10.1016/j.icarus.2014.01.018.

Weitz, C.M., Sullivan, R.J., Lapotre, M.G.A., Rowland, S.K., Grant, J.A., Baker, M., Yingst, R.A., 2018. Sand grain sizes and shapes in Eolian Bedforms at Gale crater. Mars. Geophys. Res. Lett. 45, 9471–9479. https://doi.org/10.1029/2018GL078972.

Westoby, M.J., Brasington, J., Glasser, N.F., Hambrey, M.J., Reynolds, J.M., 2012. 'Structure-from-motion' photogrammetry: a low-cost, effective tool for geoscience applications. Geomorphology 179, 300–314. https://doi.org/10.1016/j.geomorph.2012.08.021.

Williams, R.D., 2012. DEMs of Difference. Geomorphological Techniques.

Zelenyi, L.M., Korablev, O.I., Rodionov, D.S., Novikov, B.S., Marchenkov, K.I., Andreev, O.N., Larionov, E.V., 2015. Scientific objectives of the scientific equipment of the landing platform of the ExoMars-2018 mission. Sol. Syst. Res. 49, 509–517. https://doi.org/10.1134/S0038094615070229.

COLLEGE DOCTORAL PAYS DE LA LOIRE
ED MATIERE, MOLECULES MATERIAUX ET GEOSCIENCES

Nantes Université

Titre : Influence de la dégradation de la glace sur les paysages planétaires

Mots clés : permafrost, modélisation analogique, Mars, cartographie

Résumé : Cette thèse présente de nouvelles connaissances sur le lien entre glace du sol et géomorphologie, dans des contextes terrestres et martiens. J'étudie deux morphologies : les molards et les polygones de contraction thermique. Sur Terre, les molards sont des cônes de débris que l'on trouve dans les dépôts de glissements de terrain. Ils ont été récemment identifiés comme étant formés à partir de blocs de sédiments cimentés par la glace, transportés par un glissement de terrain, et s'étant dégradés dans ses dépôts. Ce sont potentiellement des marqueurs précis, à la fois temporels et spatiaux, de la dégradation du permafrost de montagne. Dans ma thèse, je propose donc d'étudier les molards de façon systématique grâce à une approche de modélisation analogique, dont les modèles sont reconstruits régulièrement grâce à un système de photogrammétrie automatisé que j'ai développé. Je présente également une étude qui suggère la présence de molards sur Mars dans les éjectas du cratère Hale, et qui les utilise pour obtenir des informations sur l'histoire géologique de ces éjectas. Dans cette thèse j'étudie également les polygones de contraction thermique, qui sont des réseaux de fractures résultant de la contraction thermique de la glace du sol. Sur Terre, la mise en place de glace d'eau ou de sédiments dans ces fractures peut former des polygones avec des morphologies différentes. Sur Mars, l'on observe des polygones ayant des dimensions et des morphologies similaires. Dans ma thèse, je présente donc une étude dans laquelle nous étudions les polygones de contraction thermique d'Utopia Planitia, et concluons à la présence d'eau liquide dans le proche passé de la planète. Je développe également une étude des polygones de contraction thermique en parallèle des unités géomorphologiques qui les portent, ce qui me permet d'obtenir des informations à la fois sur le timing de formation des polygones, et sur l'histoire géologique de ces unités.

Title : Influence of ice degradation on planetary landscapes

Keywords : permafrost, analogue modelling, Mars, mapping

Abstract : The present thesis aims at getting new understandings on how ground water ice and periglacial processes influence surface geomorphology on Earth and on Mars. I am hence investigating two periglacial landforms: molards and thermal-contraction polygons. On Earth, molards are cones of loose debris found in landslide deposits. It was recently attested that they are former ice-cemented blocks of sediment, that were transported by a landslide and progressively degraded within its deposits into conical shapes. They could represent accurate spatial and temporal markers of the degradation of mountain permafrost. Therefore, I provide here a systematic way to study molards, based on analogue modelling experiments monitored by an automated time-lapse photogrammetry system I developed. I also present a study on the firstly-identified potential martian molards, that provide insights into the geological setting of the ejecta from the Hale crater. Terrestrial thermal-contraction polygons are known to result from the thermal contraction of ground ice, which forms surficial networks of polygonal fractures. Water or lithic material can infill those fractures, and with repeated freeze-thaw cycles of water generate polygons with various morphologies. On Mars, polygons of similar dimensions and showing similar morphologies are observed. Therefore, I present here a study that investigates martian thermal-contraction polygons in Utopia Planitia, concluding on the geologically recent activity of liquid water in the area. I also present a study that investigates thermal-contraction polygons located on geomorphological units in Utopia Planitia, providing insights into both the timing of formation of thermal-contraction polygons and the geological history of the area.